DOT/FAA/AR-00/64

Turbine Rotor Material Design

Office of Aviation Research
Washington, D.C. 20591

December 2000

Final Report

DISTRIBUTION STATEMENT A
Approved for Public Release
Distribution Unlimited

This document is available to the U.S. public through the National Technical Information Service (NTIS), Springfield, Virginia 22161.



U.S. Department of Transportation
Federal Aviation Administration

20010403 086

NOTICE

This document is disseminated under the sponsorship of the U.S. Department of Transportation in the interest of information exchange. The United States Government assumes no liability for the contents or use thereof. The United States Government does not endorse products or manufacturers. Trade or manufacturer's names appear herein solely because they are considered essential to the objective of this report. This document does not constitute FAA certification policy. Consult your local FAA aircraft certification office as to its use.

This report is available at the Federal Aviation Administration William J. Hughes Technical Center's Full-Text Technical Reports page: actlibrary.tc.faa.gov in Adobe Acrobat portable document format (PDF).

Technical Report Documentation Page

1. Report No.	2. Government Accession No.	3. Recipient's Catalog No.
DOT/FAA/AR-00/64		

4. Title and Subtitle	5. Report Date
TURBINE ROTOR MATERIAL DESIGN	December 2000
	6. Performing Organization Code

7. Author(s)			8. Performing Organization Report No.
G. R. Leverant*	M. P. Enright*	C. Fischer†	18-7445
R. C. McClung*	G. G. Chell*	D. Lehmann††	
Y.-T. Wu*	K. S. Chan*	K. Green†††	
H. R. Millwater*	P. C. McKeighan*	J. Bartos***	
D. S. Riha*	M. Gorelik**	N. Howard***	
		S. Srivatsa***	

9. Performing Organization Name and Address		10. Work Unit No. (TRAIS)
*Southwest Research Institute 6220 Culebra Road 18/128 San Antonio, TX 78238	†Scientific Forming Technologies, Corp. 5038 Reed Road Suite 255 Columbus, OH 43220	
**AlliedSignal 111 South 34th St. P.O. Box 52181 Phoenix, AZ 85072-2181	††Pratt & Whitney 400 Main Street M/S 163-24 East Hartford, CT 06108	11. Contract or Grant No. 92-G-041
***General Electric 1 Neumann Way Cincinnati, OH 45212-6301	†††Rolls-Royce Allison 2001 South Tibbs Ave. S.C. W05 Indianapolis, IN 46241	

12. Sponsoring Agency Name and Address	13. Type of Report and Period Covered
U.S. Department of Transportation Federal Aviation Administration Office of Aviation Research Washington, DC 20591	Final Report
	14. Sponsoring Agency Code ANE-110

15. Supplementary Notes

The FAA William J. Hughes Technical Center Technical Monitor was Joseph Wilson.

16. Abstract

Premium grade titanium alloys are used for fan and compressor rotors and disks in aircraft turbine engines. Occasional upsets during processing can result in the formation of metallurgical anomalies referred to as hard alpha (HA). Although rare, low-cycle fatigue cracks initiated by HA have led to uncontained engine failures that resulted in fatal accidents such as the incident at Sioux City, Iowa, in 1989. In a report issued by the Federal Aviation Administration (FAA) after the accident at Sioux City, it was recommended that a damage tolerance approach be implemented to explicitly address HA anomalies, with the objective of enhancing conventional rotor life management methodology. The probabilistic, damage tolerance code developed in this program for low-cycle fatigue of titanium rotors/disks is intended to supplement, not replace, the current safe-life design. The code is called Design Assessment of Reliability With INspection (DARWIN) and was developed in collaboration with AlliedSignal Engines, General Electric Aircraft Engines, Pratt & Whitney, and Rolls-Royce Allison. DARWIN integrates finite element stress analysis, fracture mechanics analysis, nondestructive inspection simulation, and probabilistic analysis to assess the risk of rotor fracture. Supplementary tasks performed in this program in support of code implementation included the generation of fatigue crack growth data for Ti-64, Ti-6242, and Ti-17β in high vacuum; determination of the crack initiation behavior of artificial and natural HA defects embedded in plates of Ti-64; and development of a forging microcode to predict the movement, shape and orientation of HA anomalies during processing from ingot to billet, and from billet to a disk forging.

17. Key Words	18. Distribution Statement
Turbine engines, Disks, Rotors, Titanium, Hard alpha, Low-cycle fatigue, Probabilistic, Damage tolerance code, Crack initiation and growth, Forging code	This document is available to the public through the National Technical Information Service (NTIS) Springfield, Virginia 22161.

19. Security Classif. (of this report)	20. Security Classif. (of this page)	21. No. of Pages	22. Price
Unclassified	Unclassified	356	

ACKNOWLEDGEMENTS

The success of this large and complex program would not have been possible without the substantial contributions of many different people working for many different organizations. The list of specific names cited in these acknowledgments is inevitably incomplete, and the authors apologize for any inadvertent omissions.

The support of the Federal Aviation Administration is deeply appreciated. In particular, Tim Mouzakis of the New England Regional Center, and Bruce Fenton and Joe Wilson of the William J. Hughes Technical Center, are thanked for their consistent encouragement and guidance.

The cooperation and direction provided by the four partner engine companies was essential and invaluable. Lead staff from these companies played a crucial role on the program Steering Committee and/or on many individual technical tasks. Some of these lead staff contributed to this report as authors while others worked behind the scenes to ensure that tasks were successfully planned and completed. Specific faces changed from year to year as organizations changed. The substantial contributions of Jon Tschopp and Nikki Howard (General Electric); Gary Peters and Darryl Lehmann (Pratt & Whitney); Joe Adams, Chet Date, and Michael Gorelik (AlliedSignal); and Nick Provenzano, Chuck Teague, Doug Herrmann, and Ken Green (Rolls-Royce Allison) are all gratefully acknowledged.

The Rotor Integrity Subcommittee (RISC) of the Aerospace Industries Association (AIA) was largely responsible for the initial formulation of the program, and they continued to provide essential guidance and oversight throughout the program.

The Engine Titanium Consortium (ETC) maintained close contact with the Turbine Rotor Material Design (TRMD) program and provided a variety of support to specific activities. Lisa Brasche (Iowa State), Kevin Smith (P&W), and Jon Bartos, General Electric Aircraft Engines (GEAE) are thanked for their cooperation and assistance.

Many other technical staff made important contributions to specific technical tasks on the program. Again, this list is invariably incomplete, but represents the desire of the authors to acknowledge and thank all those who generated data, performed analysis, developed software, and otherwise supported the program.

Effect of Forging on Defect Morphology. Wei-Tsu Wu (Scientific Forming) played a key role in development of the forging analysis microcode. Lee Perocchi, General Electric Corporate Research and Development (GE CRD), was responsible for manufacturing the hard alpha specimens for the constitutive property testing. Andy Nagy, Southwest Research Institute (SwRI), designed the specialized test fixtures for the constitutive property testing, and Forrest Campbell (SwRI) performed these complex experiments. Mike Keller (GEAE) assisted with the nondestructive evaluation (NDE) inspection of the forgings.

Crack Nucleation and Growth Data and Modeling. Barney Lawless (GEAE) and Yancey Gill (AlliedSignal) were lead test engineers for the generation of vacuum fatigue crack growth data. Bob Piascik (NASA-Langley) provided experimental data on vacuum level effects.

Lee Perocchi (GE CRD) was responsible for manufacturing the artificially seeded hard alpha nucleation specimens. Art Nicholls (SwRI) conducted the hard alpha nucleation tests and analyzed test data, and Ali Minachi (SwRI) provided NDE support to locate defects in the RMI Titanium Co. contaminated billet study (CBS) specimens. Tom Mills (Air Force Research and Development Laboratory, Wright-Patterson Air Force Base) provided electronic files of appropriate data from the Damage Tolerant Design Handbook. Don Raizenne (National Research Council of Canada) provided the fatigue crack growth (FCG) data from the Advisory Group for Aerospace Research and Development (AGARD) round robin program.

Probabilistic Integration Design Code Development and Sensitivity Studies. In addition to the primary developers of Design Assessment of Reliability With INspection (DARWIN) who appear among the authors of this report, Steven Johns, Simeon Fitch, and Justin Meyer (SwRI) were responsible for development of the DARWIN graphical user interface (GUI). Kirsten Koble (SwRI) provided GUI testing support and also supported the development of the user's manual chapter on the GUI. Software developers of the Flight_Life module were Chris Kuhlman, Yi-Der Lee, and Matthew Ferrell (SwRI).

Ruth Pollard, Lori Salas, Patty Soriano, and Loretta Mesa (SwRI) are thanked for their skilled clerical assistance in preparing this large and complex final report. Roxanne Kerr (SwRI) provided important administrative assistance in support of the DARWIN user's manual and workshop.

TABLE OF CONTENTS

		Page
EXECUTIVE SUMMARY		xv
1.	INTRODUCTION	1-1
1.1	Objective	1-1
1.2	Background	1-1
1.3	Scope of Report	1-2
2.	APPROACH, RESULTS, AND DISCUSSION	2-1
2.1	Distribution of Hard Alpha Anomalies in Titanium	2-1
2.2	Effect of Forging on Hard Alpha Anomaly Morphology	2-1
2.2.1	Constitutive Properties for Titanium Disk Alloys	2-1
2.2.2	Constitutive Properties for Hard Alpha Anomalies	2-1
2.2.3	Development of Constitutive Relationships for Hard Alpha	2-9
2.2.4	Forging Microcode Development	2-12
2.2.5	Forging Experiments to Validate Microcode	2-42
2.2.6	Parametric Benchmarking of Forging Microcode on Actual Disk Geometries	2-55
2.3	Crack Nucleation Behavior of Hard Alpha Anomalies	2-65
2.3.1	Specimens and Test Procedures	2-65
2.3.2	Results	2-67
2.3.3	Relevance to Industry Field Experience	2-73
2.4	Fatigue Crack Growth Behavior of Titanium Alloys	2-74
2.4.1	Fatigue Crack Growth Data in Vacuum	2-74
2.4.2	Life Scatter in Fatigue Crack Growth Data for Ti-6Al-4V in Air	2-85
2.5	Development of Probabilistic Design Code	2-96
2.5.1	Stress Processing	2-97
2.5.2	Flight_Life Fracture Mechanics Module	2-104
2.5.3	Probabilistic Driver	2-108
2.5.4	Graphical User Interface	2-111

2.5.5 Verification and Sensitivity Studies 2-118
2.5.6 Code Quality Assurance 2-124

2.6 Technology Transfer Workshops 2-126

3. CONCLUDING REMARKS 3-1

4. REFERENCES 4-1

APPENDICES

A—The Development of Anomaly Distributions for Aircraft Engine Titanium Disk Alloys

B—Experimental Characterization of the Constitutive Properties of Hard Alpha

C—Development of Constitutive Equations for Hard Alpha

D—Microlevel Simulations of Hard Alpha During Forging

E—Forging Procedures and Simulations

F—Compilation of General Electric Results for Conventional and Multizone Inspections of Seeded and RMI Billets/Forgings

G—Nondestructive Evaluation (NDE) and Metallography of Pancake Forging Containing RMI CBS Defect B1BW3-A

H—Static and Fatigue Testing of Synthetic and Naturally Occurring Hard Alpha Defects to Characterize Cracking Behavior

I—Fatigue Crack Growth Rate Testing of Three Titanium Rotor Alloys in Vacuum

J—DARWIN Analysis of Advisory Circular (AC) Test Case

LIST OF FIGURES

Figure		Page
2-1	Compressive Stress-Strain Curves of Hard Alpha Ti for Five Different Nitrogen Contents in Weight Percent	2-2
2-2	Compressive Stress-Strain Curves of Hard Alpha Ti With 12 wt.% N for Three Different Test Temperatures	2-3
2-3	Load Displacement Curves of Indirect Tension Tests of Hard Alpha Ti With Four Different Nitrogen Contents	2-4
2-4	Comparison of Fracture Strength of Hard Alpha Ti Tested in Compression and Indirect Tension	2-4
2-5	Experimental Results of Average Stress Versus Average Strain for Indentation Tests of Hard Alpha Ti With Various Nitrogen Contents	2-5
2-6	Comparison of Engineering Stress-Strain Curves of Hard Alpha Ti With Various Nitrogen Contents Tested in Plane Strain Compression at a Strain Rate of 0.01 s^{-1}	2-6
2-7	The Flow Stress (Y) and Fracture Stress (Y_i) of Hard Alpha as a Function of Pressure, P	2-6
2-8	Flow and Fracture Stresses of Hard Alpha Increase With Increasing Nitrogen Content at Different Slopes	2-7
2-9	Flow Stress of Hard Alpha With Nitrogen Content ≤ 4 wt.% as a Function of Strain Rate	2-8
2-10	Fracture Strengths of Hard Alpha Ti as a Function of Strain Rate	2-8
2-11	Semilog Plot of Flow or Fracture Stress, Y_i, as a Function of Pressure, $P = 1/3 \sum_{k=1}^{3} \sigma_{kk}$	2-10
2-12	Experimental Correlation and Least-Square Fit of the Flow or Fracture Stress, Y_n, of Hard Alpha as a Function of Nitrogen Content	2-11
2-13	Comparison of the Calculated Fracture Stress of the Intact Materials and the Flow Stress of the Failed Material	2-11

2-14	Comparison of Calculated and Measured True Stress-Strain Curves of Hard Alpha Ti with 2 wt.% N for Two Strain Rates	2-13
2-15	Measured True Stress-Strain Curves Compared to Model Calculations for Two Strain Rates	2-13
2-16	Comparison of Calculated and Measured Flow and Fracture Stresses of Hard Alpha Ti	2-14
2-17	Flow Chart Illustrating Basic Sequence of Operations for Preparing and Running a Microlevel Simulation	2-15
2-18	Geometry Definition Window from GUI Showing Multiple Boundary Capability	2-16
2-19	User Interface for Defining Microvolume Geometry and Location in Macrolevel Simulation	2-18
2-20	User Interface for Defining Object Geometry, Mesh, and Properties in Microvolume	2-18
2-21	Microvolume Boundary Shape as Defined by Point Tracking Boundary Nodes	2-19
2-22	Simulation Controls Window From Microlevel Simulation Template	2-19
2-23	Comparison of Experimental and Simulated Engineering Stress-Strain Data for 2% Nitrogen Hard Alpha at Strain Rates of 0.01 and 1.0 per Second at 1750°F	2-21
2-24	Comparison of Experimental and Simulation Results for the Fracture Behavior of 4% and 6% Nitrogen Hard Alpha at 1750°F at a Strain Rate of 1.0 per Second	2-22
2-25	Meshing Based on Boundary Nodes	2-23
2-26	Mesh of an Object With Two Internal Holes	2-23
2-27	Seed 29 Microlevel Simulation: Initial Mesh	2-25
2-28	Seed 29 Microlevel Simulation: Initial Damage Distribution	2-26
2-29	Seed 29 Microlevel Simulation: Damage Distribution at Step 100	2-27
2-30	Seed 29 Microlevel Simulation: Damage Distribution at Step 200	2-28
2-31	Seed 29 Microlevel Simulation: Damage Distribution at Step 400	2-29

2-32	Seed 29 Microlevel Simulation: Damage Distribution at Step 600	2-30
2-33	Seed 29 Microlevel Simulation: Effective Stress Distribution at Step 800	2-31
2-34	Seed 29 Microlevel Simulation: Effective Stress Distribution at Step 900	2-32
2-35	Seed 29 Microlevel Simulation: Effective Stress Distribution at Step 950, After Backflow Forging	2-33
2-36	Seed 29 Microlevel Simulation: Final Geometry of Diffusion Zone and Microvolume	2-34
2-37	Inclusion Strain as a Function of Forging Macrostrain	2-37
2-38	Inclusion Strain Dependence on Inclusion Nitrogen Contents of 4% and 8%	2-37
2-39	Inclusion Strain Dependence on Diffusion Zone Nitrogen Contents of 1% and 3%	2-38
2-40	Inclusion Strain Dependence on Diffusion Zone to Inclusion Size Ratios of 2 and 4	2-38
2-41	Inclusion Strain Dependence on Inclusion Aspect Ratios of 1 and 3	2-39
2-42	Inclusion Strain Dependence on Strain Rates of 0.1 and 1.0 per Second	2-39
2-43	Inclusion Strain Dependence on Temperatures of 1550° and 1750°F	2-40
2-44	Inclusion Strain Dependence on Pressures of 10 and 100 ksi	2-40
2-45	Jet Engine Titanium Quality Committee Data for Defect Elongation vs Billet Elongation as Analyzed by RISC	2-42
2-46	Outline of Dogbone Forging With Phantom Lines Showing Machined Part	2-43
2-47	Outline of Backflow Forging With Phantom Lines Showing Machined Part	2-43
2-48	Machine Drawing of Dogbone Forging	2-44
2-49	Machine Drawing of Backflow Forging	2-44
2-50	Sonic Shape of Disk Forgings	2-45
2-51	DEFORM™ Point Tracking of Hard Alpha Seeds in Dogbone Forging at Start, 50% Deformation and 100% Deformation	2-47

2-52	DEFORM™ Point Tracking of Hard Alpha Seeds (a) Prior to Dogbone Formation, (b) After Dogbone Formation, (c) at 50% Deformation During Backflow Forging, and (d) at 100% Deformation at Completion of Backflow Forging	2-48
2-53	Effective Strain Contours in Dogbone (Left) and Backflow (Right) Forgings	2-49
2-54	RMI CBS Indications for Processing to Pancake Shape	2-50
2-55	B3W2-G Pancake Defect Location Prediction (Based on Billet Inspection) Compared to Location From Pancake Inspections	2-52
2-56	B3W2-E Pancake Defect Location Prediction (Based on Billet Inspection) Compared to Location From Pancake Inspections	2-53
2-57	B3W2-E Disk Defect Location Prediction (Based on Billet Inspection) Compared to Location From Pancake/Disk Inspections	2-53
2-58	B1BW3-B Pancake Defect Location Prediction (Based on Billet Inspection) Compared to Location From Pancake Inspections	2-54
2-59	B1BW3-B Disk Defect Location Prediction (Based on Billet Inspection) Compared to Location From Pancake/Disk Inspections	2-54
2-60	Fan Disk Forging	2-56
2-61	Compressor Disk Forging	2-56
2-62	DEFORM™ Point Tracking of Simulated Hard Alpha Defects in Fan Disk Forging at Start and 100% Deformation	2-57
2-63	DEFORM™ Point Tracking of Simulated Hard Alpha Defects in Compressor Disk Forging at Start and 100% Deformation	2-57
2-64	Effective Strain Contours for Fan Disk Forging (Top) and Compressor Disk Forging (Bottom)	2-58
2-65	Effective Strain Contours at Different Stages of the Forging Process: P/N 68014, Inclusion 1	2-59
2-66	Final Deformation of the Four Inclusions in P/N 68014	2-61
2-67	Final Deformation of the Four Inclusions in P/N 68696	2-63
2-68	Photograph of a Typical Synthetic Hard Alpha Defect Specimen	2-66

2-69	Cracking in the HA Core and Through the Diffusion Zone in a High-Nitrogen, Large-Defect Specimen	2-68
2-70	Crack Length Measurements and Ultrasonic, Acoustic Emission, and Potential Drop Output for a Large, High-Nitrogen Surface Defect Subjected to Static Loading	2-68
2-71	Metallographic Sections After Testing of Interior Defect Specimen SHI-1 (Small, High Nitrogen) in (a) the Central Region of the Defect and (b) in a Diffusion Zone Endcap	2-70
2-72	Summary Metallographic Sections Made From HA-IS-D1 After Static and Fatigue Testing	2-71
2-73	Fracture Surfaces for Two Large, Interior Defect Specimens Subjected to Fatigue Loading	2-72
2-74	Fracture Surfaces for Two Naturally Occurring Defect (Surface and Interior) Specimens Subjected to Fatigue Loading Conditions	2-73
2-75	Microstructures of (a) Ti-6Al-4V, (b)Ti-6Al-2Sn-4Zr-2Mo+Si, and (c) Ti-17	2-75
2-76	Fatigue Crack Growth Data for Ti-6Al-4V at Constant ΔK and Different Vacuum Levels	2-77
2-77	Vacuum FCG Data for Ti-6Al-4V at 75°F (24°C)	2-79
2-78	Vacuum FCG Data for Ti-6Al-4V at 400°F (204°C)	2-79
2-79	Vacuum FCG Data for Ti-6Al-2Sn-4Zr-2Mo+Si at 75°F (24°C)	2-80
2-80	Vacuum FCG Data for Ti-6Al-2Sn-4Zr-2Mo+Si at 600°F (316°C)	2-80
2-81	Vacuum FCG Data for Ti-6Al-2Sn-4Zr-2Mo+Si at 1000°F (538°C)	2-81
2-82	Vacuum FCG Data for Ti-17 at 75°F (24°C)	2-81
2-83	Vacuum FCG Data for Ti-17 at 750°F (399°C)	2-82
2-84	Comparison of Vacuum Data With Air Data From DTDH for Ti-6Al-4V at 75°F (24°C) and $R = 0$	2-82
2-85	Comparison of Vacuum Data With Air Data From DTDH for Ti-6Al-4V at 75°F (24°C) and $R = 0.75$	2-83

2-86	Comparison of Vacuum Data With Air Data From DTDH for Ti-6Al-4V at 300°-600°F (149°-316°C) and $R = 0$	2-83
2-87	Comparison of Vacuum Data With Air Data From DTDH for Ti-6Al-2Sn-4Zr-2Mo+Si at 75°F (24°C) and $R = 0$	2-84
2-88	Comparison of Vacuum Data With Air Data From DTDH for Ti-6Al-2Sn-4Zr-2Mo+Si at 75°F (24°C) and $R = 0.5$	2-84
2-89	Bilinear Regression to Sample AGARD Data Set	2-88
2-90	Summary of Actual/Predicted Life Ratios for AGARD Regressions	2-89
2-91	Summary of FCG Regression Constants for AGARD CT Specimens	2-90
2-92	Summary of FCG Regression Constants for AGARD CC Specimens	2-91
2-93	Crack Length Histories for Simulated AGARD FCG Tests (Upper Line Only)	2-93
2-94	Crack Length Histories for Simulated AGARD FCG Tests (Bilinear Only)	2-94
2-95	Coefficient of Variation of Fatigue Life as a Function of Crack Size for AGARD Simulations	2-95
2-96	Coefficient of Variation of Fatigue Life as a Function of ΔK for AGARD and Industry Simulations	2-96
2-97	DARWIN Code Capability	2-97
2-98	DARWIN Code Framework	2-98
2-99	Schematic of the Crack Models CC01 (Corner Crack), EC02 (Embedded Crack), and SC02 (Surface Crack) Contained in Flight_Life	2-100
2-100	Mapping of Crack Models CC01, EC02, and SC02 to the Global Geometry Coordinate System Containing the Finite Element Model of the Structure	2-100
2-101	A Simple Example of the Rainflow Counting Procedures Employed in DARWIN	2-101
2-102	The Stress Gradient Along a Path that Goes Through the Center of the Crack is Needed by Flight_Life	2-102
2-103	Example of How the Crack Path Defined in the Fracture Mechanics Crack Model is Mapped Into the Global System Used in the Finite Element Model in Order to Determine the Stresses Along the Path	2-102

2-104	The Residual Stress Resulting From Shakedown is Performed Using the Load Step That Produces the Maximum Stress at the Center of the Initial Crack	2-104
2-105	Example of the Results of a Shakedown Analysis Showing the Elastically Determined Stress Distribution Normal to the Crack Plane $(\sigma_Z)_{elastic}$, the Calculated Plastically Relaxed Stress $(\sigma_Z)_{relax}$, and the Resulting Residual Stress $(\sigma_Z)_{residual}$	2-104
2-106	Crack Geometries Available in Flight_Life	2-105
2-107	Fatigue Crack Growth Data Representation Options Available in Flight_Life	2-107
2-108	Illustration of Fast Sampling Method	2-111
2-109	Pre- and Postprocessing Approach	2-112
2-110	Example of Zone Definition	2-113
2-111	Disk Assessment	2-114
2-112	Disk Assessment Per Cycle	2-115
2-113	Zone Assessment Example	2-115
2-114	Risk Contribution Factors	2-116
2-115	Max Stress Intensity Factors vs Cycles	2-117
2-116	Max-Min Stress Pair Along Plate	2-117
2-117	Influence of Stress Factor COV on Probability of Fracture at 20,000 Cycles	2-119
2-118	Influence of Stress Factor Median on Probability of Fracture at 20,000 Cycles	2-120
2-119	Influence of Life Scatter COV on Probability of Fracture at 20,000 Cycles	2-120
2-120	Optimum Mean Inspection Time for Minimum Probability of Fracture at 20,000 Cycles	2-121
2-121	Influence of Inspection Time COV on Optimum Mean Inspection Time for Minimum Probability of Fracture at 20,000 Cycles	2-122
2-122	Influence of Inspection Time COV on Probability of Fracture at 20,000 Cycles	2-122
2-123	Comparison of the Influences of Stress, Life Scatter, and Inspection Time COVs on Probability of Fracture at 20,000 Cycles	2-123

2-124 Influence of Maximum Defect Area on Exceedance Curve on Probability of Fracture at 20,000 Cycles 2-124

2-125 Summary Flowchart of Darwin Process Control 2-125

2-126 Web-Based System for Tracking DARWIN Bugs and Code Enhancements 2-126

LIST OF TABLES

Table Page

2-1 Design of Experiment Variables 2-36

2-2 Input for Regression Analysis 2-41

2-3 Description of Forgings Used in the Validation Study 2-45

2-4 Description of Artificial Seeds and Associated Validation Cases Evaluated in Seeded Forgings 2-46

2-5 Seed Locations in Mults Used to Produce Seeded Forgings 2-49

2-6 Defect Locations from Billet, Pancake, and Disk Inspections 2-51

2-7 Room Temperature Tensile Properties of Titanium Rotor Alloys Tested 2-75

2-8 Summary of Vacuum FCG Test Conditions 2-75

EXECUTIVE SUMMARY

Premium grade titanium alloys, formerly processed by double vacuum arc remelting (VAR) and now processed by triple VAR, or hearth melt (HM) plus VAR, are used for fan and compressor rotors and disks in aircraft turbine engines. Occasional upsets during processing can result in the formation of metallurgical anomalies referred to as hard alpha (HA). These anomalies are nitrogen-rich alpha titanium that are brittle and often have microcracks and microvoids associated with them. Although rare, these anomalies have led to uncontained engine failures that resulted in fatal accidents such as the incident at Sioux City, Iowa, in 1989. In a report issued by the Federal Aviation Administration (FAA) after the accident at Sioux City, it was recommended that a damage tolerance approach be implemented to explicitly address HA anomalies, with the objective of enhancing conventional rotor life management methodology. The approach adopted and summarized in this report is based on probabilistic fracture mechanics. This enhancement is intended to supplement, not replace, the current safe-life design methodology.

The probabilistic, damage tolerance code developed in this program for low-cycle fatigue of titanium rotors/disks containing HA anomalies is called Design Assessment of Reliability With INspection (DARWIN). It was developed in collaboration with AlliedSignal Engines, General Electric Aircraft Engines, Pratt & Whitney, and Rolls-Royce Allison. DARWIN is a computer program that integrates finite element stress analysis, fracture mechanics analysis, nondestructive inspection simulation, and probabilistic analysis to assess the risk of rotor fracture. It computes the probability of fracture as a function of flight cycles, considering random defect occurrence and location, random inspection schedules, and several other random variables. Both Monte Carlo and advanced, fast integration methods are integral to the probabilistic driver. A fracture mechanics module, called Flight_Life, is also incorporated in the code. In addition, a user-friendly graphical user interface (GUI) is available to handle the otherwise difficult task of setting up the problem for analysis and viewing the results.

A workshop was held at Southwest Research Institute™ (SwRI™) in San Antonio, TX, on May 18-20, 1999, to transfer the DARWIN technology developed in this program to the engine industry and government. An overview of all program tasks, as well as a demonstration of the GUI for DARWIN, was provided on the first day. Hands-on training on the use of the GUI and probabilistic driver was provided on the second and third days with instruction provided by SwRI staff and members of the industry steering committee. Representatives of nine engine manufacturers from the United States, Germany, England, France, and Canada were among the 41 attendees. Other attendees included representatives of the FAA, Transport Canada, NASA, and the U.S. Air Force.

Among the supplementary tasks performed in this program in support of code implementation was the generation of crack growth data for Ti-64, Ti-6242, and Ti-17β in high vacuum. This data is important because most incidents invoking cracking from HA have originated at subsurface locations. In fact, the crack growth data at low ranges of stress intensity factor was found to be considerably slower in vacuum than in air for all three alloys at ambient temperature as well as elevated temperature and at various R ratios. This data will be used, along with other

new data, to update the HA anomaly distribution in a follow-on FAA program. The current anomaly distribution was calibrated to field experience using crack growth data generated in air.

A second supplementary task was conducted to determine the crack initiation behavior of artificial and natural HA defects embedded in plates of Ti-6Al-4V. Nitrogen content of the HA varied from 1.6 to 6 weight percent. It was found that crack initiation for surface-connected HA and its associated diffusion zone occurred at very low stresses while, based on acoustic emission monitoring, higher stresses, comparable to those experienced at stress concentrations in disks, appeared to be needed to initiate cracks in subsurface HA. Based on the limited testing conducted to date for both seeded and natural defects, an incubation period occurred in all cases prior to the onset of established crack growth in the titanium matrix. However, until additional testing and analysis can be done, it is appropriate to apply the current conservative industry assumption that, should HA be present in a high stress location, the presence of a sharp crack in the matrix should be assumed upon initial loading for computing the low-cycle fatigue life of a component.

Another task involved the development of a forging microcode to predict the movement, shape, and orientation of HA anomalies during processing from ingot to billet and from billet to a disk forging. This microcode was integrated with a commercially available forging code called DEFORM^{TM}. Mechanical properties, both flow and fracture of HA were obtained on synthetically produced material of various nitrogen contents. Constitutive relationships for flow and fracture of HA under multiaxial stresses were developed on the basis of the experimental results and are embedded in the microcode. Prediction of the behavior of HA using this microcode will be used to check the assumptions made in the original development of the HA defect distribution by the Rotor Integrity Subcommittee (RISC) of the Aerospace Industries Association. The microcode will also be utilized to update the defect distribution and to provide information to nondestructive evaluation (NDE) experts on how the HA presents itself (orientation and shape) to the ultrasonic beam during ultrasonic inspection of various disk locations. An industry workshop on the use of the code was held on June 15-16, 1999, at Scientific Forming Technologies Corporation in Columbus, OH.

1. INTRODUCTION.

1.1 OBJECTIVE.

The objective of this program was to develop a probabilistically based, damage tolerance design code to augment the current safe-life approach for life management of commercial aircraft gas turbine rotors/disks. The design code is not intended to replace existing design methods but to provide an additional tool that the engine manufacturers can use for reliability assessment. Initial application of the code focused on melt-related anomalies (hard alpha (HA)) in titanium. Supplemental tests were also performed to determine the mechanical properties of hard alpha and titanium disk alloys, and a forging code was developed to predict the shape and orientation of hard alpha anomalies during processing.

1.2 BACKGROUND.

Aircraft turbine engine industry experience has shown that the occurrence of material and manufacturing anomalies can potentially degrade the structural integrity of high-energy rotors. Conventional rotor life management methodology does not explicitly address the occurrence of these types of anomalies. The conventional methodology is founded on the assumption of nominal material and manufacturing conditions. Under nominal conditions, the methodology provides a structured process for the design and life management of high-energy rotors. This process provides assurance of structural integrity throughout the service life of the rotor (safe-life). Undetectable material and manufacturing anomalies represent a departure from the assumed nominal conditions. To quantify the extent of such anomalies, the Federal Aviation Administration (FAA) requested reconstitution of the Society of Automotive Engineers (SAE) committee on uncontained turbine engine rotor events [1]. While no adverse trends were identified by the committee, concern has been expressed that the projected increase in airline passenger traffic at a rate of some 3.5 percent per annum will lead to a noticeable increase in the number of accidents per year due to uncontained engine failures. Engine uncontained rotor events continue to cause catastrophic commercial aircraft accidents at very low but at a constant rate.

As a result of the Sioux City accident in 1989, the FAA in 1991 requested that industry, through the Aerospace Industries Association (AIA), review available techniques to see whether a damage tolerance approach could be introduced to reduce the rate of uncontained rotor events. The industry working group, Rotor Integrity Subcommittee (RISC) of the Aerospace Industries Association, concluded that the conventional rotor life management methodology could be enhanced to address anomalous conditions. This program was initiated in 1995 in response to the AIA recommendations, the FAA "Titanium Rotating Component Review Team Report" [2], Advisory Group for Aerospace Research and Development (AGARD) [3], National Aeronautics and Space Administration (NASA) [4], and Air Force [5, 6] experience and recommendations on damage tolerance concepts and operational experience for gas turbine disk alloys.

The program team was established through an FAA grant awarded to Southwest Research Institute, with partners AlliedSignal, Rolls-Royce Allison, General Electric, and Pratt &

Whitney. A steering committee was formed with representatives from each organization to provide guidance on program priorities and direction to the FAA.

1.3 SCOPE OF REPORT.

This report summarizes the results of Phase I of this grant dealing with development of the hard alpha defect distribution (section 2.1); the influence of forging on the shape and orientation of hard alpha anomalies (section 2.2); the mechanical properties of hard alpha embedded in a titanium matrix (section 2.3); the vacuum fatigue crack growth properties of three titanium disk alloys and life scatter in fatigue crack growth data (section 2.4); the development of a probabilistic code and associated graphical user interface (section 2.5); and the transfer of the technology to industry and government (section 2.6).

2. APPROACH, RESULTS, AND DISCUSSION.

2.1 DISTRIBUTION OF HARD ALPHA ANOMALIES IN TITANIUM.

Development of anomaly distributions for HA in titanium disk alloys was initiated by the RISC of the AIA in 1991. The RISC analyzed data was gathered by the Jet Engine Titanium Quality Committee (JETQC) between 1990 and 1993. The data represented hard alpha finds in billet and bar that had been ultrasonically inspected.

While the available data were limited, it served as the basis for an extensive analysis performed by RISC to develop HA anomaly distributions that are applicable to Ti-64, Ti-6242, and Ti-17β. The final distributions were set based upon calibration to actual field experience of the commercial airliner fleet. The background information, analytical procedures and associated assumptions, and the actual distributions are summarized in appendix A. This appendix is a paper prepared by a subteam of the RISC.

2.2 EFFECT OF FORGING ON HARD ALPHA ANOMALY MORPHOLOGY.

As discussed in appendix A, the HA defect distribution developed by the AIA Rotor Integrity Subcommittee was based on several assumptions regarding the geometrical changes experienced by a HA anomaly when an ingot is converted to a billet and eventually a disk forging. To test the validity of these assumptions, a deformation microcode was developed to predict the change in shape and orientation of HA anomalies during the conversion process. The information could be used to establish the nature of the anomalies that would be interrogated by ultrasonic nondestructive evaluation (NDE) methods during the billet and disk forging inspections and to assess the assumption made with respect to the flaw size used in fracture mechanics analyses. To develop the deformation microcode, the deformation and fracture constitutive properties of HA with various nitrogen contents were required. This section summarizes (1) the testing results and constitutive model development for HA, (2) the development of the deformation microcode, (3) forging experiments that were conducted on seeded and natural HA embedded in titanium to validate the microcode, and (4) analyses of representative disk geometries used to test the capabilities of the microcode.

2.2.1 Constitutive Properties for Titanium Disk Alloys.

Early in the program, constitutive properties for representative titanium disk alloys such as Ti-64, Ti-6242, and Ti-17 were made available to the program team by General Electric (GE) under a nondisclosure agreement. The contribution of this data allowed available resources to be directed at establishing the constitutive properties of HA of various nitrogen contents. These results are reported in sections 2.2.2, and 2.2.3, and appendices B and C.

2.2.2 Constitutive Properties for Hard Alpha Anomalies.

The constitutive behavior of hard alpha was characterized as a function of stress state, nitrogen content, temperature, and strain rate. The stress state was varied by employing different testing techniques and specimen geometries including (1) uniaxial compression, (2) indirect tension (Brazilian), (3) indentation, and (4) plane strain compression tests. Synthetic hard alpha test

specimens were fabricated by melting titanium metal sponge and titanium nitride (TiN) in a nonconsumable arc-melter. The nominal nitrogen contents of the test specimens were 2%, 4%, 6%, 9%, and 12%. Details of the fabrication process, specimen geometry, and test procedures of the constitutive tests are presented in appendix B. Results of the constitutive properties of HA are summarized below.

2.2.2.1 Compression Test Results.

In uniaxial compression, hard alpha Ti was ductile at 2 wt. % N, but fractured during plastic deformation at 4 wt.% N. The measured flow stress and ultimate fracture strength were consistent with GE data for 3.4 wt.% N [7]. Hard alpha Ti failed by fracture without appreciable plastic deformation for nitrogen contents at or greater than 6 wt.%. The stress-strain curves of hard alpha Ti for compression at 1750°F at a strain rate of 1 s^{-1} are presented in figure 2-1. Hard alpha Ti with 12 wt.% N failed by fracture under compression at 1700°, 1750°, and 1800°F at a strain rate of 1 s^{-1}. These results are presented in figure 2-2, which shows the fracture stress is relatively insensitive to the test temperature. The results of the compression tests are summarized in table B-2 of appendix B, which presents the test temperature, strain rate, the yield stress, fracture stress, and the mode of failure. The initial slope of the stress-strain curves for compression tests was used to determine the Young's modulus of hard alpha. These results are summarized in table B-3 in appendix B.

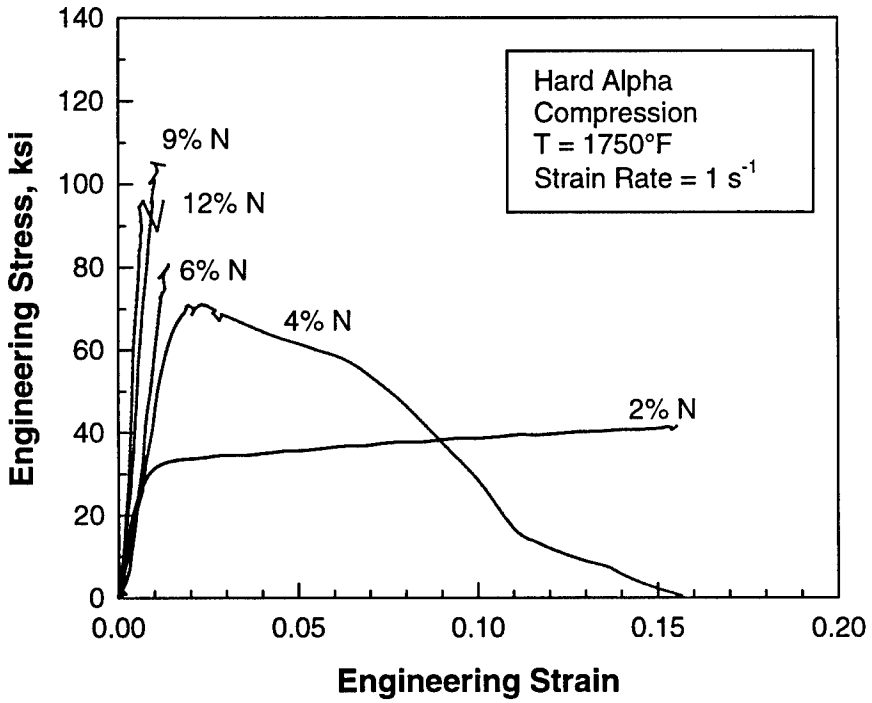


FIGURE 2-1. COMPRESSIVE STRESS-STRAIN CURVES OF HARD ALPHA Ti FOR FIVE DIFFERENT NITROGEN CONTENTS IN WEIGHT PERCENT
(Tests were conducted at 1750°F at a strain rate of 1 S^{-1}.)

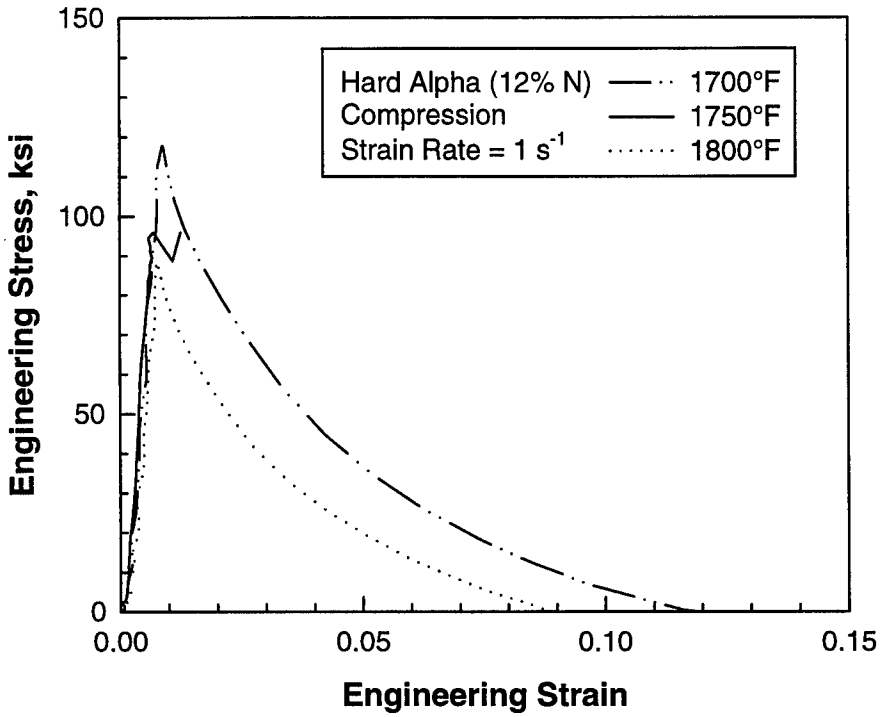


FIGURE 2-2. COMPRESSIVE STRESS-STRAIN CURVES OF HARD ALPHA Ti WITH 12 wt.% N FOR THREE DIFFERENT TEST TEMPERATURES

2.2.2.2 Indirect Tension Test Results.

The load displacement curves for the indirect tension tests of hard alpha Ti are shown in figure 2-3. The result for 2 wt.% N was invalid because of excessive plasticity. For specimens that failed by brittle fracture, an elastic stress analysis [8] was used to calculate the tensile fracture stress at the center of the disk, and the results are summarized in table B-2 of appendix B. The tensile fracture strengths of hard alpha are compared to the compressive strengths in figure 2-4, which shows that hard alpha Ti fractured at substantially lower stress in tension than in compression.

2.2.2.3 Indentation Test Results.

Indentation tests [9] of hard alpha Ti were performed on specimens with varying nitrogen content at a temperature of 1750°F at displacement rates of 0.01 and 1 in/s, which corresponded to approximate average strain rates of 0.01 and 1 s^{-1}, respectively. One test was also done at 1800°F for hard alpha Ti with 12 wt.% N. Figure 2-5 shows a plot of the average stress versus the average strain for the indentation tests at 1750°F under a strain rate of 1 s^{-1}. Hard alpha Ti with 2 wt.% N was ductile and exhibited plastic flow without fracture when tested by indentation. With 4 wt.% N, hard alpha Ti exhibited plastic flow and localized fracture after yielding. For nitrogen contents > 6 wt.%, the hard alpha Ti fractured with little plastic flow. A summary of the yield and fracture stresses for the indentation tests is presented in table B-2, appendix B.

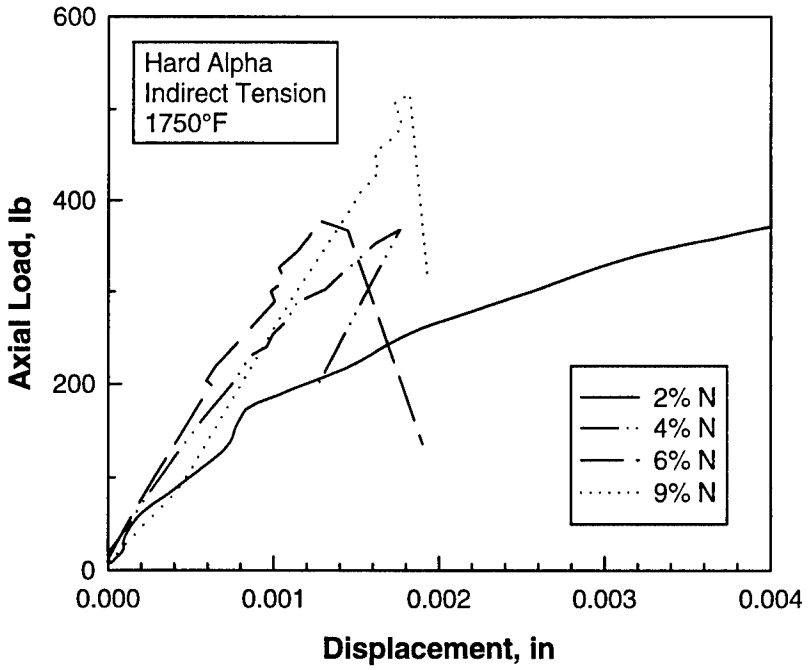


FIGURE 2-3. LOAD DISPLACEMENT CURVES OF INDIRECT TENSION TESTS OF HARD ALPHA Ti WITH FOUR DIFFERENT NITROGEN CONTENTS

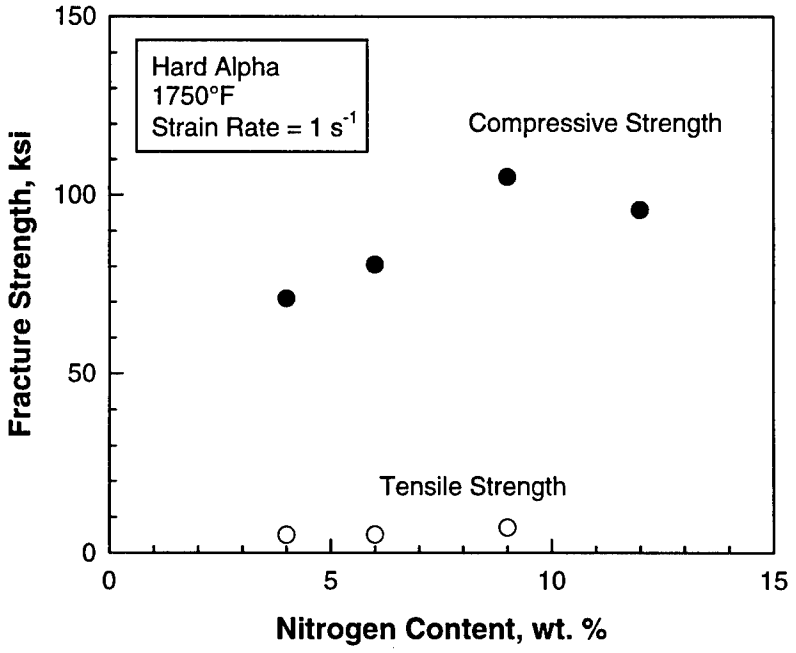


FIGURE 2-4. COMPARISON OF FRACTURE STRENGTH OF HARD ALPHA Ti TESTED IN COMPRESSION AND INDIRECT TENSION

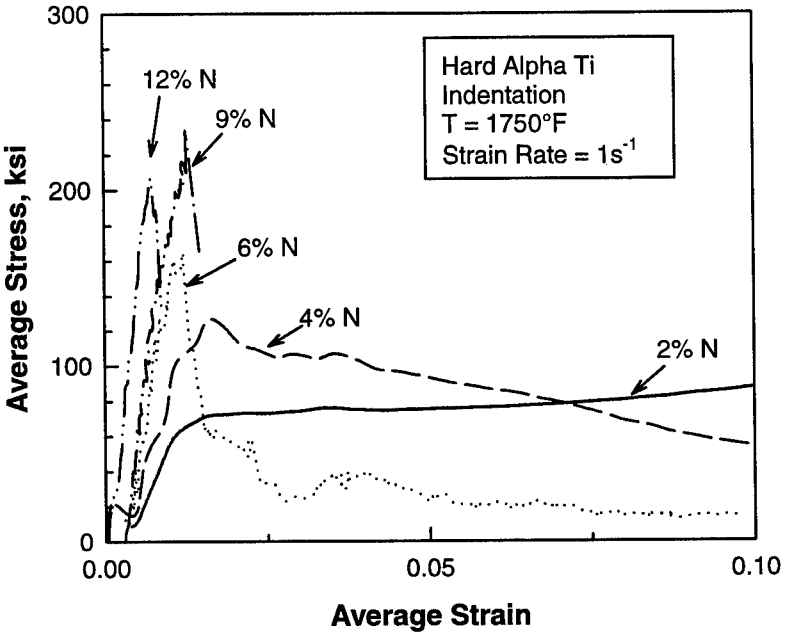


FIGURE 2-5. EXPERIMENTAL RESULTS OF AVERAGE STRESS VERSUS AVERAGE STRAIN FOR INDENTATION TESTS OF HARD ALPHA Ti WITH VARIOUS NITROGEN CONTENTS

2.2.2.4 Plane Strain Compression Test Results.

Plane strain compression tests were performed at ambient temperature by compressing the test specimen in the channel die beyond the maximum load. Typical stress-strain curves of the plane strain compression tests for a strain rate of 0.01 s^{-1} are presented in figure 2-6. For hard alpha at a given nitrogen content, the applied stress increases linearly with displacement until the maximum stress is reached. The applied stress then decreases almost linearly with increasing displacement. The load dropped beyond the peak load due to the formation of microcracks during the plane strain compression. Additional results of the plane strain compression tests for a strain of 1 s^{-1} are shown in appendix B.

2.2.2.5 Effects of Pressure.

The fracture strength, Y_i, determined for a given stress state was normalized by the fracture strength, Y_n, for uniaxial compression. The results are plotted as a function of pressure, P, normalized by Y_n in figure 2-7. Pressure is calculated as 1/3 of the sum of the principal stresses, as given by

$$P = \frac{1}{3}(\sigma_{11} + \sigma_{22} + \sigma_{33}) \tag{2-1}$$

where σ_{11}, σ_{22}, and σ_{33} are the principal stresses. The values of the ratio P/Y_n are 0.045, 1/3, and ≈ 6 for indirection tension, uniaxial compression, and indentation, respectively. The semilog

plot in figure 2-7 indicates that Y/Y_n increases linearly with log (P/Y_n). The fracture stress increases with pressure because microcracking is suppressed by a high pressure.

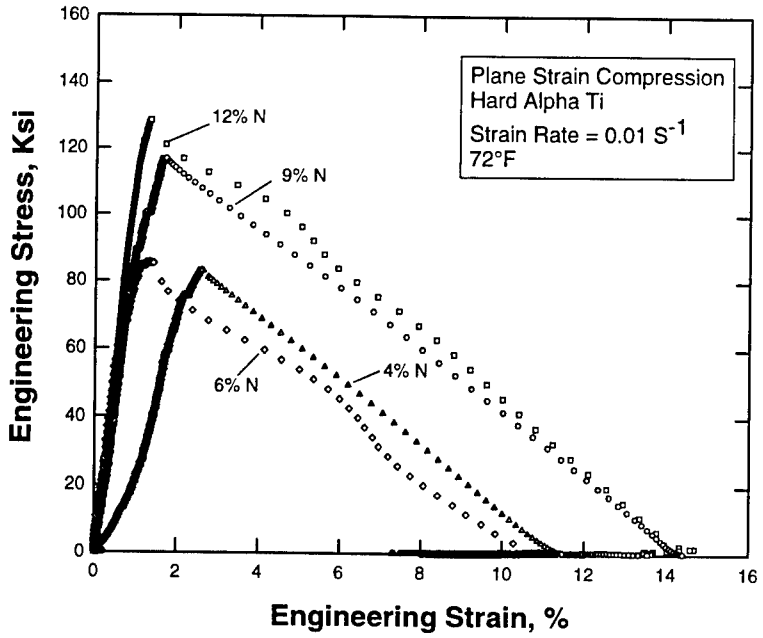


FIGURE 2-6. COMPARISON OF ENGINEERING STRESS-STRAIN CURVES OF HARD ALPHA Ti WITH VARIOUS NITROGEN CONTENTS TESTED IN PLANE STRAIN COMPRESSION AT A STRAIN RATE OF 0.01 s^{-1}

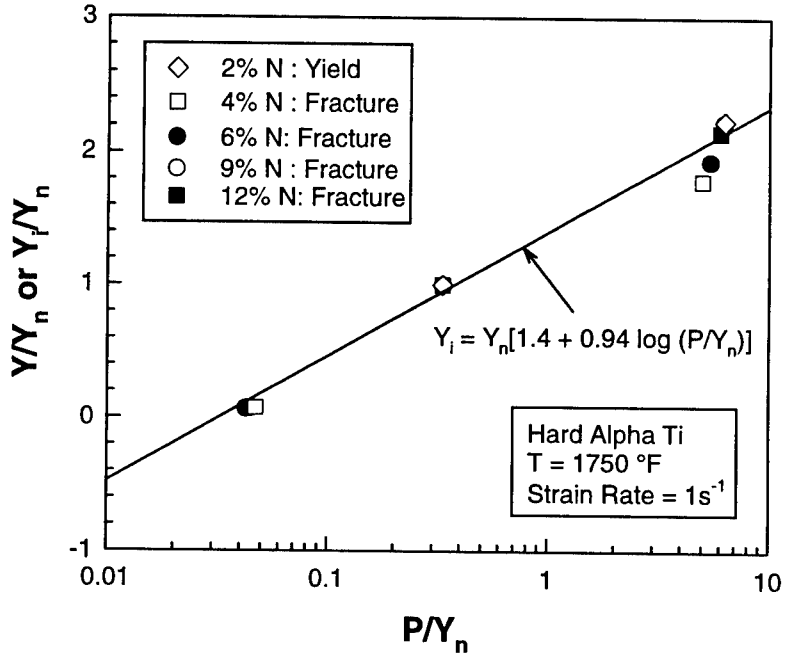


FIGURE 2-7. THE FLOW STRESS (Y) AND FRACTURE STRESS (Y_f) OF HARD ALPHA AS A FUNCTION OF PRESSURE, P

2.2.2.6 Effects of Nitrogen Content.

The dependence of the flow and fracture stresses on the nitrogen content of hard alpha is shown in figure 2-8. Both the flow stress and the fracture stress increase with increasing nitrogen content, but the rates of increase are different, as shown in figure 2-8. The flow stress of hard alpha is lower than the fracture stress at nitrogen contents below 4 wt.% N. The slope dY/dN is higher for the flow stress and the flow stress exceeds the fracture stress for nitrogen contents higher than 4 wt.% N. As a result, fracture precedes plastic flow when the nitrogen content of hard alpha is greater than 4 wt.% N.

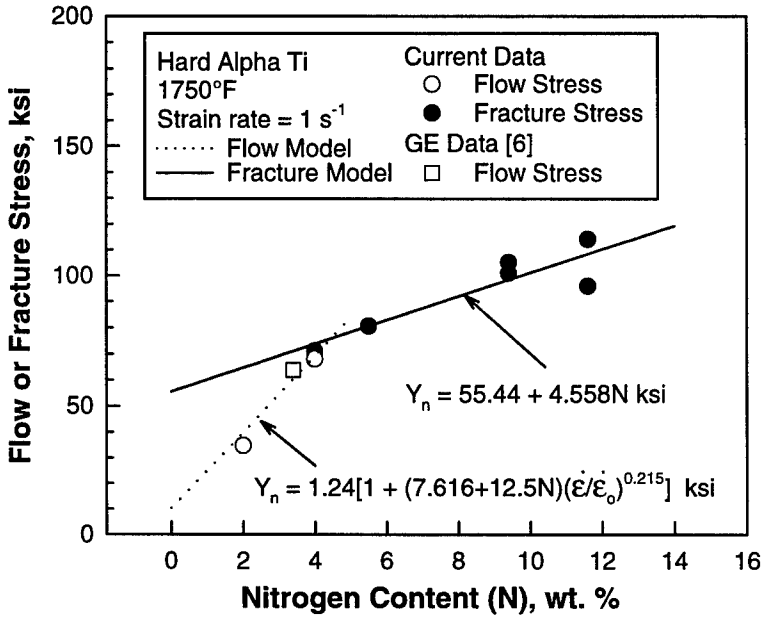


FIGURE 2-8. FLOW AND FRACTURE STRESSES OF HARD ALPHA INCREASE WITH INCREASING NITROGEN CONTENT AT DIFFERENT SLOPES

2.2.2.7 Effects of Strain Rate.

The effects of strain rate on the flow and fracture stresses of hard alpha are summarized in figures 2-9 and 2-10, respectively. As shown, the flow stress increases with increasing strain rate, see figure 2-9. On the other hand, the fracture stress of hard alpha is insensitive to the strain rate based on the experimental data for uniaxial compression and plane strain compression, see figure 2-10. The fracture stress obtained by the indentation technique shows an apparent rate sensitivity, which is not fully understood and could actually be a manifestation of the pressure effect.

2.2.2.8 Effects of Temperature.

The fracture stress of hard alpha is relatively insensitive to temperature in the range of 1700° to 1800°F, as was illustrated in figure 2-2 for hard alpha with 12 wt.% nitrogen. Comparing the plane-strain fracture stress (122.6 ksi) at ambient temperature to that for uniaxial

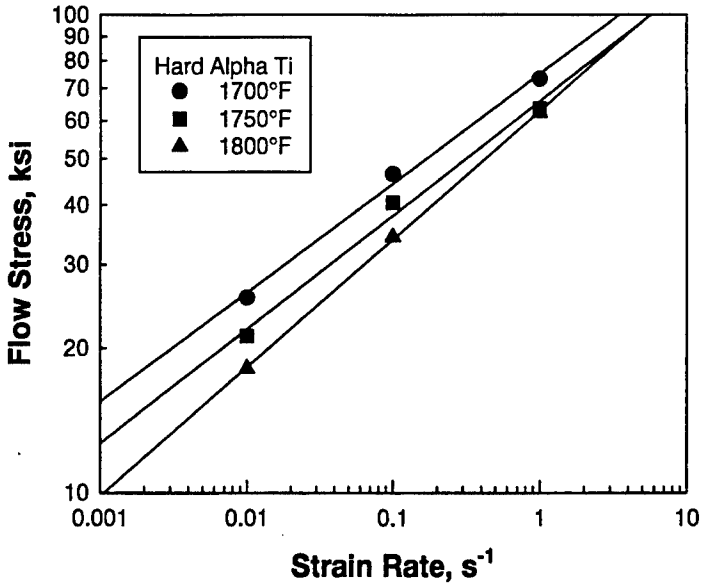


FIGURE 2-9. FLOW STRESS OF HARD ALPHA WITH NITROGEN CONTENT ≤ 4 wt.% AS A FUNCTION OF STRAIN RATE

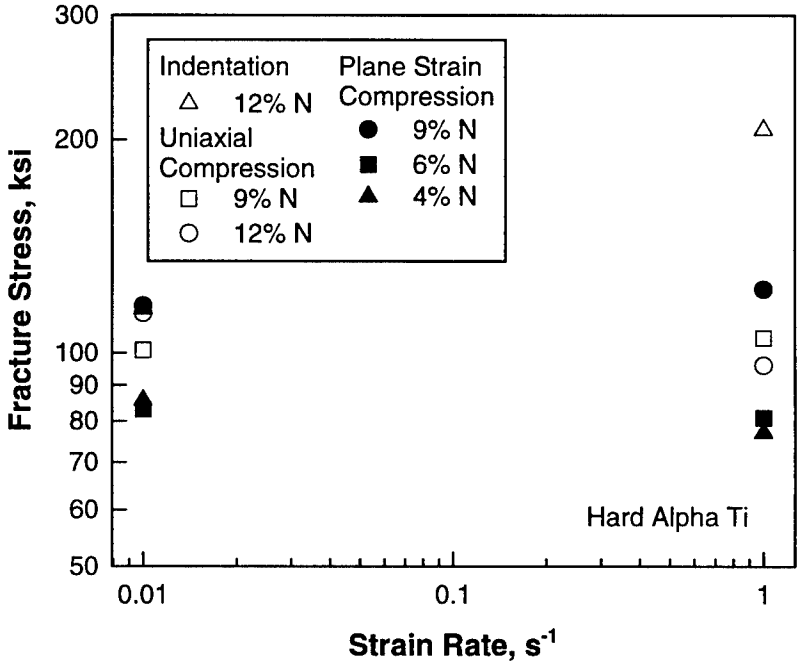


FIGURE 2-10. FRACTURE STRENGTHS OF HARD ALPHA Ti AS A FUNCTION OF STRAIN RATE

compression at 1700°F (117.8 ksi) suggests that the fracture stress may be independent of temperature from 72° to 1700°F. For hard alpha with a nitrogen content ≤ 4 wt. %, the flow stress is sensitive to the test temperature and strain rate, as shown in figure 2-9.

2.2.3 Development of Constitutive Relationships for Hard Alpha.

Experimental data indicate that hard alpha deforms plastically when the nitrogen content is less than 4 wt.%, but fractures when the nitrogen content is 4 wt.% or greater. Guided by these experimental observations, constitutive equations were developed to describe the fracture behavior of hard alpha with high nitrogen contents ($\geq$ 4 wt. % N) and the plastic flow behavior of hard alpha with low nitrogen contents ($\leq$ 4 wt. % N). These two sets of constitutive equations are summarized in this section, while details of their development are presented in appendix C.

2.2.3.1 Fracture of Hard Alpha.

Constitutive equations were developed to describe the elastic fracture of hard alpha (intact material) and the flow stress of damaged hard alpha using a continuum damage mechanics formulation. The constitutive equations are applicable to the onset and failure of hard alpha. For intact hard alpha Ti, the flow stress, Y_i, is given by

$$Y_i = Y_n\left[1.4 + 0.94 \log\left(\frac{P}{Y_n}\right)\right] \tag{2-2}$$

where P is the pressure (see equation 2-1) and Y_n is the fracture stress in uniaxial compression. The fracture stress, Y_n, is a function of the nitrogen content and is represented by

$$Y_n = 55.44 + 0.558N \tag{2-3}$$

where N is nitrogen content in weight percent and Y_n is in units of ksi. For failed hard alpha Ti, the flow stress, Y_f, is given by

$$Y_f = Y_n\left[0.14 + 0.094 \log\left(\frac{P}{Y_n}\right)\right] \tag{2-4}$$

After the initiation of fracture, the flow stress, Y_D, of the damaged material was assumed to decrease with increasing damage as given by

$$Y_D = (1 - D)Y_i + DY_f \tag{2-5}$$

where D is an internal variable representing the state of damage. The value of D is zero for intact material and is unity for failed material. The damage rate, $\dot{D}$, is represented by an evolution equation given by

$$\dot{D} = c_3\ \dot{\varepsilon} \tag{2-6}$$

where $\dot{\varepsilon}$ is the strain rate and c_3 is a model constant. The current value of the damage variable D is obtained by integrating over the loading path as

$$D = \int \dot{D}dt = \int c_3\ \dot{\varepsilon}dt \tag{2-7}$$

For multiaxial loading, $\dot{\varepsilon}$ in equations 2-6 and 2-7 is replaced by the von Mises effective strain rate, $\dot{\varepsilon}_e$.

The slope of the engineering stress-strain curves for plane strain compression tests beyond the maximum load was used to evaluate the constant c_3 in equation 2-6. The value of c_3 was dependent on the nitrogen content and increased with increasing strain rate. Specifically,

$$c_3 = 0 \text{ for } 0 \le N < 4 \ wt.\%\, N \tag{2-8}$$

since fracture did not occur in hard alpha within this range of nitrogen content. In contrast,

$$c_3 = 18.75\ \dot{\varepsilon}^{0.1516}\left(1 - e^{c_4 N}\right) \ for\ N \ge 4\ wt.\%\ N \tag{2-9}$$

where c_4 = -0.0964 (wt.% N^{-1}) and N is nitrogen content in wt.%.

The experimental data used to develop the constitutive model is shown in figures 2-11 to 2-13. Figure 2-11 illustrates that the dependence of the flow and fracture stresses of hard alpha on pressure (compression is positive here) obeys the logarithmic law as described by equation 2-2. Figure 2-12 presents the correlation between the flow or fracture stress and nitrogen content. Figure 2-13 shows a comparison of the calculated fracture stress for the intact material, equation 2-2, and the stress of the failed material determined from the indentation tests at various nitrogen levels, equation 2-6. The decrease in the flow stress of the hard alpha from the intact state to the failed state is given by equation 2-5 with the evolution of the damage state described by equation 2-6.

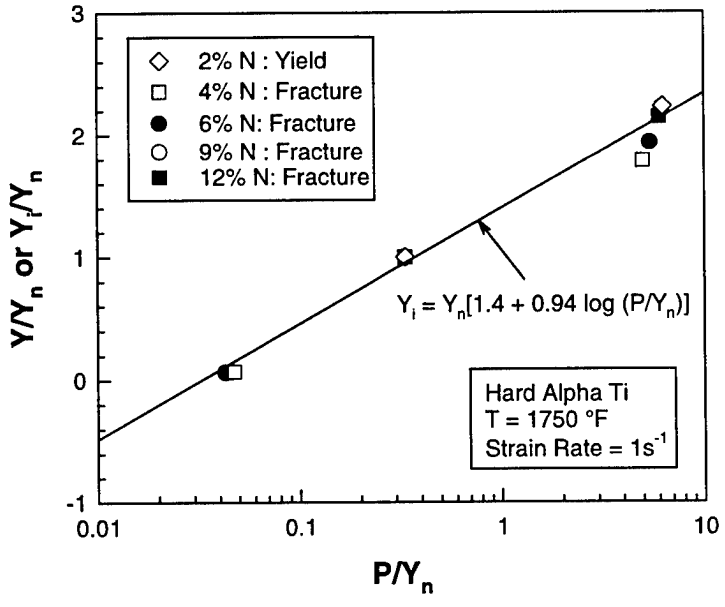


FIGURE 2-11. SEMILOG PLOT OF FLOW OR FRACTURE STRESS, Y_i, AS A FUNCTION OF PRESSURE, $P = 1/3 \sum_{k=1}^{3} \sigma_{kk}$

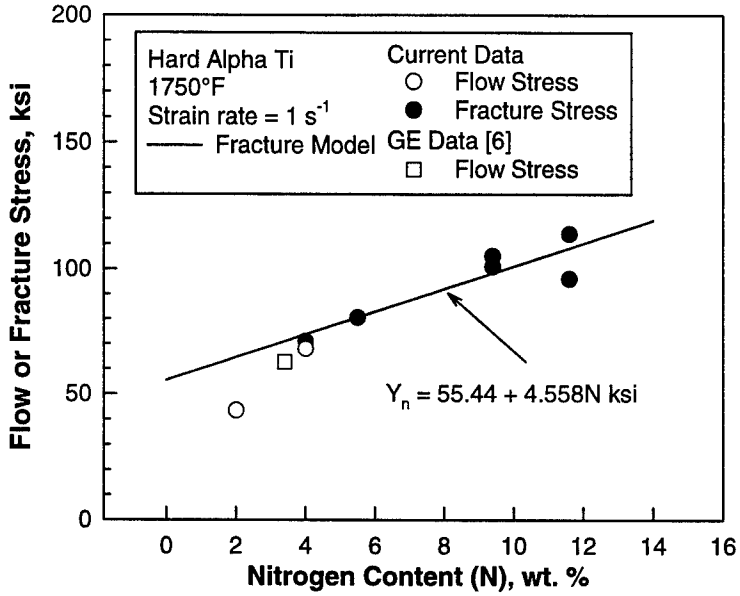


FIGURE 2-12. EXPERIMENTAL CORRELATION AND LEAST-SQUARE FIT OF THE FLOW OR FRACTURE STRESS, Y_n, OF HARD ALPHA AS A FUNCTION OF NITROGEN CONTENT
(The least-square fit applies to the fracture stress only.)

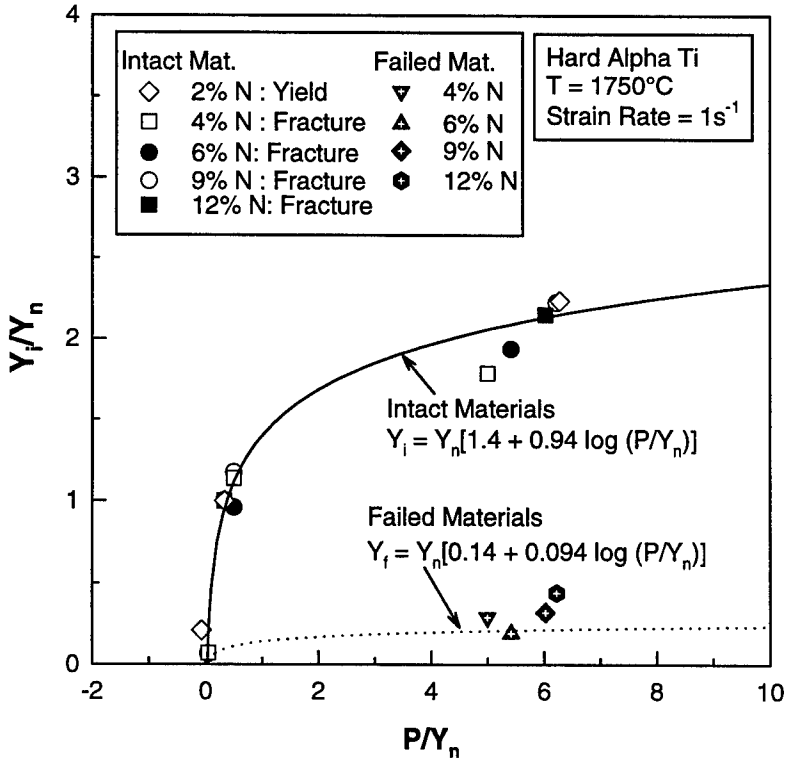


FIGURE 2-13. COMPARISON OF THE CALCULATED FRACTURE STRESS OF THE INTACT MATERIALS AND THE FLOW STRESS OF THE FAILED MATERIAL

2.2.3.2 Plastic Flow of Hard Alpha.

A set of constitutive equations was developed to describe the plastic flow of hard alpha Ti with a low nitrogen content ($0 < N \leq 4$ wt.%). This range of nitrogen content includes much of the diffusion zone between the hard alpha nugget and the Ti matrix. For $0 \leq N \leq 4$ wt.%, the flow stress, Y, of hard alpha Ti is given by

$$Y = Y_n F(P) \tag{2-10}$$

where Y_n is the flow stress of hard alpha under uniaxial compression. $F(P)$ is a function of the pressure, P, and is given by

$$F(P) = 1 \text{ for } N = 0 \tag{2-11}$$

and

$$F(P) = 1.4 + 0.94 \log(P/Y_n) \text{ for } 0 < N \leq 4 wt.\%. \tag{2-12}$$

The flow stress, Y_n, is a function of strain and strain rate as described by

$$Y_n = 1.24[1 + (7.616 + 12.5N)\ (\dot{\varepsilon}/\dot{\varepsilon}_0)^{0.215}] \tag{2-13}$$

where the reference strain rate, $\dot{\varepsilon}_o$, is 1 sec^{-1}.

Comparison of the calculated and measured stress-strain curves for 2%N and 3.4%N are shown in figures 2-14 and 2-15, respectively. The GE data [6] have been corrected for adiabatic heating using an analysis procedure provided by GE. No correction for adiabatic heating was deemed necessary for the current data because of the absence of softening in this set of data. The model overpredicts the flow stress of 2%N at 1 sec^{-1} because an average value of the strain rate exponent for both GE and current data was used. The GE data for 3.4 wt.% N was more rate sensitive than the current data for 2 and 4 wt.% N. The discrepancy is considered minor and is well within experimental scatter. The comparison of the calculated and measured flow and fracture stresses as a function of nitrogen content, in figure 2-16, shows good agreement between model and experiment.

2.2.4 Forging Microcode Development.

Forming process modeling using the finite element method (FEM) has become a core technology in the forging industry to analyze, evaluate, and optimize metal forming processes. Due to capabilities such as automatic meshing and remeshing, multiple deforming objects, ease of use, etc., the commercial forming code DEFORM™* has been extensively used by industry for modeling of billet conversion, rolling, extrusion, cold forging, hot forging, and isothermal forging, among others. DEFORM™ provides information such as material flow, temperature,

*Available from Scientific Forming Technologies Corp., Columbus, OH.

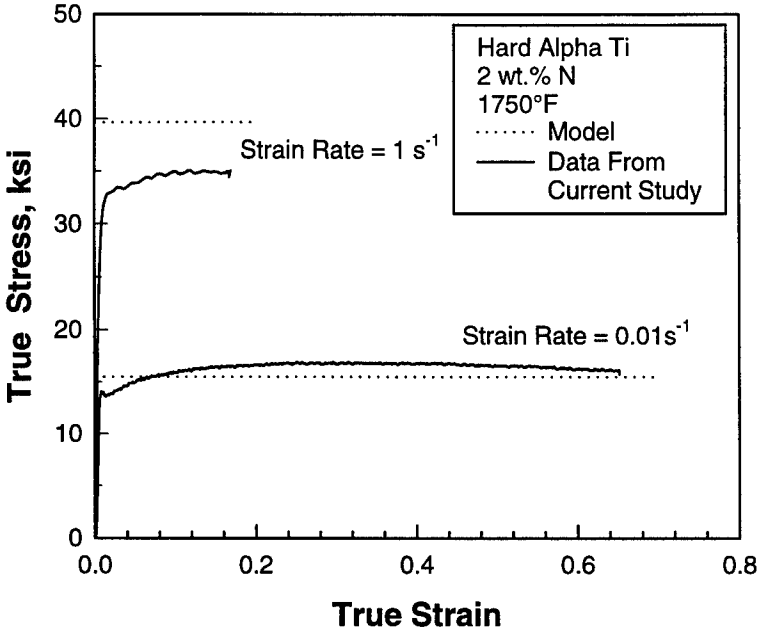


FIGURE 2-14. COMPARISON OF CALCULATED AND MEASURED TRUE STRESS-STRAIN CURVES OF HARD ALPHA Ti WITH 2 wt.% N FOR TWO STRAIN RATES

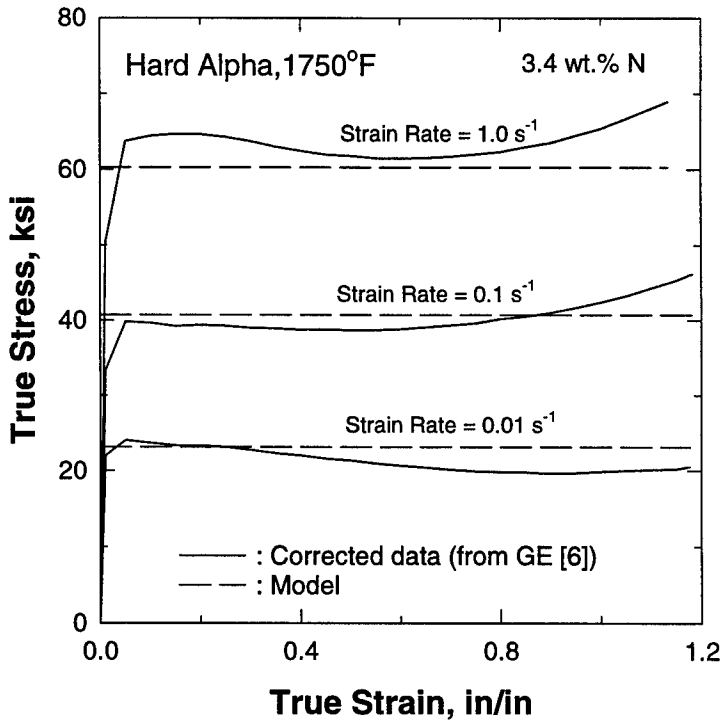


FIGURE 2-15. MEASURED TRUE STRESS-STRAIN CURVES COMPARED TO MODEL CALCULATIONS FOR TWO STRAIN RATES

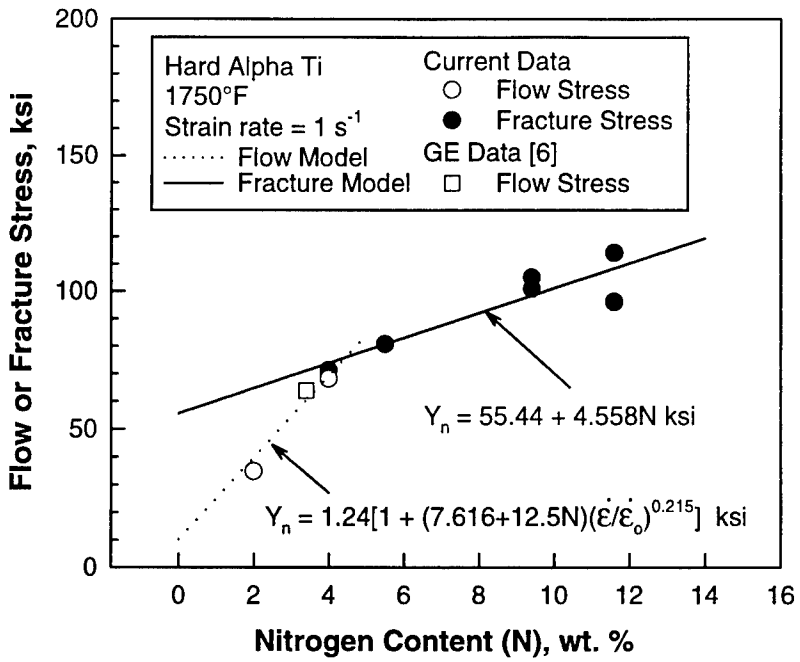


FIGURE 2-16. COMPARISON OF CALCULATED AND MEASURED FLOW AND FRACTURE STRESSES OF HARD ALPHA Ti

strain, strain rate, stress, and damage distribution. In the present effort, the capabilities of the commercial code DEFORM™-2D were extended to simulate hard alpha particle evolution during forming processes.

The objective of this task was to develop a finite element microcode to simulate the evolution of a hard alpha inclusion during forming processes. The code is intended to simulate

- the interaction and deformation among the hard alpha inclusion, nitrogen diffusion zone, and parent material during the forming process.
- degradation of strength of the hard alpha particle due to fracture by using a continuum damage mechanics constitutive model.

Due to the extreme size ratio between the full-scale part and the defect, a two-step macro-microlevel simulation was adopted. First, the entire forging process was simulated (macrolevel) using material properties for the titanium alloy and assuming that the presence of the inclusion has no effect on the bulk flow behavior of the material. Second, a small region around the inclusion was identified, the geometry and key material properties of the inclusion were defined, and a small ring of the matrix material with the nitrogen diffusion zone and hard alpha inclusion was forced through the same deformation pattern as the original material (microlevel simulation).

2.2.4.1 Approach.

Several enhancements to DEFORMTM-2D were required in order to implement the two-step simulation procedure. The preprocessor was modified to extend the geometry definition to multiple surfaces in order to include the presence of holes, and a template was created to extract data from the macrolevel simulation and generate input data for the microlevel simulation. In addition, because complicated shapes of hard alpha and the diffusion zone evolved during forging, improvements were implemented in the meshing method, including the capability to generate a mesh using predefined boundary nodes. New boundary condition codes were defined to control the movement of the microvolume in the microlevel simulation. The interpolation routine was modified to properly interpolate these boundary condition codes and the associated position functions. With respect to the FEM engine, the positions of the boundary nodes in the microvolume were defined as a function of time. During the microlevel simulation, the velocity of these boundary nodes was calculated based on the current position and the given trajectory path.

A method was investigated to model fracture of hard alpha by splitting elements into two and locally remeshing the objects. This approach was abandoned due to resource limitations and unresolved technical issues. Instead, a continuum damage mechanics-based constitutive model was used to simulate the fracture and degradation of hard alpha (see section 2.2.3.1).

The sequence of operations for preparing and running a microlevel simulation, based on macrolevel simulation results, is illustrated in figure 2-17.

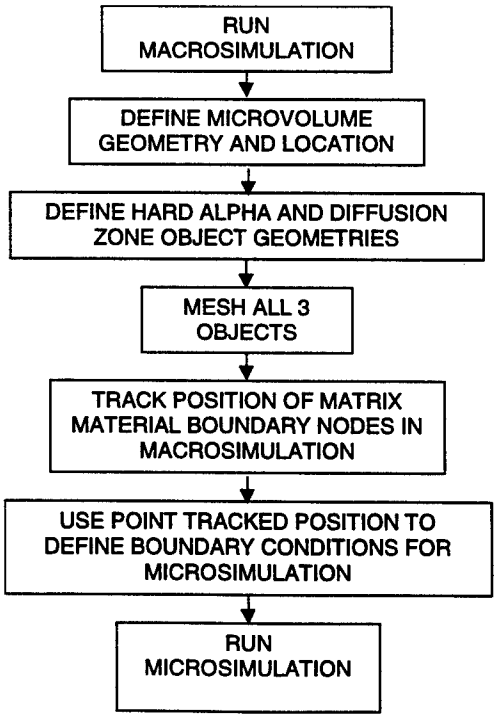


FIGURE 2-17. FLOW CHART ILLUSTRATING BASIC SEQUENCE OF OPERATIONS FOR PREPARING AND RUNNING A MICROLEVEL SIMULATION

2.2.4.2 Accommodation of Geometries With Holes.

The DEFORM™-2D preprocessor had to be modified to properly accommodate geometries with holes. Geometry in DEFORM™ is defined by boundary curves. A solid object is defined by a single curve. If holes are introduced, each hole is defined by a separate internal boundary curve. The graphical user interface (GUI) was modified to allow the user to input multiple curves and access each curve individually, as shown in figure 2-18.

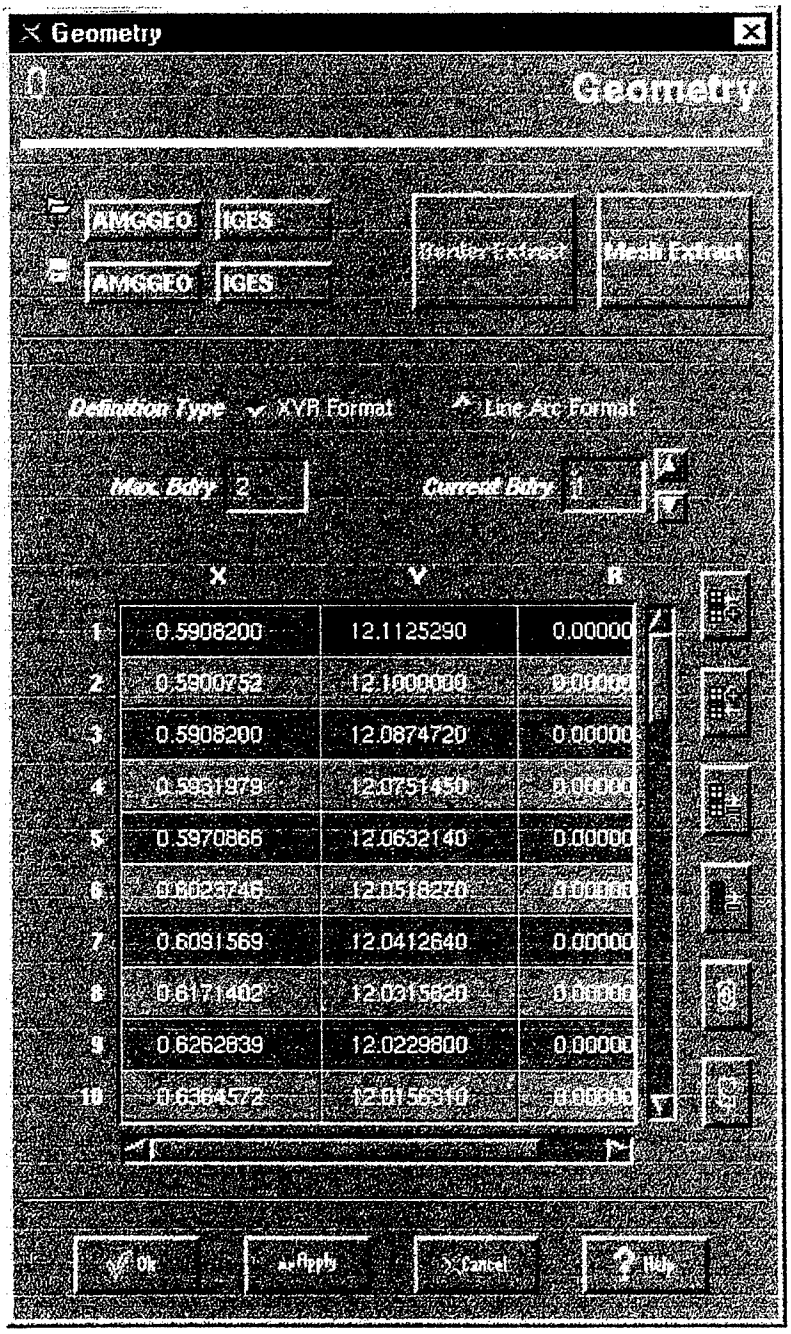


FIGURE 2-18. GEOMETRY DEFINITION WINDOW FROM GUI SHOWING MULTIPLE BOUNDARY CAPABILITY

2.2.4.3 Microlevel Simulation Template.

A graphical user interface was developed to aid the user in preparing data for microlevel simulations. Using the template, the user can:

- define the microlevel simulation problem ID and title
- select the macrolevel simulation data
- select location and shape of microvolume
- define shape of the hard alpha, diffusion zone, and matrix material
- mesh the hard alpha, diffusion zone, and matrix material
- track the boundary of the matrix material from the start to the end of the macrolevel simulation
- set relations between the three regions
- define the simulation controls for the microlevel simulation
- specify the material data
- generate a complete keyword file to run a microlevel simulation

A DEFORM™-2D macrolevel simulation database is necessary because it supplies critical data including geometry evolution, pressure, and temperature changes to the microlevel simulation. After prompting the user to select a macrolevel simulation database, the template allows the user to select the starting step (time) for the microlevel simulation and the microvolume geometry at this step (figure 2-19). Automatic microvolume geometry definition is provided for circles and rectangles. Arbitrary shapes can be defined by importing Automatic Mesh Generation GEOmetry (AMGGEO) geometries generated in the standard DEFORM™-2D preprocessor.

After the position and geometry of the microvolume have been defined, the hard alpha inclusion and diffusion zone are defined and the user is guided through generating meshes on each object (figure 2-20). Nitrogen content can be defined as a constant value or as a function of radius for each object. Temperature can be defined as a constant value, or it can be extracted from the macrolevel simulation database and used as an input function of time during the microlevel simulation.

After the microvolume objects have been meshed, the shape of the microvolume boundary is tracked in the macrolevel simulation as a function of time, and these are specified as boundary conditions for the microlevel simulation (figure 2-21).

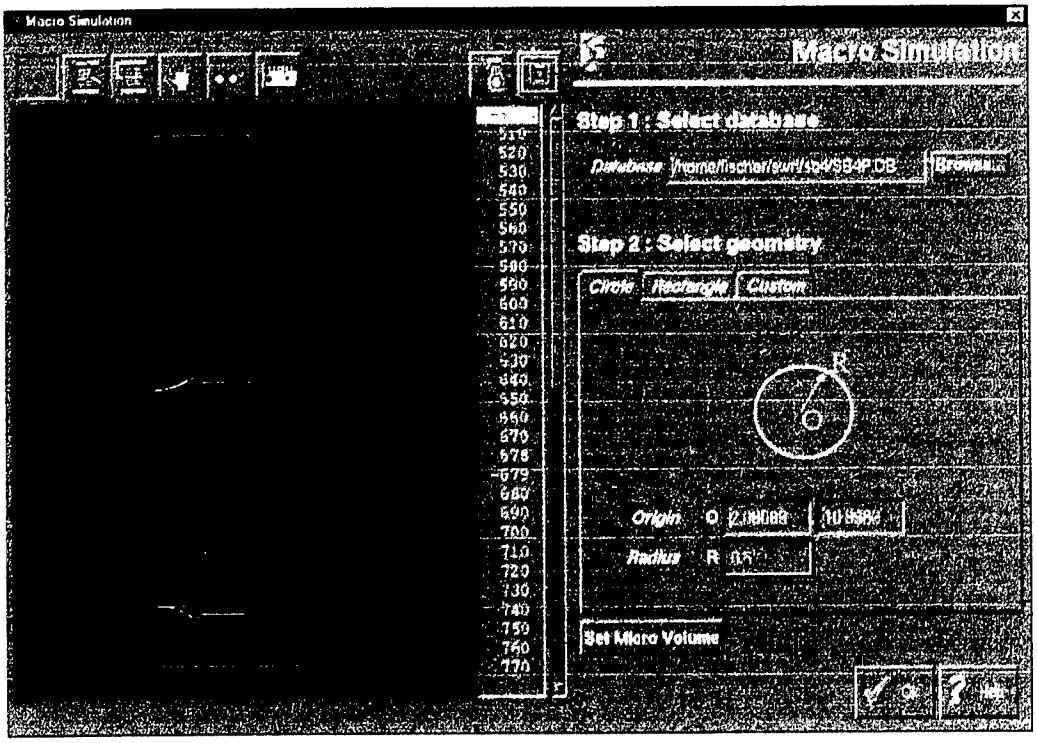


FIGURE 2-19. USER INTERFACE FOR DEFINING MICROVOLUME GEOMETRY AND LOCATION IN MACROLEVEL SIMULATION

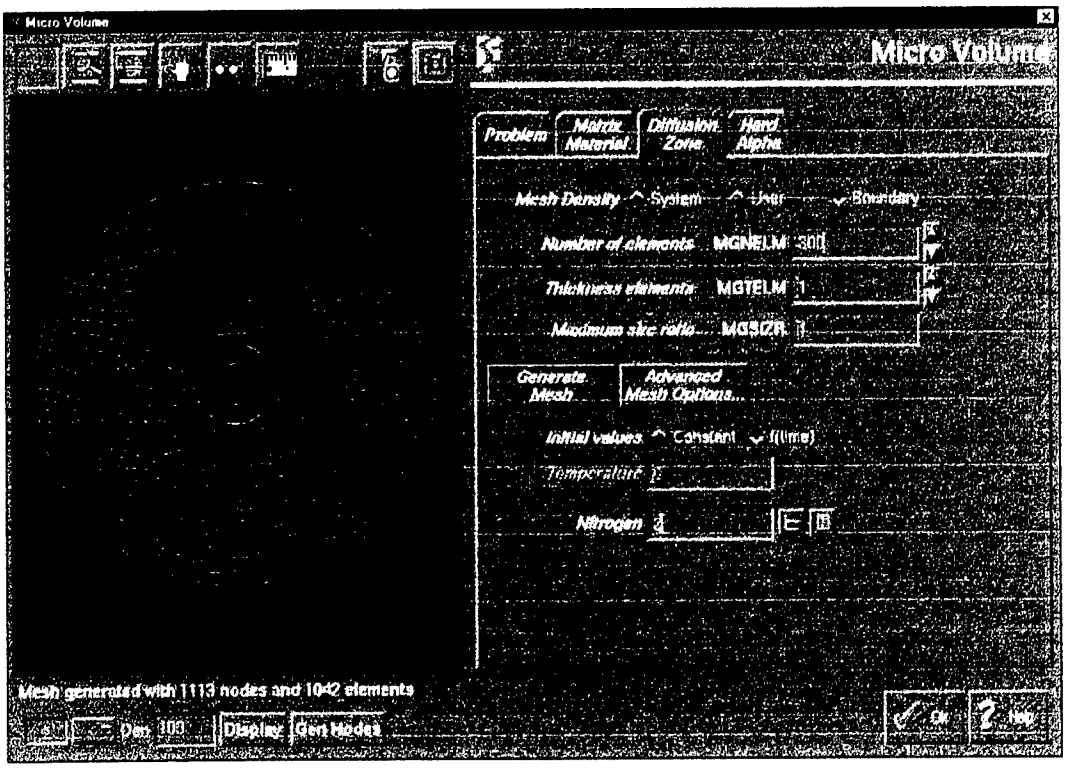


FIGURE 2-20. USER INTERFACE FOR DEFINING OBJECT GEOMETRY, MESH, AND PROPERTIES IN MICROVOLUME

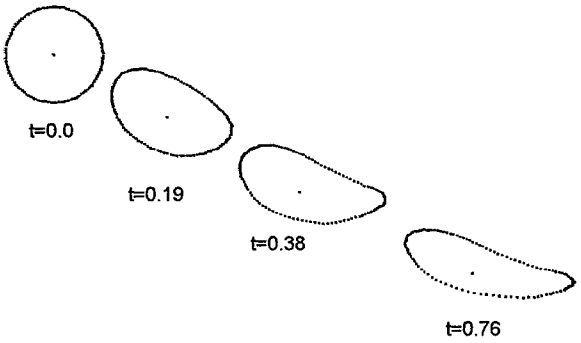


FIGURE 2-21. MICROVOLUME BOUNDARY SHAPE AS DEFINED BY POINT TRACKING BOUNDARY NODES

By default, interface boundary conditions are set as sticking. That is, each diffusion zone node on the boundary between the diffusion zone and the hard alpha object is fixed in its relative position on the boundary of the hard alpha object. These settings may be modified in the inter-object interface boundary conditions window.

Material data is specified in a DEFORM™ keyword file. Simulation controls such as process duration, total number of simulation steps, and time interval per step can be defined in the Simulation Controls window, see figure 2-22. Reasonable values are given as default values in each field.

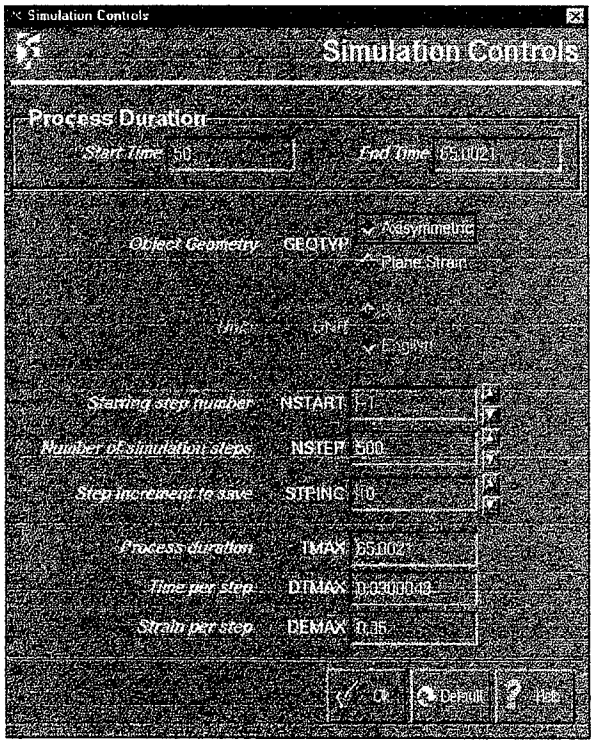


FIGURE 2-22. SIMULATION CONTROLS WINDOW FROM MICROLEVEL SIMULATION TEMPLATE

After the problem setup has been completed in the template, a DEFORM™-2D keyword file can be written out. This keyword is read into the DEFORM™-2D preprocessor. If desired, additional editing of simulation data can be performed at this time. The simulation database can then be checked and generated and the simulation run as any other DEFORM™ simulation.

2.2.4.4 Implementation of Constitutive Equations in DEFORM™-2D.

The constitutive model for plastic flow of hard alpha titanium using continuum damage mechanics (see section 2.2.2) was incorporated into DEFORM™-2D via user-defined FORTRAN subroutines. Several simulations of simple compression tests were run to verify constitutive models and the DEFORM™-2D flow stress routine for hard alpha titanium with nitrogen content ranging from 2% to 12%. Engineering stress-strain curves were created from the results of these simulations and compared to experimental stress-strain curves (see section 2.2.4.5). Based on these comparisons, the constitutive equation implementation was modified to give good agreement between DEFORM™ simulations and experimental results while maintaining stability and convergence within the FEM solver. The primary modification was the addition of a pseudoelastic region in which the elastic region in the experimental data is modeled as a linearly hardening plastic region. This representation is realistic for monotonic loading to failure as experienced by hard alpha during ingot breakdown and forging to disk shape.

The flow, fracture, and crushing behavior of hard alpha is modeled as a softening flow stress in DEFORM™-2D. The hard alpha object is always modeled as a single object, but it deforms more easily as it is fractured. This approach shows good agreement with actual continuum behavior and has the advantage of significantly lower computation time costs than those incurred with element splitting. The governing constitutive equations for flow and fracture were discussed in section 2.2.3.

As DEFORM™-2D is executed, the flow stress is calculated for each of four Gauss integration points in each linear quadrilateral element. The flow stress calculation is repeated for each iteration until convergence is achieved for a particular time step. After the solution has converged, the damage parameter is calculated once for each element using the strain, strain rate, temperature, and pressure variables at the end of the time step.

Since the constitutive behavior is extremely sensitive to pressure, an accurate pressure value is necessary. The hydrostatic stress at the center of the microvolume is tracked by the template and the pressure distribution stored in a file. If the file containing the hydrostatic stress for the microvolume is present, the pressure values are used by the flow stress subroutines during execution. Otherwise, pressure values derived from dilatational strains in the macrolevel simulation are used.

During execution, damage begins accumulating after the stress-strain state has reached the failure criterion. If damage has begun accumulating, flow stress is calculated using the mixture rule. If damage has not begun accumulating, the flow stress is calculated based on strain and the pseudoelastic Young's modulus. If the current effective stress is less than the yield stress and damage has not begun accumulating, a zero value is returned for damage. Once damage begins

accumulating, it continues to accumulate, even if the effective stress falls back below the failure stress.

2.2.4.5 Validation of Flow Stress Models.

Two methods were used to validate the flow stress models as implemented in DEFORM™. First, uniaxial compression tests (section 2.2.2.1) were simulated. Second, the stress-strain history was tracked in a microlevel simulation and compared to the experimental data.

The compression tests were simulated in DEFORM™ and compared to results of experiments. The sample size simulated was a 0.25-inch-diameter cylinder 0.5 inch high. Very good lubrication was assumed, and the tests were performed at a constant strain rate. Typical results for the 2% nitrogen diffusion zone material are shown in figure 2-23. A comparison of experimental and simulated failure stress is shown in figure 2-24. Note that the comparison in figure 2-24 is for the experimental fracture stress with the peak position of the predicted stress-strain curves. Good agreement was found with the compression test data. Good agreement with compression test data was also found using point tracking of the stress-strain history of 2% nitrogen diffusion zone material.

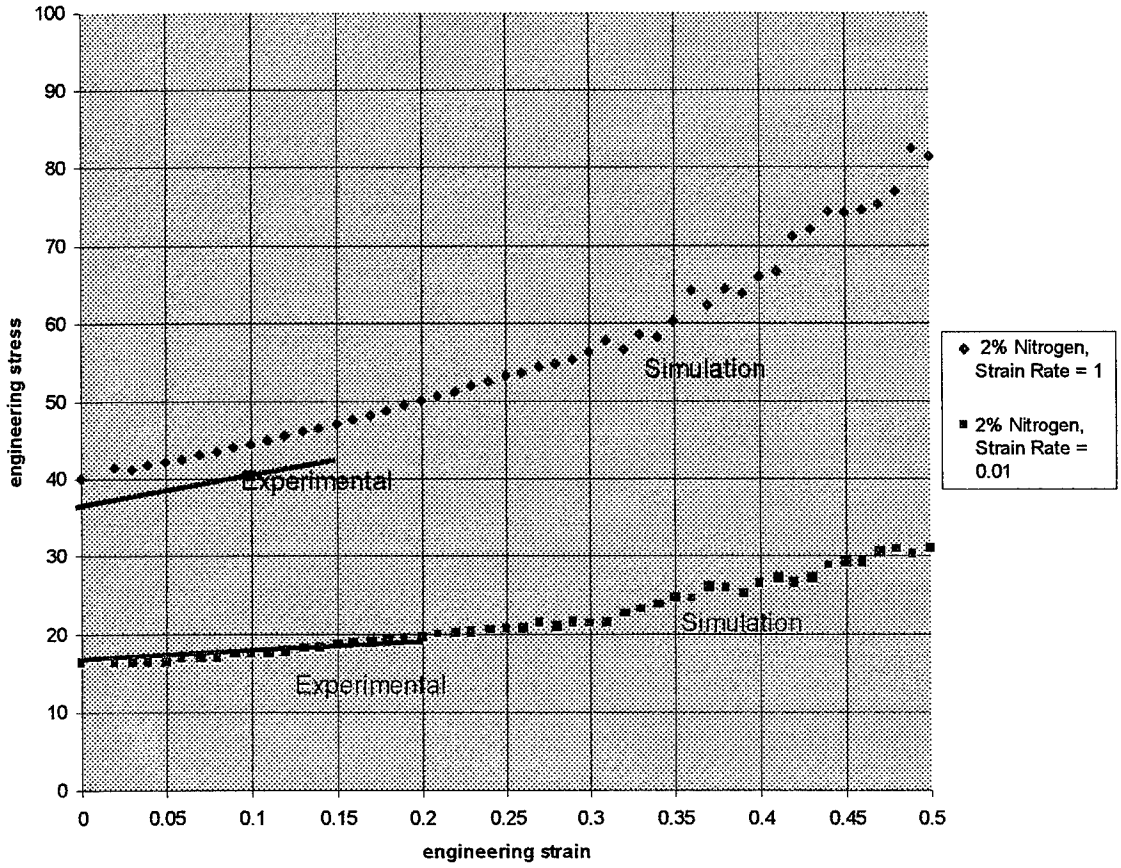


FIGURE 2-23. COMPARISON OF EXPERIMENTAL AND SIMULATED ENGINEERING STRESS-STRAIN DATA FOR 2% NITROGEN HARD ALPHA AT STRAIN RATES OF 0.01 AND 1.0 PER SECOND AT 1750°F

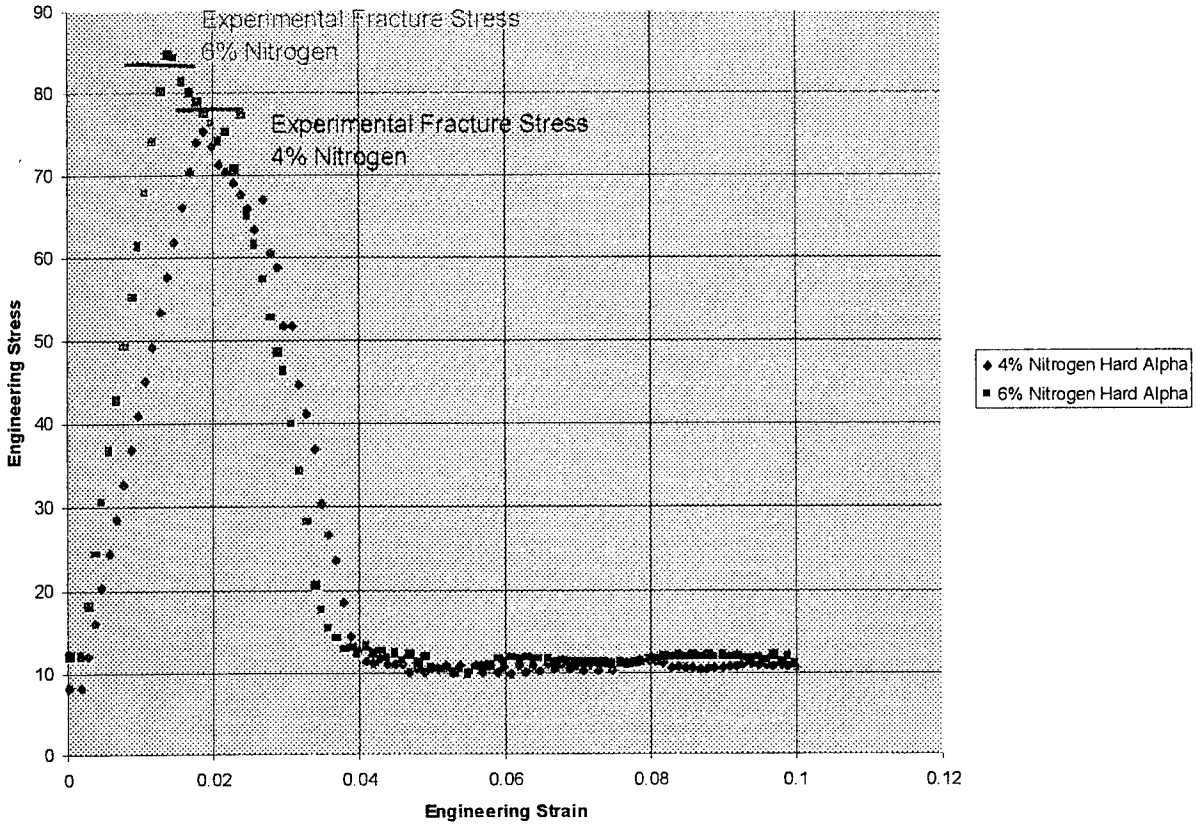


FIGURE 2-24. COMPARISON OF EXPERIMENTAL AND SIMULATION RESULTS FOR THE FRACTURE BEHAVIOR OF 4% AND 6% NITROGEN HARD ALPHA AT 1750°F AT A STRAIN RATE OF 1.0 PER SECOND

2.2.4.6 Mesh Generation and Interpolation.

Due to the special requirements of the microcode in modeling the hard alpha, diffusion zone, and matrix material, the DEFORM™ mesh generator was further enhanced to include the following capabilities:

- Generate a mesh based on given boundary nodes. During the microlevel simulation, the shape of the microvolume is determined by tracking the boundary nodes. The user must have control of the spacing of the boundary nodes to have precise control of the shape of the microvolume (figure 2-25).
- Generate a mesh for the object with an internal hole (figure 2-26).
- Interpolate boundary condition functions from the old mesh to the new mesh.
- Properly interpolate sticking boundary conditions on internal boundaries.

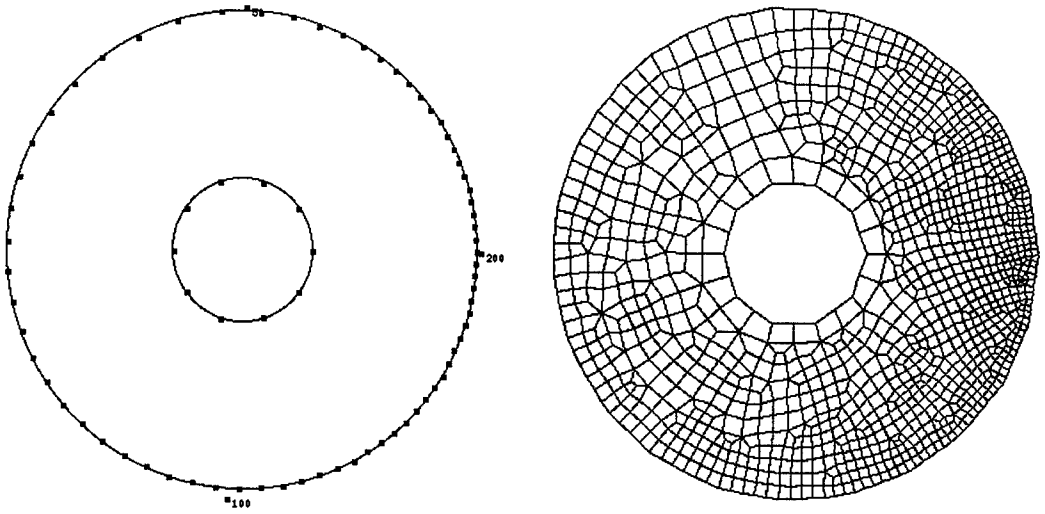


FIGURE 2-25. MESHING BASED ON BOUNDARY NODES

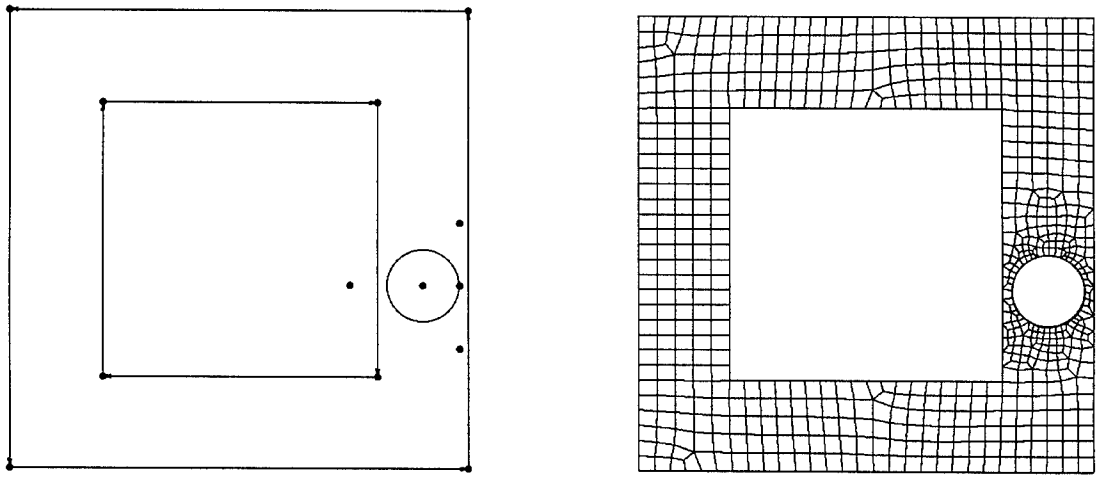


FIGURE 2-26. MESH OF AN OBJECT WITH TWO INTERNAL HOLES

2.2.4.7 Microcode Assessment.

Four microlevel simulations were performed to assess the DEFORM™ microlevel simulation procedure. A macrolevel simulation of seeded billet SB-4 with the hard alpha inclusion centered at the measured radial-axial location of seeds 29, 33, 37, and 41 (see section 2.2.5) was used as macrolevel analysis.

A DEFORM™-2D multiple-operation macrolevel simulation master file of mult SB-4 was the starting point. The operation sequence included:

- Initialize temperature
- Heat transfer during transfer from furnace to die
- Heat transfer while resting on dies
- Dogbone forging
- Initialize temperature
- Heat transfer during transfer from furnace to die
- Heat transfer while resting on dies
- Backflow forging

For any titanium forging, chilling during transfer from the furnace and resting on the die before forging have a significant influence on flow behavior during forging and thus must be accounted for in the DEFORM™ simulation. However, the movement controls in the microlevel simulation are based on the elapsed time in the DEFORM™ database. For the hard alpha simulation to run without the dwell between operations, the time count was adjusted before the second forming operation.

Seed 29 was a cylindrical seed 0.100″ diameter by 0.100″ high with the axis of the cylinder oriented in the hoop direction. The measured radial-axial position was 0.69″ × 12.10″. The inclusion core was modeled as a circle with a radius of 0.050″. The diffusion zone had a radius of 0.100″. A microvolume radius of 0.500″ was simulated. The nitrogen content of the inclusion was a uniform 12%. The nitrogen content of the diffusion zone decreased linearly from 4% at the inside diameter (ID) to 0% at the outside diameter (OD).

Absolute boundary density was used in specifying the mesh density for each object. At the completion of the simulation, a boundary node density of 145 nodes/inch was used for the hard alpha inclusion. A boundary density of 80 nodes/inch was used for both the inside and outside diameters of the diffusion zone. A boundary density of 120 nodes/inch was used for the inside of the microvolume, and 33 nodes per inch for the outside.

Screen captures showing initial mesh, geometry, damage, and stress evolution are shown in figure 2-27 through figure 2-36. Simulations of seeds 33, 37, and 41 are shown in appendix D.

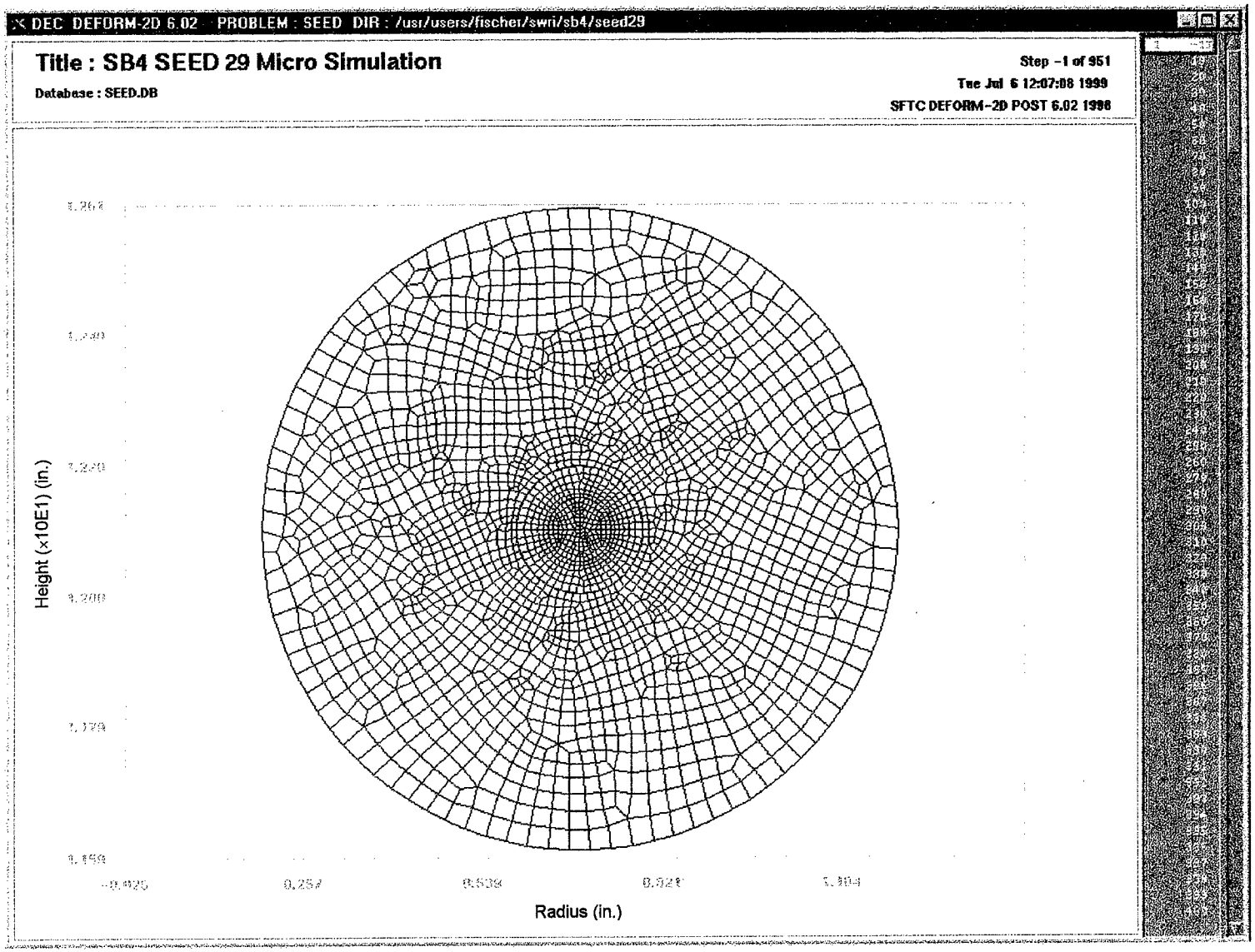


FIGURE 2-27. SEED 29 MICROLEVEL SIMULATION: INITIAL MESH

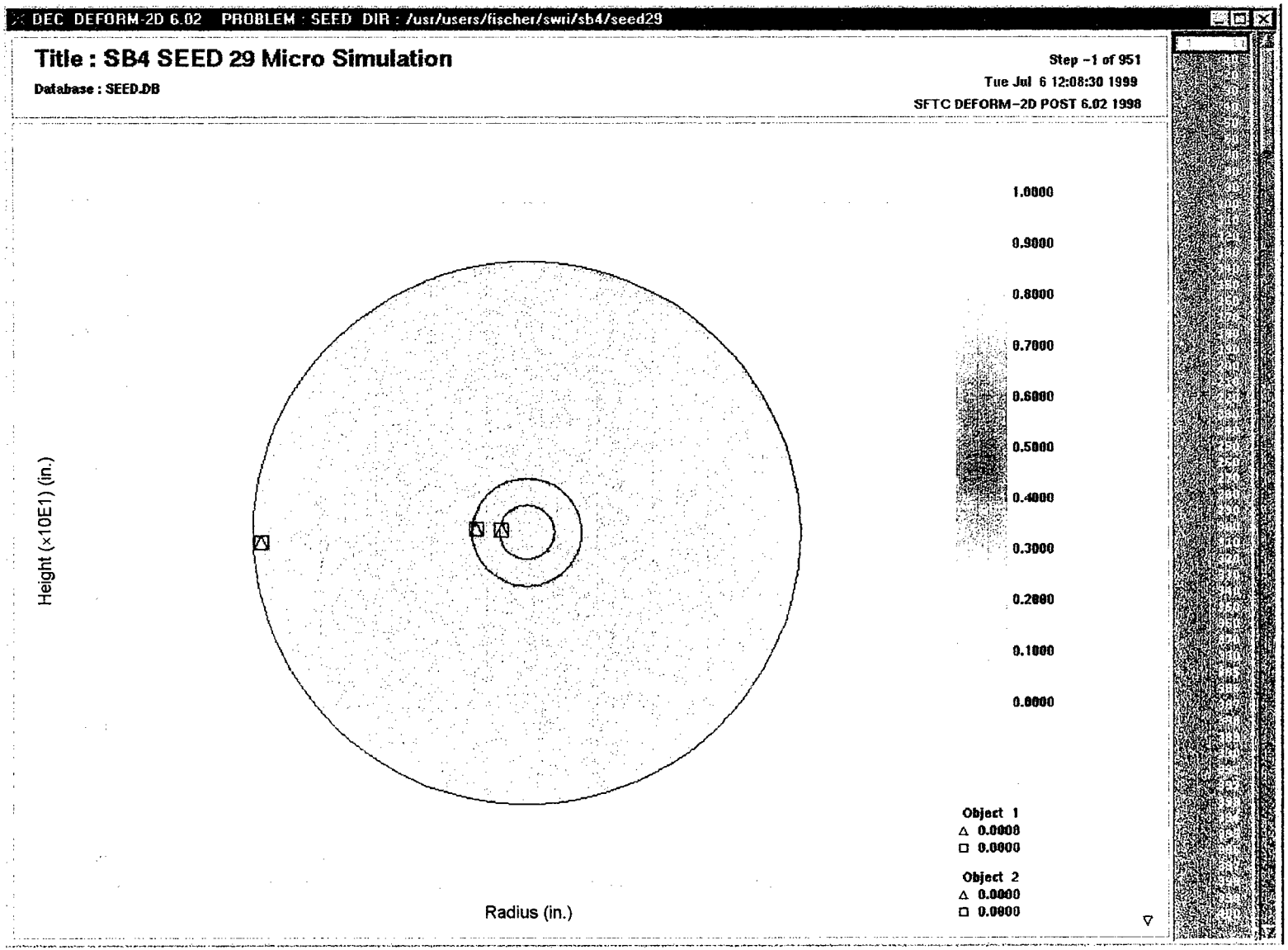


FIGURE 2-28. SEED 29 MICROLEVEL SIMULATION: INITIAL DAMAGE DISTRIBUTION

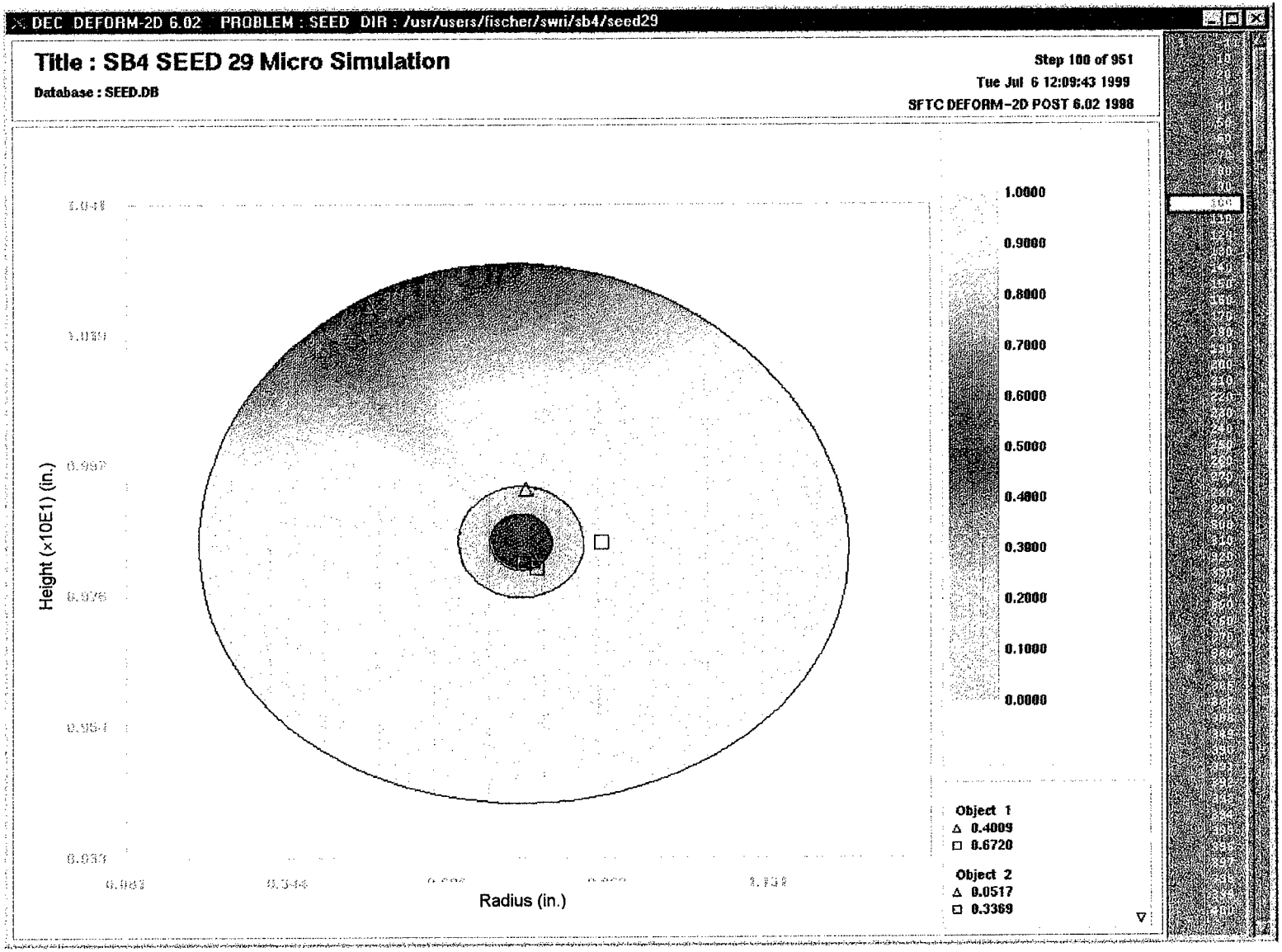


FIGURE 2-29. SEED 29 MICROLEVEL SIMULATION: DAMAGE DISTRIBUTION AT STEP 100

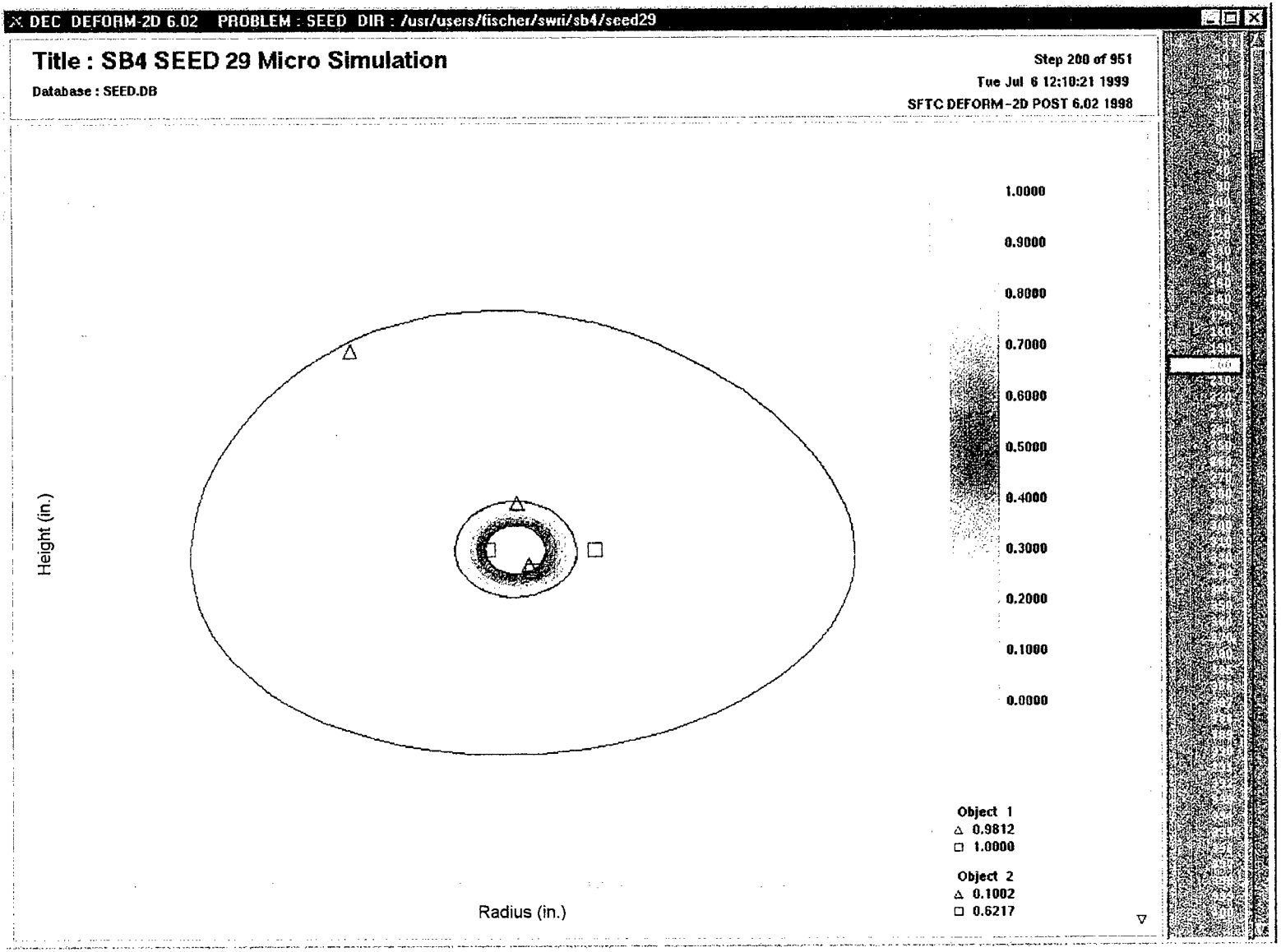


FIGURE 2-30. SEED 29 MICROLEVEL SIMULATION: DAMAGE DISTRIBUTION AT STEP 200

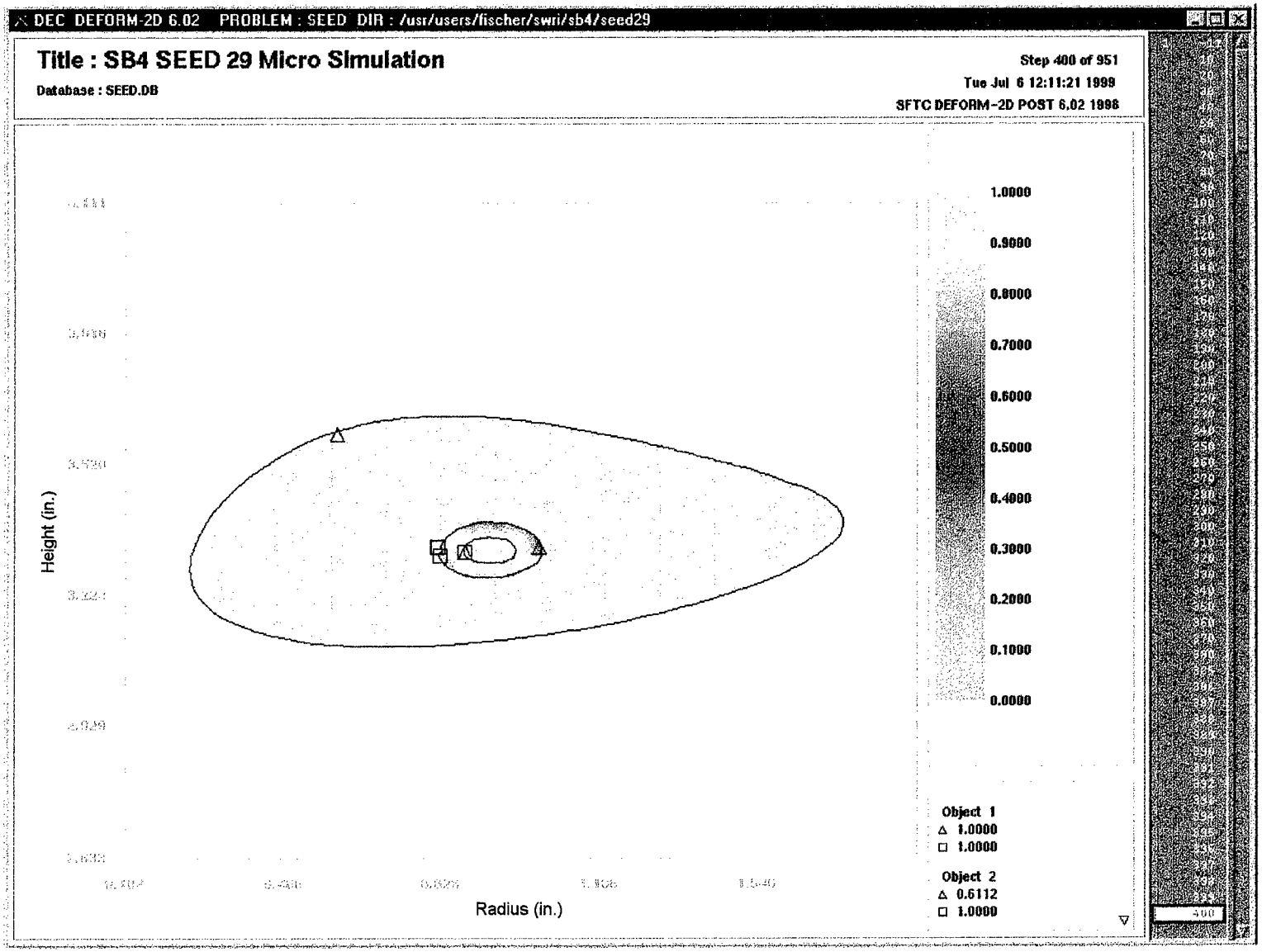


FIGURE 2-31. SEED 29 MICROLEVEL SIMULATION: DAMAGE DISTRIBUTION AT STEP 400

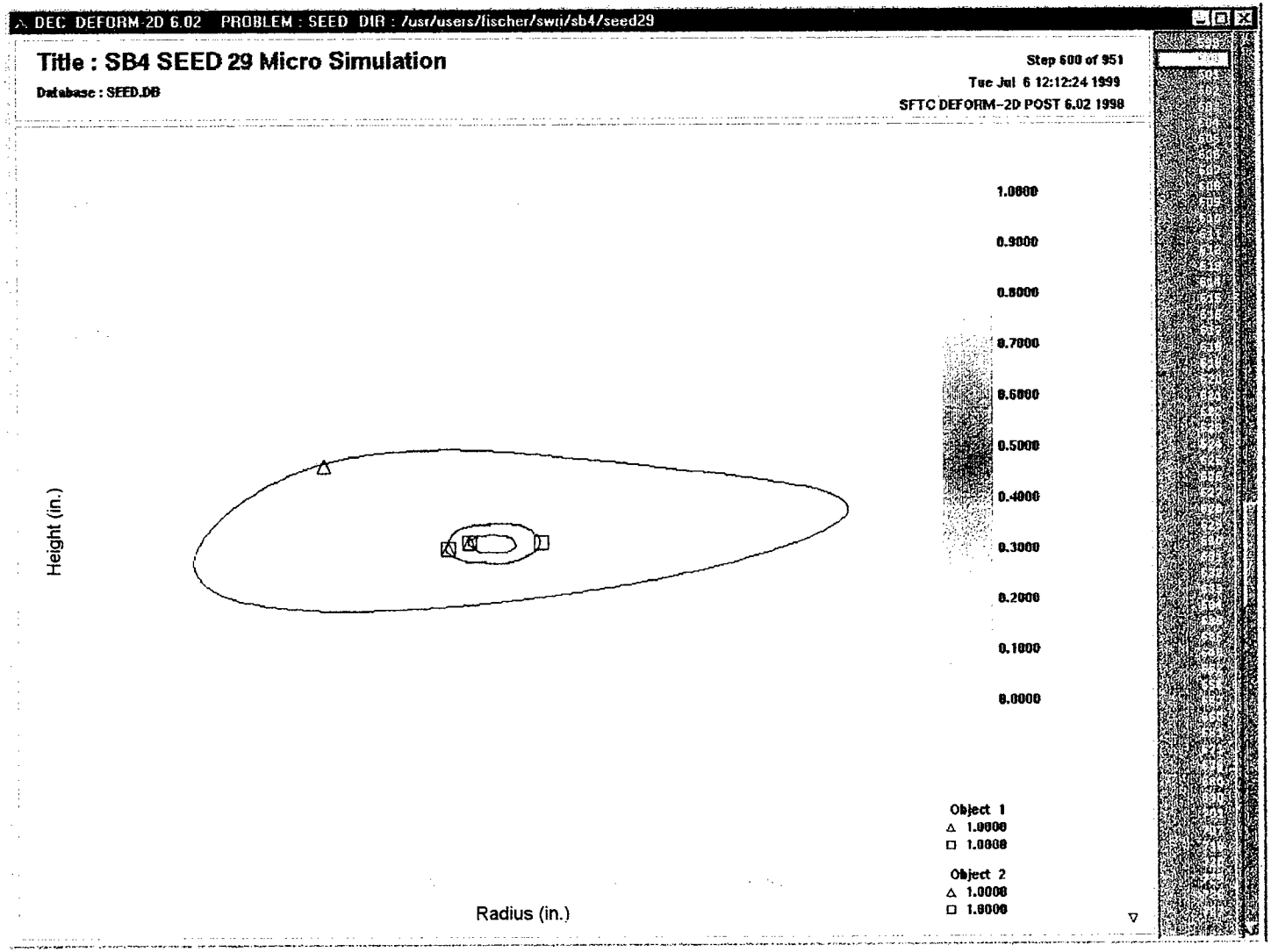


FIGURE 2-32. SEED 29 MICROLEVEL SIMULATION: DAMAGE DISTRIBUTION AT STEP 600
(Note that damage is fully saturated.)

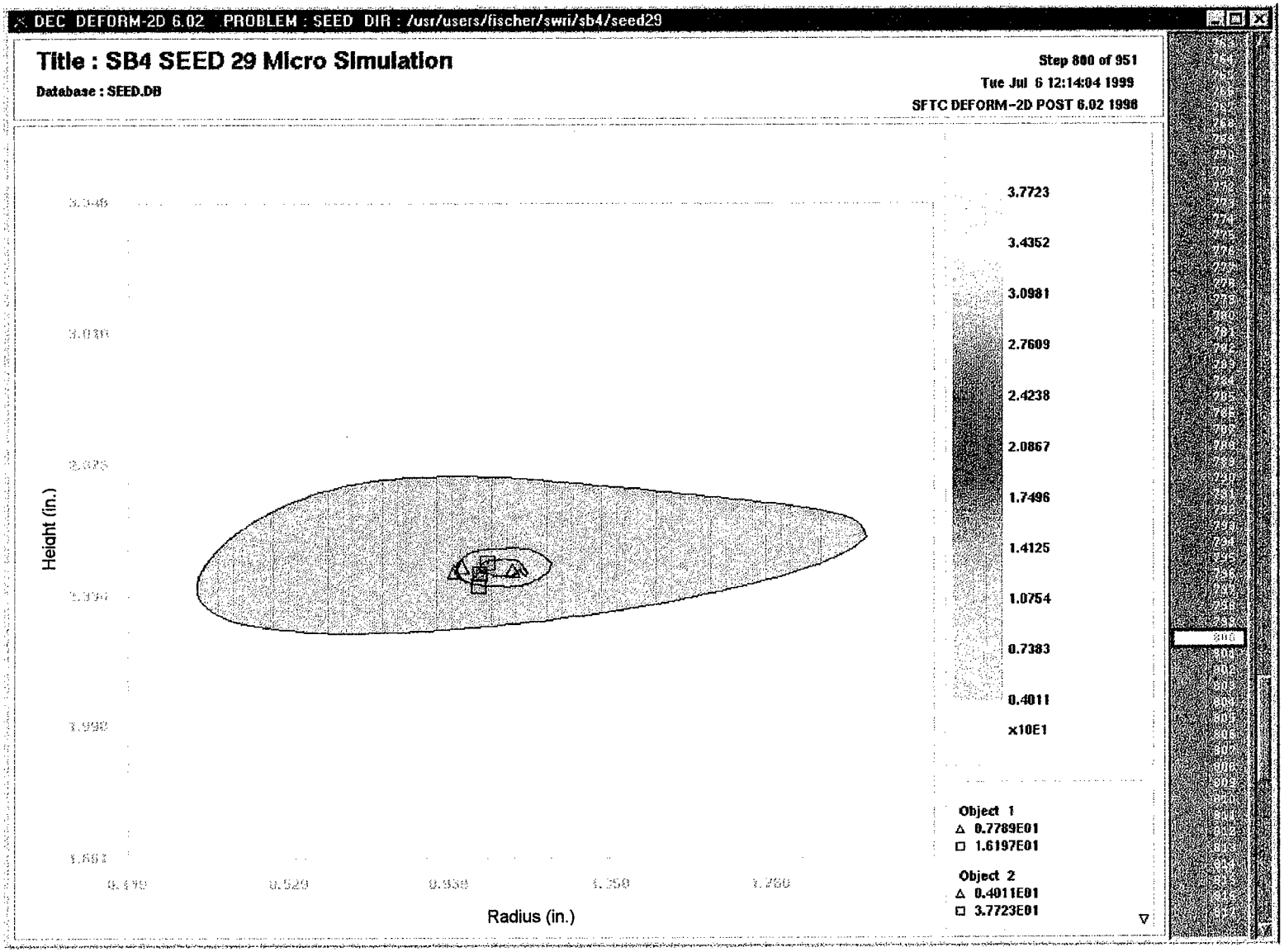


FIGURE 2-33. SEED 29 MICROLEVEL SIMULATION: EFFECTIVE STRESS DISTRIBUTION AT STEP 800

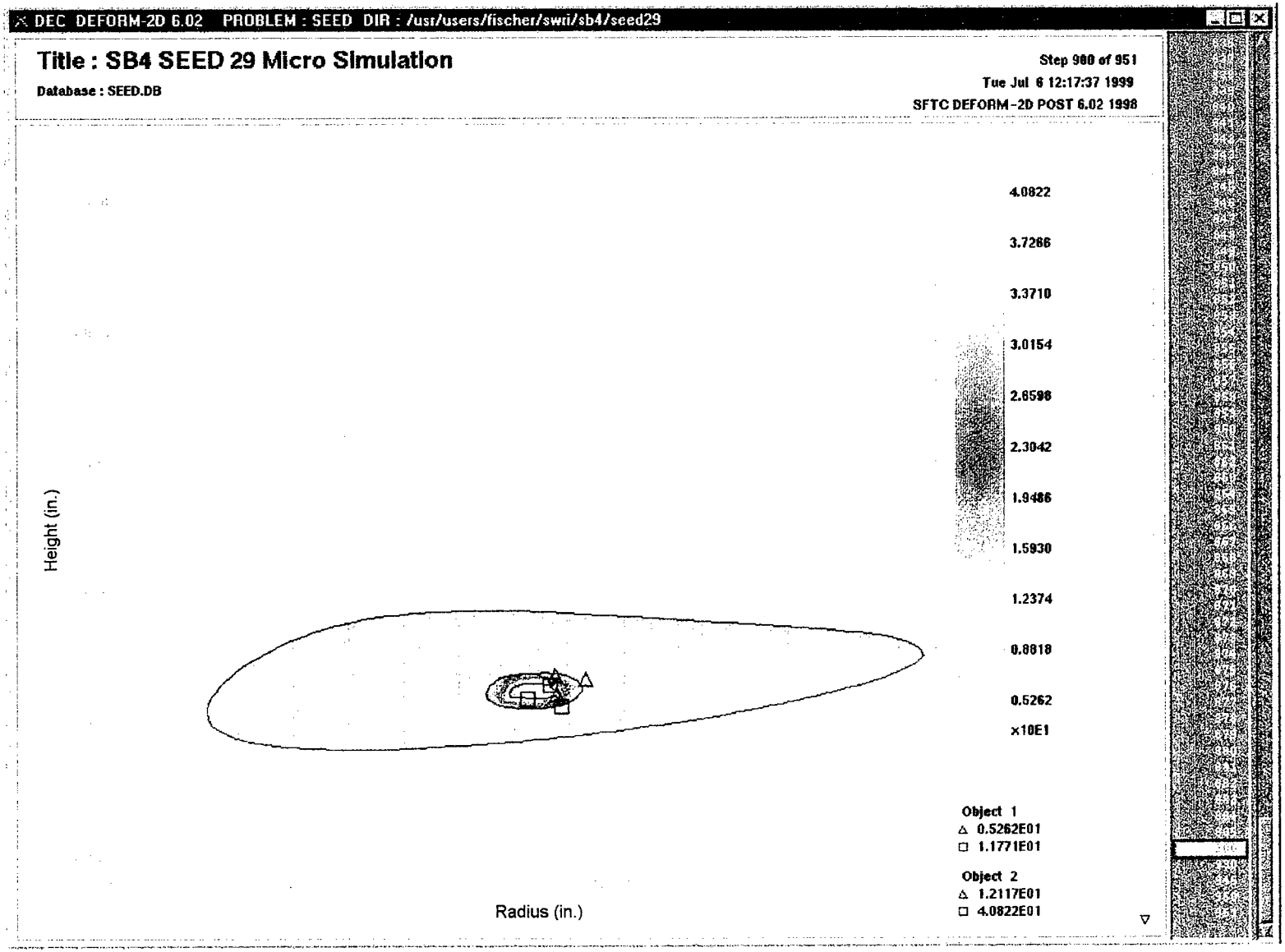


FIGURE 2-34. SEED 29 MICROLEVEL SIMULATION: EFFECTIVE STRESS DISTRIBUTION AT STEP 900

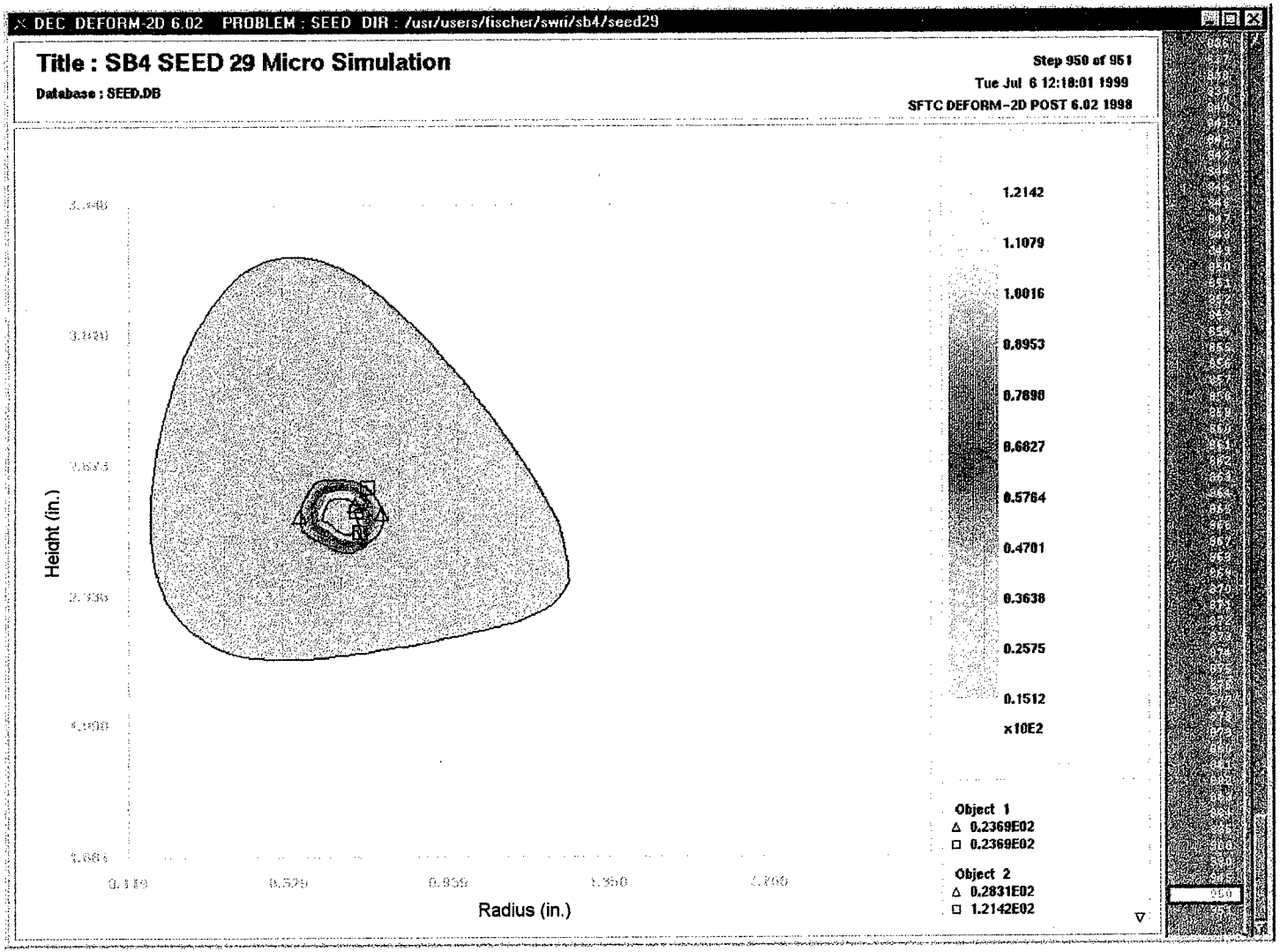


FIGURE 2-35. SEED 29 MICROLEVEL SIMULATION: EFFECTIVE STRESS DISTRIBUTION AT STEP 950, AFTER BACKFLOW FORGING

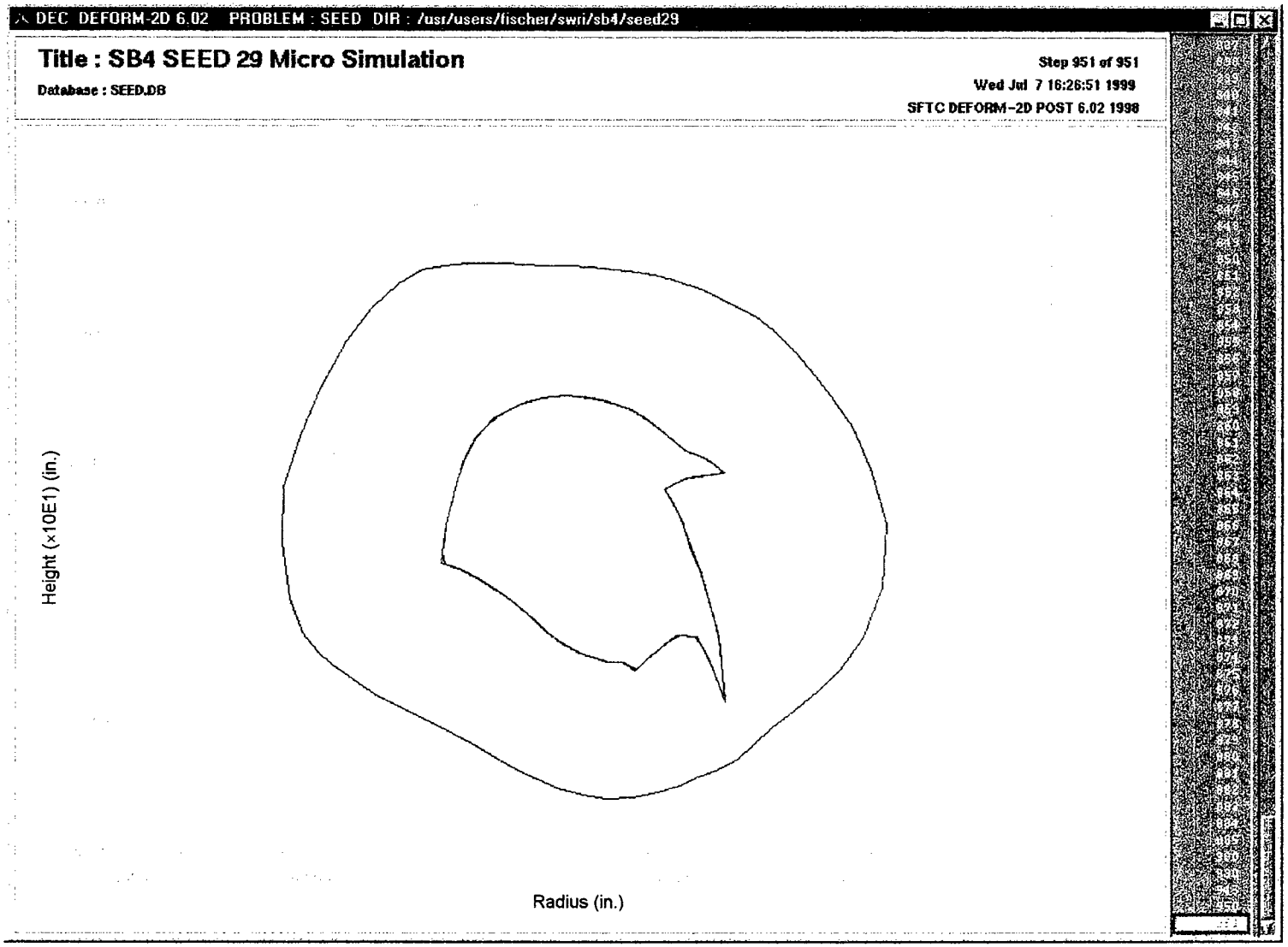


FIGURE 2-36. SEED 29 MICROLEVEL SIMULATION: FINAL GEOMETRY OF DIFFUSION ZONE AND MICROVOLUME

The simulations ran smoothly for 200-300 steps with occasional automatic remeshes, until certain regions of the microvolume began undergoing large deformations. These large localized deformation rates led to very frequent remeshings. Depending on the simulation, 150 to 400 remeshings occurred. Most of the remeshings occurred automatically without intervention due to the robust mesh generator. Several, however, required manual intervention to repair the mesh and continue the simulation. Certain modifications were made to the DEFORM™ software to improve remeshing robustness in these cases. DEFORM™ was designed not to allow more than one remeshing in a step. This was intended to prevent infinite loops if a bad mesh was generated. However, with multiple deforming objects, it prevented two objects from being remeshed on the same step and caused some stops. A new feature was added for a second remesh request on a given restart step. If the remesh request was from the same object that had just been remeshed, the simulation is still stopped. However, if the remesh request is from a different object, the remeshing will commence and the simulation will continue.

The large localized rate of deformations led to extremely high localized strain rates. A maximum strain per step setting of 0.05 had been imposed to maintain the accuracy of the simulation and prevent excessive mesh degradation. However, this limit also produced extremely small time steps and, combined with the frequent remeshings, very large database file sizes. In addition, large nonuniform deformation of the matrix material object made remeshing with the originally specified boundary nodes impractical. Thus, it was necessary to implement a method for interpolating boundary node position functions based on adjoining functions.

In the originally proposed approach, which is currently implemented, all outer boundary nodes of the matrix material object follow a predetermined path. The volume of the microvolume is forced to dilate or contract based on the boundary conditions from the macrolevel analysis. In DEFORM™, volume constancy is enforced using a large penalty constant [10]. The velocity field in the microlevel simulation must satisfy both the position boundary condition (predetermined volume path) and volume constancy (large penalty on velocity fields with nonconstant volume). It was suspected that incompatibility of the position boundary condition and volume constancy of the interior caused difficulties in convergence and extremely localized deformation. By reducing the penalty constant, the constraint for volume constancy was relaxed. All convergence difficulties disappeared and the simulations ran to completion with less frequent remeshings and much more reasonable time stepping.

2.2.4.9 Postprocessing of Microlevel Simulation Output.

The deformation microcode is based on a 2D axisymmetric or plane strain model. To more accurately establish the shape of the hard alpha anomaly, relationships were generated between the defect deformation and the forging macrostrain, and then these relationships were used to approximate the 3D defect deformation in a forging. This capability will be used eventually to update the hard alpha defect distribution.

Parametric studies with the microcode were performed to evaluate the influence of the following variables on defect deformation. All the major variables that influence the deformation of the inclusion were included.

- Nitrogen content in the inclusion
- Nitrogen content in the surrounding diffusion zone
- The size of the diffusion zone relative to the inclusion size
- Initial shape of the inclusion defined as its aspect ratio
- Macroforging strain rate
- Macroforging temperature
- Hydrostatic pressure

The microcode was run with various values of the above variables. The runs were defined based on Design of Experiment (DOE) principles to obtain the most information from the fewest number of runs. A full factorial matrix of 2**7 (=128) runs was made. A UNIX-based script file was developed which automatically setup each run, submitted the simulation, extracted the strain information from the output data base, and stored the results in a file compatible for statistical analysis using the software package MINITAB. The finite element mesh consisted of approximately 100 elements in the inclusion, 400 in the diffusion zone, and 700 in the base material. Each simulation was completed in 300 time steps with a macrostrain of 0.005 per time step to reach a final macrostrain of 1.5. Each run took about 30 minutes, on average, on a HP C160 workstation.

A low and a high level for each of the seven variables listed above were selected to represent the extremes for that variable. The microcode was run-up to a total macrostrain of 1.5, and the inclusion strain was extracted from the output at a total of six intermediate and final values of the macrostrain. A total effective strain of 1.5 corresponds to: (a) a diameter reduction of about 47% during ingot conversion (i.e., 20″ diameter reduced to about 10″ diameter) or (b) a height reduction of about 78% during upsetting of a billet (i.e., 10″ high mult reduced to 2.2″ high). The DOE levels of variables are shown in table 2-1.

TABLE 2-1. DESIGN OF EXPERIMENT VARIABLES

No.	Variable	Variable Name	High and Low levels
1.	HN2	Inclusion N2 content (%)	4, 8
2.	DN2	Diffusion zone N2 content (%)	1, 3
3.	DZH	Ratio of diffusion zone size to inclusion size	2, 4
4.	ASP	Aspect ratio of inclusion	1, 3
5.	STR	Strain rate (1/sec)	0.1, 1.0
6.	TEM	Temperature (°F)	1550, 1750
7.	PRS	Hydrostatic pressure (ksi)	10, 100
8.	STM	Macroforging strain	0.25, 0.5, 0.75, 1.0, 1.25, 1.5

The results of all the 128 runs are shown in figure 2-37. This figure shows at a glance the overall dependence of the inclusion strain as a function of the forging macrostrain.

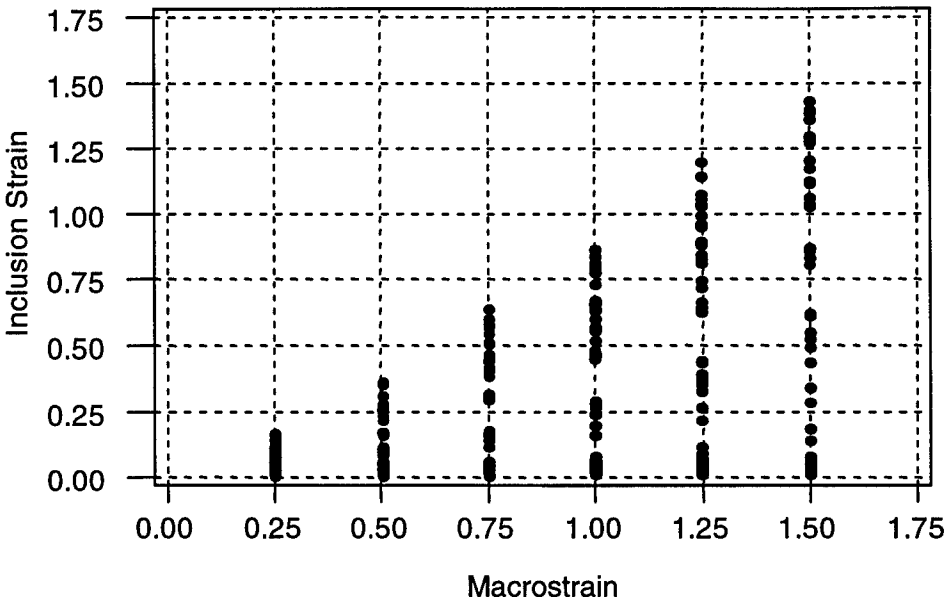


FIGURE 2-37. INCLUSION STRAIN AS A FUNCTION OF FORGING MACROSTRAIN

Figures 2-38 to 2-44 show the dependence of the inclusion strain on each independent variable, the data being averaged out over the other variables. A discussion of the dependence of inclusion strain on each variable follows.

a. Nitrogen content in the inclusion (figure 2-38): The dependence on the inclusion nitrogen content is not very significant at 4% and 8%. The inclusion flow stress is higher at 8% than at 4%, which results in a lower inclusion strain at 8%. The nitrogen dependence of the flow stress of failed hard alpha is given by (55.44 + 4.558N) ksi. Therefore, the difference in flow stress at 4% and at 8% nitrogen contents is about 25%, which is not very significant.

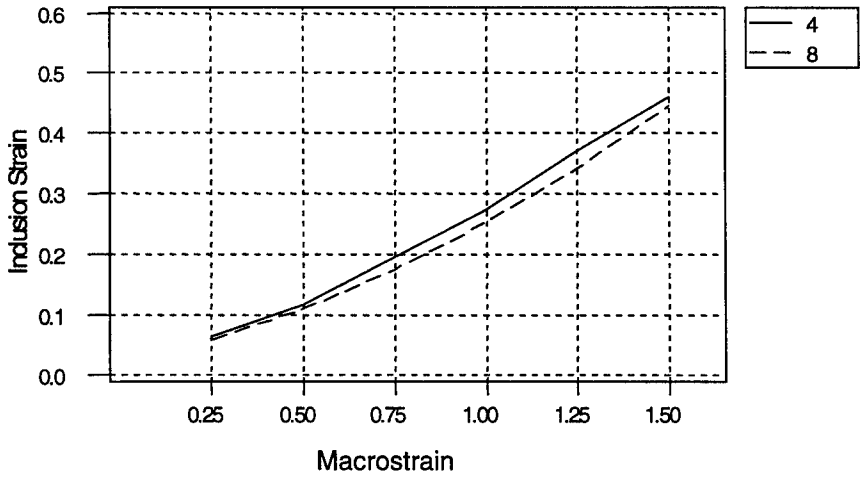


FIGURE 2-38. INCLUSION STRAIN DEPENDENCE ON INCLUSION NITROGEN CONTENTS OF 4% AND 8%

b. Nitrogen content in the surrounding diffusion zone (figure 2-39): The higher the nitrogen content of the diffusion zone, the higher its flow stress and, therefore, the higher the strain imparted to the inclusion. However, if the diffusion zone has a higher flow stress, it would itself deform less and, therefore, would be less able to impart a smaller strain to the inclusion. The overall effect on the inclusion strain is a balance of these two factors.

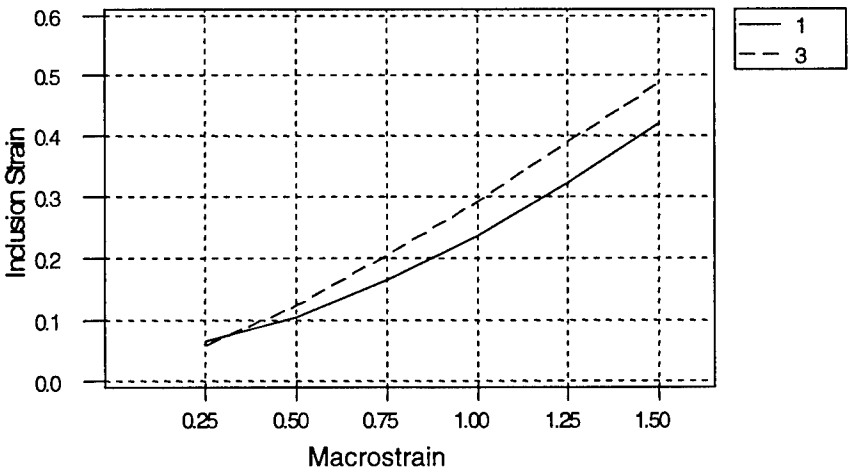


FIGURE 2-39. INCLUSION STRAIN DEPENDENCE ON DIFFUSION ZONE NITROGEN CONTENTS OF 1% AND 3%

c. The size of the diffusion zone relative to the inclusion size (figure 2-40): The inclusion strain increases as the size of the diffusion zone relative to the inclusion increases. As the diffusion zone gets larger, there is a larger volume of higher flow stress material (as compared to the base material) surrounding the inclusion, which causes the inclusion to undergo more deformation.

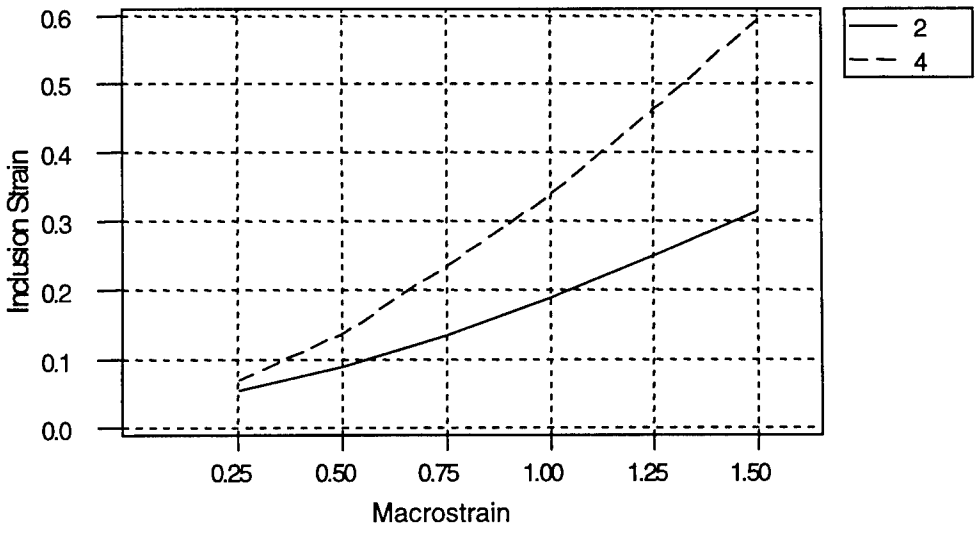


FIGURE 2-40. INCLUSION STRAIN DEPENDENCE ON DIFFUSION ZONE TO INCLUSION SIZE RATIOS OF 2 AND 4

d. Initial shape of the inclusion defined as its aspect ratio (figure 2-41): The aspect ratio is defined as the ratio of the dimension in the direction of the tensile strain direction to that in the direction of the compressive strain. A spherical inclusion (aspect ratio 1) undergoes less strain than one elongated in the tensile strain direction (aspect ratio 3). The geometry of the inclusion has an influence on how the stresses from the deformation of the base material get transmitted to the inclusion and hence on its deformation.

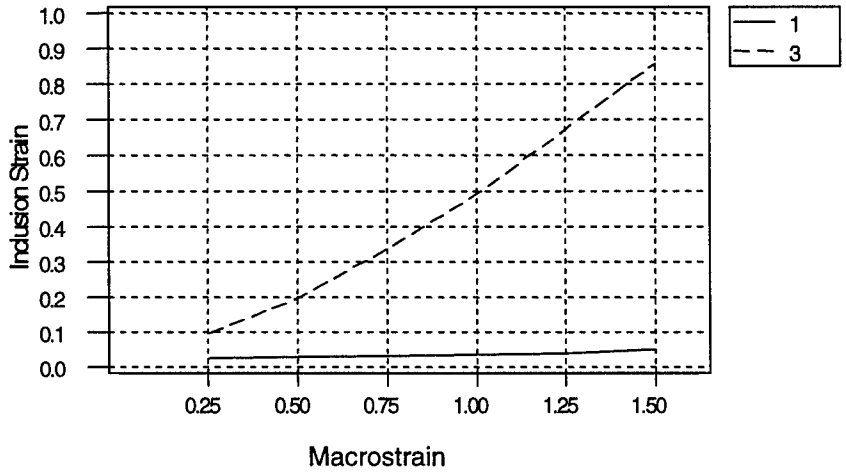


FIGURE 2-41. INCLUSION STRAIN DEPENDENCE ON INCLUSION ASPECT RATIOS OF 1 AND 3

e. Macroforging strain rate (figure 2-42): As the macroforging strain rate increases, the flow stress of the base material increases relative to that of the inclusion and the diffusion zone. This is because the flow stress of the base material is more sensitive to strain rate than the flow stress of the inclusion or the diffusion zone. This causes the flow stress differential between the base material and the inclusion to decrease with increasing strain rate resulting in larger inclusion strains at higher strain rates.

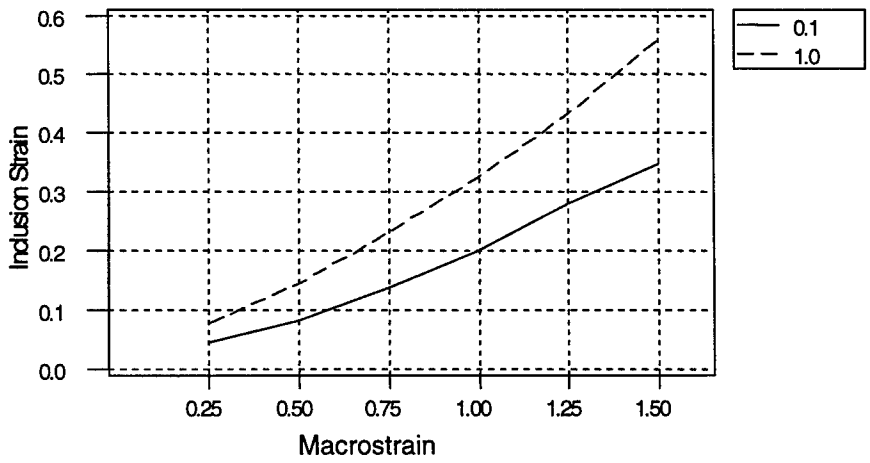


FIGURE 2-42. INCLUSION STRAIN DEPENDENCE ON STRAIN RATES OF 0.1 AND 1.0 PER SECOND

f. Macroforging temperature (figure 2-43): As the forging temperature decreases, the flow stress of the base material increases relative to that of the inclusion and the diffusion zone. This is because the flow stress of the base material is more sensitive to temperature than the flow stress of the inclusion or the diffusion zone. This causes the flow stress differential between the base material and the inclusion to decrease with decreasing temperature resulting in larger inclusion strains at lower temperatures.

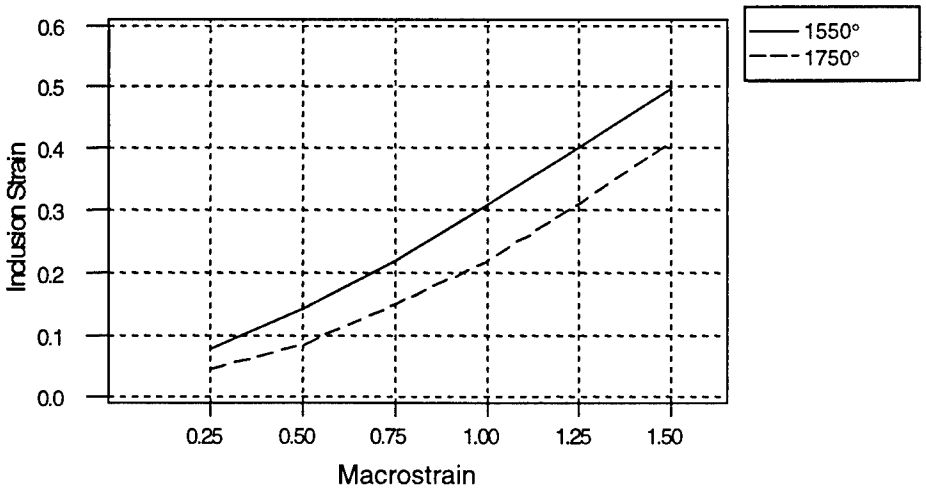


FIGURE 2-43. INCLUSION STRAIN DEPENDENCE ON TEMPERATURES OF 1550° AND 1750°F

g. Hydrostatic pressure (figure 2-44): The inclusion strain shows a very weak pressure dependence. The pressure enters the inclusion flow stress as a log term, which causes its influence to be small. The microcode has the option of specifying the pressure-time relation through an input file or calculating the pressure internally from the dilatational strain and the penalty constant. The microcode was run both ways, and the results were almost identical, providing another confirmation of the weak pressure dependence.

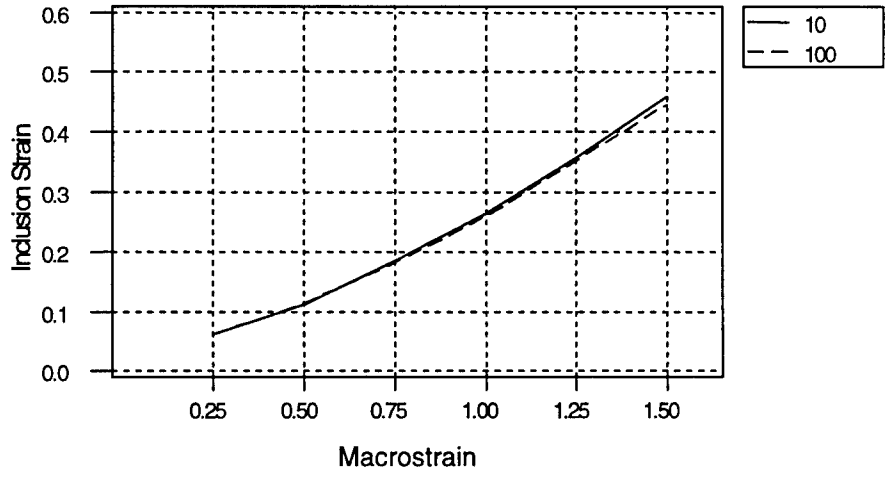


FIGURE 2-44. INCLUSION STRAIN DEPENDENCE ON PRESSURES OF 10 AND 100 ksi

A regression analysis was conducted to obtain the inclusion strain as a function of the variables investigated. In order to obtain a good fit and keep all the coefficients about the same order of magnitude, the independent variables were normalized in the (-1,1) range as in table 2-2.

TABLE 2-2. INPUT FOR REGRESSION ANALYSIS

No.	Variable	Variable Number	2 levels	Normalized
1.	HN2	Inclusion N2 content (%)	4, 8	hn=(HN2-6)/2
2.	DN2	Diffusion zone N2 content (%)	1, 3	dn=(DN2-2)/1
3.	DZH	Diffusion: Inclusion size	2, 4	dh=(DZH-3)/1
4.	AST	Aspect ratio of inclusion	1, 3	as=(ASR-2)/1
5.	STR	Strain rate (1/sec)	0.1, 1.0	sr=(STR-0.55)/0.45
6.	TEM	Temperature (°F)	1550, 1750	te=(TEM-1650)/100
7.	PRS	Pressure (ksi)	10,100	pr=(PRS-55)/45
8.	STM	Macroforging strain		Not normalized

The following equation was obtained relating the inclusion strain to the normalized values of the variables investigated:

$$\begin{aligned} STH = {} & -0.038970 - 0.008196\,hn + 0.020389\,dn + 0.066993\,dh + 0.203279\,as \\ & + 0.056756\,sr - 0.035618\,te - 0.002320\,pr + 0.31641\,stm \end{aligned} \qquad (2\text{-}14)$$

R-sq, which indicated the goodness-of-fit, equaled 60.5%. An R-sq value of 90% or greater indicates a very good fit. So the goodness-of-fit was moderate with this data. The sign of the coefficients confirmed the observations from the other plots. A negative coefficient indicated that the inclusion strain decreases as the value of that variable increases and vice versa.

Figure 2-45 shows JETQC data for hard alpha analyzed by RISC (see appendix A). The similarity of this plot to the computed results in figure 2-37 is apparent.

The DOE-based runs were used to develop a correlation between the forging induced macrostrain and the inclusion deformation. After the forge modeling of the component forging is completed, the forging macrostrain components in the three directions are available throughout the forging. These strain components can be converted to equivalent inclusion strain components using the relationships developed here. The inclusion strains can then be used to modify the defect distribution to be used in lifing analysis. This results in an approximation of the 3D defect deformation in a forging from a 2D micromodel This could provide zone dependent scaling factors to the defect distribution based on macrodeformation modeling of the component forging process. With this procedure the need for running the micromodel for each individual point in the forging with different strain components is avoided, and this significantly reduces the required effort. The regression equations developed here can be used with DEFORM^{TM}-2D or 3D output for billet conversion and for component forging.

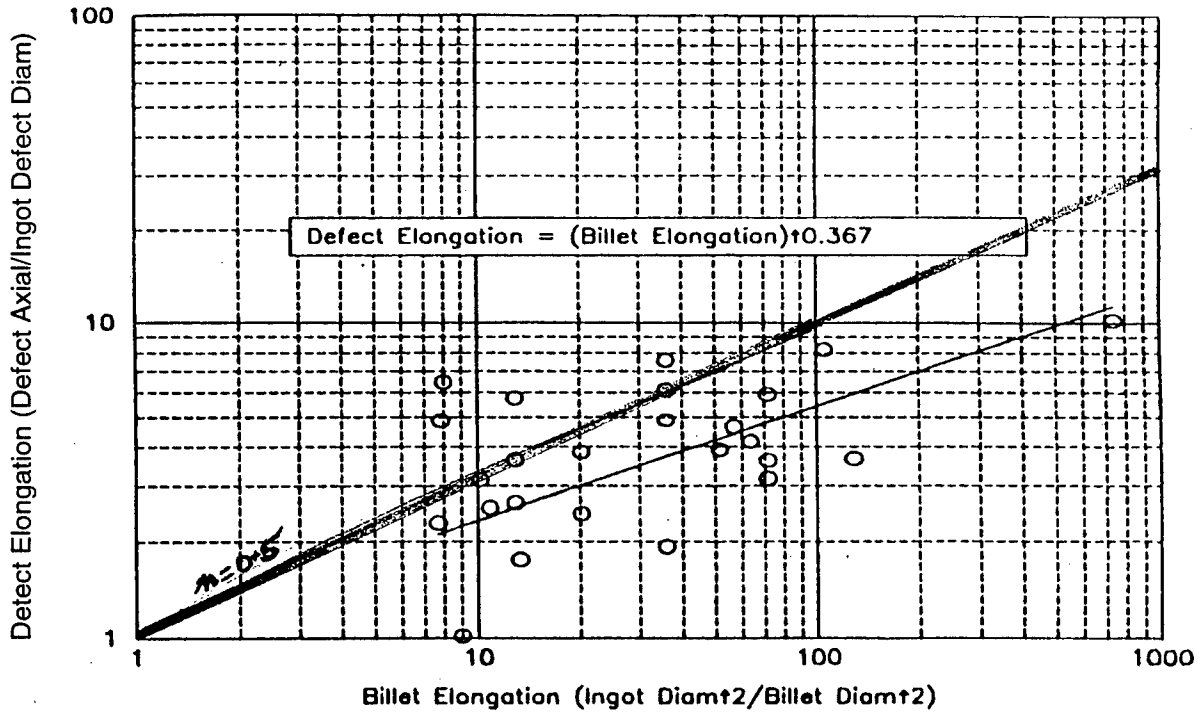
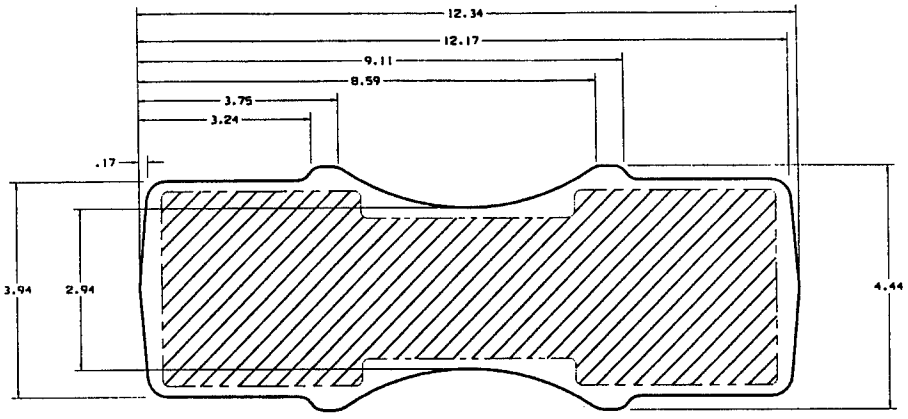


FIGURE 2-45. JET ENGINE TITANIUM QUALITY COMMITTEE DATA FOR DEFECT ELONGATION VS BILLET ELONGATION AS ANALYZED BY RISC
(Note the similarity to the computed results in figure 2-37. N = 0.5 corresponds to defect deformation equaling the billet deformation.)

2.2.5 Forging Experiments to Validate Microcode.

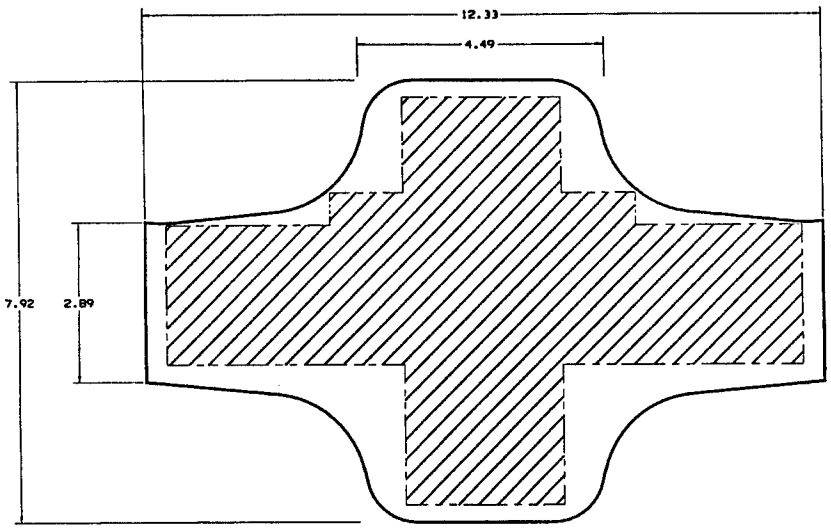
The objective of this task was to validate the DEFORM^{TM}-2D microcode's ability to predict the morphology of simulated hard alpha defects, as parts containing defects undergo a typical forging conversion operation. (Completion of the validation studies will occur in a follow-on program that includes metallographic characterization of the hard alpha defects evaluated in the forgings described in this section.) Further validation of the DEFORM^{TM} forging model was provided by the prediction and detection of the movement of hard alpha defects upon forging typical rotor shapes.

Three different forged shapes were selected for the microcode validation. Two of the shapes were stylized rotor forging shapes designated "dogbone" and "backflow." The dogbone shape (figure 2-46) represented a typical flat disk with a thickened rim area. The backflow shape (figure 2-47) had a heavy hub, thinner rim, and was forged from a dogbone forging produced in an interim operation. Both forgings weighed nominally 75 lbs. The purpose of the backflow shape was to create metal flow outward during the initial dogbone forging operation and then reverse the metal flow inward toward the hub, making it possible to determine the effect of reverse metal flow on hard alpha particles. After arriving at acceptable forging shapes for both parts, machining drawings were created, as shown in figures 2-48 and 2-49. The dogbone and backflow parts were forged at Schlosser Forge Company using hot-die techniques.



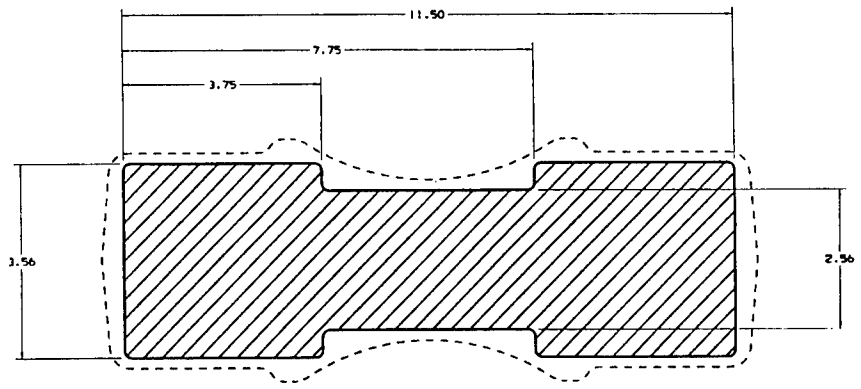
Note: Dimensions shown are approximate. Schlosser Forge Co. will guarantee parts to clean-up within 0.060 of Finish Dimensions. Local deviations and grindouts are acceptable and are not reason for rejection.
Ref. B/P # 95-G-041
Forge wt. 73.0 CALC

FIGURE 2-46. OUTLINE OF DOGBONE FORGING WITH PHANTOM LINES SHOWING MACHINED PART



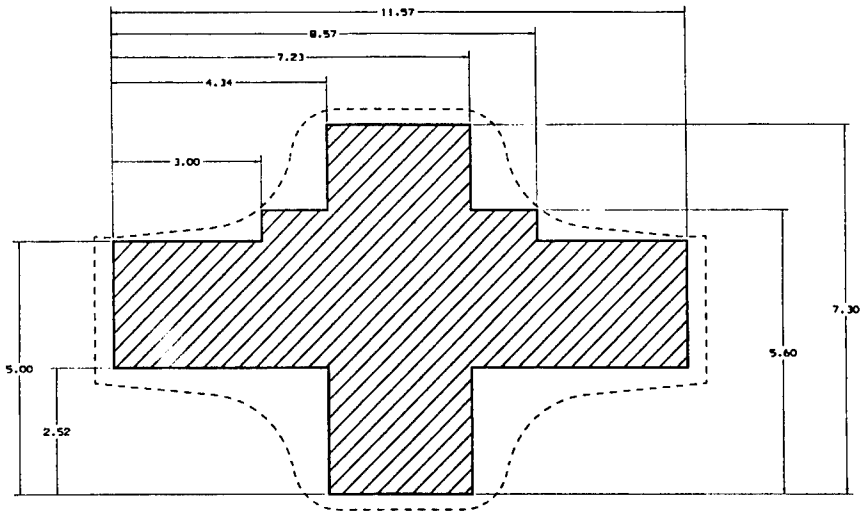
Note: Dimensions shown are approximate. Schlosser Forge Co. will guarantee parts to clean-up within 0.060 of Finish Dimensions. Local deviations and grindouts are acceptable and are not reason for rejection.
Ref. B/P # 95-G-041
Forge wt. 73.0 CALC

FIGURE 2-47. OUTLINE OF BACKFLOW FORGING WITH PHANTOM LINES SHOWING MACHINED PART



Note: All dimensions ± 0.03 unless otherwise noted.

FIGURE 2-48. MACHINE DRAWING OF DOGBONE FORGING



Note: All dimensions ± 0.03 unless otherwise noted.

FIGURE 2-49. MACHINE DRAWING OF BACKFLOW FORGING

The third shape (figure 2-50) selected for the validation effort was an actual current production engine component manufactured by Pratt & Whitney (P&W). The engine disks were produced at P&W Georgia by first forging simple pancake shapes and then finishing them in a second press forging operation. Both the pancakes and the engine disks were forged using isothermal press forging. Photos for the mults, pancakes, and disks are included in appendix E.

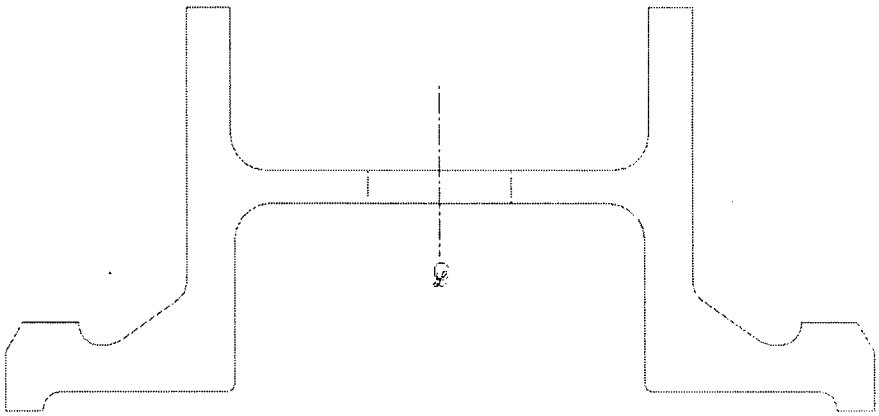


FIGURE 2-50. SONIC SHAPE OF DISK FORGINGS

Input stock for the forgings was from two basic sources. Six forgings (three dogbone, one backflow, and two engine) were produced using Ti-64 mults with multiple artificial hard alpha seeds. An additional three forgings (two engine and one pancake) were produced from RMI Titanium Co. Contaminated Billet Study (RMI CBS) billets furnished by the Engine Titanium Consortium (ETC) and containing natural hard alpha defects. All billets were nominally 6.0 to 6.5 inches in diameter. Table 2-3 describes the forging identification, configuration, and hard alpha type.

TABLE 2-3. DESCRIPTION OF FORGINGS USED IN THE VALIDATION STUDY

Forging Description				
Forging Number	Interim Shape	Final Shape	Billet Type	Number of Defects
SB-1	N/A	Dogbone	Seeded	6
SB-2	N/A	Dogbone	Seeded	6
SB-3	N/A	Dogbone	Seeded	4*
SB-4	Dogbone	Backflow	Seeded	4*
SB-5	Pancake	Engine	Seeded	4
SB-6	Pancake	Engine	Seeded	1
B1BW3-B	Pancake	Engine	RMI CBS	1
B3W3-E	Pancake	Engine	RMI CBS	1
B3W2-G	N/A	Pancake	RMI CBS	1
* Each defect consisted of multiple cluster				

The seeds in the mults for the dogbone and backflow forgings, SB-1 through SB-4, and the disk forgings, SB-5 and SB-6, were placed by the GE Corporate Research & Development Center (GE CRD). The artificial hard alpha seeds were produced by GE CRD using a proprietary process. Multiple seeds were used in the seeded forgings, as listed in table 2-4. Forgings SB-1 and SB-2 had six seeds each. Forgings SB-3 and SB-4 had four seeds each, with each defect containing multiple clusters of four seeds.

TABLE 2-4. DESCRIPTION OF ARTIFICIAL SEEDS AND ASSOCIATED VALIDATION CASES EVALUATED IN SEEDED FORGINGS

	Seed Description			
	Seed Number	N2	Description	Validation Case
SB-1	1	Was Beta	Was Beta shell	Elongation of defect
	2	Was Beta	Was Beta shell	Elongation of defect
	3	12%	High N2 with diffusion zone	Fracture and voiding
	4	12%	High N2 with diffusion zone	Fracture and voiding
	5	12%	High N2 without diffusion zone	Fragmentation
	6	12%	High N2 without diffusion zone	Fragmentation
SB-2	7	Was Beta	Was Beta shell	Elongation of defect
	8	Was Beta	Was Beta shell	Elongation of defect
	9	12%	High N2 with diffusion zone	Fracture and voiding
	10	12%	High N2 with diffusion zone	Fracture and voiding
	11	12%	High N2 without diffusion zone	Fragmentation
	12	12%	High N2 without diffusion zone	Fragmentation
SB-3	13,14,15,16	12%	High N2 with diffusion zone (4 seed cluster)	Reconstitution of multiple seeds
	17,18,19,20	12%	High N2 with diffusion zone (4 seed cluster)	Reconstitution of multiple seeds
	21,22,23,24	12%	High N2 with diffusion zone (4 seed cluster)	Reconstitution of multiple seeds
	25,26,27,28	12%	High N2 with diffusion zone (4 seed cluster)	Reconstitution of multiple seeds
SB-4	29,30,31,32	12%	High N2 with diffusion zone (4 seed cluster)	Reconstitution of multiple seeds
	33,34,35,36	12%	High N2 with diffusion zone (4 seed cluster)	Reconstitution of multiple seeds
	37,38,39,40	12%	High N2 with diffusion zone (4 seed cluster)	Reconstitution of multiple seeds
	41,42,43,44	12%	High N2 with diffusion zone (4 seed cluster)	Reconstitution of multiple seeds
SB-5	45,46,47,48	12%	High N2 with diffusion zone	Fracture and voiding
SB-6	49	12%	High N2 with diffusion zone	Fracture and voiding

Seed placement in the mults for the forgings was facilitated by using a DEFORM™ macrolevel forging simulation and its point tracking feature. The criteria for seed locations in the SB-1 through SB-4 forgings were that they must be in an inspectable (ultrasonic) location, must have at least 1.0 effective strain, and must be in a widely dispersed pattern where adjacent seeds have no influence on each other. DEFORM PC Pro running on a stand-alone 175-MHz PC was used for seed placement. Through an iterative process of DEFORM™ runs and seed location adjustment, the seeding plan was established. The results of point tracking for dogbone forgings SB-1 and SB-2 are shown in figure 2-51. The results of DEFORM point tracking for dogbone/backflow forgings SB-3 and SB-4 are shown in figure 2-52. Strain maps for the dogbone and backflow forgings are shown in figure 2-53. All of the seed locations met the inspectability and strain requirements.

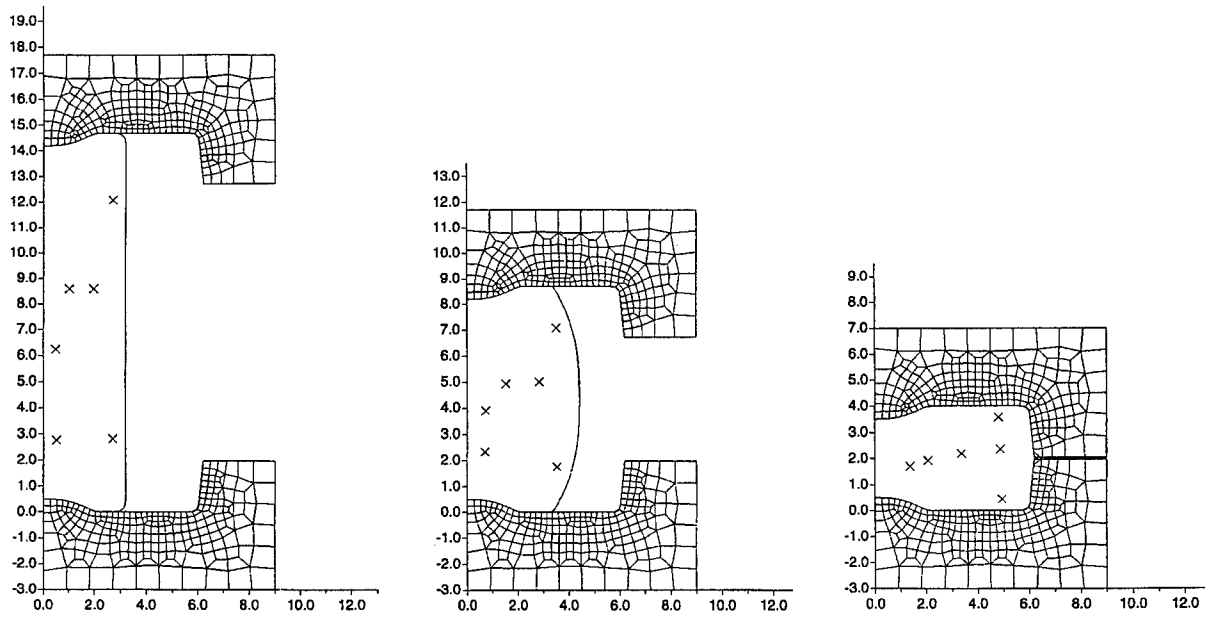


FIGURE 2-51. DEFORM™ POINT TRACKING OF HARD ALPHA SEEDS IN DOGBONE FORGING AT START, 50% DEFORMATION, AND 100% DEFORMATION
(The scales are in inches.)

The seed locations are summarized in table 2-5. The locations of the seeds are described as a height and radius in a mult of 6.4 in. diameter by 15 in. length. The seeds were produced as cylinders approximately 0.100 inch in diameter by 0.200 inch in length for the 12% nitrogen without diffusion zone. The "Was Beta" (diffusion zone only) and the 12% nitrogen with diffusion zone were cylinders approximately 0.200 inch in diameter by 0.200 inch in length. The cores in the 12% nitrogen with diffusion zone were approximately 0.100 inch in diameter by 0.100 inch in length. The orientation of the seeds was varied in each mult to assess their deformation as a function of seed orientation and strain field. Engineering drawings (P/N T847581 through T847584) describing the seeded mults are shown in appendix E for SB-1 through SB-4.

To provide material for the mults, Rolls-Royce Allison procured double-melted Ti-64 billet per AMS 4928N from Schlosser. The material was from RMI heat BB4746 and sonic inspected per AMS 2631B class A1. The mults were cut to 6.5 inches in diameter by 16.0 inches in length and shipped directly to GE CRD.

The seeded mults were fabricated by cutting the mults into four sections near the seed planes and drilling or milling holes to accept the seeds at the proper radial location and axial depth. The seeds were inserted in the holes and the holes welded shut. After cleaning, the mult sections were welded back to the original mult shape and hot isostatic pressed (HIPed) to fully bond the sections back to one piece. The mults were then turned to the final diameter dimension and cut to finished length. The mults were shipped to the GE Quality Technology Center where they were sonically inspected.

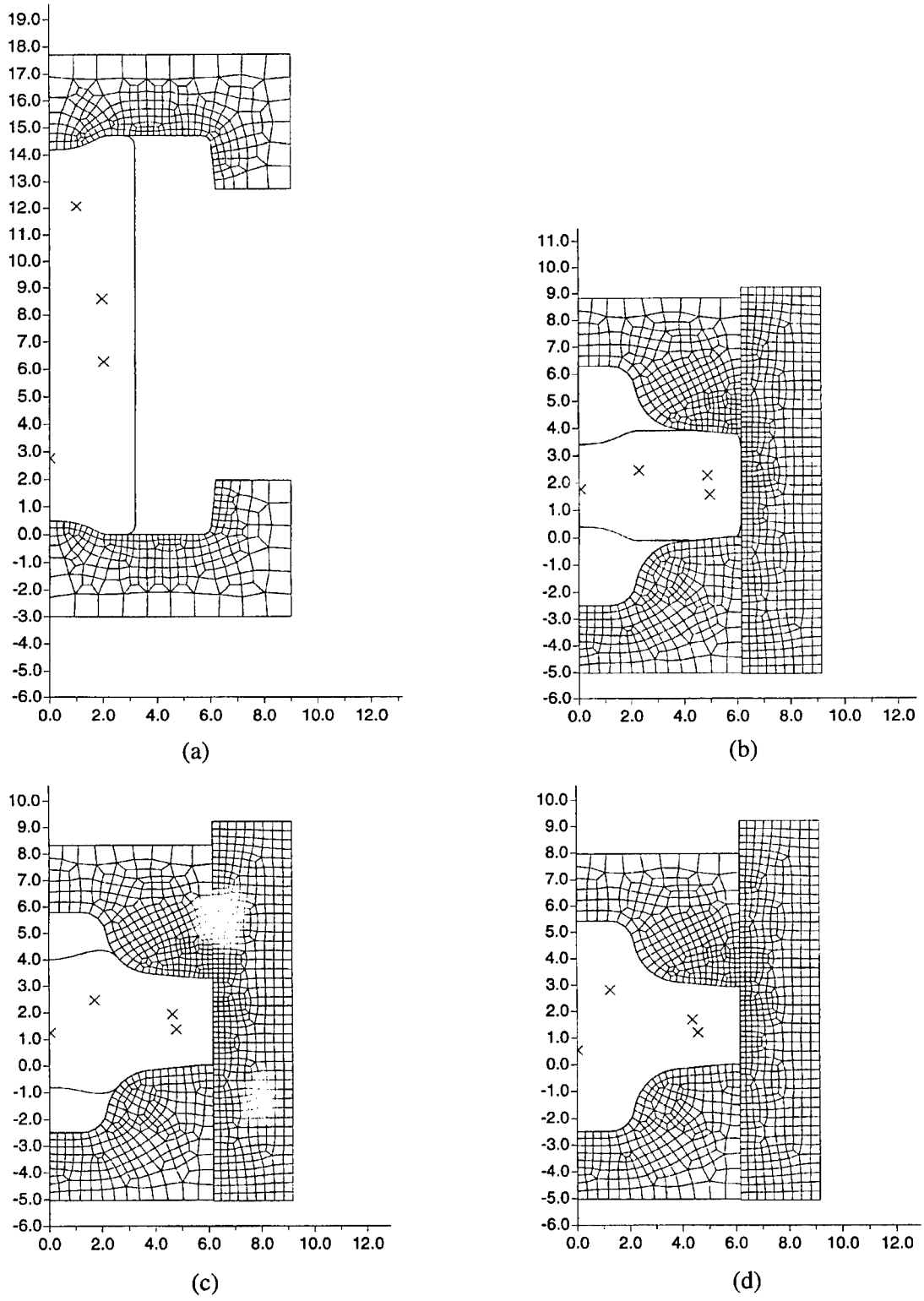


FIGURE 2-52. DEFORM™ POINT TRACKING OF HARD ALPHA SEEDS (a) PRIOR TO DOGBONE FORMATION, (b) AFTER DOGBONE FORMATION, (c) AT 50% DEFORMATION DURING BACKFLOW FORGING, AND (d) AT 100% DEFORMATION AT COMPLETION OF BACKFLOW FORGING
(The scales are in inches.)

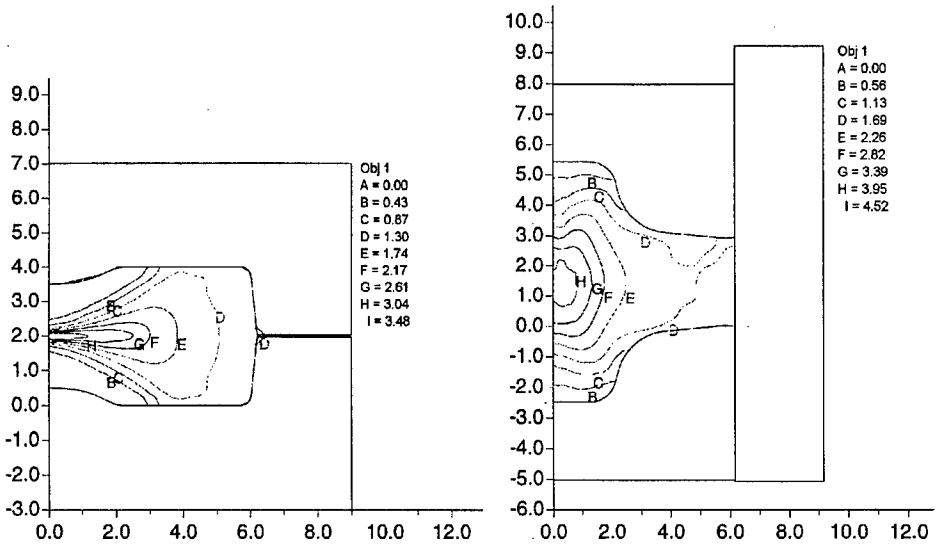


FIGURE 2-53. EFFECTIVE STRAIN CONTOURS IN DOGBONE (LEFT) AND BACKFLOW (RIGHT) FORGINGS

TABLE 2-5. SEED LOCATIONS IN MULTS USED TO PRODUCE SEEDED FORGINGS

Seed Locations Within Mult					
Mult Number	Seed Number	Height (in.)	Angle (deg)	Radius (in.)	Orientation
SB-1	1	12.15	0	2.75	Circumferential
	2	8.625	45	1	Axial
	3	8.625	180	2	Axial
	4	6.375	315	0.5	Radial
	5	2.85	225	0.5	Radial
	6	2.85	90	2.75	Circumferential
SB-2	7	12.15	0	2.75	Circumferential
	8	8.625	45	1	Axial
	9	8.625	180	2	Axial
	10	6.375	315	0.5	Radial
	11	2.85	225	0.5	Radial
	12	2.85	90	2.75	Circumferential
SB-3	13,14,15,16	12.15	0	2.75	Circumferential
	17,18,19,20	8.625	90	1	Radial
	21,22,23,24	6.375	180	2	Axial
	25,26,27,28	2.85	0	0	Axial
SB-4	29,30,31,32	12.15	0	1	Circumferential
	33,34,35,36	8.625	90	1	Radial
	37,38,39,40	6.375	180	2	Axial
	41,42,43,44	2.85	0	0	Axial
SB-5	45	1.3	0	2.1	Axial
	46	1.3	180	2.4	Axial
	47	3.8	90	1.4	Axial
	48	3.8	270	2.1	Axial
SB-6	49	1.3	0	2.1	Axial

The guideline for alignment of the defects for the pancake and disk forgings was to locate the seeds/hard alpha defects in a location that would be highly stressed during subsequent spin testing. As a result, based on the DEFORM™ point tracking, the defects were aligned in locations in the mults which were predicted to end up close to the corner of the disk bore. Figure 2-54 illustrates the locations defined for cutting the RMI CBS mults to align the hard alpha defects near the corner of the disk bore. B3W2-G, which did not get forged into a disk but was stopped at the interim pancake shape, also has its defect aligned at a location that would have ended up in the bore if it proceeded on to final disk forging. In SB-5, three additional seeds (four total) were placed in the mult. These seeds were dispersed throughout the disk at locations with varying forging strains and levels of inspectability. The defects in SB-5 were spread 90° apart from each other to prevent any interference during the forging and the inspections.

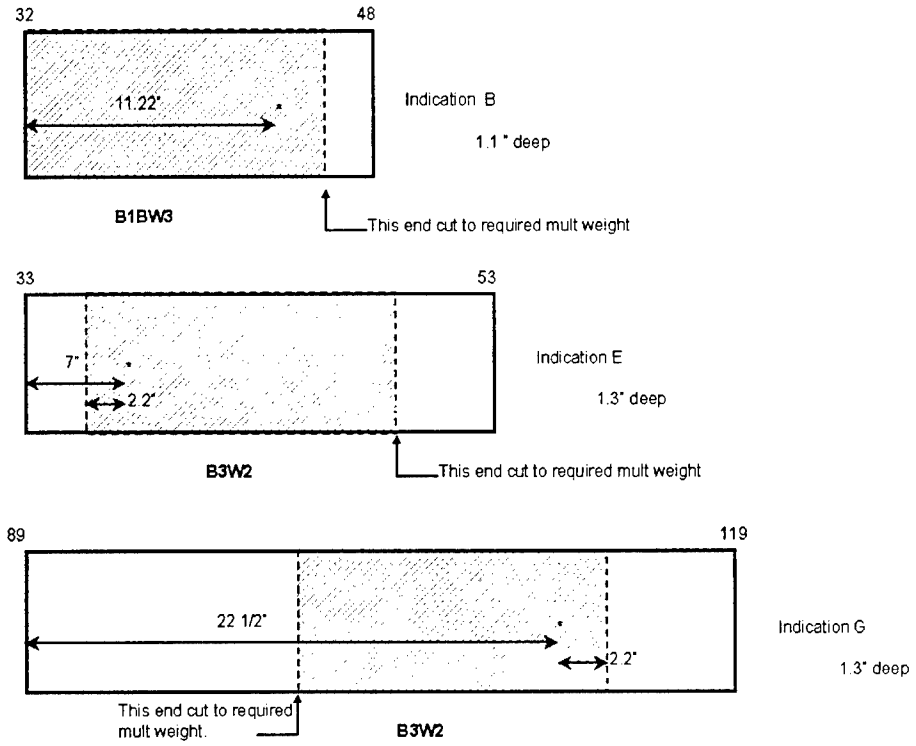


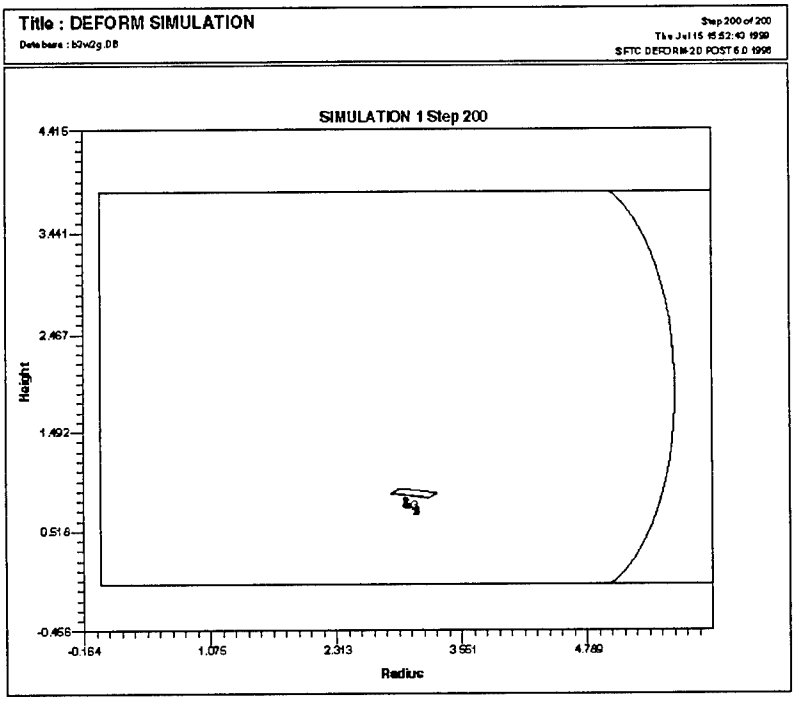
FIGURE 2-54. RMI CBS INDICATIONS FOR PROCESSING TO PANCAKE SHAPE

The inspection results for the RMI CBS billets were provided by the ETC. Initial program plans only called for GE inspections of the seeded billets, pancakes and disks, and the CBS pancakes and disks. Where permitted within the task schedule, AlliedSignal, P&W Florida, P&W Georgia, and RR-Allison also voluntarily performed additional inspections as program enhancements. Additional disk inspections will continue in a follow-on program. The full compilation of inspection results from the different companies includes a combination of production and laboratory inspections as well as standard ultrasonic, multizone, and shear wave inspections. A compilation of measured positional data for SB-5, SB-6, and the three RMI CBS forgings is shown in table 2-6. A compilation of the GE results for conventional and multizone inspections is included in appendix F. Note that the depth reported in the table in this appendix is approximately equal to 3.2″ minus the radial position reported in table 2-6.

TABLE 2-6. DEFECT LOCATIONS FROM BILLET, PANCAKE, AND DISK INSPECTIONS

Mults			
Mult Number	Seed Number	Axial Depth (in.)	Radial Position (in.)
B3W2-G	N/A	2.2	1.7
B3W2-E	N/A	2.2	1.7
B1BW3-B	N/A	1.7	1.3
SB-5	45	1.6	2.2
		N/A	2.0
	46	1.0	2.5
		N/A	2.4
	47	4.0	1.4
		N/A	1.2
	48	4.0	2.2
		N/A	1.9
SB-6	49	1.0	2.2
		N/A	2.0
Pancakes			
Pancake Number	Seed Number	Axial Depth (in.)	Radial Position (in.)
B3W2-G	N/A	0.6	3.00
		0.6	3.03
		0.6	3.02
		0.66	3.00
B3W2-E	N/A	0.6	3.26
		0.58	3.36
		0.6	3.34
		0.6	N/A
B1BW3-B	N/A	0.4	3.25
		0.37	3.35
		0.4	3.2
SB-5	45	0.35	3.15
		0.5	3.03
	46	0.25	3.75
		0.3	3.8
	47	1.25	2.75
		1.2	2.6
	48	1.1	3.9
		1.0	3.9
SB-6	49	0.4	3.1
		0.4	3.02
Disks			
Disk Number	Seed Number	Axial Depth (in.)	Radial Depth (in.)
B3W2-E	N/A	0.5	0.5
B1BW3-B	N/A	0.25	0.5
SB-5	45	0.2	0.4
	46	0.15	1.0
	47	1.5	0.25
	48	0.4	1.1 (from OD)
SB-6	49	0.5	0.25

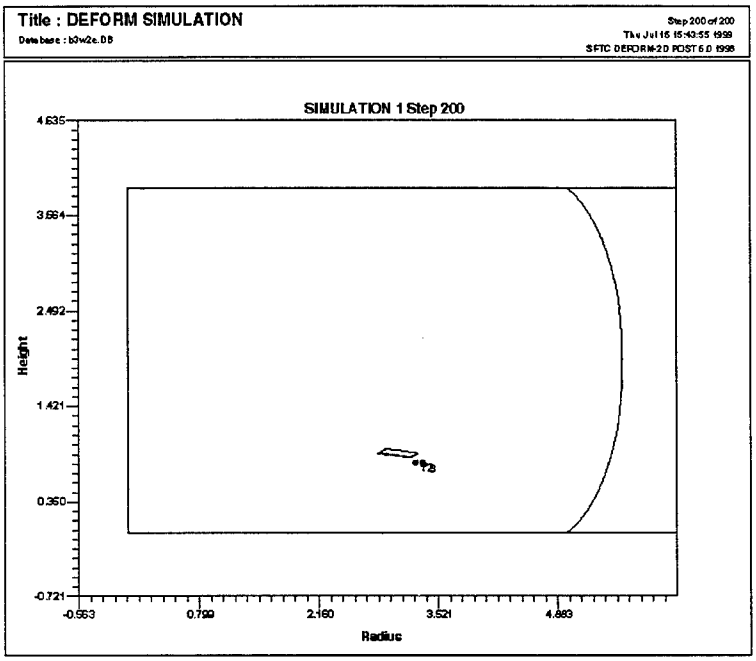
Figures 2-55 through 2-59 include comparisons of the inspection results to the DEFORM™ predictions for the CBS forgings. Flow nets were used to track the defects, as measured in the billets, through the forging process. For illustration purposes, all of the flow nets for the RMI CBS mults were assumed to be a 0.2″ by 0.2″ square, equal to the size of the seeds in SB-4 and SB-6. On the same plots are points identifying the defect locations indicated from the forging inspections. The small variation between the inspection locations in the pancakes and disks and the predictions may be attributed to the uncertainty in the assumption that the billet inspection location was at the center of the defects, to defect sizes larger than 0.2″ or to the variability in the reporting of the locations of the defects in the billets.



Net indicates location predicted by DEFORM™ based on billet UT inspection location and assumption of 0.2″ × 0.2″ defect centered at that location.

Points indicate defect locations from pancake UT inspections.

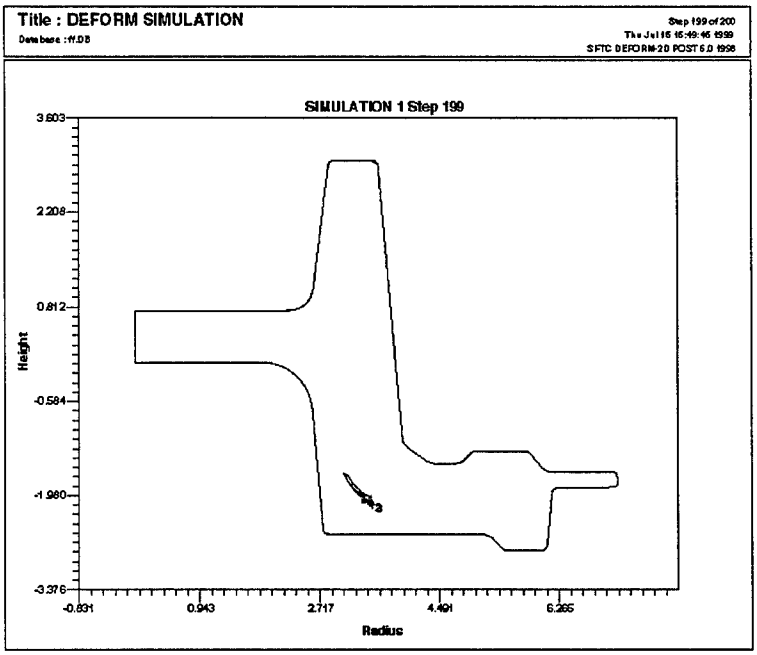
FIGURE 2-55. B3W2-G PANCAKE DEFECT LOCATION PREDICTION (BASED ON BILLET INSPECTION) COMPARED TO LOCATION FROM PANCAKE INSPECTIONS



Net indicates location predicted by DEFORM™ based on billet UT inspection location and assumption of 0.2″ × 0.2″ defect centered at that location.

Points indicate defect locations from pancake UT inspections.

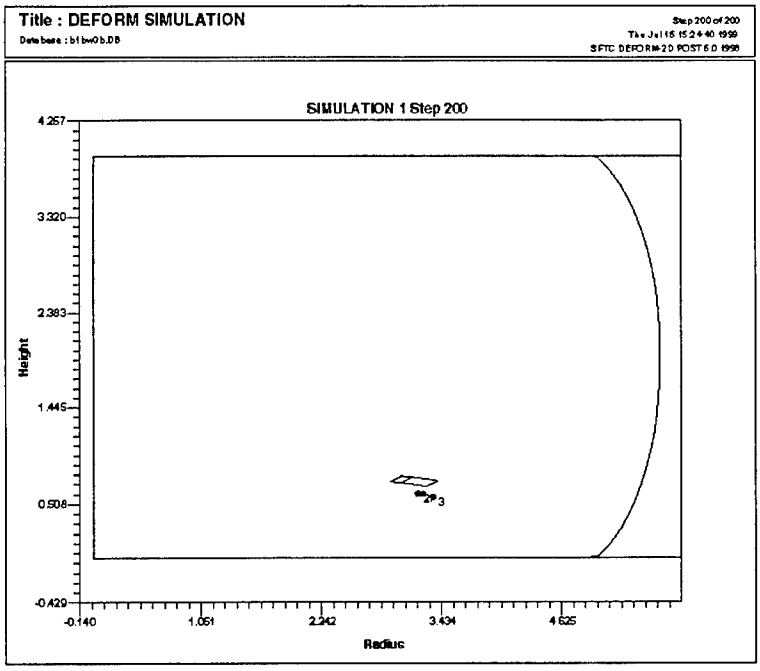
FIGURE 2-56. B3W2-E PANCAKE DEFECT LOCATION PREDICTION (BASED ON BILLET INSPECTION) COMPARED TO LOCATION FROM PANCAKE INSPECTIONS



Net indicates location predicted by DEFORM™ based on billet UT inspection location and assumption of 0.2″ × 0.2″ defect centered at that location.

Points indicate defect locations from pancake and disk UT inspections.

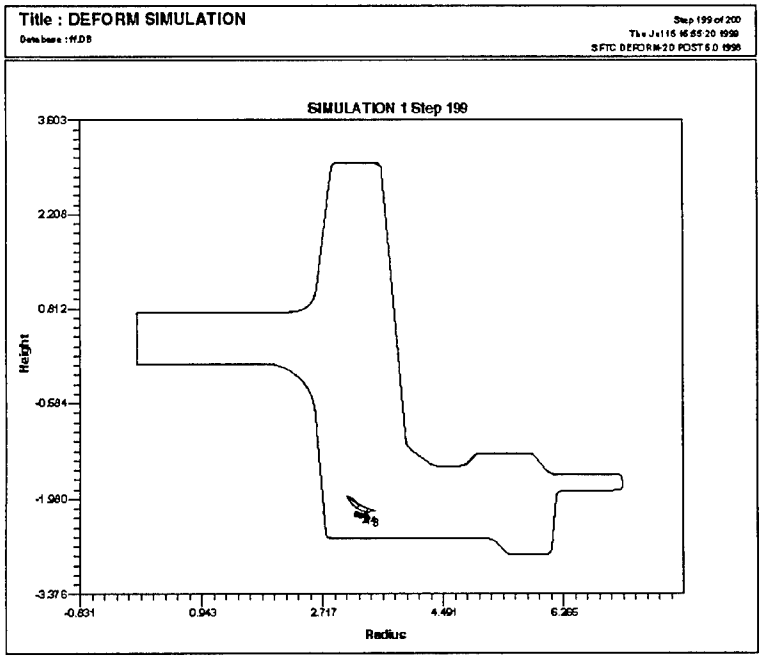
FIGURE 2-57. B3W2-E DISK DEFECT LOCATION PREDICTION (BASED ON BILLET INSPECTION) COMPARED TO LOCATION FROM PANCAKE/DISK INSPECTIONS



Net indicates location predicted by DEFORM™ based on billet UT inspection location and assumption of 0.2″ × 0.2″ defect centered at that location.

Points indicate defect locations from pancake UT inspections.

FIGURE 2-58. B1BW3-B PANCAKE DEFECT LOCATION PREDICTION (BASED ON BILLET INSPECTION) COMPARED TO LOCATION FROM PANCAKE INSPECTIONS



Net indicates location predicted by DEFORM™ based on billet UT inspection location and assumption of 0.2″ × 0.2″ defect centered at that location.

Points indicate defect locations from pancake and disk UT inspections.

FIGURE 2-59. B1BW3-B DISK DEFECT LOCATION PREDICTION (BASED ON BILLET INSPECTION) COMPARED TO LOCATION FROM PANCAKE/DISK INSPECTIONS

Figures E-14 through E-25 in appendix E compare the inspection results to the seed placement and DEFORM™ predictions for the seeded mults and forgings, SB-5 and SB-6. The flow nets were placed in the DEFORM™ mult models matching the size and locations of the seeds and were tracked through the forging process. As with the RMI CBS forgings, points identifying the locations from the inspections were plotted for comparison. The differences between the inspection results and the predictions were generally within the variability of the inspections. Many of the inspection results were located within or on the edge of the flow net throughout the forging process.

The results of these experiments have demonstrated that the DEFORM™ macrolevel code can accurately predict the movement of defects through an isothermal forging process to both an interim pancake shape and a final disk shape. Metallographic evaluation of the seeded forgings for validation of the DEFORM™ microcode will be done in a follow-on FAA program. A preliminary nondestructive inspection and metallographic evaluation of a HA defect in a pancake forging produced at Schlosser from the RMI CBS billet B1BW3-A (see appendix F) is summarized in appendix G.

2.2.6 Parametric Benchmarking of Forging Microcode on Actual Disk Geometries.

A series of parametric studies on selected titanium rotating components in commercial service were conducted to validate the hard alpha deformation microcode. A thorough review of Rolls-Royce Allison fan rotor and compressor disk components resulted in the selection of two components that could be used in this exercise. The criteria for selecting the components were:

- Must be in commercial service
- Titanium alloy
- Produced by press forging

The components selected were the AE 3007 fan disk (figure 2-60) and the AE 2100/3007 Stage 14 compressor disk (figure 2-61). The fan disk is produced by Wyman-Gordon in Ti-64 alloy and the compressor disk is produced by Sifco in Ti-6242 alloy. The fan disk is produced by press forging in a highly contoured closed die. The compressor disk, being a relatively simple, flat shape, is press forged as a pancake in open dies.

Roll-Royce Allison worked with Wyman-Gordon and Sifco to establish DEFORM™ forging models for each part. Both forgers use DEFORM™ in their forging die design operations and agreed to share key word files with Rolls-Royce Allison to run the models in-house. This was successfully accomplished and both models were run at Rolls-Royce Allison. For the fan disk, Rolls-Royce Allison used proprietary Wyman-Gordon flow stress data for Ti-64 to run the macromodel. The data were retained at Rolls-Royce Allison when the key word files were sent to GEAE to run the microcode. The Ti-6242 flow stress data used to run the compressor disk were obtained in the embedded keyword files found in DEFORM™.

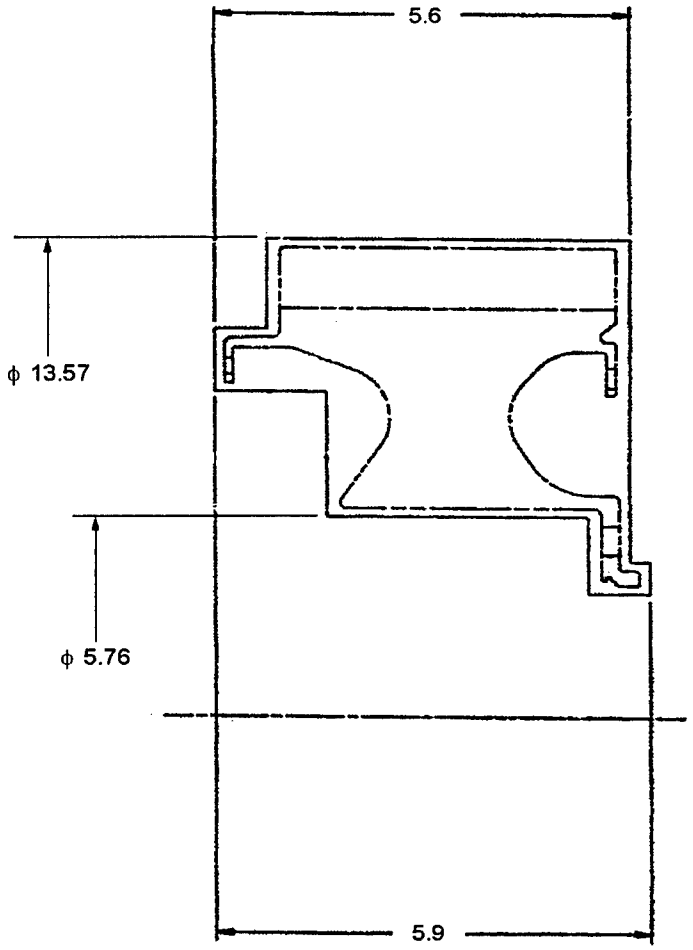


FIGURE 2-60. FAN DISK FORGING

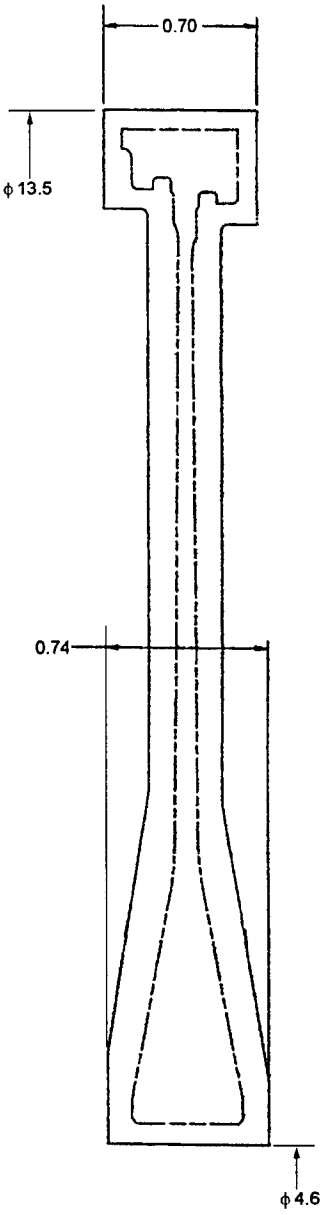


FIGURE 2-61. COMPRESSOR DISK FORGING

Subsequent to processing both macromodels, locations in both forgings that represented critical microvolumes for the hard alpha microcode analysis were selected. The locations approximately represent bore center, bore edge, mid-web, and blade root attachment in the finished components. These locations are shown in the point tracking runs, in figure 2-62 for the fan disk and figure 2-63 for the compressor disk. The strain maps for these components are shown in figure 2-64. The outputs of the analysis were then sent to General Electric Aircraft Engines (GEAE) for the microcode analysis. It should be noted the DEFORM PC Pro version does not have the capability to run the microcode, and for this reason, it was decided to have GEAE run the Rolls-Royce Allison-provided macrocodes on the workstation version of DEFORM™.

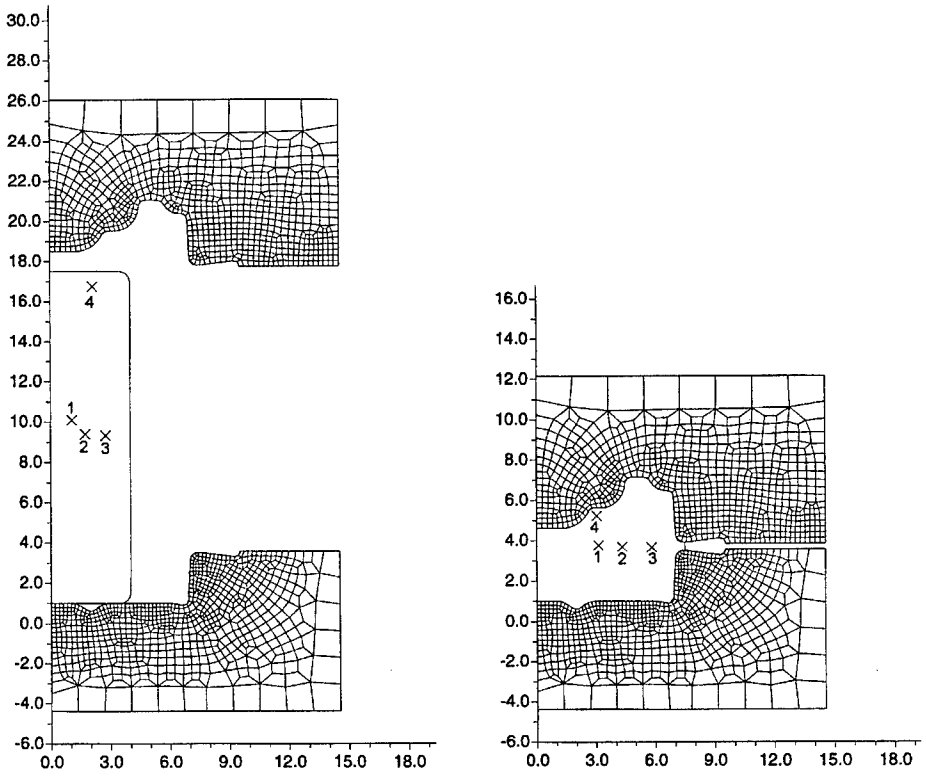


FIGURE 2-62. DEFORM™ POINT TRACKING OF SIMULATED HARD ALPHA DEFECTS IN FAN DISK FORGING AT START AND 100% DEFORMATION

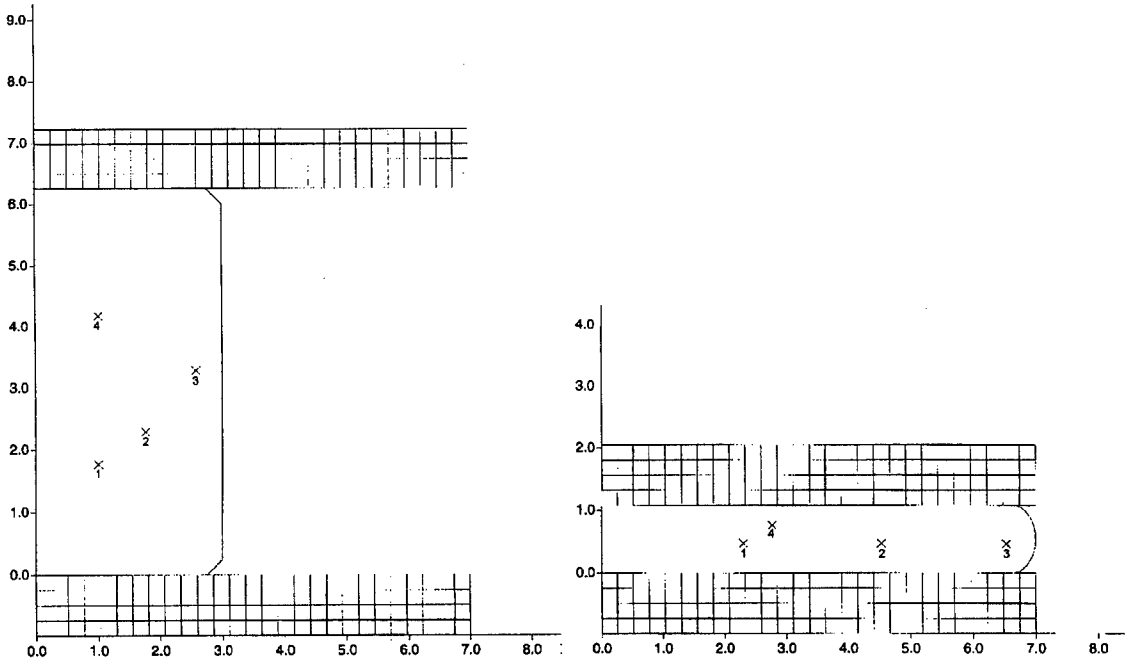


FIGURE 2-63. DEFORM™ POINT TRACKING OF SIMULATED HARD ALPHA DEFECTS IN COMPRESSOR DISK FORGING AT START AND 100% DEFORMATION

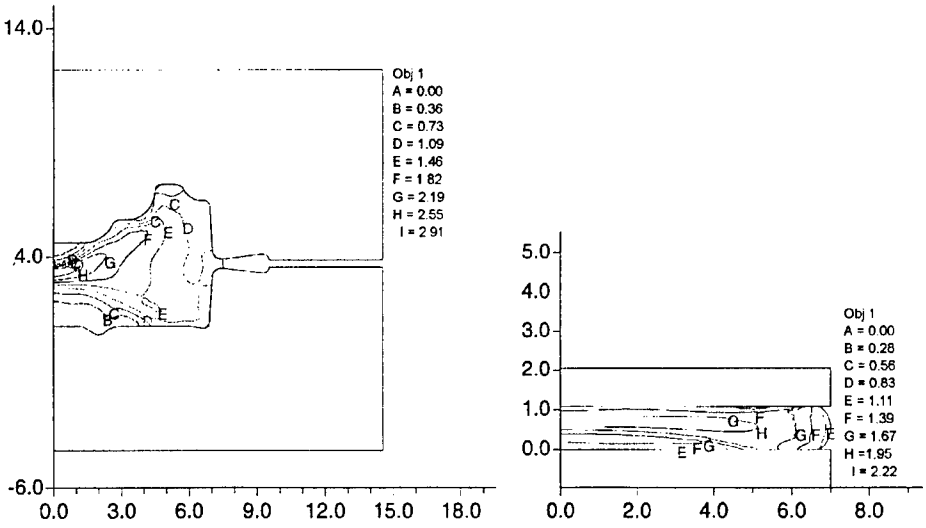


FIGURE 2-64. EFFECTIVE STRAIN CONTOURS FOR FAN DISK FORGING (TOP) AND COMPRESSOR DISK FORGING (BOTTOM)

The two Rolls-Royce Allison forgings used for parametric benchmarking of the microcode were identified as follows:

- Part Number (P/N) 68014, Stage 14 compressor disk, Ti-6242, forged by Sifco
- P/N 68696, fan disk, Ti-64, forged by Wyman-Gordon

Details of the micromodel are:

- Nitrogen content: 2% in diffusion zone and 4% in nugget (average values)
- Indication location in billet: Four locations as shown in figures 2-62 and 2-63

Figure 2-65 shows the strain contours and the shape of Inclusion No. 1 in P/N 68014 at four different stages of the forging process. Figures 2-66 and 2-67 show the strain contours and the shapes of the four inclusions at the end of the forging process for both parts. These figures show the following.

- The strain in the inclusion is less than that in the matrix material. This confirms the results of section 2.2.4.9 relating the inclusion strain to the matrix material strain.

- The strain in the matrix material is, in general, higher immediately adjacent to the inclusion than the average strain within the microvolume. This is because the inclusion is more difficult to deform and so more of the overall deformation has to be accommodated by the matrix material.

- The strain in the matrix material is tensile at the ends of the major axis of the inclusion and is compressive at the ends of the short axis of the inclusion. Voids are likely to open up in the regions of high tensile strain.

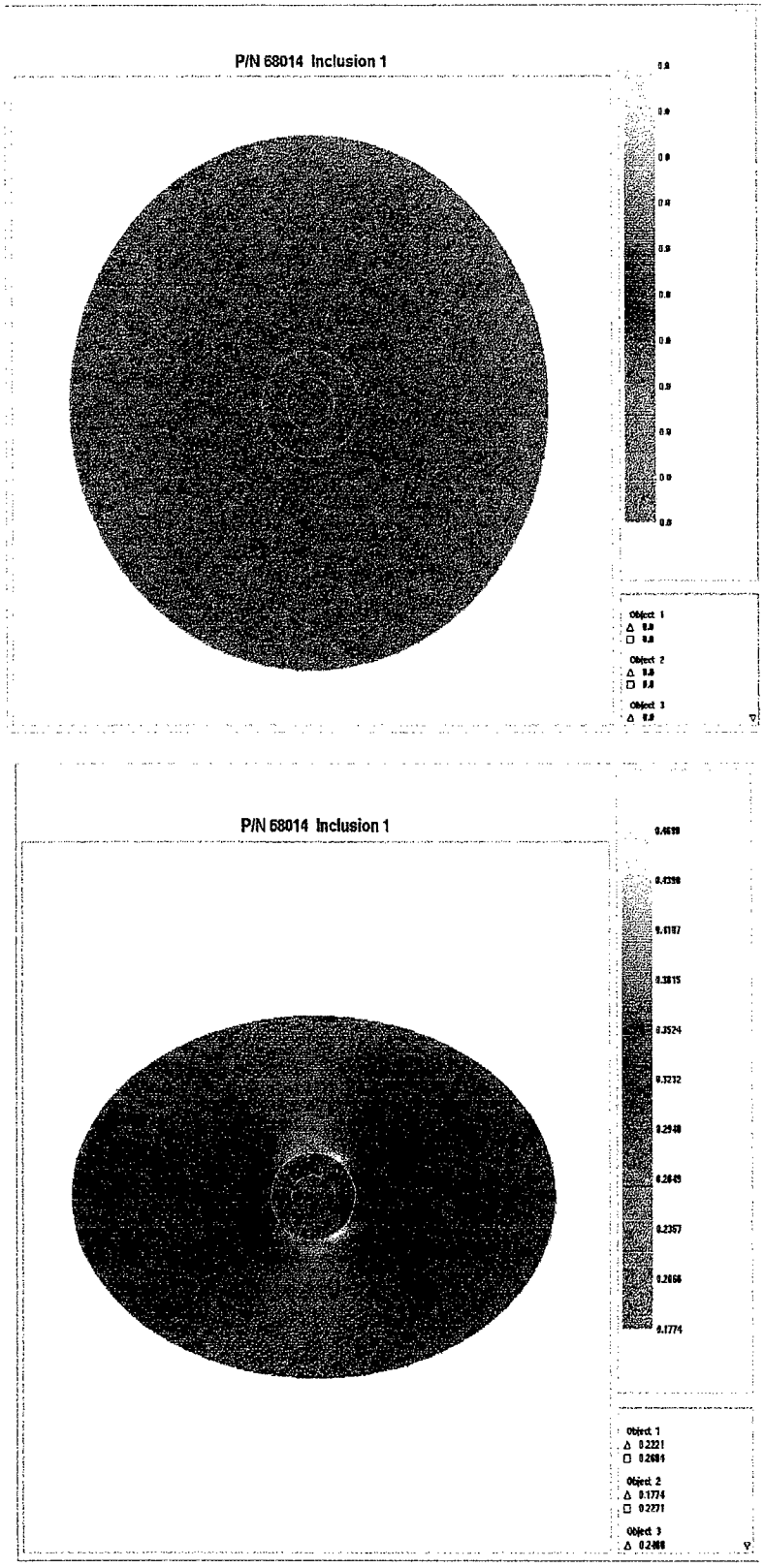


FIGURE 2-65. EFFECTIVE STRAIN CONTOURS AT DIFFERENT STAGES OF THE FORGING PROCESS: P/N 68014, INCLUSION 1

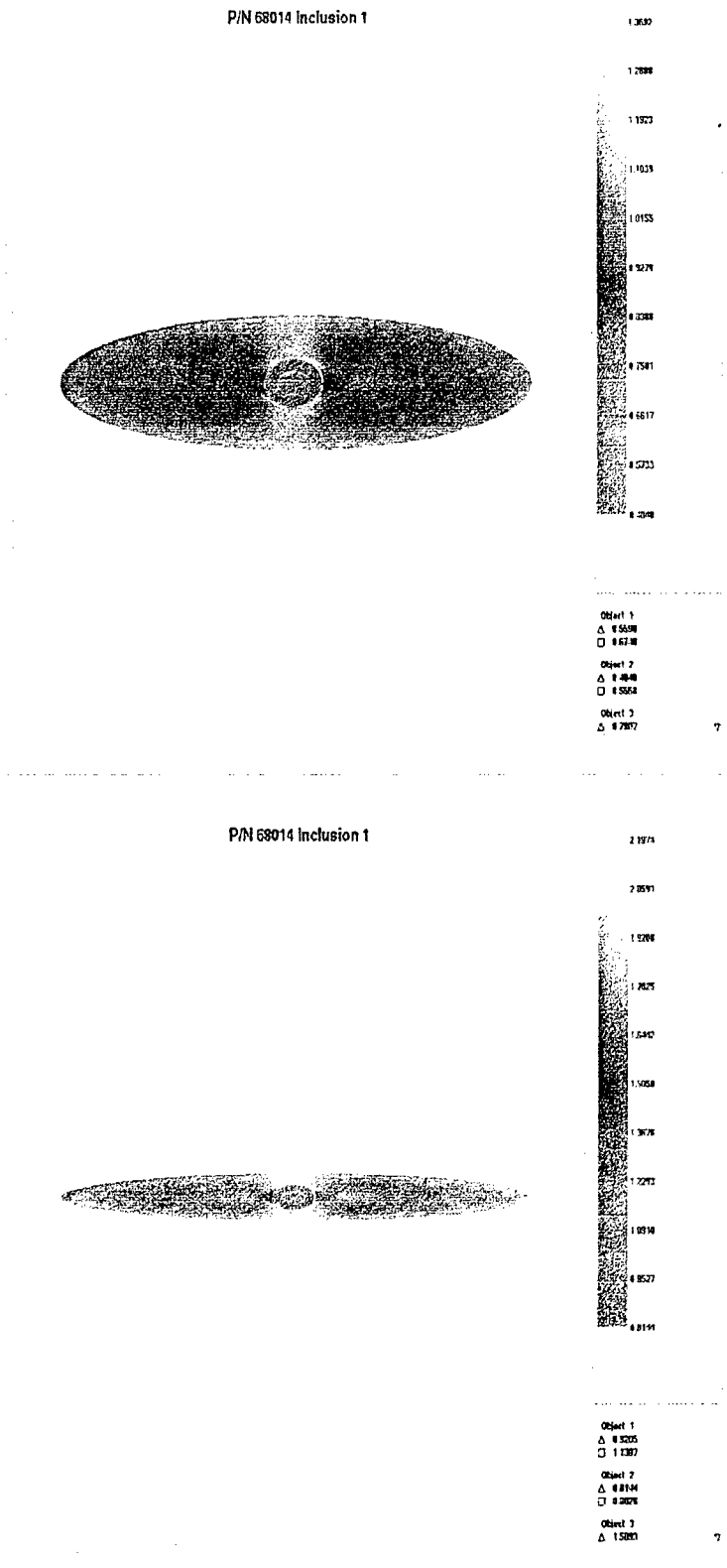


FIGURE 2-65. EFFECTIVE STRAIN CONTOURS AT DIFFERENT STAGES OF THE FORGING PROCESS: P/N 68014, INCLUSION 1 (Continued)

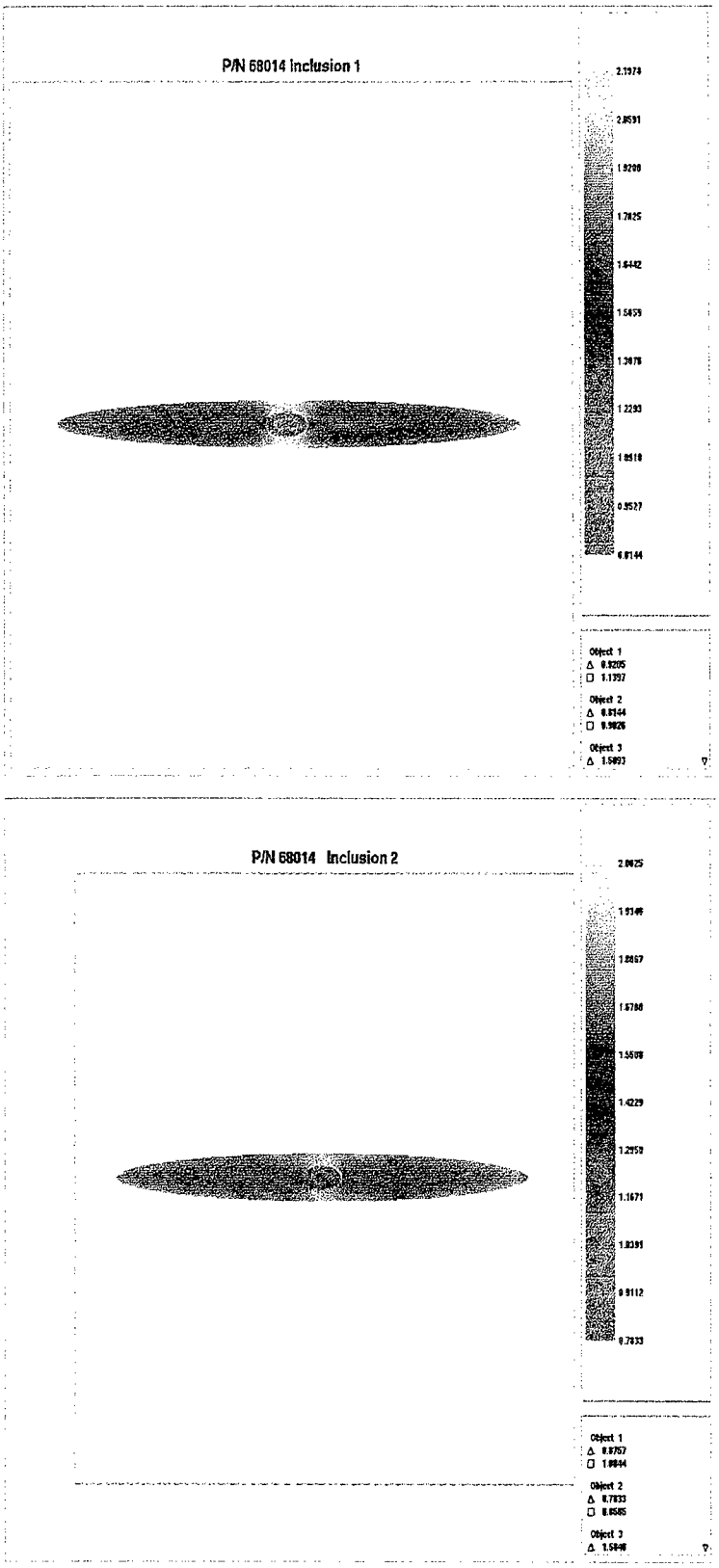


FIGURE 2-66. FINAL DEFORMATION OF THE FOUR INCLUSIONS IN P/N 68014

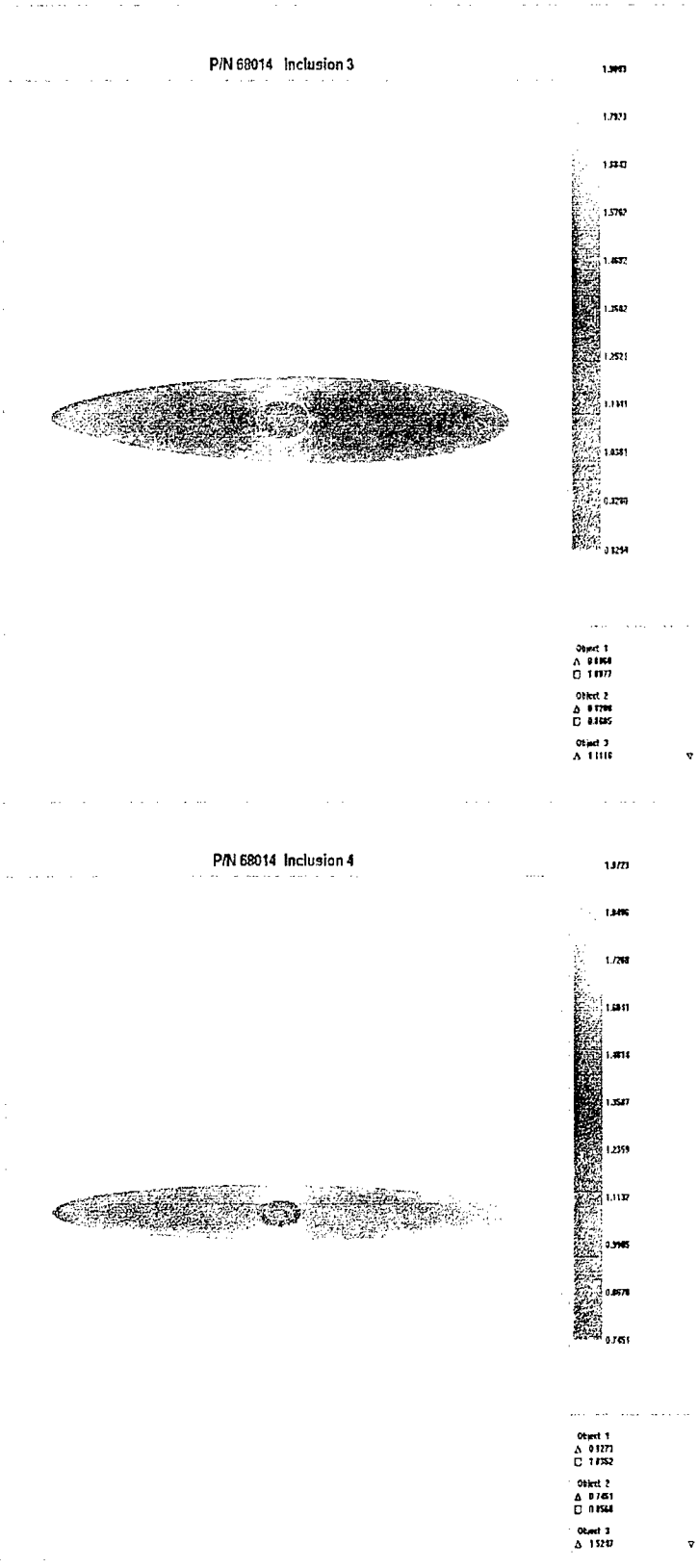


FIGURE 2-66. FINAL DEFORMATION OF THE FOUR INCLUSIONS IN P/N 68014 (Continued)

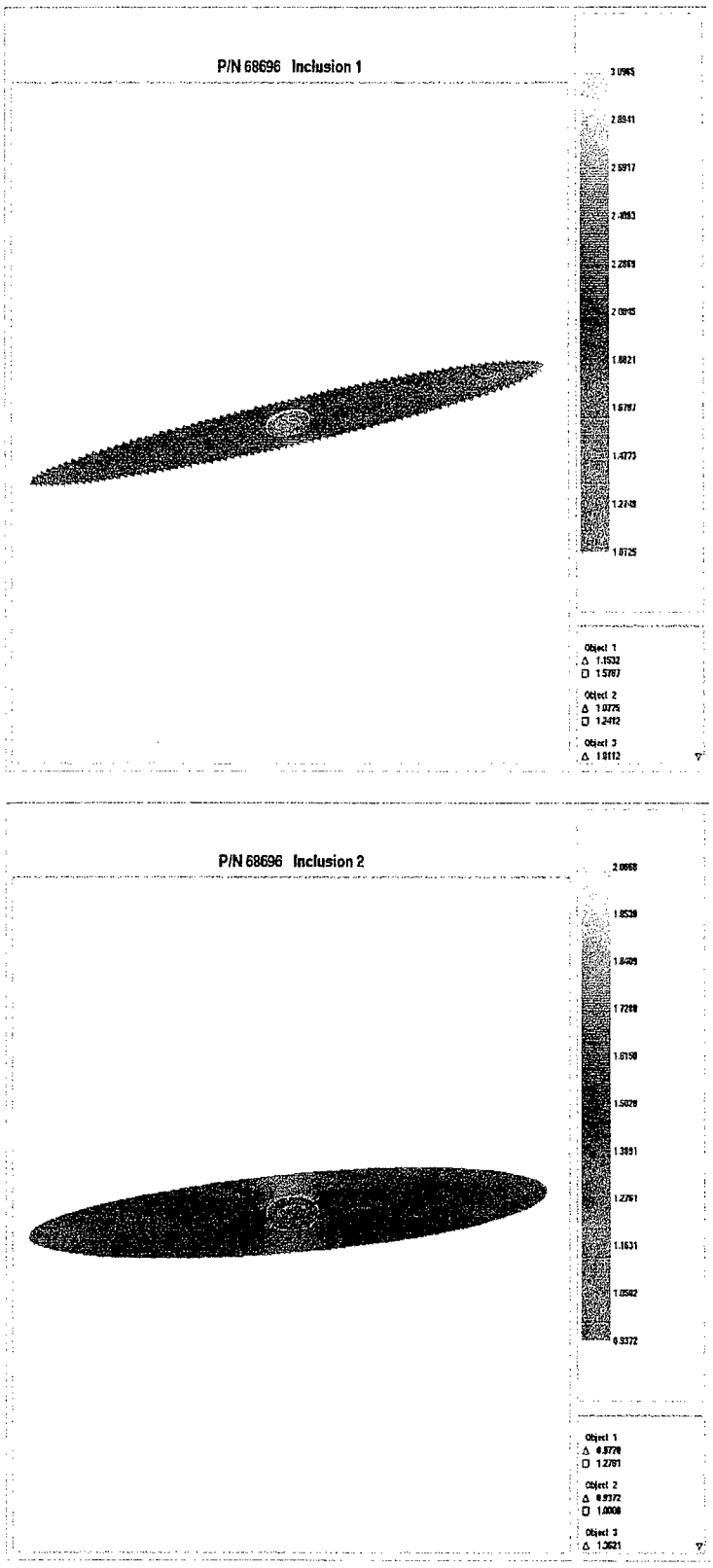
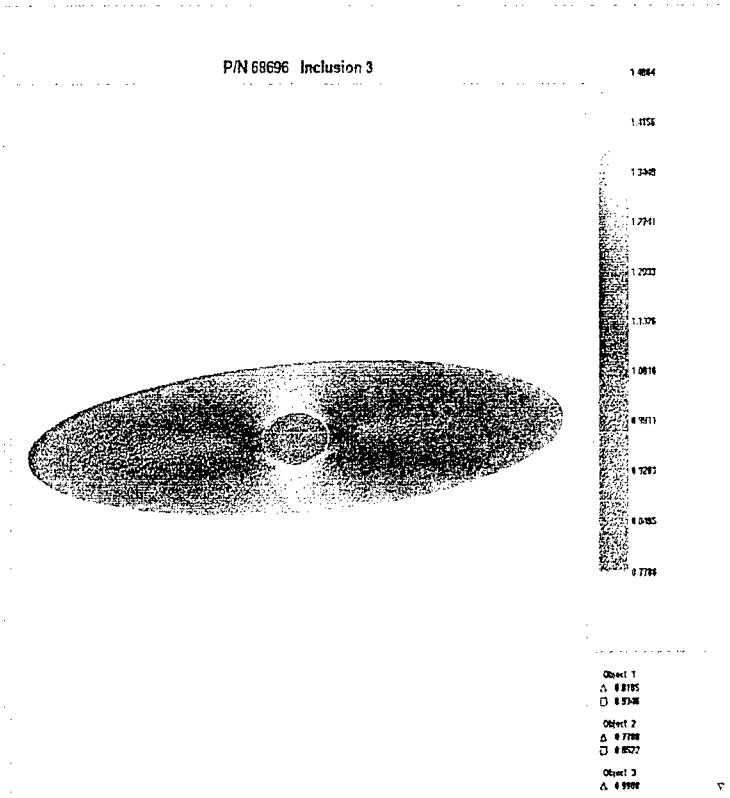


FIGURE 2-67. FINAL DEFORMATION OF THE FOUR INCLUSIONS IN P/N 68696



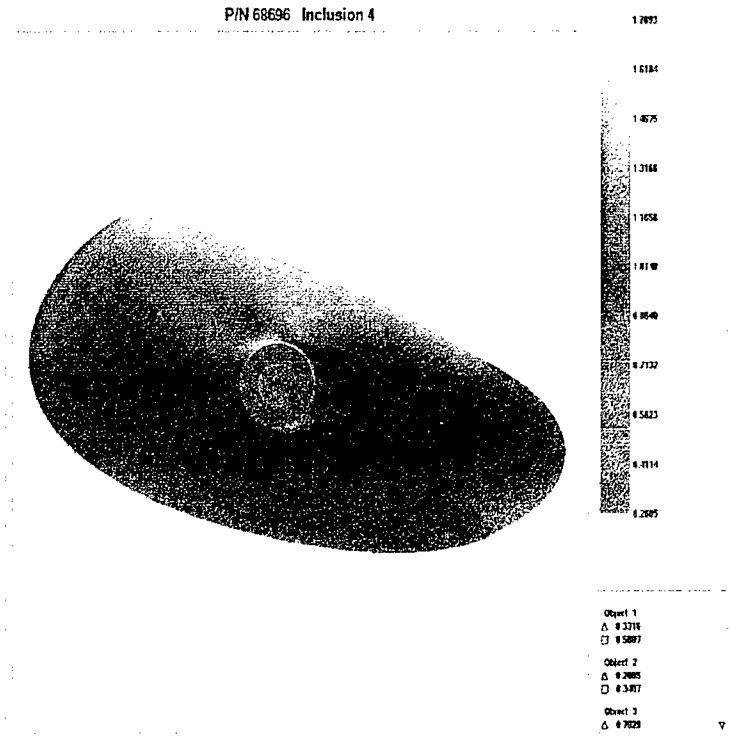


FIGURE 2-67. FINAL DEFORMATION OF THE FOUR INCLUSIONS IN P/N 68696 (Continued)

2.3 CRACK NUCLEATION BEHAVIOR OF HARD ALPHA ANOMALIES.

Hard alpha anomalies are often extensively voided and cracked in the final forged rotor configuration. Current life prediction methodologies commonly assume that an initial fatigue crack size equal to the size of the HA region (high nitrogen core plus surrounding diffusion zone) is present at the beginning of life. This assumption could be overly conservative, however, for smaller HA anomalies and zones with lower nitrogen content, which may be less likely to be extensively cracked and voided after the forging process and, hence, more difficult to detect using NDE. Consequently, these anomalies may play a significant role in the probabilistic risk assessment, especially considering that a relatively larger number of these smaller defects are postulated to remain in the rotor upon entry into service. Therefore, it is useful to assess the cracking tendencies of the HA anomalies under static and fatigue loading in order to evaluate the possibility that some nonzero crack nucleation life could be included in the fatigue life prediction methodology.

An experimental program was conducted to characterize the damage evolution that occurs in and around hard alpha anomalies. Mechanical tests were conducted on reduced gage section specimens of Ti-6Al-4V containing either synthetic or naturally occurring hard alpha material. The details of this program are documented at some length in appendix H, but a short synopsis is given here for convenience.

2.3.1 Specimens and Test Procedures.

The synthetic anomalies were created artificially by GE CRD using techniques originally developed to manufacture specimens for NDE studies. These cylindrical anomalies with surrounding synthetic diffusion zone were distinguished by their core nitrogen content (nominal 1.6%, 2.7%, or 6%), location (embedded or surface breaking), and size (core diameter approximately 0.031″ or 0.078″, with proportional diffusion zone size). Defects were manufactured separately and inserted into blocks of Ti-6Al-4V, which were then HIPed before being machined to final specimen dimensions. The axis of the defect cylinder was oriented across the specimen thickness, normal to the loading axis. A photograph of a typical synthetic HA specimen with a surface defect is given in figure 2-68.

Microprobe and hardness scans were conducted on a representative 6% nitrogen surface defect specimen. The hard alpha core was measured to be about 5% nitrogen (weight percent). The nitrogen level dropped sharply to an approximately constant value of about 1% within 2 mils of the core-diffusion zone interface. This level was maintained over a distance of about 20 mils before gradually decaying to near-zero levels near the interface between the 38-mil-wide diffusion zone and the matrix material. The hardness profile revealed a corresponding gradient in mechanical properties. Measured Rockwell C hardnesses ranged from about 30 in the matrix material to a high approaching 70 in the defect core.

A small number of similar test specimens were machined from selected RMI CBS (contaminated billet study) billets. These specimens were machined in such a way that NDE indications thought to be HA defects, or related voids or diffusion zones, were located in the gage section with an appropriate orientation, either surface exposed or internal. These specimens were more

expensive to develop, and did not permit specific selection of size or nitrogen content, but did provide a valuable comparison with the synthetic specimens. An RMI-CBS specimen with a surface connected defect was noted to contain a significant void, along with numerous microcracks extending from the void into the diffusion zone, prior to mechanical testing.

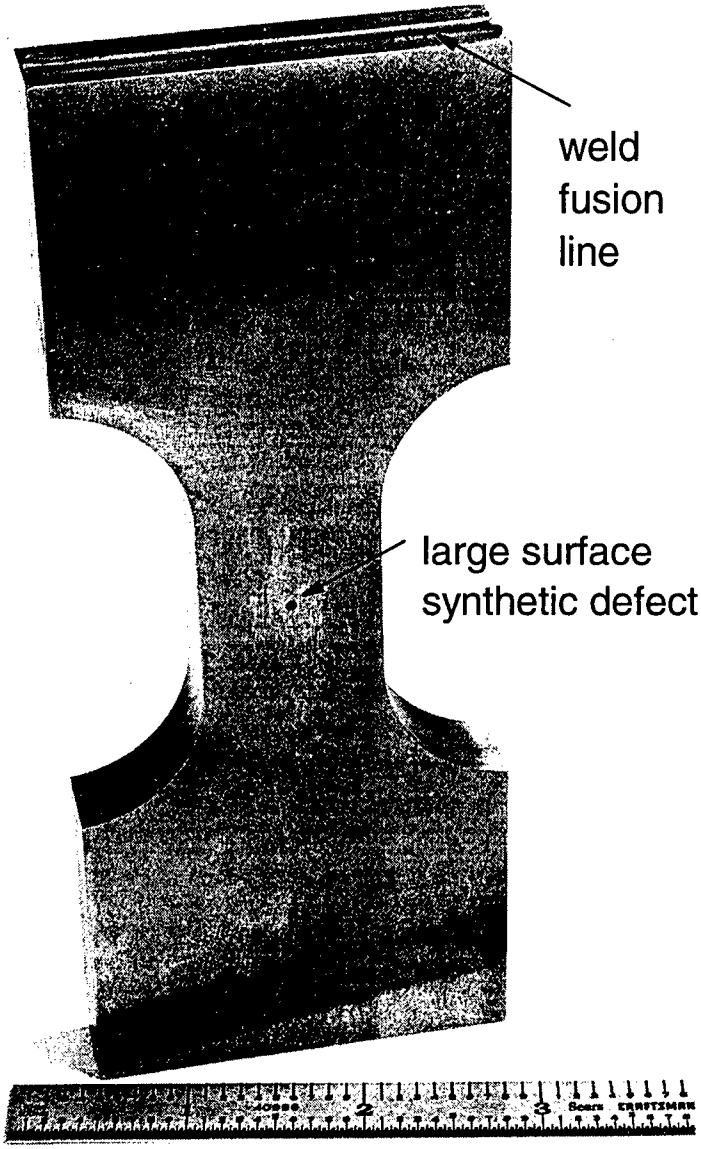


FIGURE 2-68. PHOTOGRAPH OF A TYPICAL SYNTHETIC HARD ALPHA DEFECT SPECIMEN

Cracking behavior was characterized by several different means. Cracking in defects that were surface connected could be monitored by direct visual observation at low magnification. Nonvisual methods—acoustic emission (AE), direct-current electric potential drop (PD), and ultrasonic (UT) time of flight—were used for both surface and internal defects. These methods were especially important for the embedded defects where visual observation during the test was

not possible. The simple ultrasonic methods employed during early testing proved less useful than the AE and PD methods and hence were discontinued during later tests. A simple two-microphone AE system was used during early tests, while a more sophisticated six-microphone system with source location capability was used during later tests. Posttest fractographic analysis and progressive metallurgical sectioning were employed on select specimens (particularly embedded defects) to characterize cracking in detail and correlate it with the nonvisual, indirect transducer data recorded during the test.

Testing was performed in a 200-kip capacity MTS Systems Corporation (MTS) servohydraulic test frame with hydraulic wedge grips. Applied loads were either monotonic (quasi-static) or cyclic (fatigue). All tests were performed at room temperature. Loads in the monotonic tests were applied incrementally, stopping at each load level to record transducer output. This was especially important for crack length measurement in the case of the surface defects. Maximum applied stresses in the monotonic tests ranged from 50 to 120 ksi.

Fatigue tests were run in continuous cycling at 2 Hz with stops at prescribed cycle counts for data recording, even though some data were continuously recorded with computer acquisition. These tests were conducted at a stress ratio ($R = \sigma_{min}/\sigma_{max}$) of 0.1 with constant load amplitudes. In some tests, groups of high stress ratio ($R = 0.7$) cycles were periodically applied in attempts to form marker bands on the fracture surface to aid posttest interpretation. Maximum fatigue stresses ranged from 40 to 100 ksi. Some tests were continued until specimen separation while other tests were halted prior to failure and the specimen either sectioned or broken open by static loading.

2.3.2 Results.

2.3.2.1 Monotonic Tests.

Monotonically loaded synthetic specimens with surface-connected defects exhibited cracking at relatively low stress levels. First cracking in the defect core was generally observed at applied stresses ranging from 5 to 15 ksi. Cracks first formed in the diffusion zone at around 20 to 40 ksi, and the diffusion zone was often fully cracked when the applied stresses reached 50 to 100 ksi. Cracks did not appear to extend into the matrix material in any of these monotonic tests.

Typical cracking in a monotonically loaded surface defect specimen is shown in figure 2-69. Multiple cracks were observed in both core and diffusion zone. Cracks arrested at the diffusion zone-matrix interface, although crack tip plastic deformation extended into the matrix material.

The nonvisual transducers were generally successful at detecting early core cracking as well as progressive cracking into the diffusion zone. Figure 2-70 compares signals from AE, PD, and UT transducers with visually measured crack length as static load is increased. All nonvisual methods indicated first cracking at around 8 ksi and approximately linear, albeit incremental, increases in crack length as stresses increased to 50 ksi.

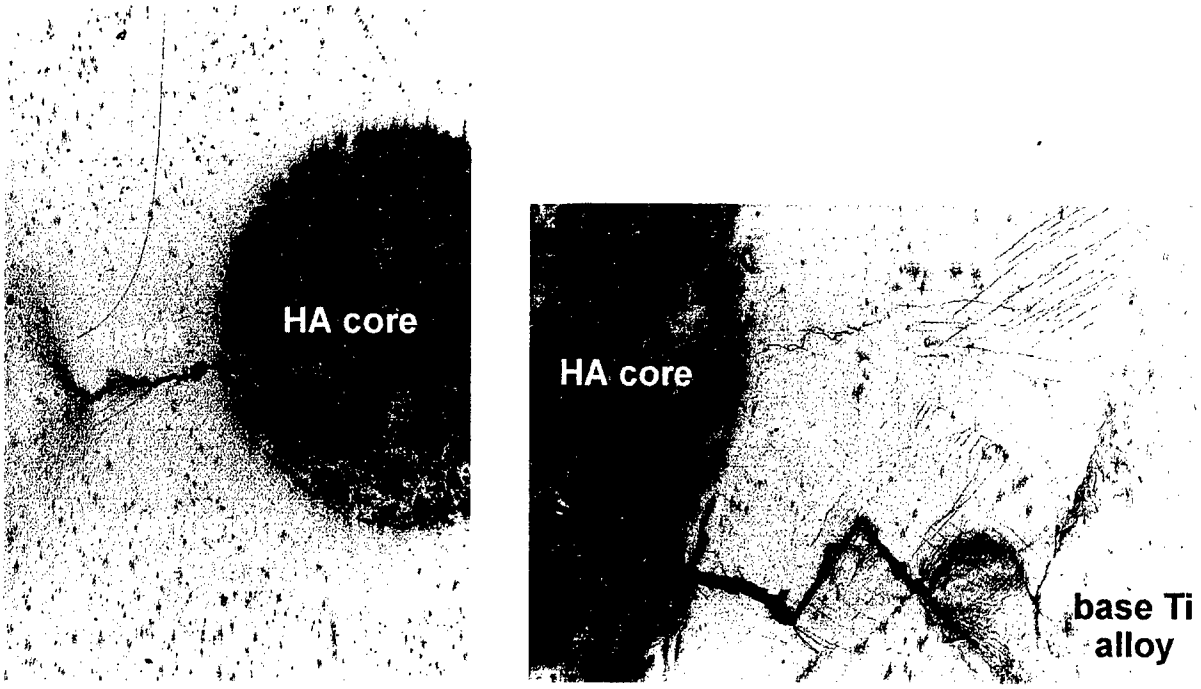


FIGURE 2-69. CRACKING IN THE HA CORE AND THROUGH THE DIFFUSION ZONE IN A HIGH-NITROGEN, LARGE-DEFECT SPECIMEN

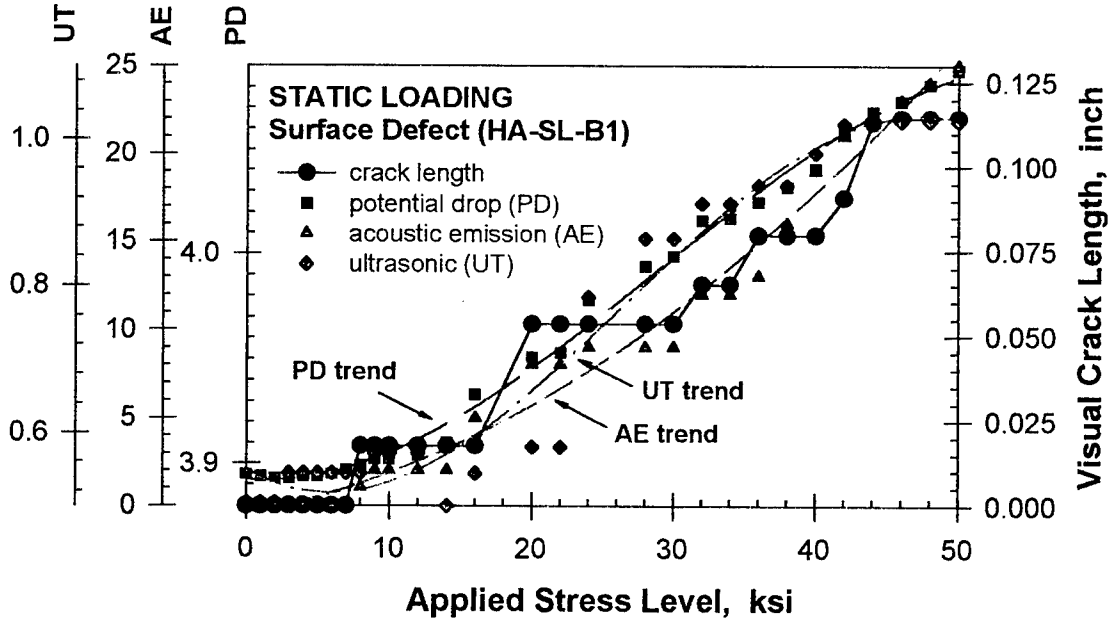


FIGURE 2-70. CRACK LENGTH MEASUREMENTS AND ULTRASONIC, ACOUSTIC EMISSION, AND POTENTIAL DROP OUTPUT FOR A LARGE, HIGH-NITROGEN SURFACE DEFECT SUBJECTED TO STATIC LOADING

Monotonically loaded synthetic specimens with embedded defects generally exhibited a substantially higher resistance to cracking. Nonvisual transducers (AE and PD) indicated limited cracking events at stresses around 20 to 40 ksi, but substantial signals were observed only when applied stresses exceeded 80 to 100 ksi. Posttest fractography of some specimens exhibited only limited core cracking, even at these high terminal stresses, although other specimens with internal defects exhibited extensive core and diffusion zone cracking. An example is shown in figure 2-71, a small 6% nitrogen internal defect specimen loaded statically to 120 ksi. Note that the core was shattered, but the diffusion zone was still not fully cracked. Some cracks were observed along the interface between the diffusion zone (DZ) and matrix.

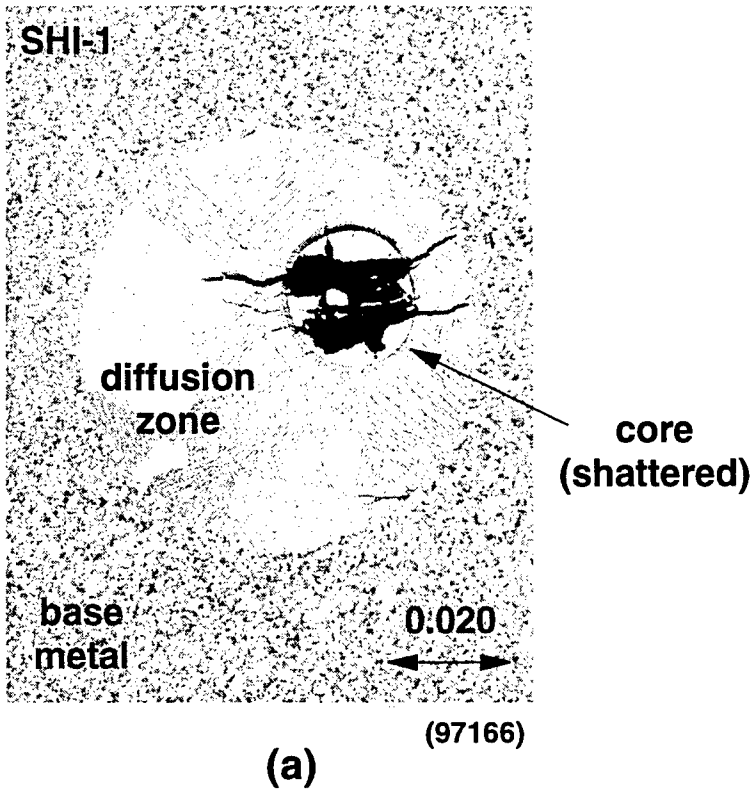
2.3.2.2 Fatigue Tests.

Core and diffusion zone cracks formed quite early in fatigue specimens with synthetic surface defects. This behavior is consistent with the low monotonic fracture strengths. These cracks then grew into the matrix relatively quickly under continued fatigue cycling.

Significantly different behavior was observed for interior defects under fatigue cycling. Figure 2-72 schematically illustrates a typical damage state for these specimens. The metallographic sections indicate numerous sites of unconnected cracking. The damage tended to be distributed throughout the core and diffusion zone, with more cracking observed in the larger diffusion zone. This tendency towards extensive, unconnected cracking may be indicative of a more damage tolerant microstructure. Had damage been more highly localized and concentrated in a connected manner, presumably less cycling (i.e., energy) would be required to form a continuous crack growing into the matrix.

The fatigue tests with synthetic internal defects were more complex to analyze, but provided some particularly interesting results. The amount of fatigue crack growth observed on the posttest fracture surface (aided, in some cases, by marker bands) corresponding to a known number of applied fatigue cycles was compared to predictions of crack growth performed with the Flight_Life fracture mechanics module in the Design Assessment of Reliability With INspection (DARWIN) computer code. Vacuum fatigue crack growth properties for Ti-6Al-4V at room temperature (see section 2.4.1 and appendix I) were employed in the analysis since the embedded cracks were isolated from the atmosphere. Flight_Life analyses for tests in which the initial and final crack sizes and shapes were distinct (due to marker bands) and regular were used to obtain confidence in the analysis. These validation analyses successfully predicted high stress ratio marker band widths and predicted the number of cycles for observed major cycle ($R = 0.1$) growth within a factor of two.

The initial crack size for crack growth from the defect was assumed to be an ellipse with total area and aspect ratio set equal to the observed dimensions of the original defect core plus diffusion zone. This corresponds approximately to the current industry design practice for probabilistic rotor lifing in which a fatigue crack equal in size to the HA defect is assumed to be present and growing on the first fatigue cycle. The only difference is that the design practice assumes a circular crack while the Flight_Life analysis permitted noncircular shapes for increased accuracy in the comparisons.



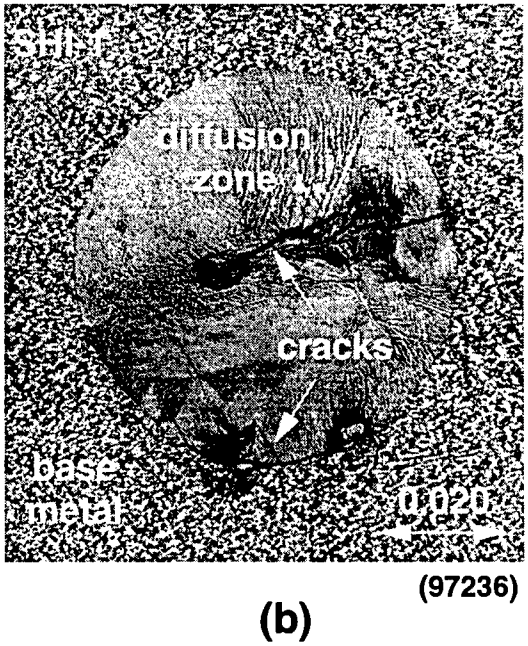
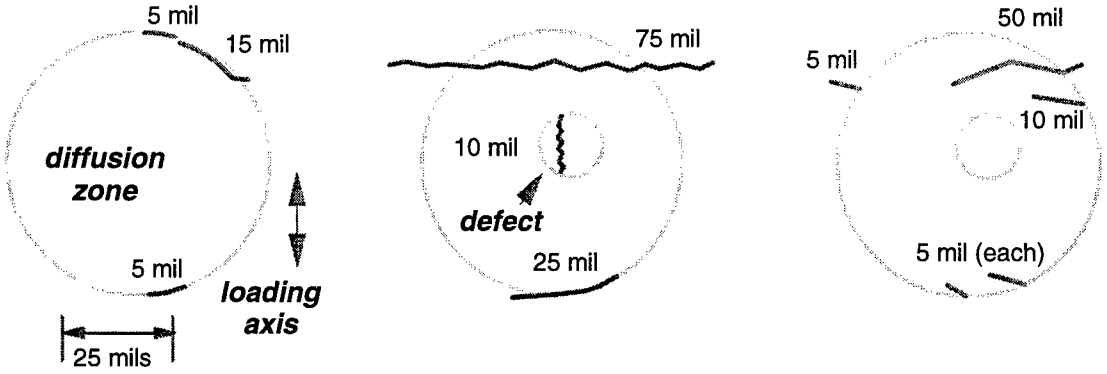


FIGURE 2-71. METALLOGRAPHIC SECTIONS AFTER TESTING OF INTERIOR DEFECT SPECIMEN SHI-1 (SMALL, HIGH NITROGEN) IN (a) THE CENTRAL REGION OF THE DEFECT AND (b) IN A DIFFUSION ZONE ENDCAP



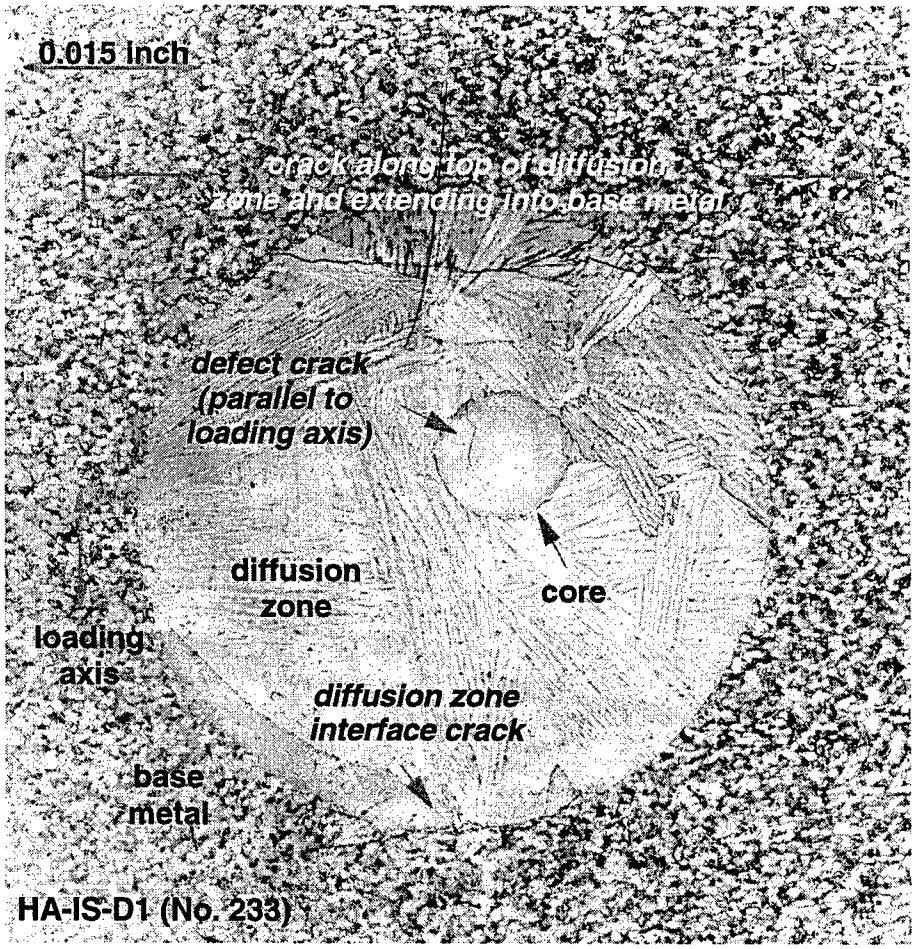
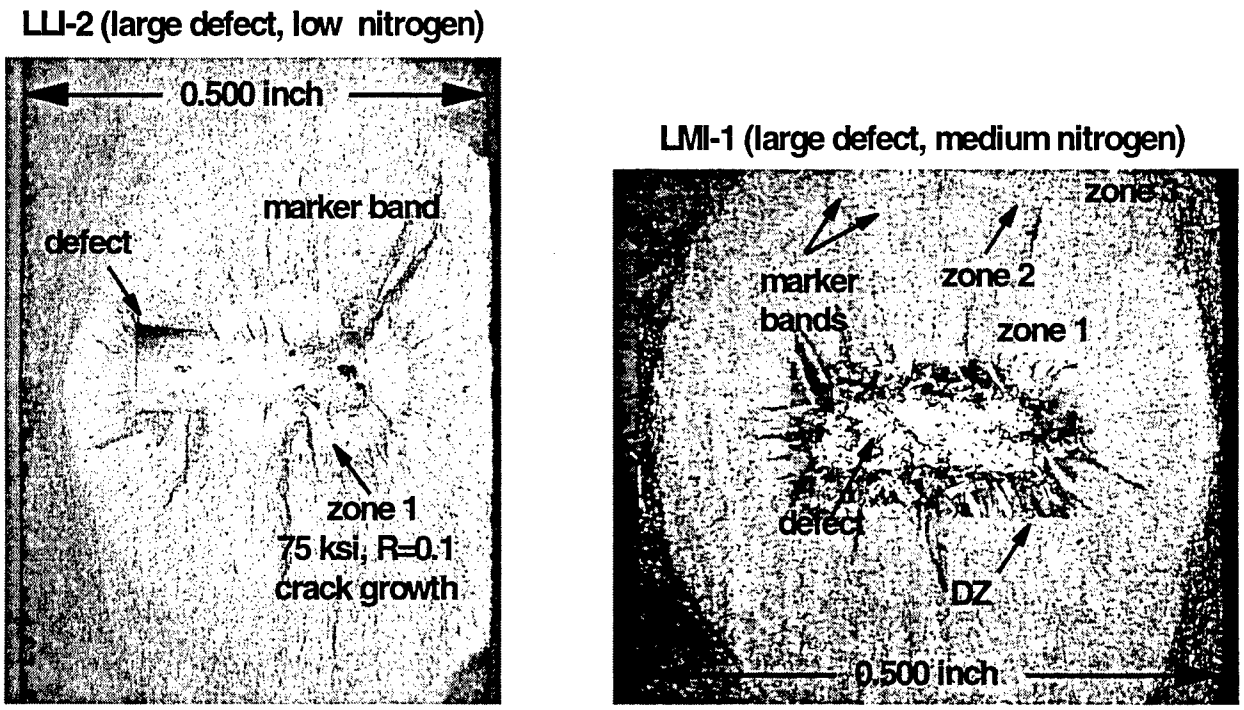


FIGURE 2-72. SUMMARY METALLOGRAPHIC SECTIONS MADE FROM HA-IS-D1 AFTER STATIC AND FATIGUE TESTING

Two fatigue tests with maximum stresses of 50 ksi exhibited no detectable fatigue crack growth into the matrix, even after 10,000 to 25,000 fatigue cycles were applied. Flight_Life analysis predicted that the fatigue crack in one of the specimens should have grown to failure.

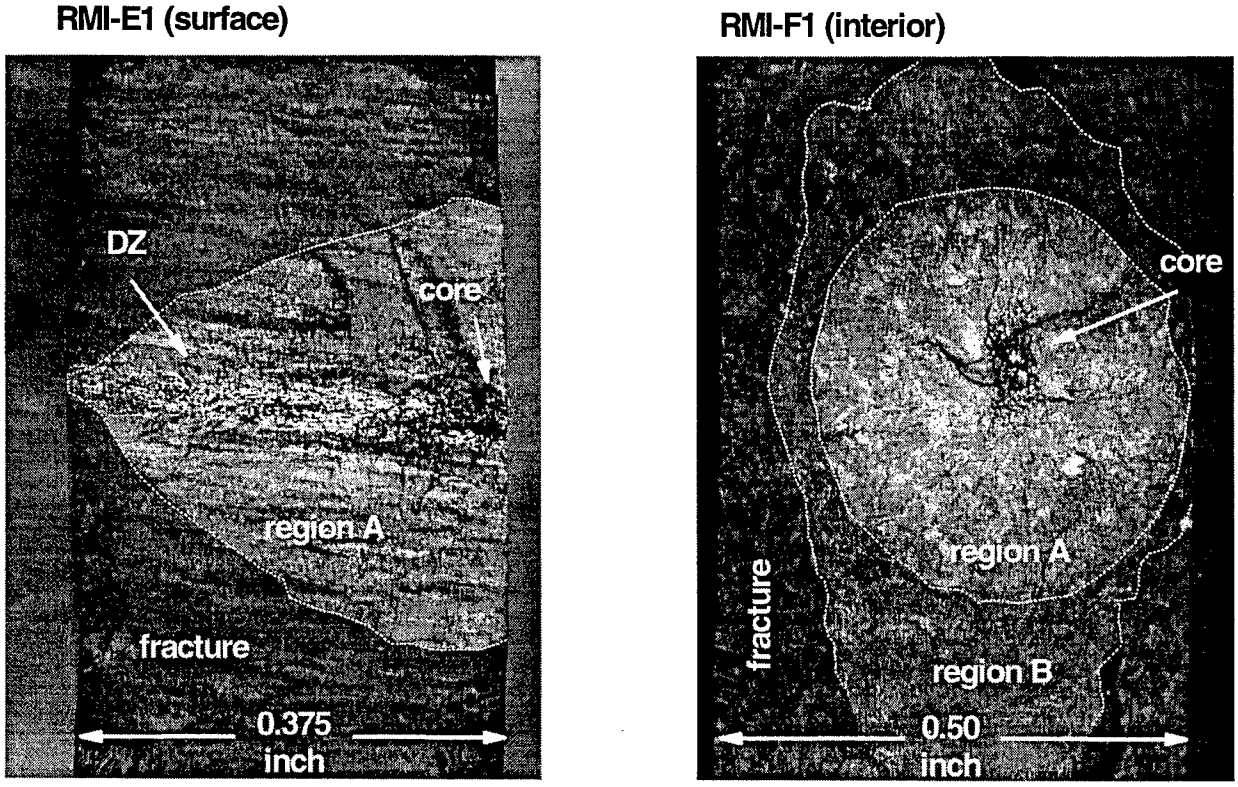
Two fatigue tests with maximum stresses of 75 ksi did grow fatigue cracks to failure but required considerably more fatigue cycles to grow the crack than predicted by the Flight_Life analysis. In both of these tests, 10,000 fatigue cycles were applied to grow the crack from the initial defect to an intermediate size clearly delineated by marker banding, as shown in figure 2-73. In both cases, Flight_Life analyses indicated that this amount of crack growth should have occurred in about 2,500 cycles. The difference between the 2,500 cycles (predicted) and the 10,000 cycles (experimental) may be attributable to a nucleation period required to fully crack the defect and form a stable, growing fatigue crack in the matrix.



(a) (b)

FIGURE 2-73. FRACTURE SURFACES FOR TWO LARGE, INTERIOR DEFECT SPECIMENS SUBJECTED TO FATIGUE LOADING

Fatigue tests were conducted on two specimens from the RMI CBS material. These results appeared to be qualitatively consistent with the synthetic defect tests. Fracture surfaces are shown in figure 2-74. The first RMI CBS test (RMI E1) was conducted on a specimen with a surface defect and a diffusion zone that extended well into the specimen. Crack growth along the surface proceeded quickly, as in the synthetic tests. However, the patterns of cracking observed on the posttest fracture surface indicated that the diffusion zone did not crack immediately but that the fatigue crack initiated and grew incrementally along the diffusion zone during the test.



(a) (b)

FIGURE 2-74. FRACTURE SURFACES FOR TWO NATURALLY OCCURRING DEFECT (SURFACE AND INTERIOR) SPECIMENS SUBJECTED TO FATIGUE LOADING CONDITIONS

In the second RMI CBS test, the size of the embedded defect was not known until after the test. Fatigue cycling began at a maximum stress of 50 ksi. Although some AE activity was observed early in the test, it diminished, and so the maximum stress was increased to 62 ksi. Similar increases and then decreases in AE activity motivated another increase in stress to 75 ksi and finally to 100 ksi. The specimen fractured during 100 ksi cycling with clear evidence of significant fatigue crack growth prior to fracture. Posttest Flight_Life analysis indicated that, although no fatigue crack growth was predicted at 50 ksi and 62 ksi, substantial crack growth should have occurred at 75 ksi, and failure should have occurred relatively quickly—even from the initial defect size—at 100 ksi. Again, the difference between experimentally applied cycles and Flight_Life calculations suggests some nucleation period.

2.3.3 Relevance to Industry Field Experience.

In summary, HA anomalies cracked at low static stress levels when the anomalies were located at the surface, although crack extension into the matrix was problematic under static loading. Fatigue crack growth into the matrix from surface defects occurred relatively quickly.

Embedded HA anomalies exhibited substantially higher resistance to cracking under static load but still cracked substantially at applied stresses around 80 to 120 ksi. Low stress ratio fatigue

tests at applied maximum stresses ranging from 75 ksi to 100 ksi did exhibit growth into the matrix and eventual specimen failure. However, comparisons of observed cracking with Flight_Life predictions suggested that some significant number of fatigue cycles could be required to form a dominant, growing fatigue crack in the matrix in both the synthetic and RMI CBS defect specimens. This is consistent with the metallographic observations of distributed, discontinuous cracking in the defect core and diffusion zone. At lower stresses, fatigue crack growth into the matrix might not occur at all, even if predicted stress intensities based on initial defect sizes were greater than the fracture mechanics threshold.

However, it must be emphasized that this very small number of synthetic and natural HA tests represents a very limited parameter range. Furthermore, these tests may not be fully representative of actual hardware under actual service conditions. Actual hardware would have experienced a complete forging operation after defect formation, and it is possible that this forging operation would have either nucleated more severe initial cracks in the hard alpha anomaly or even grown cracks into the matrix itself. There is some industry experience suggesting that some rotor fatigue cracks nucleated at hard alpha defects did, in fact, begin growing in the matrix at the very beginning of life. However, it is not known at the present time how the conditions in those events (defect size, applied stress level, etc.) compare to the current test matrix. It is possible that larger defects, or defects in higher stress fields, would form a matrix fatigue crack much more quickly.

Until additional testing and analysis are performed, it seems appropriate to continue to use the current conservative industry assumption: assume a growing fatigue crack in the matrix on the first fatigue cycle with initial size equal to the size of the defect core plus the diffusion zone. However, additional testing and analysis should be performed to understand any differences between laboratory tests and industry field experience and to quantify any nonnegligible nucleation life of practical significance.

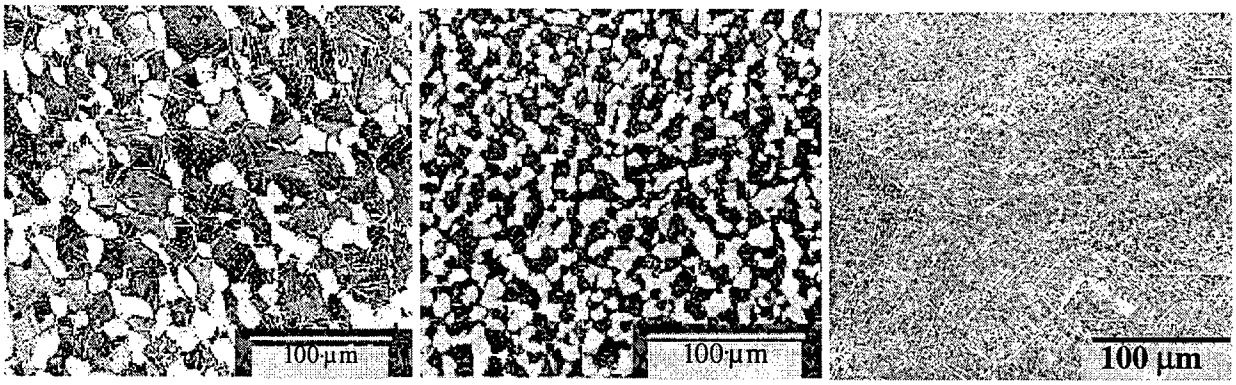
2.4 FATIGUE CRACK GROWTH BEHAVIOR OF TITANIUM ALLOYS.

2.4.1 Fatigue Crack Growth Data in Vacuum.

Hard alpha anomalies most commonly occur at subsurface locations. Since any fatigue cracks that nucleate at these anomalies are not exposed to the atmosphere, they grow in a vacuum-like environment. Numerous researchers have noted a difference between fatigue crack growth (FCG) rates in air and vacuum for titanium alloys [11–20]. However, these investigations have generally been limited to a single stress ratio (typically $R = 0.1$) and a single temperature (typically ambient). Information on systematic changes in vacuum behavior with stress ratio or temperature has not been available. Of greater significance, insufficient vacuum data are available to support a complete lifing system for FCG in turbine engine rotors, and therefore, it is difficult to accurately evaluate the risk associated with crack nucleation at subsurface HA anomalies. For this reason, a test program was conducted to develop baseline design data for fatigue crack growth of titanium rotor alloys in a vacuum environment. A complete documentation of the test procedures and results is provided in appendix I.

2.4.1.1 Materials and Test Procedures.

Experiments were conducted on three rotor-grade titanium alloys: Ti-6Al-4V, Ti-6Al-2Sn-4Zr-2Mo+Si, and Ti-17. All specimens were machined from triple vacuum arch remelt (VAR) melted production forgings. The Ti-6-4 was alpha + beta forged, solution heat treated below the beta transus, water quenched, and then overaged. The Ti-6-2-4-2 was alpha + beta forged, solution heat treated below the beta transus, rapid air cooled, and aged. The Ti-17 was forged above the beta transus, and then solution heat treated below the beta transus, water quenched, and aged. The resulting microstructures are shown in figure 2-75. Room temperature tensile properties are summarized in table 2-7.



(a) (b) (c)

FIGURE 2-75. MICROSTRUCTURES OF (a) Ti-6Al-4V, (b) Ti-6Al-2Sn-4Zr-2Mo+Si, AND (c) Ti-17

TABLE 2-7. ROOM TEMPERATURE TENSILE PROPERTIES OF TITANIUM ROTOR ALLOYS TESTED

Material	σ_{YS} (ksi)	σ_{ULT} (ksi)	% RA	% elongation
Ti-6-4	140	152	37	15
Ti-6-2-4-2	133	145	35	18
Ti-17	155	170	12	21

Vacuum FCG rate tests were conducted for a matrix of multiple temperatures and stress ratios at GEAE and AlliedSignal Engines following the standard test procedures used by those companies for the generation of design data. Test conditions are summarized in table 2-8.

TABLE 2-8. SUMMARY OF VACUUM FCG TEST CONDITIONS

Material	Test Lab	Stress Ratios	Temperatures (°F)
Ti-6-4	GEAE	0, 0.5, 0.75	75, 400
Ti-6-2-4-2	AlliedSignal Engines	0.05, 0.5, 0.75	75, 600, 1000
Ti-17	GEAE	0, 0.6	75, 750

Although the tests were conducted at different sites, similar test procedures were followed. Region II (Paris regime) tests were conducted with small surface crack tension, SC(T), specimens, also known as Kb bar specimens [21]. These specimens had a nominal gage section of 168 × 400 mils (GEAE) or 226 × 450 mils (AlliedSignal Engines) with a semicircular electrodischarge machining (EDM) notch of approximate dimensions 7 × 14 mil (GEAE) or 10 × 20 mil (AlliedSignal Engines) in the center of the wide face. Tests in the near-threshold regime were conducted at AlliedSignal Engines on the same SC(T) geometry and at GEAE on single edge notch button head (SENBH) specimens with a 100 mil × 400 mil gage section and a 15 mil (EDM) notch.

Crack lengths were monitored using the DC electric potential drop method [21], with crack sizes posttest corrected from visual measurements of marked initial and final crack dimensions on the fracture surfaces. Stress intensity factors were calculated from the Newman-Raju solution [22] for SC(T) and the Harris solution [23] for SENBH. Tests were conducted under either constant load or constant ΔK-gradient (increasing or decreasing) at constant R, where the ΔK-gradient was as high as ±20/inch (AlliedSignal Engines) or ±30/inch (GEAE). Research at the engine companies has indicated that these gradients, which are more severe than the recommendations of ASTM E647, do not significantly influence the measured growth rates, and are necessary to obtain adequate data on small specimens [24]. Crack growth rates were calculated with incremental polynomial methods. Vacuum levels were better than 10^{-7} Torr for all tests. Test frequencies were either 1 Hz (some ambient and 400°F tests) or 0.33 Hz (all other tests). Brief studies found no difference in growth rates between these two frequencies at the conditions where the faster frequency was employed.

2.4.1.2 Vacuum Level Effects Study.

It is not clear from the literature what vacuum level is adequate to maintain the full effect of vacuum on FCG rates. Irving and Beevers [12] cited general evidence for other materials of the existence of a critical pressure below which no further effect on growth rates would be observed with changes in vacuum pressure. The only evidence they could cite for titanium was unpublished research of James on Ti-5Al-2½Sn, where no difference was found between FCG rates at 10^{-5} Torr and $3(10)^{-8}$ Torr. Sugano et al. [25] found that the total fatigue lives of notched commercially pure titanium were an order of magnitude longer at 10^{-5} Torr compared to slightly higher pressures. Bache et al. [20] found no difference in FCG rates for Ti-6Al-4V between lab air and 10^{-2} Torr pressures but a large difference at 10^{-6} Torr.

A brief study of vacuum level effects was conducted at NASA Langley Research Center on the Ti-6Al-4V forging material tested in this program. The study employed an ultrahigh vacuum chamber with an assortment of pumps and gages capable of a wide range of pressures down to $3(10)^{-10}$ Torr. Constant ΔK FCG tests were conducted at 400°F (204°C) and f = 0.33 Hz with a pin-loaded extended compact tension specimen [26], also known as the extended single edge cracked tension specimen. Fatigue crack length was monitored continuously via crack mouth opening compliance with visual confirmation via a long focal length optical microscope at 400×.

Sample results from the brief NASA Langley vacuum level study are shown in figure 2-76 for ΔK = 18 ksi$\sqrt{\text{in.}}$, R = 0.05. The graph of crack length vs cycles highlights extremely small

changes in *da/dN* under constant ΔK and different vacuum levels. Because it is difficult to maintain a perfectly constant vacuum level, each region of crack growth is characterized by a range of vacuum levels. A factor of two reduction in *da/dN* was observed when the vacuum was changed from 10^{-4} to 10^{-5} Torr, but negligible variations in growth rates were observed for vacuum levels ranging from 10^{-5} to 10^{-9} Torr. A test at ΔK = 9 ksi$\sqrt{in.}$, R = 0.5 found no significant variation in *da/dN* between vacuum levels of 10^{-6} and 10^{-9} Torr but found a clear increase in *da/dN* at 10^{-5} Torr. Obviously, this brief, informal study does not definitively resolve the vacuum level question, and further testing at much lower growth rates (very near threshold) would be of particular value. However, the limited data available suggest that vacuum levels better than 10^{-6} Torr have been adequate to capture full vacuum effects for engineering purposes and, therefore, the 10^{-7} Torr or better levels employed at GEAE and AlliedSignal Engines were sufficient.

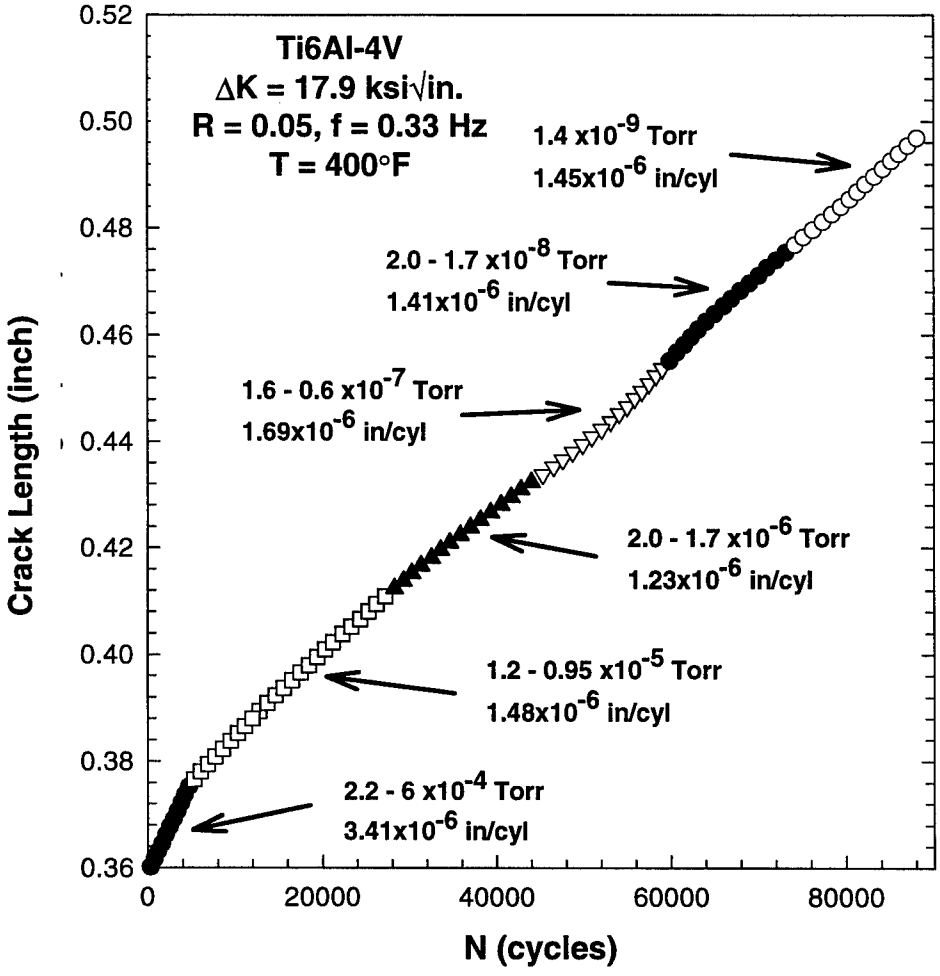


FIGURE 2-76. FATIGUE CRACK GROWTH DATA FOR Ti-6Al-4V AT CONSTANT ΔK AND DIFFERENT VACUUM LEVELS

2.4.1.3 Test Results.

Vacuum FCG results for Ti-6-4 at 75° and 400°F (24° and 204°C) for stress ratios of $R = 0, 0.5$ and 0.75 are shown in figures 2-77 and 2-78. The data demonstrated typical stress ratio and temperature effects for this material as observed in testing in air. Changing temperature from 75° to 400°F did not affect vacuum FCG rates significantly except at the highest mean stresses ($R = 0.75$).

Vacuum FCG rates for Ti-6-2-4-2 at 75°, 600°, and 1000°F (24°, 316°, and 538°C) for stress ratios of $R = 0.05$, 0.5, and 0.75 are shown in figures 2-79, 2-80, and 2-81. Again, the data demonstrated typical stress ratio and temperature effects. Mean stress effects were more pronounced at higher temperatures. No temperature effects were evident between 75°F and 600°F at $R = 0.05$ and 0.5, but temperature effects were seen at all stress ratios for 1000°F and at $R = 0.75$ for 600°F.

Vacuum FCG rates for Ti-17 at 75° and 750°F (24° and 315°C) for stress ratios of $R = 0$ and 0.6 are shown in figures 2-82 and 2-83. No significant temperature effects were observed.

The significance of the vacuum behavior becomes much clearer when compared directly with FCG rate data in laboratory air. Representative comparisons of the vacuum data with the trends of relevant air data from the Damage Tolerant Design Handbook (DTDH) [27] are shown in figures 2-84 through 2-88. In each case, the vacuum and air data exhibited the same growth rates in the upper Paris regime. The vacuum FCG rates were considerably slower in the near-threshold regime, and the apparent thresholds under vacuum conditions were significantly higher than under ambient conditions. Similar vacuum vs. air trends were seen at all combinations of material, stress ratio, and temperature where available data permitted direct comparisons, including elevated temperature tests with Ti-6Al-2Sn-4Zr-2Mo+Si. (See appendix I) These trends were in agreement with the literature data cited earlier at lower stress ratios and temperatures.

Regressions of all the data were conducted to obtain constants for fatigue crack growth equations contained in the DARWIN computer code. All data were fitted with single linear Paris relationships at individual combinations of temperature and stress ratio. Independent analyses were performed to obtain stress intensity factor range threshold (ΔK_{th}) values at each temperature and stress ratio. Constants for Walker and Newman crack closure stress ratio models were obtained at each temperature. Appendix I includes graphical documentation of all regressions and tabulations of all regression constants.

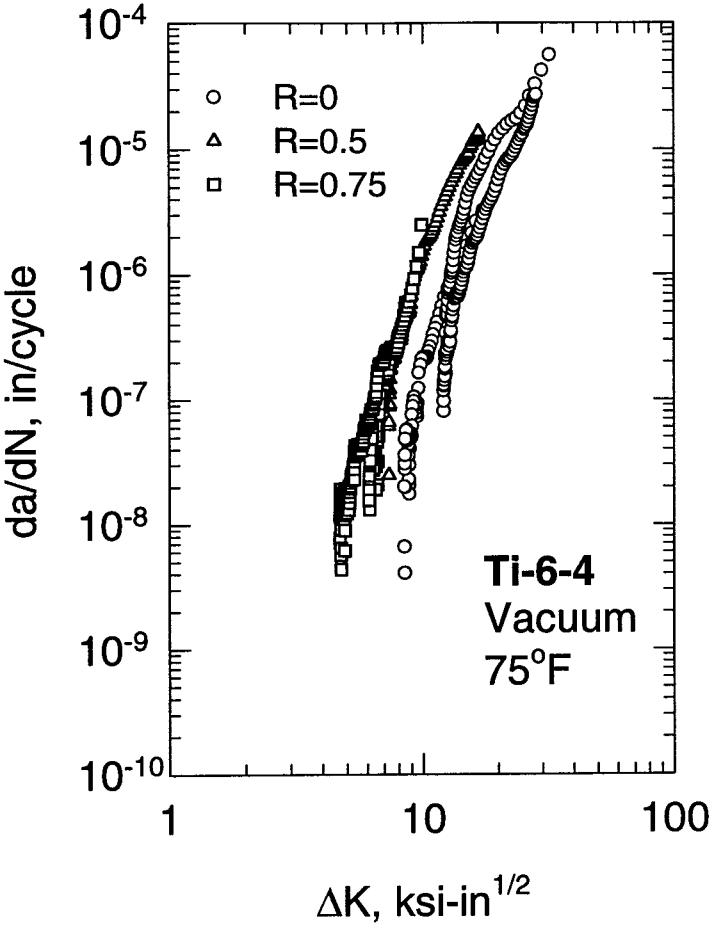


FIGURE 2-77. VACUUM FCG DATA FOR Ti-6Al-4V AT 75°F (24°C)

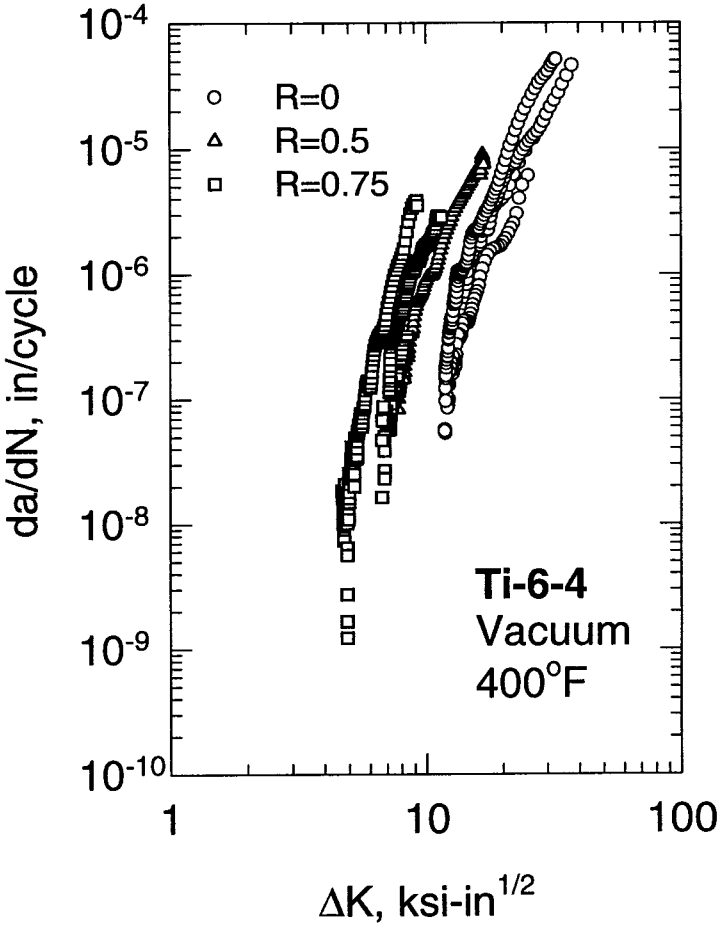


FIGURE 2-78. VACUUM FCG DATA FOR Ti-6Al-4V AT 400°F (204°C)

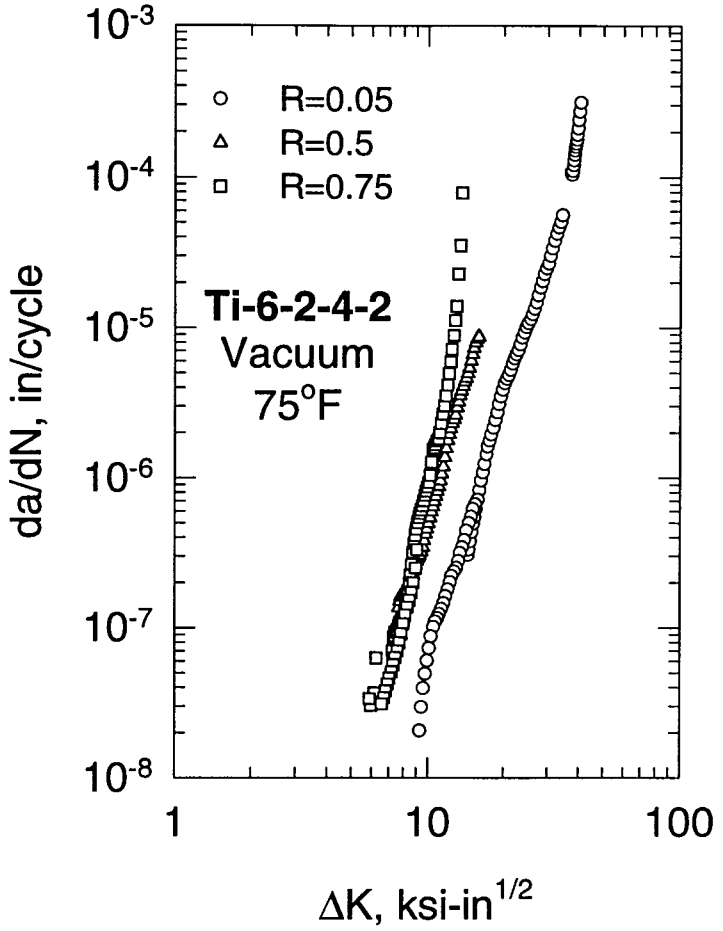


FIGURE 2-79. VACUUM FCG DATA FOR Ti-6Al-2Sn-4Zr-2Mo+Si AT 75°F (24°C)

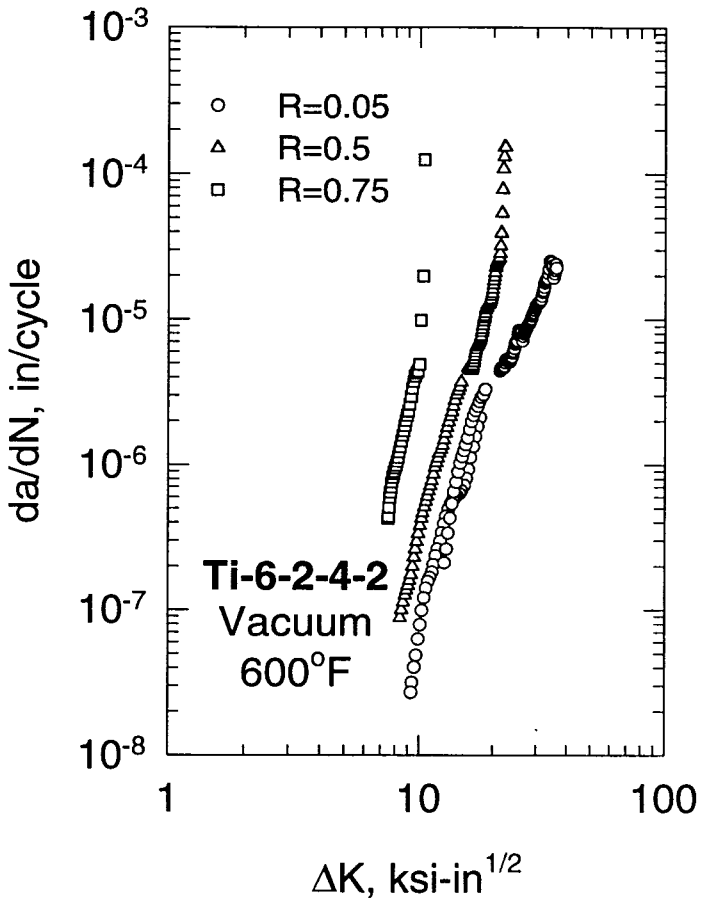


FIGURE 2-80. VACUUM FCG DATA FOR Ti-6Al-2Sn-4Zr-2Mo+Si AT 600°F (316°C)

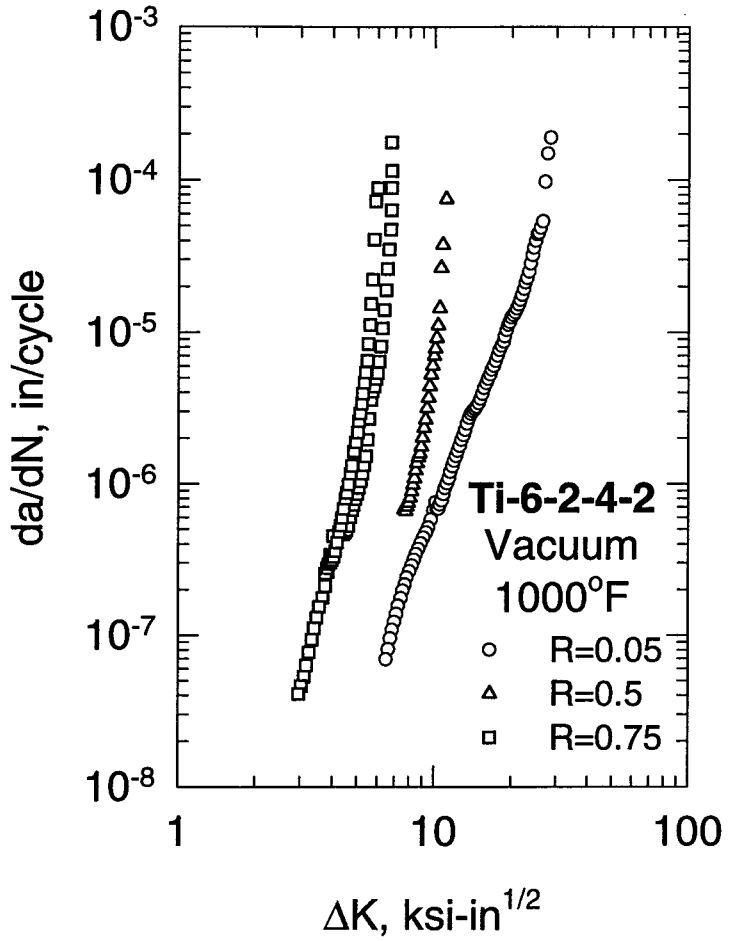


FIGURE 2-81. VACUUM FCG DATA FOR Ti-6Al-2Sn-4Zr-2Mo+Si AT 1000°F (538°C)

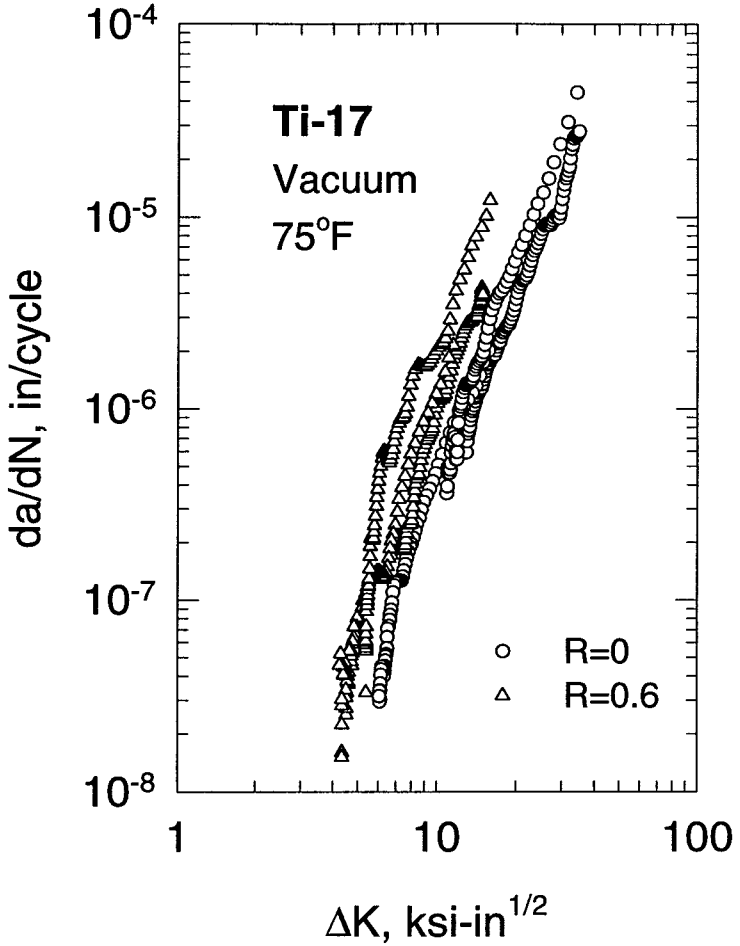


FIGURE 2-82. VACUUM FCG DATA FOR Ti-17 AT 75°F (24°C)

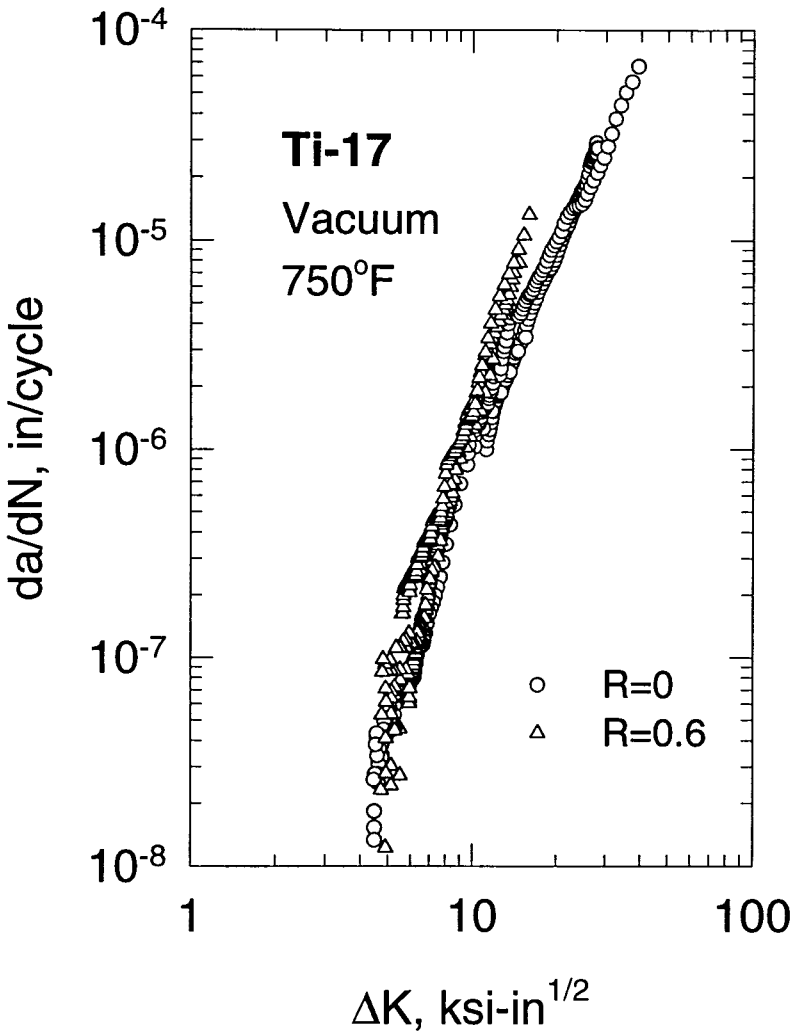


FIGURE 2-83. VACUUM FCG DATA FOR Ti-17 AT 750°F (399°C)

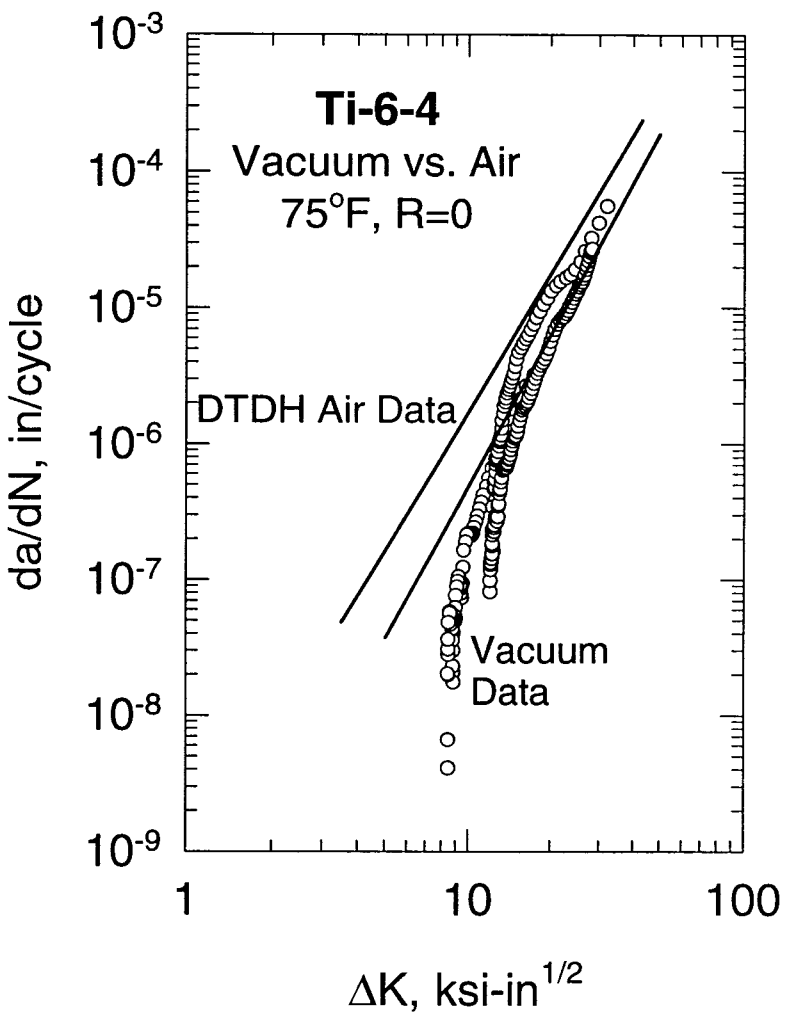


FIGURE 2-84. COMPARISON OF VACUUM DATA WITH AIR DATA FROM DTDH FOR Ti-6Al-4V AT 75°F (24°C) AND $R = 0$

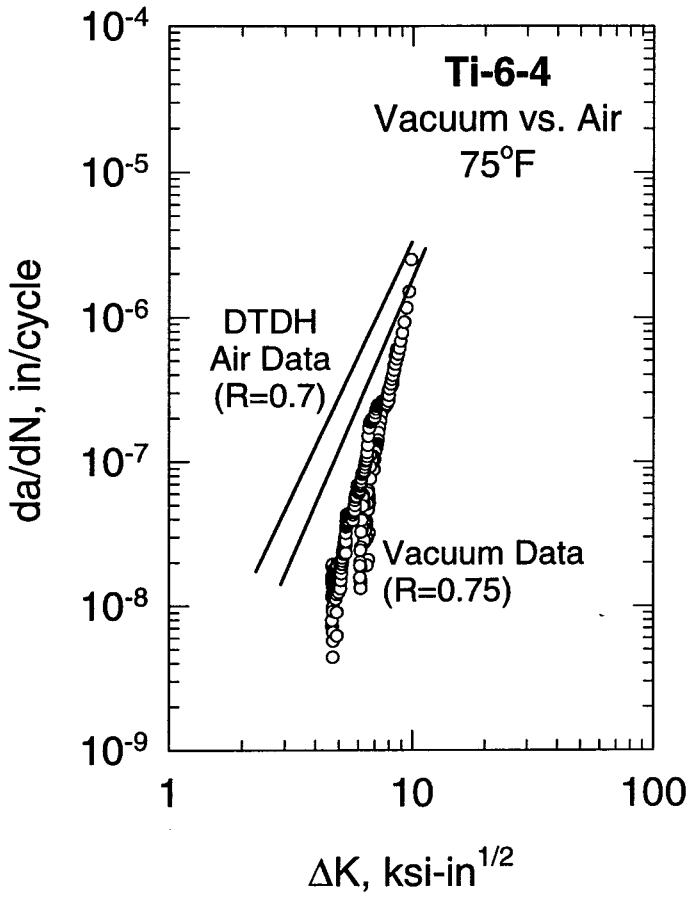


FIGURE 2-85. COMPARISON OF VACUUM DATA WITH AIR DATA FROM DTDH FOR Ti-6Al-4V AT 75°F (24°C) AND $R = 0.75$

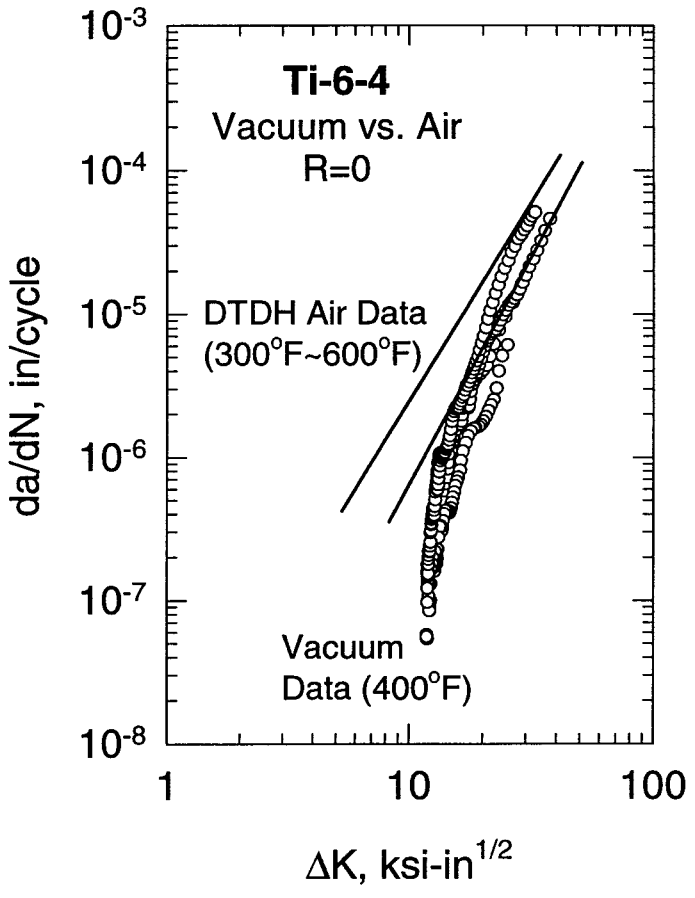


FIGURE 2-86. COMPARISON OF VACUUM DATA WITH AIR DATA FROM DTDH FOR Ti-6Al-4V AT 300°-600°F (149°-316°C) AND $R = 0$

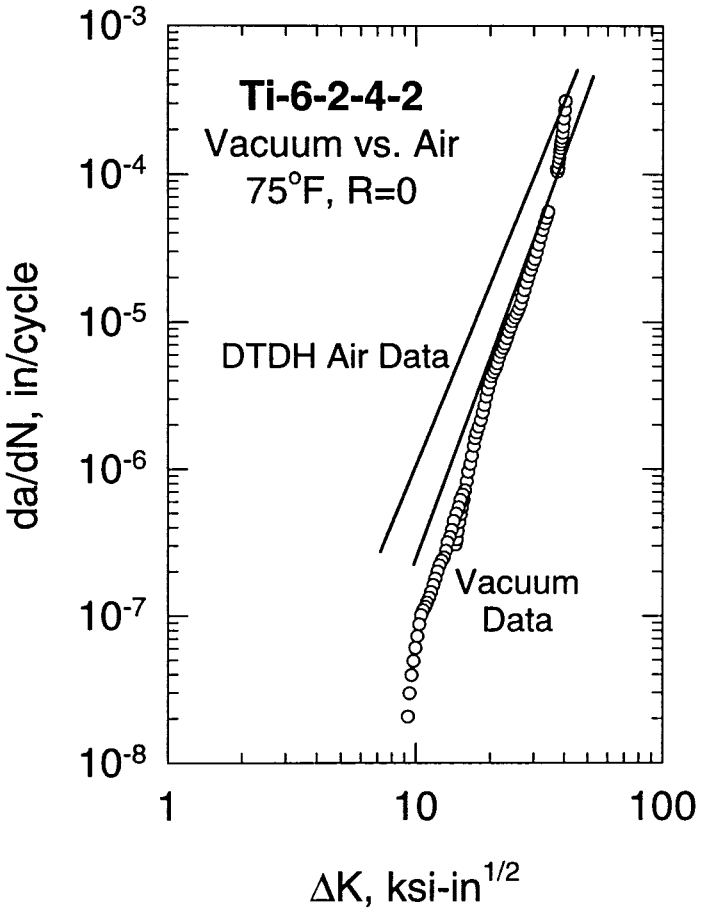


FIGURE 2-87. COMPARISON OF VACUUM DATA WITH AIR DATA FROM DTDH FOR Ti-6Al-2Sn-4Zr-2Mo+Si AT 75°F (24°C) AND $R = 0$

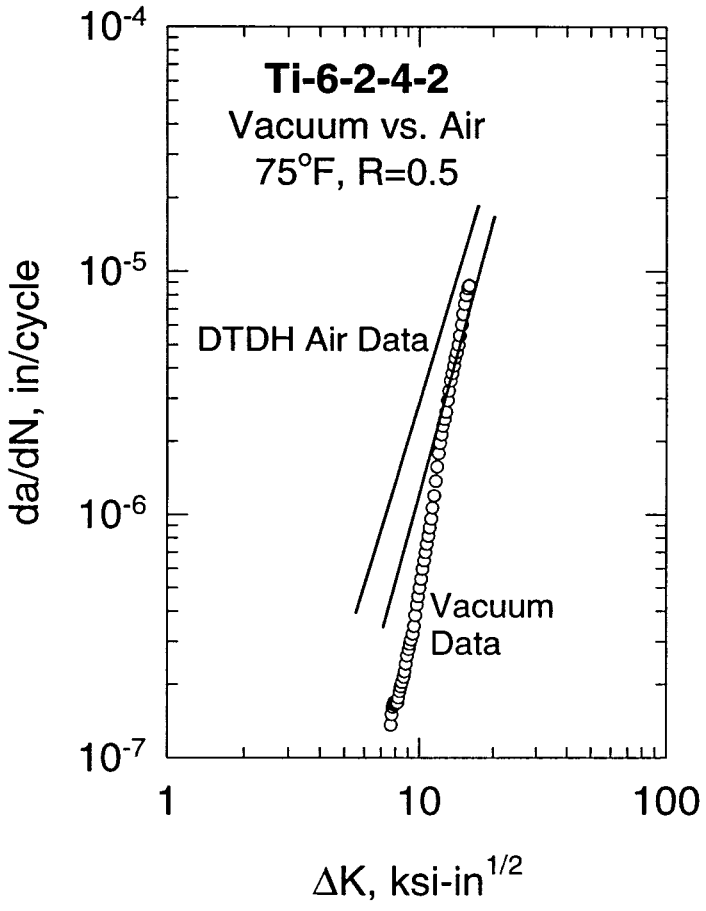


FIGURE 2-88. COMPARISON OF VACUUM DATA WITH AIR DATA FROM DTDH FOR Ti-6Al-2Sn-4Zr-2Mo+Si AT 75°F (24°C) AND $R = 0.5$

2.4.2 Life Scatter in Fatigue Crack Growth Data for Ti-6Al-4V in Air.

2.4.2.1 Background.

The enhanced life management process for turbine engine rotors is based on probabilistic damage tolerance methods, in which the various uncertainties that impact lifetime calculations are directly factored into those calculations. These uncertainties include the probability of occurrence of a hard alpha defect, the size of that defect, the probability that the defect will be missed by NDE, and any uncertainties in the rotor stress analysis. Another uncertainty of potential importance is variability in the crack growth analysis itself: the calculated lifetime for a flaw of a given initial size and shape.

Uncertainty in the lifetime calculation can arise from at least two different sources. The first source of variability is inherent scatter in the crack growth rate itself. Fatigue crack growth is inherently a stochastic phenomenon due to the local interactions between a complex crack geometry and a complex microstructure. An individual crack will speed up or slow down as it grows through different features in the microstructure, and overall microstructural variations between different samples of the same nominal material will introduce further scatter in growth rates.

A second source of variability in lifetime calculations can be labeled modeling error. Most fatigue crack growth equations are based on multivariable regressions of multiple data sets that have been lumped together. Any inexactness in these largely empirical formulations describing the resistance to FCG will lead to errors in life prediction for certain combinations of variables. Similarly, any inexactness in calculations of the crack driving force—for example, error in a stress-intensity factor solution based on an idealized crack geometry in an idealized stress field—will further degrade the accuracy of the resulting life prediction.

A comprehensive treatment of all these potential sources of error is beyond the scope of the current study. Instead, the current brief study had the goal of quantifying only the material scatter contribution to the uncertainty in the lifetime calculation. Available replicate data from simple coupon experiments were analyzed to characterize the inherent scatter in typical Ti-6Al-4V FCG behavior. These results provide insight into the minimum scatter that should be considered in any probabilistic damage tolerance analysis of titanium rotors and provide a starting point for any future consideration of other sources of life scatter.

2.4.2.2 Sources of Data.

Undoubtedly the largest available set of replicate fatigue crack growth data for a Ti-6Al-4V rotor alloy was generated in the AGARD "Engine Disc Cooperative Test Programme" completed in 1988 [28, 29]. Twelve laboratories from seven countries participated in a tightly controlled round-robin test program. Fatigue crack growth rate data were generated with two different specimen geometries (compact tension, (CT) and corner crack, (CC)) under room temperature, constant amplitude loading at $R = 0.1$. A common set of detailed test procedures was followed by all participants. All specimens were machined from two nominally identical fan disk forgings supplied by Rolls-Royce. The forgings were in the conventional ($\alpha+\beta$) solution treated and aged (STA) condition, resulting in a duplex microstructure of primary α and platelet α in β. About 70

fatigue crack growth tests were reported in the core program. Complete tabulations of the original test data (*a, N, da/dN*, and ΔK values) were made available to the current study.

Additional fatigue crack growth data were made available to Southwest Research Institute from some of the individual engine companies on the turbine rotor material design (TRMD) program team. These proprietary design data were supplied under the terms of nondisclosure agreements that preclude any detailed description in this report. The proprietary data were analyzed following the same general procedures applied to the AGARD data in order to evaluate the generality of any conclusions reached from the AGARD data. All proprietary data analyzed in this task were also taken from tests on standard specimens machined from rotor forgings of Ti-6Al-4V in the conventional metallurgical condition. Tests were conducted at room temperature and a stress ratio nominally $R = 0.1$.

2.4.2.3 Analysis Procedure.

Development of the statistical analysis procedure itself is of particular importance to insure the engineering relevance of the results. The procedure adopted was designed to minimize any contributions from modeling error. Furthermore, the procedure deliberately focused on describing scatter in the lifetime to reach certain crack sizes rather than scatter in crack growth rate. Statistical methods that focus on growth rate scatter sometimes fail to adequately address the variability in the growth rate of a single crack as it grows versus the variability of one crack versus another. As a result, rate scatter methods sometimes fail to accurately describe scatter in the calculated total lifetime, which is the final result of greatest importance.

The first step in the analysis procedure was to fit the data from each individual crack growth test with a suitable engineering FCG equation. Tailoring of each equation to a specific set of data helps to ensure that the regression itself will not introduce substantial additional (modeling) error. In fact, a verification calculation was performed for each specimen by integrating the resulting regression equation between the initial and final crack lengths for that specimen in order to predict the lifetime of the specimen and comparing this prediction with the actual lifetime. If the difference was substantial, then the data set and regression were revisited to determine if any artifacts had been missed.

Some data were censored from this analysis process based on engineering judgement. In a few cases, the fatigue crack growth data from a particular test exhibited such dramatic deviations from commonly observed behavior that some fundamental problem with the performance of the test was implied. In other cases, the available data from a particular test covered such a narrow range of crack sizes (i.e., the amount of data was so limited) that any regression was inherently unstable. About ten percent of the tests were removed from consideration for one of these reasons.

In other cases, individual data points from the very beginning or the very end of a specific test were censored if those points exhibited substantial deviations from conventional linearity. Deviations at the beginning of a data set generally reflect some irregularity in the crack shape as it evolves from the initial notch/precrack or some artificial influence of the notch or precracking process. Deviations at the end of a data set typically represent the superposition of static mode crack growth as instability is approached or the superposition of time-dependent or

plasticity effects as cracks become long and stresses become large in the remaining ligament. Neither of these classes of deviations is significant to the fundamental scatter issues at hand, but both types of deviations can significantly degrade the quality of the regression over the range of normal data.

It was not possible to evaluate the scatter in life from the actual test results since every specimen had a slightly different initial and final crack size, and many specimens had slightly different applied loads. However, generation of a complete set of regression constants for each and every test specimen did make a meaningful comparison possible. The regression constants from all specimens were used to make a set of life predictions, as many life predictions as there were specimens, but each with a common applied cyclic load and common initial and final crack lengths. The resulting set of simulated fatigue lifetimes were then analyzed to determine appropriate statistical distribution parameters.

2.4.2.4 Results.

The results of this analysis process for the AGARD round-robin data are illustrated in the following figures.

A simple bilinear Paris equation was found to be an appropriate regression form for the data (note that none of the available AGARD data extended down to near-threshold growth rates). This bilinear relationship can be written as

$$\frac{da}{dN} = A_0 \ \Delta K^{n_0} \tag{2-15}$$

for $\Delta K \leq \Delta K^*$ and

$$\frac{da}{dN} = A_1 \ \Delta K^{n_1} \tag{2-16}$$

for, $\Delta K \leq \Delta K^*$ where ΔK^* is the "knee" in the bilinear curve.

An example of this bilinear form is shown in figure 2-89 in comparison to the experimental data set from which the regression was derived. The knee where the upper and lower lines intersected typically occurred around 16 to 19 ksi$\sqrt{\text{in}}$. In some of the AGARD data sets, all of the available data were either above or below this knee and so a single linear regression was more appropriate.

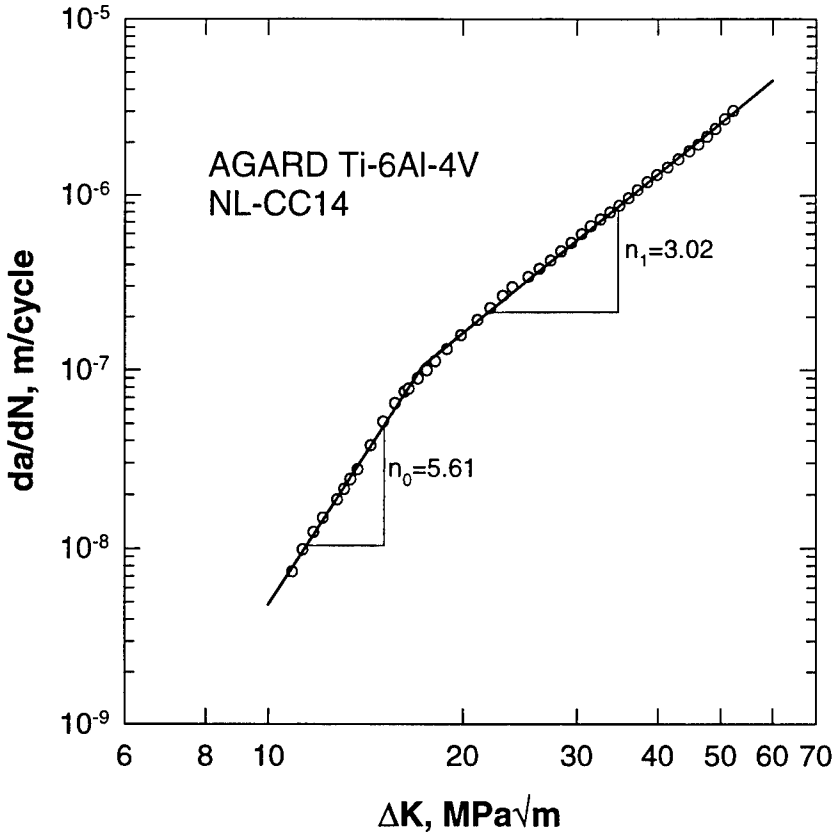


FIGURE 2-89. BILINEAR REGRESSION TO SAMPLE AGARD DATA SET

All of the resulting regressions were validated by integrating each resulting equation and comparing the result against the experimentally observed life. The resulting comparisons of actual vs predicted lifetime ratios are summarized in figure 2-90. Note that most predictions were accurate within a few percent, and all except one were accurate within five percent. Therefore, modeling error has been minimized by fitting each test specimen with its own equation.

The resulting pairs of $A_0 - n_0$ and $A_1 - n_1$ are shown graphically in figure 2-91 for the regressions from the AGARD CT specimen and in figure 2-92 for the regressions from the AGARD CC specimen. The A-n pairs are segregated because of a slight specimen dependence of the regressions. The different acronyms in the figure legends denote the different laboratories participating in the round-robin test program. These graphs demonstrate a general log-linear relationship between A and n that has often been observed in the literature for a variety of different materials. Clearly, A and n are not fully independent variables. Any probabilistic treatment that attempts to describe scatter in growth rates on the basis of scatter in crack growth rate properties (i.e., scatter in A and n) must address this relationship appropriately. Some treatments in the literature that address scatter in FCG rates by holding the slope n constant and varying the intercept A are inherently unsatisfactory and may easily overpredict variability.

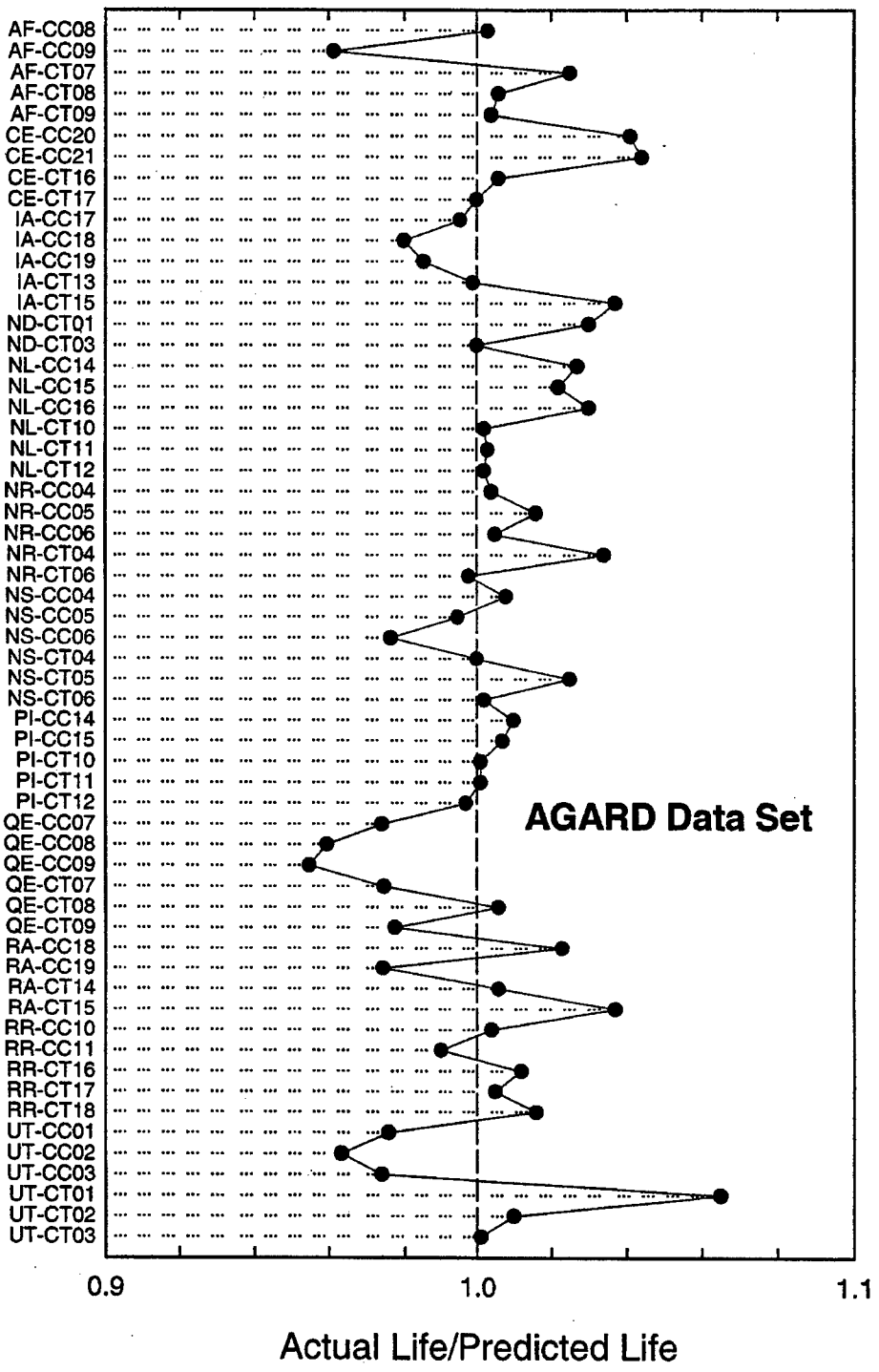
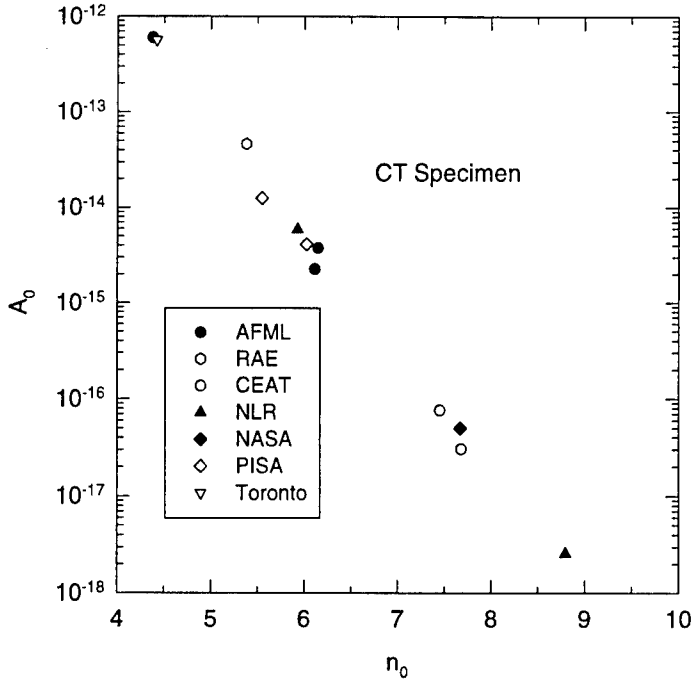


FIGURE 2-90. SUMMARY OF ACTUAL/PREDICTED LIFE RATIOS FOR AGARD REGRESSIONS



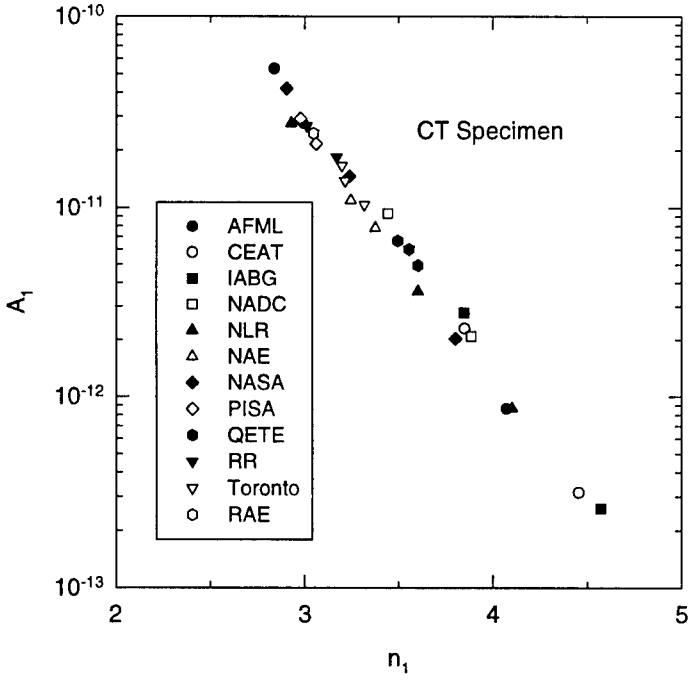
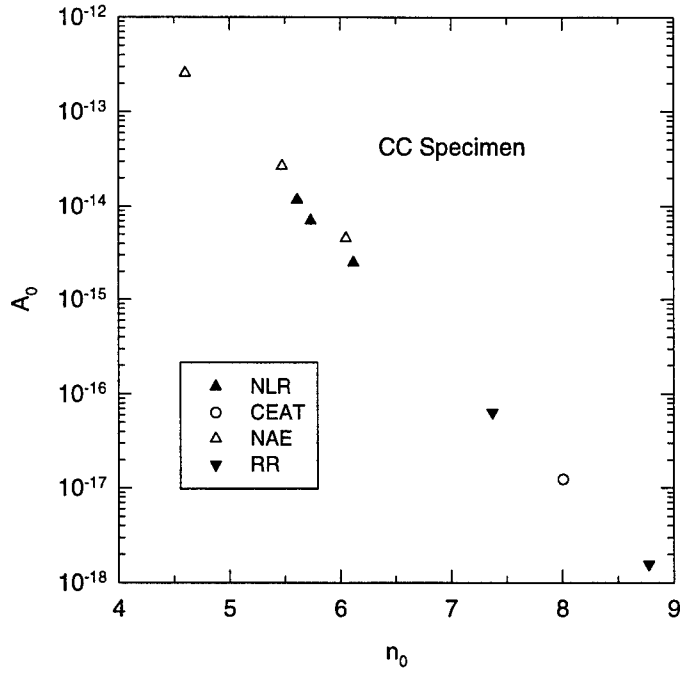


FIGURE 2-91. SUMMARY OF FCG REGRESSION CONSTANTS FOR AGARD CT SPECIMENS



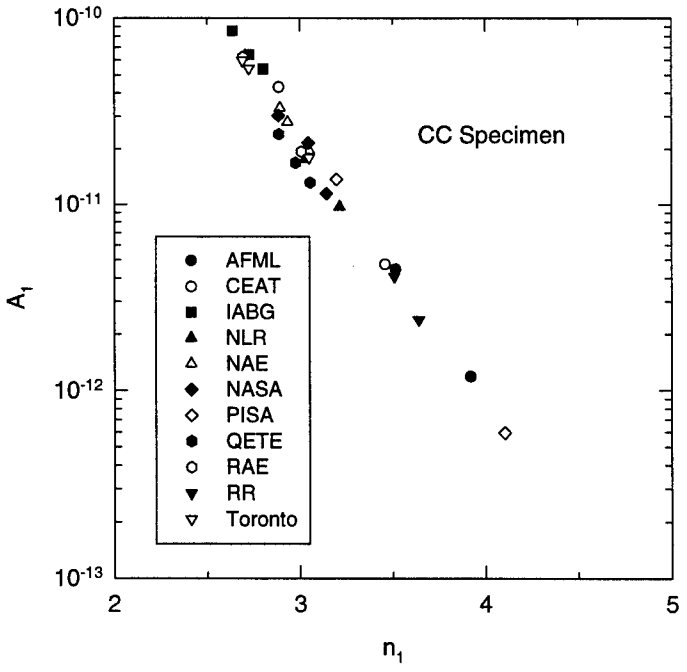


FIGURE 2-92. SUMMARY OF FCG REGRESSION CONSTANTS FOR AGARD CC SPECIMENS

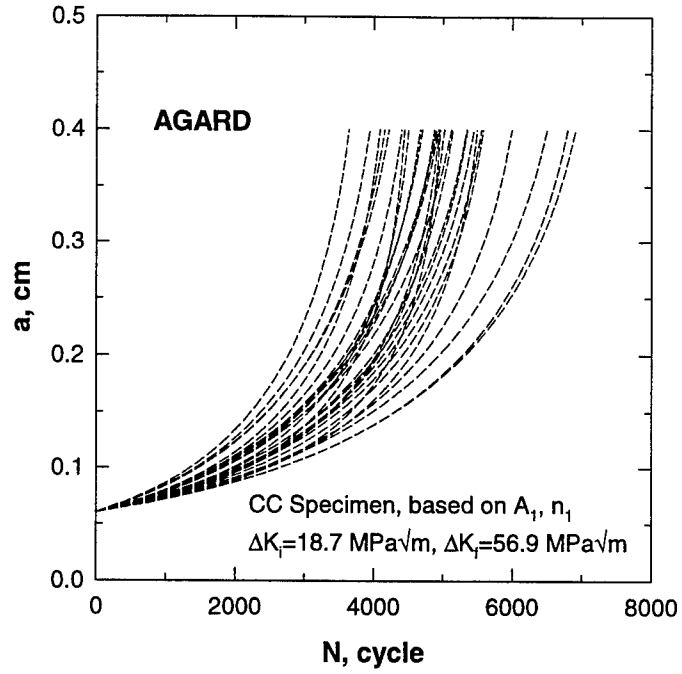
In the current work, however, scatter is being treated not on the basis of scatter in the FCG equation parameters but directly on the basis of scatter in the total fatigue life. It was not possible to directly analyze the scatter in the actual experimental lives from the AGARD tests since each test was conducted with slightly different initial and final crack lengths and sometimes a different applied cyclic load. Therefore, all the pairs of A and n values were used to construct a series of simulated tests, each test having the same initial and final crack length and the same applied cyclic load.

The resulting graphs of calculated crack length vs cycles (a vs N) for the simulated tests based on the upper line of the bilinear equation are shown in figure 2-93. The graphs for the simulations based on the full bilinear equation are shown in figure 2-94. The number of simulations is smaller in figure 2-94 because some of the data sets only permitted regression of the upper line or the lower line due to the range of ΔK spanned.

The simulations generated analytical data on each specimen for the number of fatigue cycles to reach specified crack lengths. The resulting data were evaluated statistically to determine appropriate distribution types and estimated statistical parameters. Both lognormal and Weibull distributions were acceptable representations of most data, but the lognormal was chosen because it appeared to be a slightly more suitable form in many cases.

The coefficient of variation (COV) of the estimated lognormal distribution was calculated at a series of incremental crack lengths from the estimated mean and standard deviation. The COV is plotted as a function of crack length in figure 2-95 for the CC and CT geometries. These calculated COV values are based only on those simulations from AGARD specimens that originally yielded a bilinear regression (i.e., those that covered an adequately wide range of ΔK in the original test data). Note that the COV is higher for smaller crack sizes (lower values of ΔK on the lower line of the bilinear form) and then gradually decreases as the cracks grow. This trend indicates that scatter is greater for smaller cracks closer to the threshold regime but that this scatter tends to average out more evenly as cracks get longer.

As mentioned earlier, some additional replicate FCG data was made available to Southwest Research Institute (SwRI) from some of the individual engine companies on the TRMD program team, and these proprietary data were analyzed following the same general procedures applied to the AGARD data. The bilinear equation was again found to be a suitable form. Because of the proprietary nature of the data, the final results of the statistical analyses are shown in a sanitized form. Figure 2-96 shows changes in COV for the lognormal distributions derived from the crack growth simulations, plotted here as a function of applied ΔK rather than crack size. The COV values from two different engine company data sets are graphed alongside the previous AGARD results. The comparison indicates that the general COV trends are the same for all four data sets, gradually decreasing with increasing ΔK. Specific calculated COV values vary somewhat, ranging from 0.3 – 0.5 below ΔK = 15 ksi$\sqrt{\text{in}}$, to 0.1 – 0.4 in the upper Paris regime.



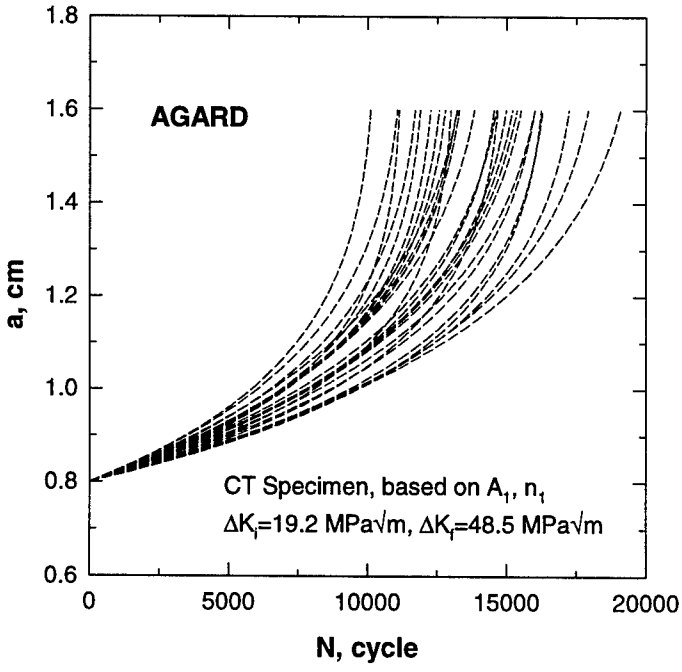
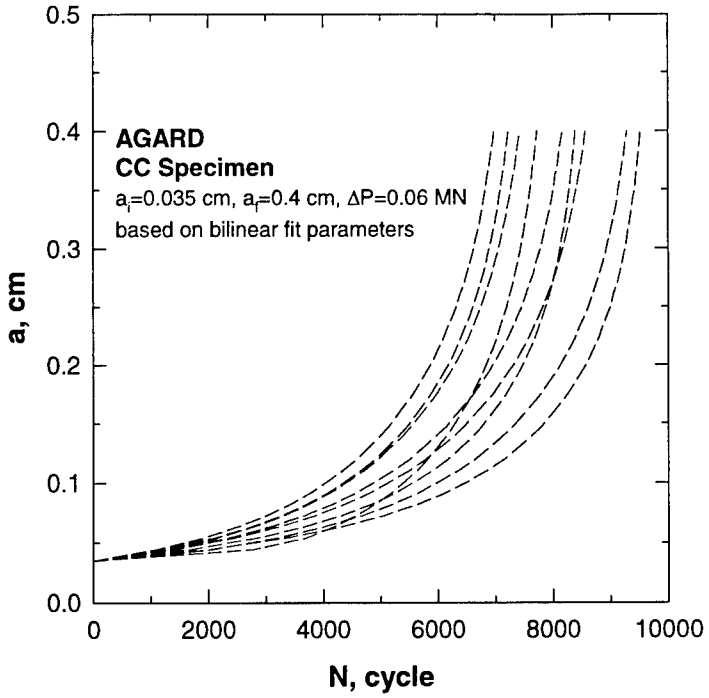


FIGURE 2-93. CRACK LENGTH HISTORIES FOR SIMULATED AGARD FCG TESTS (UPPER LINE ONLY)



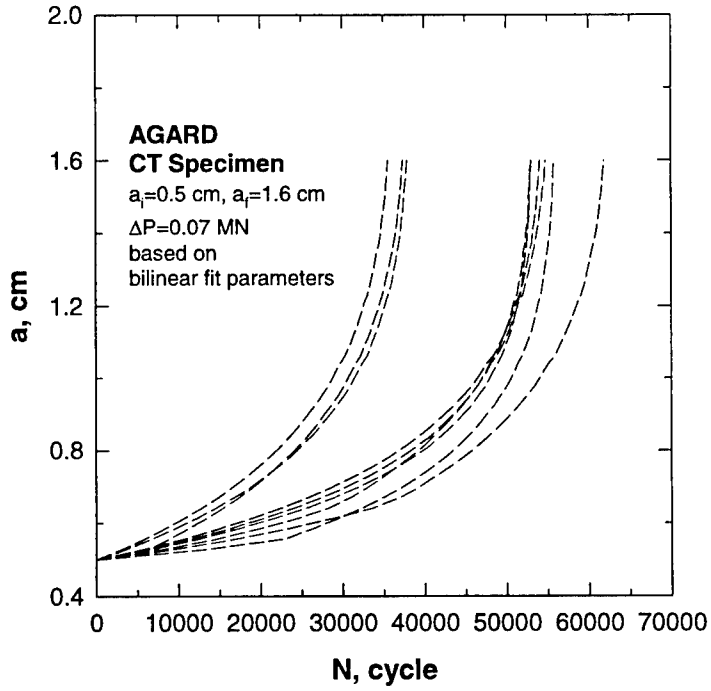
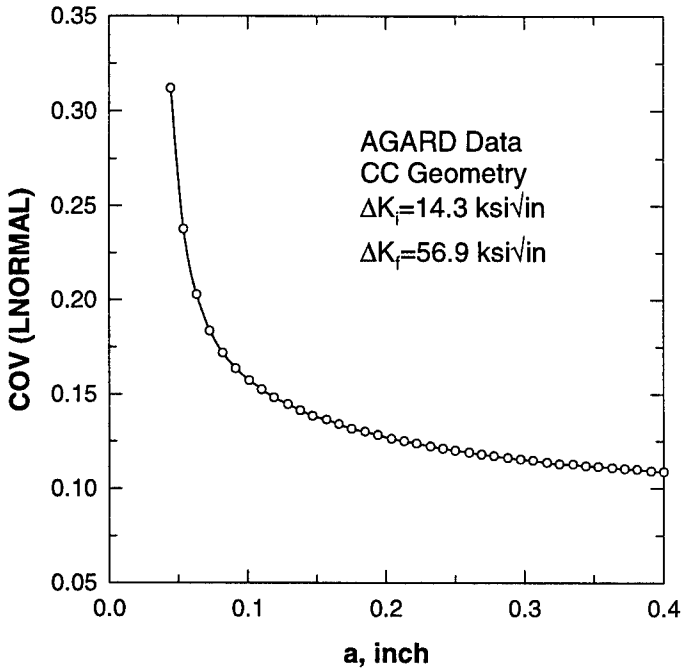


FIGURE 2-94. CRACK LENGTH HISTORIES FOR SIMULATED AGARD FCG TESTS (BILINEAR ONLY)



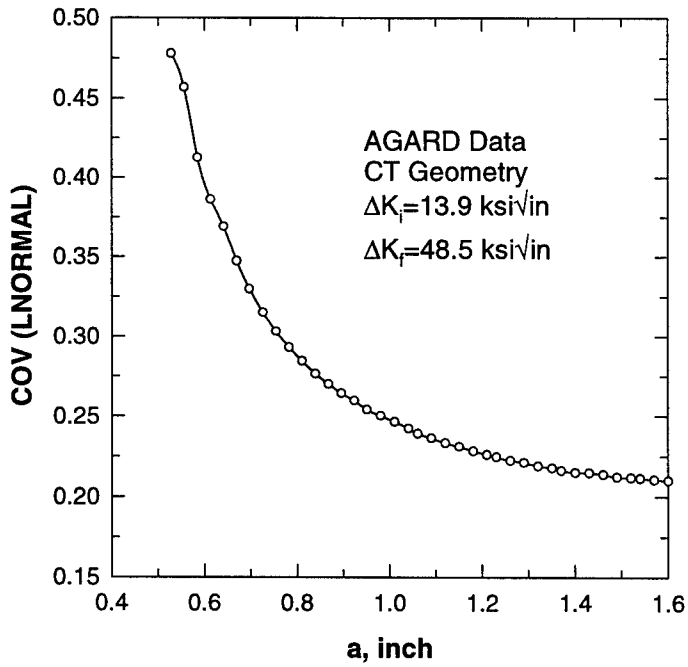


FIGURE 2-95. COEFFICIENT OF VARIATION OF FATIGUE LIFE AS A FUNCTION OF CRACK SIZE FOR AGARD SIMULATIONS

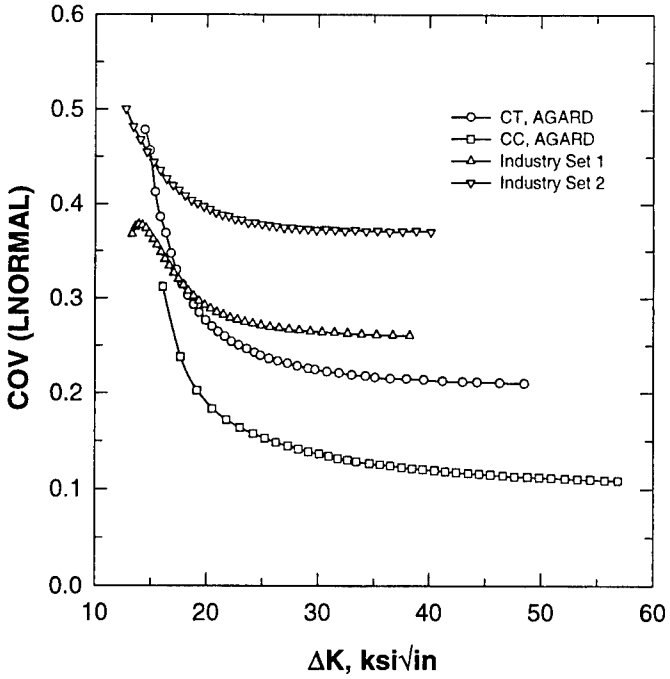


FIGURE 2-96. COEFFICIENT OF VARIATION OF FATIGUE LIFE AS A FUNCTION OF ΔK FOR AGARD AND INDUSTRY SIMULATIONS

2.4.2.5 Discussion.

It is important to remember that these COV values represent only scatter in inherent material properties and do not include additional variability due to modeling error. Additional study is needed to investigate the numerical contribution of modeling error to total life scatter. However, the limited study conducted to date has provided some initial guidance on the nature and magnitude of life scatter. Sensitivity studies comparing the contributions of this life scatter to total risk against the contributions of other uncertain variables (e.g., initial flaw size, probability of detection, etc.) should provide guidance on the level of detail required to treat life scatter adequately.

2.5 DEVELOPMENT OF PROBABILISTIC DESIGN CODE.

DARWIN is a computer program that integrates finite element stress analysis, fracture mechanics analysis, nondestructive inspection simulation, and probabilistic analysis to assess the risk of rotor fracture with in-service inspection. DARWIN computes the probability of fracture as a function of flight cycles considering random defect occurrence and location, random inspection schedules, multiple inspections, and other random variables. The current capability of DARWIN 3.2, verified using three rotor models and released in July 1999 is summarized in figure 2-97.

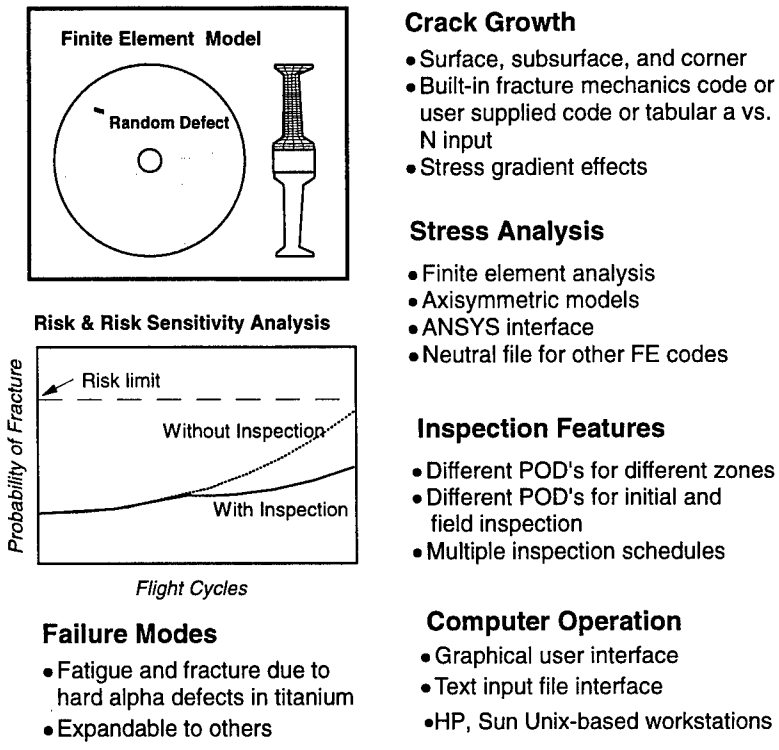


FIGURE 2-97. DARWIN CODE CAPABILITY

The focus of the code development was on titanium disks with hard alpha anomalies as the critical source of potential rotor fracture. New capabilities for treating other materials will be developed in a follow-on FAA program.

The basic approach implemented in DARWIN is to divide the disk into a number of zones, compute the risk due to the growth of a defect in each of the zones, and integrate the risks. Figure 2-98 illustrates the code framework based on the zone-based methodology.

Section 2.5.1 reviews stress processing methodology and section 2.5.2 summarizes the fracture mechanics module, Flight_Life. The probabilistic analysis driver of the Flight_Life analysis is summarized in section 2.5.3. A GUI, described in section 2.5.4, has been developed to assist the users in preparing the DARWIN analysis input and in viewing the results. Section 2.5.5 provides a summary of validation examples and design sensitivity studies. The DARWIN software Quality Assurance (QA) process is summarized in section 2.5.6.

A comprehensive description of DARWIN capabilities is provided in the User's Manual [30].

2.5.1 Stress Processing.

The structure is divided into zones for risk based analyses. The stress-processing module provides stress gradient, cycle pairing, and temperature information for each zone to the fracture mechanics module Flight_Life. Zone specific information is required to relate the finite element geometry to the appropriate fracture mechanics models available in Flight-Life and then to map

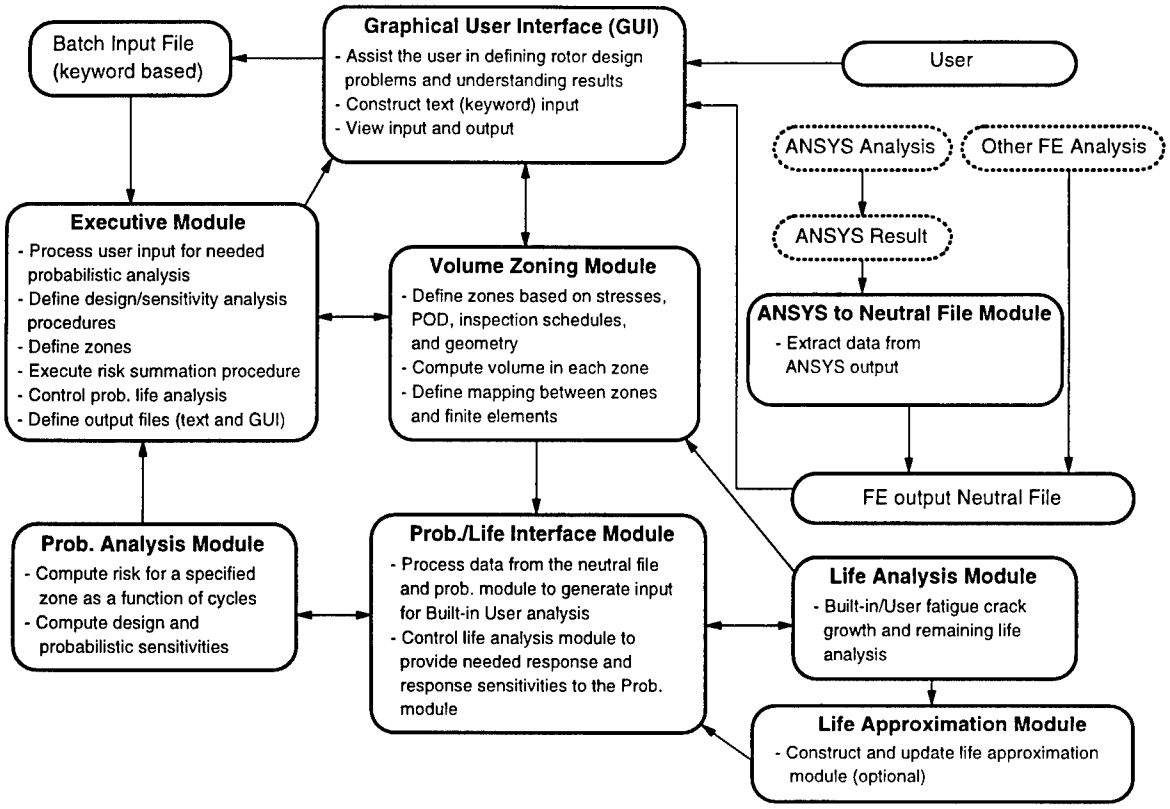


FIGURE 2-98. DARWIN CODE FRAMEWORK

the crack location and the gradient path from the model back to the finite element geometry. The stress-processing module also computes the zone volume from the finite element model of the structural geometry. The following steps are performed for each zone during stress processing:

1. The element corresponding to each point along the crack path is located, identified, and the local coordinates of each element are recorded.
2. The stress at each point on the crack path is determined corresponding to the maximum and minimum stress for each load step using interpolation techniques based on element shape functions.
3. Cycle pairing is performed for fatigue analysis automatically by DARWIN using the ASTM Simplified Rainflow Counting for Repeating Histories Algorithm.
4. The volume of each zone is computed based on the elements comprising each zone.

Further details about stress processing can be found in the DARWIN User's Manual [30].

2.5.1.1 Stress Files.

Stress data are input to DARWIN through finite element result files (that can be either Finite Element Analysis Code (ANSYS) specific files or so-called neutral files) or a reduced stress file generated in a previous DARWIN run. Each stress file can contain multiple-load cases and multiple files can be entered to define the load steps to be used in the analysis.

Although stress input is organized by missions, only one of the missions can be used at any one time in the current version of DARWIN. The stress files are listed sequentially under each mission number. All files have to be of the same type, i.e., either ANSYS, neutral, or a single reduced stress file. Stress pairing to generate the cyclic load spectrum is performed automatically using a rainflow counting method.

Currently, axisymmetric finite element models are used for the risk analysis. However, other element types can be present in the finite element results files.

2.5.1.1.1 ANSYS and Neutral Results Files.

Portions of the System for Integrated Engineering Structural and Thermal Analysis (SIESTA) [31] program developed by GE Aircraft Engines have been incorporated into the DARWIN program to enable it to read finite element geometry and nodal stresses and temperatures from either ANSYS 5.x results files or from neutral files. Neutral files consist of a unified input file and a unified output file and are text-based files that use keywords and modifiers to delineate finite element quantities. A neutral file has a defined format enabling the results from other finite element analysis programs besides ANSYS to be used.

2.5.1.1.2 Reduced Stress File.

A reduced file provides a very concise summary of the stress data needed for a risk analysis compared to the information contained in either an ANSYS file or a neutral file. The reduced stress file contains the information that defines the stress gradient for each zone. DARWIN creates this file after it has processed an ANSYS results file or a neutral file. A subsequent run of DARWIN can use a reduced stress file generated in a previous run provided the new problem uses the same zone definitions (crack orientation, position, type, plate orientation, and stress input). However, it is not necessary for the new problem to have the same material properties, inspection schedule, or risk parameters. Use of a reduced stress file can result in a significant reduction in computational effort, especially if there are many time steps and/or a large number of elements employed in the finite element model.

2.5.1.2 Zone Definition and Flaw Location.

Each zone has a number of attributes that are used in a DARWIN analysis. These attributes are provided in the zone definition and include information such as the numbers of the mesh elements in the zone and, crucial to the fracture mechanics modeling, crack related data. The elements in the zone are used to compute the zone volume. The crack data contains information needed by Flight_Life, such as:

- crack model (corner, embedded, or surface),
- orientation of the plane containing the crack (radial, axial, or hoop),
- location of the crack with respect to a global coordinate system,
- dimensions of the fracture mechanics model geometry (width and thickness), and
- direction of the stress distribution acting on the crack (expressed with respect to the global coordinate system).

DARWIN uses the crack information to relate the finite element geometry and stress analysis results to the fracture mechanics model in Flight_Life. Figure 2-99 shows a schematic of three crack models in Flight_Life. These models are all constructed for cracks in rectangular plates (referred to as fracture mechanics plates). Since most structural geometries are not rectangular, it is necessary to map the plate to the global geometry of the structure. Figure 2-100 shows examples of this mapping for corner (CC01), embedded (EC02), and surface (SC02) crack models. The stress variations along paths that go through the centers of the cracks are needed in order to evaluate the stress intensity factors for crack models EC02 and SC02. In the case of corner cracks, the stress gradients along two paths that correspond to the two surfaces that include the crack are needed.

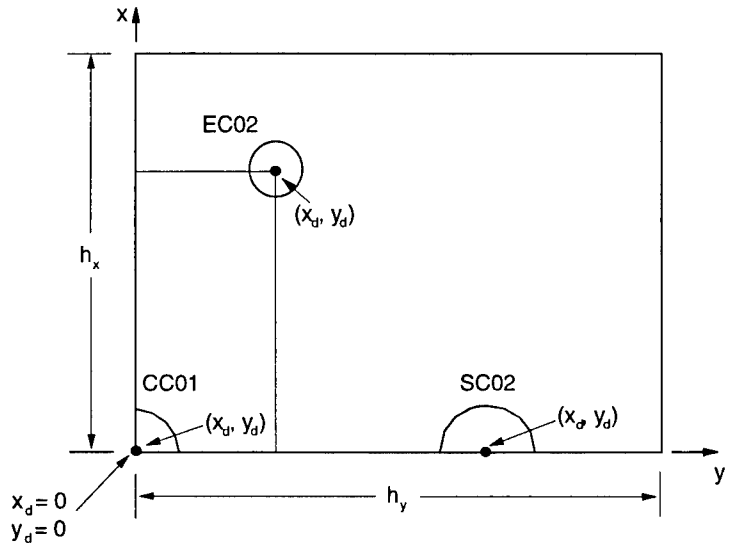


FIGURE 2-99. SCHEMATIC OF THE CRACK MODELS CC01 (CORNER CRACK), EC02 (EMBEDDED CRACK), AND SC02 (SURFACE CRACK) CONTAINED IN Flight_Life

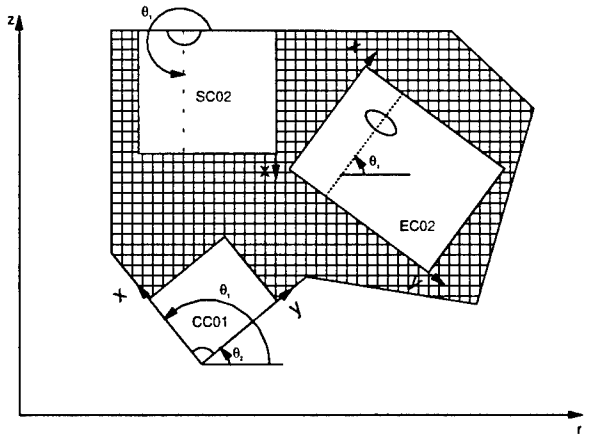


FIGURE 2-100. MAPPING OF CRACK MODELS CC01, EC02, AND SC02 TO THE GLOBAL GEOMETRY COORDINATE SYSTEM CONTAINING THE FINITE ELEMENT MODEL OF THE STRUCTURE

2.5.1.3 Rainflow Counting.

The DARWIN program contains an automated rainflow counting routine to determine the maximum and minimum cycle pairs for each zone based on the user input load step history. The algorithm is based on the ASTM Simplified Rainflow Counting for Repeating Histories [32] and has the following characteristics:

- the repeating histories contain no half cycles and
- every cycle is closed; i.e., it has a well-defined maximum and minimum load.

An example rainflow counting analysis from reference [33] was used to test the DARWIN code. The stress history from the stress analysis is shown in figure 2-101(a). The results of reordering the loading history such that the history begins with a load step corresponding to a maximum peak or minimum valley are in figure 2-101(b). Figure 2-101(c) shows the paired load steps resulting from the rainflow analysis. The pairs are depicted in the figure as shaded and hatched areas. Load Step 3 is paired with load Step 0 to form the maximum and minimum loads in a cycle, respectively. Similarly, load Step 5 is paired with load Step 4, load Step 7 is paired with load Step 6, and load Step 1 is paired with load Step 2.

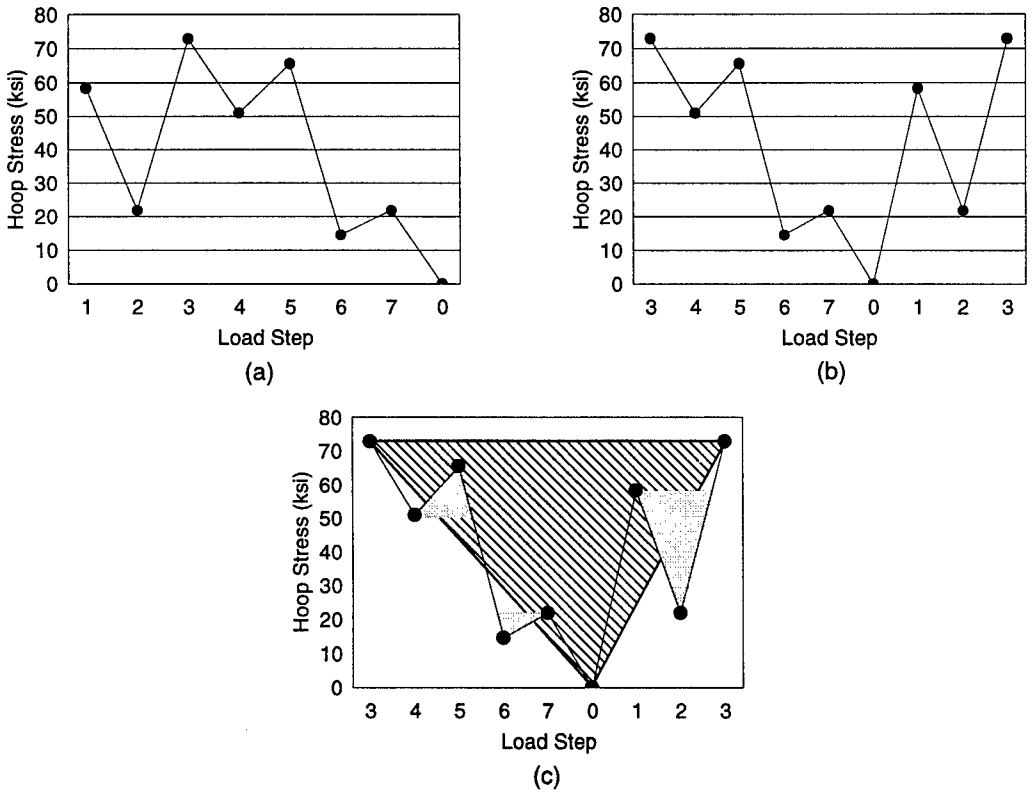


FIGURE 2-101. A SIMPLE EXAMPLE OF THE RAINFLOW COUNTING PROCEDURES EMPLOYED IN DARWIN

((a) Load history resulting from stress analysis of a mission that consists of a number of loads steps, (b) Reordering of the load history so that it begins with a peak stress and finishes with a peak stress, and (c) Paired load steps resulting from the rainflow analysis.)

2.5.1.4 Stress Gradients.

The variation of stress along a path that goes through the center of a crack (see figure 2-102) is needed by Flight_Life to compute crack tip driving forces. In addition, this stress gradient is used in computing the residual stress resulting from stress relaxation and redistribution (shakedown) due to localized plastic deformation in the structure (see section 1.5). The stress paths are mapped from the fracture mechanics plate[1] to the global structural model used in the finite element stress analysis. Figure 2-103 provides a simple example of the mapping procedure. This figure illustrates how points 1, 2, 3 etc., on the crack path defined with respect to the crack model (a surface crack, SC02) are mapped onto the global structure model. Evaluation of the stresses at the points 1, 2, 3 etc., in the global system is performed using the finite element shape functions to interpolate the stress values in the elements that coincide with the crack path.

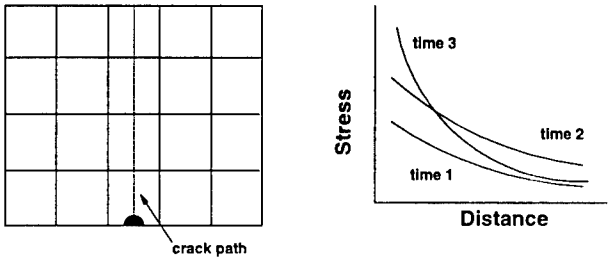


FIGURE 2-102. THE STRESS GRADIENT ALONG A PATH THAT GOES THROUGH THE CENTER OF THE CRACK IS NEEDED BY Flight_Life
(This figure shows a typical crack path for a surface crack and typical stress gradients corresponding to various load steps in a mission.)

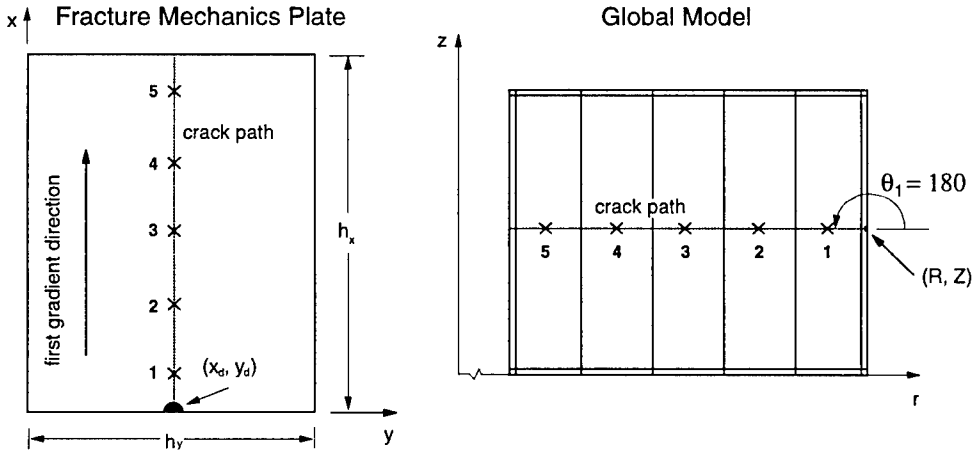


FIGURE 2-103. EXAMPLE OF HOW THE CRACK PATH DEFINED IN THE FRACTURE MECHANICS CRACK MODEL IS MAPPED INTO THE GLOBAL SYSTEM USED IN THE FINITE ELEMENT MODEL IN ORDER TO DETERMINE THE STRESSES ALONG THE PATH

[1] The disk structure is idealized for fracture mechanics analysis as a rectangular region, i.e., a fracture mechanics plate. This idealization permits the use of many existing stress intensity factor solutions.

The stress gradients are represented analytically by polynomial expressions. The orders of the polynomials used to fit the stress data along the crack paths are based on the number of stress values being fitted. The maximum order of the polynomial used in the fit is six. A stress output summary provides percent error of the true stress compared with the polynomial fit.

2.5.1.5 Shakedown Residual Stress Implementation in DARWIN.

The Darwin program includes a module, SHAKEDOWN, which is used to evaluate the residual stresses resulting from stress relaxation due to plastic deformation associated with local plasticity at stress raisers (such as geometrical discontinuities, grooves, and notches) during over-spin testing and service cycling. When the applied load is removed, the plastically deformed local region unloads elastically and the residual plastic strains produced by tensile yielding result in compressive residual stresses at the root of the stress concentrator. As a consequence of these compressive residual stresses, further cycling produces only elastic deformations and the structure is said to have undergone shakedown. The shakedown residual stresses are static stresses and although they do not influence the cyclic crack tip driving force, they change the stress ratio (ratio of minimum to maximum loads in a cycle). Compressive static stresses will lower the stress ratio and result in a slower cyclic crack growth rate and a longer calculated lifetime. In addition, compressive stresses will reduce the crack tip driving force, resulting in a greater calculated critical crack size that in turn will extend the cyclic lifetime of the component. Hence, there are clearly benefits in implementing a shakedown routine in DARWIN.

The SHAKEDOWN module converts the results of a linear elastic stress analysis into an approximate elastic-plastic stress distribution from which the shakedown residual stress is derived. The shakedown methodology accounts for multiaxial stress states by using values of the elastically determined stress components. Neuber's rule is employed to evaluate the relaxed stresses. Monotonic stress-strain properties are used to evaluate shakedown due to over-spin testing, and the cyclic properties are used to assess shakedown during service. The shakedown routine maintains force balance between the elastic and elastic-plastic stress solutions for the stress component acting normal to the crack plane. The methodology assumes that plastic deformation occurs only at a single free surface (e.g., the root of a stress raiser). The shakedown analysis is limited to two-dimensional problems where the results of stress analysis can be represented on a single plane. Two shakedown analyses are performed for assessments involving corner cracks (crack geometry CC01). These analyses use the stress distributions along the two free surfaces that form the corner containing the crack. If the shakedown analysis is performed with respect to service conditions that involve more than one load step, then DARWIN determines the most onerous load step for use in the analysis by utilizing the stresses at the maximum loads of each step. The stress values at the center of the initial crack are employed in this procedure (see figure 2-104) together with the temperature at which the maximum stressing occurs and the level of multiaxial stressing. A detailed description of the stress relaxation methodology is included in appendix C of the DARWIN User's Manual [30].

The output of the SHAKEDOWN module consists of

- the shakedown residual stress distribution as a function of position and
- the plastically relaxed stress components as a function of position.

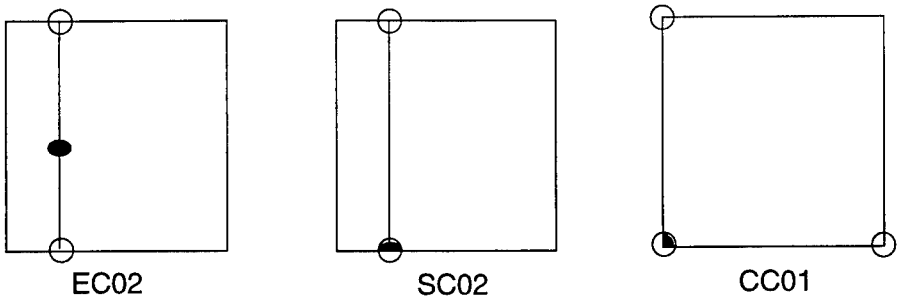


FIGURE 2-104. THE RESIDUAL STRESS RESULTING FROM SHAKEDOWN IS PERFORMED USING THE LOAD STEP THAT PRODUCES THE MAXIMUM STRESS AT THE CENTER OF THE INITIAL CRACK
(The figure illustrates these locations (full symbols) for embedded (EC02), surface (SC02), and corner (CC01) crack models.)

An example of the stresses generated at a notch is shown in figure 2-105. This figure displays the calculated stress normal to the crack plane (σ_z) normalized by the yield stress (σ_o) plotted against the distance ahead of the notch tip (x) normalized by the notch tip radius (r). The original elastic based stress solution, the plastically relaxed stress, and the residual stress resulting from shakedown are shown in the figure.

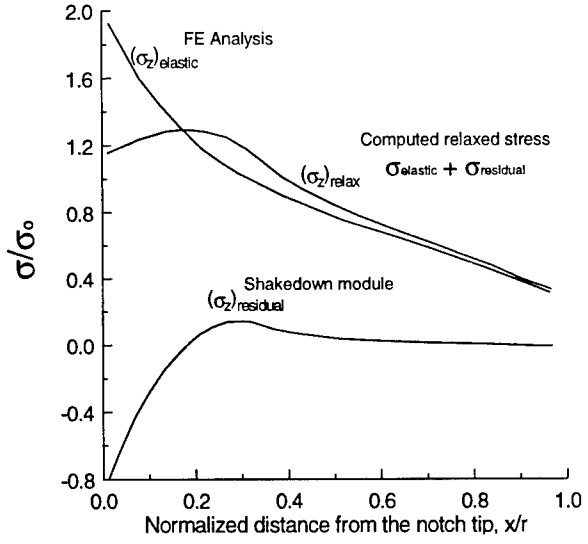


FIGURE 2-105. EXAMPLE OF THE RESULTS OF A SHAKEDOWN ANALYSIS SHOWING THE ELASTICALLY DETERMINED STRESS DISTRIBUTION NORMAL TO THE CRACK PLANE $(\sigma_z)_{elastic}$, THE CALCULATED PLASTICALLY RELAXED STRESS $(\sigma_z)_{relax}$, AND THE RESULTING RESIDUAL STRESS $(\sigma_z)_{residual}$

2.5.2 Flight_Life Fracture Mechanics Module.

DARWIN analysis includes fracture mechanics (FM) life calculations. The DARWIN user has the option of interfacing DARWIN with a user-supplied FM computer code or of inputting user-supplied crack size vs cycles information that was output from a user-supplied FM code.

However, DARWIN also includes an integrated FM module called Flight_Life that has been tailored for the probabilistic rotor analysis problem. Because Flight_Life is integral to DARWIN, it is more convenient and more efficient to use than an external user-supplied code. Flight_Life contains a variety of key FM capabilities and methods that have been defined by the engine industry with additional new technology developed by SwRI. This section provides an overview of the capabilities of Flight_Life. Further details are available in the DARWIN User's Manual [30].

Flight_Life currently includes a suite of six stress-intensity factor (K) solutions needed for rotor analysis, including the quarter-elliptical corner crack (CC01), the semi-elliptical surface crack (SC02), the elliptical embedded crack (EC02), the elliptical embedded crack approaching a free surface (EC03), the embedded through crack (TC01), and the surface through crack (TC02). These six geometries are shown schematically in figure 2-106. All crack models assume a rectangular plate shape. Most K solutions were adapted from existing codes and have been validated against benchmarks from the literature or other FM codes wherever possible. The CC01 solution was taken directly from the Fatigue Crack Growth Computer Program (NASGRO) code [34] while SC02, EC02, TC01, and TC02 were adapted from the SwRI internal code K calculation (KCALC). The EC03 solution was developed from EC02 specifically for Flight_Life, and other improvements were made to some of the KCALC solutions, such as the implementation of improved side surface effects.

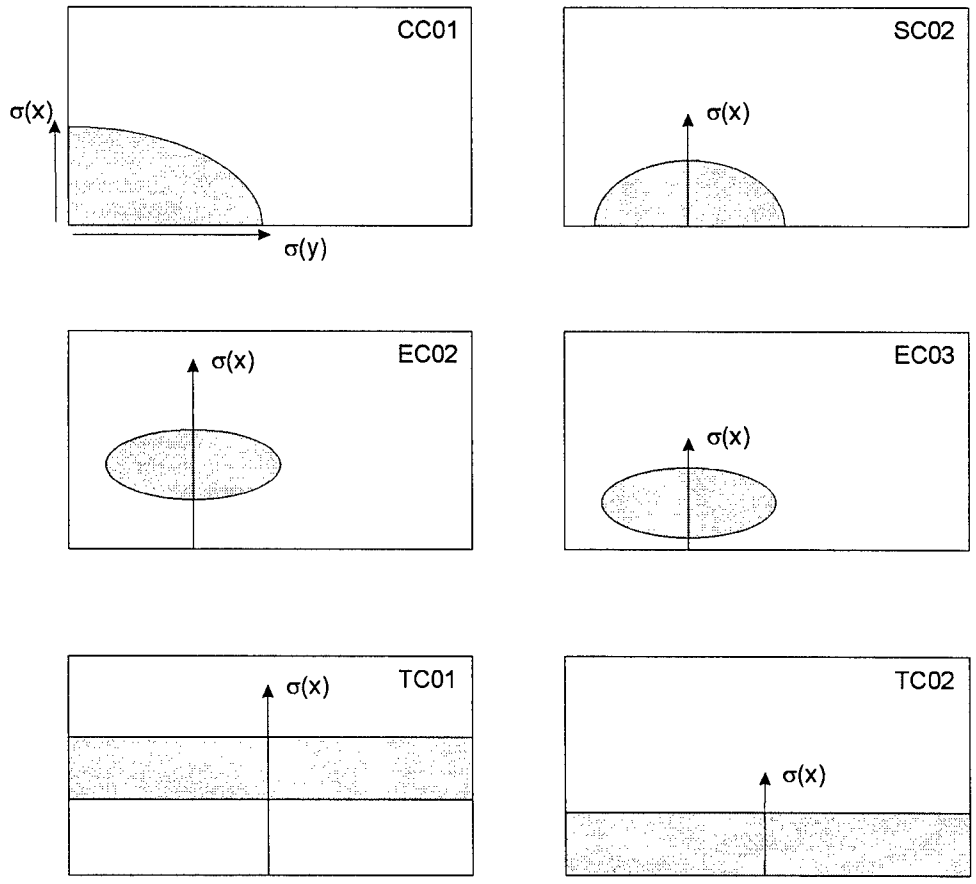


FIGURE 2-106. CRACK GEOMETRIES AVAILABLE IN Flight_Life

All cracks can be placed anywhere in the rectangular plate (the effects of nearby free surfaces are addressed appropriately). The growth of three dimensional cracks is calculated independently at multiple degrees of freedom (DOF) around the crack perimeter (2 DOF for CC01, 3 DOF for SC02, and 4 DOF for EC02/EC03), so crack shapes are allowed to evolve naturally as the crack grows. The CC01 and SC02 solutions incorporate a loss-of-constraint factor (the NASGRO beta-factor) at points where the crack perimeter intersects a free surface. All solutions except CC01 accept univariant 6^{th}-order polynomial stress gradients. The polynomial coefficients may be fitted by DARWIN to finite element (FE) stress results. The use of polynomial representations for stress distributions and the corresponding influence functions for determining K values makes Flight_Life computationally faster than would be the case if weight function approaches had been used to calculate K. The CC01 solution (from NASGRO) accepts uniform stresses or linear stress gradients along the two sides of the plate that include the crack. Stress inputs to the K solutions may include redistributed (residual) stresses calculated by the shakedown module to account for localized plasticity that can occur at stress concentrators, as described in section 2.5.1.5.

All possible crack geometry transitions, such as the breakthrough of an embedded crack to a surface crack, are automated. Specific transitions enabled include EC02 → EC03 and SC02; EC03 → SC02; SC02 → CC01, TC01, and TC02; CC01 → TC02; and TC01 → TC02. Cracks transition whenever the validity limits of the K solution are reached, or whenever the crack tip plastic zone reaches the edge of the plate. Transitioning logic includes recharacterization of the crack shape to maintain equivalent cracked area and approximate recharacterization of the applied stresses if the crack growth direction after transitioning is different from the direction used to specify the pretransitioning stress gradient. The important material property change as embedded cracks transition into surface cracks (and therefore change environments) is also included, although this feature has been disabled at the present time since the default defect distributions in DARWIN are all based on calculations with air data. FCG rates in titanium rotor alloys can be significantly different in air vs vacuum environments, as discussed in section 2.4.1.

For convenience, Flight_Life includes a variety of different FCG equations and stress ratio models that are commonly used by major engine companies. Available FCG equations currently include single linear Paris, bilinear Paris, hyperbolic sine, and sigmoidal. FCG rate data can also be entered as tables of da/dN vs ΔK values. These options are shown schematically in figure 2-107. Available models for including stress ratio effects in FCG equations include explicit Walker and crack closure formulations. Stress ratio interpolation based on a point-by-point Walker construction is available for tabular da/dN vs ΔK data. Temperature interpolation of FCG properties is available for both equations and tabular data, or properties can be selected at the nearest or next highest temperature in the database.

To facilitate computational efficiency in calculating fatigue lifetimes, the crack growth routines in Flight_Life have an automatic integration step refinement capability. This feature enables a coarse step size to be used during the integration process when crack propagation rates are small and a fine step to be implemented when the rates increase. This capability is particularly important in reducing run times when the Flight_Life module is called frequently by DARWIN in a probabilistic life assessment.

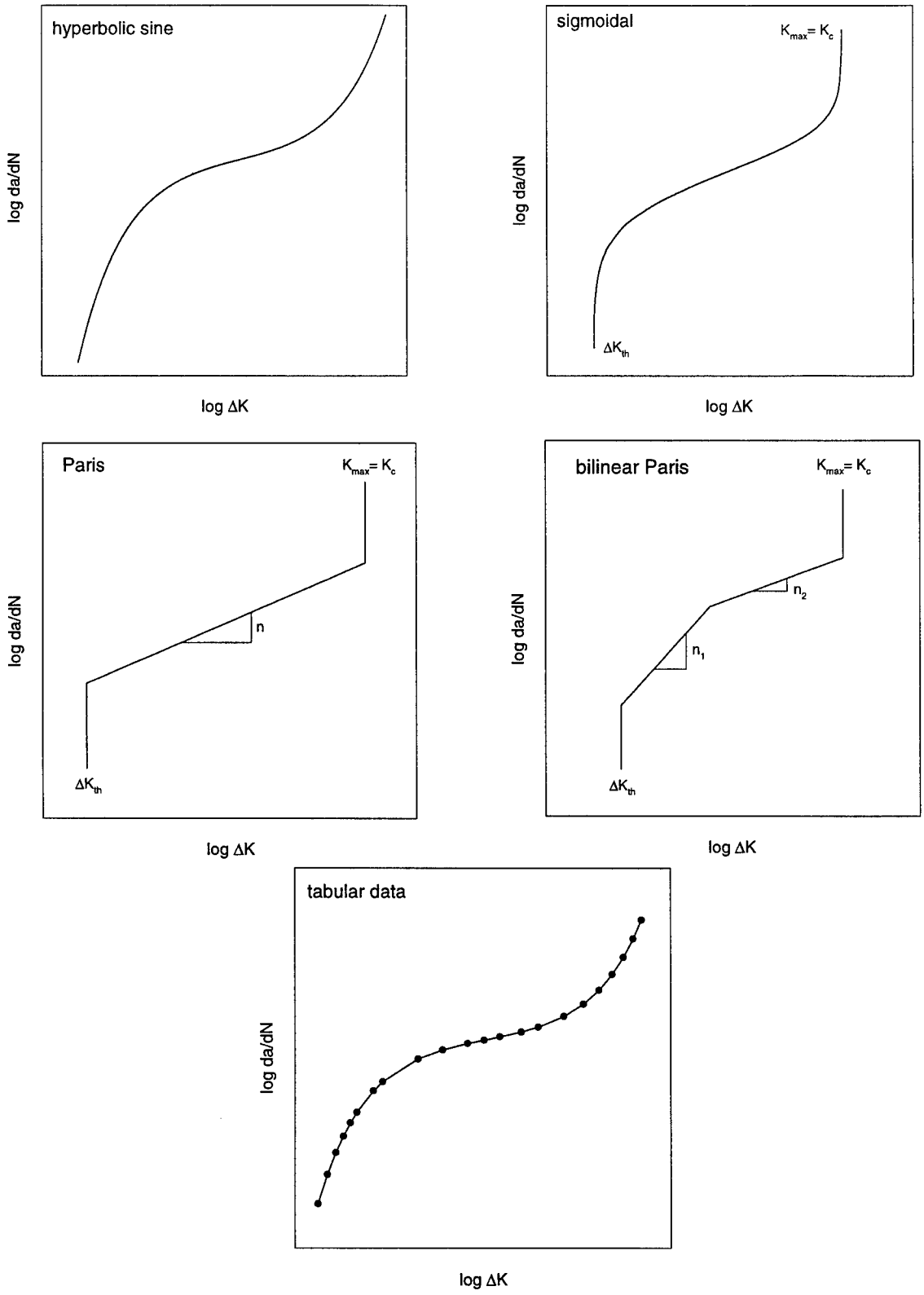


FIGURE 2-107. FATIGUE CRACK GROWTH DATA REPRESENTATION OPTIONS AVAILABLE IN Flight_Life

Flight_Life can be run as part of a probabilistic DARWIN reliability analysis, and it can also be run independently in a deterministic mode. Output from deterministic solutions includes full histories of crack size, location, area, and K_{max}; before-and-after summaries of any crack transitions that may have occurred; and failure information.

2.5.3 Probabilistic Driver.

This section summarizes the probabilistic analysis methodology developed and implemented as a probabilistic analysis driver in DARWIN. More details are included in the DARWIN User's Manual [29].

2.5.3.1 Probability of Fracture.

In considering the structural integrity of a titanium rotor disk containing hard alpha anomalies, the potential random variables include defect size and location, stress, material properties, and the time and effectiveness of the inspections. The effectiveness of an inspection is characterized by the probability of detection (PoD).

Given an initial defect in a disk, the defect size and the stress intensity factor K will increase as a function of flight cycles, which consists of variable amplitude loading. Failure is predicted when the maximum K exceeds the fracture toughness K_C, i.e.,

$$g(X,Y,t) = K_C - K(X,Y,t) \leq 0 \tag{2-17}$$

in which the failure function, g(X, Y, t), is a function of input variables and time:

$$g(X,Y,t)) = g(X_1,X_2,\ldots X_n,Y_1,Y_2,\ldots Y_m,t) \tag{2-18}$$

in which X is a vector of input variables unrelated to inspections, Y is a vector of input variables related to inspections, and t is flight hours. A negative or zero g(X, Y, t) represents a failure event.

The probability of failure is:

$$p_f = P\left[g(X,Y,t) \leq 0\right] \tag{2-19}$$

DARWIN's analysis output includes the probability of disk fracture as a function of flight cycles, with and without inspection. For reliability design assessment, the two important numbers are probability-of-failure per flight cycle with and without inspection.

In the current version of DARWIN, there are three X random variables. One is the defect size, and the other two are related to the stress and life models. The stress uncertainty has been modeled as follows:

$$\sigma = X_1 \cdot \sigma_{FEM} \tag{2-20}$$

where X_1 is the stress multiplier, a random variable accounting for the errors in geometry and numerical (e.g., finite element) modeling. Similarly, a practical stochastic life model has been defined as:

$$N - X_2 \cdot N_{model} \tag{2-21}$$

where N_{model} is the life model, calculated by the Flight_Life module in DARWIN, and X_2 is the life scatter random variable.

The Y random variables are the PoDs and shop visit times, currently modeled as normally distributed random variables.

2.5.3.2 Zone-Based Risk Integration Method.

The defects can in general be randomly distributed within the disk. To account for the location uncertainty, a zone-based risk integration method has been developed and implemented. In short, the method divides the structure into a manageable number of zones, computes the risk in each of the zones taking account of the probability of defect occurrence, and sums the risks.

If F_i is defined as a failure event due to an initial defect in zone i (i from 1 to m), then the risk of a disk failure is the probability union of all the F_i's:

$$p_f[disk] = P[F_1 \cup F_2 \cup \ldots \cup F_m] \tag{2-22}$$

If the occurrence rate of significant defects (i.e., with sizes that could cause failure) is small, such that, given a significant defect in a zone the probability of having other significant defects in the same disk is negligible, then the above equation can be simplified as:

$$p_f[disk] \approx \sum_{i=1}^{m} P[F_i] \tag{2-23}$$

Thus, under the assumption of rare occurrence of significant defects, summing the zone risks can approximate the total risk.

The zone-based approach has a major advantage in that each zone can have its own defect occurrence rate and other X and Y parameters, and it allows the analyst to identify and focus on critical zones for design and inspection planning. DARWIN 3.2 provides risk contribution factors for all the zones in the disk.

2.5.3.3 Probabilistic Analysis Methods.

There are two probabilistic analysis approaches implemented in DARWIN. One is Monte Carlo simulation, which is relatively slow but is very robust and can be as accurate as desired by increasing the number of random samples. The other is a fast sampling approach that focuses analysis on the initial conditions (defect size and other random variables) that would result in lives shorter than the user-specified service life, without inspection. By reducing analysis

regions, the second approach is significantly more efficient than Monte Carlo. Since a hard alpha defect is a rare event, DARWIN ignores the probability of having two or more defects of significant size in a disk.

a. Monte Carlo Method—Monte Carlo random simulation is time consuming but is the most robust and easy method to implement for complicated problems. This method has the most flexibility for future expansion and can be used to provide reference solutions to verify other faster methods. The Monte Carlo method implemented in DARWIN is zone based and the user can specify a different number of samples in different zones.

b. Fast Sampling Method—The optimal design and maintenance of disks requires fast analysis to provide a quick turnaround of reliability analysis for design and inspection planning. The importance-sampling method developed for DARWIN focuses analysis on the initial conditions (defect size and other random variables) that would result in lives shorter than the user-specified service life, without inspection.

The fast, importance-sampling procedure is illustrated in figure 2-108 for random initial defects with deterministic stress and no life scatter. In general, when the stress and life scatter are random, the probabilistic analysis procedure includes the following steps:

a. Calculate the probability of failure without inspection, $\overline{p}_f$, by numerical integration.

b. Generate, in the following sequence, a selected number of realizations of life scatter, stress multiplier, and defect in the failure domain. The failure domain, denoted as Ω, is defined as the random variable space in which all the predicted lives are shorter than the service life.

   - Randomly generate a life scatter according to its probability density function (PDF) in the failure region.
   - Randomly generate a stress multiplier according to its PDF in the failure region, given the life scatter.
   - Randomly generate a defect according to its PDF in the failure region, given the life scatter and the stress multiplier.

c. Using the above failure-only samples, perform a Monte Carlo simulation of crack growth and inspection processes to determine the number of disks removed by inspection.

d. The probability of failure with inspection is calculated as:

$$p_f \text{ (with inspection)} = \overline{p}_f \text{(without inspection)} \cdot \frac{\text{Number of failures with inpsection}}{\text{Total number of samples in } \Omega} \quad (2\text{-}24)$$

By generating samples directly in the failure domain, the importance-sampling approach is significantly more efficient than generating samples in the entire random variable space, particularly when $\overline{p}_f$ is very small.

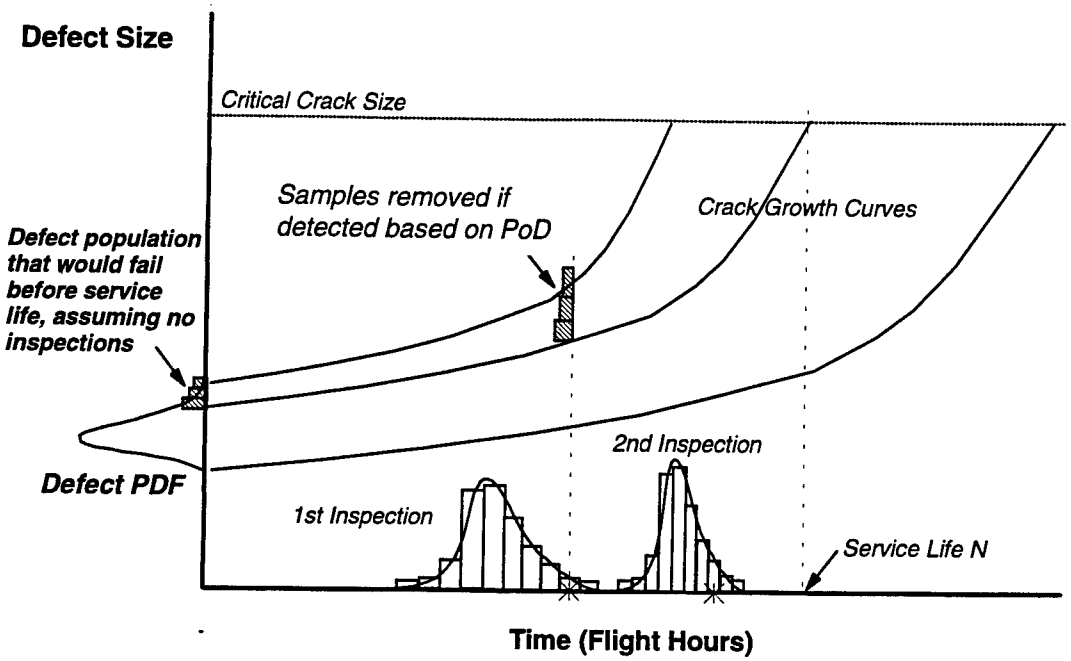


FIGURE 2-108. ILLUSTRATION OF FAST SAMPLING METHOD

2.5.4 Graphical User Interface.

DARWIN contains a highly customized GUI. The GUI is designed as a pre- and postprocessor to the risk assessment code. This relationship is shown in figure 2-109. (More details on the GUI can be found in chapter 7 of the DARWIN User's Manual).

Briefly, the GUI contains the following capabilities:

2.5.4.1 Preprocessing.

- develop zones—group element, set defect location, fracture model, applied stresses
- import and view defect distributions
- import and view probability of detection curves
- import and view fatigue crack growth material properties
- develop inspection schedules

2.5.4.2 Postprocessing (Graphical Displays).

- Risk Assessment
  - Overall disk assessment
  - Disk assessment/cycle
  - Individual zone risk assessments
  - Risk contribution factors

- Fracture Mechanics
  - Maximum stress intensity factor vs cycles for each zone
  - Defect area vs cycles for each zone
  - Stress max and min load pairs for each load block for each zone
- Processing

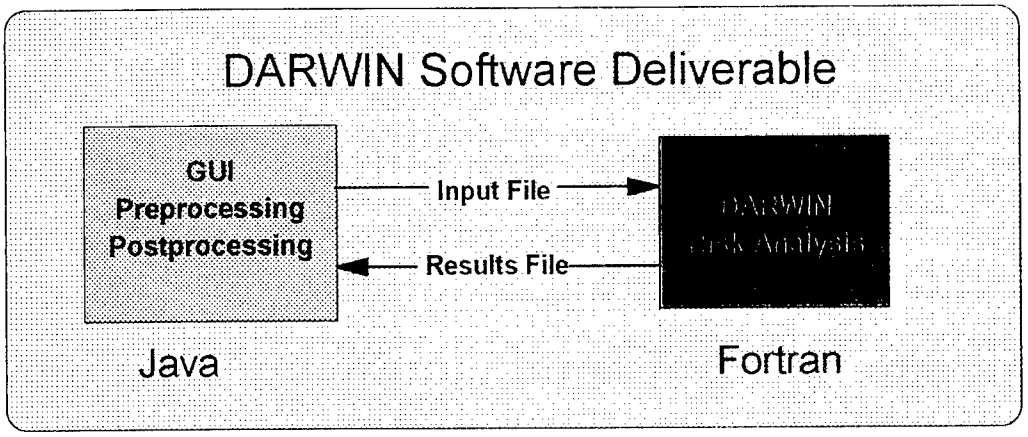


FIGURE 2-109. PRE- AND POSTPROCESSING APPROACH

A major emphasis of the GUI is to assist the user in the development of risk zones. A zone is a grouping of material such that all material parts in the zone have a generally uniform stress state the same fatigue crack growth properties, inspection schedules, PoD curves, and defect distribution. In other words, the risk computed for any subregion of material of the zone will be the same; thus, the subregions are grouped into a zone. The risk results obtained by locating a defect in any particular portion of a zone are assumed representative of the zone in general. The results for a zone are obtained independently from any other zone.

The definition of the zone requires visualization of the finite element stress results. These results are presented to DARWIN in the form of neutral files for the particular geometry and stresses. Figure 2-110 shows an example screen shot of a zone being defined. An axisymmetric finite element model is shown, color coded by hoop stress value (axis of rotation is horizontal, parallel to bottom of the disk). Zone 10 is being defined. The white circle is the location of the defect. The rectangular plate is used to approximate the real disk geometry—with the plate geometry being used for fracture mechanics calculations. The arrow from the top of the plate to the bottom is used to define the path along which stress gradients will be extracted from the finite element model and used during the fracture mechanics calculations.

The GUI provides a number of tools for selecting elements to encompass a zone, locating the defect, defining/adjusting the plate and for selecting material, probability of detection, defect distribution, and inspection schedule properties of the zone.

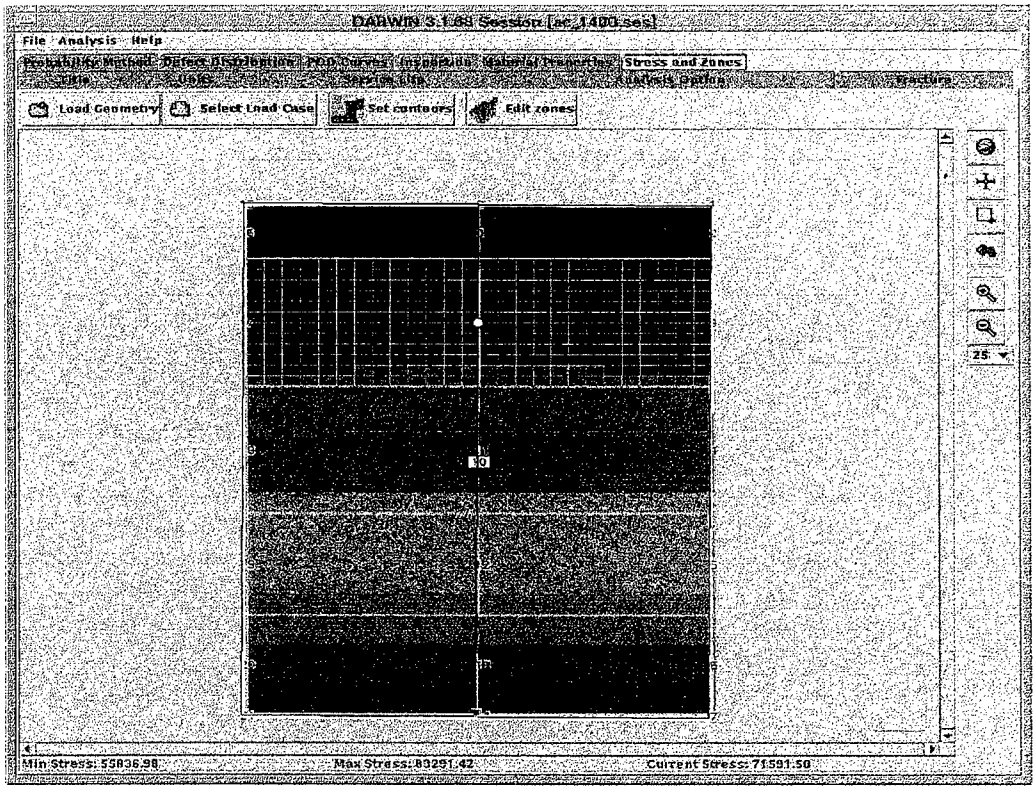


FIGURE 2-110. EXAMPLE OF ZONE DEFINITION

The postprocessing capabilities are intended to graphically display the results of the risk assessment, deterministic fracture mechanics analysis, and stress processing. The risk assessment results include the overall disk risk assessment, the overall disk risk assessment on a per cycle basis, each zone risk assessment, and risk contribution factors showing the relative contribution of each zone to the disk risk. The deterministic fracture mechanics analysis results are based on the behavior of a 10-mil radius flaw located in each zone and grown as a function of cycles. The 10-mil size is an arbitrary starting size and is used for information purposes only prior to conducting the probabilistic analysis.

The GUI can be used to plot the behavior of the maximum stress intensity factor (K_{max}), and defect area as a function of cycles for each zone. These results provide the engineer an assessment of the behavior of a defect in the zone.

The stress processing results show the behavior of the stress load pairs (min and max) over the plate. These stress results are a result of shakedown analysis to determine residual stress effects and rainflow counting to determine significant loadings and load pairing for fatigue analysis. The results are shown plotted as a function of normalized plate distance. The initial flaw location is also shown on each plot. These results are presented for each zone.

Examples of the plotting capabilities are given in the following subsections.

2.5.4.3 Disk Assessment.

Disk assessment shows the probability of fracture of the entire disk as a function of cycles for the cases with and without inspection. The View Data box can be selected to display a table of numerical results. An example of graphical display is given in figure 2-111.

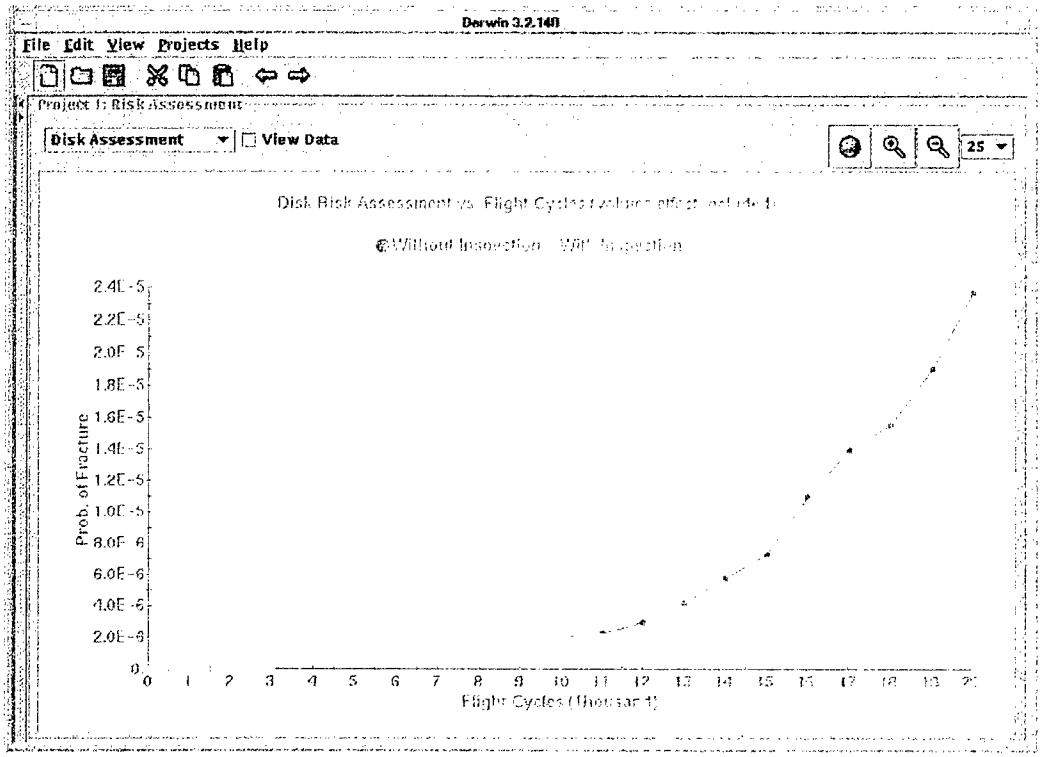


FIGURE 2-111. DISK ASSESSMENT

2.5.4.4 Disk Assessment Per Cycle.

The disk assessment per cycle displays the probability of fracture of the entire disk divided by the number of cycles as a function of cycles for the cases with and without inspection. This gives the average failure rate per cycle. The cycle value used to divide into the disk assessment varies as a function of the cycles. For example, the results at 10,000 cycles are obtained by dividing the probability of fracture at 10,000 cycles by 10,000. The View Data box can be selected to display a table of numerical results. An example of a graphical display is shown in figure 2-112.

2.5.4.5 Probability of Fracture Per Zone.

The probability of fracture for each individual zone can be plotted. The results for each zone can be turned on or off by clicking on the zone number in the plot legend. The View Data box can be selected to display a table of numerical results. The volume effect can be turned on or off by clicking the "Volume Effect" box at the bottom of the screen. (The volume effect is the probability of having a defect and is based on the defect distribution for the zone and the zone volume.) An example is shown in figure 2-113.

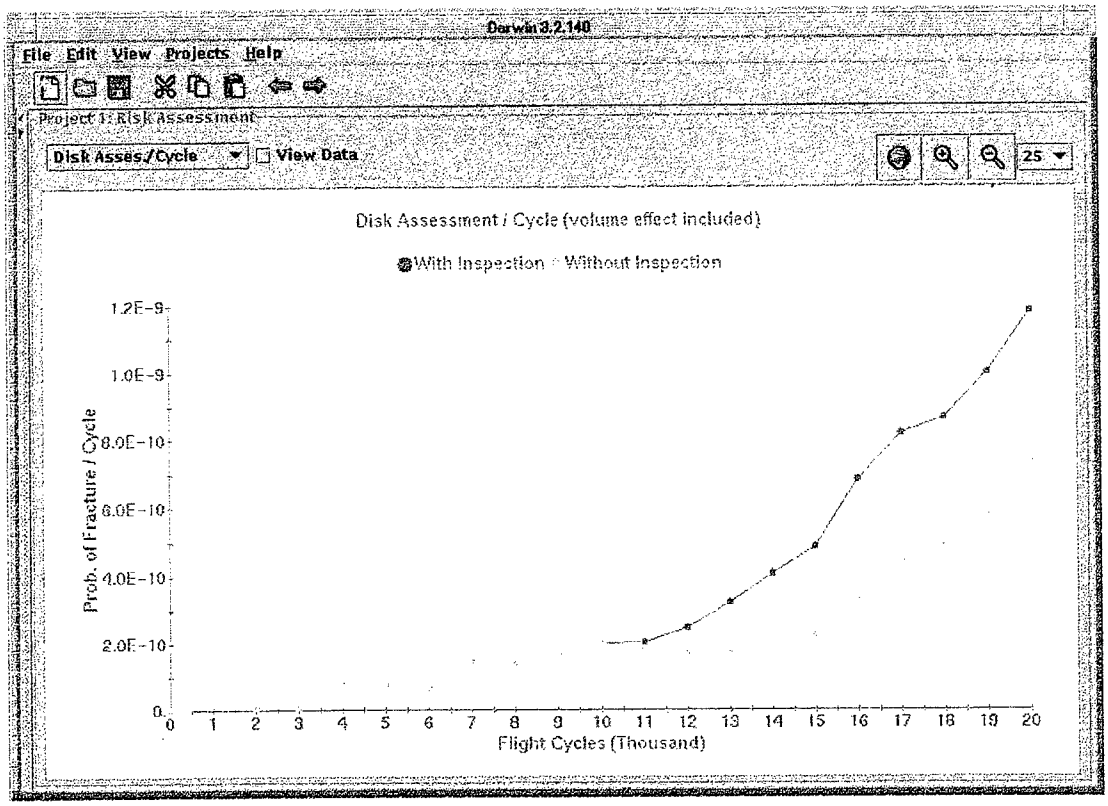


FIGURE 2-112. DISK ASSESSMENT PER CYCLE

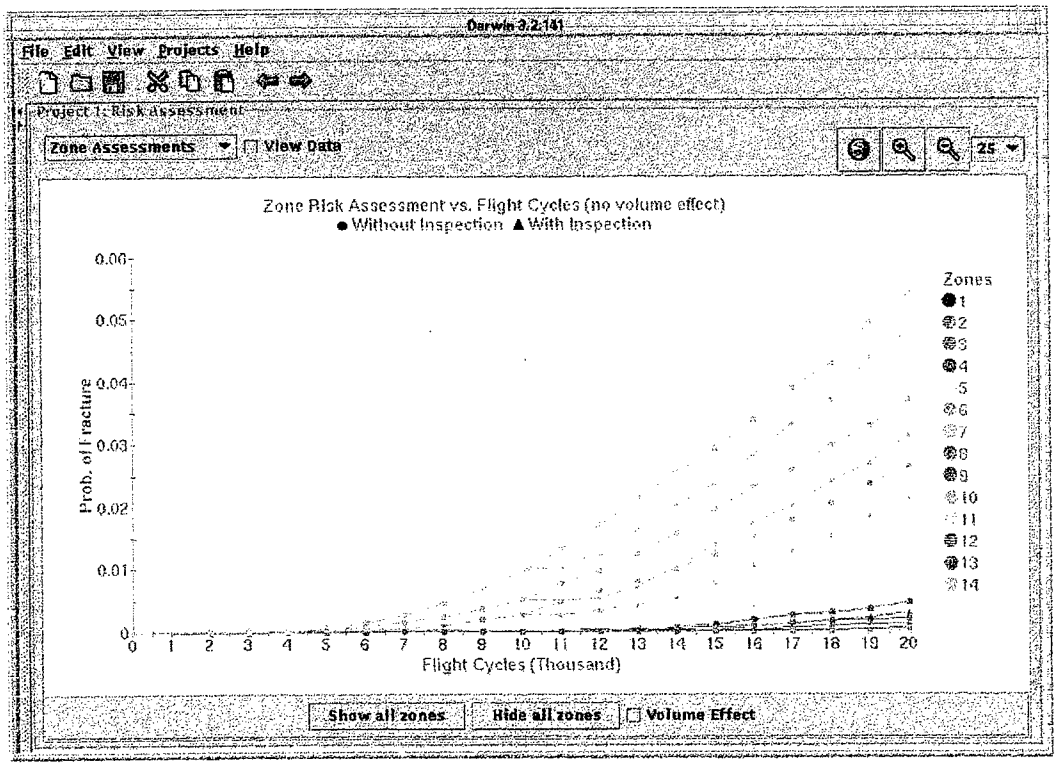


FIGURE 2-113. ZONE ASSESSMENT EXAMPLE

2.5.4.6 Risk Contribution Factors.

The risk contribution factors show the contribution of each zone risk to the overall disk risk. The results for each zone can be turned on or off by clicking on the zone number in the plot legend. The total risk contribution of all selected zones in percent is shown in the text box at the bottom of the plotting window.

The user can click the view data button to see a table of the numerical results. The rows corresponding to all selected zones are highlighted in the table. The user can also select zones by clicking the corresponding row in the view data table. An example is shown in figure 2-114.

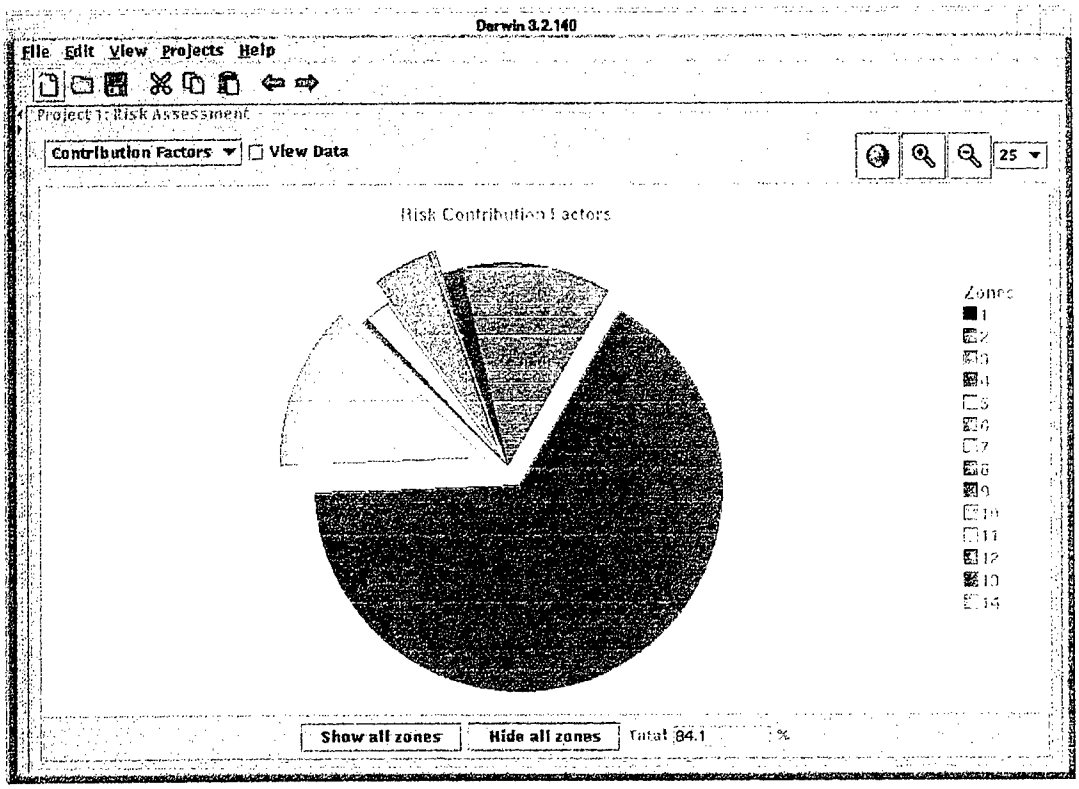


FIGURE 2-114. RISK CONTRIBUTION FACTORS

2.5.4.7 Maximum Stress Intensity Factor vs. Cycles.

The maximum stress intensity factor versus cycles can be plotted for each zone. The maximum stress intensity value is the maximum value computed at any time during a loading cycle. The results for each zone can be turned on or off by clicking on the zone number in the plot legend. An example is shown in figure 2-115.

2.5.4.8 Stress Processing.

The stress results along the plate in normalized coordinates are shown for the max and min load pairs for each zone. In addition, the polynomial fit is also shown. The crack origin is shown as a square on each line. An example is shown in figure 2-116.

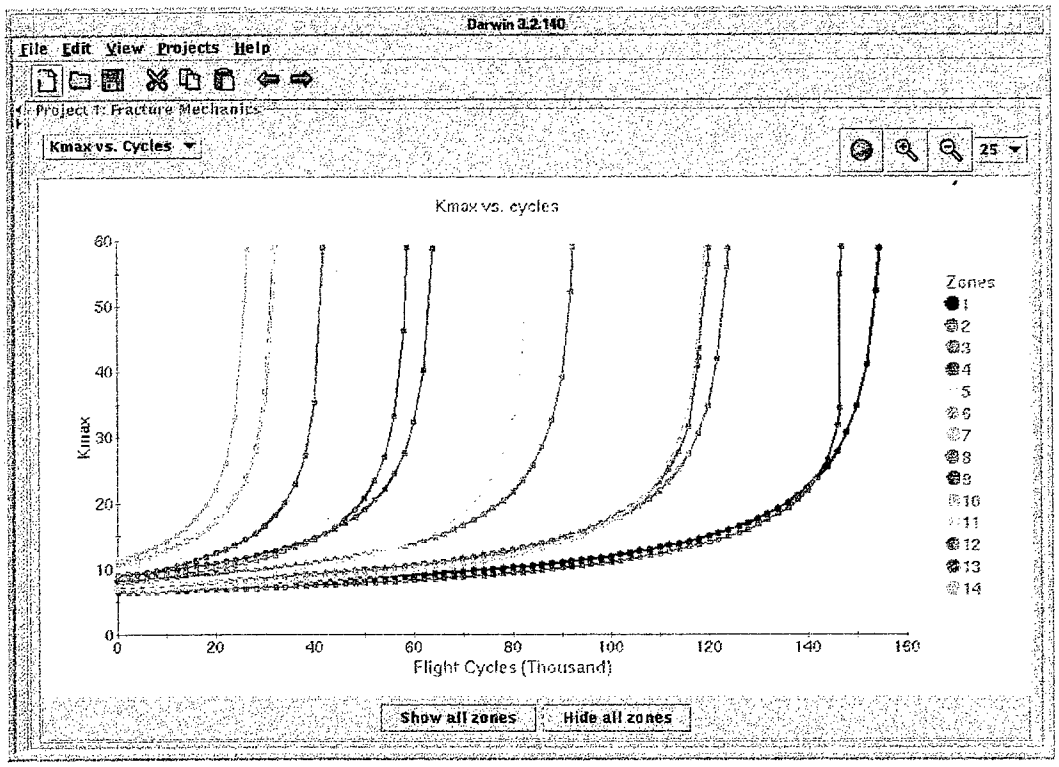


FIGURE 2-115. MAX STRESS INTENSITY FACTORS VS CYCLES

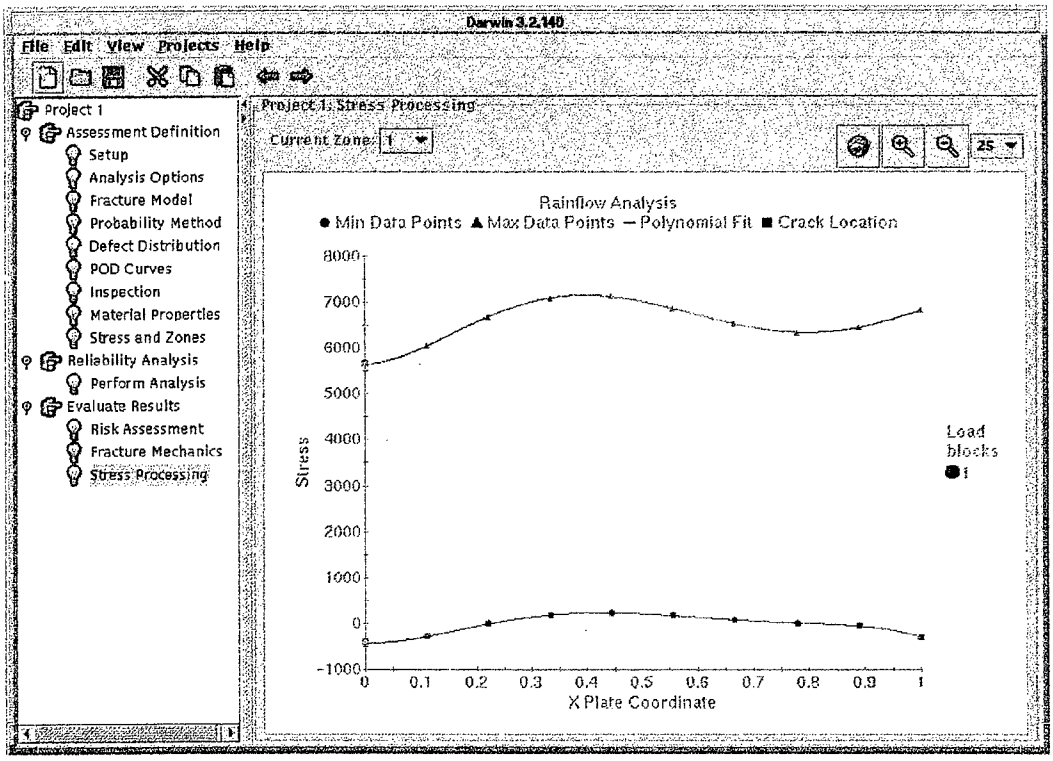


FIGURE 2-116. MAX-MIN STRESS PAIR ALONG PLATE

2.5.5 Verification and Sensitivity Studies.

DARWIN 3.2 was verified using both the Advisory Circular (AC) test case (see appendix J) and an impeller rotor model. The base cases for these problems have uniform material properties, one inspection, a single load case, and a single defect distribution. Risk computations were performed using both Monte Carlo simulation (10,000 and 100,000 samples) and importance sampling (100 and 400 samples). Fracture mechanics computations were performed using both the Flight_Life and life approximation function (LAF) methods. Stress processing was verified using both ANSYS and neutral files. Over 50 example problems were included in the verification procedure.

DARWIN 3.2 results were compared with previously validated DARWIN 3.1 results for the HP and SUN Unix platforms. Results obtained from the two risk computation methods (i.e., Monte Carlo simulation, importance sampling) were compared to identify bugs and estimate the error associated with the importance-sampling method. Results obtained from the two fracture mechanics methods (i.e., Flight_Life, LAF) were compared to estimate approximation error associated with the LAF method. Additional problems will be added in the future for further verification of DARWIN results.

The purpose of the sensitivity studies was to investigate the sensitivity of the probability of fracture with respect to several random variables. The AC test case was selected for this work. An overview description of the AC test case is presented in appendix J. For a complete description of the AC test case (including input/output data files and descriptions of random variables) see the Darwin User's Manual (Version 3.2). The stress factor and the life scatter were both lognormally distributed with median = 1.0 and with user-defined COV. The inspection time was normally distributed. The same parameters were applied to all zones.

Sensitivity studies were conducted by varying stress factor median and COV, life scatter COV, inspection time mean value and COV, and the maximum area in the defect exceedance curve (appendix A). The COV values were varied from 0% to 30% in 5% increments. The stress factor median was varied from 0.7 to 1.3 in 0.1 increments. Mean inspection times were varied from 1,000 cycles to 20,000 cycles in 1,000 cycle increments. The maximum defect area (defect exceedance curve) was set at values ranging from 1,000 mil^2 to 200,000 mil^2 (i.e., 1,000; 2,000; 5,000; 10,000; 20,000; 50,000; 100,000; and 200,000 mil^2). The defect exceedance values associated with the selected maximum defect areas were computed using linear interpolation or extrapolation on a log-log (base 10) scale.

Other parameters that could be considered, but have not been studied to date, include the PoD, the number of zones, the location of defects, and the thickness of the onion skin (surface elements). The issues associated with these parameters are more involved and likely more sensitive to design details. They will be addressed in the future if the sensitivity results prove to be valuable in providing insights and useful design guidelines.

As shown in figure 2-117, the stress factor COV has a significant influence on the probability of fracture at 20,000 cycles (P_f) and increases nonlinearly with increasing stress COV. The P_f associated with 30% stress COV is more than an order of magnitude higher than the P_f

associated with 0% stress COV for both the inspection and no inspection cases. The difference in the probability of fracture at 20,000 cycles for no inspection versus inspection, $P_{f_noinsp} - P_{f_insp}$, increases slightly with increasing COV. Overall, the P_f reduction is relatively small compared with the P_f increase due to increasing COV.

In figure 2-118, the influence of the stress factor median on P_f is shown. Similar to the stress factor COV, the influence of the stress factor median on P_f is significant and increases three to four orders of magnitude for the stress factor median range 0.7 to 1.3.

The results of figures 2-117 and 2-118 suggest that reducing the stress or stress variation, if possible, is an effective way of reducing P_f, perhaps more effective than implementing inspection.

The influence of the life scatter COV on the probability of fracture at 20,000 cycles is shown in figure 2-119. As the life scatter COV is increased from 0% to 30%, P_f increases 60% to 80% for the inspection and no inspection cases. The P_f reduction due to inspection is approximately constant for the range of COV studied.

In figure 2-120, the effect of varying the mean inspection time is shown for deterministic inspection (i.e., inspection time COV = 0). P_f reaches the minimum when the inspection is performed at approximately 14,000 cycles.

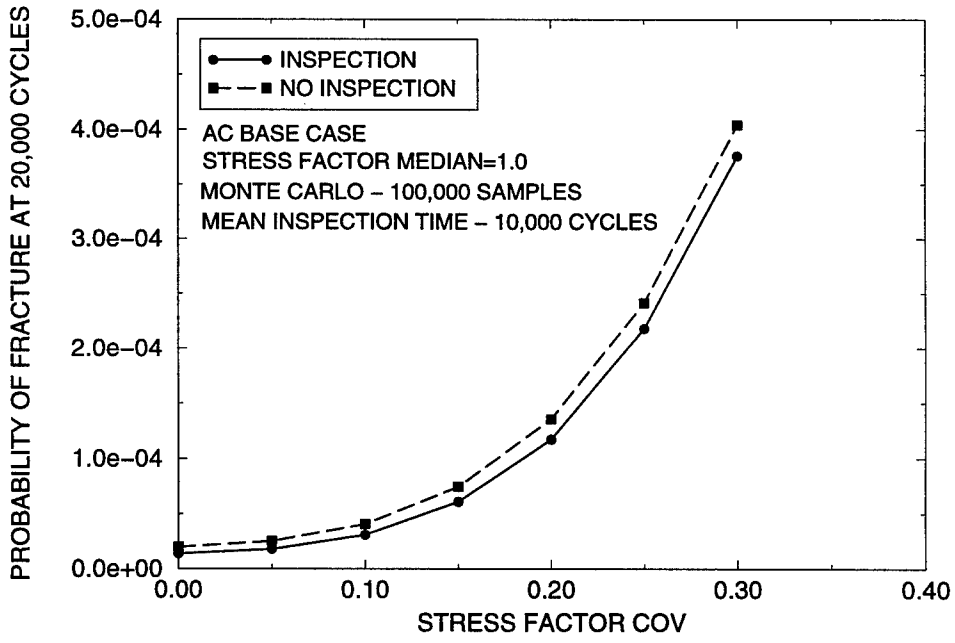


FIGURE 2-117. INFLUENCE OF STRESS FACTOR COV ON PROBABILITY OF FRACTURE AT 20,000 CYCLES
(AC base case, stress factor median = 1.0, mean inspection time = 10,000 cycles, Monte Carlo simulation @ 100,000 samples.)

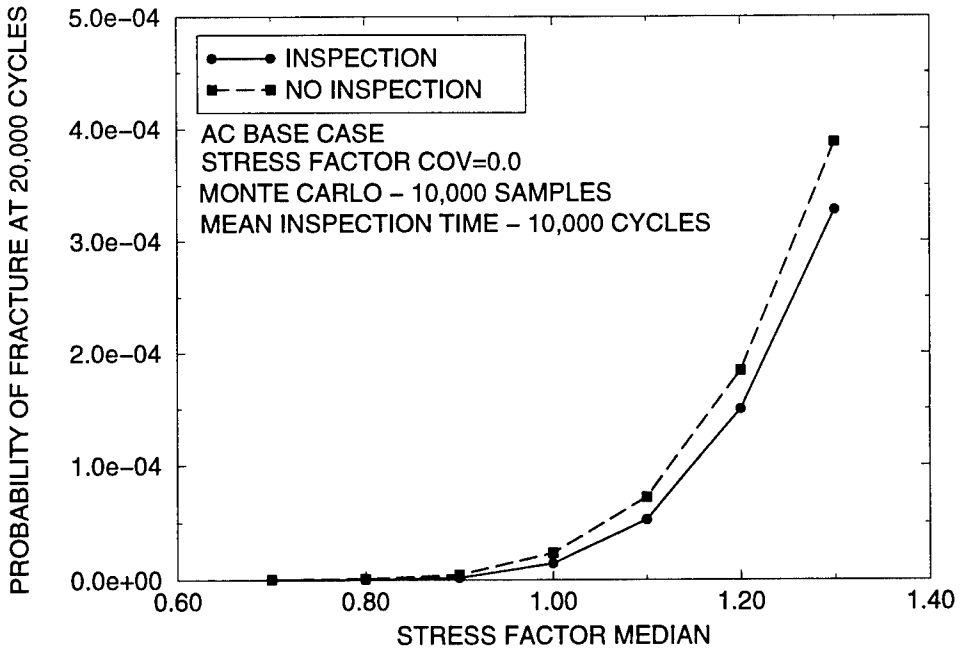


FIGURE 2-118. INFLUENCE OF STRESS FACTOR MEDIAN ON PROBABILITY OF FRACTURE AT 20,000 CYCLES
(AC base case, stress factor COV = 0, mean inspection time = 10,000 cycles, Monte Carlo simulation @ 10,000 samples.)

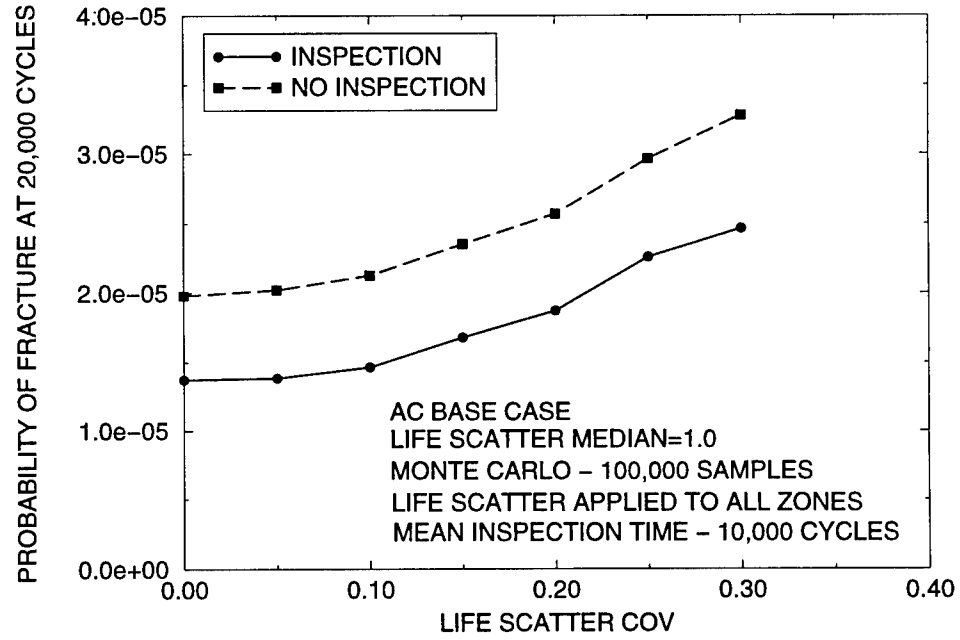


FIGURE 2-119. INFLUENCE OF LIFE SCATTER COV ON PROBABILITY OF FRACTURE AT 20,000 CYCLES
(AC base case, life scatter median = 1.0, mean inspection time = 10,000 cycles, Monte Carlo simulation @ 100,000 samples.)

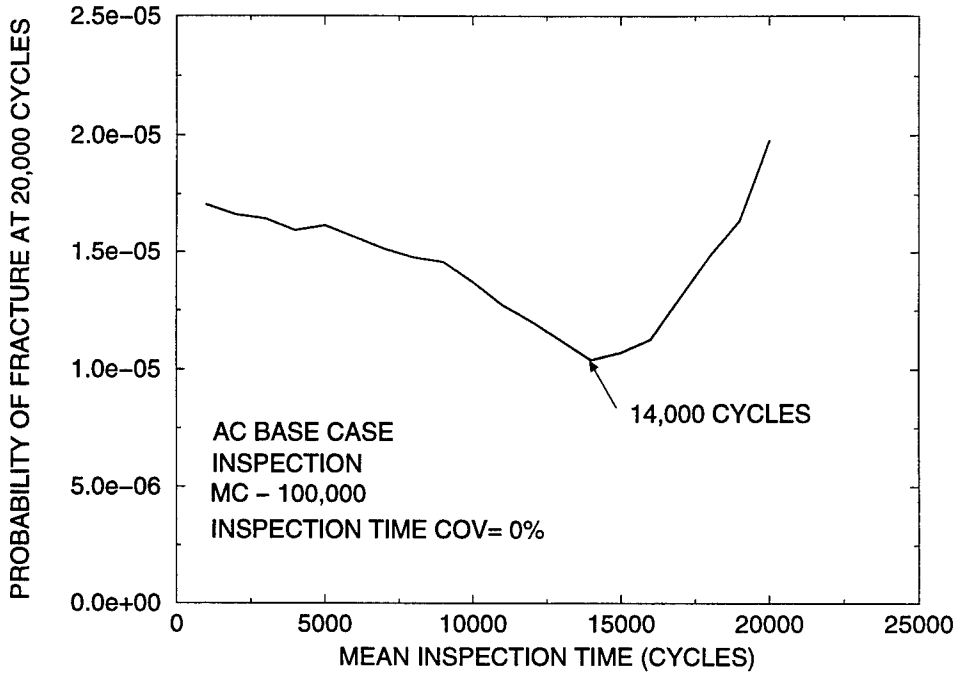


FIGURE 2-120. OPTIMUM MEAN INSPECTION TIME FOR MINIMUM PROBABILITY OF FRACTURE AT 20,000 CYCLES
(AC base case, inspection time COV = 0.0,
Monte Carlo simulation @100,000 samples.)

The inspection time COV has an influence on the value of the optimum mean inspection time that minimizes the probability of fracture at 20,000 cycles. In figure 2-121, it can be observed that the optimum mean inspection time varies from 12,000 cycles to 14,000 cycles for inspection time COVs ranging from 0% to 30%.

In figure 2-122, the influence of inspection time COV on probability of fracture at 20,000 cycles is shown for a mean inspection time of 10,000 (AC baseline) cycles. Also shown are failure probabilities for the optimum mean inspection times associated with minimum probability of fracture at 20,000 cycles. It can be observed that P_f is relatively insensitive to inspection time COV if the inspection is performed at 10,000 cycles. If the optimum mean inspection time is used, however, P_f may be significantly lower than that for 10,000 cycles and increases with increasing COV values. This result suggests that the optimal mean inspection time depends on inspection time COV and that finding optimal mean inspection times can generate the lower bound of P_f. Additional analyses are underway to develop the lower bound.

A comparison of the influences of stress, life scatter, and inspection time COVs on P_f is shown in figure 2-123. It can be observed that stress COV has a dominant effect on P_f. In fact, the P_f associated with 10% stress COV is larger than the failure probabilities associated with 30% COV for life scatter and inspection time. This illustrates that a reduction in the stress COV has more influence on reducing P_f as compared to the life scatter and inspection time COVs.

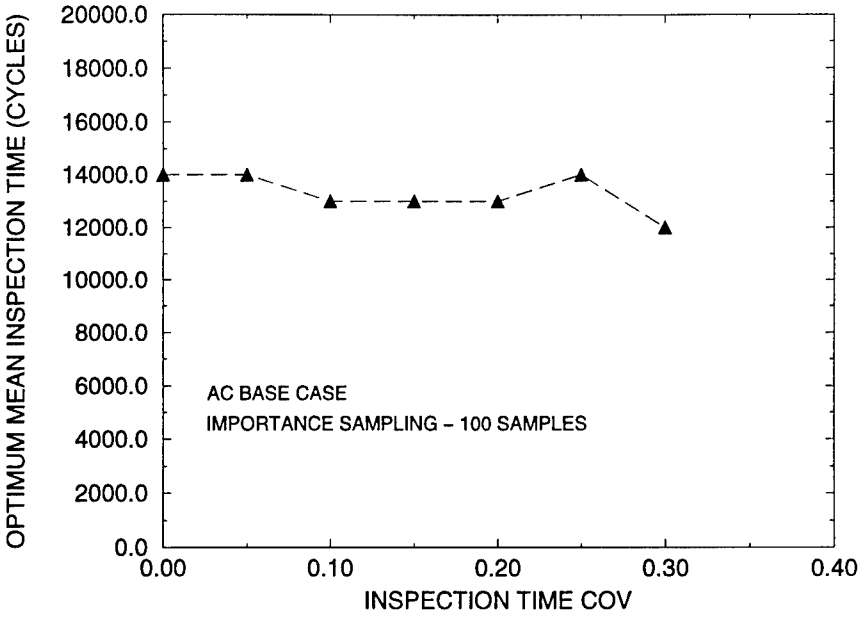


FIGURE 2-121. INFLUENCE OF INSPECTION TIME COV ON OPTIMUM MEAN INSPECTION TIME FOR MINIMUM PROBABILITY OF FRACTURE AT 20,000 CYCLES
(AC base case, importance sampling @100 samples.)

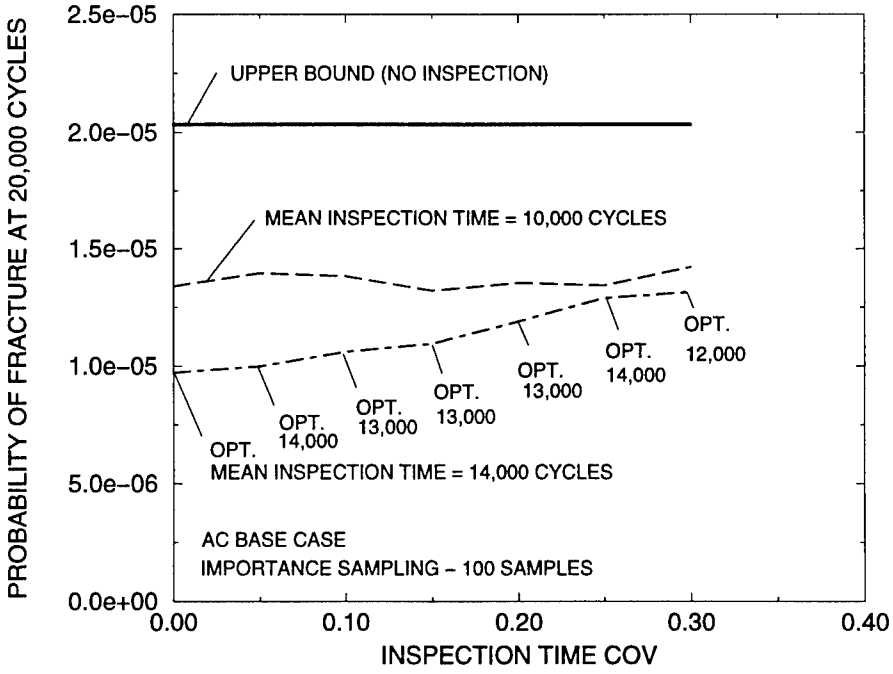


FIGURE 2-122. INFLUENCE OF INSPECTION TIME COV ON PROBABILITY OF FRACTURE AT 20,000 CYCLES
(AC base case, importance sampling @100 samples.
Mean inspection time = 14,000 cycles is the optimal inspection time at COV = 0.)

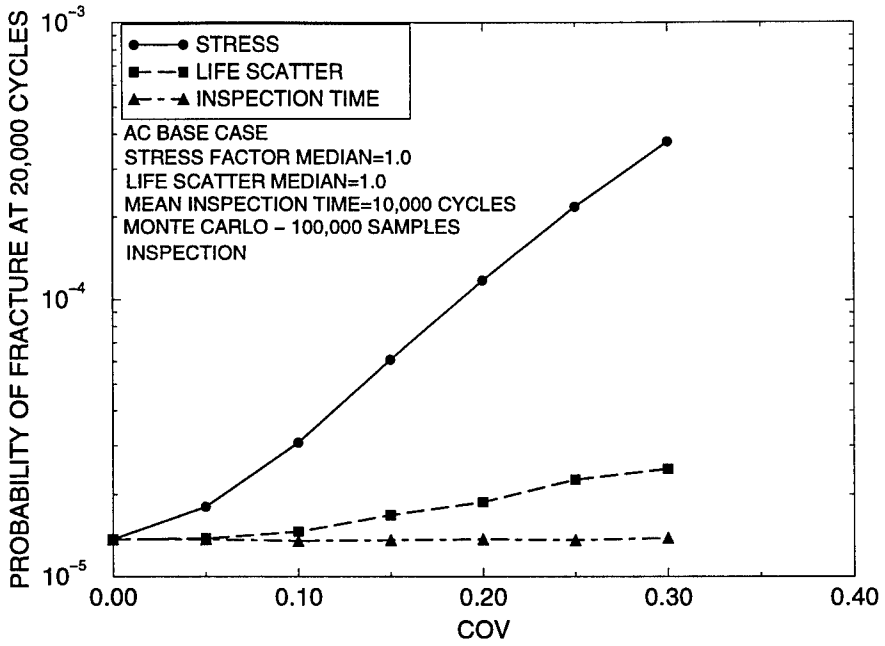


FIGURE 2-123. COMPARISON OF THE INFLUENCES OF STRESS, LIFE SCATTER, AND INSPECTION TIME COVS ON PROBABILITY OF FRACTURE AT 20,000 CYCLES (AC base case, stress factor median = 1.0, life scatter median = 1.0, mean inspection time = 10,000 cycles, Monte Carlo simulation @100,000 samples.)

In figure 2-124 the influence of the maximum defect area of the exceedance curve is shown for maximum defect areas ranging from 1,000 to 200,000 mil^2. It can be observed that the most significant increases in P_f occur in the range of 1,000 - 5,000 mil^2. In this region, P_f increases roughly up to six (or more) times its value for both the inspection and no inspection cases. $P_{f_noinsp} - P_{f_insp}$ increases with increasing maximum defect area.

Based on the above results, the following conclusions can be made:

a. Relative to life scatter and inspection time variability, the stress median or COV has a dominant effect on P_f. Reducing the stress or stress variation, if possible, is an effective way of reducing P_f, perhaps more effective than implementing inspection.

b. Inspection time variability does not have a significant impact on P_f, particularly if the mean inspection time is not at the optimal time.

c. Optimal mean inspection time depends on the inspection time COV.

d. The most critical defect sizes are in the range of 1,000 - 5,000 mil^2. Very large defects (> 5,000 mil^2) do not significantly increase P_f because the probability of occurrence is relatively small.

These conclusions were derived based on the AC test case and should be used with caution.

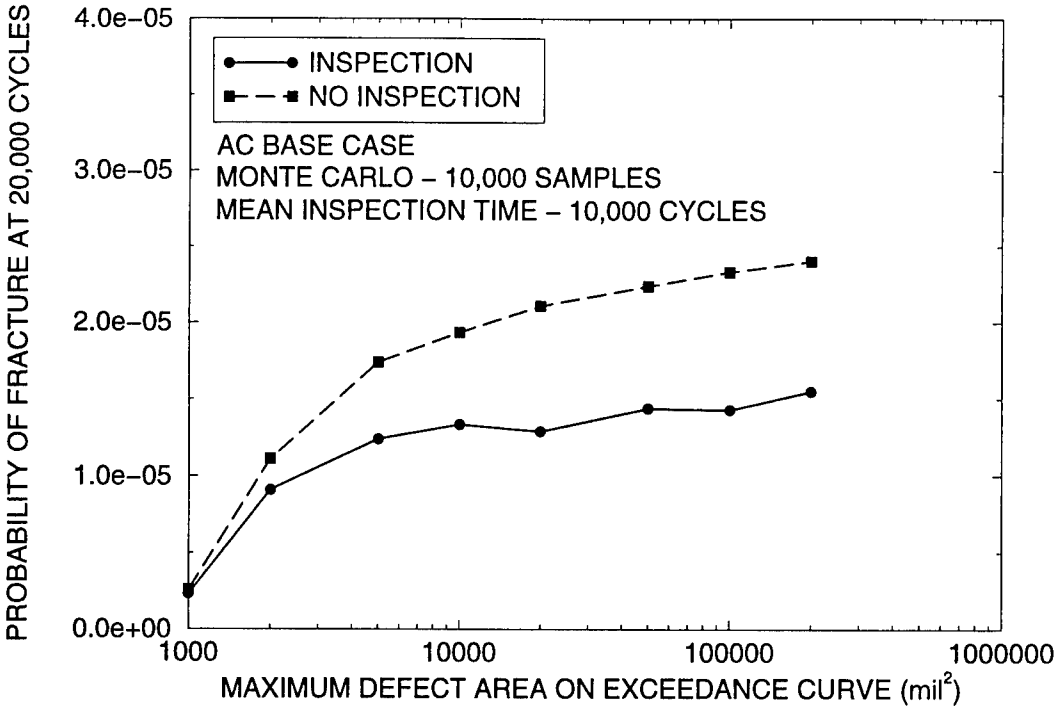


FIGURE 2-124. INFLUENCE OF MAXIMUM DEFECT AREA ON EXCEEDANCE CURVE ON PROBABILITY OF FRACTURE AT 20,000 CYCLES
(AC base case, mean inspection time = 10,000 cycles, Monte Carlo simulation @10,000 samples.)

2.5.6 Code Quality Assurance.

DARWIN QA focused on review and control of software development activities and code revision control. DARWIN QA procedures consist of process control for software development activities and configuration management for code revision control.

Process control (PC) is used to manage software development activities. The objective of PC is to ensure that all software modifications are documented and reviewed prior to being incorporated into released versions of the DARWIN code. A summary flowchart of DARWIN process control is shown in figure 2-125. When modification requests (e.g., bug fixes, enhancements) are received, they are entered into the Software Modification Database. The web-based system for user entry of DARWIN bugs and code enhancements is shown in figure 2-126. When the code modification/verification and documentation tasks associated with a modification are completed, the proposed modification is reviewed by an independent member of the DARWIN team. Upon approval, the proposed modification is applied to the source code. The associated documentation and verification/validation problems are updated as necessary.

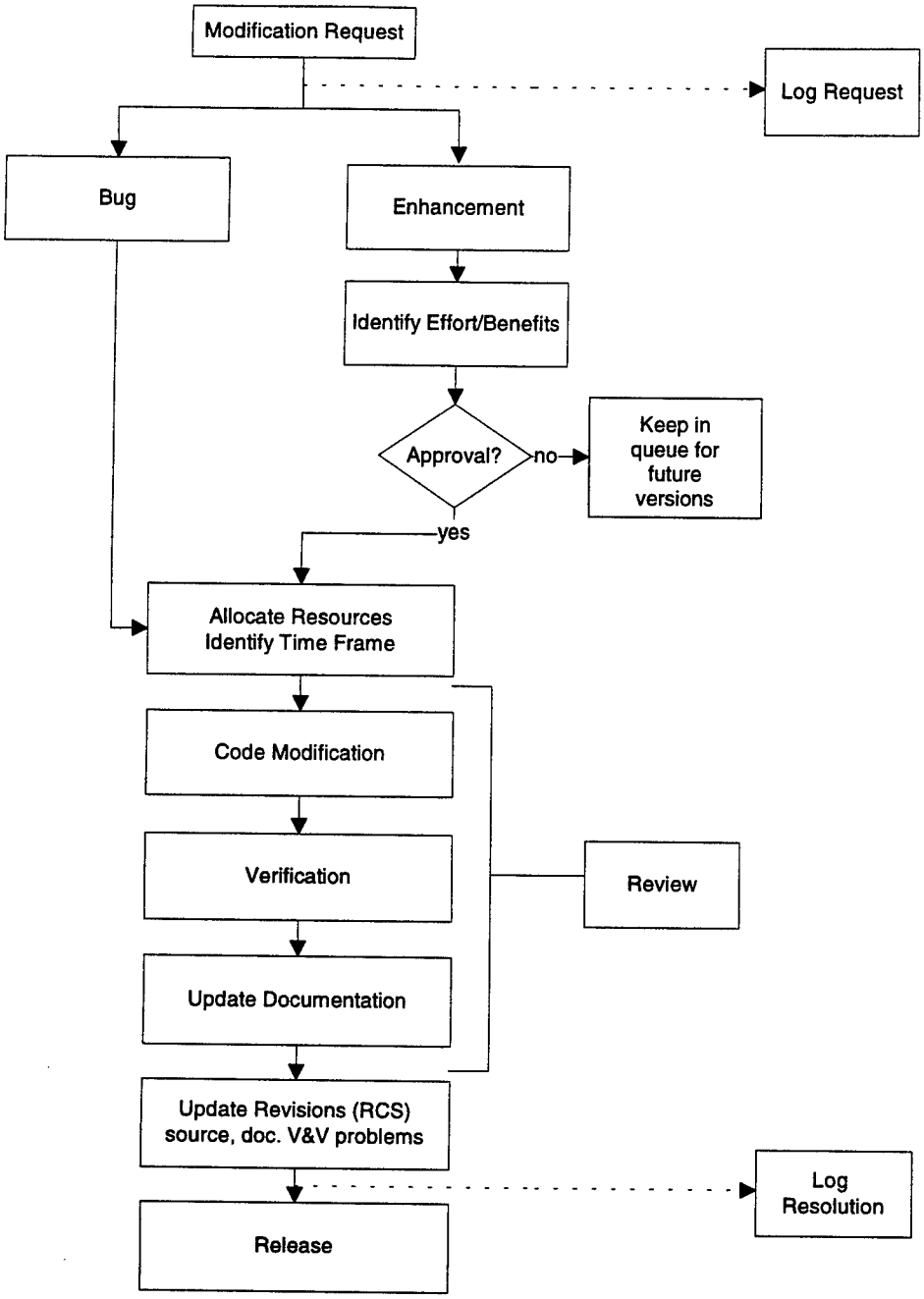


FIGURE 2-125. SUMMARY FLOWCHART OF DARWIN PROCESS CONTROL

Configuration management is used to control and track revisions to DARWIN. The Revision Control System (RCS) utilities of the HP development platform are used to maintain the source code, verification/validation problems, and associated documentation. The Concurrent Versions System (CVS, a configuration management utility similar to RCS) is used to maintain the DARWIN GUI. A revision control procedure is also used for the DARWIN Fortran program in which incremental versions are saved manually (CVS will be used in the future). In addition, complete copies of all DARWIN releases are maintained for future reference.

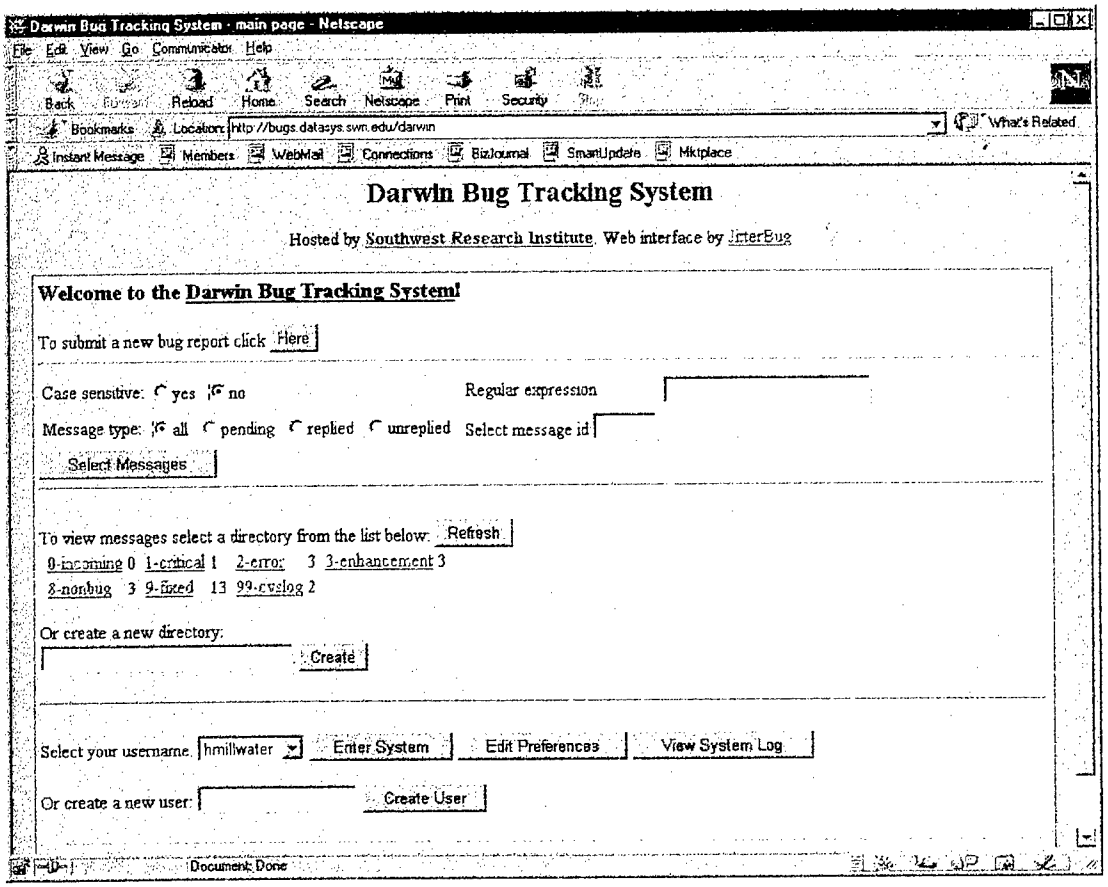


FIGURE 2-126. WEB-BASED SYSTEM FOR TRACKING DARWIN BUGS AND CODE ENHANCEMENTS

2.6 TECHNOLOGY TRANSFER WORKSHOPS.

A workshop was held at SwRI in San Antonio, TX, on May 18-20, 1999, to transfer the technology developed in this program to industry and government. An overview of all program tasks, as well as a demonstration of the GUI for DARWIN, were provided on the first day. Hands-on training on the use of the GUI and probabilistic driver was provided on the second and third days with instruction provided by SwRI staff and members of the industry steering committee. Representatives of nine engine manufacturers from the United States, Germany, England, France, and Canada were among the 41 attendees. Other attendees included representatives of the FAA, Transport Canada, NASA, and the U.S. Air Force.

On June 15-16, 1999, a workshop was held at Scientific Forming Technologies Corporation (SFTC) in Columbus, Ohio, to transfer the DEFORM^{TM} microcode technology to industry. Eight representatives were present from the melting and casting vendors, the forging vendors, and the engine manufacturers. Instruction was provided by SFTC staff and an engine company representative.

3. CONCLUDING REMARKS.

A probabilistic, damage tolerance code was developed in this program for low-cycle fatigue of titanium rotors/disks containing HA anomalies. It is called DARWIN and was developed in collaboration with AlliedSignal Engines, General Electric Aircraft Engines, Pratt & Whitney, and Rolls-Royce Allison. DARWIN is a computer program that integrates finite element stress analysis, fracture mechanics analysis, nondestructive inspection simulation, and probabilistic analysis to assess the risk of rotor fracture. It computes the probability of fracture as a function of flight cycles, considering random defect occurrence and location, random inspection schedules, and several other random variables. Both Monte Carlo and advanced, fast integration methods are integral to the probabilistic driver. A fracture mechanics module, called Flight_Life, is also incorporated in the code. In addition, a user-friendly GUI is available to handle the otherwise difficult task of setting up the problem for analysis and viewing the results.

A workshop was held at SwRI in San Antonio, TX, on May 18-20, 1999, to transfer the DARWIN technology developed in this program to the engine industry and government. An overview of all program tasks, as well as a demonstration of the GUI for DARWIN, was provided on the first day. Hands-on training on the use of the GUI and probabilistic driver was provided on the second and third days with instruction provided by SwRI staff and members of the industry steering committee. Representatives of nine engine manufacturers from the United States, Germany, England, France, and Canada were among the 41 attendees. Other attendees included representatives of the FAA, Transport Canada, NASA, and the U.S. Air Force.

Among the supplementary tasks performed in this program in support of code implementation was the generation of crack growth data for Ti-64, Ti-6242, and Ti-17β in high vacuum. This data are important because most incidents invoking cracking from HA have originated at subsurface locations. In fact, the crack growth data at low ranges of stress intensity factor was found to be considerably slower in vacuum than in air for all three alloys at ambient temperature as well as elevated temperature and at various R ratios. This data will be used, along with other new data, to update the HA anomaly distribution in a follow-on FAA program. The current anomaly distribution was calibrated to field experience using crack growth data generated in air.

A second supplementary task was conducted to determine the crack initiation behavior of artificial and natural HA defects embedded in plates of Ti-6Al-4V. Nitrogen content of the HA varied from 1.6 to 6 weight percent. It was found that crack initiation for surface-connected HA and its associated diffusion zone occurred at very low stresses while based on acoustic emission monitoring, higher stresses, comparable to those experienced at stress concentrations in disks, appeared to be needed to initiate cracks in subsurface HA. Based on the limited testing conducted to date for both seeded and natural defects, an incubation period occurred in all cases prior to the onset of established crack growth in the titanium matrix. However, until additional testing and analysis can be done, it is appropriate to apply the current conservative industry assumption that, should HA be present in a high stress location, the presence of a sharp crack in the matrix should be assumed upon initial loading for computing the low-cycle fatigue life of a component.

Another task involved the development of a forging microcode to predict the movement, shape, and orientation of HA anomalies during processing from ingot to billet and from billet to a disk forging. This microcode was integrated with a commercially available forging code called DEFORM™. Mechanical properties, both flow and fracture, of HA were obtained on synthetically produced material of various nitrogen contents. Constitutive relationships for flow and fracture of HA under multiaxial stresses were developed on the basis of the experimental results and are embedded in the microcode. Prediction of the behavior of HA using this microcode will be used to check the assumptions made in the original development of the HA defect distribution by the RISC of the Aerospace Industries Association. The microcode will also be utilized to update the defect distribution and to provide information to NDE experts on how the HA presents itself (orientation and shape) to the ultrasonic beam during ultrasonic inspection of various disk locations. An industry workshop on the use of the code was held on June 15-16, 1999, at Scientific Forming Technologies Corporation in Columbus, OH.

4. REFERENCES.

1. "Uncontained Turbine Engine Rotor Events," Report by FAA/SAE Committee, 1994.

2. "Titanium Rotating Components Review Team Report," Federal Aviation Administration, December 14, 1990.

3. "Damage Tolerance Concepts for Critical Engine Components," Advisory Group for Aerospace Research and Development (AGARD), Conference Proceedings No. 393, 1985.

4. J. C. Newman, Jr., "Contribution From NASA Langley Research Center on the AGARD Engine Disc Programme," private correspondence.

5. P. G. Roth, "Probabilistic Rotor Design System (PRDS) Phase I," AFWAL Report WL-TR-92-2011, May 1992.

6. J. D. Adamson, E. P. Fox, and J. E. Malone, "Probabilistic Design System-Phase I and II Interim Report," Contract F33615-92-C-2219, December 1995.

7. M. Gigliotti, General Electric Corporate Research and Development, Internal Report, 1991.

8. M.C. Shaw, P.M. Braiden, and G.J. DeSalvo, "The Disk Test for Brittle Materials," *Journal of Engineering for Industry*, Transactions of the ASME, Vol. 97, Ser. B, No. 1, pp. 77-87, 1975.

9. D. Tabor, The Hardness of Metals, Oxford University Press, New York, 1951.

10. S. Kobayashi, S.I. Oh, and T. Altan, Metal Forming and the Finite Element Method, Oxford University Press, New York, 1989.

11. D. A. Meyn, "An Analysis of Frequency and Amplitude Effects on Corrosion Fatigue Crack Propagation in Ti-8Al-1Mo-1V," *Metallurgical Transactions*, Vol. 2, pp. 853-865, 1971.

12. P. E. Irving and C. J. Beevers, "The Effect of Air and Vacuum Environments on Fatigue Crack Growth Rates in Ti-6Al-4V," *Metallurgical Transactions*, Vol. 5, pp. 391-398, 1974.

13. H. Doker and D. Munz, "Influence of Environment on the Fatigue Crack Propagation of Two Titanium Alloys," *The Influence of Environment on Fatigue*, MEP Ltd, London, pp. 123-130, 1977.

14. J. A. Ruppen and A. J. McEvily, "Influence of Microstructure and Environment on the Fatigue Crack Growth Fracture Topography of Ti-6Al-2Sn-4Zr-2Mo-0.1Si," *Fractography and Materials Science, ASTM STP 733*, pp. 32-50, 1981.

15. M. Peters, A. Gysler, and G. Lutjering, "Influence of Texture on Fatigue Properties of Ti-6Al-4V," *Metallurgical Transactions*, Vol. 15A, pp. 1597-1605, 1984.

16. S. J. Gao, G. W. Simmons, and R. P. Wei, "Fatigue Crack Growth and Surface Reactions for Titanium Alloys Exposed to Water Vapor," *Materials Science and Engineering*, Vol. 62, pp. 65-78, 1984.

17. L. S. Vesier and S. D. Antolovich, "Fatigue Crack Propagation in Ti-6242 as a Function of Temperature and Waveform," *Engineering Fracture Mechanics*, Vol. 37, pp. 753-775, 1990.

18. R. Foerch, A. Madsen, and H. Ghonem, "Environmental Interactions in High-Temperature Fatigue Crack Growth of Ti-1100," *Metallurgical Transactions*, Vol. 24A, pp. 1321-1332, 1993.

19. J. Petit, W. Berata, and B. Bouchet, "Fatigue Crack Growth Behavior of Ti-6Al-4V at Elevated Temperature," *Titanium '92 Science and Technology*, TMS, Warrendale, PA, pp. 1819-1826, 1993.

20. M. R. Bache, W. J. Evans, and M. McElhone, "The Effects of Environment and Internal Oxygen on Fatigue Crack Propagation in Ti-6Al-4V," *Materials Science and Engineering*, Vol. A234-236, pp. 918-922, 1997.

21. R. H. Van Stone and T. L. Richardson, "Potential-Drop Monitoring of Cracks in Surface-Flawed Specimens," *Automated Test Methods for Fracture and Fatigue Crack Growth, ASTM STP 877*, pp. 148-166, 1983.

22. J. C. Newman, Jr. and I. S. Raju, "Stress Intensity Factor Equations for Cracks in Three-Dimensional Finite Bodies," *Fracture Mechanics: Fourteenth Symposium—Volume 1, ASTM STP 791*, pp. I-238-I-265, 1983.

23. D. O. Harris, "Stress Intensity Factors for Hollow Circumferentially Notched Round Bars," *Journal of Basic Engineering*, Vol. 89, pp. 49-54, 1967.

24. J. W. Sheldon, K. R. Bain, and J. K. Donald, "Investigation of the Effects of Shed-Rate, Initial K_{max}, and Geometric Constraint on ΔK_{th} in Ti-6Al-4V at Room Temperature," to be published in *International Journal of Fatigue*.

25. M. Sugano, S. Kanno, and T. Satake, "Fatigue Behavior of Titanium in Vacuum," *Acta Metallurgica*, Vol. 37, pp. 1811-1820, 1989.

26. R. S. Piascik, J. C. Newman, Jr., and J. H. Underwood, "The Extended Compact Tension Specimen," *Fatigue and Fracture of Engineering Materials and Structures*, Vol. 20, pp. 559-563, 1997.

27. Damage Tolerant Design Handbook, WL-TR-94-4053, CINDAS/USAF, Vol. 2, 1994.

28. A. J. A. Mom and M. D. Raizenne, "AGARD Engine Disc Cooperative Test Programme," AGARD Report 766, August 1988.

29. M. D. Raizenne, "Fatigue Crack Growth Rate Data for AGARD TX114 Engine Disc Cooperative Test Programme," Laboratory Memorandum ST-479, National Aeronautical Establishment, Ottawa, Canada, September 1987.

30. "Design Assessment of Reliability With INspection," Version 3.2, User's Manual, Southwest Research Institute, July 1999.

31. "System for Integrated Engineering Structural and Thermal Analysis (SIESTA) User's Manual," Version I.00, GEAE, October 1995.

32. "Standard Practices for Cycle Counting in Fatigue Analysis," *Annual Book of ASTM Standards*, American Society of Testing and Materials, Vol. 03.01, pp. 710-718, 1999.

33. J. Bannantine, J. Comer, and J. Handrock, Fundamentals of Metal Fatigue Analysis, Prentice-Hall, Inc., New Jersey, 1990.

34. "Fatigue Crack Growth Computer Program NASGRO," Version 3.00, Theoretical and Operational Manual, JSC-22267B, NASA Johnson Space Center, 1999.

APPENDIX A—THE DEVELOPMENT OF ANOMALY DISTRIBUTIONS FOR AIRCRAFT ENGINE TITANIUM DISK ALLOYS

Authors: Sub-team to the Aerospace Industries Association Rotor Integrity Sub-Committee

1.0 Abstract

The Aerospace Industries Association (AIA) Rotor Integrity Sub-Committee* ("industry committee") has proposed an enhanced damage tolerance design strategy for critical rotating titanium parts, in response to recommendations made in the FAA Titanium Rotating Components Review Team Report, December 14, 1990. This design strategy employs a probabilistic relative risk assessment methodology intended to reduce the rate of uncontained rotor events. A key part of constructing this strategy was the development of the hard alpha (Nitrided titanium) anomaly distribution (occurrence rate and size of the anomalies present in the finished part material), and the benchmarks to measure the results of the assessments [engine and component Design Target Risk (DTR) values]. The DTR is the metric that determines the acceptability of new designs and the appropriateness of proposed field actions.

The industry committee put in place our sub-team to establish the hard alpha anomaly distribution and develop a methodology for the committee to determine the DTRs. We developed the distribution through a series of analytical modeling steps, based on behavioral observations, that simulate the manufacturing process of a titanium rotating component from ingot conversion through forging inspection. The simulation incorporates three dimensional size information from detected and analyzed hard alpha, inspection capability, and inspection find rates to determine a baseline distribution shape. The initial estimated distribution was adjusted based on certain Commercial Engine service experience of the industry committee members. This adjustment was necessary since the analytical process involved a set of difficult to evaluate assumptions, leading to multiple potential solutions. Once we established the anomaly distribution, based on the complex set of assumptions and experience, the industry committee determined DTRs for both the engine and individual components. The industry committee arrived at the DTR values by consensus using results of analytical simulations from each member company. The proposed DTRs represent a significant reduction in estimated number of hard alpha uncontained rotor events when compared to the baseline period; 1984 to 1989, as reported in the SAE SP 1270 report.

The steps taken to develop the hard alpha anomaly distribution and the DTR values are presented in this paper. This information is applicable to titanium disk alloys (i.e., Ti 6-4, Ti 6-2-4-6, and Ti 17β) manufactured after 1995.

2.0 Introduction

Historically, the conventional design and life management of aircraft gas turbine engine disks have involved a methodology (i.e., "Safe Life") founded on the premise of nominal material and manufacturing variability (common cause). While the industry has put in place strict material process controls and in-process inspections, gas turbine industry experience demonstrates that material anomalies, while extremely infrequent and sometimes not detectable with standard non-destructive testing (NDT) methods, exist and have the potential to degrade the structural integrity of high energy rotating components.

Damage tolerance is one way of improving recognition of potential anomalies which can result from inherent material structure, material processing, component design, manufacturing or usage. These potential anomalies are addressed through the incorporation of fracture resistant design, fracture mechanics, manufacturing process control, and/or nondestructive inspection.

---

* FAA/AIA collaboration and industry committee initiative to improve commercial aircraft safety. The AIA Rotor Integrity Sub-Committee member companies are listed in Section 9.0 Acknowledgments.

Regions in titanium of interstitially stabilized alpha phase that, on rare occasion, can arise from the local presence of high nitrogen or oxygen concentrations. These regions typically exhibit higher hardness and lower ductility then the surrounding material.

An FAA/Industry agreed upon relative risk design target value. This "benchmark" is the standard against which probabilistic assessment results will be compared. Stated in terms of component or engine level events per engine flight cycle, calculated over the projected life of the components in the engine.

A subset of the industry committee membership tasked with working technical details for the industry committee damage tolerance proposal. The Sub-Team membership is listed in section 9.0 Acknowledgments.

Copyright © 1997 by the AIA Rotor Integrity Sub-Committee. Published by the American Institute of Aeronautics and Astronautics, Inc. with permission.

The FAA established the Titanium Review Team after the 1989 Sioux City accident to evaluate the material process control, manufacture, and field management of titanium alloy rotating turbine engine components. The FAA Titanium Review Team Report (issued in December 1990) recommended that the industry review available techniques to determine whether the introduction of additional damage tolerance concepts could reduce the rate of uncontained rotor events. The industry established the AIA Rotor Integrity Sub-Committee ("industry committee") to address this FAA recommendation.

The industry committee concluded that current technology could enhance the conventional design and life management process to address anomalous conditions. It has proposed that an additional damage tolerance element be added to conventional design procedures to augment the FAA and industry efforts to minimize the occurrence of uncontained rotor events. In response to a FAA request for prioritization of this undertaking, the industry committee focused its initial efforts on the issues associated with potential hard alpha in rotors manufactured from titanium alloys (e.g. Ti 6-4, Ti 6-2-4-6, and Ti 17β).

The proposed process change will result in damage tolerance assessments on all new critical titanium alloy rotor designs in the form of fracture mechanics-based probabilistic analyses. The results will be compared against specified Design Target Risk (DTR) values. Designs satisfying the targets will be considered acceptable. If a design does not meet the DTRs, the engine manufacturer has several options to achieve the desired target, including component redesign, material change/process improvements, manufacturing inspection improvements, in-service inspections, and any combinations of the above.

Since the analysis inputs are subject to variability, the results of these assessments are not considered to be "exact" or "absolute [1]". Never the less they are a "relative calculation" to be used as an engineering guideline by the engine industry to select design and/or field actions which minimize the chances of uncontained rotor events.

The industry committee put in place our sub-team to establish the hard alpha anomaly distribution and develop a methodology for the committee to determine the DTRs.

The scarcity of hard alpha data combined with the issue that the available data was not in the appropriate form, suggested the need for an analytical process to estimate the appropriate data to develop and validate the hard alpha anomaly distribution. The titanium hard alpha anomaly distribution was developed through a series of analytical modeling steps, based on behavioral observations, that simulate the manufacturing process from billet conversion to final machining. The simulation incorporates three dimensional size information from detected and analyzed hard alpha, inspection capability (agreed to by the industry committee), and inspection find rates to determine a baseline distribution. The final distribution was estimated by adjusting the hard alpha frequency of the baseline distribution to achieve an approximate correlation with commercial engine service experience for a baseline period, 1984 through 1989, as reported in SAE SP 1270. This adjustment attempted to reconcile an analytical process that involved an initial set of assumptions that were difficult to validate, and led to multiple solutions.

Once the anomaly distribution was established, the industry committee determined Design Target Risk (DTR) values specifically for hard alpha anomalies. Targets specific to hard alpha were necessary since the process to determine the DTRs used the estimated hard alpha anomaly distribution as an input. The industry committee arrived at the DTR values by consensus using results of analytical simulations from each member company. The proposed DTRs represent a significant reduction in estimated number of hard alpha uncontained rotor events when compared to the baseline period.

3.0 Review of Available Data

Our goal was the development of a hard alpha anomaly distribution that applies to fully machined finished components for future engine designs. Unfortunately, as in many undertakings of this nature, the requisite data did not exist to directly determine this distribution, which required size and frequency data for the rare hard alpha present in finished parts. The available data were for anomalies found by inspection and removed from the in-process material. Specifically this information included the following:

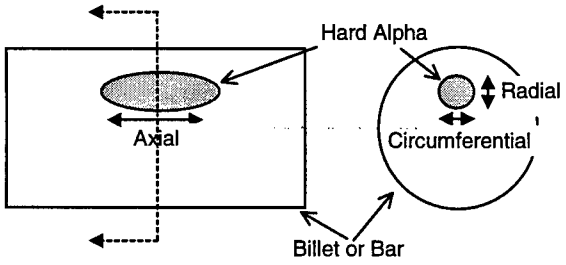
- Jet Engine Titanium Quality Committee (JETQC) data for double and triple vacuum arc remelt (VAR) titanium alloys (e.g. Ti 6-4, Ti 6-2-4-2, and

[1] The term absolute typically describes risk analysis that includes an accurate portrayal of all significant variables and is rigorously calibrated to past experience.

Ti 17β). The data was recorded from 1990 to mid 1992 and consisted of:

- The number of billet and bar hard alpha ultrasonic inspection finds
- The weight (in pounds) of material inspected
- Two dimensional size data (radial and circumferential) for all of the hard alpha finds. (note: sometimes including an estimate of the axial length) See Figure 3.1
- Three-dimensional size data (radial, circumferential, and axial) for a limited number of finds. Size data was based on detailed metallurgical sectioning of the hard alpha.

Figure 3.1. Hard Alpha Reference Directions Inside the Billet or Bar



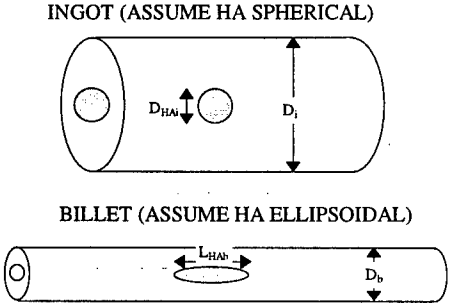
- Probability of Detection (POD)* estimates for the in-process billet and bar ultrasonic inspections
- Estimate of the number of sonic shape** hard alpha finds
- Hard alpha find data from titanium rotor proof testing

Individual sub-team member's review of the available data revealed several significant observations regarding the development of the hard alpha anomaly distribution. They were:

1. Hard alpha were deformed in the billet and bar proportional to the amount of elongation in the ingot to billet/bar transformation.
2. The find rate (number of hard alpha per unit weight) for bars was greater than the find rate for billets.
3. Sonic shape finds were no more than 10 % of the billet finds.
4. There were indications of an underlying hard alpha distribution that ultrasonic inspection apparently did not detect.

A sub-team member made the first observation based an analysis of the JETQC hard alpha three dimensional size data which showed that hard alpha detected in bars tended to be more elongated in the axial direction than those detected in billets. In addition, the hard alpha cross sectional area in the circumferential-radial plane was typically larger for the billet finds than it was for the bar finds. This was true for both the two and three dimensional JETQC data. These observations suggested that the ingot to billet/bar transformation stretched the hard alpha in the axial direction during the ingot to billet/bar transformation and the amount of deformation was a function of the amount of ingot to billet/bar elongation.

Figure 3.2. Hard Alpha Deformation Schematic



The sub-team member conceived a hard alpha deformation theory to explain these observations. This team member assumed that hard alpha is spherical in the ingot, and that as the ingot is elongated into a billet or bar, the spherical hard alpha is elongated in the same direction as the ingot, without change of volume, into an ellipsoid of circular cross section. A schematic of this theory is shown in Figure 3.2.

Figure 3.3 is a plot of the JETQC three dimensional data in terms of billet/bar elongation verses hard alpha elongation. The team member evaluated the data to determine a mathematical model that describes the observed hard alpha deformation behavior. The sub-team decided to use only the three dimensional JETQC data since the two dimensional data lacked the axial dimension required to calculate the equivalent

---

* POD is a quantitative statistical measure of the probability of detecting a particular type of material anomaly over a range of sizes for a specific non-destructive inspection technique.

** A geometric shape machined from a forging to enable ultrasonic inspection of the material.

Component spin test at elevated conditions to screen for anomalies in the material that could be detrimental in service. This test is conducted after ultrasonic inspection and prior to field service.

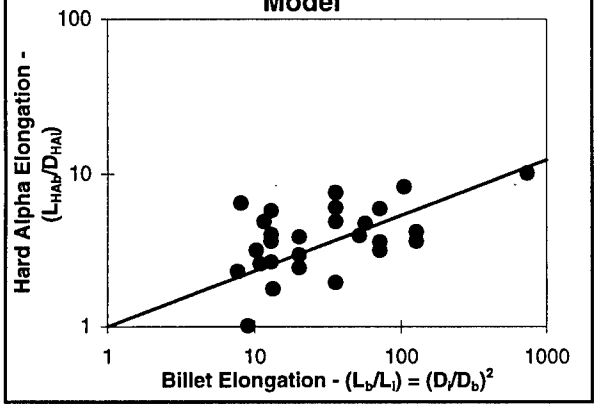
volume and associated diameter for the hard alpha anomaly in the ingot.

After considerable experimentation with more complex relationships the team member concluded that a simple model was the most appropriate. We adopted the following model based on our team member's recommendation:

$$L_{HA_b} = D_{HA_i} \times \left(\frac{D_i^2}{D_b^2} \right)^{0.364}$$

Where L_{HAb} is the length of the hard alpha in the billet, D_{HAi} is the diameter of the hard alpha in the ingot, D_i is the ingot diameter, and D_b is the billet or bar diameter.

Figure 3.3. Hard Alpha Elongation Model



The team member's second observation suggested that hard alpha in a bar was more inspectable than in a billet. As billet and bar material generally comes from the same ingot source, the team member concluded, on the average, bars should not contain any more hard alpha than the billets. Three contributing factors are: 1) hard alpha deformation in a bar creates a larger inspectable cross-sectional area than in the billet; 2) the bar material was inspected with a more sensitive ultrasonic inspection; and, 3) the smaller diameter of the bar means there is less material to inspect through. Overall, this member's observation supported the argument that the find data could not be used directly to determine the hard alpha distribution present in finished parts. We adopted our team member's conclusion.

The sub-team used the first two observations as fundamental building blocks for construction of the simulation model and the third and fourth observations as process checks on the results estimated by the model.

4.0 Development of the Baseline Distribution

The hard alpha deformation model combined with the observed effects of the in-process ultrasonic inspections provided the foundation for developing a simulation model to determine the required data for estimating the hard alpha distribution. However, our sub-team as well as the total industry committee recognized that an analytical procedure alone may not yield the final distribution, due to the uncertainty in the data and the process itself. Therefore, the industry committee anticipated a need to correlate with field experience of in-service components.

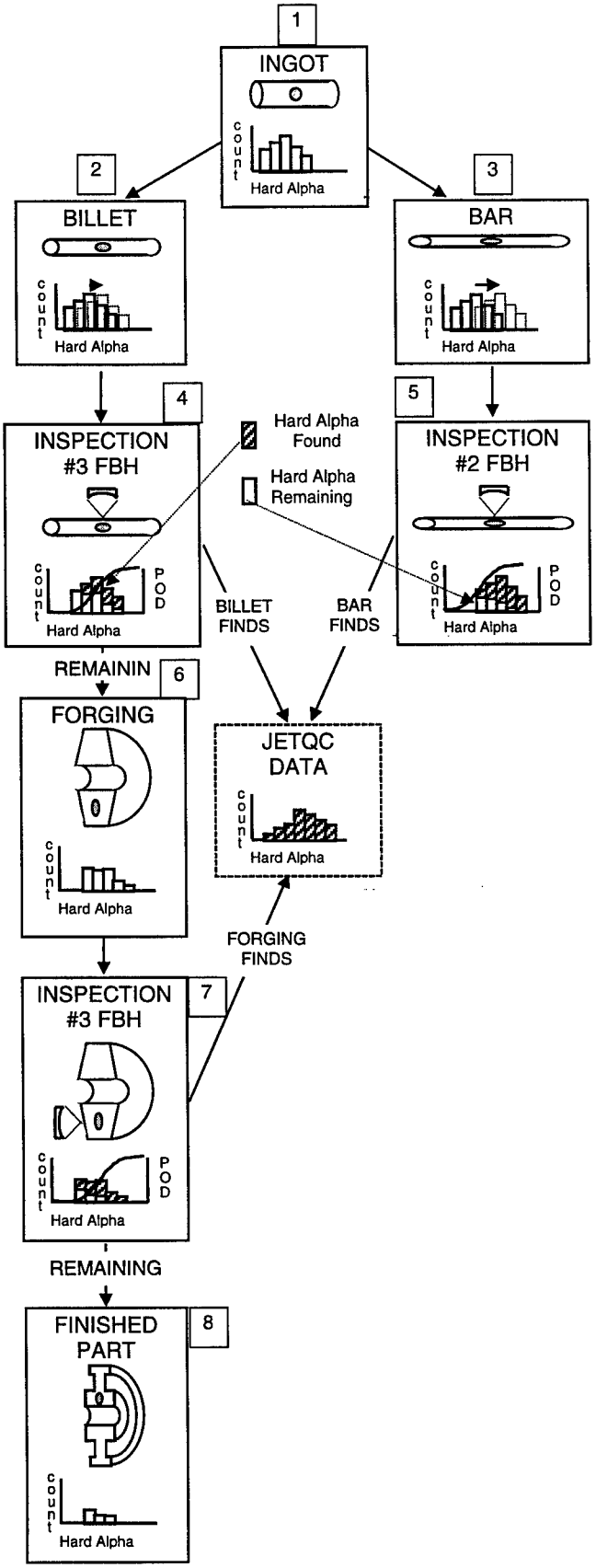
The steps we used to establish the final hard alpha distribution are discussed in sections 4.1 through 4.4.

4.1 Titanium component manufacturing process model description

Figure 4.1 shows the titanium component process model we developed to estimate the required data for the baseline hard alpha anomaly distribution. The model assumes that both bar and billet material originate from the same initial ingot distribution, frame 1. From this point the model splits into paths, one for billet material and one for bar. In frames 2 and 3 the deformation model is applied to create the billet and bar pre-inspected distributions. In frames 4 and 5, each distribution is inspected with the appropriate ultrasonic inspection POD curve [#2 flat bottom hole (FBH) for the bar and #3 FBH for the billet]. These inspections yield two types of data, estimated number of billet and bar finds, and the post inspected billet distribution. Frame 6 represents the pre-inspected sonic shape distribution, we assumed that the forging process had little impact on the hard alpha size and shape. In frame 7 performing the ultrasonic sonic inspection with the appropriate POD curve (#3 FBH) results in the post-sonic or baseline finished part distribution and an estimated number of sonic inspection finds, shown in frame 8.

Ultrasonic calibration standard consisting of a block of material containing holes of varying diameters. The diameters of the holes are specified in multiples of 1/64".

Figure 4.1. Titanium Component Process Model



4.2 Derivation of the Baseline Anomaly Distribution

Derivation of the baseline hard alpha distribution breaks down into 5 main steps.

1. Construction of an ingot relative size distribution, based on three-dimensional JETQC data, and the #2 and #3 flat bottom hole POD curves.
2. Conversion of the ingot relative size distribution to billet and bar relative size distributions implementing the deformation model.
3. Estimation of the number of billet and bar finds and post inspected billet distribution, applying the appropriate POD curve.
4. Determination of the position of the ingot distribution (on the probability axis) that achieves a match with the number of finds in the JETQC data for both the billet and bar material.
5. Conformation of results against the sonic shape inspection find rate and the undetected hard alpha distribution.

The following discussion is further elaboration on the above steps.

Step 1 - Construction of the ingot relative size distribution. We estimated the ingot relative size distribution using the JETQC three-dimensional billet and bar find data and associated inspection POD. Two-dimensional size information was also available, however a strong correlation between the two-dimensional and three-dimensional sizes did not exist. Therefore, we did not use the two-dimensional size data for this purpose.

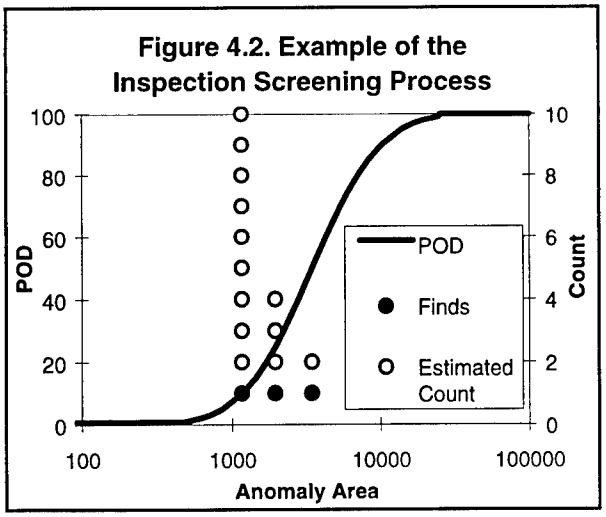
The analytical process involved estimating the pre-inspected number of hard alphas for a given size as a function of the ultrasonic inspection. First, we calculated the hard alpha ellipsoidal cross sectional area presented to the inspection field. We used the root mean square of the radial and circumferential dimensions due to the uncertainty in the melter's reporting of the actual orientation of these two dimensions.

$$A_{HA_e} = \frac{\Pi}{4} \times Axial \times \sqrt{\frac{Radial^2 + Circumferential^2}{2}}$$

We screened the area of each anomaly in the billet against the appropriate POD curve (#2 or #3 FBH) to estimate how many anomalies were present prior to the inspection as shown in Figure 4.2. For example, if the POD for a given find size is 50% this implies that a second anomaly of this size existed in the

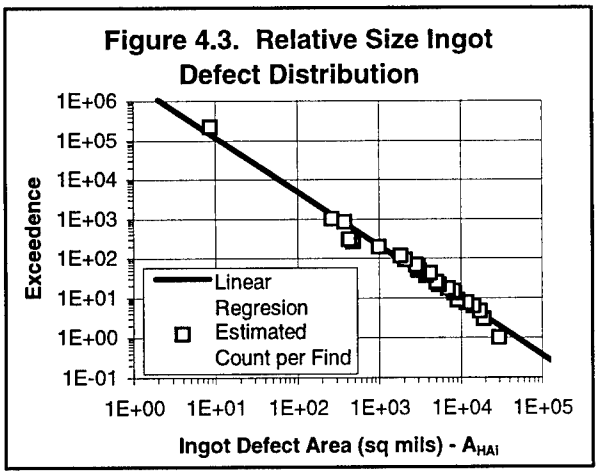
pre-inspected material. The screening process for each find is characterized by the following expression:

$$\#Anomalies_{A_{HA_i}} = {}^{1}\!/\!_{POD_{A_{HA_i}}}$$



With the pre-inspection count for each billet and bar find estimated, we calculated the ingot circular cross sectional anomaly area, assuming constant volume as described by the following expression:

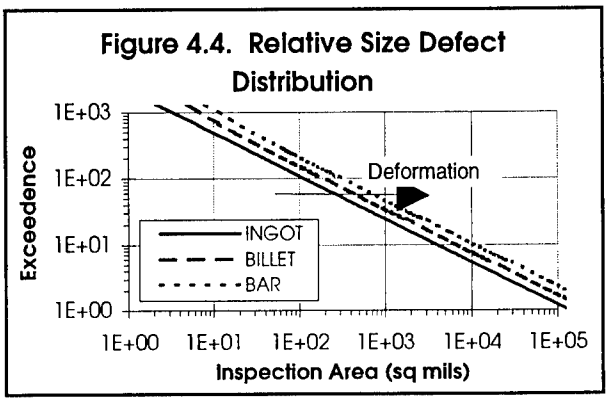
$$A_{HA_i} = \frac{\Pi}{4}(Axial \times Radial \times Circumferential)^{2/3}$$



We combined the total number of billet and bar anomalies and analyzed the data to determine an expression that best fit the data. A linear regression of the log-log data shown in Figure 4.3 yielded the best fit. The following expression defined the baseline ingot distribution shape.

$$\log(ExceedenceCount) = intercept + slope \times \log(A_{HA_i})$$

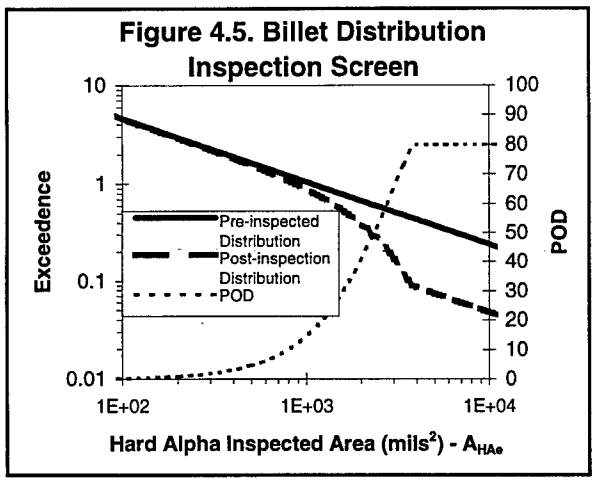
Step 2 - Conversion of ingot to billet/bar distributions. Once we established the ingot relative size distribution, we applied the deformation model to transform the ingot distribution into billet and bar distributions as shown in Figure 4.4. We used the average ingot, billet, and bar diameters from the complete set of two dimensional JETQC finds to accomplish this result.



Step 3 - Estimation of inspection finds and post inspected billet distribution. We estimated the number of hard alpha finds from billet and bar inspections by screening the above billet and bar distributions with the appropriate ultrasonic inspection POD curve (#3 FBH and #2 FBH for billet and bar respectively) as shown in Figure 4.5. We conducted the screening process through numerical integration of the pre-inspected distributions with the appropriate POD curves per the following expressions:

$$\text{Re}\,mainingHA = \sum (TotalHA_i - TotalHA_{i+1}) \times \left[1 - POD\left(\frac{x_i + x_{i+1}}{2}\right)\right]$$

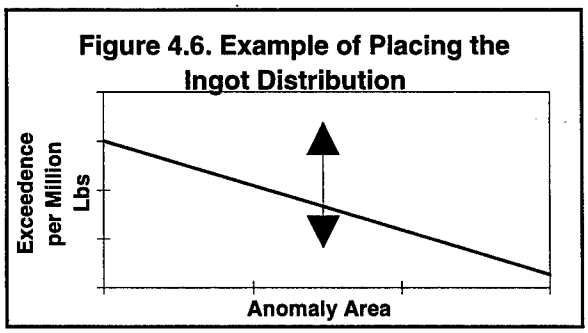
$$FoundHA = \sum (TotalHA_i - TotalHA_{i+1}) \times POD\left(\frac{x_i + x_{i+1}}{2}\right)$$



We compared the estimated find rates to find rates reported by the JETQC.

Bar = 1.0 finds/million pounds
Billet = 0.6 finds/million pounds

Step 4 - Determining the position of the distribution. The sub-team determined the final position of the baseline distribution using an iterative process. We adjusted the ingot distribution hard alpha frequency (shifted up or down on the exceedence axis as shown in Figure 4.6) and repeated steps 2



and 3 until we achieved a match with the JETQC find rate data. By forcing a match to the JETQC frequency data, we essentially transformed the relative size distribution into an exceedence distribution per unit volume.

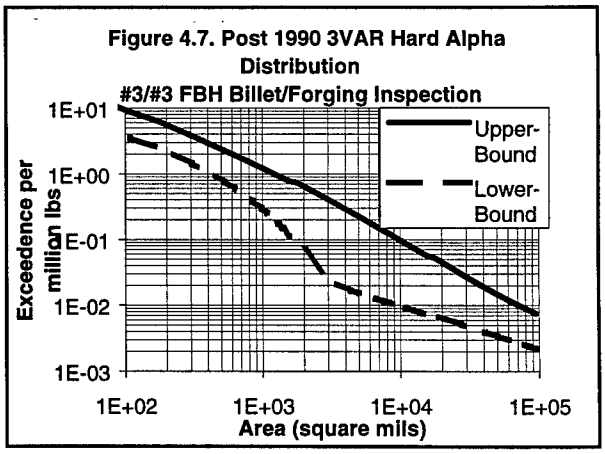
After several iterations of this process, it became apparent that we could not achieve a simultaneous match to the JETQC billet and bar finds, and we had a problem with the model. We decided to investigate the effects of potential variation in the POD curves. While the problem could have been caused by several other variables, we believed it was appropriate to explore the effects of variation in the POD. We made our decision based on our knowledge of the limited amount of data available to estimate the POD curves, therefore, causing uncertainty in these estimates. Future plans, as discussed in section 8.0, include the evaluation of how other variables effect the solution.

Our investigation included the variation in the POD curve mean and standard deviation, and a cap on the maximum achievable POD. [We explored the cap to assess the possibility that larger anomaly sizes saturate the ultrasonic inspection beam, thus after a certain size the POD would not increase]. The billet #3 FBH and bar #2 FBH curves were modified on a consistent basis. These studies resulted in a range of possible anomaly distributions which all "fit" the analytical model.

Step 5 - Checks against other independent data. In all cases, our estimated number of finds at the sonic shape was less than 10% of the billet finds, meeting the sonic find check. In addition, the distributions we derived by using the cap POD curves coincidentally displayed the characteristics of the underlying hard alpha distribution not detected by ultrasonic inspection. This observation influenced the industry committee's final selection of the distribution, as discussed in the next section.

4.3 Field Experience Calibration

Recognizing the limitations of the process for determining the distribution, our sub-team recommended to the industry team that we use each industry committee member's titanium rotor event rate experience to select the final shape and position of the



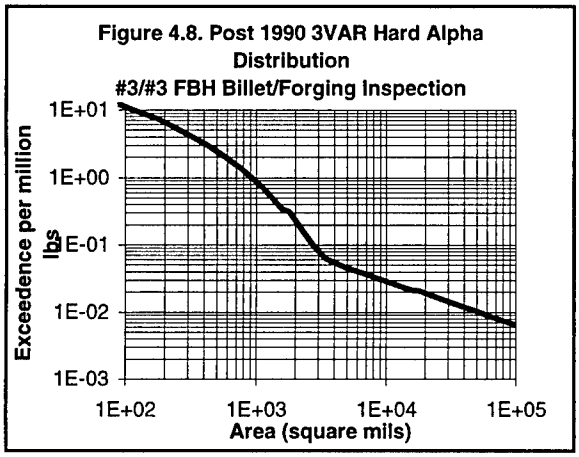
distribution. The industry committee adopted our recommendation. From the range of possible solutions, we determined a best estimate of an upper-bound and lower-bound distribution as shown in Figure 4.7.

Since the parts with field experience (to be used for correlation) were manufactured prior to 1990,

we created upper and lower bound distributions representative of the manufacturing processes for that hardware. We generated a family of upper-bound and lower-bound curves, which reflected typical ultrasonic inspection levels that were generally performed during this period. Also, we adjusted the frequency values to reflect the melting practices of the period, including double VAR, triple VAR, etc., based on limited industry data.

We provided this family of curves to the industry committee member companies so that they could perform probabilistic assessments and compare estimated number of events to their specific actual field experience. Each company then noted which curve, upper-bound or lower-bound, best represented its experience and reported how to adjust the exceedence axis (or hard alpha frequency) of the curves to achieve correlation.

We complied the responses and provided them to the industry committee for review. The industry committee reached a consensus agreement to use the



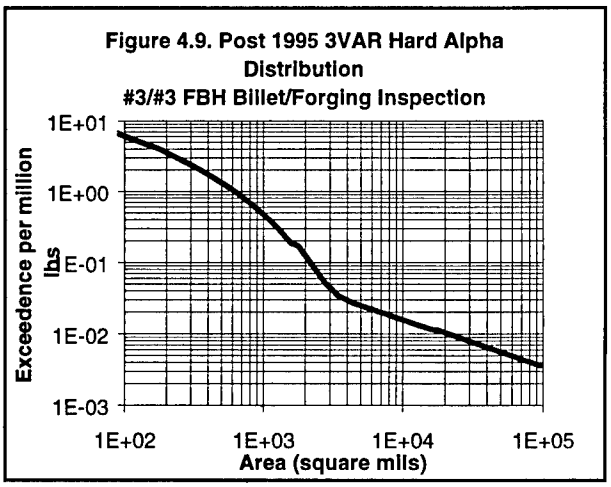
lower-bound curve with a 3 X increase on the exceedence values (or hard alpha frequency) as shown in Figure 4.8. The industry committee concluded that the lower-bound curve shape best represented the effects of in-process inspections and the underlying distribution of hard alpha not detected by ultrasonic inspection.

Because of the manner in which the final distribution was derived, we consider it to be approximately correlated to industry experience.

4.4 Post 1995 Hard Alpha Anomaly Distribution.

A considerable amount of time had elapsed from the initial development of the hard alpha distribution to the time the industry committee planned to submit their damage tolerance proposal to the FAA. Recognizing that the JETQC had collected more data over this time interval, we decided to review their most recent database to determine if a significant change in hard alpha find rates had occurred. Our analysis of the updated database showed an approximate 50% reduction for rotor grade material. We proposed to the industry committee that the 1990 hard alpha be updated to reflect our findings. The industry committee agreed to modify the 1990 distribution prior to submitting the their recommendations to the FAA.

We updated the 1990 distribution by scaling its exceedence values (or hard alpha frequency) down by the ratio of the change in hard alpha rates from 1995 to 1990 (0.54). This modified distribution became the post 1995 hard alpha distribution, as shown in Figure 4.9.



5.0 Design Target Risk (DTR)

With the hard alpha distribution complete, we developed an approach for the industry committee to generate data that they could use to establish component and engine level DTRs for the design of new titanium rotating parts. The approach consisted of analytical studies conducted by each industry committee member that simulated goal reductions in the industry hard alpha event rate. The industry committee arrived at the DTRs by consensus using the results of these analytical reduction studies.

The industry committee's goal was to develop DTR levels that would provide a substantial reduction in the hard alpha related event rate for the new engines in the future fleet relative to the existing commercial fleet characterized by the SAE SP 1270 reporting period. Absolute DTRs were not possible due the uncertainty of the inputs to the probabilistic

assessments, particularly the hard alpha distribution. Therefore, the industry committee concluded that only a relative reduction had validity. Reduction targets of 3, 6, and 15 X were selected to guide the simulation process. The industry committee's intent was to make the maximum reduction consistent with the practical constraints of engine design and commercial engine use.

During the SAE SP 1270 reporting period the commercial transport fleet accumulated 220 million engine flight cycles and experienced 3 titanium melt related events. For the purposes of this simulation the industry committee assumed that the size of the commercial fleet will double in the next 20 years. They selected a six year time period to define the future fleet, consistent with the SAE reporting period, which suggested that the fleet would accumulate 440 million engine flight cycles. The industry committee also assumed that new engines designed to the damage tolerance criteria would account for 1/2 of the engine cycles of the future fleet, or 220 million engine flight cycles.

Each industry committee member independently estimated reductions in event rates by comparing the estimated event rate of two hypothetical fleets, one representing titanium components in operation at the time of the SAE SP 1270 report period (existing fleet) and the other made up of new parts designed to the proposed damage tolerance criteria (future fleet). The hypothetical fleets were based on each member's own components, essentially assuming that the commercial fleet was made up of 100% of their engines

Each industry committee member computed the number of engine components in its hypothetical commercial fleets based on its cyclic mix of engines, number of titanium stages in each engine, and the individual component life limits, so that the total number of engine cycles was 250 million (The industry committee agreed to use 250 million engine flight cycles to simplify the calculations). The following tables provide an example of how the industry committee members determined the engine cyclic mix and number of components to populate their hypothetical fleets.

Example - Engine Cyclic Mix

Engine	Cyclic Mix	Engine Cycles
ENG - 1	20%	50 E06
ENG -2	80%	200 E06
Total	100%	250 E06

Example - Total Number of Components In the Fleet

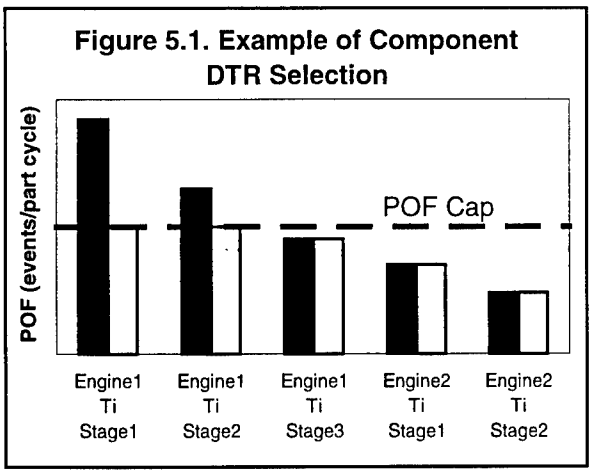
Engine	Titanium Stage	Life Limit Cycles	Engine Cycles	Calculated # of Components
ENG - 1	1	20000	50 E06	2500
	2	20000	50 E06	2500
	3	10000	50 E06	5000
ENG - 2	1	20000	200 E06	10000
	2	10000	200 E06	20000
			Total Fleet	40000

Once the industry committee members defined the mix and number of components in their hypothetical fleets, they selected the appropriate anomaly distribution and estimated the probability of fracture (POF) for each component in the hypothetical existing fleet. Field inspections were included as applicable. The committee members classified each titanium component by material melt process, time period, and level of in-process inspection using categories established during the hard alpha distribution development as discussed in section 4.3. The estimated number of events (ENE) was then calculated using the following expression:

$$ENE = \sum_{j=1}^{E} \sum_{i=1}^{n} \left(POF_i * N_i * Limit_i \right)_j$$

Where POF is the component probability of fracture (events/part cycle), E is the number of engines, j is an individual engine, n is the number of titanium stages per engine, N is the total number of components in the fleet for a given stage, *Limit* is the component service life limit. This ENE calculation provided a baseline number of events for the existing fleet that was used as a bench mark to calculate the potential reductions for the future fleet.

Next each industry committee member changed the material for each part to the 1990 vintage and recalculated the event rate to reflect the improvements in material processing. If the baseline to 1990 material event rate reduction was less than the target value, each industry committee member determined a maximum component POF such that the target reduction was achieved. The maximum component POF was established by replacing the higher risk parts with lower risk parts until the target was met, essentially assuming redesign, as shown in Figure 5.1.



Each industry committee took the component DTR as the maximum component POF allowed in order to meet the event rate reduction goal. They then computed the POF for each engine by summing the individual component POF values for an engine using the capped values from the component DTR exercise. Each industry committee member took the maximum engine POF as the engine level DTR.

A member of our sub-team assembled all of the results from each industry committee member and presented them to the industry committee for review. The entire industry committee evaluated the combined results and agreed to the following values for engine and component level DTRs.

Level	DTR (Events/Part Cycle)
Engine	5.0 E-09
Component	1.0 E-09

The estimated event reduction based on the above values was different for each individual company, as a function of its particular mix of component characteristics (vintage of material, component stress levels, number of engines, etc.). The range of reduction for the industry was approximately 3 to 10 X. The industry committee gave greater weight to results from engine companies with more component experience during the 1984 through 1989 time period. For those engine manufacturers the reduction could be as high as 8 to 10 X.

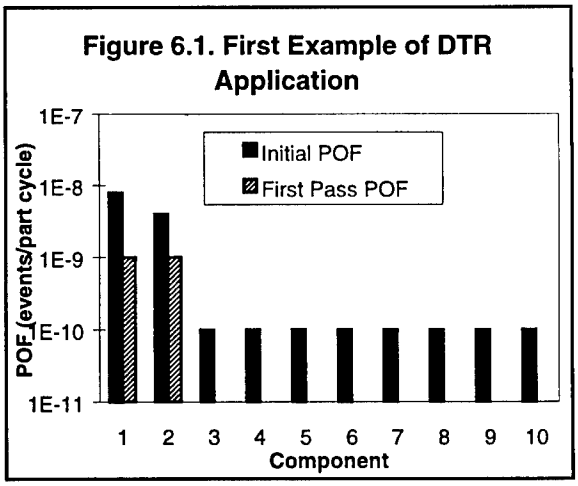
6.0 Customization and/or Future Modifications

Since the titanium hard alpha distribution is only "roughly" correlated to industry experience, and the industry committee based the DTR values on studies using the hard alpha distribution, these DTRs are not "absolute" values. In addition, this integrated approach of developing the DTRs from analytical studies using the hard alpha distribution suggests that the DTRs and hard alpha distribution are highly interdependent. Therefore, the industry committee recommends that any company specific anomaly distributions be developed using a methodology similar to that described in this paper. Failure to do so may result in component estimated event rate reductions inconsistent with those previously stated.

7.0 DTR Application and Projected Impact

As noted in the introduction, the industry committee has proposed fracture mechanics based probabilistic assessments to evaluate the damage tolerance capability of future titanium rotating component designs. Action to reduce the relative risk of a future rotor design should be based on whether or not the design satisfies the component and engine level DTRs. The role of the two DTRs will be a function of the component relative risk profile for the engine. The engine DTR will typically control the overall relative risk, while the component DTR prevents concentration of relative risk into one single component.

We considered two examples to illustrate the application of the DTRs. The first is a hypothetical engine with titanium components that have a high/low relative risk profile, and the second is an engine with a uniform component relative risk (or POF) profile.

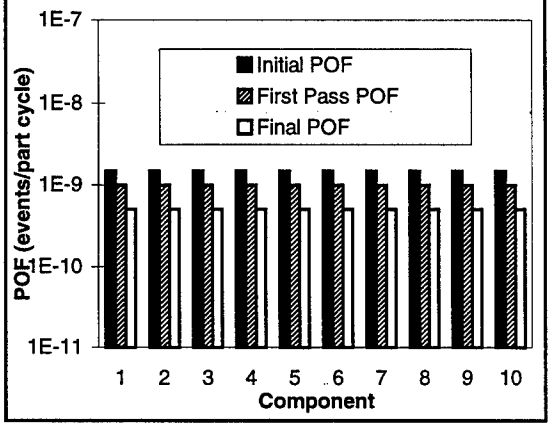


Probabilistic assessment results for the first example, are shown as the black bars in Figure 6.1. The POF for components 1 and 2 are higher than the rest of the parts, and exceed the component and engine DTRs of 1 E-09 (events/cycle) and 5E-09 (events/cycle) respectively. Since the DTRs are exceeded, redesign or a field plan should be considered.

Quantitative trade studies can be performed to determine the influence of key variables such as potential inspection methods, inspection frequency, stress levels, material selection, and life limits. Variations of these design and/or field management actions can be evaluated to achieve the DTRs. Assuming these evaluations yield the results denoted by the shaded bars in Figure 6.1 for components 1 and 2, the engine POF would be 2.8 E-09 (events/part cycle), which is less than the 5.0 E-09 (events/part cycle) DTR. Thus, both the component and engine DTRs would be satisfied.

In the second example the initial probabilistic assessment results, again shown as the black bars in Figure 6.2, depict a uniform component POF profile.

Figure 6.2. Second Example of DTR Application



In contrast to the first example, all of the components are at the same POF and exceed the component DTR. Like the first example, the engine DTR has not been achieved. In this case, redesign or a field action plan should be considered for all of the components. Assuming the shaded bars in Figure 6.2 denote the results of a first pass at such actions, all of the parts meet the component DTR. However, the engine POF is still grater than the engine DTR [(10 E-09 (event/part cycle) vs. 5 E-09 (events/part cycle)] and further action should be considered. Assuming the open bars in Figure 6.2 denote the results of additional action, the engine POF drops to 5 E-09 (events/part cycle). Thus both the component and engine DTRs are satisfied.

Reference 5 contains detailed examples of the fracture mechanics-based probabilistic assessment process, the accompanying methodology, and standardized input data.

8.0 Future Work

Realizing the importance of this effort, the FAA awarded a grant to Southwest Research Institute which, teamed with four members of industry (AlliedSignal, Allison, GE Aircraft Engines, and Pratt & Whitney), is working to further develop the hard alpha anomaly distribution, as well as completion of several other related tasks. In addition the Engine Titanium Consortium (ETC), also sponsored by the FAA, is working to improve the quality of the POD estimates used in the development of the hard alpha distribution and the damage tolerance probabilistic assessments. A future update to the hard alpha distribution is planned to be completed in the next two to three years.

9.0 Acknowledgments

The authors acknowledge the significant amount of time and resources that each member company of the AIA Rotor Integrity Sub-Committee put into development of the hard alpha anomaly distribution and the DTRs. Industry members of the AIA Rotor Integrity Sub-Committee are: AlliedSignal, Allison, GE Aircraft Engines, MTU, Pratt & Whitney, Pratt & Whitney of Canada, Rolls Royce, SNECMA, Sundstrand, and Williams International.

In addition, the authors acknowledge the excellent team work, cooperation, and technical creativity of the individual sub-team members. The sub-team membership consisted of Dr. Joseph Casey (GEAE), Barry Kalb (GEAE), Nichola Little (GEAE), Mike McNelly (Allison), Gary Peters (P&W), Nick Provenzano (Allison), and Jon Tschopp (GEAE).

10.0 References

1. SAE/FAA Committee On Uncontained Turbine Rotor Events, Report No. AIR 1537, Data Period 1962-1975.
2. SAE/FAA Committee On Uncontained Turbine Rotor Events, Report No. AIR 4003, Data Period 1976-1983.
3. To be published SAE Special Report On Uncontained Turbine Rotor Events, Report No. SP 1270, Data Period 1984-1989.
4. Hard alpha find data provided by the Jet Engine Quality Committee (JETQC) for the 1990 through 1995 time period.
5. Industry Recommendations Regarding an Enhanced Life Management Process for Titanium Rotating Parts, prepared by the AIA Rotor Integrity Sub-Committee, submitted by the AIA to the FAA, November 27, 1996.

APPENDIX B—EXPERIMENTAL CHARACTERIZATION OF THE CONSTITUTIVE PROPERTIES OF HARD ALPHA

B.1 MATERIAL.

Synthetic hard alpha specimens for the constitutive property testing were fabricated at General Electric Corporate Research and Development (GE CRD) Hard alpha ingots were prepared by melting titanium metal sponge and titanium nitride (TiN) powder in a nonconsumable arc-melter. Each of the ingots was melted three times. The ingot was turned over and weighted between each melt. Subsequently, the arc-melted hard alpha alloy ingots were hot isostatically pressed (HIPed) at 1200°C under 30 ksi pressure for 4 hours to close any solidification porosity. The HIPed ingot was then cut by electrodischarge machining (EDM) to yield two thin diametrical slices (< 0.1 inch thick, each). One slice was metallographically polished and examined to assure microstructural homogeneity. The other slice was cut (for example, with a diamond saw) into small pieces for chemical analysis. Oxygen analysis was carried out via a fusion technique (LECO Corporation), while nitrogen analysis was performed via acid dissolution and titration. Analysis of the nitrogen content for the synthetic hard alpha is shown compared to the target values in table B-1.

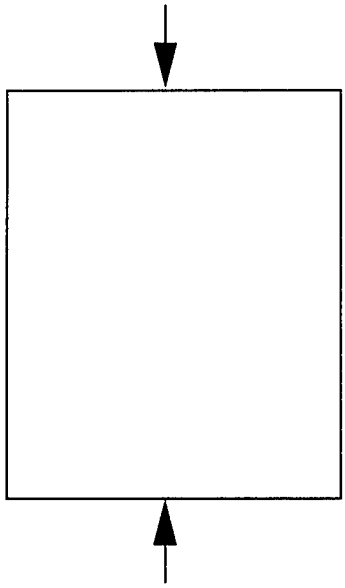
TABLE B-1. NITROGEN CONTENTS OF SYNTHETIC HARD ALPHA SPECIMENS

Specimen	Target N_2 Content	Measured N_2 Content
2N	2%	2%
4N	4%	4%
6N	6%	5.5%
9N	9%	9.4%
12N	12%	11.6%

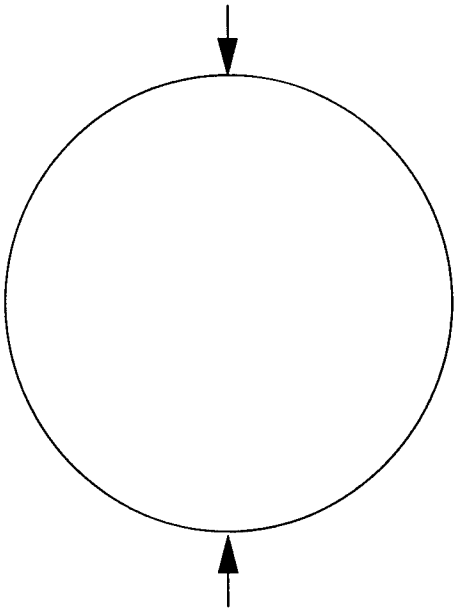
Test specimens were fabricated from the HIPed ingots by EDM. The compression test specimens were 0.25-inch-diameter cylinders, 0.5 inch in height. The indirect tension specimens were thin disks 0.375 inch in diameter and 0.125 inch in thickness. Both the indentation and plane strain compression test specimens were 0.25-inch cubes. After EDM, the flat surfaces of the test specimens were ground. They were then etched in a solution of 60 vol.% distilled water, 30 vol.% nitric acid, 10% hydrofluoric acid to clean surfaces and rinsed in propanol. All the specimens were tested in the as-received condition at Southwest Research Institute (SwRI) after inspection for surface cracks.

B.2 EXPERIMENTAL PROCEDURES.

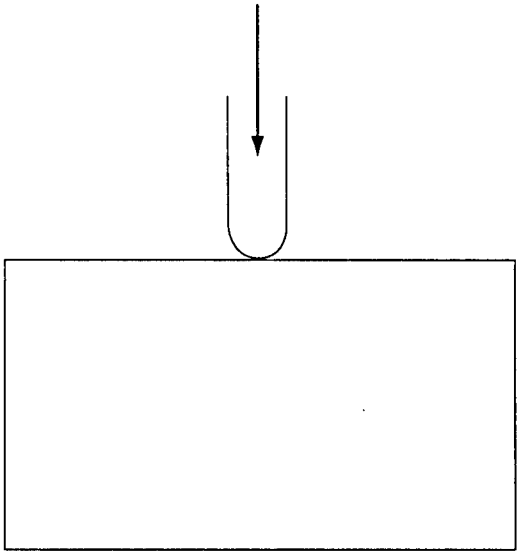
The constitutive behavior of hard alpha was characterized as a function of temperature, strain rate, nitrogen content, and stress state. The stress state was varied by employing different testing techniques and specimen geometries. As summarized in figure B-1, the constitutive tests include (a) uniaxial compression, (b) indirect tension (Brazilian), (c) indentation, and (d) plane strain compression tests. Indirect tension tests were preferred over conventional tensile tests because it is extremely difficult to fabricate tensile specimens of hard alpha due to its brittleness. The procedures of the various constitutive tests are described below.



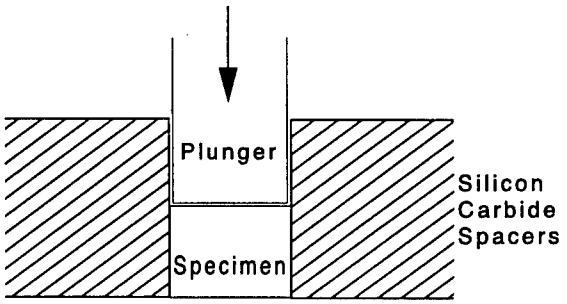
(a) Uniaxial compression of a cylindrical bar specimen



(b) Indirect tension by compressing a thin disk on edge



(c) Indentation of a cube specimen by an indentor with a semispherical tip



(d) Plane strain compression of a cube specimen

FIGURE B-1. TESTING TECHNIQUES USED TO CHARACTERIZE THE STRESS-STRAIN BEHAVIOR OF HARD ALPHA UNDER VARIOUS STRESS STATES

B.2.1 COMPRESSION TESTS.

Compression tests were conducted on cylindrical bars 0.25 inch in diameter and 0.5 inch in height. Testing was conducted in a servo-hydraulic testing machine equipped with induction heating unit. To eliminate friction, boron nitride, a spray lubricant, was applied to the interface

between the silicon carbide loading blocks and the test specimen. The test temperatures were 1700°, 1750°, and 1800°F while the strain rates were 0.01 and 1 s^{-1}. The nominal nitrogen contents of the test specimens were 2, 4, 6, 9, and 12 percent nitrogen by weight, as shown in table B-1. All tests except the 2% N specimens were conducted under displacement-controlled conditions because of little or no plastic flow in these materials. The 2% N specimens exhibited substantial plastic deformation, so testing was conducted under computer-controlled constant strain rate conditions. Load-displacement data were measured using a computer data acquisition system and subsequently converted into stress-strain data.

B.2.2 INDIRECT TENSION TESTS.

The indirect tension (Brazilian) tests were conducted by compressing circular thin disks on edge using the same experimental setup described earlier for the compression tests. The disk specimens were 0.125 inch in thickness and 0.375 inch in diameter. Small cracks were detected in some of the disk specimens prior to testing and they were not used. Testing was performed on crack-free specimens of several nitrogen contents at 1750°F under a strain rate of 1 s^{-1}. One test was performed on a specimen (B6N-A) with a small crack oriented perpendicular to the compression axis. This small crack was closed during testing and did not affect the test result. For comparison, one test was also performed at a strain rate of 0.01 s^{-1}. Load-displacement curves were measured up to fracture, which occurred at the center of the specimens.

B.2.3 INDENTATION TESTS.

Indentation tests were conducted on 0.25-inch cube specimens using a silicon carbide indentor and the same experimental setup used in the compression tests. The indentor was semispherical with a 0.06-inch radius. Indentation tests were performed on specimens with five different nitrogen contents (2, 4, 6, 9, and 12 wt. % N). All tests were conducted at 1750°C under displacement controlled conditions that corresponded to average strain rates of 1 and 0.01 s^{-1}. Load was measured as a function of indentation depth and the test was terminated when a large load drop occurred or after the indentation depth exceeded a distance equal to the radius (0.06 inch) of the indentor. For 2% N specimens, the indentor penetrated completely into the hard alpha without causing cracking or fracture to the cube specimen. For higher nitrogen contents (> 4% N), large cracks formed at the center of the specimen causing it to fracture into several small pieces.

B.2.4 PLANE STRAIN COMPRESSION TESTS.

Plane strain compression tests were conducted by compressing a flat plunger onto a 1/4″ cube specimen in a die with a rectangular channel that prevented expansion of the specimen in the width direction. Schematics of the apparatus for the plane strain compression tests are presented in figure B-2. Testing was performed at ambient temperature under constant displacement rates. The compliance of the servo-hydraulic test system was first obtained for the strain rates of interest, which were 0.01 s^{-1} and 1 s^{-1}. Plane strain compression tests were then performed and load-displacement data were measured. After testing, the compliance curve was then subtracted from the measured load-displacement data to obtain the actual load–displacement response of the test specimen. Plane strain compression tests were performed for 2N, 4N, 6N, and 9N materials at 1 s^{-1} and for 2N, 4N, 6N, 9N, and 12N at 0.01 s^{-1}. All tests were conducted beyond the

maximum load where the specimen fractured and straining continued until the applied load dropped to almost zero. Postfracture straining was necessary to characterize the damage-induced softening response of the hard alpha under constrained conditions.

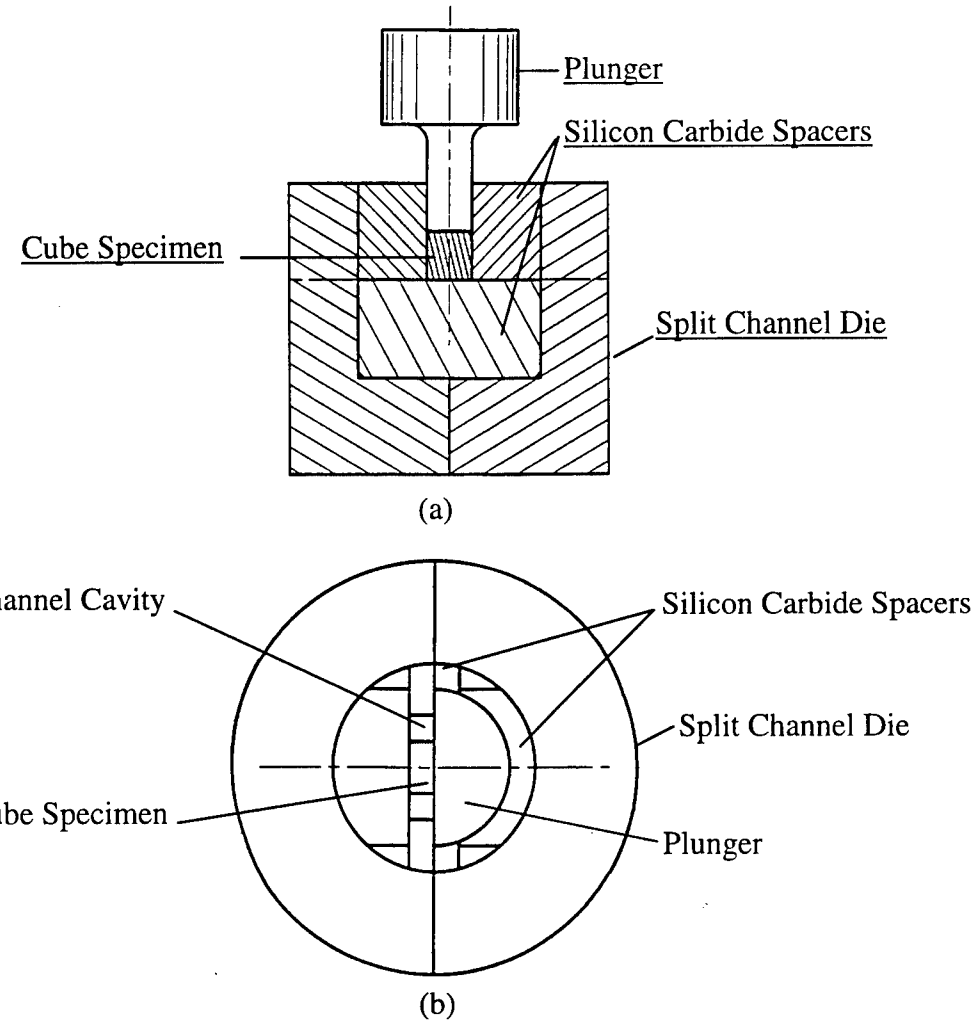


FIGURE B-2. SCHEMATICS OF THE PLANE STRAIN COMPRESSION TEST APPARATUS ((a) side view and (b) top view)

B.3 EXPERIMENTAL RESULTS.

B.3.1 COMPRESSION TESTS.

Table B-2 summarizes the results of the compression tests. The table includes test temperature, strain rate, yield stress, fracture stress, and the mode of failure. The initial slope of the stress-strain curves for compression tests was used to determine an approximate Young's modulus for hard alpha. These results, summarized in table B-3, show that the Young's modulus of hard alpha increases with increasing nitrogen content. In uniaxial compression, hard alpha Ti was ductile at 2 wt.% N, but fracture intervened during plastic deformation at 4 wt.% N. The measured flow stress and ultimate fracture strength were consistent with GE data for 3.4 wt.% N [B-1], which is also shown in table B-2. Hard alpha Ti failed by fracture without appreciable plastic deformation for nitrogen contents at or greater than 6 wt.%. The stress-strain curves of hard alpha Ti for compression at 1750°F under a strain rate of 1 s^{-1} are presented in figure B-3, and those for a strain rate of 0.01 s^{-1} are shown in figure B-4. Hard alpha Ti with 12 wt.% N failed by fracture under compression at 1700°, 1750°, and 1800°F and a strain rate of 1 s^{-1}. These results are presented in figure B-5.

B.3.2 INDIRECT TENSION (BRAZILIAN) TESTS.

Five Brazilian specimens were tested by edge compression of thin disks. Two of these specimens contained 2 wt.% N, which were very ductile and did not fail by fracture. The indirect tension test performed on this alloy composition was therefore invalid. The remaining three crack-free Brazilian specimens were tested and they failed by elastic fracture, yielding valid values of the fracture stress. One specimen that contained a very small crack near the edge was also tested with the known crack aligned normal to the applied compressive stress. A summary of the Brazilian tests is presented in table B-2. Tensile test results from GE CRD for hard alpha with 2.5 wt.% N [B-1] are also included in table B-2.

The load displacement curves for the indirect tension tests of hard alpha Ti are shown in figure B-6. The result for 2 wt.% N was invalid because of excessive plasticity. For specimens that failed by brittle fracture, the elastic stress analysis [B-2] was used to analyze the data. According to this analysis, the tensile fracture stress at the center of a thin disk under edge compression is 1/3 of the peak compression stress applied at the edge. Using this method, the peak load at fracture was used to calculate the tensile fracture stress at the center of the disk and the results are summarized in table B-2. In addition, the tensile fracture strength results are compared against those in compression in figure B-7, which shows that hard alpha Ti fractured at substantially lower stress in tension than in compression.

TABLE B-2. A SUMMARY OF YIELD STRESS (σ_y) AND FRACTURE STRESS (σ_f) OF HARD ALPHA Ti TESTED IN COMPRESSION, INDIRECT TENSION, INDENTATION, AND PLANE STRAIN COMPRESSION

Specimen	T, °F	N, wt.%	Strain Rate, sec^{-1}	σ_y, ksi	σ_f, ksi	Type	Comment
2N-A	1750	2	1	30	>43.5	C	Yielding, no fracture
4N-A	1750	2	1	68	70.95	C	Yielding, no fracture
6N-A	1750	5.5	1	—	80.5	C	Fracture, no yielding
9N-A	1750	9.4	1	—	105.1	C	Fracture, no yielding
12N-A	1750	11.6	1	—	95.92	C	Fracture, no yielding
GE (3.4 wt.% N)	1750		1	50.23	62.6	C	Yielding, GE data [B-1]
4N-B	1750	4	0.01	33.4	46.4	C	Yielding/Fracture
9B-B	1750	9.4	0.01	—	100.9	C	Fracture, no yielding
12N-C	1750	11.6	0.01	—	114	C	Fracture, no yielding
12N-D	1700	11.6	1	—	117.8	C	Fracture, no yielding
12N-E	1800	11.6	1	—	88.6	C	Fracture, no yielding
B2N-A	1750	2	1	—	—	B	Yielding, invalid test
B4N-A	1750	4	1	—	5.02	B	Fracture, no yielding
B4N-B	1750	4	0.01	—	4.48	B	Fracture, no yielding
B6N-A	1750	5.5	1	—	5.14	B	Fracture, no yielding
B9N	1750	9.4	1	—	7.12	B	Fracture, no yielding
GE (2.54 wt.% N)	1750		—	6.3	10.4	T	Yielding/Fracture, GE data [B-1]
S2N-1	1750	2	1	67.1	—	I	Yielding
S4N-2	1750	4	1	126.8	126.8	I	Yielding/Fracture
S6N-1	1750	5.5	1	—	155.8*	I	Fracture
S9N-1	1750	9.4	1	—	233.7*	I	Fracture
S12N-1	1750	11.6	1	—	206.6*	I	Fracture
S12N-4	1750	11.6	1	—	217.0*	I	Fracture
S4N-1	1750	4	0.01	69.4	—	I	Yielding/Fracture
S12N-2	1750	11.6	0.01	—	115.5*	I	Fracture
S2N-3	72	2	1	—	—	P	No yielding, no fracture
S2N-4	72	2	1	—	—	P	No yielding, no fracture
S4N-4	72	4	1	—	80.9	P	Fracture, no yielding
S6N-3	72	5.5	1	—	77.1	P	Fracture, no yielding
S9N-3	72	9.4	1	—	123.6	P	Fracture, no yielding
S4N-3	72	4	0.01	—	83.1	P	Fracture, no yielding
S6N-2	72	5.5	0.01	—	85.6	P	Fracture, no yielding
S9N-2	72	9.4	0.01	—	116.7	P	Fracture, no yielding
S12N-5	72	11.6	0.01	—	128.4	P	Fracture, no yielding
S12N-6	72	11.6	0.01	—	116.7	P	Fracture, no yielding

C: Compression Tests T: Tensile Tests P: Plane Strain Compression Tests
B: Brazilian Tests (indirect tension tests) I: Indentation Tests

* Results based on P/2.8

TABLE B-3. YOUNG'S MODULUS OF HARD ALPHA Ti AT 1750°F

Specimen	Nitrogen Content, wt.%	E, psi
2N	2.0	6.0×10^6
4N	4.0	4.1×10^6
6N	5.5	7.4×10^6
9N	9.4	11.9×10^6
12N	11.6	18.1×10^6

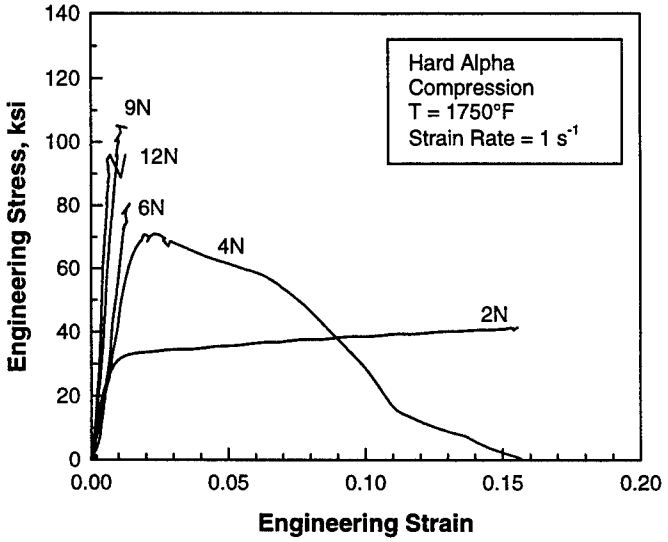


FIGURE B-3. COMPRESSION STRESS-STRAIN CURVE OF HARD ALPHA Ti FOR FIVE DIFFERENT NITROGEN CONTENTS IN WEIGHT PERCENT

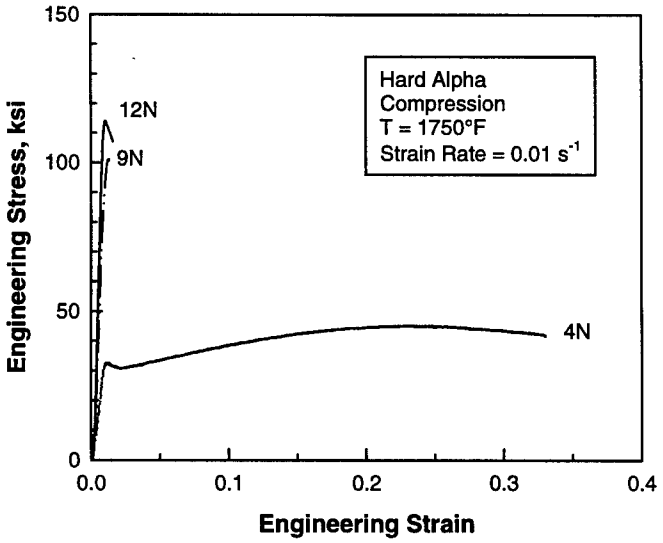


FIGURE B-4. COMPRESSION STRESS-STRAIN CURVE OF HARD ALPHA Ti FOR THREE DIFFERENT NITROGEN CONTENTS IN WEIGHT PERCENT

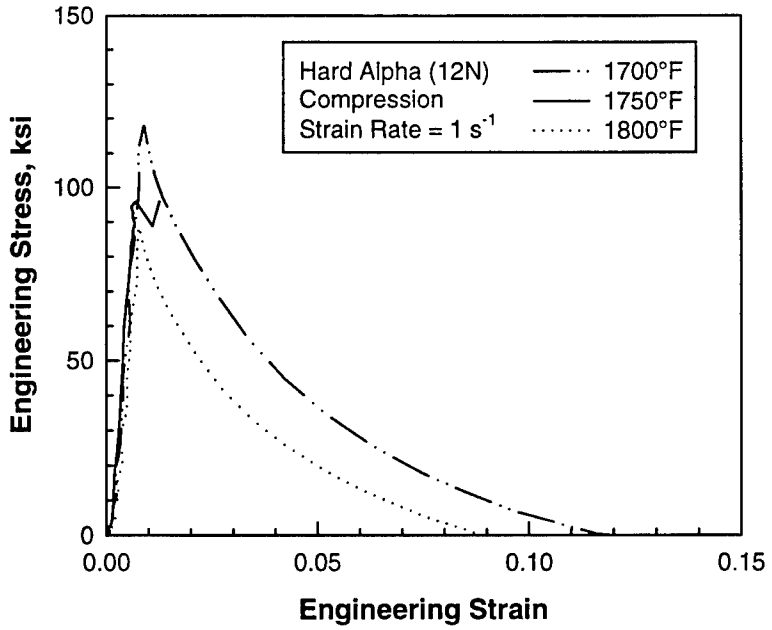


FIGURE B-5. COMPRESSIVE STRESS-STRAIN CURVES OF HARD ALPHA Ti WITH 12 wt.% N FOR THREE DIFFERENT TEST TEMPERATURES

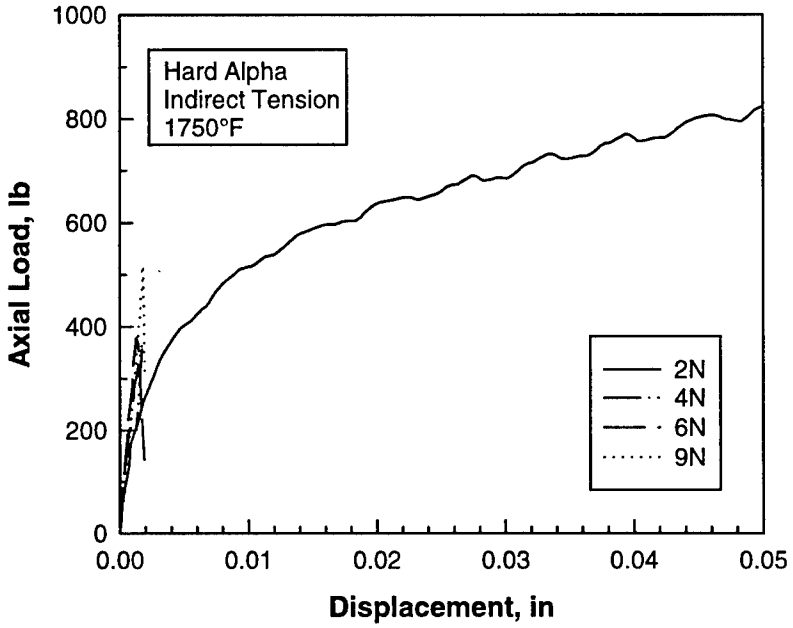


FIGURE B-6. LOAD DISPLACEMENT CURVES OF INDIRECT TENSION TESTS OF HARD ALPHA Ti WITH FOUR DIFFERENT NITROGEN CONTENTS

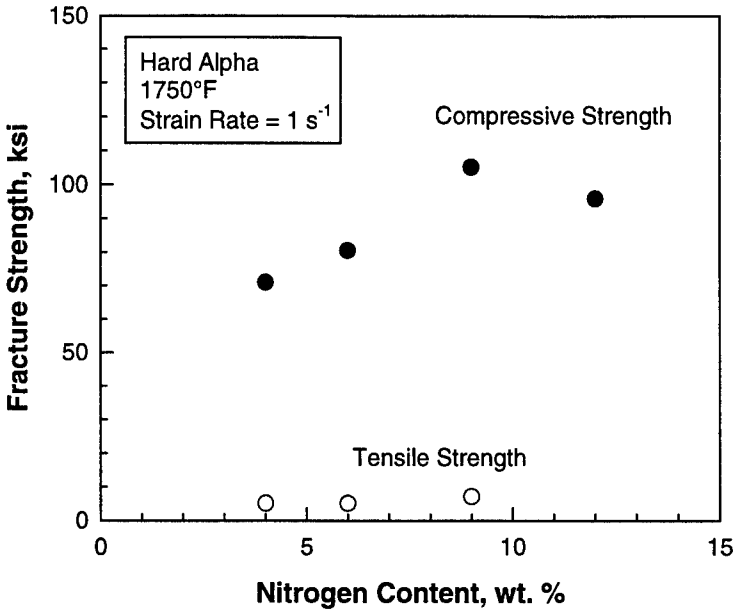


FIGURE B-7. COMPARISON OF FRACTURE STRENGTH VALUES OF HARD ALPHA Ti TESTED IN COMPRESSION AND BY INDIRECT TENSION

B.3.3 INDENTATION TESTS.

Indentation tests of hard alpha Ti were performed as a function of nitrogen content at 1750°F for displacement rates of 0.01 and 1 in./s, which corresponded to approximate, average strain rates of 0.01 and 1 s^{-1}, respectively. One test was also performed at 1800°F for hard alpha Ti with 12 wt.% N. A summary of the indentation tests is presented in table B-2 together with compression, Brazilian, and plane strain compression tests.

Figure B-8 shows a plot of the average pressure versus the average strain for the indentation tests at 1750°F (954°C) under a strain rate of 1 s^{-1}. Hard alpha Ti with 2 wt.% N was ductile and exhibited plastic flow without fracture when tested by indentation. With 4 wt.% N, hard alpha Ti exhibited plastic flow and localized fracture after yielding. For nitrogen contents > 6 wt.%, hard alpha Ti showed fracture with little plastic flow.

The indentation test results were analyzed using a method attributed to Tabor [B-3, B-4]. For a perfectly plastic material, the average pressure, P, for indentation by a spherical indentor under full plasticity conditions is related to the flow stress, Y_n, at a given strain according to reference B-3.

$$Y_n = P/2.8 \tag{B-1}$$

and the corresponding strain is given by references B-3 and B-4

$$\varepsilon = 0.2(d/D) \tag{B-2}$$

where d is the diameter of the indentation and D is the diameter of the indentor. Equations B-1 and B-2 were used to obtain the yield and fracture stresses, and the average true strain and strain rate of hard alpha Ti during indentation, assuming constrained yielding occurred under the indentor during indentation of both low and high nitrogen materials. The diameter of the indentation, d, was approximated by the penetration depth or displacement. These assumptions were justified and supported by the plane strain test results to be discussed in the next section. A summary of the yield and fracture stresses for the indentation tests is presented in table B-2, together with the compression and Brazilian test results. Tensile test results from GE CRD for hard alpha with 2.5 wt. % N [B-1] are also included in table B-2.

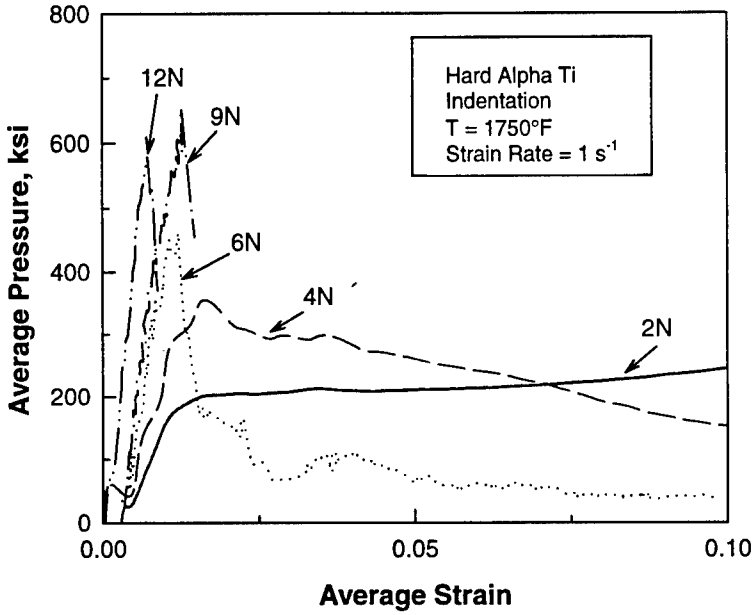


FIGURE B-8. EXPERIMENTAL RESULTS OF AVERAGE PRESSURE VERSUS AVERAGE STRAIN FOR INDENTATION OF HARD ALPHA Ti WITH VARIOUS NITROGEN CONTENTS

B.3.4 PLANE STRAIN COMPRESSION TESTS.

Plane strain compression tests were performed at ambient temperature by compressing the test specimen in the channel die beyond the maximum load to characterize the softening response due to damage and microcracking. Ambient temperature tests were used because the fracture stresses of hard alpha were found to be insensitive to the test temperature. A typical stress-strain curve of the plane strain compression test is presented in figure B-9, which shows the applied stress increases linearly with displacement until a maximum stress is reached. Subsequently, the applied stress decreases almost linearly with increasing displacement. Load drop beyond the peak load was the consequence of the formation of microcracks by plane strain compression.

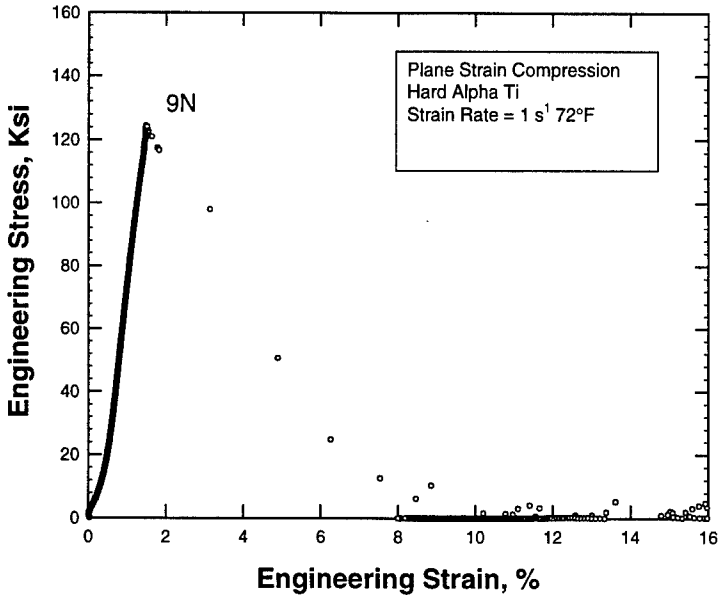
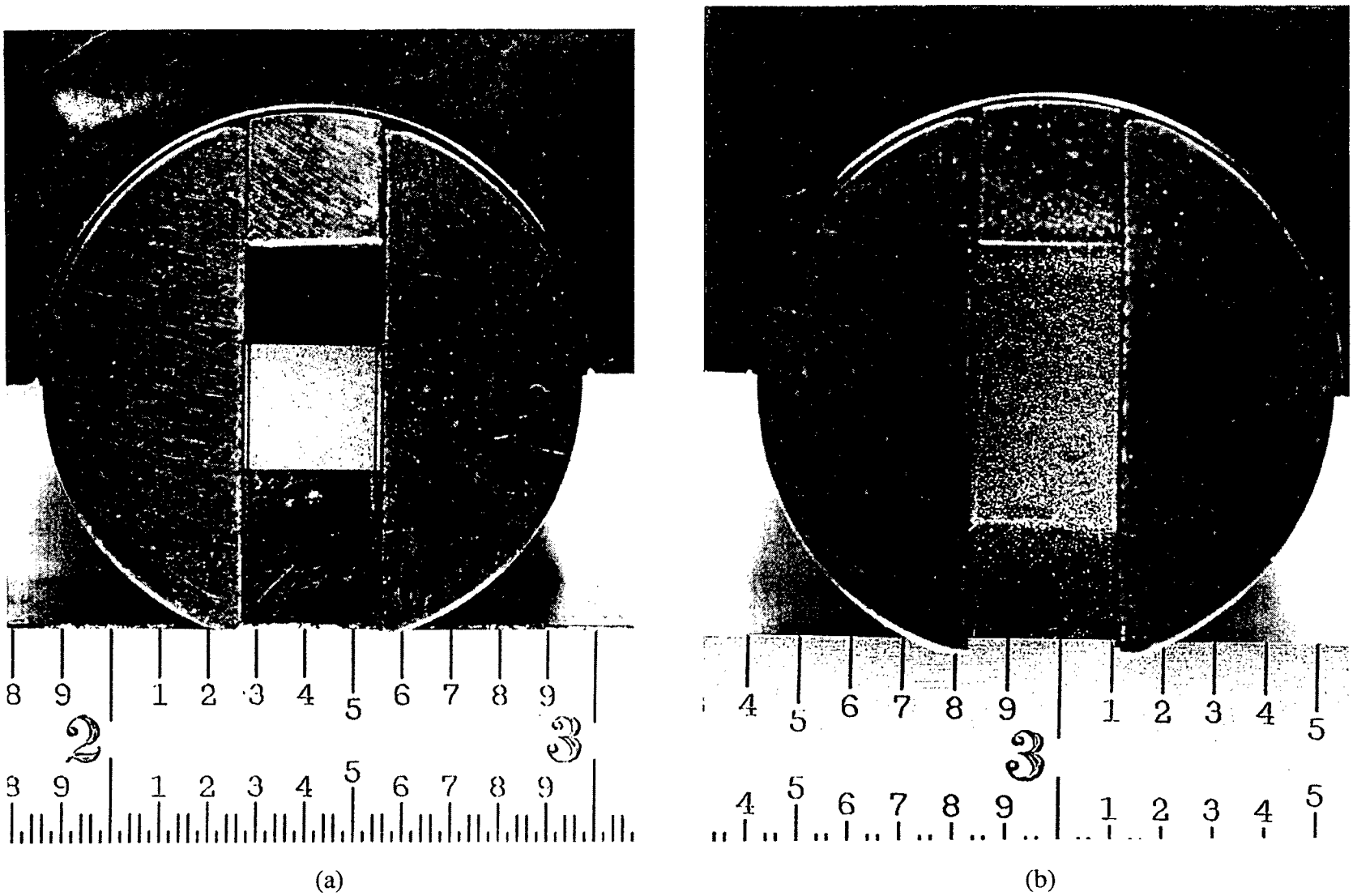


FIGURE B-9. A TYPICAL ENGINEERING STRESS-STRAIN CURVE OF HARD ALPHA Ti OBTAINED BY PLANE STRAIN COMPRESSION AT AMBIENT TEMPERATURE

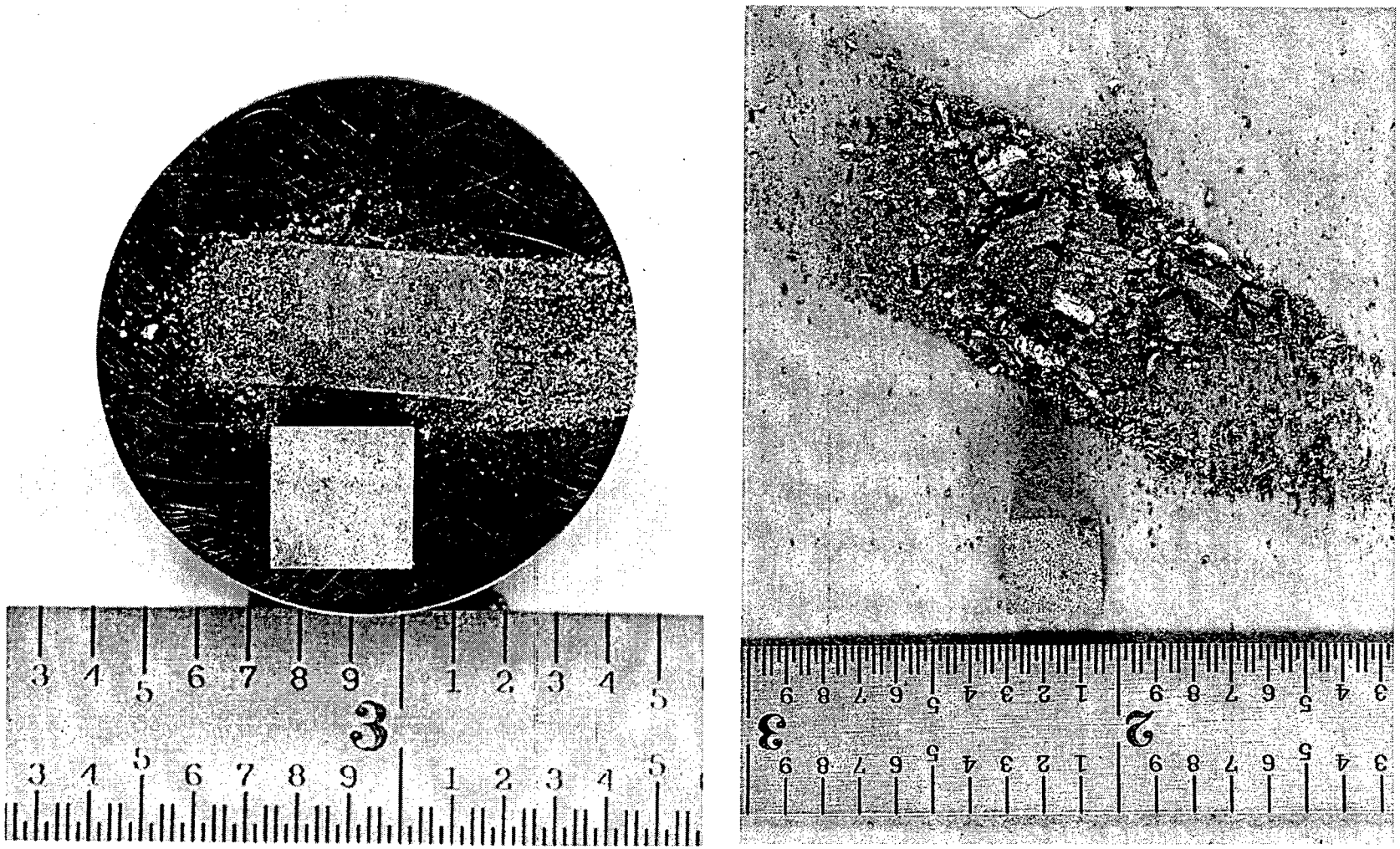
Figure B-10 shows a comparison of the test specimen of 4N before and after plane strain compression. Before testing, the specimen was in the form of a cube of intact material, see figure B-10(a), but it became a rectangular block of compacted powders after testing, see figure B-10(b). Removing the specimen from the test fixture caused some powders to separate from the block for the 4N material, see figure B-11(a). For the 6N, 9N, and 12N materials, the test specimens disintegrated into small particles and fine powders when they were removed from the test fixture, as shown in figure B-11(b) for the 12N material.

Comparisons of the engineering stress-strain curves for hard alpha Ti are shown in figures B-12 and B-13 for strain rates of 0.01 s^{-1} and 1 s^{-1}, respectively. Engineering stress-strain data for the 2N material are not shown in figures B-12 and B-13 because the material did not plastically deform or fracture when loaded to the maximum load capacity of the 10 kips test machine.



(a) (b)

FIGURE B-10. TOP VIEW OF THE PLANE STRAIN SPECIMEN IN THE TEST FIXTURE
((a) before testing and (b) after testing)



(a) (b)

FIGURE B-11. COMPOSITION OF TESTED AND UNTESTED PLANE STRAIN SPECIMENS OF HARD ALPHA Ti FOR TWO NITROGEN CONTENTS ((a) 4% N and (b) 12% N)

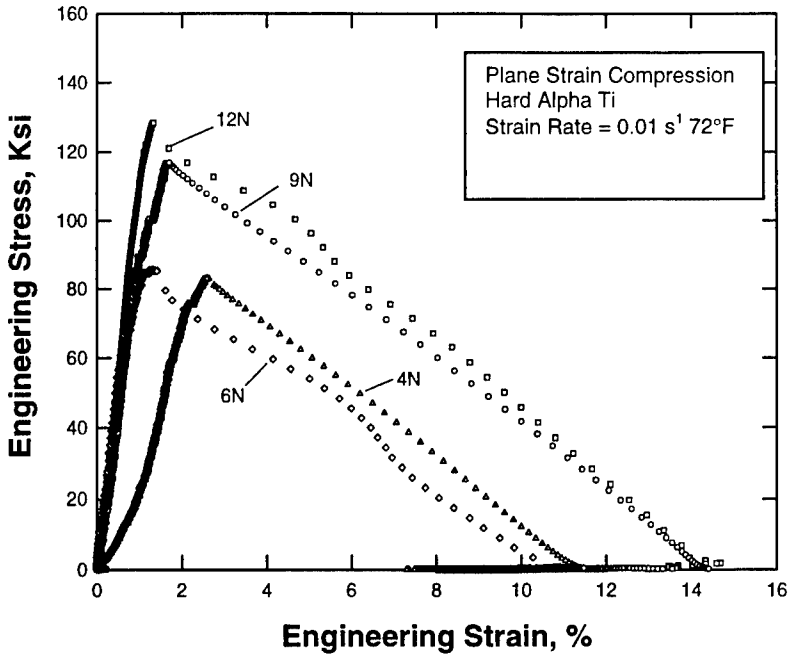


FIGURE B-12. COMPARISON OF ENGINEERING STRESS-STRAIN CURVES OF HARD ALPHA Ti WITH VARIOUS NITROGEN CONTENTS TESTED BY PLANE STRAIN COMPRESSION AT A STRAIN RATE OF 0.01 s^{-1}

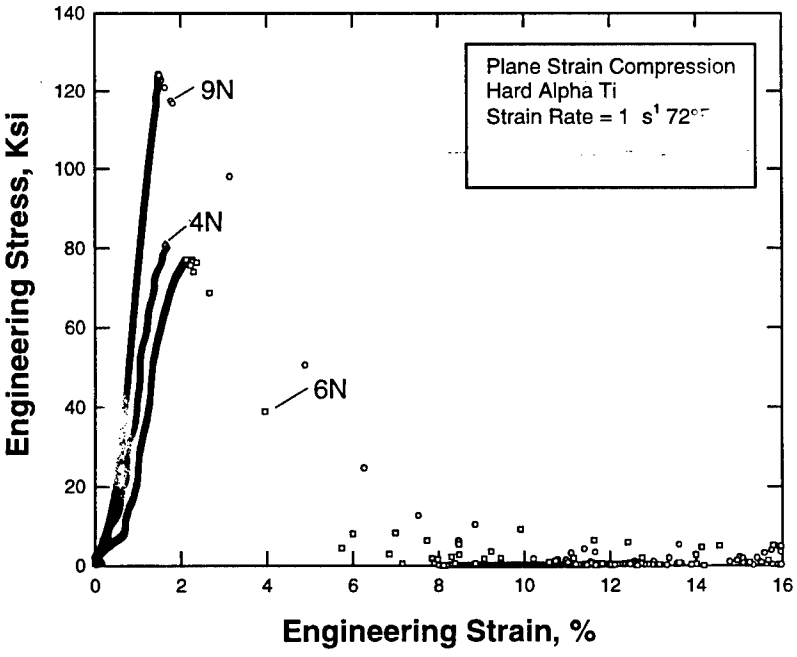


FIGURE B-13. COMPARISON OF ENGINEERING STRESS-STRAIN CURVES OF HARD ALPHA Ti WITH VARIOUS NITROGEN CONTENTS TESTED BY PLANE STRAIN COMPRESSION AT A STRAIN RATE OF 1 s^{-1}

B.4 DISCUSSION.

B.4.1 DEFORMATION AND FRACTURE CHARACTERISTICS.

The deformation and fracture characteristics of hard alpha test specimens at 1750°F (954°C) or 1800°F (900°C) are summarized in figures B-14, B-15, and B-16 for compression, Brazilian, and indentation test specimens, respectively. In all three cases, hard alpha with 2 wt.% N was ductile and deformed without fracture. Hard alpha Ti with 4 wt.% N exhibited plastic flow followed by fracture, while hard alpha Ti with 6 wt.% N or greater fractured into small fragments without showing evidence of plastic flow.

A close-up view of the compression specimens with 2 wt.% N (2N) and 4 wt.% N (4N) is presented in figure B-17, which shows the absence of apparent cracks or voids in the 2N specimen and the presence of voids and cracks in the 4N material. In the Brazilian tests, the cylindrical disk of the 2 wt.% N material (B2N) was flattened into a more rectangular shape without causing cracking. Cracks formed in the center of the flattened disk in the 4 wt. % N material (B4N), figure B-18.

Indentation of the hard alpha Ti with 4 wt.% N showed strain softening after yielding at both 0.01 and 1 s^{-1} strain rates, see figure B-18. Examination of the deformed and fractured specimens indicated the presence of several large cracks that fragmented the test specimens. In addition, many microcracks were also observed at the bottom of the indentation, suggesting that the softening effect was probably the consequence of damage or microcracking associated with plastic flow under the indentor. The fragmented specimens and the microcracks at the bottom of the indent are shown in figures B-19 and B-20 for strain rates of 0.01 and 1 s^{-1}, respectively.

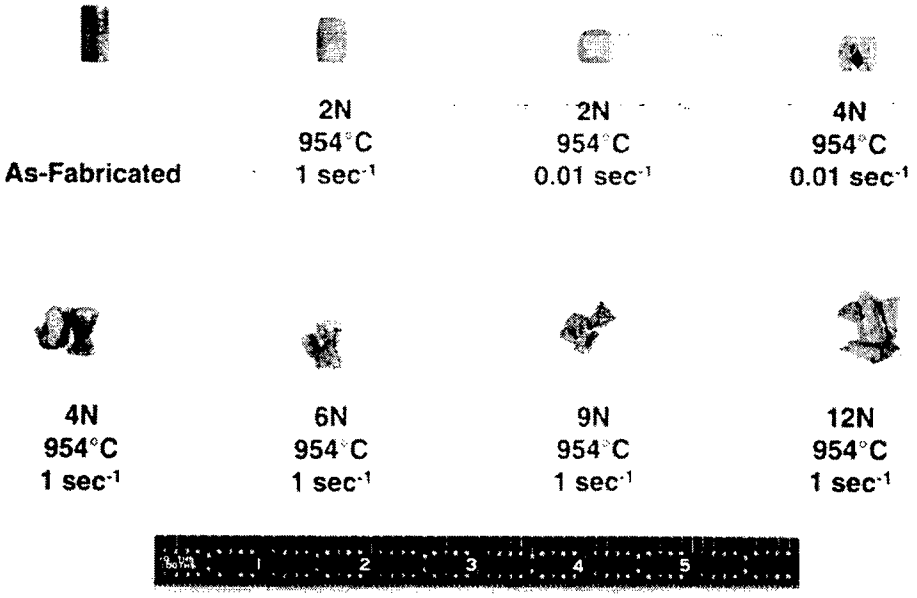


FIGURE B-14. GEOMETRIES OF DEFORMED AND FRACTURED COMPRESSION HARD ALPHA SPECIMENS COMPARED TO THE AS-FABRICATED CONDITION

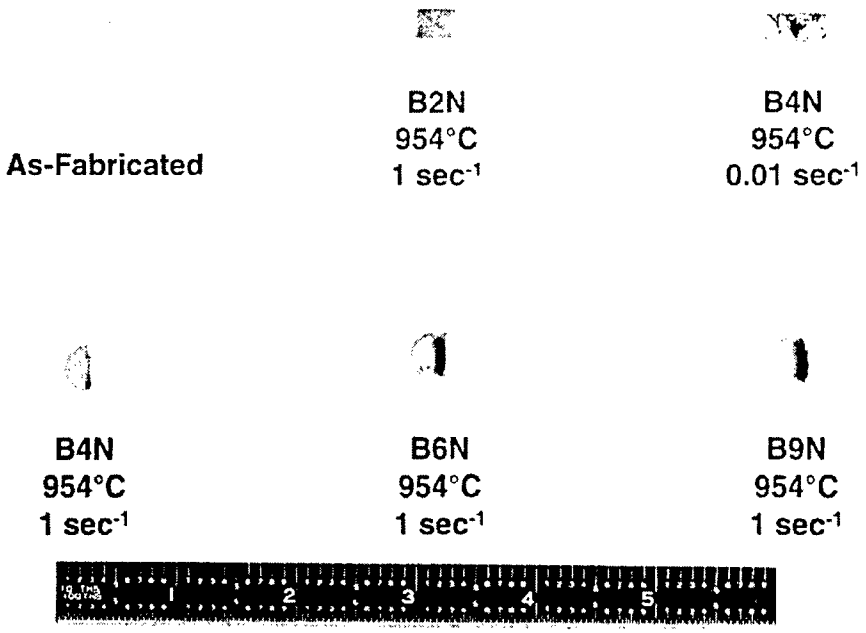


FIGURE B-15. GEOMETRIES OF DEFORMED AND FRACTURED HARD ALPHA BRAZILIAN SPECIMENS COMPARED TO THE AS-FABRICATED CONDITION

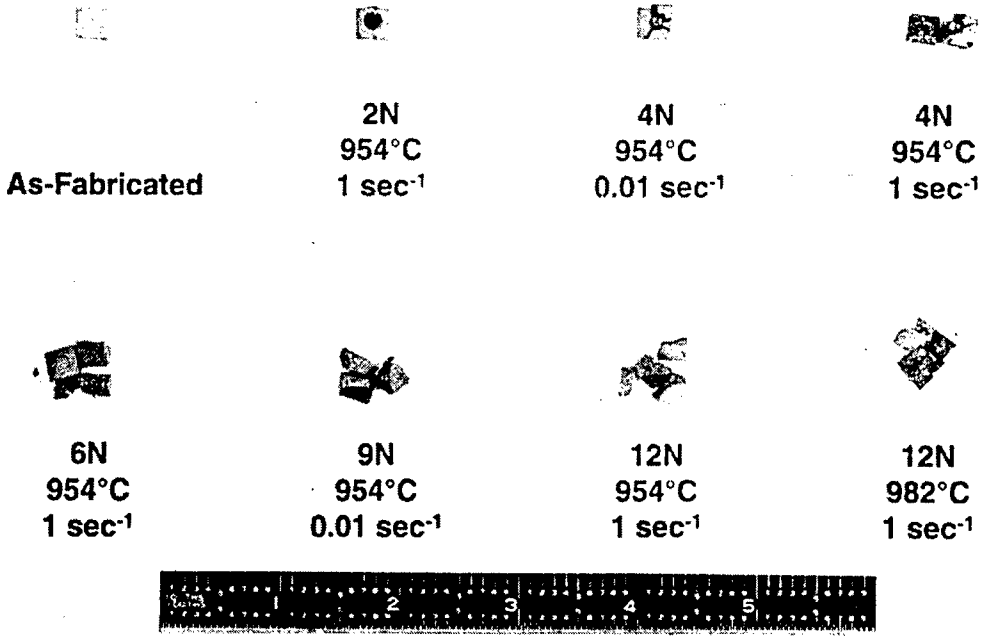


FIGURE B-16. GEOMETRIES OF DEFORMED AND FRACTURED HARD ALPHA INDENTATION SPECIMENS COMPARED TO THE AS-FABRICATED CONDITION

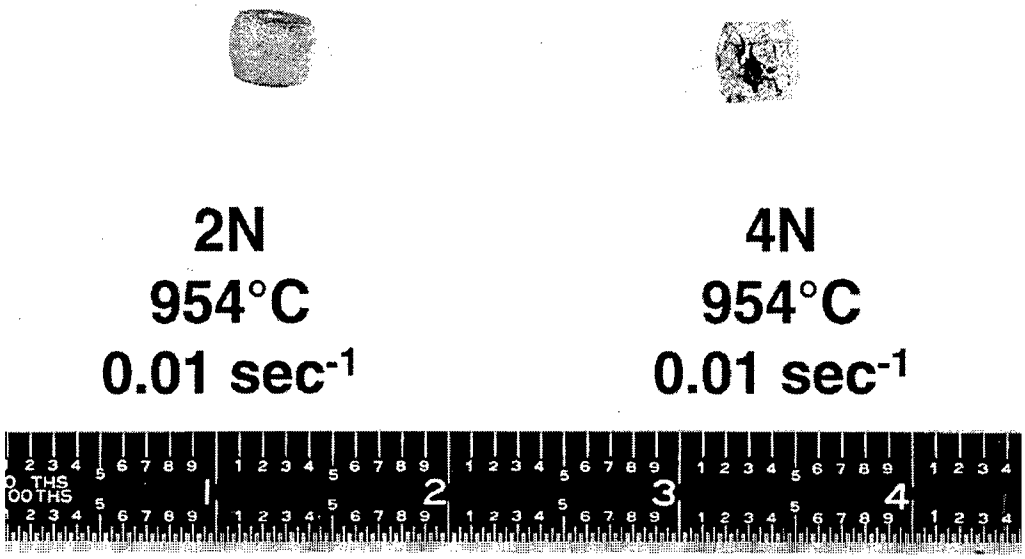


FIGURE B-17. DEFORMED COMPRESSION SPECIMEN FOR HARD ALPHA WITH 2 wt.% N COMPARED TO THAT FOR 4 wt.% N

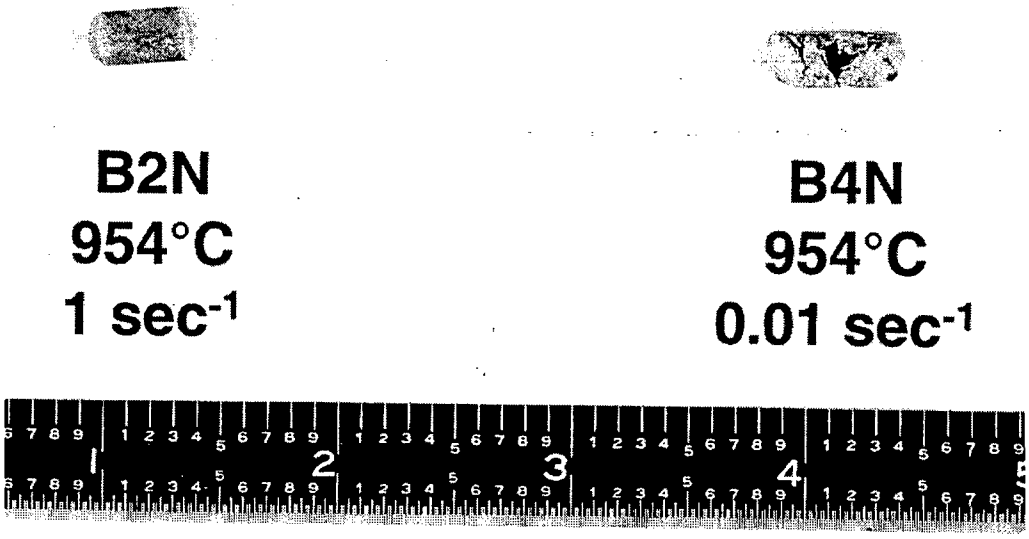
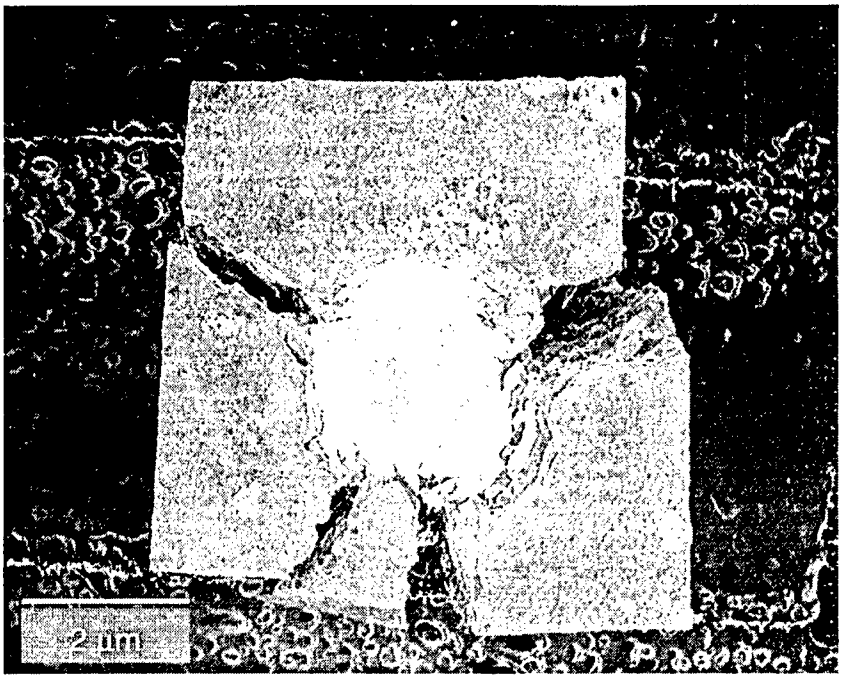
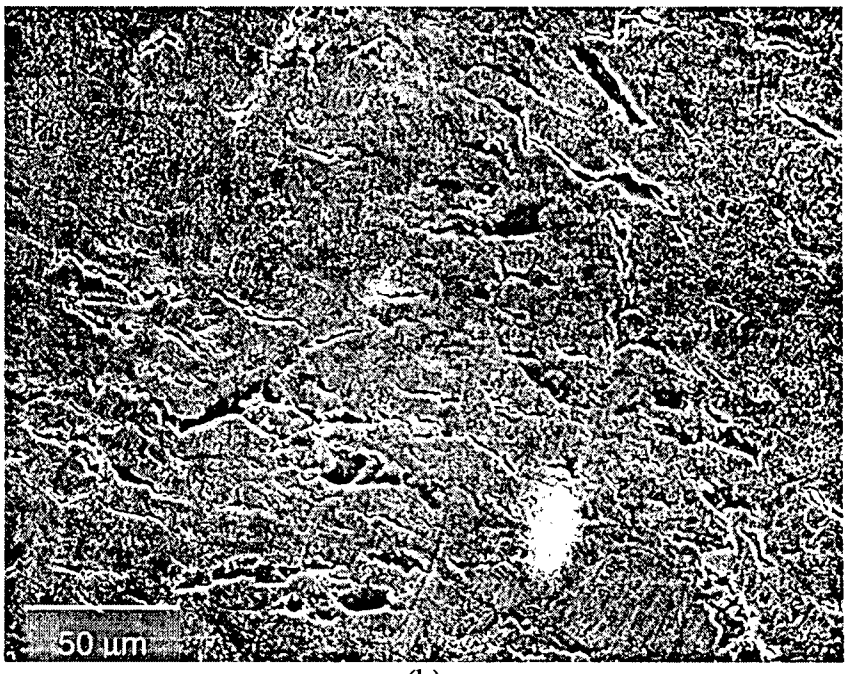


FIGURE B-18. DEFORMED BRAZILIAN SPECIMEN FOR HARD ALPHA WITH 2 wt.% N COMPARED TO THAT FOR 4 wt.% N

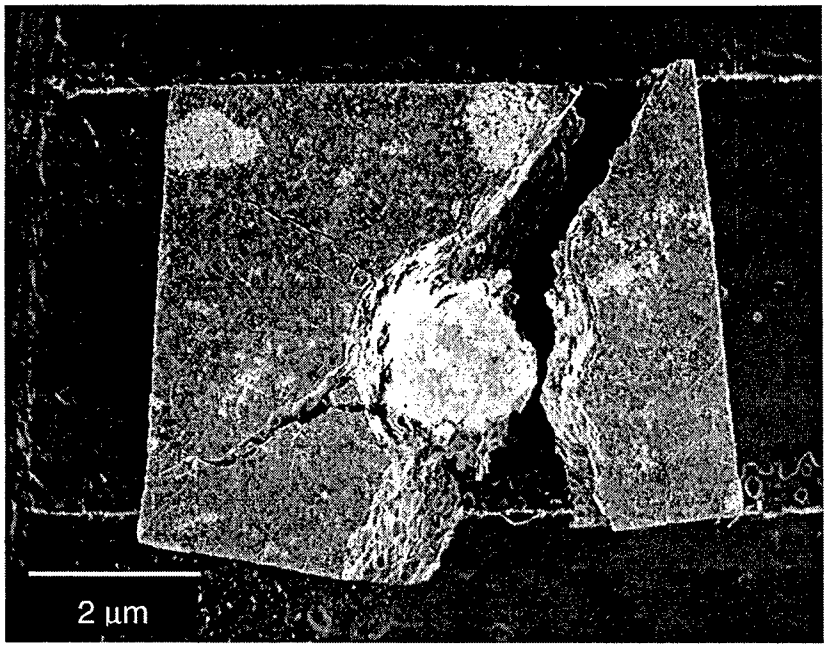


(a)

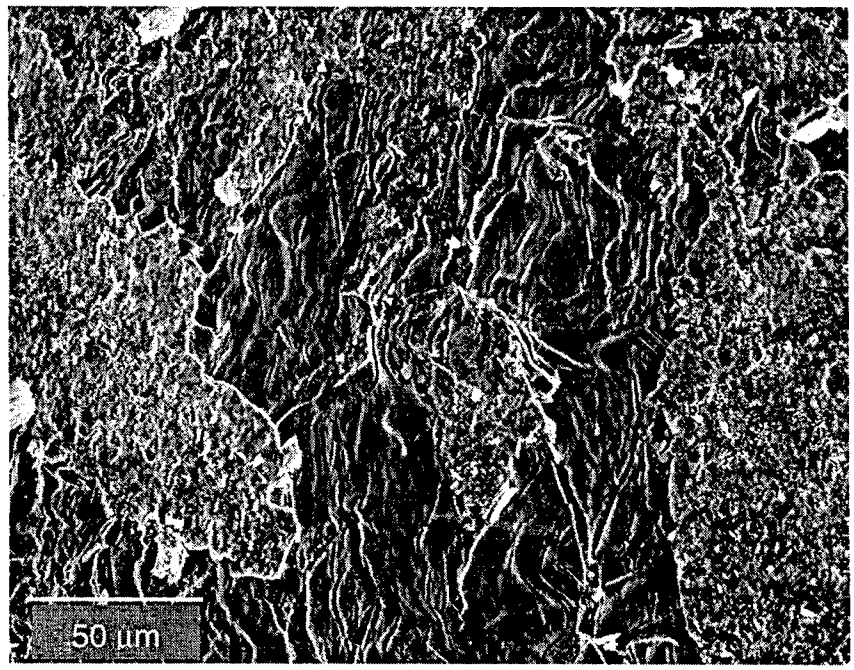


(b)

FIGURE B-19. FRACTURE INDENTATION SPECIMEN (a) AND MICROCRACKS AT THE BOTTOM OF THE INDENT (b) FOR HARD ALPHA WITH 4 wt.% N TESTED AT A SLOW STRAIN RATE (0.01 sec^{-1})



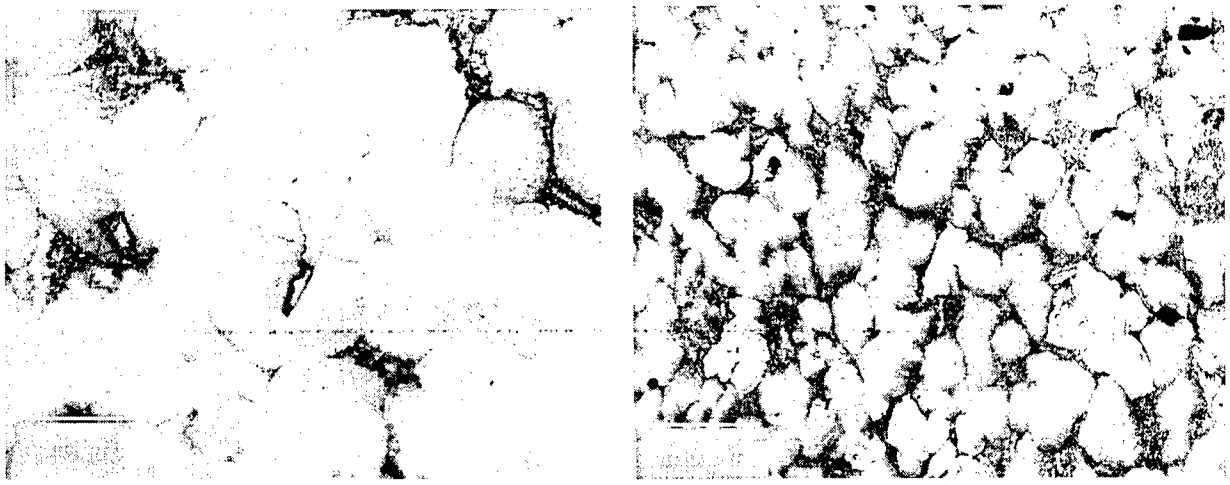
(a)



(b)

FIGURE B-20. FRACTURED INDENTATION SPECIMEN (a) AND MICROCRACKS AT THE BOTTOM OF THE INDENT (b) FOR HARD ALPHA WITH 4 wt.% N TESTED AT A RELATIVELY HIGH STRAIN RATE (1 sec^{-1})

The flow stress of hard alpha with 2% N is dependent on the mean stress (pressure) even though microcracks are not apparent. To understand this pressure-dependent flow behavior better, metallography was performed on sectioned Brazilian, compression, and indentation test specimens. The results, presented in figure B-21, show the presence of microcracks and voids in the Brazilian test specimen, see figure B-21(a). Voids are present in the compression specimen, see figure B-21(b), as well as in the material below the indent in the indentation specimen, see figure B-21(c). Compared to the as-received specimens, there were considerably more voids in the deformed specimens. There were no cracks in the compression and indentation specimens. Thus, the microcracking process appears to be suppressed at higher pressures and is responsible for the pressure-dependent plastic flow behavior observed in the 2N material.



(a) (b)

(c)

FIGURE B-21. DAMAGE PROCESS IN HARD ALPHA WITH 2 wt.% N
((a) Microcracks in the Brazilian specimen, (b) Voids in the compression specimen, and (c) Voids in the indentation specimen.)

B.4.2 EFFECTS OF PRESSURE.

The fracture strength, Y_i, determined for a given stress state was normalized by the fracture strength, Y_n, for uniaxial compression. The results are plotted as a function of pressure, P, normalized by Y_n in figure B-22. Pressure is calculated as 1/3 of the sum of the principal stresses, as given by

$$P = \frac{1}{3}(\sigma_{11} + \sigma_{22} + \sigma_{33}) \tag{B-3}$$

where σ_{11}, σ_{22}, and σ_{33} are the principal stresses. The values of the ratio P/Y_n are 0.045, 1/3 and ≈ 6 for indirection tension, uniaxial compression, and indentation, respectively. The semilog plot in figure B-22 indicates that Y/Y_n increases linearly with log (P/Y_n). The fracture stress increasing with pressure because microcracking is suppressed by a high pressure.

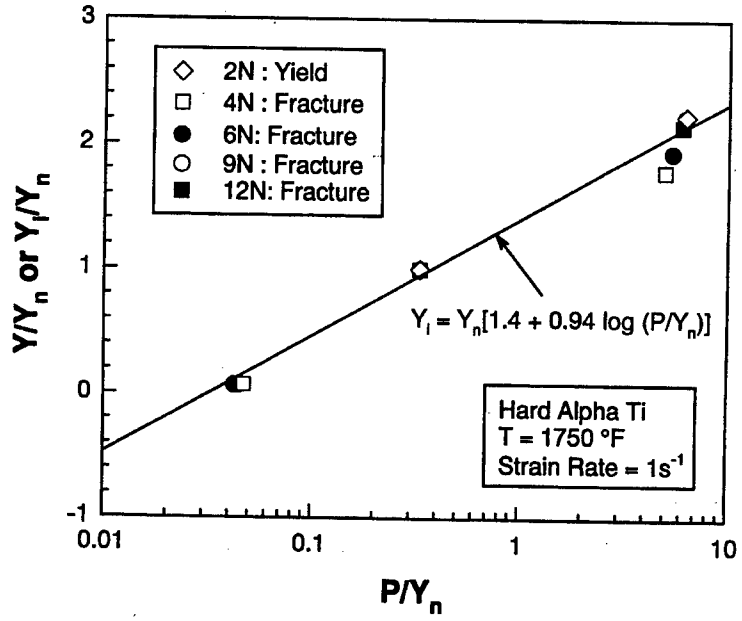


FIGURE B-22. THE FLOW STRESS (Y) AND FRACTURE STRESS (Y_i) OF HARD ALPHA INCREASES WITH INCREASING PRESSURE, P (All parameters are normalized by the flow or fracture stress for uniaxial compression.)

B.4.3 EFFECTS OF NITROGEN CONTENT.

The dependence of the flow and fracture stresses on nitrogen content of hard alpha is delineated in figure B-23. Both the flow stress and the fracture stress increase with increasing nitrogen content, but the rates of increase are different, as shown in figure B-22. The flow stress of hard alpha is lower than the fracture stress at nitrogen contents below 4 wt.% N. The slope dY/dN is higher for the flow stress and the flow stress exceeds the fracture stress for nitrogen contents higher than 4 wt.% N. As a result, fracture precedes plastic flow when the nitrogen content of hard alpha is greater than 4 wt.% N.

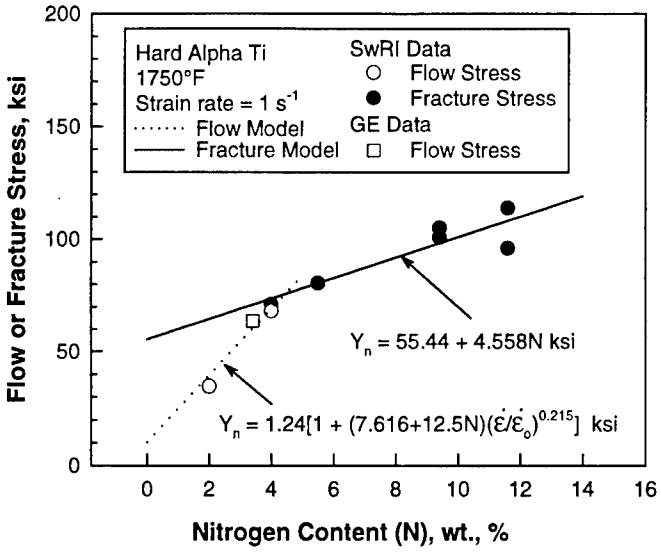


FIGURE B-23. FLOW AND FRACTURE STRESSES OF HARD ALPHA INCREASE WITH INCREASING NITROGEN CONTENTS AT DIFFERENT SLOPES

B.4.4 EFFECTS OF STRAIN RATE.

The effects of strain rate on the flow and fracture stresses of hard alpha are summarized in figures B-24 and B-25, respectively. The result indicates that the flow stress increasing with increasing strain rates, see figure B-24. On the other hand, the fracture stress of hard alpha is insensitive to the strain rate, based on the experimental data for uniaxial compression and plane strain compression, see figure B-25. The fracture stress obtained by the indentation technique shows an apparent rate sensitivity, which is not fully understood and could actually be a manifestation of the pressure effect.

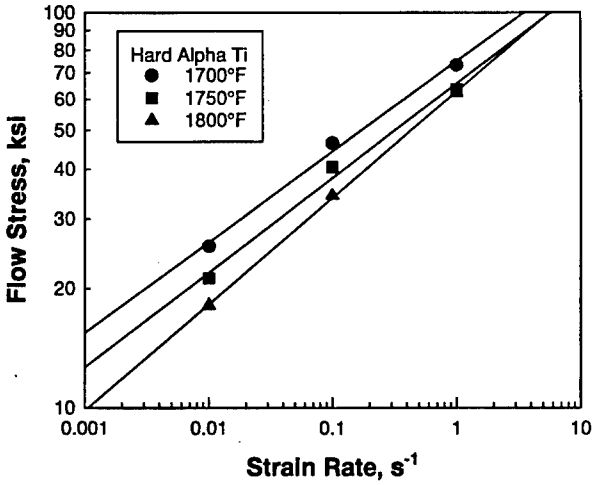


FIGURE B-24. FLOW STRESS OF HARD ALPHA WITH NITROGEN CONTENT ≤ 4 wt.% INCREASES WITH INCREASING STRAIN RATE

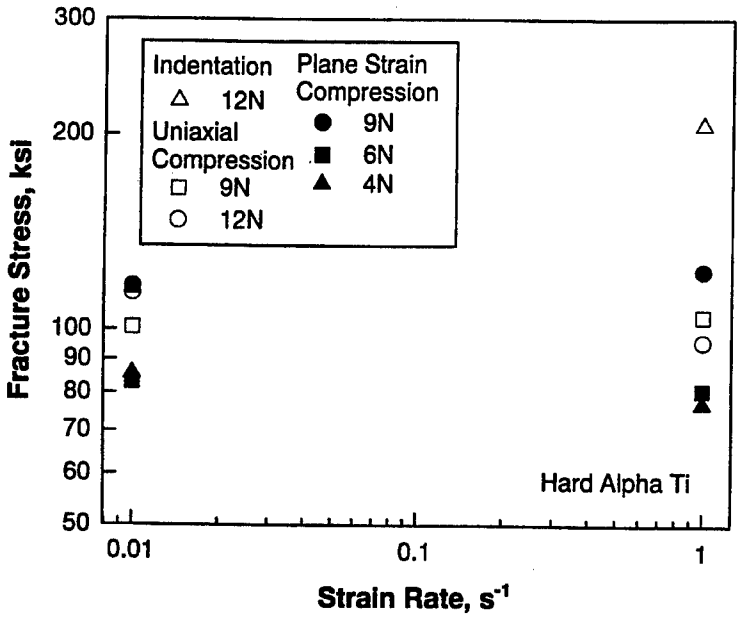


FIGURE B-25. FRACTURE STRENGTHS OF HARD ALPHA Ti AT TWO STRAIN RATES SHOW LITTLE OR NO RATE DEPENDENCE

B.4.5 EFFECTS OF TEMPERATURE.

The fracture stress of hard alpha is relatively insensitive to temperature in the range of 1700° to 1800°F, as illustrated in figure B-5 for hard alpha with 12 wt.% nitrogen. Comparison of the plane-strain fracture stress (122.6 ksi) at ambient temperature against that for uniaxial compression (117.8 ksi) suggests that the fracture stress may be independent of temperature from 72° to 1700°F. For hard alpha with a nitrogen content ≤ 4 wt.%, the flow stress is sensitive to the test temperature and strain rate, as shown in figure B-24.

B.5 REFERENCES.

B-1. M. Gigliotti, GE CRD Internal Report, 1991.

B-2. M.C. Shaw, P.M. Braiden, and G.J. DeSalvo, "The Disk Test for Brittle Materials," *Journal of Engineering for Industry*, Transactions of the ASME, Vol. 97, Ser. B, No. 1, pp. 77-87, 1975.

B-3. D. Tabor, The Hardness of Metals, Oxford University Press, New York, 1951.

B-4. G.E. Dieter, Jr., Mechanical Metallurgy, McGraw-Hill, New York, pp. 286-289, 1961.

APPENDIX C—DEVELOPMENT OF CONSTITUTIVE EQUATIONS FOR HARD ALPHA

C.1 FRACTURE OF HARD ALPHA.

This section summarizes the constitutive equations developed for describing the elastic fracture of hard alpha (intact material) and the failure stress of damaged hard alpha as a function of damage using a continuum damage mechanics formulation. These constitutive equations are applicable to describing the onset and the evolution of failure of hard alpha. For intact material, the flow or fracture stress, Y_i, of hard alpha is given by

$$Y_i = Y_n\left[X + Z\ log\left(\frac{P}{\sigma_e}\right)\right]\left(1 + c_0\,\varepsilon^{c_1}\right)\left[1 + d_0\left(\frac{\dot{\varepsilon}}{\dot{\varepsilon}_0}\right)^{d_1}\right] \qquad \text{(C-1)}$$

where Y_i = flow or fracture stress

Y_n = flow or fracture stress under uniaxial compression

P = pressure = $\dfrac{\sigma_1 + \sigma_2 + \sigma_3}{3}$ (compression is positive)

σ_e = Mises effective stress

$\dot{\varepsilon}$ = strain rate

$\dot{\varepsilon}_0$ = reference strain rate

ε = strain

X, Z = constants related to pressure effects

c_0, c_1 = constants related to strain hardening effects

d_0, d_1 = constants related to strain rate hardening

and σ_1, σ_2, and σ_3 are the principal stresses. In equation C-1, Y_n is the flow or fracture stress of hard alpha under uniaxial compression; this parameter is considered a function of nitrogen content only. The second term in the right-hand side (RHS) of equation C-1 represents the increase in the flow or fracture stress with increasing pressure, P. Strain hardening and strain rate hardening are represented by the third and fourth terms on the RHS of equation C-1, respectively. The parameters X, Z, c_0, c_1, d_0, and d_1 are model constants that are evaluated from experimental data. The reference strain rate, $\dot{\varepsilon}_0$, can be taken to be 1 s^{-1} for convenience.

The onset of fracture is given by Y_i. After the initiation of fracture, the failure stress, Y_D, is considered to decrease with increasing damage according to the expression given by

$$Y_D = (1 - D)Y_i + DY_f \qquad \text{(C-2)}$$

where D is an internal variable representing the state of damage. The value of D is zero for intact material but it has a value of unity when the material fails completely. The damage rate, $\dot{D}$, is represented by an evolution equation given by

$$\dot{D} = c_3\ \dot{\varepsilon} \qquad \text{(C-3)}$$

where $\dot{\varepsilon}$ is the strain rate and c_3 is a model constant. The current value of the damage variable D is obtained as

$$D = \int \dot{D} dt = \int c_3 \, \dot{\varepsilon} dt \tag{C-4}$$

by integrating over the loading path. For multiaxial loading, $\dot{\varepsilon}$ in equations C-1 and C-4 is replaced by the von Mises effective strain rate, $\dot{\varepsilon}_e$.

The fracture stress, Y_n, under uniaxial compression shows a linear correlation with the nitrogen content and can be represented by

$$Y_n = \gamma_0 + \gamma_1 N \tag{C-5}$$

where γ_0 and γ_1 are correlation coefficients. Linear regression of the experimental data, figure C-1, allows determination of the values of γ_0 and γ_1, leading to γ_0 = 55.44 ksi and γ_1 = 4.558 ksi/wt.% N.

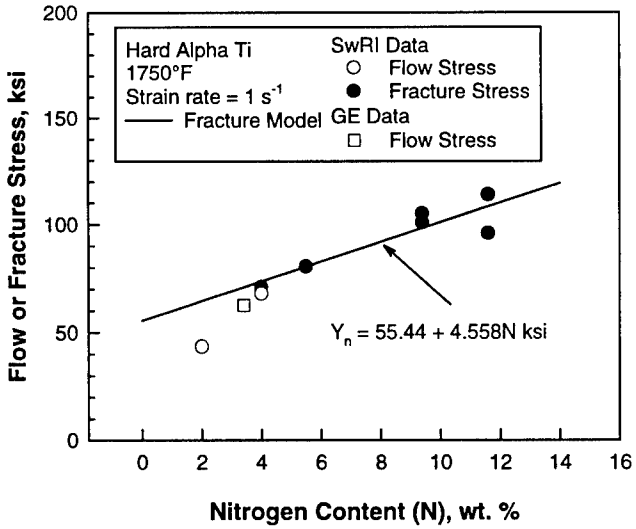


FIGURE C-1. EXPERIMENTAL CORRELATION AND LEAST-SQUARE FIT OF THE FLOW OR FRACTURE STRESS, Y_n, OF HARD ALPHA AS A FUNCTION OF NITROGEN CONTENT (The least-square fit applies to the fracture stress only.)

For fracture of hard alpha Ti, both strain hardening and strain rate hardening are absent. Thus, c_0 = 0 and d_0 = 0. For uniaxial compression, $\sigma_e = Y_n$ at the onset of inelastic flow. Then, equation C-1 is reduced to

$$Y_i = Y_n \left[X + Z \, log \left(\frac{P}{Y_n} \right) \right] \tag{C-6}$$

with X = 1.4 and Z = 0.94. The value of X and Z were obtained from a plot of Y_i/Y_n versus P/Y_n in a semilog plot, figure C-2, and performing a regression analysis of the experimental data.

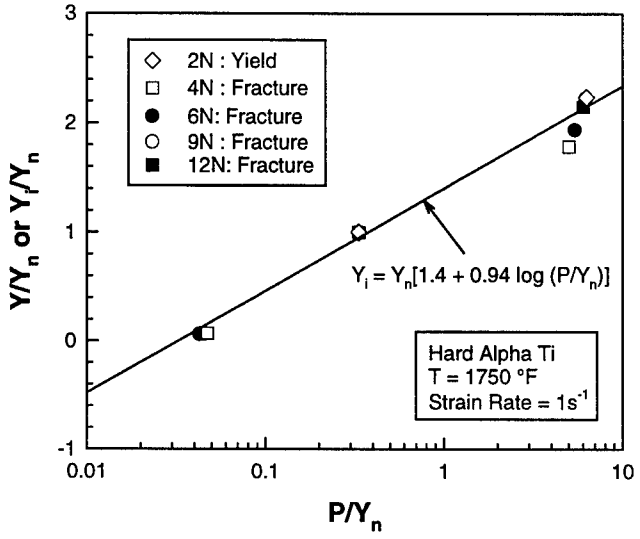


FIGURE C-2. SEMILOG PLOT OF FLOW OR FRACTURE STRESS, Y_i, AS A FUNCTION OF PRESSURE, $P = \sigma_{kk}/3$ (Both Y_i and P are normalized by the uniaxial compression flow or fracture stress, Y_n.)

For failed hard alpha Ti, the failure stress, Y_f, is expressed as

$$Y_f = Y_n\left[X + Z\ log\left(\frac{P}{Y_n}\right)\right] \tag{C-7}$$

with X = 0.14 and Z = 0.094. These values of X and Z were obtained based on the "flow stress" of the completely failed specimens in the indentation tests.

The slope of the engineering stress-strain curves for plane strain compression tests beyond the maximum load was used to evaluate the constant c_3 in the damage evolution equation in the constitutive model for hard alpha Ti. The value of c_3 was sensitive to nitrogen content and increased with increasing strain rate. Specifically,

$$c_3 = 0 \text{ for } 0 \le N < 4\ wt.\%\ N \tag{C-8}$$

since fracture did not occur in hard alpha within this range of nitrogen content. In contrast,

$$c_3 = 18.75\ \dot{\varepsilon}^{0.1516}\left(1 - e^{c_4 N}\right)\ for\ N \ge 4\ wt.\%\ N \tag{C-9}$$

with c_4 = -0.0964 (wt.% N^{-1}) and N is nitrogen content in wt.%. For $\dot{\varepsilon}$ = 1 sec^{-1}, equation C-2 gives the c_3 values as shown in table C-1.

TABLE C-1. VALUES OF c_3 AS A FUNCTION OF NITROGEN CONTENT

N, wt.%	c_3
4	6
5	8
9	11
12	13

The experimental basis for the constitutive model is provided by the results shown in figures C-1 to C-3. Figure C-2 illustrates that the dependence of the flow and fracture stresses of hard alpha on pressure (compression is positive here) obeys a logarithmic law as described by equation C-6, which is a simplification of the more general form in equation C-1. Figure C-1 presents the correlation between the flow or fracture stress and nitrogen content. Figure C-3 shows a comparison of the calculated fracture stress for the intact material, equation C-6, and the stress of the failed material determined from the indentation tests at various nitrogen levels, equation C-7. The decrease in the flow stress of the hard alpha from the intact state to the failed state is given by equation C-2 with the evolution of the damage state described by equation C-3. The minimum pressure in the unloading portion of pressure-strain values (figure B-8) was used to obtain the Y_f values, from which $X = 0.14$ and $Z = 0.094$ in equation C-7 were determined and shown in figure C-3. The linear damage rate formulation, equation C-3, is suggested by plane strain compression data shown in figures B-13 and B-14, which show the stress decreases linearly with increasing strain. The value of d_0 was determined to be zero from a plot of fracture stress versus strain rate in figure B-25, which shows that with the exception of one data point, the fracture stress is essentially independent of strain rate.

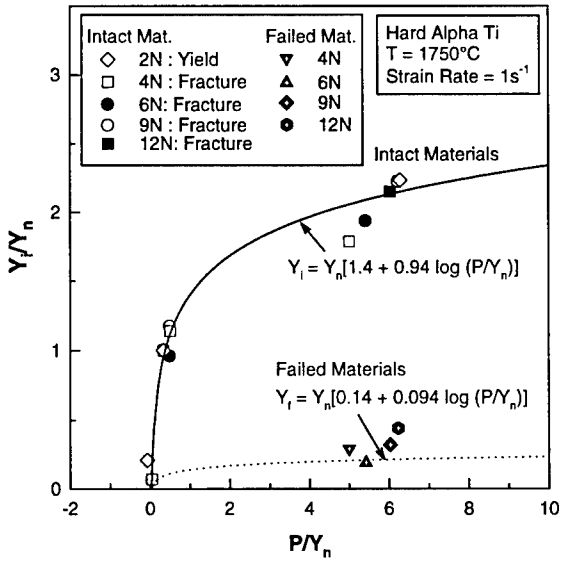


FIGURE C-3. COMPARISON OF THE CALCULATED FRACTURE STRESS OF THE INTACT MATERIALS AND THE FLOW STRESS OF THE FAILED MATERIAL

It should be noted that equation C-6 gives $Y_i/Y_n \leq 0$ when $P/Y_n \leq 0.0324$. The negative value means tensile strength as tension is taken to be negative. Y_i can be taken to be the tensile strength, which is $\approx$ 6 ksi. This leads to Y_i/Y_n = -0.14, which can be used as the failure stress for $P/Y_n \leq 0.023$.

C.1.1 PLASTIC FLOW OF HARD ALPHA.

This section summarizes the constitutive equations developed for describing the plastic flow of hard alpha Ti containing a low nitrogen content ($0 < N \leq 4$ wt.%). For $0 \leq N \leq 4$ wt.%, the flow stress, Y, of hard alpha Ti is given by

$$Y = Y_n F(P) \tag{C-10}$$

where Y_n is the flow stress of hard alpha under uniaxial compression. $F(P)$ is a function of the pressure, P, and is given by

$$F(P) = 1 \text{ for } N = 0 \tag{C-11}$$

and

$$F(P) = X + Z \log\left(P/Y_n\right) \text{ for } 0 < N \leq 4 wt.\% \tag{C-12}$$

with $X = 1.4$ and $Z = 0.94$.

The flow stress, Y_n, is a general function of strain and strain rate as described by

$$Y_n = Y_o\left[1 + c_o \varepsilon^{c_1}\right]\left[1 + d_o\left(\frac{\dot{\varepsilon}}{\dot{\varepsilon}_o}\right)^{d_1}\right] \tag{C-13}$$

where Y_o, c_o, c_1, d_o, and d_1 are constants, ε is strain and $\dot{\varepsilon}_o$ is the reference strain rate, and $\dot{\varepsilon}$ is the strain rate. The values of these constants are as follows:

Y_o = 1.24 ksi
c_o = c_1 = 0 (no hardening)
d_1 = 0.215
$\dot{\varepsilon}_o$ = 1 sec^{-1}

The value of d_o is a function of nitrogen content, N, and is given by

$$d_o = 7.616 + 12.5N \tag{C-14}$$

which leads to

$$Y = Y_n[1.4 + 0.94 log\,(P/Y_n)] \tag{C-15}$$

$$Y_n = 1.24[1 + (7.616 + 12.5N)(\dot{\varepsilon}/\dot{\varepsilon}_0)^{0.215}] \tag{C-16}$$

as the flow equations for hard alpha Ti with a low N content ($0 < N \leq 4$ wt.%).

The values of X and Z for 2N were determined from experimental data that include tensile test results from General Electric (GE) [C-1] and uniaxial compression tests as well as indentation tests performed at Southwest Research Institute (SwRI). The correlation of equation C-12 with the flow stress data for 2N is presented in figure C-3. The same function is applicable to treat fracture of hard alpha with higher nitrogen contents. For the case of 2N, $Y = Y_i$ in figure C-3.

The strain rate sensitivity exponent, d_1, in equation C-13 was determined for GE results for 3.4 wt. % N [C-1] and SwRI data for 2 and 4 wt.% N. The d_1 value for 3.4 wt.% N is 0.26, and it is 0.17 for both 2 and 4 wt.% N. An average value of $d_1 = 0.215$ is used for these low N content materials ($0 < N \leq 4$ wt.%). A comparison of the model calculation and experimental data on the dependence of flow stress vs nitrogen content is shown in figure C-4 for two strain rates.

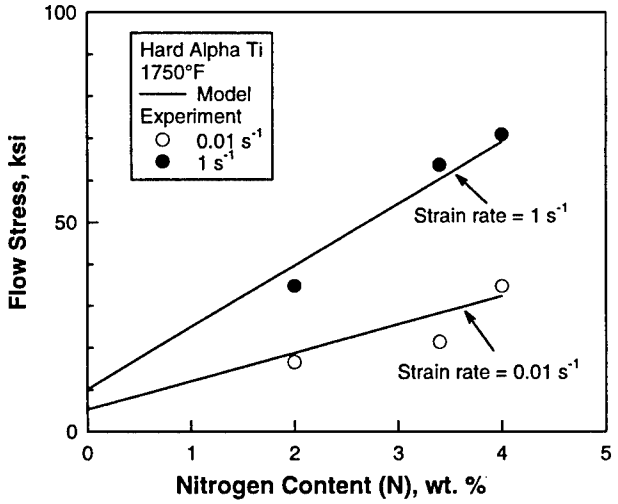


FIGURE C-4. CALCULATED AND MEASURED FLOW STRESS OF HARD ALPHA Ti AS A FUNCTION OF NITROGEN CONTENTS FOR TWO STRAIN RATES

Uniaxial compression tests of hard alpha Ti with 2N (SwRI data) show a small strain hardening. In contrast, the data for 3.4 wt.% N (GE data) [C-1] show strain hardening, followed by softening, and then hardening again at larger strains. For simplicity, strain hardening and softening are both ignored by approximating hard alpha as a nonhardening material. Comparison of the calculated and measured stress-strain curves for 2N and 3.4N are shown in figures C-5 and C-6, respectively. The GE data have been corrected for adiabatic heating using an analysis procedure provided by GE. No correction for adiabatic heating was deemed necessary for

the SwRI data because no softening was observed in this set of data. The model overpredicts the flow stress of 2N at 1 sec^{-1} because an average value of d_1 (d_1 = 0.215) for both GE and SwRI data was used in this calculation. The GE data for 3.4 wt.% N was more rate sensitive than the SwRI data for 2 and 4 wt.% N. The discrepancy is considered minor and is well within experimental scatter. A comparison of the calculated and measured flow and fracture stresses is shown in figure C-7 as a function of nitrogen content, which shows good agreement between model and experiment.

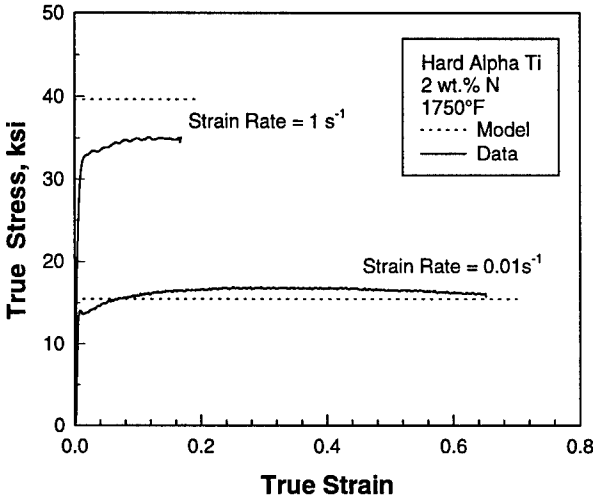


FIGURE C-5. COMPARISON OF CALCULATED AND MEASURED TRUE STRESS-STRAIN CURVES OF HARD ALPHA Ti WITH 2 wt.% N FOR TWO STRAIN RATES

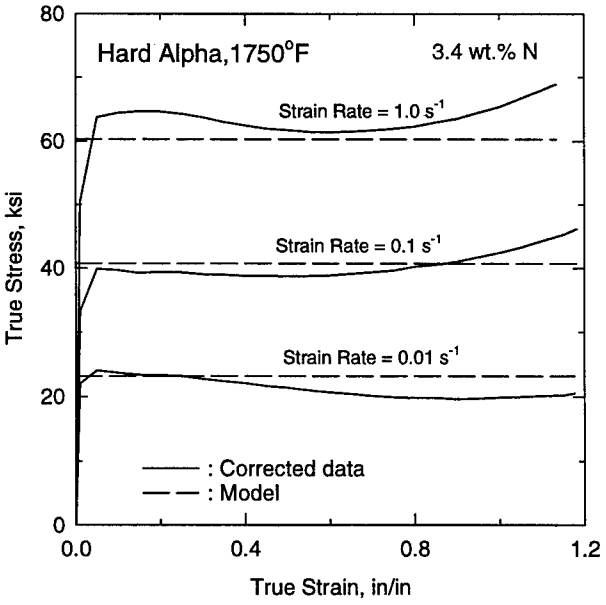


FIGURE C-6. MEASURED TRUE STRESS-STRAIN CURVES COMPARED TO MODEL CALCULATIONS FOR TWO STRAIN RATES
(The experimental data (GE data) were corrected for adiabatic heating.)

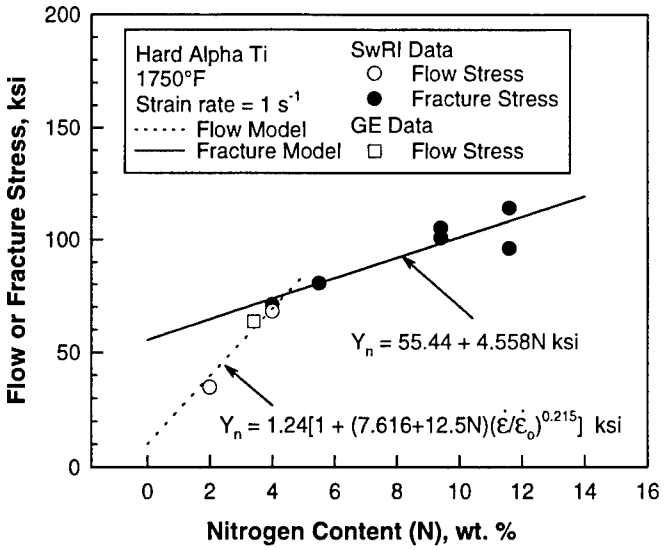


FIGURE C-7. COMPARISON OF CALCULATED AND MEASURED FLOW AND FRACTURE STRESSES OF HARD ALPHA Ti

C.2 REFERENCE.

C-1. M. Gigliotti, GE CRD Internal Report, 1991.

APPENDIX D—MICROLEVEL SIMULATIONS OF HARD ALPHA DURING FORGING

D.1 SEED 33.

Seed 33 was a cylindrical seed 0.100″ in diameter and 0.100″ high, with the axis of the cylinder oriented in the radial direction. The measured radial-axial position was 2.39″ × 9.00″. The inclusion was modeled as a square with an edge length of 0.100″. The diffusion zone was a square with an edge length of 0.200″. The microvolume was a square with an edge length of 1.000″. The nitrogen content of the inclusion was a uniform 12%. The nitrogen content of the diffusion zone decreased linearly from 4% at the inside surface to 0% at the outside surface.

As with Seed 29, several meshing schemes were experimented with before a proper value was determined. At the completion of the simulation, a boundary node density of 130 nodes/inch was used for the hard alpha inclusion. A boundary density of 90 nodes/inch was used for both the inside and outside of the diffusion zone. A boundary density of 120 nodes/inch was used for the inside of the microvolume, and 33 nodes/inch were used on the outside.

Screen captures showing initial mesh, geometry, damage, and flow stress evolution are shown in figure D-1 through figure D-7.

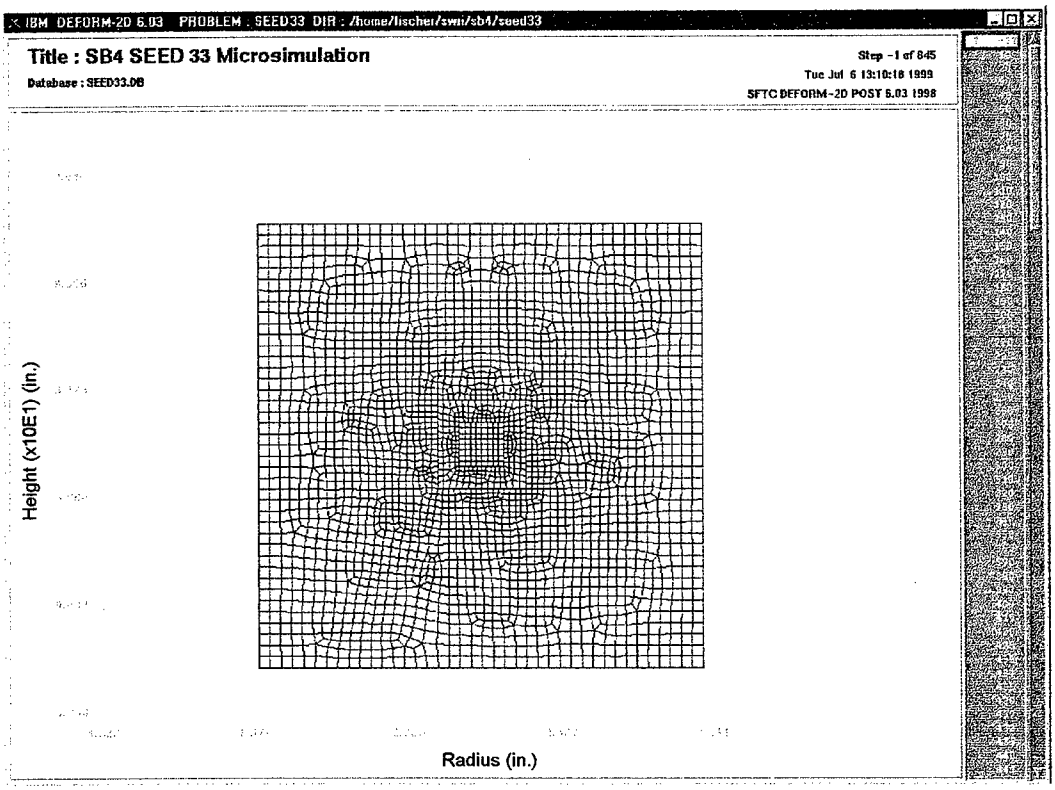


FIGURE D-1. SEED 33 MICROLEVEL SIMULATION, INITIAL MICROVOLUME MESH

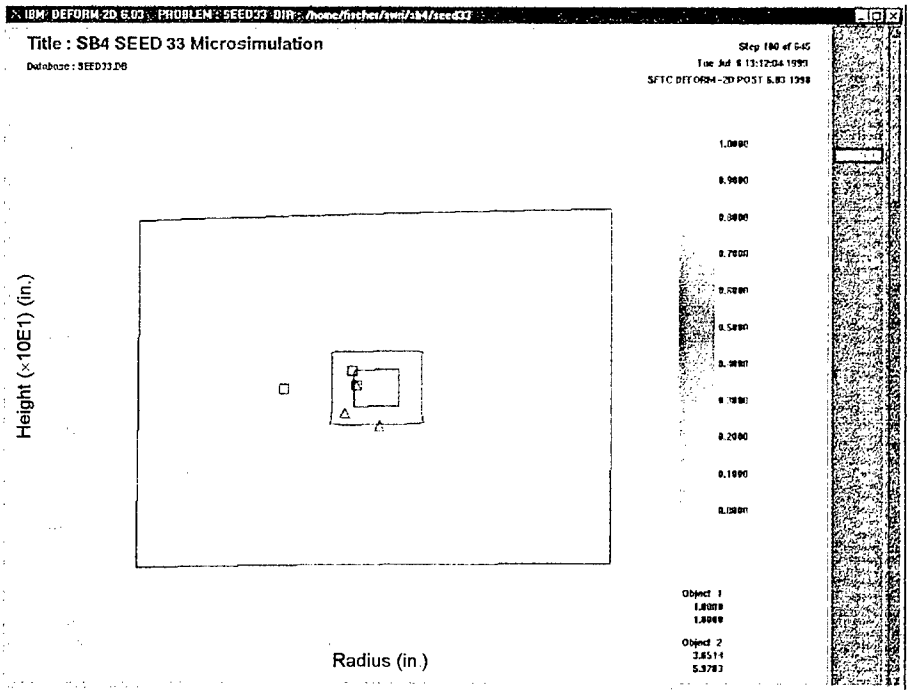


FIGURE D-2. SEED 33 MICROLEVEL SIMULATION, DAMAGE DISTRIBUTION AT STEP 100 (Note that damage is saturated in all objects.)

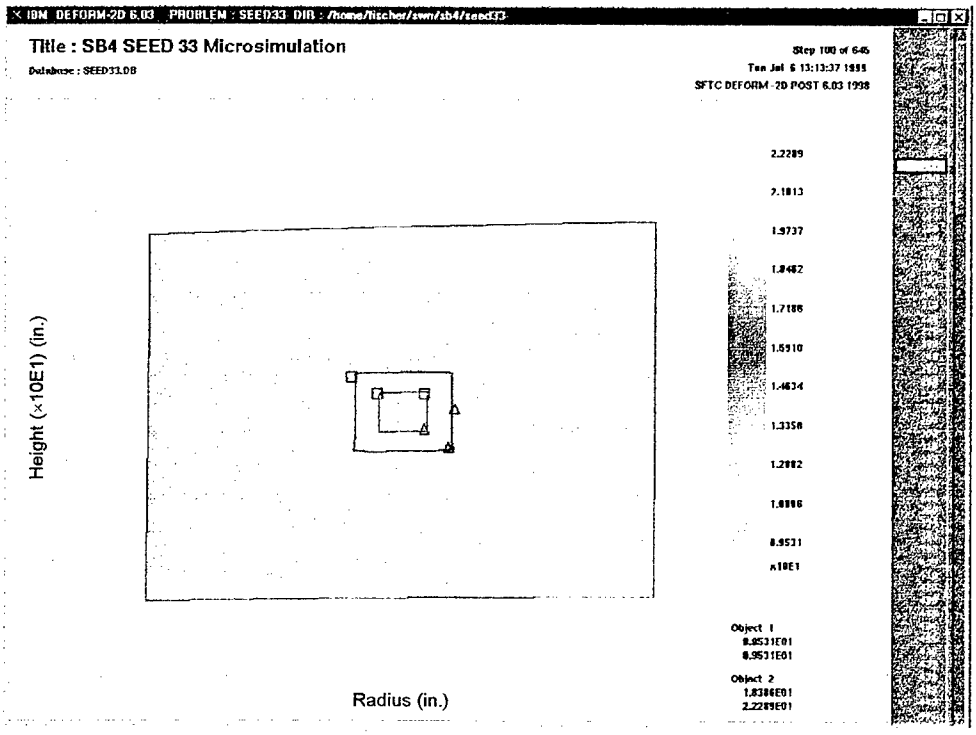


FIGURE D-3. SEED 33 STEP 100, EFFECTIVE STRESS DISTRIBUTION (Note very low flow stress in failed hard alpha inclusion.)

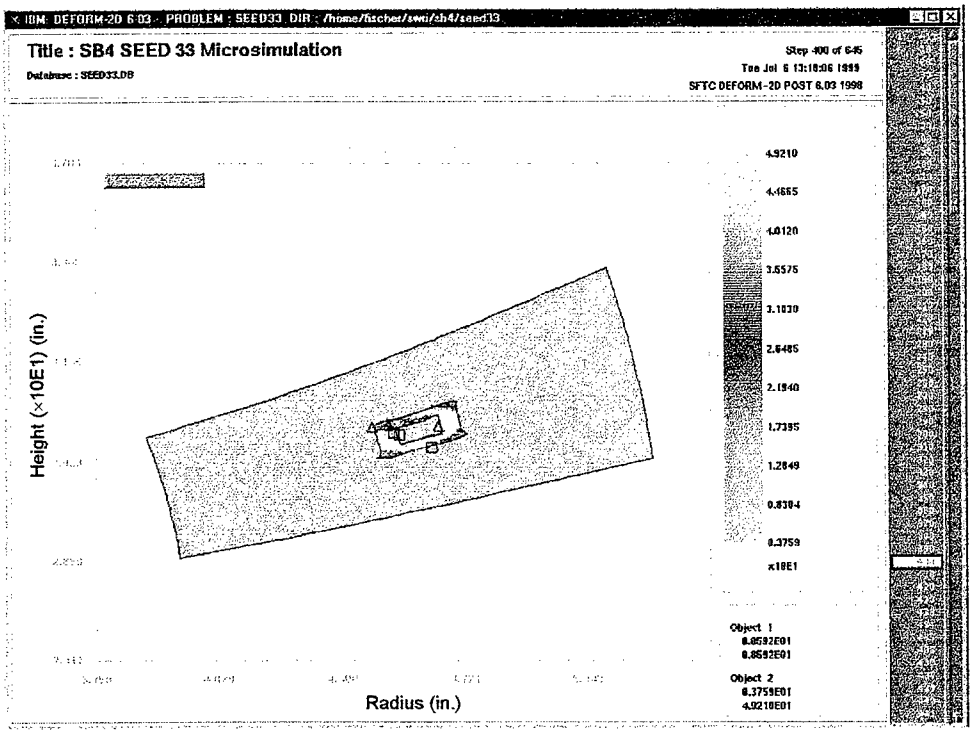


FIGURE D-4. SEED 33 STEP 400, STRESS DISTRIBUTION

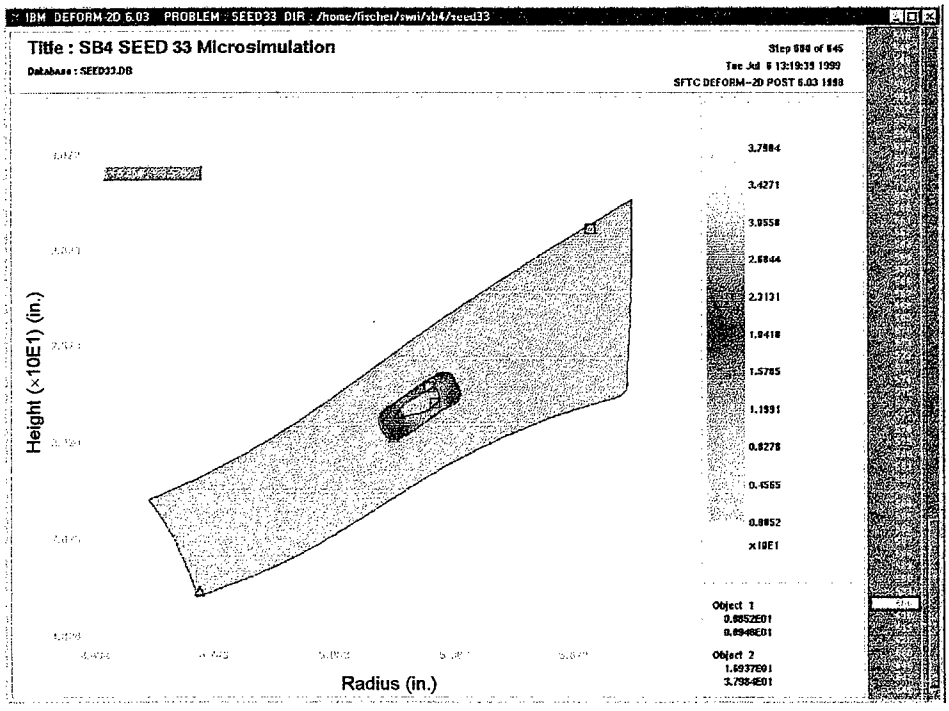


FIGURE D-5. SEED 33 STEP 600, STRESS DISTRIBUTION

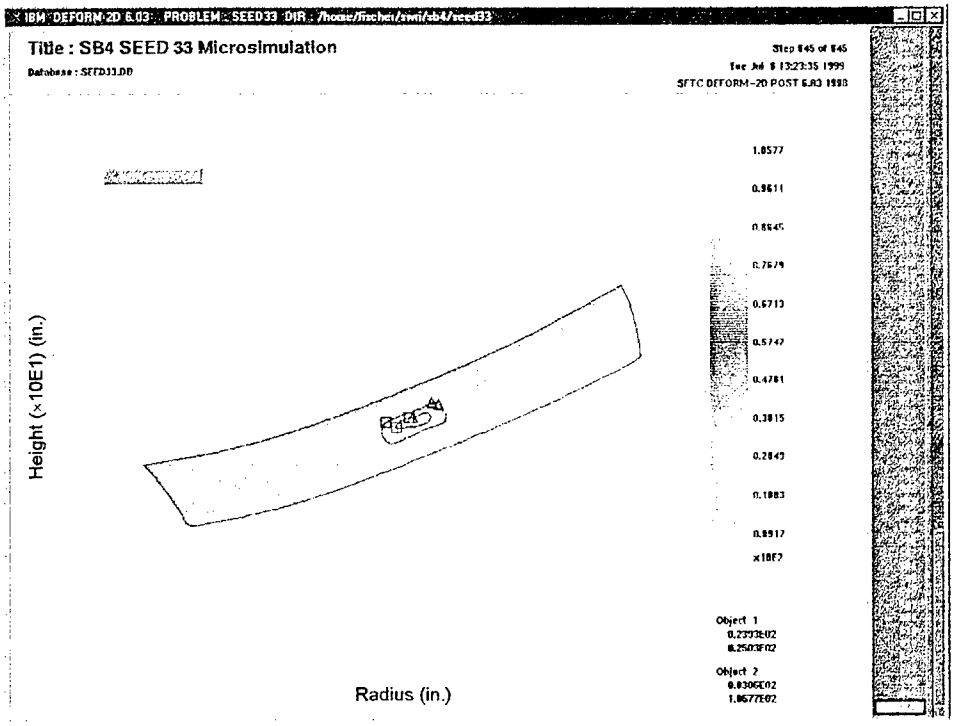


FIGURE D-6. SEED 33 STEP 645, FINAL EFFECTIVE STRESS DISTRIBUTION IN MICROVOLUME

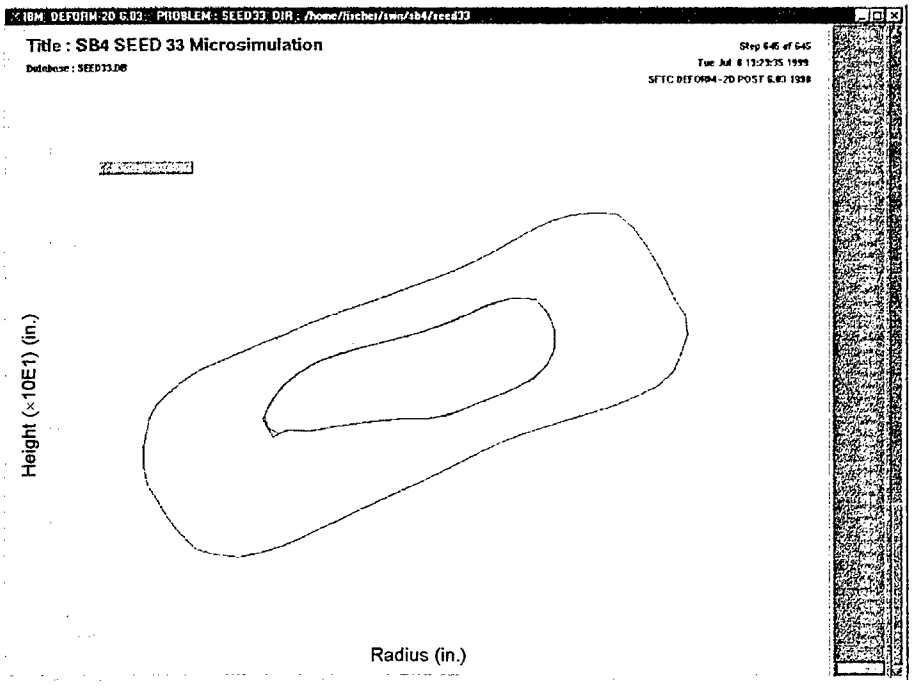


FIGURE D-7. SEED 33, FINAL SHAPE OF HARD ALPHA INCLUSION AND DIFFUSION ZONE

D.2 SEED 37.

Seed 37 was a cylindrical seed 0.100″ diameter by 0.100″ high with the axis oriented radially. The measured radial position was 1.990″. An average position of 6.575″ was used for the axial position. The geometry and nitrogen content in this microlevel simulation was the same as was used for Seed 33.

In the Seed 37 microlevel simulation, the hard alpha inclusion object completely penetrated the diffusion zone at Step 616 and led to a geometric configuration in which the simulation could not be continued because of the violation of fundamental assumptions regarding the simulation. A detail of the hard alpha and diffusion zone is shown in figure D-8.

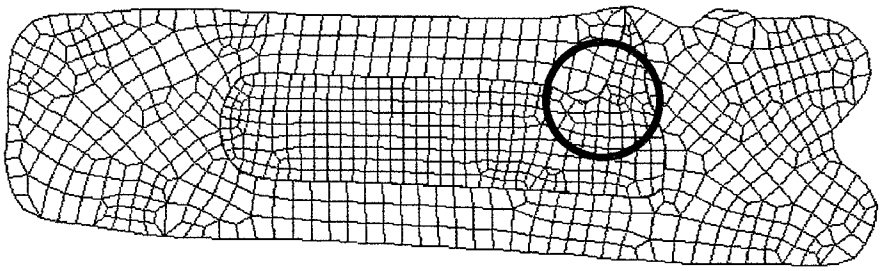


FIGURE D-8. DETAIL OF HARD ALPHA AND DIFFUSION ZONE OF SEED 37 AT STOPPING POINT IN MICROLEVEL SIMULATION
(Note that the hard alpha has completely penetrated the diffusion zone.)

The boundary node mesh density on the hard alpha inclusion was 191 nodes/inch. The density on both the internal and external boundaries of the diffusion zone was 135 nodes/inch. The density on the internal boundary of the matrix material was 170 nodes/inch and on the external boundary was 50 nodes/inch. The diffusion zone was master to both the hard alpha and matrix material.

Screen captures showing the initial mesh and the evolution of geometry, damage, and flow stress are shown in figures D-9 through D-14.

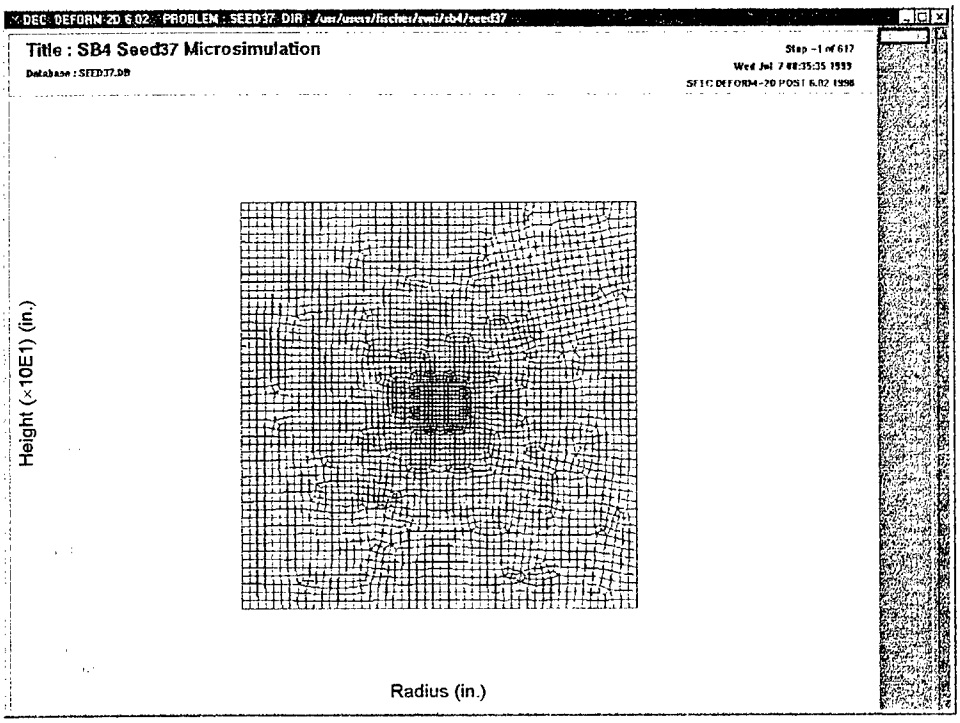


FIGURE D-9. SEED 37, INITIAL MESH CONFIGURATION

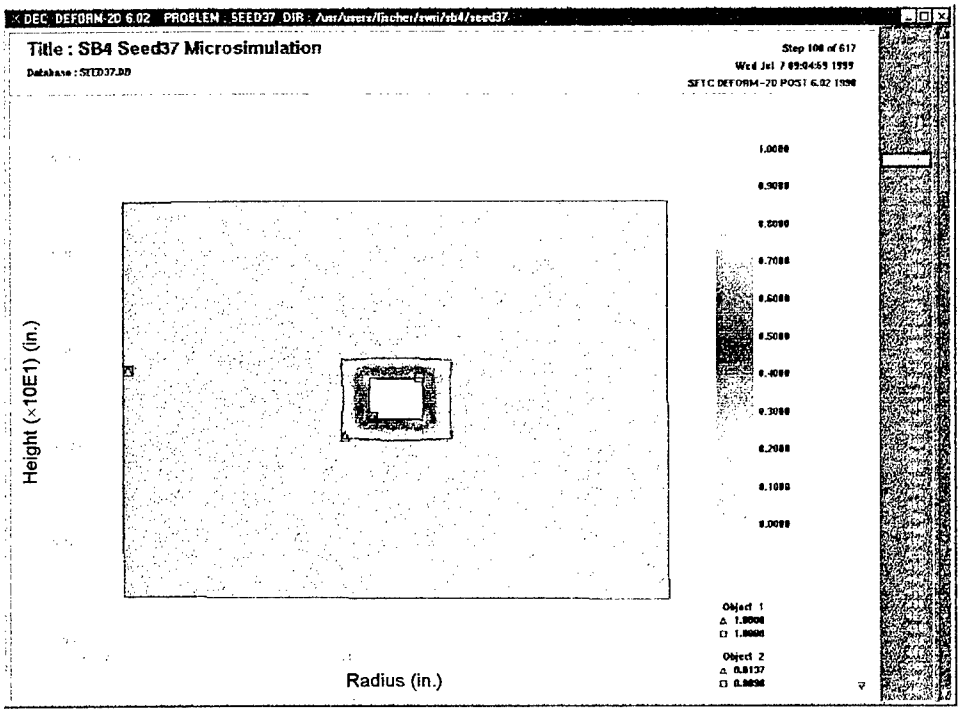


FIGURE D-10. SEED 37 STEP 100, DAMAGE DISTRIBUTION

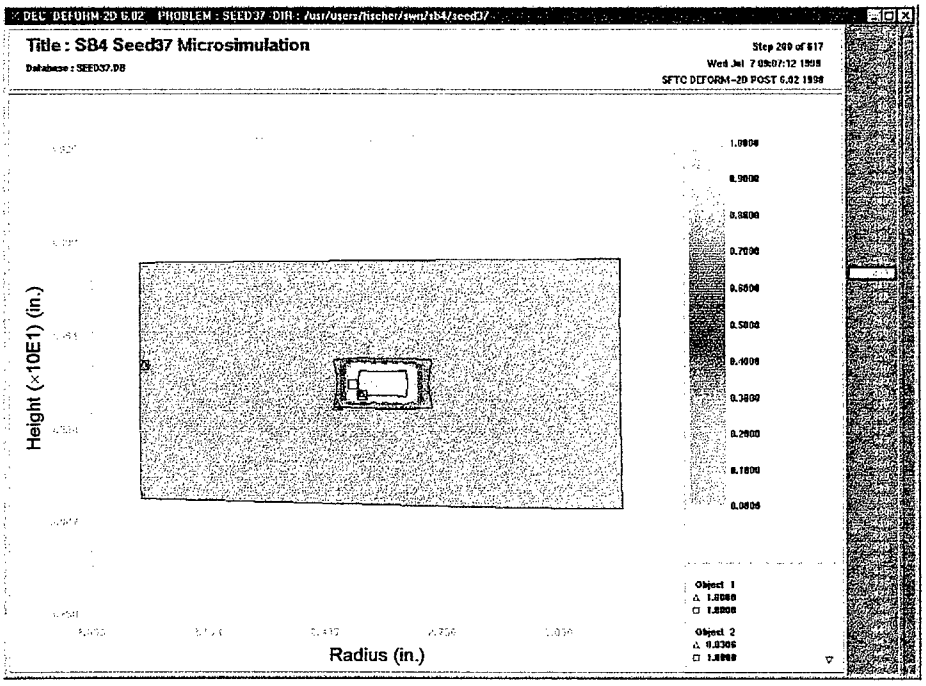


FIGURE D-11. SEED 37 STEP 200, DAMAGE DISTRIBUTION

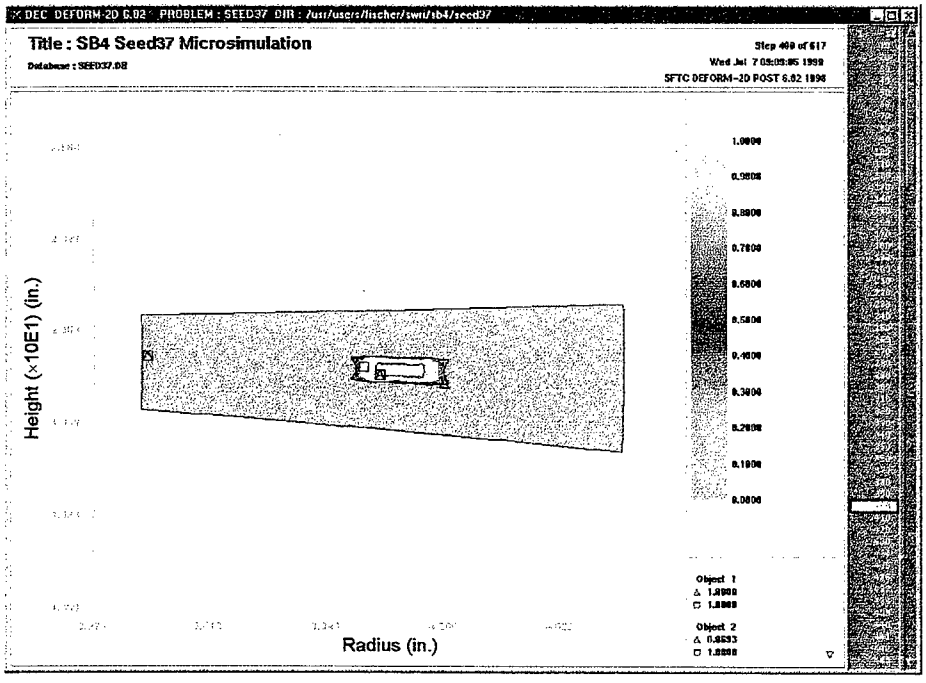


FIGURE D-12. SEED 37 STEP 400, DAMAGE DISTRIBUTION

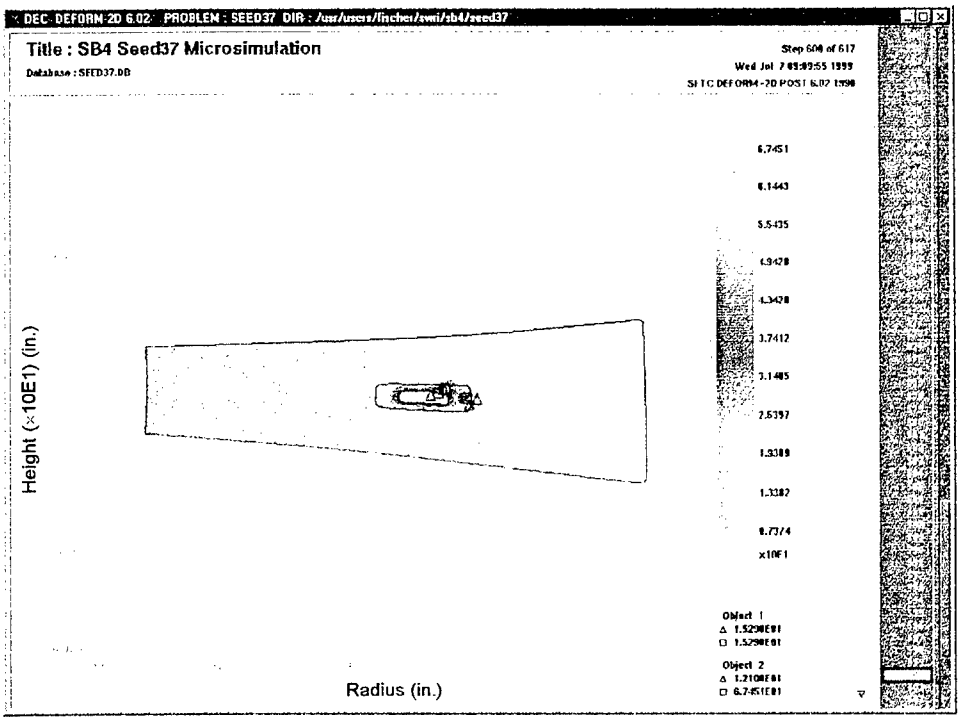


FIGURE D-13. SEED 37 STEP 600, STRESS DISTRIBUTION

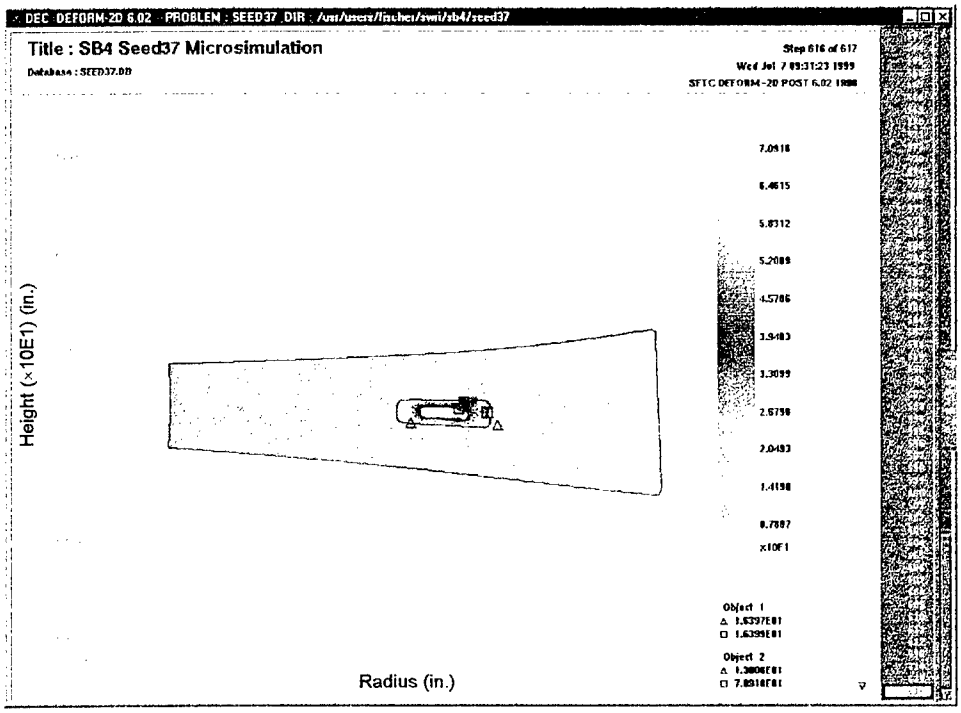


FIGURE D-14. SEED 37 STEP 616, STRESS DISTRIBUTION

D.3 SEED 41.

Seed 41 was located along the centerline of the part, at a height of 2.75". The inclusion was modeled as a circle. Since it is on the centerline, it is clipped to a half-circle with a radius of 0.050". The diffusion zone, also clipped, had an assumed radius of 0.100", and the microvolume had a radius of 0.500". The nitrogen content of the inclusion was a uniform 12%. The nitrogen content of the diffusion zone decreased linearly from 4% at the inside diameter (ID) to 0% at the outside diameter (OD).

A uniform mesh density was used for each object. Approximately 50 elements were used for the hard alpha inclusion, 100 elements for the diffusion zone, and 1000 elements for the matrix material.

Results are shown in figures D-15 through D-23.

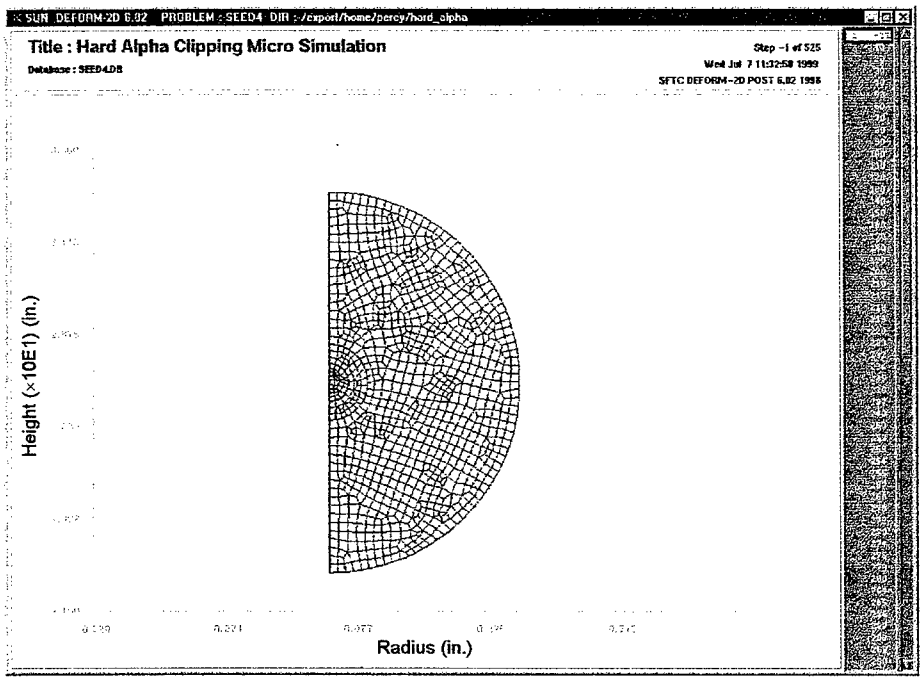


FIGURE D-15. SEED 41 INITIAL MESH
(Geometry is clipped at center line due to rotational (axial) symmetry.)

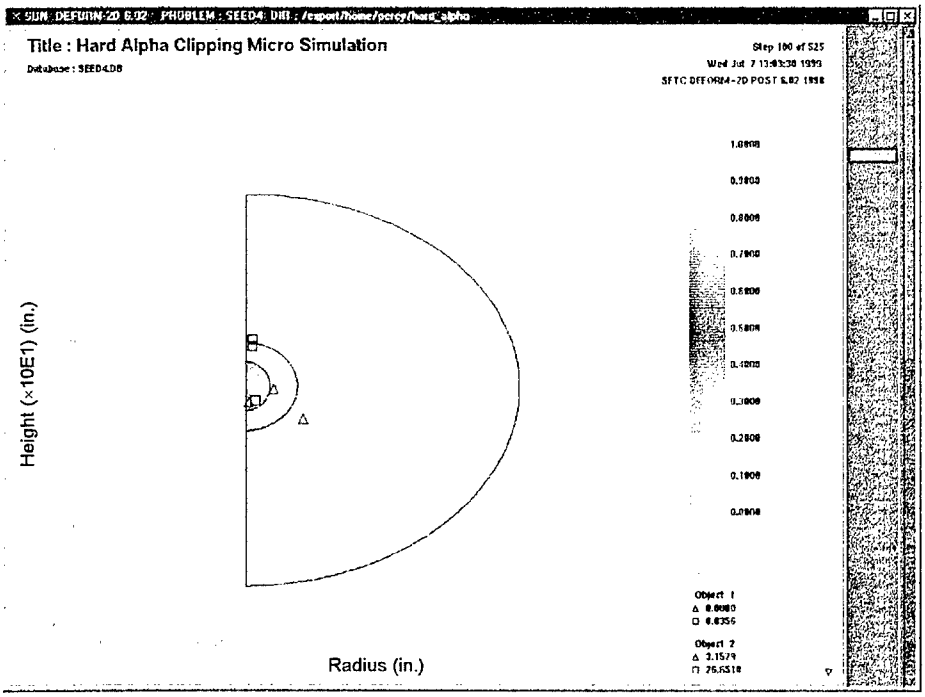


FIGURE D-16. SEED 41 STEP 100, DAMAGE DISTRIBUTION
(Note that damage has not begun to accumulate in hard alpha nugget. Damage in diffusion zone and matrix material is inconsequential.)

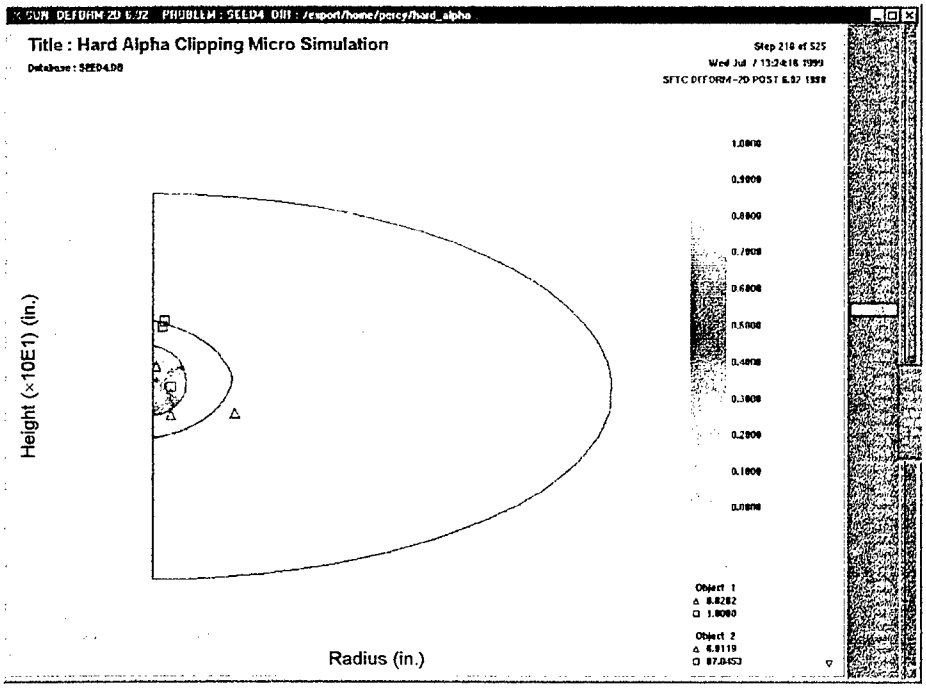


FIGURE D-17. SEED 41 STEP 218, DAMAGE DISTRIBUTION
(Note that damage is beginning to accumulate in the hard alpha object.)

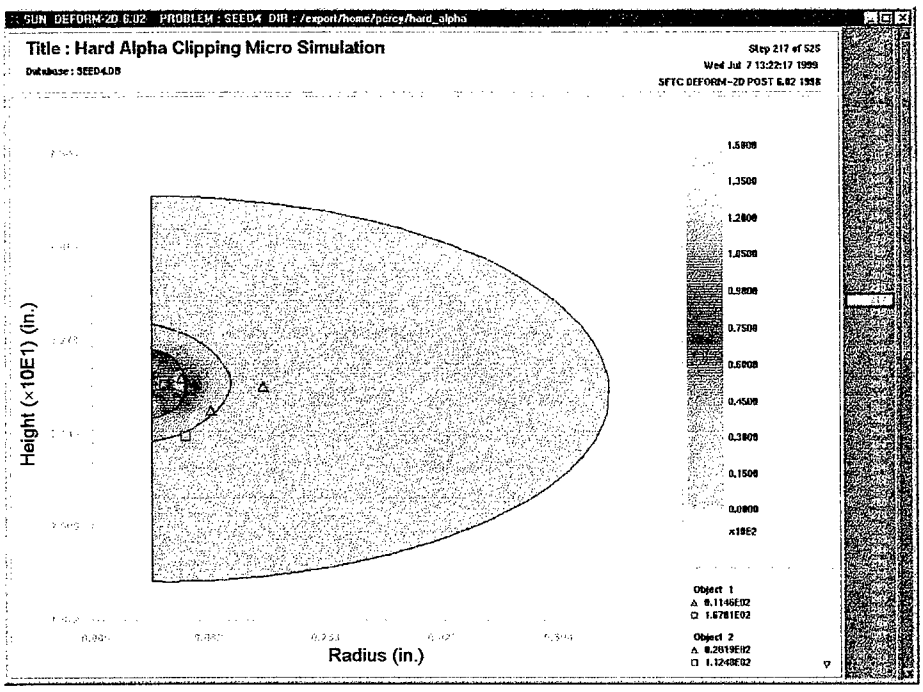


FIGURE D-18. SEED 41 STEP 217, STRESS DISTRIBUTION
(Note high stress in the hard alpha object, particularly the undamaged area.)

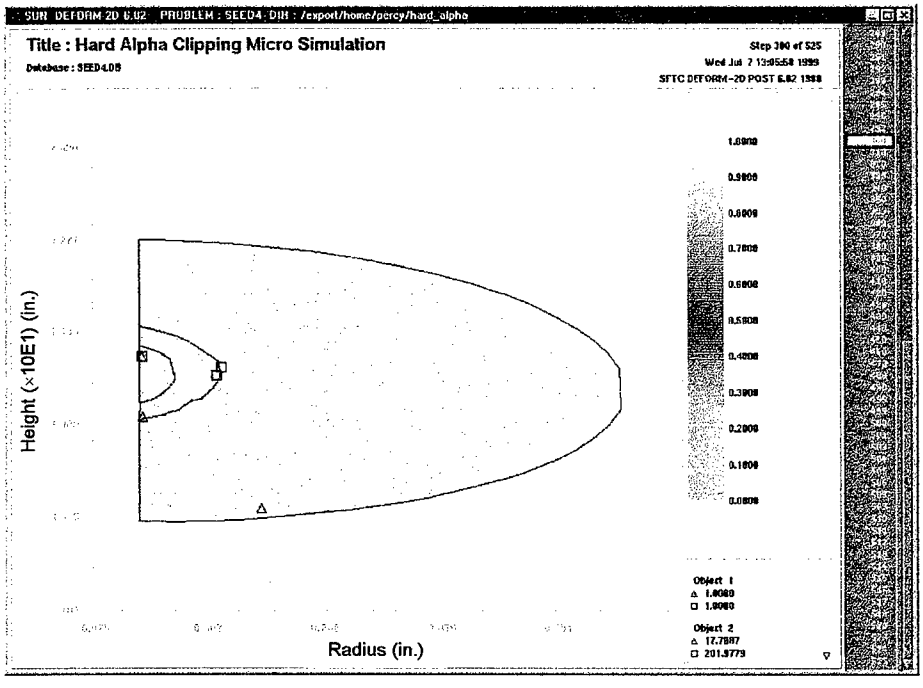


FIGURE D-19. SEED 41 STEP 300, DAMAGE DISTRIBUTION
(Note that damage has saturated in the hard alpha object.)

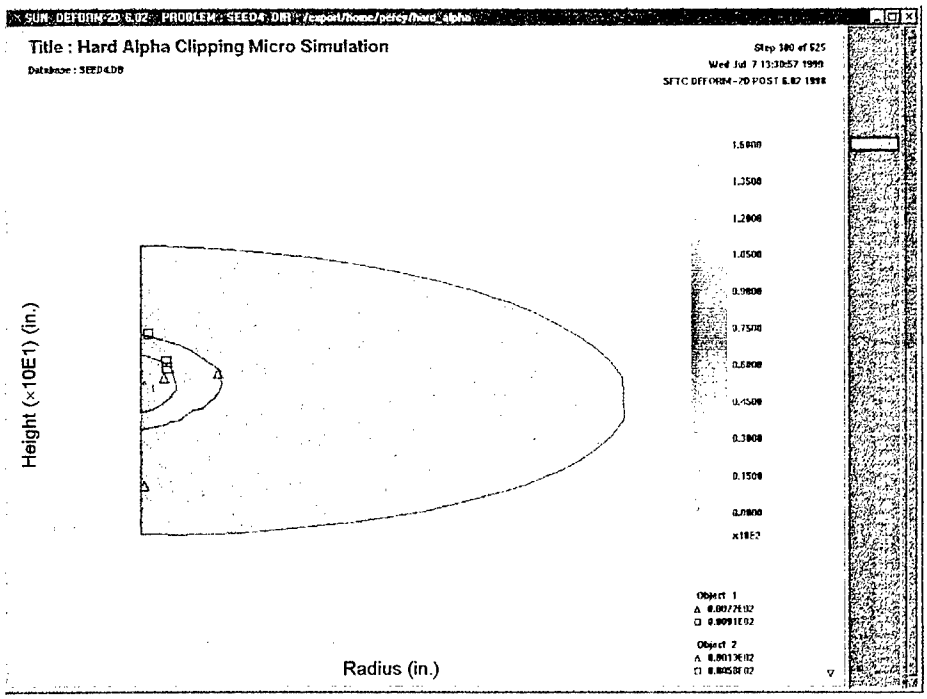


FIGURE D-20. SEED 41 STEP 300, STRESS DISTRIBUTION
(Note that the stress has dropped considerably from step 217.)

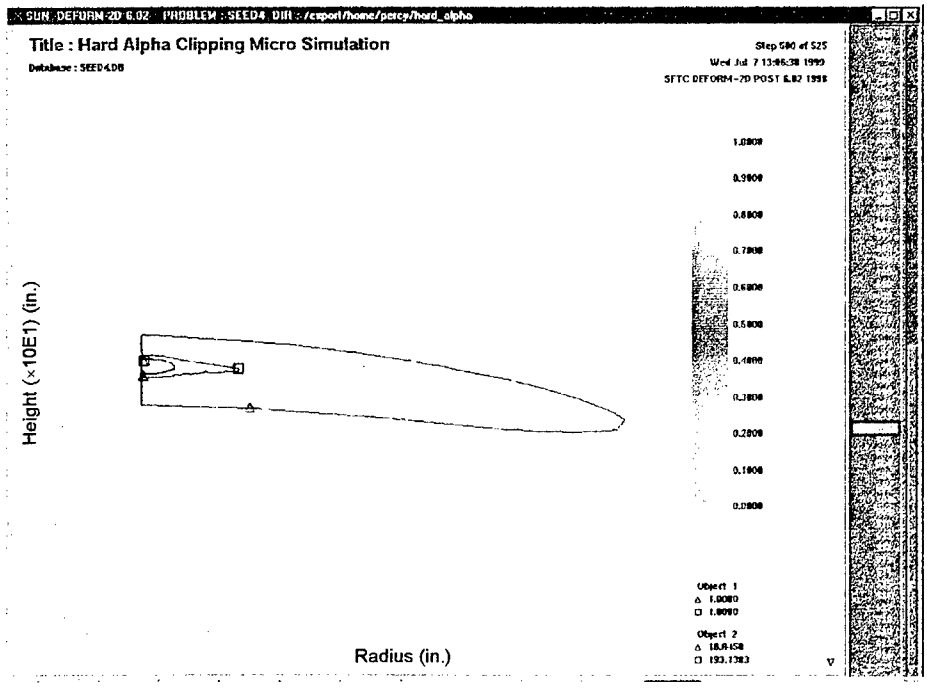


FIGURE D-21. SEED 41 STEP 500, DAMAGE DISTRIBUTION

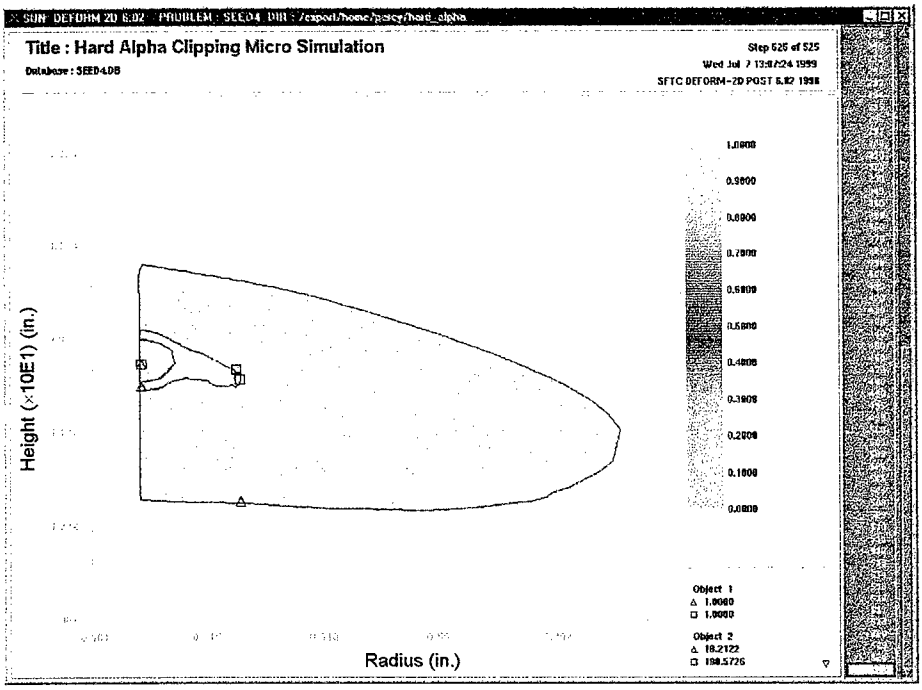


FIGURE D-22. SEED 41 STEP 525, DAMAGE DISTRIBUTION AND GEOMETRY AFTER BACKFLOW FORGING

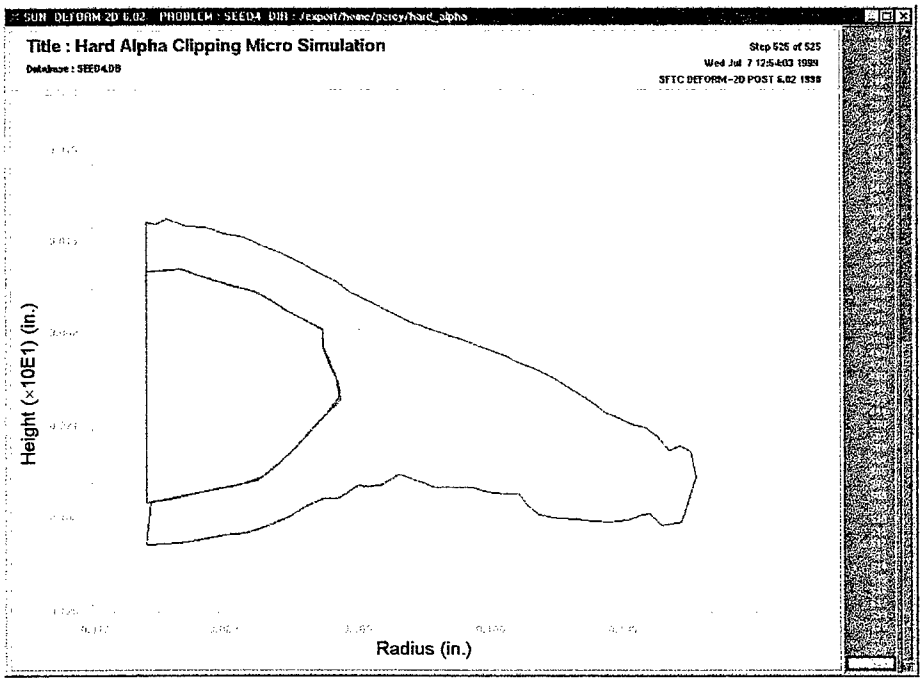


FIGURE D-23. SEED 41, FINAL GEOMETRY OF HARD ALPHA AND DIFFUSION ZONE

APPENDIX E—FORGING PROCEDURES AND SIMULATIONS

E.1 FORGING PROCEDURES OF PANCAKES AND DISKS AT PRATT & WHITNEY (P&W) GEORGIA.

Initial rough cutting of the Ti 6-4 CBS and seeded mults to an oversized length was completed through General Electric's Quality Technology Center (GE-QTC) facility. The mults were all clearly marked to identify locations of the defects and where to cut for final machining. The Contaminated Billet Study (CBS) mults (figure E-1) were then shipped to P&W in Columbus, Georgia, for final machining to the forging weight (figure E-2). A dimple was placed in the center of the mults for alignment in the forging press was also used to monitor the pancake orientation. Isothermal forging to an interim pancake shape was completed at P&W GA (figure E-3) followed by machining to a sonic shape (figure E-4). The slight distortion in the pancake forgings is attributed to the small diameter of the CBS mults.

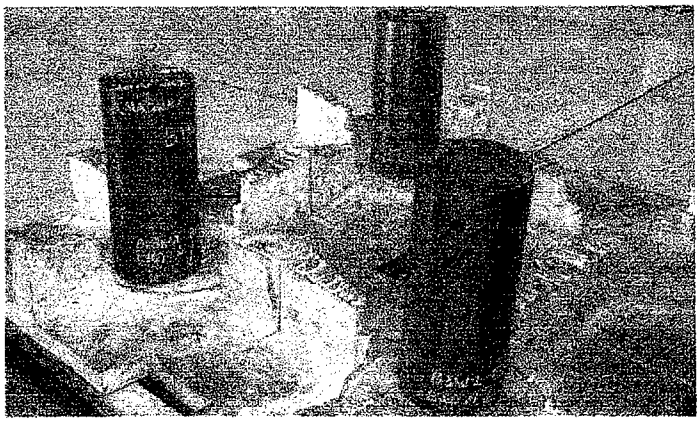


FIGURE E-1. RMI CBS MULTS AS RECEIVED AT P&W GEORGIA

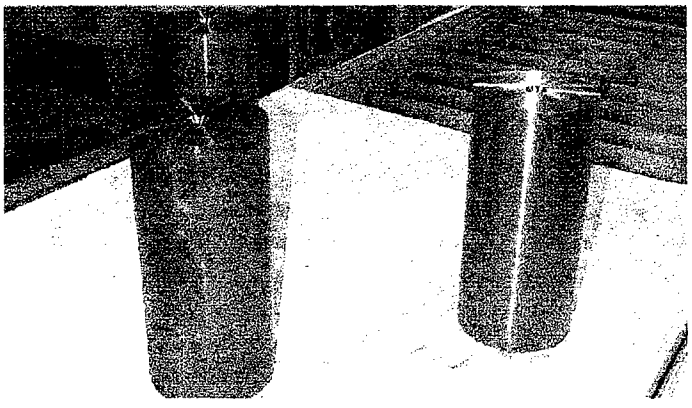
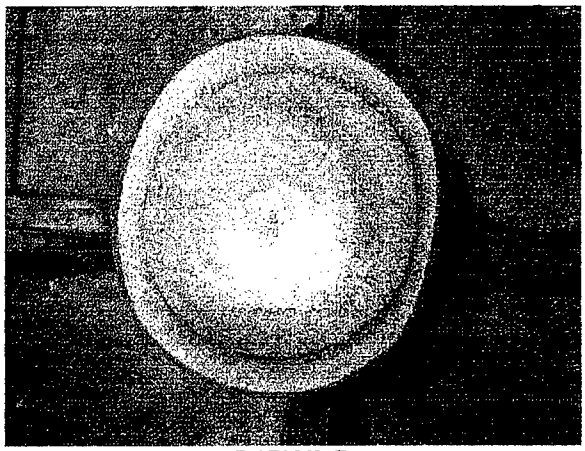
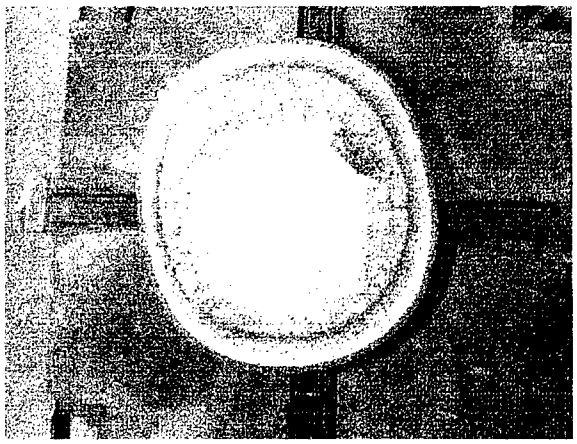


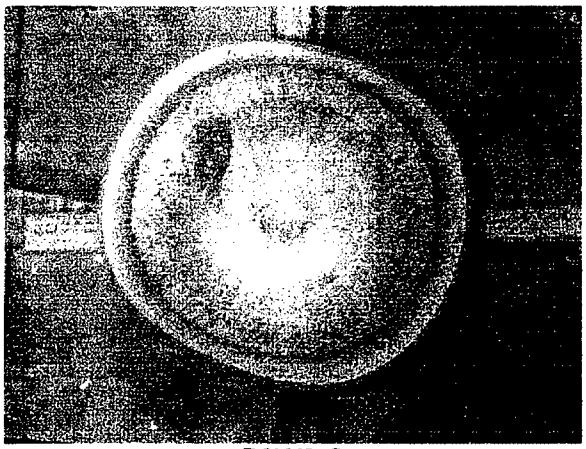
FIGURE E-2. RMI CBS MULTS MACHINED TO FORGING LENGTH



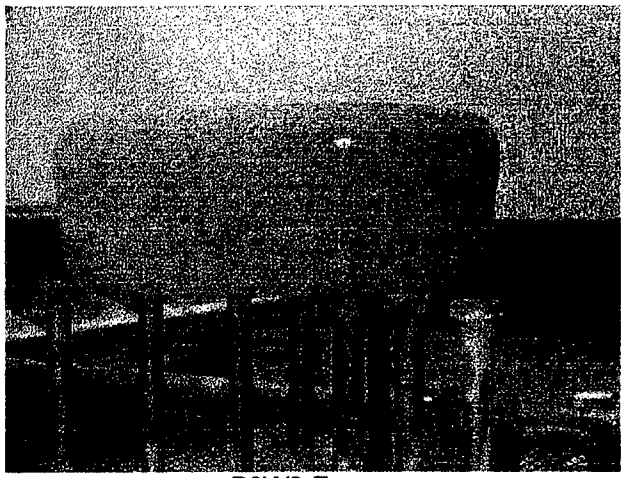
B1BW3-B



B3W2-E



B3W2-G



B3W2-E



B3W2-G

FIGURE E-3. RMI CBS PANCAKES

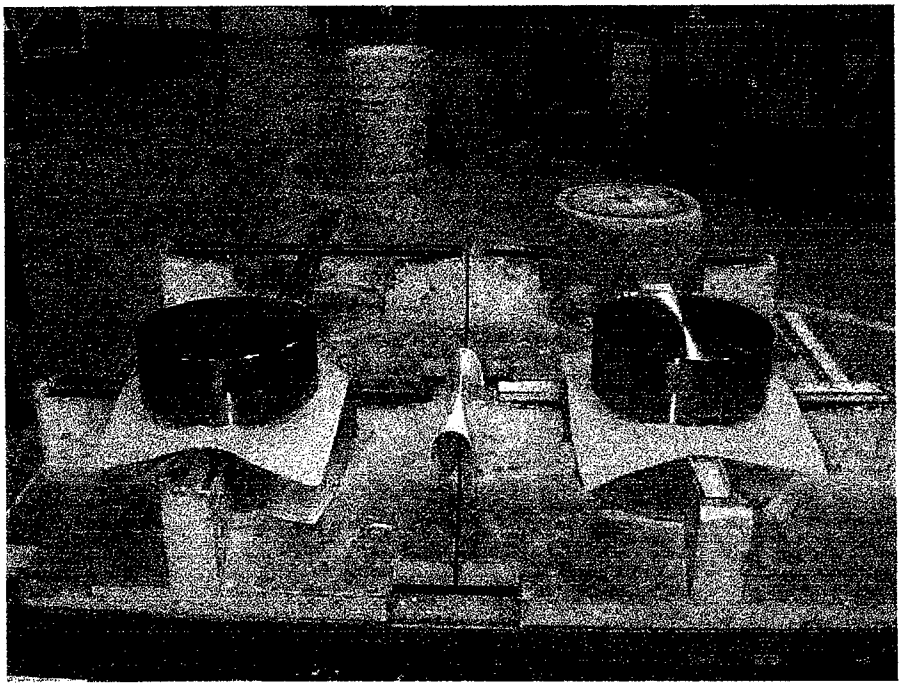


FIGURE E-4. RMI CBS PANCAKES MACHINED TO SONIC SHAPE

Seed placement in SB-5 and SB-6 was completed by the GE Corporate Research and Development (CRD) Center. The mults were then inspected at GE-QTC and P&W FL. As with the CBS mults, the seeded mults were then shipped to P&W GA for final machining to the forging weight (figure E-5), isothermal pancake forging (Figure E-6), and machining to a sonic shape (figure E-7). The larger diameter seeded mults did not experience the distortion observed in the CBS pancakes.

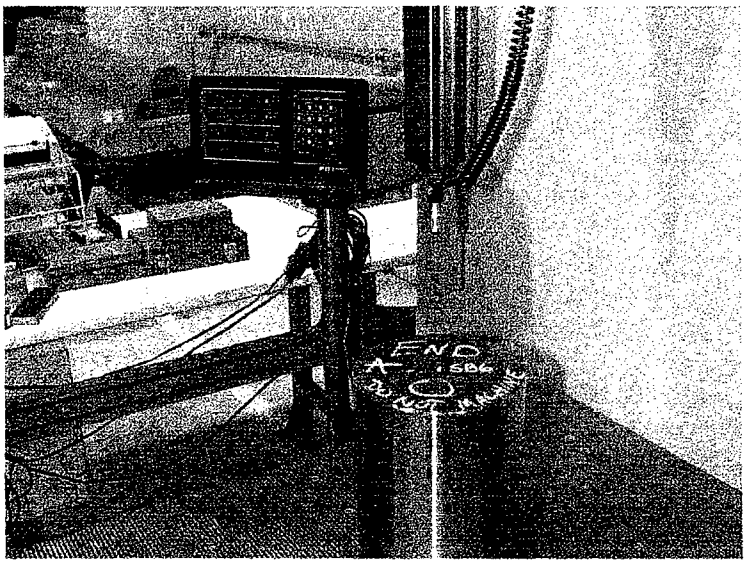
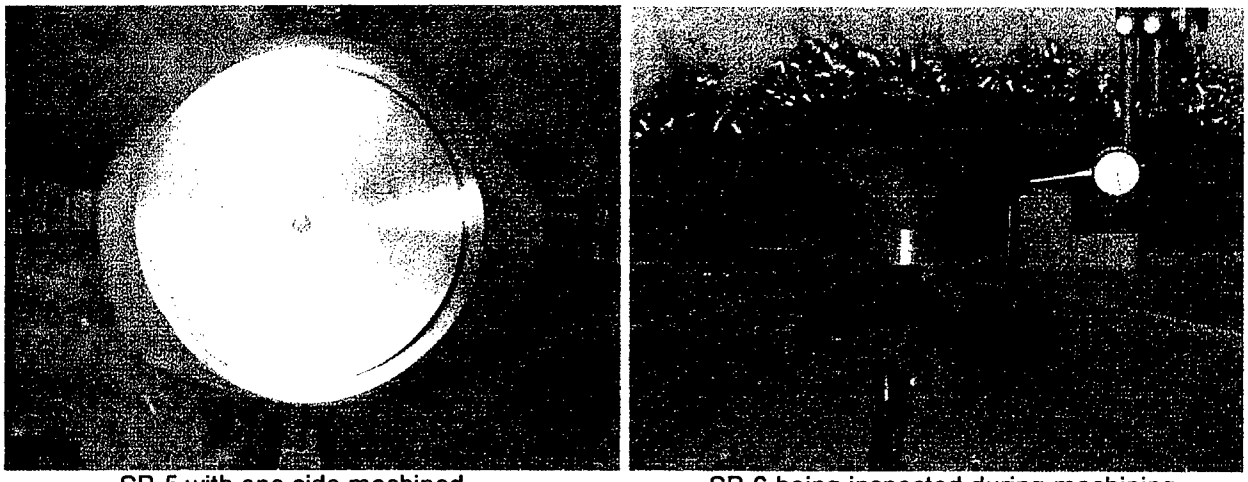


FIGURE E-5. SEEDED MULT SB-6 AS RECEIVED AT P&W GEORGIA



FIGURE E-6. SEEDED PANCAKE SB-6



SB-5 with one side machined

SB-6 being inspected during machining

FIGURE E-7. MACHINING OF SEEDED PANCAKES TO SONIC SHAPE

Following ultrasonic inspections four of the pancakes were isothermal forged into a final disk shape (figure E-8), heat treated, and machined to a sonic shape (figure E-9) at P&W GA.

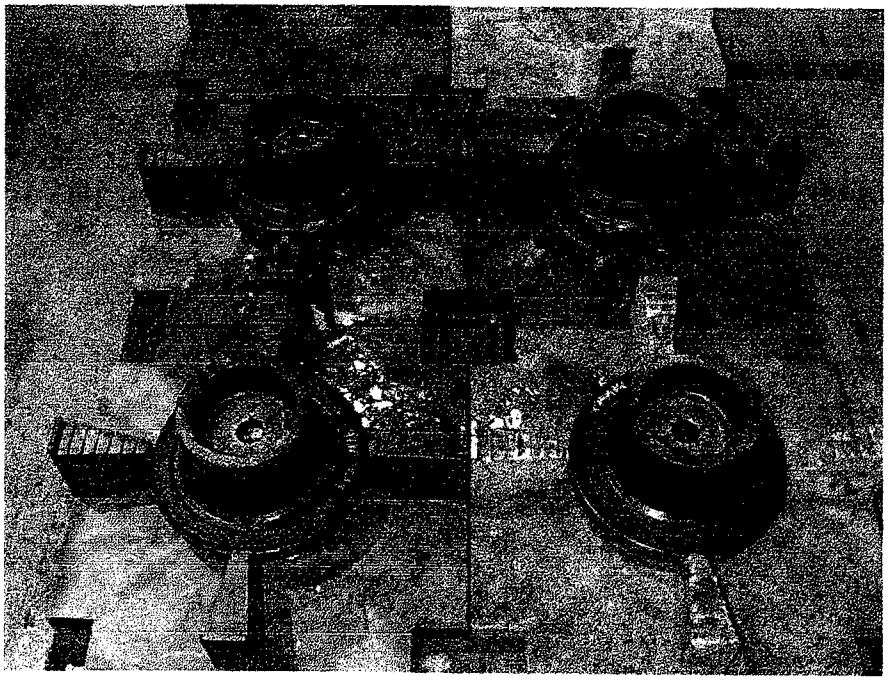


FIGURE E-8. FORGED DISKS AWAITING HEAT TREATMENT

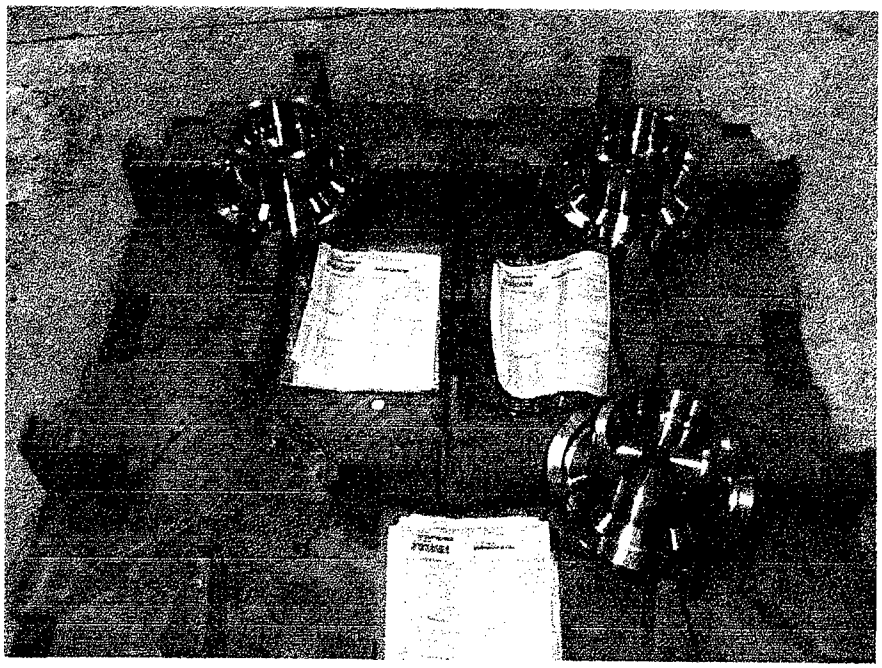


FIGURE E-9. THREE OF THE FOUR DISKS MACHINED TO SONIC SHAPE

E.2 SEED PLACEMENT IN MULTS SB-1, -2, -3, AND -4.

The engineering drawing of seeds placement in mults SB-1, -2, -3, and -4 are shown in figures E-10, E-11, E-12, and E-13.

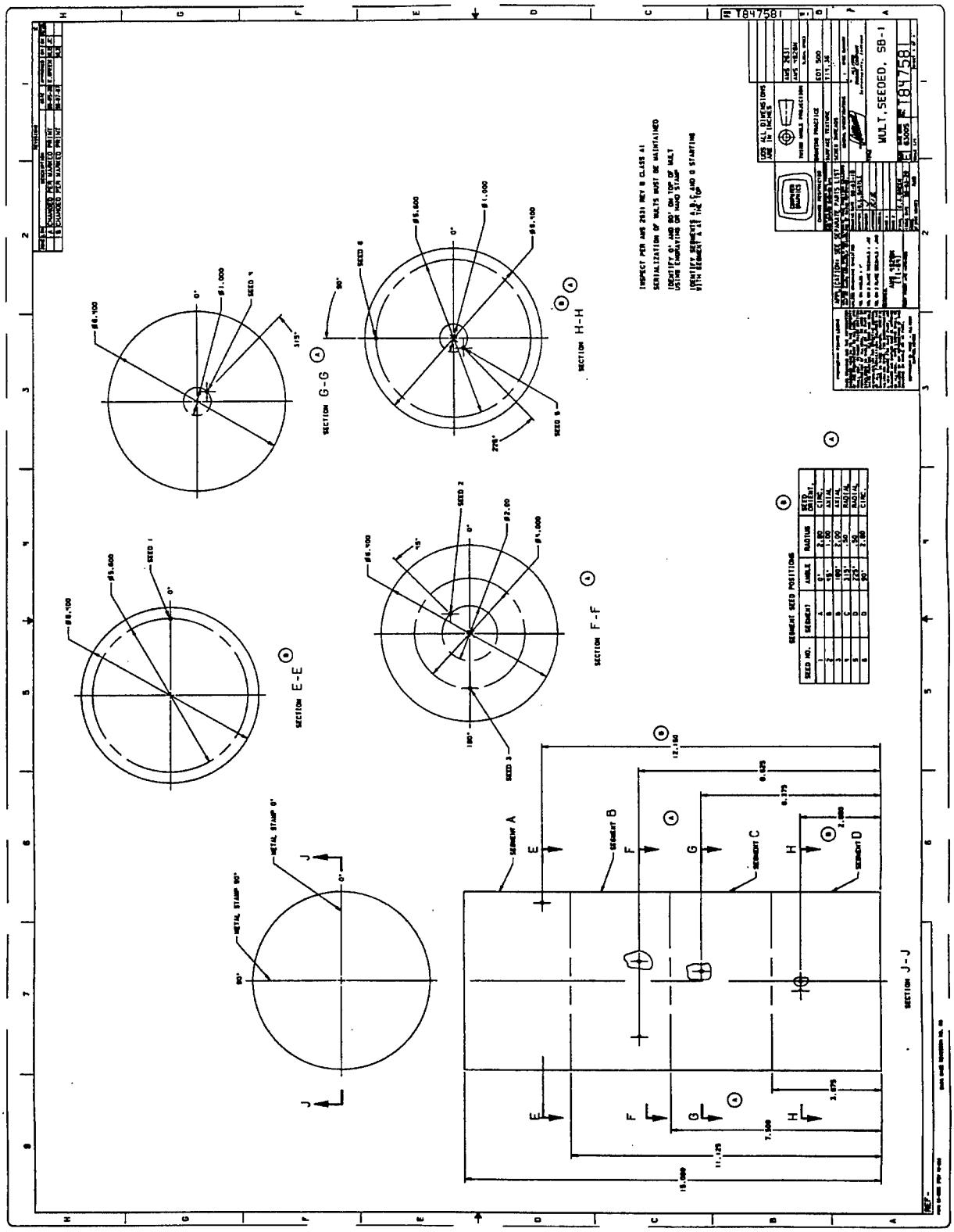


FIGURE E-10. ENGINEERING DRAWING OF SEED PLACEMENT IN MULT SB-1

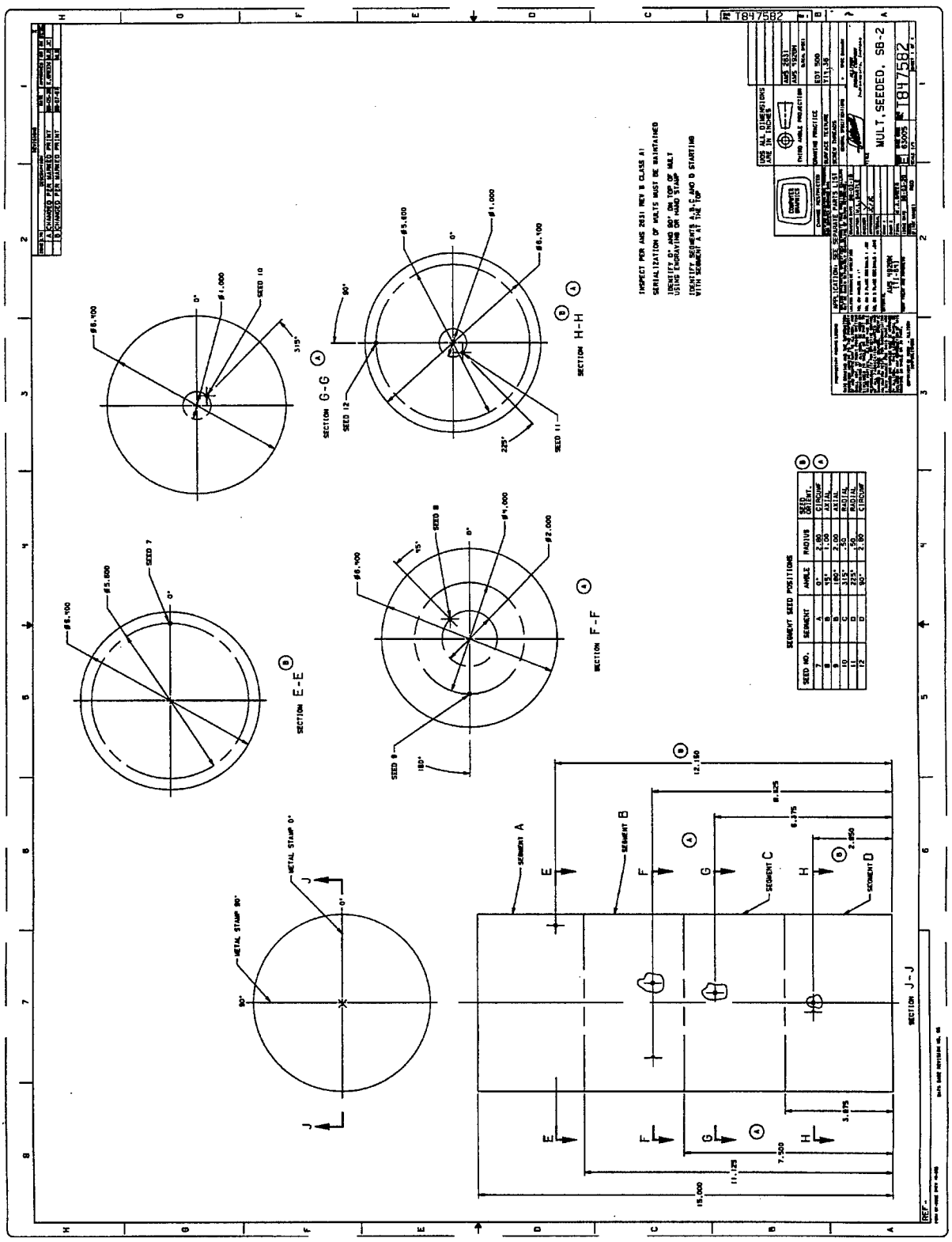


FIGURE E-11. ENGINEERING DRAWING OF SEED PLACEMENT IN MULT SB-2

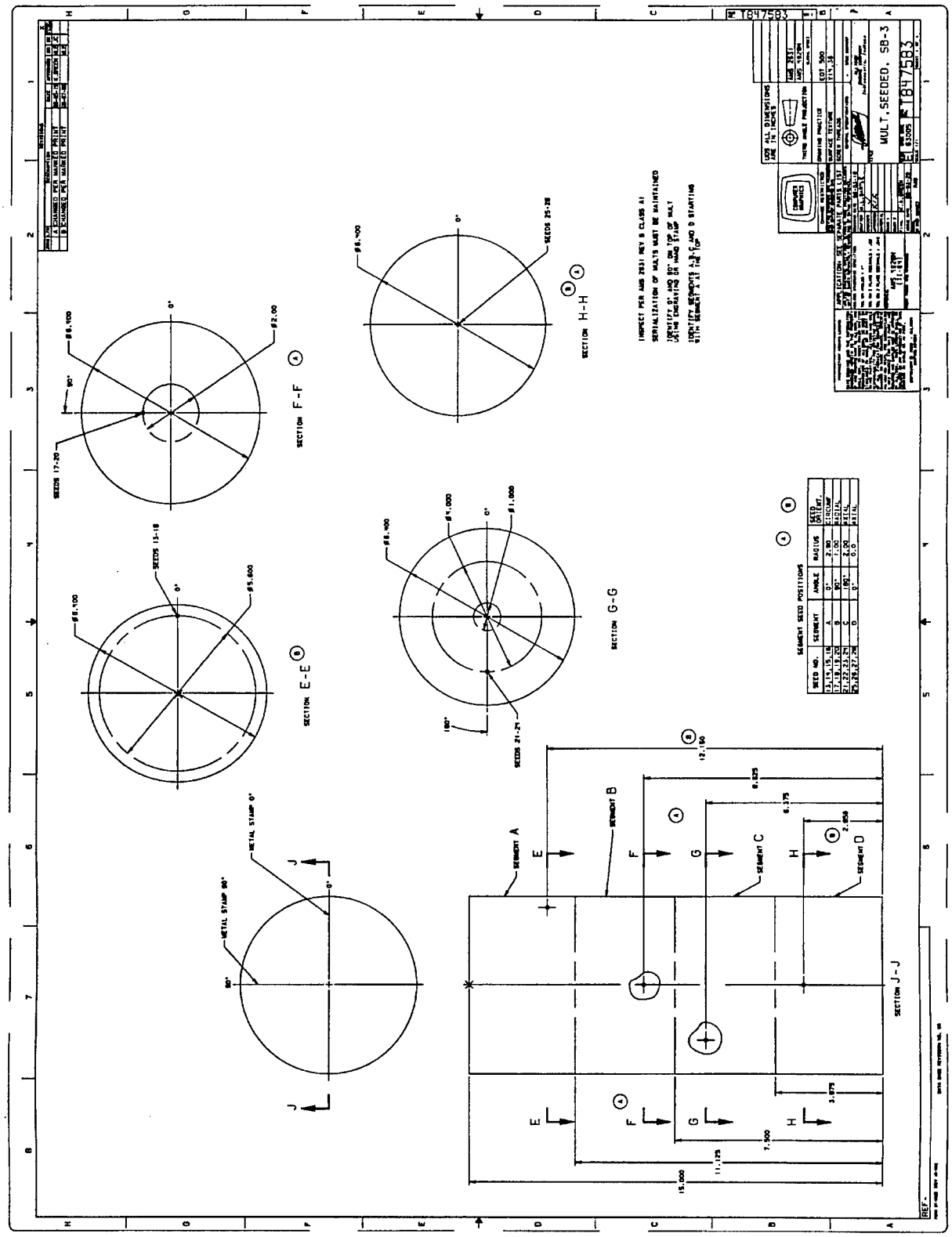


FIGURE E-12. ENGINEERING DRAWING OF SEED PLACEMENT IN MULT SB-3

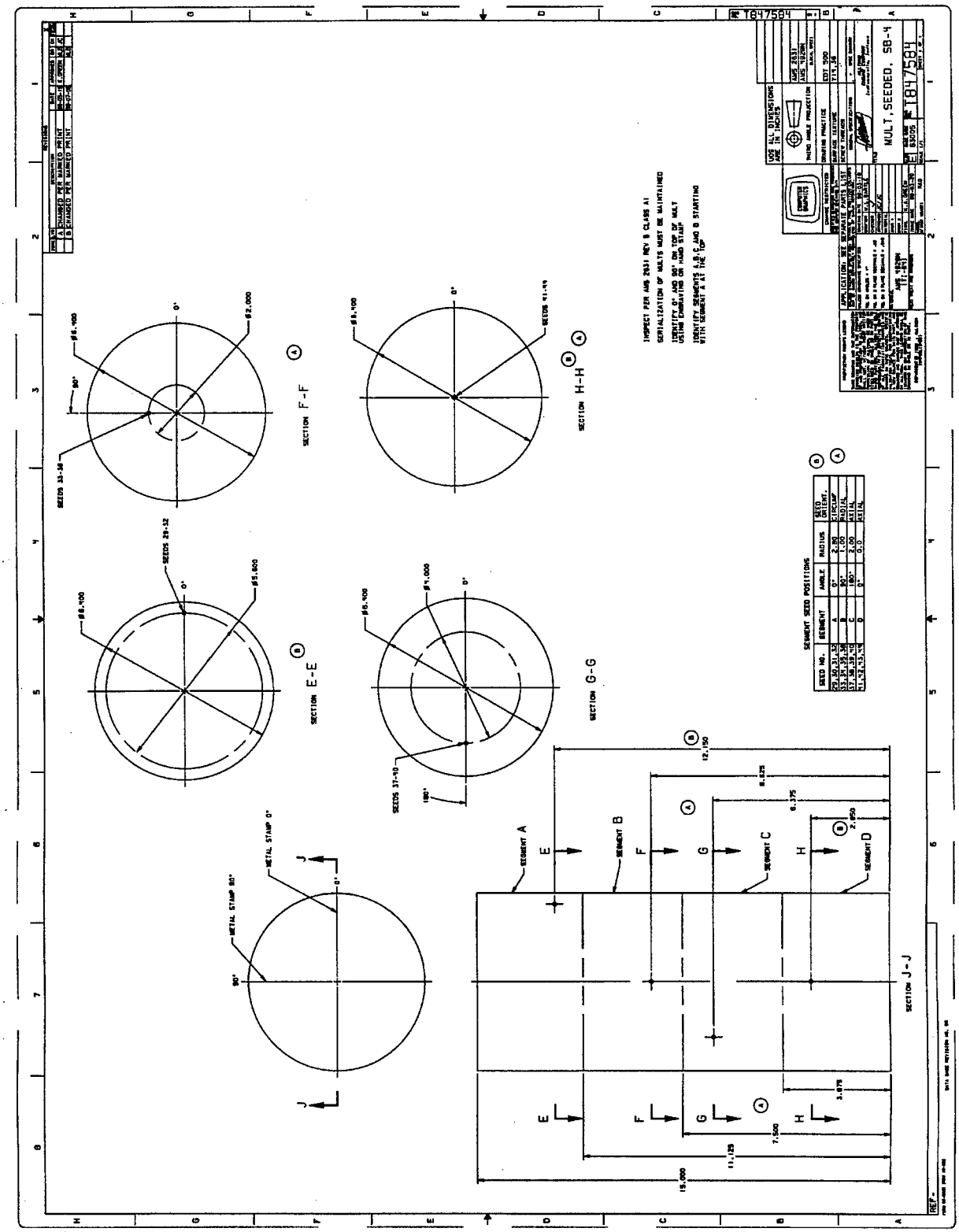
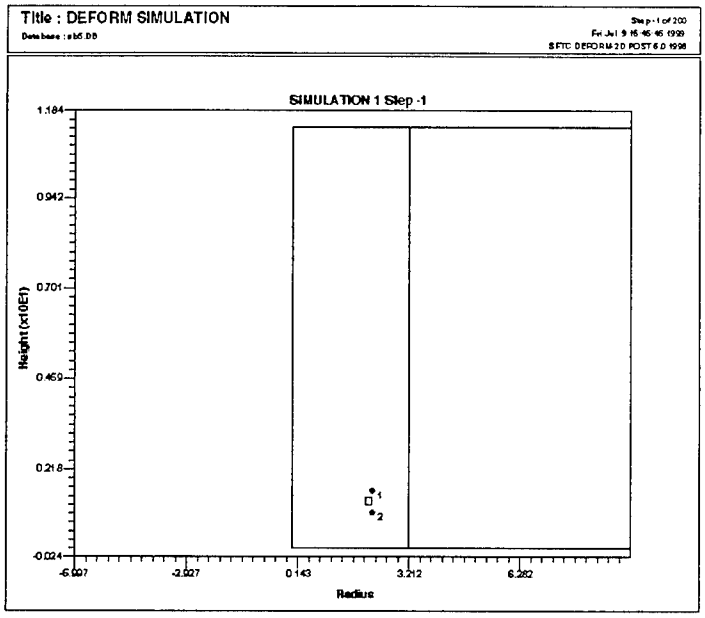


FIGURE E-13. ENGINEERING DRAWING OF SEED PLACEMENT IN MULT SB-4

E.3 COMPARISON OF PREDICTED AND MEASURED SEED LOCATIONS.

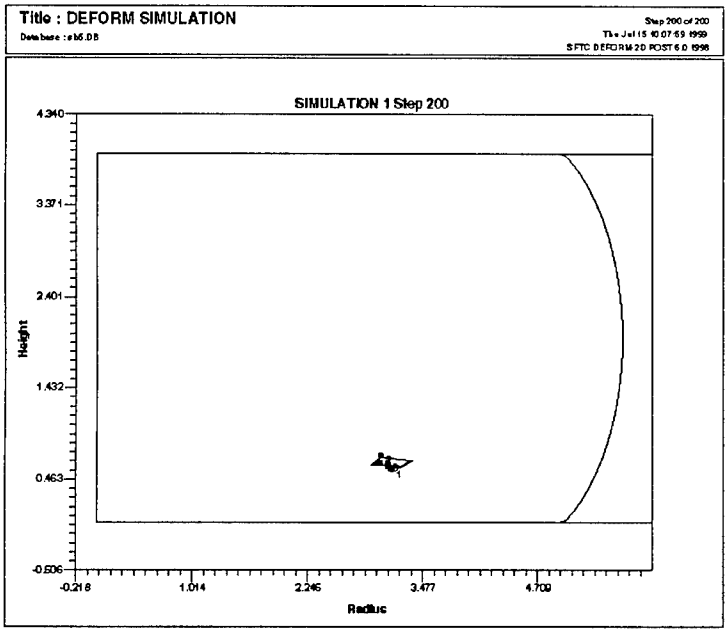
A comparison of the predicted and measured seed locations in forgings SB-5 and SB-6 are shown in figures E-14 through E-25.



Net indicates location of seed placement.

Points indicate defect locations from mult UT inspections.

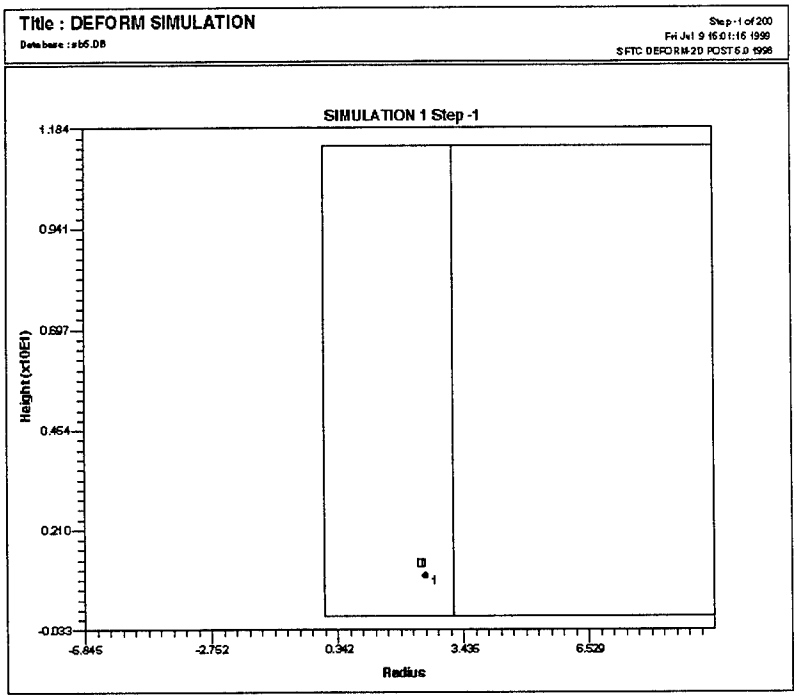
FIGURE E-14. SB-5 SEED 45 AND SB-6 SEED 49 PLACEMENT COMPARED TO LOCATIONS IDENTIFIED BY INSPECTION



Net indicates location predicted by DEFORM™ based seed placement.

Points indicate defect locations from pancake UT inspections.

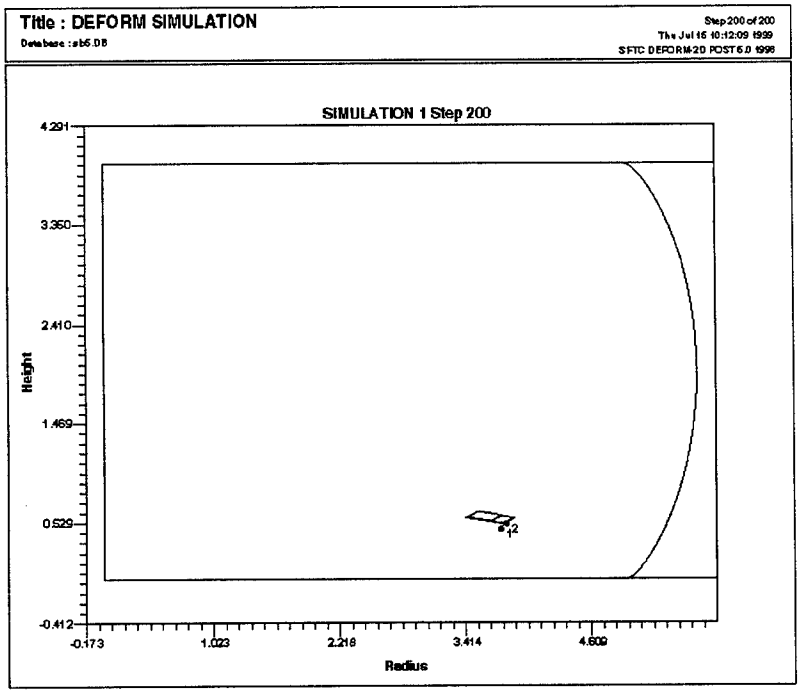
FIGURE E-15. SB-5 SEED 45 AND SB-6 SEED 49 DEFORM PREDICTION COMPARED TO LOCATIONS IDENTIFIED BY INSPECTION



Net indicates location of seed placement.

Point indicates defect location from mult UT inspection.

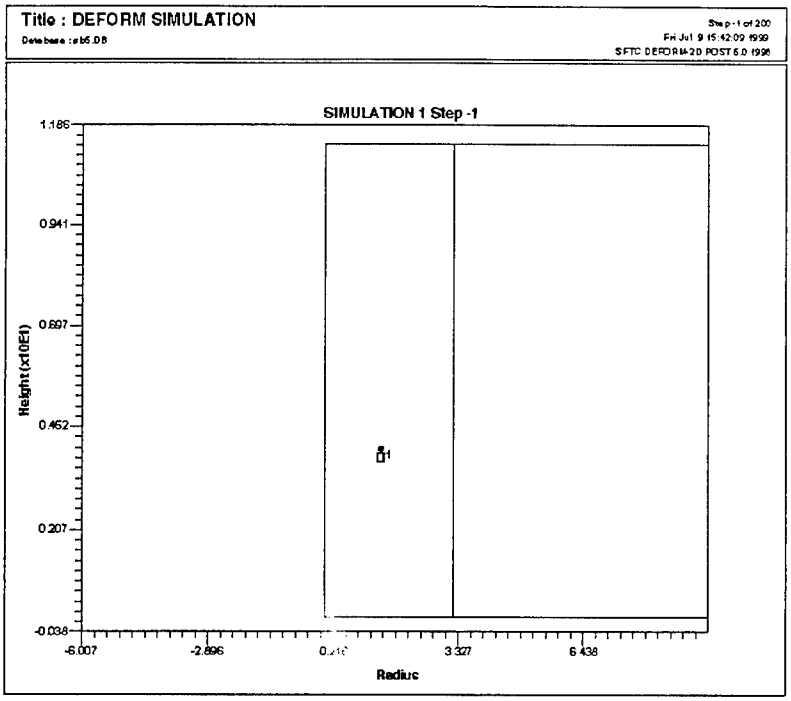
FIGURE E-16. SB-5 SEED 46 PLACEMENT COMPARED TO LOCATION IDENTIFIED BY INSPECTION



Net indicates location predicted by DEFORM™ based on seed placement.

Points indicate defect locations from pancake UT inspections.

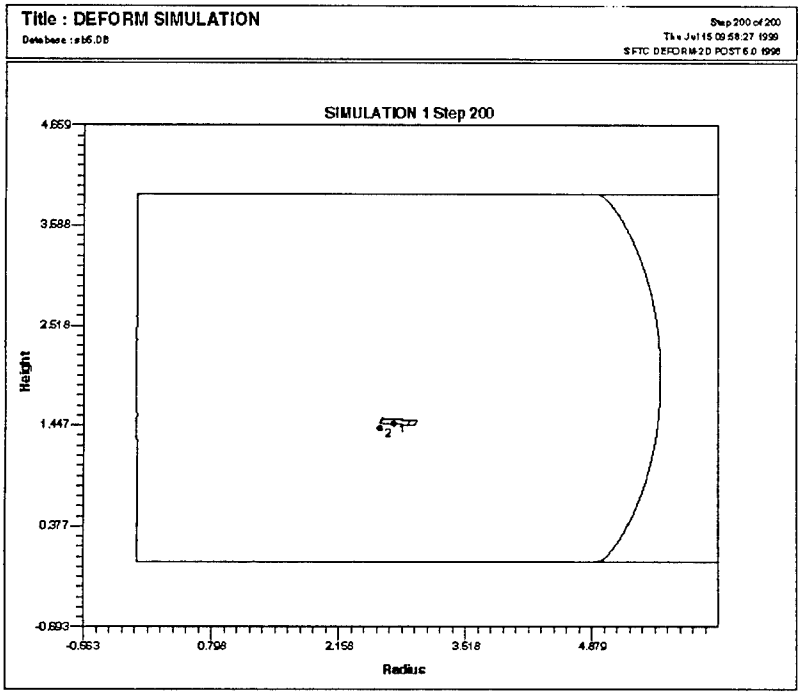
FIGURE E-17. SB-5 SEED 46 DEFORM PREDICTION COMPARED TO LOCATIONS IDENTIFIED BY INSPECTION



Net indicates location of seed placement.

Point indicates defect location from mult UT inspections.

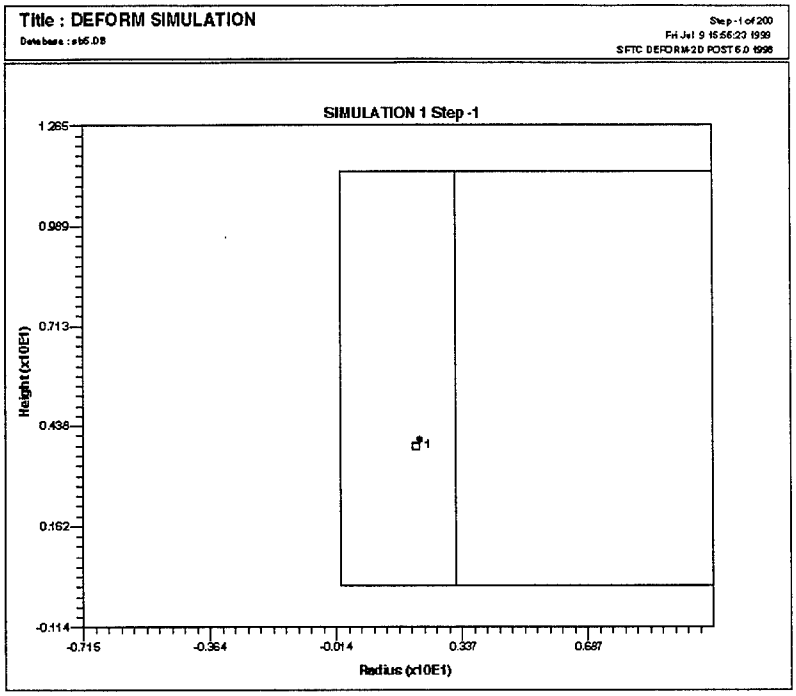
FIGURE E-18. SB-5 SEED 47 PLACEMENT COMPARED TO LOCATION IDENTIFIED BY INSPECTION



Net indicates location predicted by DEFORM™ based on seed placement.

Points indicate defect locations from pancake UT inspections.

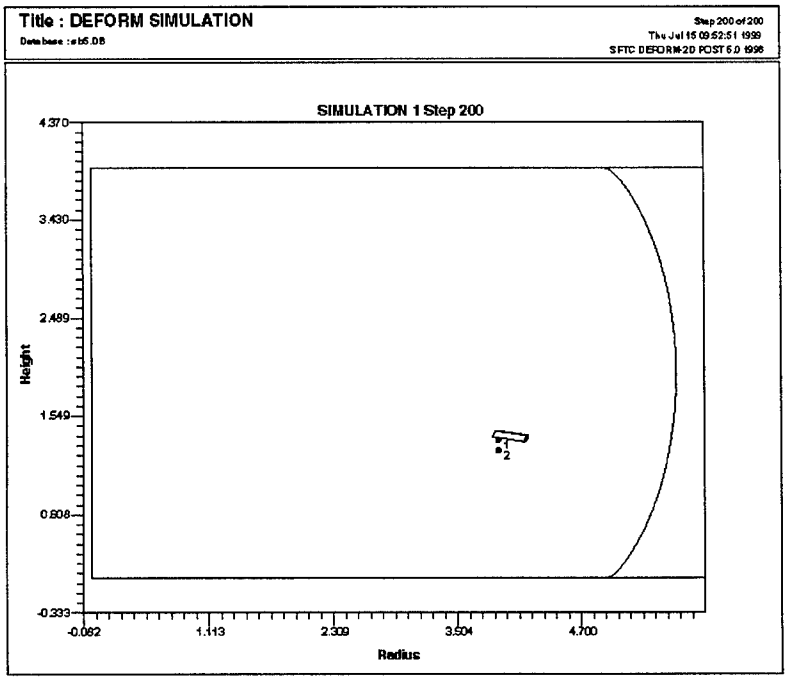
FIGURE E-19. SB-5 SEED 47 DEFORM PREDICTION COMPARED TO LOCATIONS IDENTIFIED BY INSPECTION



Net indicates location of seed placement.

Point indicates defect locations from mult UT inspection.

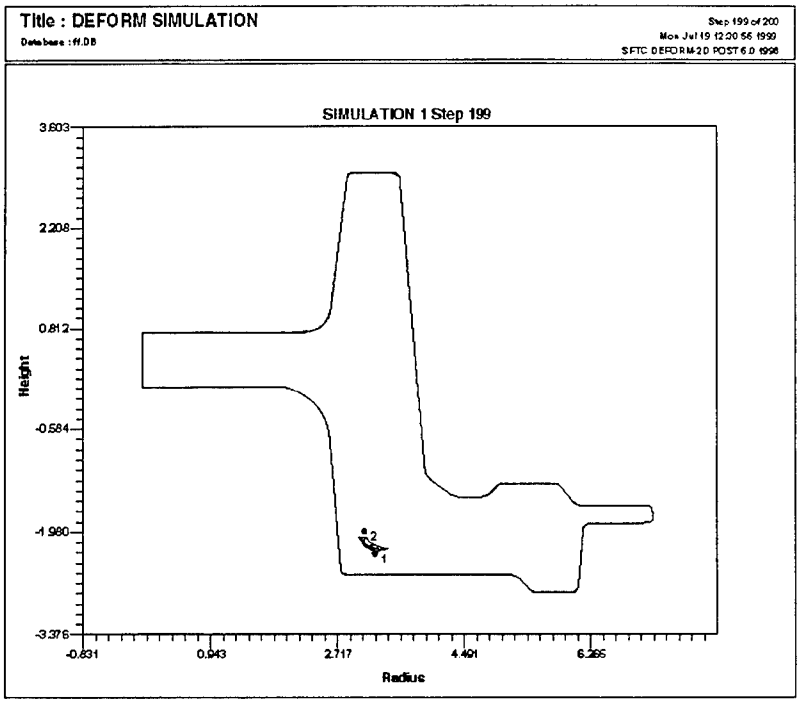
FIGURE E-20. SB-5 SEED 48 PLACEMENT COMPARED TO LOCATION IDENTIFIED BY INSPECTION



Net indicates location predicted by DEFORM™ based on seed placement.

Points indicate defect locations from pancake UT inspections.

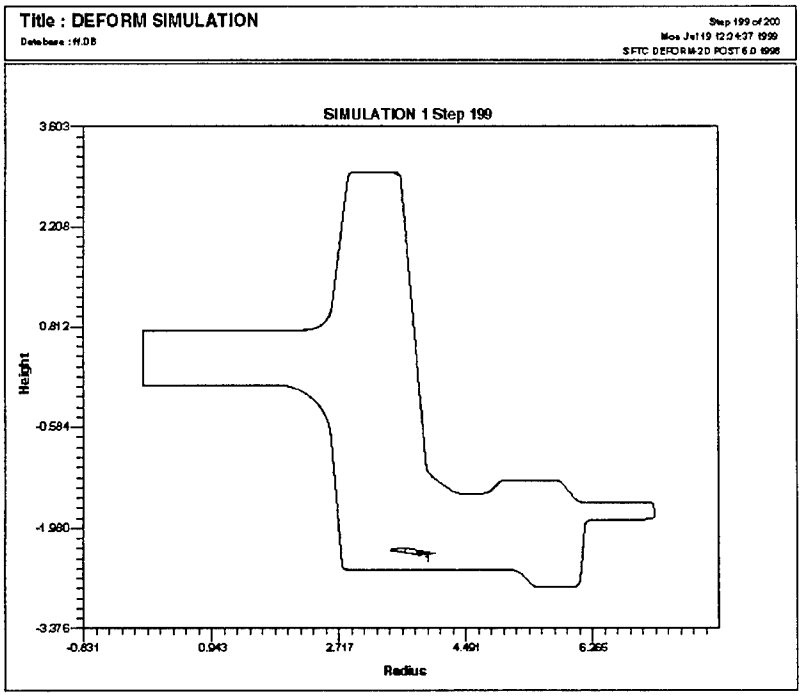
FIGURE E-21. SB-5 SEED 48 DEFORM PREDICTION COMPARED TO LOCATIONS IDENTIFIED BY INSPECTION



Net indicates location predicted by DEFORM™ based on seed placement.

Points indicate defect locations from disk UT inspections.

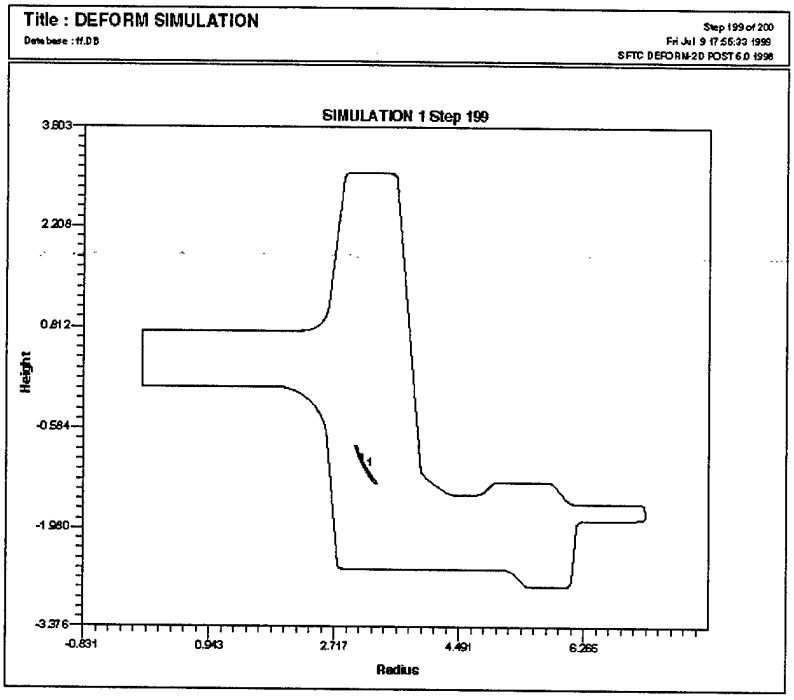
FIGURE E-22. SB-5 SEED 45 AND SB-6 SEED 49 DEFORM PREDICTION COMPARED TO LOCATIONS IDENTIFIED BY INSPECTION



Net indicates location predicted by DEFORM™ based on seed placement.

Point indicates defect location from disk UT inspection.

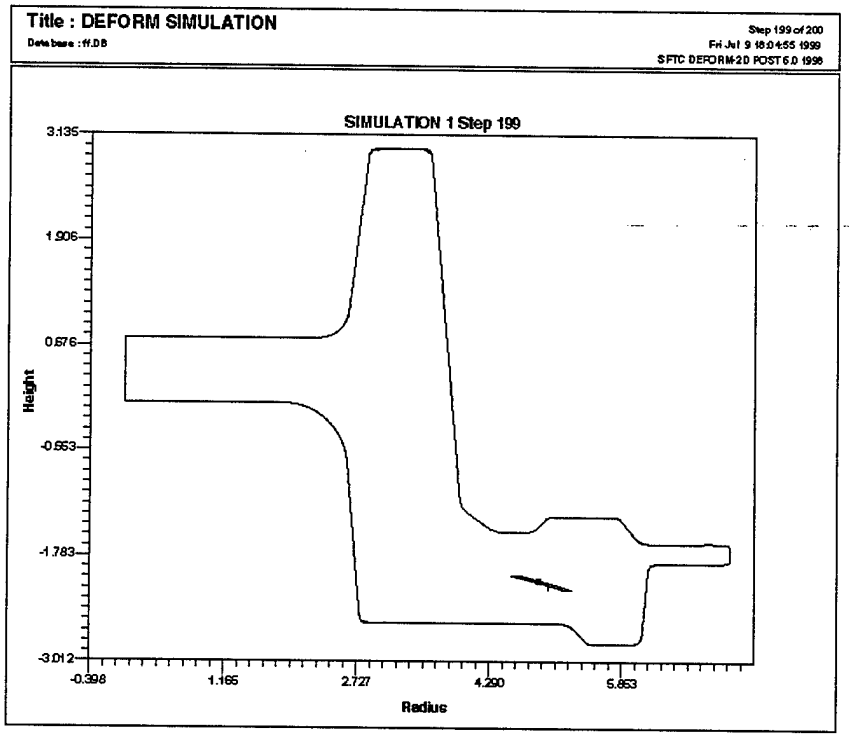
FIGURE E-23. SB-5 SEED 46 DEFORM PREDICTION COMPARED TO LOCATION IDENTIFIED BY INSPECTION



Net indicates location predicted by DEFORM™ based on seed placement.

Point indicates defect location from disk UT inspection.

FIGURE E-24. SB-5 SEED 47 DEFORM PREDICTION COMPARED TO LOCATION IDENTIFIED BY INSPECTION



Net indicates location predicted by DEFORM™ based on seed placement.

Point indicates defect location from disk UT inspection.

FIGURE E-25. SB-5 SEED 48 DEFORM PREDICTION COMPARED TO LOCATION IDENTIFIED BY INSPECTION

APPENDIX F—COMPILATION OF GENERAL ELECTRIC RESULTS FOR CONVENTIONAL AND MULTIZONE INSPECTIONS OF SEEDED AND RMI BILLETS/FORGINGS

TRMD Billet and Pancake Forging Data Summary

Column	a	b	c	d	e	f	g	h	i	j	k	l	m	n	o	p	q	r	s	t	u		v	w	x
	Billet Conventional				**Billet Multizone**										**Forging Conventional**								**Forging Multizone**		
Sample ID (# of Ind)	Ind #	U/T Depth	% of #3 FBH	S/N	HIP Depth	Zone	U/T Depth	HIP Axial	U/T Axial	% of #2 FBH	S/N	Ave Noise % #2	Dev Noise % #2	Peak Noise % #2	side	10 MHz-Zone	U/T Depth	Radial Dist	5 MHz-Zone	U/T Depth	Radial Dist		10 MHz-Zone	U/T Depth	Radial Dist
SB-1	1	N/I*	N/I*	N/I*	0.4	1	0.4	12.2	12.3	125+	7.7	13.75	2.5	23.75											
(6)	2	N/I*	N/I*	N/I*	2.2	3	2.2	8.6	8.5	125+	6.9	11.25	2.5	27.5											
	3	N/I*	N/I*	N/I*	1.2	2	1.2	8.6	8.6	125+	8.3	12.5	2.5	25											
	4	N/I*	N/I*	N/I*	2.7	4	2.5	6.4	6.5	125+	9.2	11.25	2.5	23.75											
	5	N/I*	N/I*	N/I*	2.7	4	2.7	2.9	3	121	9.8	11.25	2.5	23.75											
	6	N/I*	N/I*	N/I*	0.4	1	0.4	2.9	3	75	7.9	11.25	1.25	18.75											
SB-2	7	N/I*	N/I*	N/I*	0.4	1	0.4	12.2	12.3	111	10.8	13.75	1.25	22.5											
(6)	8	N/I*	N/I*	N/I*	2.2	3	2.2	8.6	8.6	78	4.6	13.75	2.5	26.25											
	9	N/I*	N/I*	N/I*	1.2	2	1.1	8.6	8.6	118	6.9	15	3.75	28.75											
	10	N/I*	N/I*	N/I*	2.7	4	2.7	6.4	6.5	125+	6.8	16.25	2.5	31.25											
	11	N/I*	N/I*	N/I*	2.7	4	2.7	2.9	3	98	5.2	13.75	2.5	31.25											
	12	N/I*	N/I*	N/I*	0.4	1	0.4	2.9	3	121	15.2	12.5	2.5	21.25											
SB-3	13-16	N/I*	N/I*	N/I*	0.4	1	0.4	12.2	12.2	125+	17.3	20	2.5	26.25											
(4)	17-20	N/I*	N/I*	N/I*	2.2	3	1.8	8.6	8.7	125+	8	12.5	2.5	27.5											
	21-24	N/I*	N/I*	N/I*	1.2	2	1	6.4	6.6	125+	7.7	12.5	3.75	26.25											
	25-28	N/I*	N/I*	N/I*	3.2	4	3.2	2.9	3.4	75	1.3	17.5	3.75	43.75											
SB-4	29-32	N/I*	N/I*	N/I*	2.2	3	2.5	12.2	12.3	125+	7.2	16.25	3.75	31.25											
(4)	33-36	N/I*	N/I*	N/I*	1.2	1	0.8	8.6	9.2	125+	13.4	20	2.5	28.75											
	37-40	N/I*	N/I*	N/I*	1.2	2	1.2	6.4	6.5	123	11.2	11.25	2.5	25											
	41-44	N/I*	N/I*	N/I*	3.2	4	3.2	2.9	3	120	8.7	16.25	3.75	28.75											
SB-5	45	N/I*			1.1	2	1	1.3	1.4	130	7.5	14	3.125	29.88	A	1	1	3.9	2	1.2	3.9		3	1.4	3.9
(4)															B	N/D**			2	2.1			6	2.1	3.9
	46	N/I*			0.8	1	0.7	1.3	1.4	84	8.1	12.5	3.125	25.2	A	1	0.3	3.8	2	1	3.8		3	1	3.8
															B	N/D**			2	2.3			5	2.3	3.8
	47	N/I*			1.8	3	1.8	4	3.9	73	6.4	12.5	3.125	25.2	A	1	1.2	2.6	2	0.5	2.6		1	0.4	2.6
															B	N/D**			2	2.9			6	3	2.6
	48	N/I*			1.1	2	1	4	3.9	110	6.8	14	3.125	28.32	A	1	0.5	3	N/D**		3		2	0.4	3
															B	N/D**			2	3			6	3	3
SB-6	49	N/I*			1.1	2	1	1.3	1.4	109	5.5	15	3.75	30	A	1	0.4	3	2	0.5	3		2	0.5	3
(1)															B	N/D**			2	2.9			6	2.9	3
B1BW3-B	1	N/D**	*	*	N/A	2	1	N/A	N/A	200	7.6	N/C	N/C	N/C	A	1	0.4	3.2	N/D**		32		1	0.4	3.2
(1)															B	N/D**			2	3			6	3	3.2
B3W2-E	1	1	92	4.5***	N/A	2	1.3	N/A	N/A	266	12.5	N/C	N/C	N/C	A	1	0.6	3.34	2	0.6	3.8		2	0.6	3.8
(1)															B	N/D**			2	2.9			6	2.8	3.8
B3W2-G	1	1.5	100		N/A	2	1.3	N/A	N/A	177	5.9	N/C	N/C	N/C	A	1	0.6	3	2	0.6	3		2	0.6	3
(1)															B	N/D**			2	2.8			6	2.8	3
B1BW3-A		N/I*	*	*	N/A	1	0.9	N/A	N/A	141	3.92	N/C	N/C	N/C	A	1	.388****	9****	*	*	*		1	0.4	9

* = not inspected

N/C = Not calculated

**** = Not found by conventional inspection. Found by Pratt & Whitney modified inspection.

*** = Signal/Noise ratios determined using Multizone software and provided for information only – normally not determined for conventional inspections

APPENDIX G—NONDESTRUCTIVE EVALUATION (NDE) AND METALLOGRAPHY OF PANCAKE FORGING CONTAINING RMI CBS DEFECT B1BW3-A

This appendix will cover the ultrasonic inspection and metallographic evaluation of hard alpha defect B1BW3-A as it was detected in both the billet and pancake forging forms. The hard alpha defect B1BW3-A was obtained from the Engine Titanium Consortium's (ETC) Contaminated Billet Study (CBS) billets. The CBS study is described in more detail in program progress reports prepared by the ETC for the Federal Aviation Administration (FAA) William J. Hughes Technical Center. While some details of the billet study will be presented here, this appendix will concentrate on the evaluation of the pancake forging manufactured from the CBS billet.

G.1 ULTRASONIC EVALUATION OF THE PANCAKE FORGING.

A section approximately 17 inches long was cut from one of the CBS 6-inch-diameter Ti-6Al-4V billets and forged by Schlosser Forge into a pancake approximately 1 inch thick by 21 inches in diameter. After minor surface preparation, the pancake forging was ultrasonically inspected using conventional and multizone inspection techniques.

A conventional inspection was conducted by Pratt & Whitney (P&W) at their West Palm Beach facility. A 10-MHz transducer was used. Although initial attempts were unsuccessful due to excessive noise levels, modification of the inspection resulted in detection of the hard alpha defect. The defect produced a reflected signal amplitude of 100% of Full Screen Height (FSH). This amplitude was approximately equal to that produced by a No. 1 Flat Bottom Hole (FBH) in their calibration sample. The indication appeared at a radius of about 9 inches and was about 0.380 inch below Side B of the pancake. The longest dimension of the indication, as measured from the ultrasonic C scan, was about 0.120 inch.

The pancake was then evaluated by General Electric (GE) Aircraft Engines at their Quality Technology Center in Cincinnati, Ohio. A multizone inspection was conducted using an F8-TLC Company 10-MHz transducer with a 3-inch focal length. The pancake surface was scanned using a 0.020-inch index, and the sensitivity was set so that the signal from the indication was not saturated (i.e., exceeded 100% FSH). The pancake thickness was divided into two 0.5-inch-thick zones for inspection. The two zones were evaluated by successively focusing the transducer on the top and bottom pancake surfaces and gating the signal so the volume of material between 0.100 inch and 0.600 inch below the surfaces was interrogated. This inspection produced an indication with amplitude of 50% FSH. This amplitude was about 62% of that produced by a No. 1 FBH in their calibration sample. The indication appeared at about the same location as determined in the P&W evaluation. The largest dimension of the indication as determined from the C scan was about 0.100 inch.

GE also performed a second inspection of the pancake using the procedure they consider to be a conventional inspection. For this evaluation, the same transducer used in the multizone inspection was applied. The transducer was again focused at the surface, and a 0.025-inch index was used. The primary difference between this inspection and the multizone was that the signal was gated between 0.100 inch and the back surface rather than the multizone approach of gating between 0.100 inch and 0.600 inch. Distance Amplitude Correction (DAC) was applied to adjust sensitivity to a uniform No. 1 FBH level throughout the pancake thickness. Results of this

inspection revealed the indication could not be detected due to the high noise level of the inspection.

Upon completion of the GE inspection of the pancake forging, the indication was cut from the forging for further evaluation. A 1-inch cube of material around the indication was machined from the pancake and ultrasonically inspected using a higher frequency transducer to obtain improved detail. An F10 Panametrics 25-MHz transducer was used, with a 0.005-inch index. A No. 1 FBH calibration was used and the signal gated between 0.250- and 0.550-inch depth of the cube. Radio Frequency (RF) waveforms were also collected from inspections of all six sides of the indication. They will be available for a more detailed characterization of the indication in conjunction with future waveform data to be collected from samples to be produced later in the program. These results confirmed the more spherical shape of the hard alpha inclusion and identified its maximum dimensions as about 0.100 by 0.100 inch. This appears to be markedly different from the elongated cigar shape noted in the billet ultrasonic inspection.

G.2 METALLOGRAPHIC EVALUATION OF THE PANCAKE FORGING.

Following ultrasonic inspection of the forged pancake, the 1-inch cube was metallographically sectioned to determine the microstructural characteristics of the indication. Orientation of the cube was identified so that the metallographic polishing would proceed along the same plane as the ultrasonic beam as it entered the forged pancake. The sample was mounted and polishing began based on the location of the indication provided by the ultrasonic inspection. As the polishing approached the location of the indication, small layers (about 0.010 inch) were removed and the specimen examined. Once the diffusion zone was detected, increments of about 0.010 inch were removed and photographs taken to document the size and characteristics of the indication.

After the indication had been polished through about 0.050 inch, a microprobe analysis was conducted to determine the elemental and interstitial chemical composition. Results of the microprobe analysis, shown in table G-1, indicate the maximum nitrogen content of this hard alpha inclusion to be about 4.9%. When viewed in conjunction with the metallographic section (Step 14) shown in figure G-1, a sharp drop in nitrogen content is seen when the probe evaluates areas just outside the white nugget area. The value of about 0.5% to 1% appears to be representative of the diffusion zone around the nugget. Also shown in figure G-1 is the results of a hardness traverse across the nugget. Note that hardness values are about 40 Rockwell C in the matrix and rise to over 60 Rockwell C in the nugget.

A large number of photos were taken at all polishing steps through the indication. When assembled, they show the character of the hard alpha as the polishing proceeded through the diffusion zone, to the nugget, and back out through the diffusion zone. Montages of the indication at these polishing steps are available but will not be included in this report. The photomicrographs shown in figures G-2 through G-6 are representative of the nugget geometry and character. Note the significant diffusion zone and the extensive cracking and voiding around the white nugget. From these photos, it is apparent that the forging operation did not close the voiding and cracking which is typical of hard alpha inclusions as they have been observed in billets by the ETC.

TABLE G-1. MICROPROBE RESULTS

Mt. 98-3598

FILE LABEL: QF(3598) 98-073
WEIGHT% DATA FOR POINTS 6 TO 26

											— In / near defect area — (min beam diameter)		
POINT	TI-K	AL-K	V-K	CR-K	SN-L	MO-L	ZR-L	SI-K	FE-K	TOTAL	O Kd *	C Kd *	N Kd *
6	90.75	7.57	2.12	0.07	0.01	0.00	0.00	0.03	0.02	100.57	< MOL	< MOL	< MOL
7	90.63	7.38	2.17	0.03	0.02	0.04	0.05	0.02	0.01	100.35	< MOL	< MOL	< MOL
8	90.99	7.42	2.13	0.04	0.00	0.03	0.07	0.02	0.02	100.72	< MOL	< MOL	< MOL
9	90.76	7.19	2.20	0.06	0.01	0.01	0.00	0.01	0.02	100.26	< MOL	< MOL	0.4
10	90.90	6.76	2.21	0.05	0.03	0.01	0.00	0.02	0.00	99.98	< MOL	< MOL	0.4
11	91.62	6.22	2.17	0.06	0.01	0.00	0.00	0.01	0.03	100.12	< MOL	< MOL	0.5
12	91.88	5.63	2.19	0.06	0.00	0.00	0.06	0.02	0.01	99.85	< MOL	< MOL	0.8
13	91.84	5.48	2.06	0.05	0.02	0.00	0.16	0.01	0.03	99.65	< MOL	< MOL	1.1
14	91.85	5.61	2.08	0.04	0.02	0.00	0.06	0.02	0.00	99.68	< MOL	< MOL	0.9
15	92.13	6.00	2.07	0.04	0.00	0.08	0.00	0.02	0.03	100.37	< MOL	< MOL	0.9
16	92.74	4.12	1.80	0.03	0.03	0.08	0.00	0.01	0.01	98.82	< MOL	< MOL	1.8
17	92.32	1.41	1.64	0.02	0.01	0.00	0.00	0.00	0.00	95.40	< MOL	< MOL	4.5
18	91.68	1.43	1.47	0.03	0.01	0.00	0.00	0.01	0.00	94.63	< MOL	< MOL	4.9
19	90.29	4.74	1.79	0.06	0.01	0.00	0.00	0.02	0.01	96.92	< MOL	< MOL	2.2
20	91.90	4.30	1.79	0.00	0.07	0.01	0.00	0.00	0.02	98.09	< MOL	< MOL	2.6
21	91.96	4.98	1.95	0.04	0.01	0.00	0.04	0.01	0.02	99.01	< MOL	< MOL	1.3
22	92.58	1.69	1.49	0.01	0.04	0.05	0.00	0.01	0.00	95.87	< MOL	< MOL	3.8
23	93.26	1.46	1.33	0.04	0.00	0.02	0.00	0.00	0.01	96.12	< MOL	< MOL	3.9
24	88.79	2.70	1.63	0.02	0.00	0.07	0.06	0.02	0.00	93.29	< MOL	< MOL	1.1
25	88.91	2.88	1.67	0.02	0.00	0.00	0.02	0.01	0.01	93.52	< MOL	< MOL	1.2
26	89.20	2.65	1.61	0.03	0.00	0.00	0.00	0.01	0.03	93.53	< MOL	< MOL	1.3

*NOTE: O, C, and N values are not absolute concentrations but are relative to an average baseline value taken well away from the defect

40.3, 43.2, 42.4, 45.8, 58.6, 66.7, 54.2, 48.9, 46.7, 42.9, 39.6, 38.0, 42.2, 39.2, 38.2, 38.3, 37.6
hardness values #1 → #20

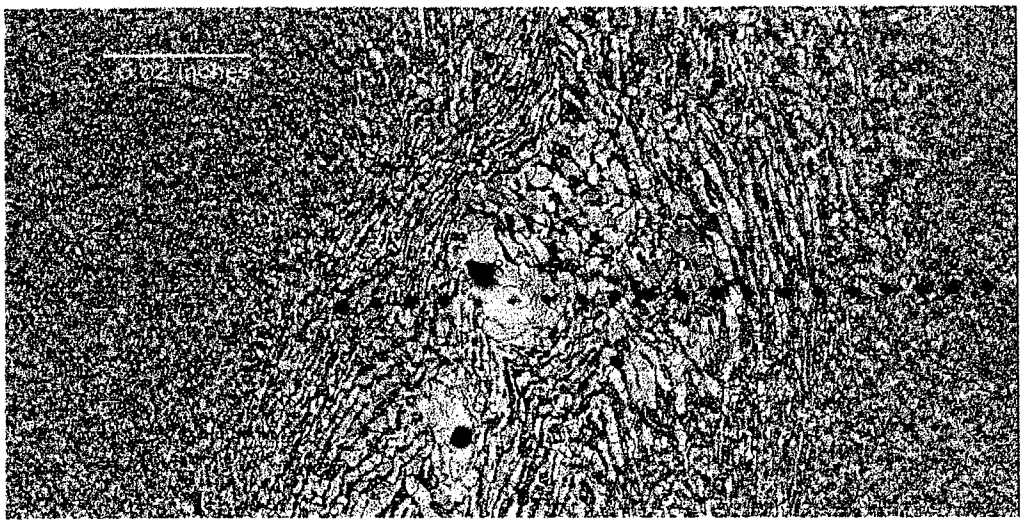


FIGURE G-1. PANCAKE B1BW3 IND, A HARD ALPHA INDICATION MT. #98-3598, STEP 14

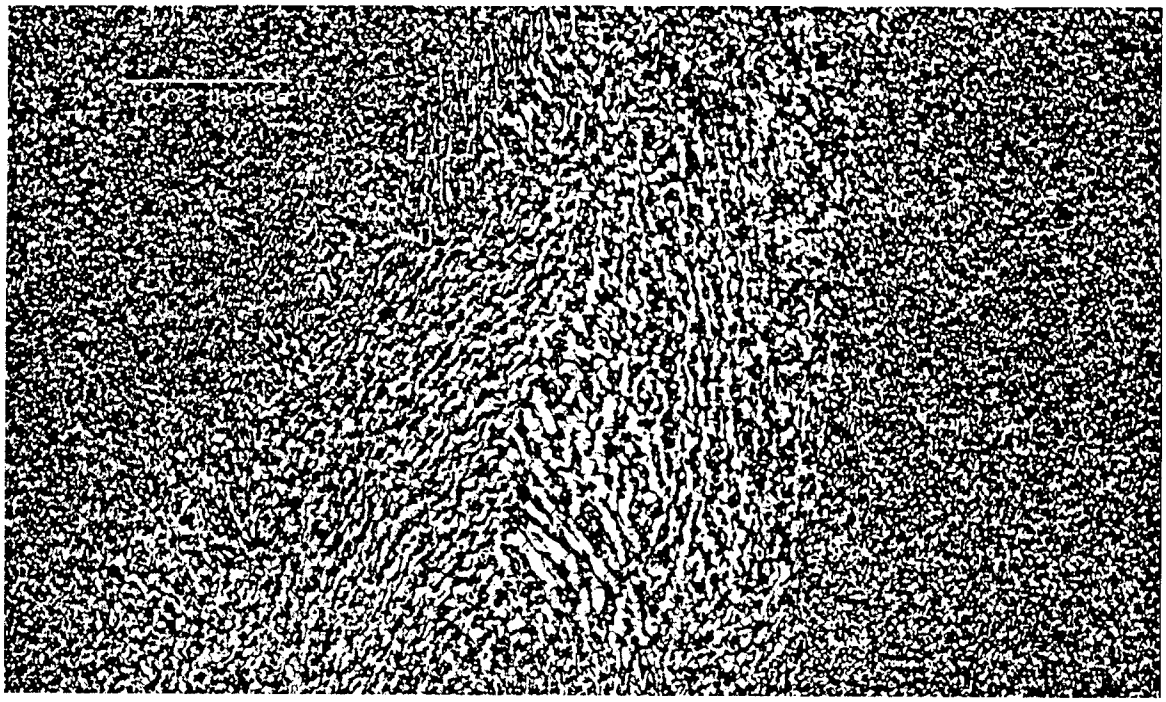


FIGURE G-2. PANCAKE B1BW3—INDICATION A—STEP 9

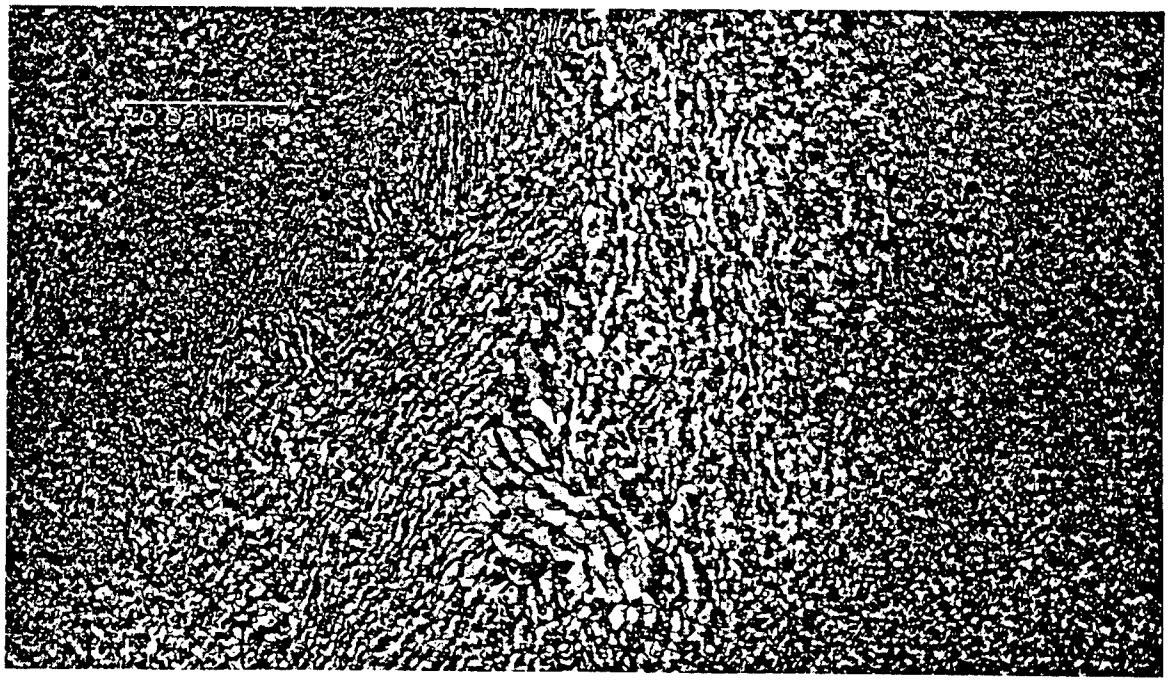


FIGURE G-3. PANCAKE B1BW3—INDICATION A—STEP 10

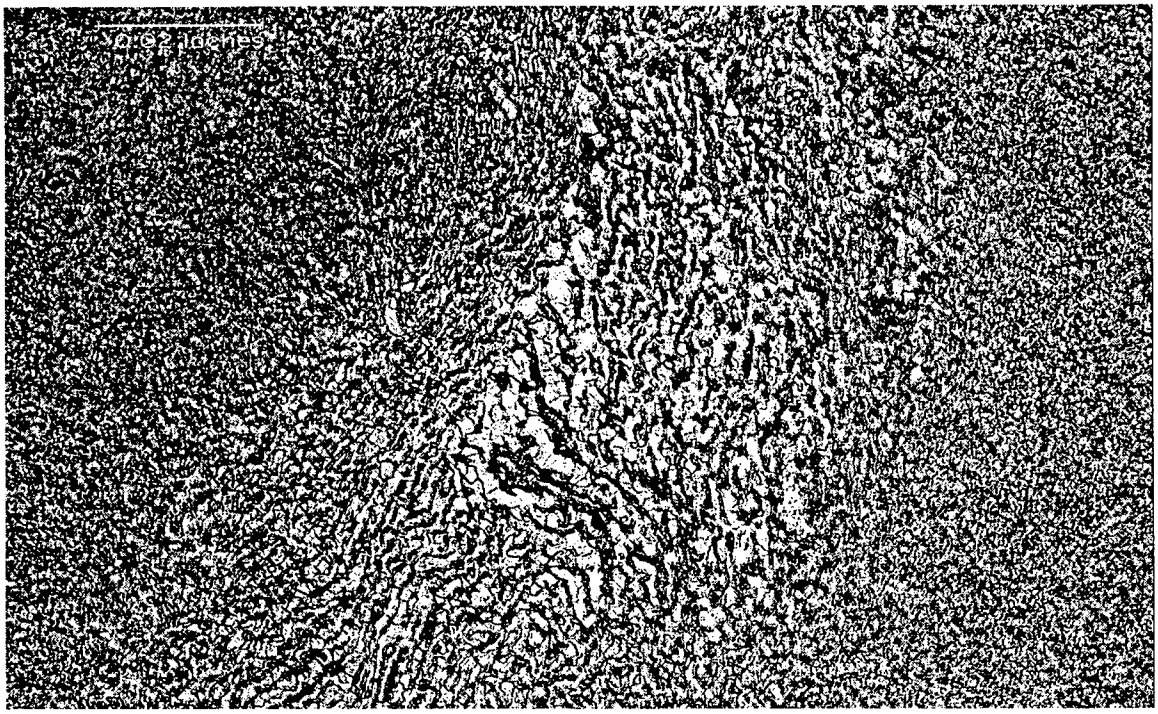


FIGURE G-4. PANCAKE B1BW3—INDICATION A—STEP 11

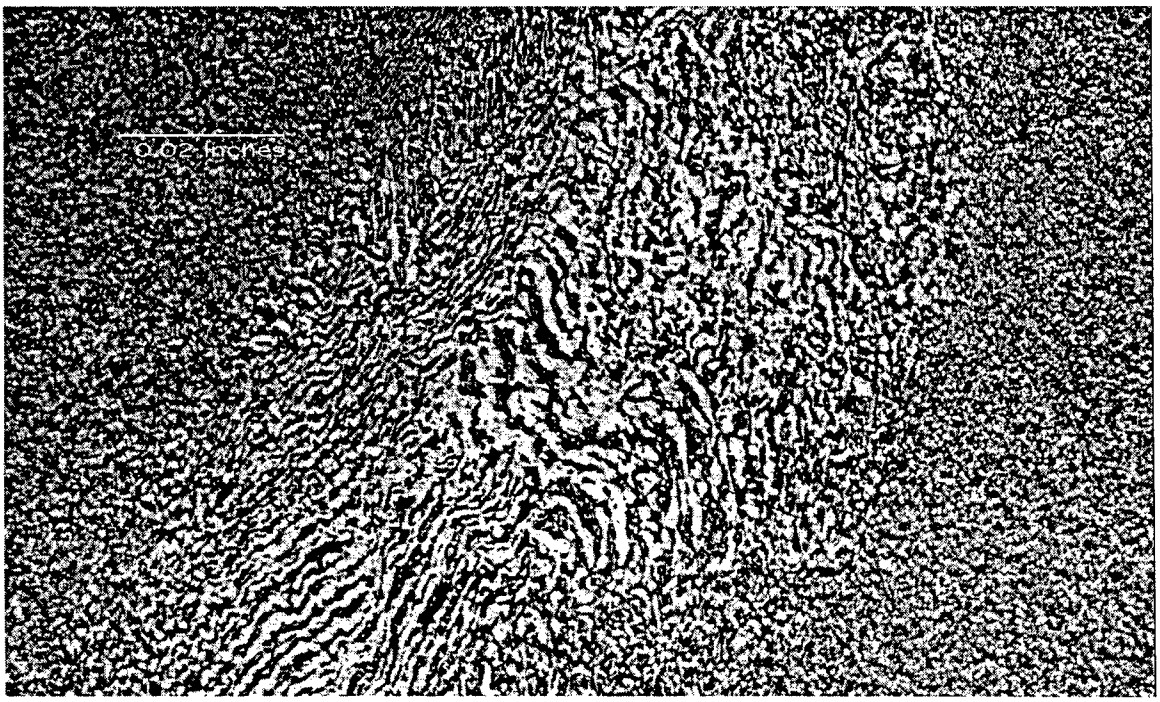


FIGURE G-5. PANCAKE B1BW3—INDICATION A—STEP 12

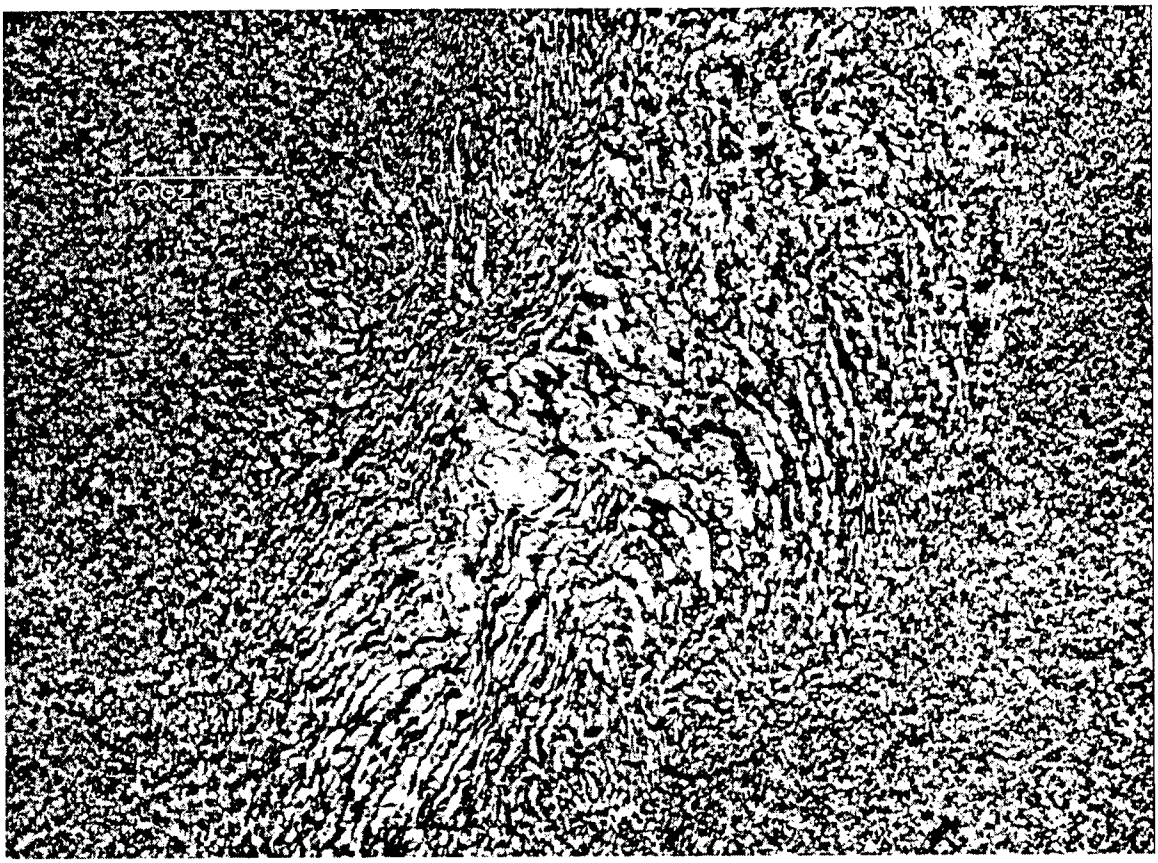


FIGURE G-6. PANCAKE B1BW3—INDICATION A—STEP 13

G.3 CONCLUSIONS FROM EVALUATION OF FORGED PANCAKE.

Based on the ultrasonic and metallographic evaluation of indication B1BW3 as it appeared in the billet and forged pancake, the following conclusions are drawn:

- Ultrasonic inspections of the forged pancake prepared from the CBS billet containing hard alpha inclusion B1BW3-A by P&W and GE resulted in detection of the hard alpha indication at about the same location in the forging. Indication amplitude results, considering the differences in transducers, equipment, and calibration standards used, were very similar i.e., between 60-100 percent of that obtained from a No. 1 FBH. Both results indicated the hard alpha to be about 0.100-0.120 inch maximum dimension.

- Comparison by GE of multizone and their version of a conventional ultrasonic inspection of the pancake (both at the No. 1 FBH sensitivity level) indicated that the hard alpha inclusion could be readily detected using the multizone technique but could not be detected using their conventional technique due to excessive noise levels.

- Based on the ultrasonic images of the hard alpha inclusion, forging appeared to change the shape of the inclusion from the cigar shape observed in the billet to a more spherical shape in the pancake forging.

- Metallographic evaluation of the hard alpha inclusion in the pancake forging indicated the presence of a significant diffusion zone and substantial cracking and voiding around the nugget. These characteristics were observed in several of the slices through the inclusion, suggesting the forging operation was not effective at closing voids and cracks which have been detected in numerous hard alpha inclusions at the billet stage of processing.

- Microprobe analysis of the hard alpha inclusion indicated a maximum nitrogen content of about 4.9% in the nugget, and about 0.5% in the diffusion zone surrounding the nugget. This level of nitrogen is typical of that found in previously evaluated hard alpha inclusions.

- Hardness measurements of the inclusion indicated about a 20 point increase in Rockwell C hardness between the matrix material and the nugget. This result agrees with previous data suggesting the nugget to be a hard, brittle inclusion relative to the surrounding matrix material.

APPENDIX H—STATIC AND FATIGUE TESTING OF SYNTHETIC AND NATURALLY OCCURRING HARD ALPHA DEFECTS TO CHARACTERIZE CRACKING BEHAVIOR

H.1 INTRODUCTION.

This document details the mechanical test activities associated with understanding how cracks initiate and nucleate from hard alpha (HA) defects in Ti-6Al-4V material. Hard alpha defects are small zones where the alpha phase has been stabilized by the presence of nitrogen introduced during the melting process. Large hard alpha anomalies are often extensively voided and cracked in the final forged rotor configuration. Current life prediction methodologies commonly assume that an initial crack size equal to the size of the HA region is present at the beginning of life. This assumption could be overly conservative, however, for smaller HA anomalies and zones with lower nitrogen content, which may be less likely to be extensively cracked and voided after the forging process and, hence, more difficult to detect using nondestructive evaluation. Consequently, these anomalies may play a significant role in the probabilistic risk assessment especially considering that a relatively larger number of these smaller defects are postulated to exist in rotor material. Therefore, it is useful to assess the cracking tendencies of the HA anomalies under static and fatigue loading in order to potentially include some nonzero crack nucleation life in the fatigue life prediction methodology.

Both synthetic defects and naturally occurring defects were mechanically tested during this program. The synthetic anomalies were created artificially using techniques pioneered by General Electric Corporate Research and Development (GE CRD) to develop inspection standards used for refining nondestructive evaluation (NDE) methods. A synthetic hard alpha defect and surrounding synthetic diffusion zone (DZ) were embedded in a Ti-6-4 plate specimen. These anomalies, consisting of both interior and surface breaking geometries, were tested both statically as well as under cyclic fatigue loading conditions. A number of size and defect composition-related variables were also examined in the matrix of testing. The naturally occurring defects were extracted from the well-documented RMI Titanium Co. contaminated billet study (RMI CBS) billets so as to explore the applicability of the synthetic defect behavior to the more relevant naturally occurring defects.

Various crack detection transducers were used to characterize the behavior. This was especially important in the case of the interior defects, where visual observation was not possible. Extensive metallurgical sectioning and fractographic analysis were also employed to characterize cracking more definitively following testing. The testing was performed using a phased approach so as to apply the lessons learned from the initial testing in the subsequent experimental work.

H.2 EXPERIMENTAL METHODS AND PROCEDURES.

The experimental work detailed herein was carried out over nearly a 3-year period. The testing was executed in two phases: an initial series of tests (Phase A) was performed to understand the influence of several of the key variables with a view toward refining the conditions and testing methods employed in the second series of tests (Phase B). Some techniques used differed

slightly between phases. The purpose of this section is to document the methods and procedures used in each and to provide a foundation for understanding the measurements performed.

H.2.1 VARIABLES INVOLVED IN THE INVESTIGATIONS.

The overall goal of this experimental subset of the overall program was to characterize the damage evolution that occurs in and around hard alpha defects. This characterization could then act to validate or refine assumptions made elsewhere in the modeling portion of the program that provides the analytical design tools. The fundamental questions addressed in this mechanical testing included:

- Quantifying the link between mechanical loading variables (stress level, static loading, and fatigue cycling) and damage evolution in and around hard alpha defects.
- Understanding the conditions that lead to crack incubation and evolution (crack initiation).
- Identifying the onset of physical cracking in the defect and diffusion zone.
- Demonstrating the features of the fatigue crack propagation that occurs after initiation in the defect leading to growth into the adjacent base metal material.

These goals were achieved by applying a variety of different crack detection transducers (as well as visual inspection where possible) to specimens with defects that were mechanically loaded. The physical phenomena monitored with these transducers included acoustic emission (AE), direct-current electric potential drop (PD) and ultrasonic time of flight (Phase A only).

A number of defect variables were also included in the matrix. These variables included:

- Defect Source: synthetically manufactured or naturally occurring.
- Defect Position: surface connected or internal surrounded completely by Ti-6-4 material.
- Defect Extent: a large and small size.
- Defect Composition: three levels of nitrogen content (low, medium, and high).

H.2.2 CREATION OF SPECIMEN BLANKS WITH A SYNTHETIC HARD ALPHA DEFECT AND DIFFUSION ZONE.

The procedures used to prepare the artificially seeded blocks and specimens were relatively complex involving multiple steps: (a) preparation of the seeds, (b) creation of the artificial diffusion zones, (c) machining of the blocks, (d) assembly of the combined seed and blocks, (e) joining and finishing of the block, and (f) machining of the specimens. These procedures were carried out by personnel at the GE CRD Center in Schenectady, NY.

First, titanium metal sponge and titanium nitride powder were added to the cold copper hearth of a nonconsumable, arc-melting furnace. The material was melted three times, measuring the weight and flipping the ingot 180 degrees between each melt. The arc-melted Ti-N was hot isostatically pressed (HIPed) at 1200°C and 30 ksi for 4 hours to close any solidification porosity.

The HIPed ingot was initially sectioned with wire electrodischarge machining (EDM) to yield two thin diametral slices each approximately 0.100 inch thick that were used to insure microstructural homogeneity and verify chemistry. Both oxygen and nitrogen analyses were performed using a fusion technique and an acid dissolution and titration method, respectively. Once the metallographic and microstructural work insured that the ingot met specification, small cylindrical pieces approximately 1 inch long were wire EDMed. These were then hand polished to eliminate machining burrs and etched in a nitric and hydrofluoric acid to clean the surfaces. The pieces were then mounted in epoxy and cut on a diamond saw to the required length to create the artificial hard-α core.

The defect cores were then removed from the epoxy by soaking in dimethylformamide and rinsing in propanol. Core diameters and lengths were measured and carefully documented. The various cores were then placed in a matrix pattern of cylindrical cavities created in a Ti-6-4 block with a cover plate mechanically clamped. The assembly was then electron beam welded (typical conditions 125 kV, 10 mA and a welding speed of 30 inches per minute) and HIPed at 1400°C at 30 ksi for 3 hours. This created a natural diffusion zone around the defect (nominally defined as the hard alpha core and the diffusion zone) that was subsequently EDMed out, along with the core to the appropriate diameter and length. The HA/DZ were then etched in a solution of distilled water, nitric acid and hydroflouric acid, and rinsed in flowing distilled water. The pieces were lastly rinsed in propanol and dried with oil-free air.

The specimen blanks, in the form of a rectangular block with embedded defects, were manufactured from either Ti-6-4 rolled rings or a forged disk. The blocks were split through the thickness and the mating surfaces were ground to insure excellent dimensional agreement. The plane of the major axis of the cylindrical defect was perpendicular to the split surfaces and a flat bottom hole of the appropriate size to insert the defect was drilled into the block. The pieces of the block were then cleaned in hot phenol (88% in water), soaked in hot Oakite-90 solvent, rinsed in hot water, and then etched in a nitric and hydrofluoric acid bath. Following etching, the parts were bathed in distilled water, rinsed in propanol, and dried with oil-free air.

The defects were then placed in the block and the cover plate positioned in place with mechanical clamps to maintain alignment during electron beam (EB) welding. The block was then welded in vacuum using the welding conditions described earlier. Following welding, the blocks were HIPed using the same pressure and time conditions as during defect manufacture but at a temperature of 900°C (below the beta transus temperature) to yield a select volume fraction of primary alpha. The resulting block was ground on all surfaces with equal amounts taken from opposite sides while carefully maintaining the orientation relative to the processing. In no case was any postfabrication heat treatment applied to the blocks, and they were tested in the as-HIPed condition.

Finally, the bond plane of the block was examined by ultrasonic NDE to assure a metallurgical bond and an absence of voids or disbonds. This final inspection was also used to physically locate the defect in the block providing dimensions defining defect position relative to the ground surfaces of the block. This defect location was critical to insuring that, when the specimens were machined, the defect was positioned in the center of the specimen gage length. Specimen blanks were provided in the form of blocks, as shown in figure H-1. For the case of

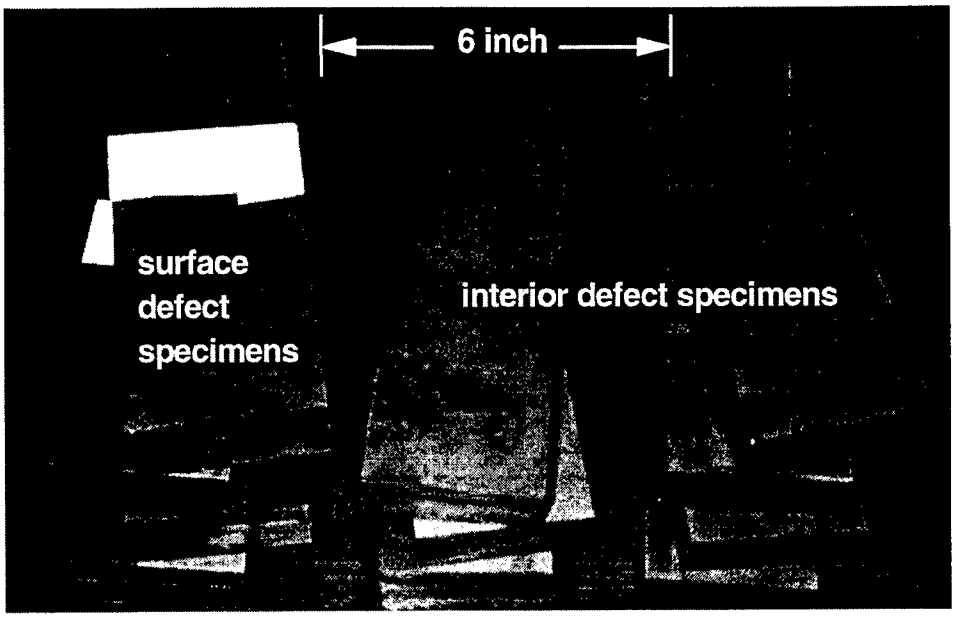


FIGURE H-1. SPECIMEN BLANKS SUPPLIED BY GE CRD PRIOR TO MACHINING INTO FINAL SPECIMEN GEOMETRY

the surface connected defect specimens, the machining blanks were created by EDMing a block with a defect located in the center of it.

H.2.3 SYNTHETIC DEFECT SPECIMEN MANUFACTURE.

The blanks containing defects shown in figure H-1 were subsequently machined into specimens suitable for mechanical testing. The dog-bone geometry used for the specimens shown in figure H-2 was suitable for either static or fatigue testing. Based on the defect position information obtained from GE CRD derived from their postmanufacture ultrasonic (UT) inspection of the blocks, a detailed set of machining instructions was then developed so as to insure that the defect was located suitably in the final machined specimens. Solid blanks yielded interior defect specimens and split blanks were machined into specimens with a surface defect. Special care was taken with the surface defect specimens to insure that the face of the specimen with the defect (an EDM surface after splitting) was subjected only to low stress, light grinding. Specimen machining was performed in accordance with detailed instructions provided to an external subcontractor, Metal Samples Inc. (Munford, AL).

The target core and diffusion zone sizes considered in the specimens are shown in figure H-3. The defect core was completely surrounded by a diffusion zone on all sides. The core and diffusion zone sizes were selected based on the range observed in the Jet Engine Titanium Quality Committee (JETQC) data. The defect cores essentially corresponded to a No. 2 (1/32-inch) and No. 5 (5/64-inch) flat-bottom hole for the small and large core, respectively. The aspect ratio (length-to-diameter ratio) of the defect core was nominally 2.5.

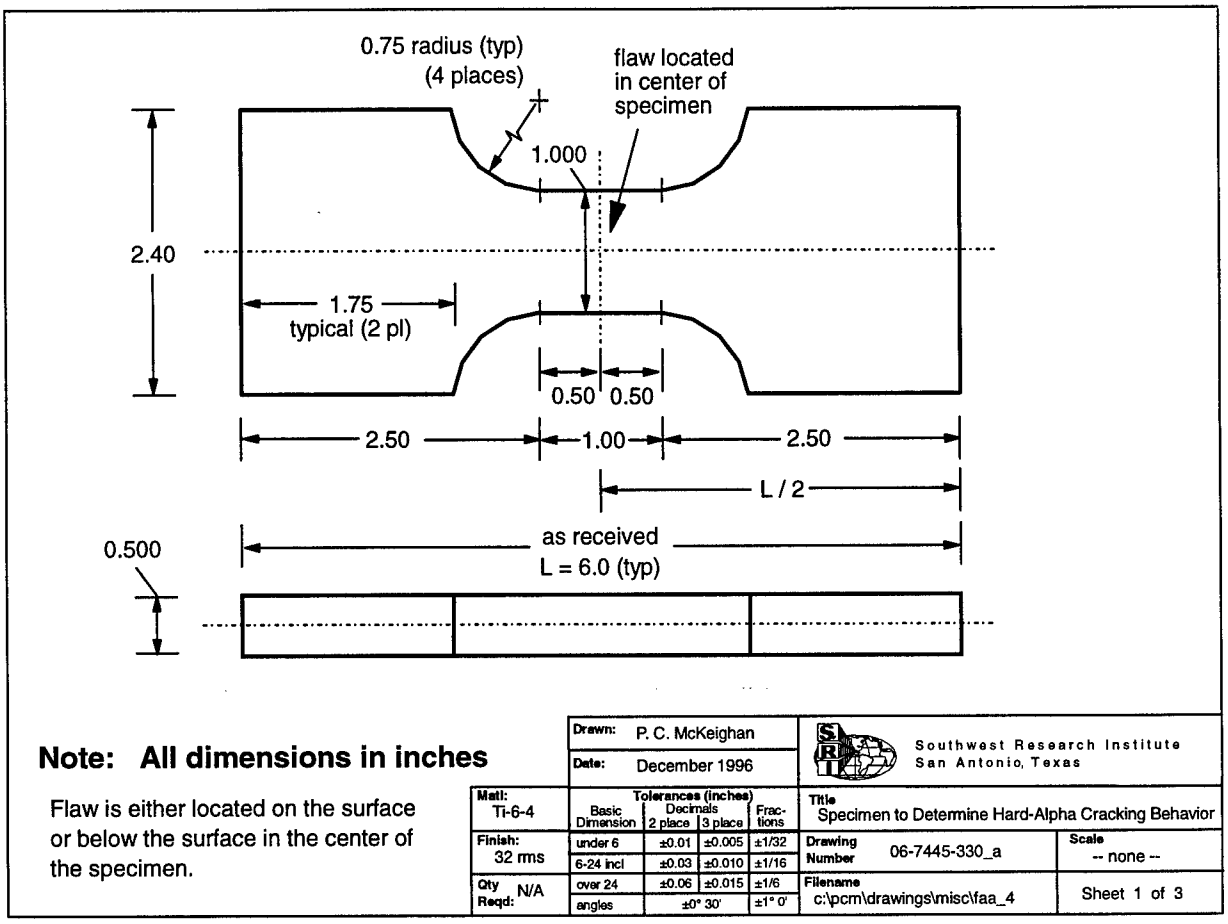
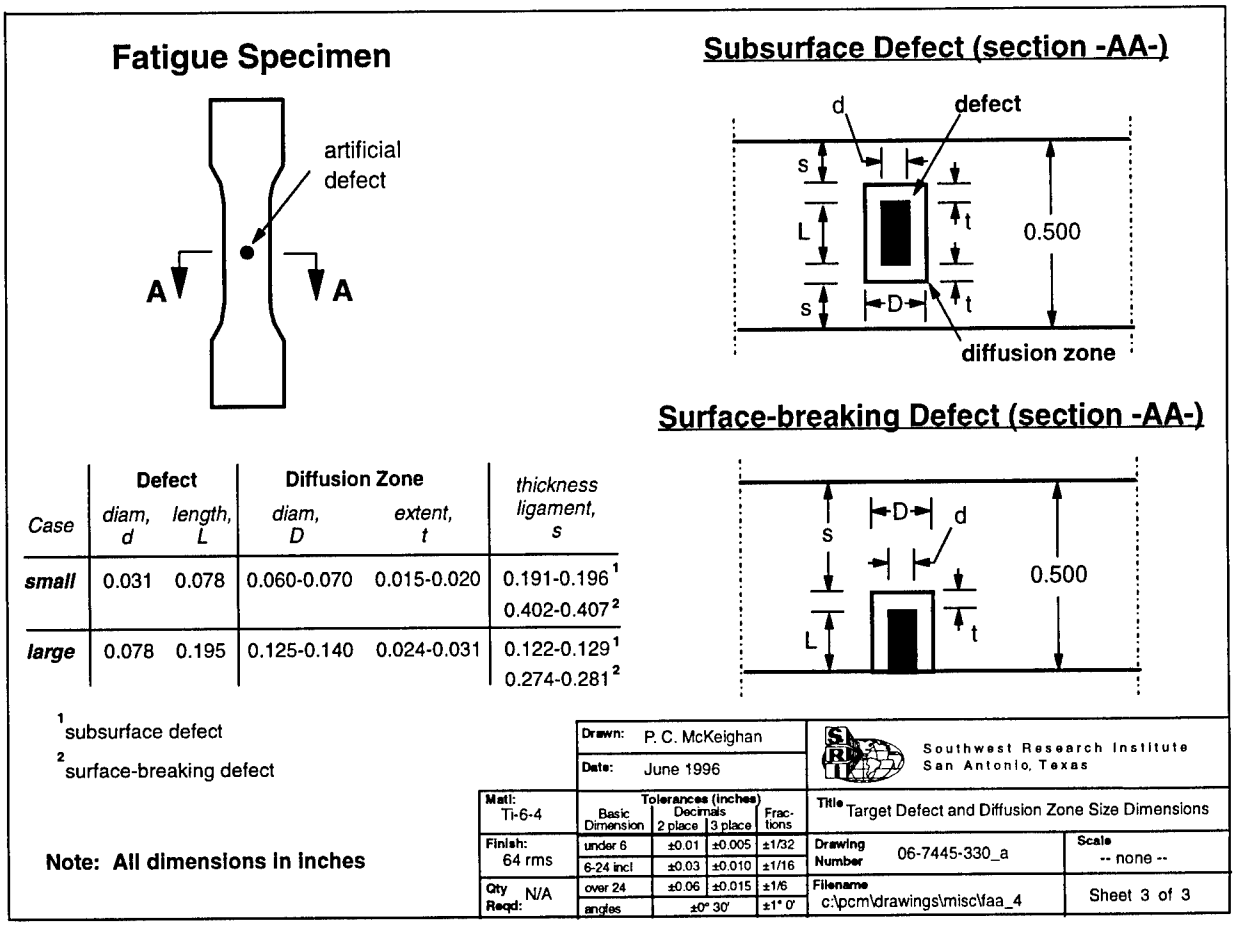


FIGURE H-2. OVERALL DIMENSIONS OF THE SYTHETIC HARD ALPHA SPECIMENS

Subsequent metallurgical sectioning of specimens that had been tested allowed comparison of actual measured HA/DZ dimensions to the theoretical targets in figure H-3. Measurements made from six specimens indicated that typical hard alpha core and diffusion zone diameters (in inches) were in the range of 0.015-0.025 (HA) and 0.055-0.070 (DZ) for the small defects and 0.060-0.075 (HA) and 0.115-0.135 (DZ) for the large defects. Furthermore, it was not unusual to observe eccentricity between the core and diffusion zone axes, which was not surprising in view of the complexity involved in the manufacture.



Case	Defect diam, d	Defect length, L	Diffusion Zone diam, D	Diffusion Zone extent, t	thickness ligament, s
small	0.031	0.078	0.060-0.070	0.015-0.020	0.191-0.196[1] 0.402-0.407[2]
large	0.078	0.195	0.125-0.140	0.024-0.031	0.122-0.129[1] 0.274-0.281[2]

[1] subsurface defect

[2] surface-breaking defect

Note: All dimensions in inches

Drawn: P. C. McKeighan				Southwest Research Institute, San Antonio, Texas
Date: June 1996				
Matl: Ti-6-4	Tolerances (inches) Basic Dimension	Decimals 2 place	3 place	Fractions
Finish: 64 rms	under 6	±0.01	±0.005	±1/32
	6-24 incl	±0.03	±0.010	±1/16
Qty Reqd: N/A	over 24	±0.06	±0.015	±1/8
	angles	±0° 30'		±1° 0'
Title: Target Defect and Diffusion Zone Size Dimensions				
Drawing Number: 06-7445-330_a				Scale: -- none --
Filename: c:\pcm\drawings\misc\faa_4				Sheet 3 of 3

FIGURE H-3. DIMENSIONS OF THE DEFECTS EMBEDDED IN THE SYNTHETIC HARD ALPHA SPECIMENS
(Both interior and surface breaker geometries are shown.)

A photograph of a final machined test specimen is shown in figure H-4. The surface defect on the face of the specimen and weld fusion line perpendicular to the thickness can clearly be noted. A systematic specimen identification numbering scheme was used with ID's vibro-etched on the grip area to track the different defect geometry and composition variables. A listing of the specimens manufactured during Phase A (9 specimens) and Phase B (17 specimens) is provided in table H-1 noting the different defect variables included in each. The form of the ID number varied between Phase A and B. In Phase A, where only 6% nitrogen composition defects were included, the ID number was of the form HA-WX-YZ where the following code was used for the W, X, Y and Z letters:

W – "S" for a surface defect, "I" for internal
X – "L" for a large defect, "S" for small
Y – overall blank ID provided by GE CRD
Z – specimen number from the blank

The greater number of variables involved in Phase B resulted in a different numbering scheme. The form of this ID, nominally WXY-Z, included the following identifiers:

W – defect size ("L" for large, "S" for small)

X – defect nitrogen composition ("H" for 6%, "M" for 2.7% and "L" for 1.6%)

Y – defect geometry ("S" for surface, "I" for internal)

Z – block ID in the case of interior defects and side of the split block in the case of the surface defects ("B" for bottom and "T" for top as identified by GE CRD)

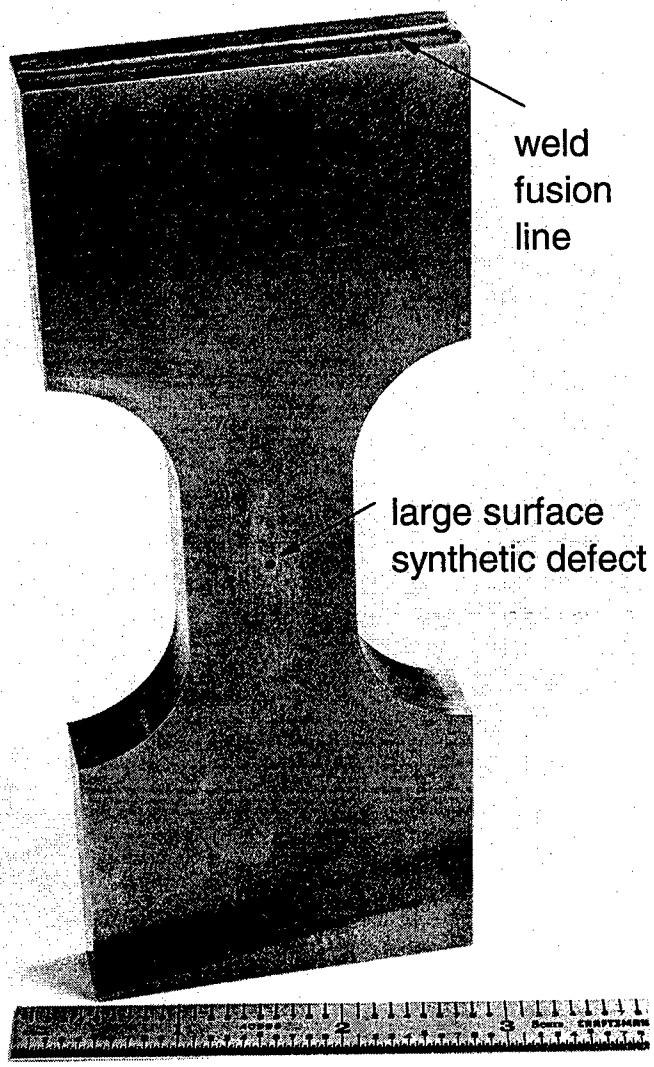


FIGURE H-4. PHOTOGRAPH OF A TYPICAL SYNTHETIC HARD ALPHA DEFECT SPECIMEN

TABLE H-1. ARTIFICIAL HARD ALPHA SPECIMENS MANUFACTURED DURING BOTH PHASES OF TESTING
(Specimens denoted with an asterisk were not tested.)

Phase	Defect Size		Defect Nitrogen Composition			Defect Position		Number of Specimen	Specimen IDs
	Small	Large	Low (1.6%)	Med (2.7%)	High (6%)	Interior	Surface		
A		✓			✓		✓	6	HA - SL - A1, A2, B1, B2*, C1 and C2*
		✓			✓	✓		1	HA - IL - F1
	✓				✓	✓		2	HA - IS - D1 and E1
B		✓			✓	✓		2	LHI - 1 and 2
		✓			✓		✓	2	LHS - B and T
	✓				✓	✓		2	SHI - 1 and 2*
	✓				✓		✓	2	SHS - B* and T
		✓		✓		✓		1	LMI
		✓		✓			✓	2	LMS - B* and T
	✓			✓			✓	2	SMS - B* and T
		✓	✓			✓		2	LLI - 1 and 2
		✓	✓				✓	2	LLS - B* and T

Two anomalous results occurred during specimen inspection that are worthwhile noting. First, during Phase A, the GE CRD UT inspection was unable to detect the interior defect in specimen HA-IS-E1. This specimen was subsequently held in reserve and not tested in Phase A. Prior to the Phase B testing, the specimen was examined using a 160 keV, realtime, microfocus X-ray equipment (MegaTech, Norcross, GA). This inspection method indicated that a defect was indeed present, albeit seeing it required knowing exactly where to look. This specimen was subsequently included in the Phase B testing.

The second unusual occurrence resulting from inspection concerned the four LMS and SMS surface defect, medium nitrogen content specimens manufactured in Phase B. When the surface defect specimens were examined visually under low power magnification, only a large diameter diffusion zone was observed and no apparent defect was visually present. Postulating that the blocks had been split in one of the diffusion zone end caps leaving the defect in one half of the blank, the defect faces of these specimens were subsequently EDMed deeper. Approximately 0.030-0.050 inch of material was removed in the unsuccessful attempt to find the defect core. These specimens, now dog-boned in two directions, were subsequently tested in the Phase B effort, recognizing that the nature of the defect was unknown.

H.2.4 NATURALLY OCCURRING DEFECT SPECIMEN MANUFACTURE.

In the case of the synthetic defects, the defect variables such as composition, size, and geometry can be controlled. However, it is unknown how well these synthetic defects mirror the behavior of natural HA defects. Consequently, a limited amount of testing was also performed using naturally occurring defects to insure that the overall behavior measured with both types of defects was consistent.

H.2.4.1 RMI Billets Supplied.

The source of the natural defects was the RMI CBS material documented in detail by the engine companies and the Engine Titanium Consortium. Lisa Brasche (Iowa State) supplied the information on the RMI billets and assisted in defining the billets available for testing. The constraining variables in this process included the geometric practicalities of manufacturing and gripping a specimen as well as the metallurgical sectioning work that has already been performed on a number of the billets. The goal was to obtain billet(s) that had a variety of defect sizes with sufficient surrounding material to machine a practical test specimen.

The final billets selected and delivered to Southwest Research Institute (SwRI) included the following (along with the defect state as determined from the CBS work):

- B2W2: An 18-inch-long billet including indication "B" reported to be 14 inches from one end and located 0.6 inch deep. This indication was reported to have a UT amplitude of 107%.

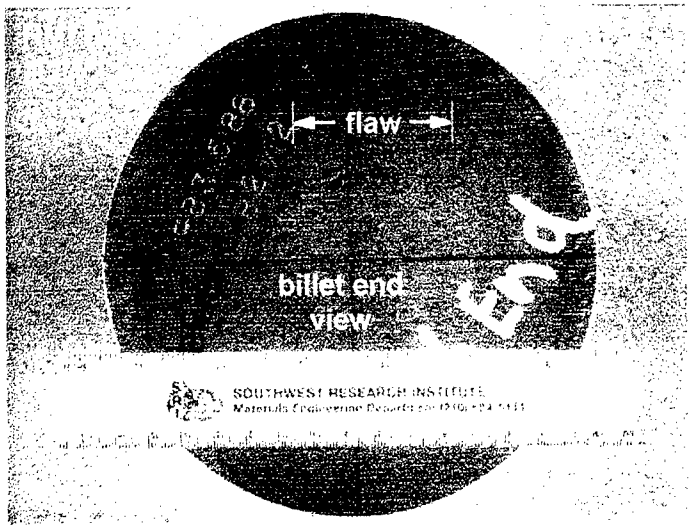
- B1AW2: A 14-inch-long billet with two indications. Indication "E" was 1 inch from the end and 1.3 inch deep. This indication was detected in three zones and had a UT amplitude of 160%. Indication "F" was reported to be 3 inches from the other end of the billet and 1.1 inches deep with a UT amplitude of 268%.

SwRI was advised to consider these defect positions as approximate only. Hence, the billets were subjected to UT examination at SwRI to determine defect position (depth and angular position) as well as extent (length along the billet).

H.2.4.2 SwRI Inspections of RMI Billets.

The billets were first visually inspected. On the stamped end of billet B2W2, a flaw on the order of 1.5 inches long was noted, as shown in the photograph in figure H-5. This flaw actually consisted of a series of connected voids. When this end of the billet was polished, another large (approximately 0.5 inch long) surface flaw located on the opposite side of the diameter was observed. Presumably, one of these two large defects corresponds to the reported "A" defect, although "A" was supposed to be 1 inch from the end of the billet, not on the end surface of the billet.

Both billets were subsequently inspected ultrasonically. A support was designed to hold the billet and allow rotating it. An azimuth scale was attached to one end of the billet to provide a reference angle for inspections. The billets were placed in a water immersion tank and a 5-MHz, 0.5-inch-diameter planar transducer was used to generate ultrasound. Although higher frequencies could produce better resolution, the 5-MHz transducer was deemed sufficient for the overall inspection. Had higher resolution been required, this could have been achieved with a more focused UT method. Due to the high speed of sound in titanium, only half of the billet was examined at each azimuth angle. The transducer was placed 1 inch above the billets. This limits reverberation signals and does not interfere with signals returned from defects in the billet.



Second defect (revealed after polishing) underneath ruler

FIGURE H-5. PHOTOGRAPH OF RMI BILLET B2W2 SHOWING THE LARGEST SURFACE FLAW VISUALLY NOTED

Scanning was carried out at a fixed azimuth angle along the length of the billet in 0.1-inch increments. The angular step between axial scans was 10°. Using data similar to that shown in figure H-6 for Flaw F in billet B1AW2E, the defects in each sample were identified.

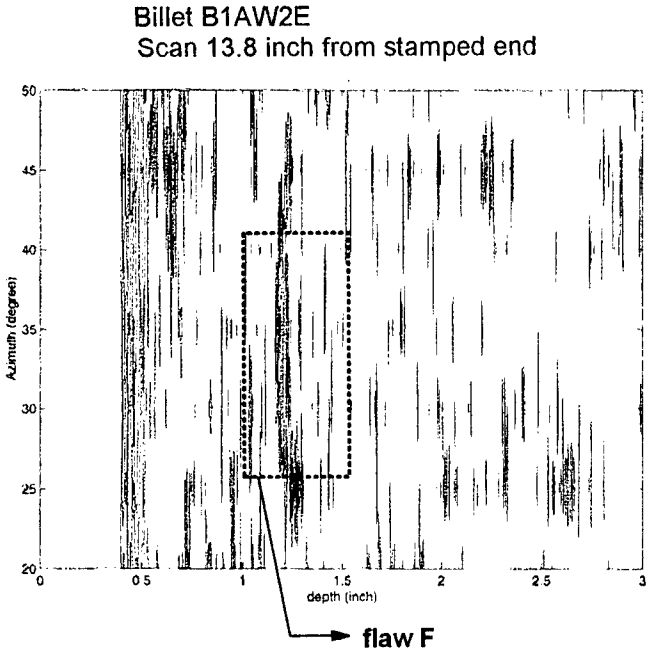


FIGURE H-6. SAMPLE ULTRASONIC SCAN PERFORMED ON THE RMI BILLETS AND USED TO LOCATE DEFECTS

H.2.4.3 Billet UT Scan Results and Subsequent Specimen Machining.

The natural defect testing was a modest effort compared to the synthetic defect testing. As a minimum, the testing was intended to mirror the interior and surface defect work assessed in the synthetic defect testing. With this in mind, three types of specimens were machined: diffusion zone only (not tested), a surface defect, and an interior defect. Machining these specimens required a detailed understanding of the largest, least-risk defects in the RMI billets for identification and cataloging. Typical results of this machining operation are shown in figures H-7 and H-8 illustrating the sectioning and specimen orientation in the RMI billets. A listing of the samples machined, along with a description of the type of natural defect, is shown in table H-2.

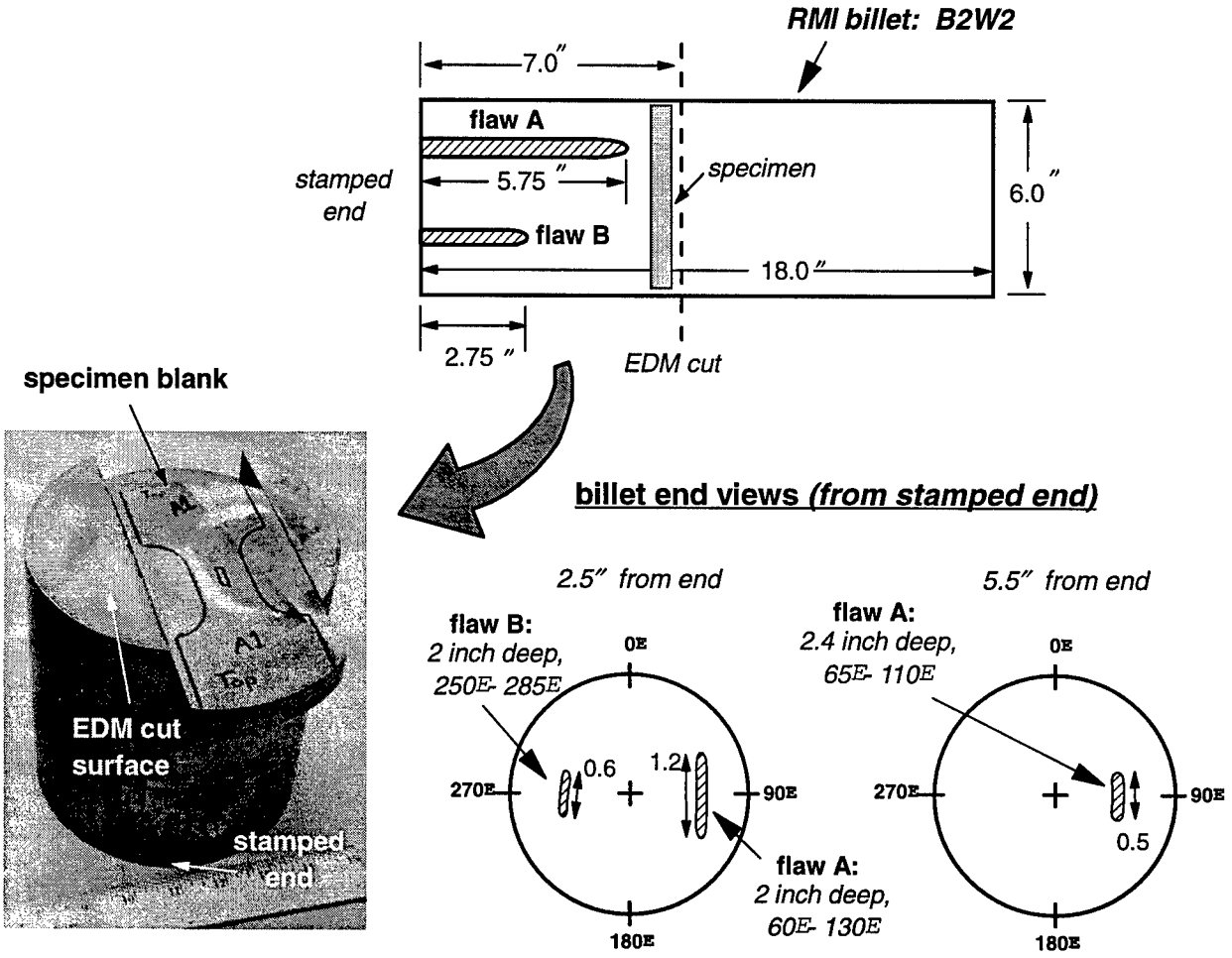


FIGURE H-7. PHOTOGRAPH OF THE BLANK REMOVED FROM THE RMI BILLET B2W2
(Specimen RMI-A1, diffusion zone only.)

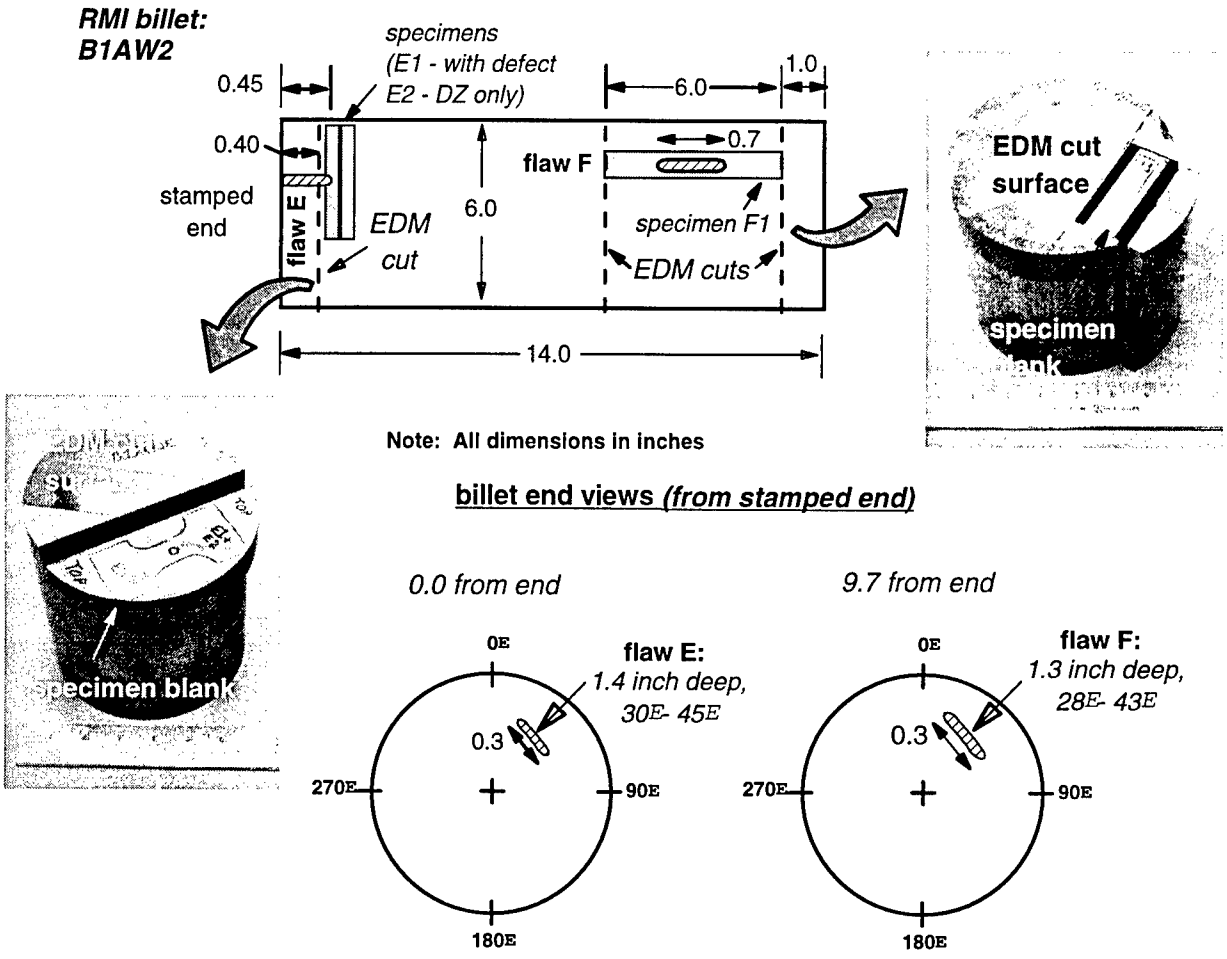


FIGURE H-8. PHOTOGRAPH OF THE BLANKS REMOVED FROM THE RMI BILLET B1AW2E (Specimens RMI-E1, -E2, and -F1.)

TABLE H-2. SPECIMENS MANUFACTURED FROM THE RMI BILLETS CONTAINING NATURALLY OCCURRING DEFECTS
(The specimen ids marked with an asterisk are untested.)

Specimen ID	RMI Billet	Flaw ID	Location	Comments
RMI-A1*	B2W2	A	diffusion zone only	Full-size specimen (rounded ends)
RMI-E1	B1AW2	E	surface defect and diffusion zone	Smaller-scale specimen
RMI-E2*		E	diffusion zone only	Smaller-scale specimen
RMI-F1		F	interior defect	Full-size specimen

In the case of RMI billet B2W2 (figure H-7), the two large defects observed on the end of the specimen were found to extend 2.75 and 5.75 inches deeper into the billet. Two billet end views are shown in figure H-7 corresponding to measurements 2.5 inches from the end (with both defects in view on the section) and 5.5 inches from the end. Presumably, the large size of this defect implied a large diffusion zone. Based on this assumption, specimen RMI-A1 (diffusion zone only) was machined approximately 0.75 inch from the identified end of Flaw A in figure H-7. This specimen was oriented such that the primary loading axis was radial relative to the forging and the assumed diffusion zone area extended through the center of the gage length presumably through the thickness of the specimen. It should be noted that no diffusion zone area was evident using a low-power light microscope on the sectioned billet after polishing and etching.

Two flaws were evident in billet B1AW2E (figure H-8) with one (Flaw E) intersecting the end of the billet. It is assumed that this is Flaw E although it is not 1 inch deep as reported, it only extended 0.45 inch from the end. This defect was used to generate the second diffusion zone specimen (RMI-E2) as well as a surface defect specimen (RMI-E1). Specimen RMI-E1 was created by sectioning the billet through the end of the flaw, hence, leaving the last 0.050 inch of Flaw E in the section where the specimen was extracted. Both of these specimens were oriented perpendicular to the major axis of the billet. Furthermore, the close proximity of the specimen to the edge of the sample required that the specimen be scaled to 75% of the size shown in figure H-2.

The surface defect specimen, RMI-E1, was further examined by polishing and etching the microstructure prior to testing. Results of this examination are shown in figure H-9. The defect, actually a void, was approximately 0.010 inch wide by 0.020 inch long. Surrounding it was a banana-shaped diffusion zone that was quite large (estimated to be 0.035 x 0.080 inch) relative to the defect size. An interesting feature of this defect is the array of microcracks that extended from the defect into the diffusion zone area. These microcracks completely surrounded the defect and typically were no longer than 0.005 inch. Although these cracks could have been a result of the EDM process used to expose the end of the defect, this is doubtful since the recast layer had been removed and the specimen was only exposed to low stress, light grinding.

The second flaw in billet B1AW2, Flaw F, was used to create an interior defect specimen. Flaw F was believed to be 0.7 inch long, and the resulting specimen, RMI-F1, was machined such that the primary loading axis was parallel to the major axis of the billet. Based on the perceived accuracy of the UT inspections and the relatively small size of the test specimen, it was believed that there was a good chance that the interior defect was not actually physically present in the specimen.

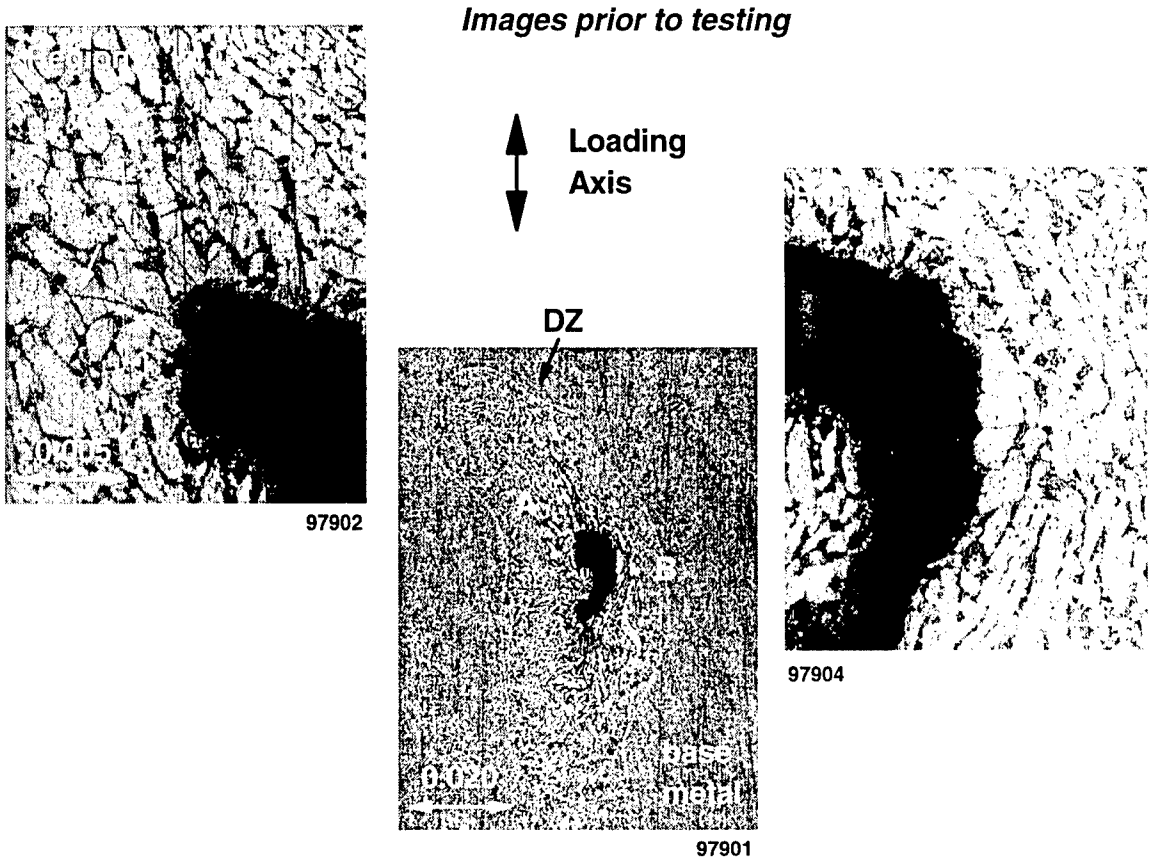


FIGURE H-9. POLISHED AND ETCHED SURFACE OF NATURAL HARD ALPHA DEFECT SPECIMEN RMI-E1 SHOWING CRACKING PRESENT PRIOR TO TESTING (See arrows.)

H.2.5 MECHANICAL LOADING CONDITIONS.

Testing was performed in a 200-kip capacity MTS System Corporation (MTS) servohydraulic test frame using an SwRI-developed closed loop controller. MTS hydraulic wedge grips (100-kip capacity) operating at 8000 psi clamping pressure were used to grip the sample as shown in figure H-10. Due to the relatively small surface area of the specimen ends, total applied load was limited to approximately 60 kip before specimen slippage occurred. The first monotonically loaded sample was performed in displacement control to determine specimen, grip, and machine behavior. Subsequent tests were all run in load control, providing improved test control. The loading train was electrically insulated so as not to provide a current path for some of the instrumentation utilized.

All testing was performed at room temperature. Monotonic tests were all run in manual control. Load was applied incrementally, stopping at each load level to record transducer output. This was especially important for crack length measurement in the case of the surface defects. Fatigue tests were run in a similar fashion, with stops at prescribed cycle counts for data recording, even though some data were continuously recorded with computer data acquisition. The cyclic loading frequency applied during fatigue testing was 2 Hz.

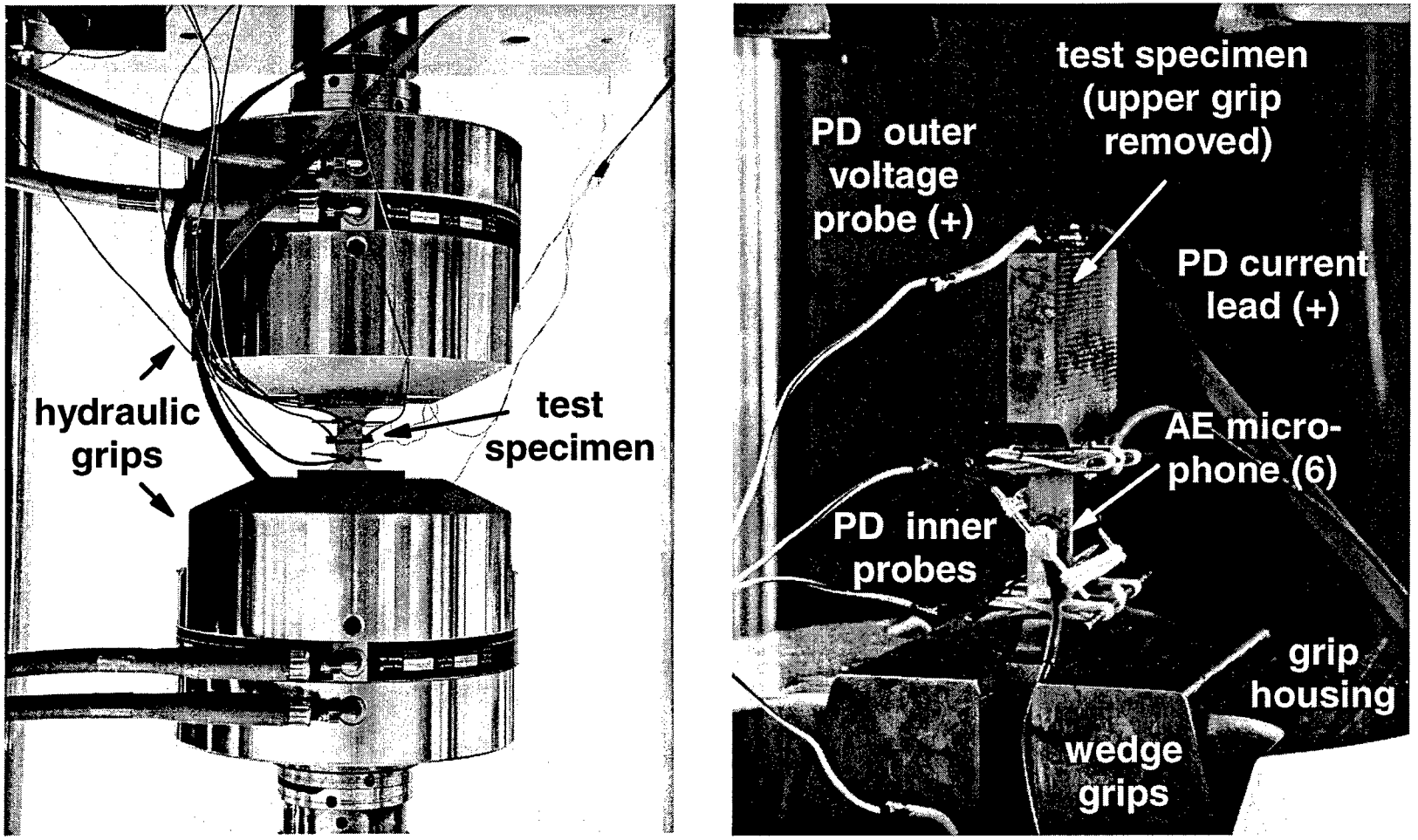


FIGURE H-10. PHOTOGRAPH OF A GRIPPED SPECIMEN AND THE ACOUSTIC EMISSION AND POTENTIAL DROP INSTRUMENTATION ATTACHED TO A SPECIMEN

The matrix of loading conditions for the synthetic defect specimens in Phase A and the static tests run in Phase B is shown in table H-3. The maximum stress levels applied were typically relatively high and in excess of 50 ksi. The conditions for the fatigue testing of the synthetic defect specimens in Phase B are shown in table H-4, while test conditions for the two RMI billet specimens are denoted in table H-5. For the fatigue tests, the maximum stress level (σ_{max}) is shown for each test along with the *R*-ratio, *R*, which is defined as the ratio of minimum to maximum load. A higher *R*-ratio test is indicative of an evaluation performed with a higher mean stress magnitude fatigue cycle.

A variable amplitude fatigue loading condition was applied to many of the tests. The rationale used was to inject a high *R*-ratio band periodically in a low *R*-ratio test so as to create a marker band on the surface of the fatigue crack. This marker band is created by a subtle change in fracture surface morphology that is typically evident under indirect lighting using a low power microscope. This technique is especially useful for (a) understanding how the crack shape evolves over time and (b) deriving incremental growth rates during the fatigue crack propagation process (by posttest matching the marker bands to specific periods in the fatigue loading). The marker band *R*-ratio used in this work was 0.7, a fairly effective level that empirically has been shown to mark a number of materials under a broad range of loading conditions. When applying the marker band, the maximum stress level used was the same as applied during the low *R*-ratio fatigue cycling. The loading frequency of the marker band was typically 5 Hz although sometimes 2 Hz if the block was sufficiently short.

The greatest challenge when using a marker band technique is knowing *a priori*, without any crack length information, how many marker band cycles to apply. The best marker band that has minimal effect on overall crack growth behavior is one that is on the order of 0.002-0.004 inch wide. Of course, controlling this is impossible without the ability to visually measure crack length or definitively know crack length at any time. Hence, the marker band method is largely empirical and the success rate on a given material without any crack length information can sometimes be poor. The success in marking a fracture surface in this manner is highly dependent upon a number of variables. For instance, fracture surface marking does not work particularly well at either low or high growth rates. Nevertheless, it can be a quite effective way to gather significant information concerning incremental crack growth rates and the progression of crack shape over time. The advantage of this, when contrasted to disadvantages such as possibly influencing the growth rate, must be assessed to determine suitability of the technique. It is also an efficient method when compared to the time consuming challenge of measuring smaller-scale fatigue features in a high-power microscope.

TABLE H-3. ARTIFICIAL HARD ALPHA SPECIMEN TEST MATRIX FOR PHASE A AND INITIAL STATIC PHASE B TESTING

Specimen ID	Defect Size		Defect Nitrogen Composition			Defect Position		Loading Type	Loading History
	Small	Large	Low (1.6%)	Med (2.7%)	High (6%)	Interior	Surface		
HA-SL-B1		✓			✓		✓	static	σ_{max} = 50 ksi
HA-SL-A2		✓			✓		✓	static	σ_{max} = 75 ksi
HA-SL-A1		✓			✓		✓	static	σ_{max} = 110 ksi
HA-SL-C1		✓			✓		✓	static/fatigue	40 ksi static, 24 kcyc σ_{max}=40 ksi R=0.05
HA-IL-F1		✓			✓	✓		static	σ_{max} = 100 ksi
HA-IS-D1	✓				✓	✓		static/fatigue	100 ksi static, 20 kcyc σ_{max}=80 ksi R=0.1
LLS-T		✓	✓				✓	static	σ_{max} = 100 ksi
LMS-T		✓		✓			✓	static	σ_{max} = 120 ksi
SMS-T	✓			✓			✓	static	σ_{max} = 120 ksi
LHS-T		✓			✓		✓	static	σ_{max} = 110 ksi
SHS-T	✓				✓		✓	static	σ_{max} = 110 ksi
LLI-1		✓	✓			✓		static	σ_{max} = 120 ksi
LHI-1		✓			✓	✓		static	σ_{max} = 100 ksi
SHI-1		✓			✓	✓		static	σ_{max} = 120 ksi

TABLE H-4. ARTIFICIAL HARD ALPHA SPECIMEN TEST MATRIX FOR PHASE B FATIGUE TESTING

Specimen ID	Defect Size		Defect Nitrogen Composition			Defect Position		Loading Type	Loading History
	Small	Large	Low (1.6%)	Med (2.7%)	High (6%)	Interior	Surface		
LHS-B		✓			✓		✓	fatigue	5 kcyc σ_{max}=50 ksi R=0.1
HA-IS-E1	✓				✓	✓		fatigue	5 kcyc σ_{max}=50 ksi R=0.1 *marker 325 kcycles, σ_{max}=50 ksi R=0.7* 5 kcyc σ_{max}=50 ksi R=0.1
LHI-2		✓			✓	✓		fatigue	5 kcyc σ_{max}=50 ksi R=0.1 *marker 340 kcycles, σ_{max}=50 ksi R=0.7* 20 kcyc σ_{max}=50 ksi R=0.1
LMI		✓		✓		✓		fatigue	10 kcyc σ_{max}=75 ksi R=0.1 *marker 2.5 kcycles, σ_{max}=75 ksi R=0.7* 0.2 kcyc σ_{max}=75 ksi R=0.1 *marker 2.0 kcycles, σ_{max}=75 ksi R=0.7* 0.2 kcyc σ_{max}=75 ksi R=0.1
LLI-2		✓	✓			✓		fatigue	20 kcyc σ_{max}=75 ksi R=0.1 *marker 203 kcyc σ_{max}=75 ksi R=0.7*

TABLE H-5. MATRIX OF TEST CONDITIONS APPLIED TO THE RMI BILLET SPECIMENS

Specimen ID	RMI Billet	Flaw ID	Applied Loading Condition
RMI - E1	B1AW2	E	**50 ksi static** 22.7 kcyc, σ_{max}=50 ksi R=0.1
RMI - F1		F	**50 ksi static** 42 kcyc, σ_{max}=50 ksi R=0.1 (7 blocks) *marker: 5.25 kcyc, σ_{max}=50 ksi R=0.7 (7 blocks)* **62 ksi static** 15 kcyc, σ_{max}=62 ksi R=0.1 (2 blocks) *marker: 2.25 kcyc, σ_{max}=62 ksi R=0.7 (2 blocks)* **75 ksi static** 24 kcyc, σ_{max}=75 ksi R=0.1 (4 blocks) *marker: 2.55 kcyc, σ_{max}=75 ksi R=0.7 (3 blocks)* **100 ksi static** 13.285 kcyc, σ_{max}=100 ksi R=0.1 (4 blocks) *marker: 2.0 kcyc, σ_{max}=100 ksi R=0.7 (3 blocks)*

H.2.6 DETECTION OF DAMAGE EVOLUTION AND CRACKING.

A number of techniques were used during testing to understand the observed cracking behavior in the test specimens. The purpose of this section is to address some of the most relevant details associated with each method. Five methods were considered—three that specifically relate to damage measurement (visual, metallographic, and acoustic emission methods) and two that infer damage by measuring some other type of phenomena (electric current field in the potential drop method and transmitted sound waveform characteristics in the ultrasonic method). Of these methods, the only definitive indicator of damage is the physical observation inherent in the visual and metallographic methods. None of the other four methods can be used for a definitive assessment of cracking or crack size without correlating information derived visually.

H.2.6.1 Visual and Metallographic Methods.

The advantage with a surface defect is that cracking can be visually observed (at least on the surface of the specimen) as the testing progresses. In practice, this observation was made with a low-power travelling microscope mounted on a vernier scale to measure feature lengths. Appropriate holds were injected into both static and fatigue testing to provide the necessary time to make the measurements. However, in the case of interior defects, visual observation was not possible unless the crack was sufficiently large to cause regions of plasticity on the polished outer faces of the specimen.

Prior to testing, the surface defect specimens were mechanically polished and chemically polished/etched with 50 ml HNO_3, 40 ml H_2O, and 10 ml HF. This was followed with a final mechanical polish with 6-micron diamond paste to produce a surface that was relatively free from smearing.

To better understand how cracking progressed in interior defects, four specimens were serially sectioned and metallographically examined to quantify the cracking behavior and how it varied along the length of the defect. These sections essentially corresponded to different positions through the thickness of the specimen. These thickness planes were oriented in a manner such that the HA/DZ zones were each circular. Destructive progressive polishing was used to expose these planes. Initially much of the virgin Ti-6-4 material was EDMed from the gage length to minimize the initial amount of polishing required. The portion of the gage length was then cold mounted in phenolic and the total thickness measured. An automatic polisher was then used to polish down until the endcap of the diffusion zone was apparent using 320-grit paper. Subsequent polishing was then performed using finer media.

After the final polish, an etchant of 85 ml H_2O, 10 ml HF, and 5 ml HNO_3 was used to highlight out the grain structure. The section was then photographically documented and polishing deeper into the section was then undertaken. This was repeated at different intervals to gain a three-dimensional sense of damage progression along the length of the HA/DZ axis.

H.2.6.2 Electric Potential Drop.

The electric PD technique has been used quite successfully for a number of years to measure crack length remotely. With this technique the disturbance in the potential field caused by a discontinuity (crack) is measured in a current-carrying body (the specimen). As the crack grows, the effective cross-sectional area of the specimen decreases and the electric resistance increases. Given a constant electrical current input, the voltage difference between two points on either side of the crack will also increase.

During this program, a pulsed direct current, dual probe-set potential drop unit was used to monitor electric potential. In a dual probe-set configuration, the voltage monitored was proportional to the ratio of the voltage from the probe set immediately adjacent to the crack to a voltage from a remote set of probes. The primary advantage with a ratio method is that both transient temperature changes as well as slight current input perturbations are automatically accounted for.

In preparing the sample for the PD measurements, both ends of the specimen were drilled and tapped for a number 10-32 machine screw in preparation for the outer PD lead attachment. Following surface polishing in the gage length, the two inner PD leads were placed on the specimen by spot welding platinum wire (0.005 inch in diameter) to the surface of the sample in two locations. Each wire was located on the centerline of the loading axis of the specimen and ±0.1 inch from the center of the defect on the face of the sample. Small stranded wire was subsequently soldered to the platinum and connected to the PD systems inner probe set inputs. The large power leads from the PD system were screw fastened to the drilled and tapped end holes in the specimen with 10-32 machine screws. The outer probe set leads were also fastened to the specimen at the same location as the power leads. A photograph of the PD lead and power input configuration is shown in figure H-10.

The best potential drop response will be manifested by a monotonic increase in PD as a crack grows between the inner set of probes. However, if the crack is not between the probes, a more complex PD response will be observed. In fact, it is possible that PD would actually decrease depending on how the crack will grow and where it is located. Although the PD method has been shown to be quite sensitive to potential field changes, calibrations between PD and crack length are available only for the simplest, most common crack configurations. In this program the PD method was applied to detect potential field change so as to infer crack growth as opposed to physically providing an indicator of crack size. In fact, given the probe positions used, the PD output signal was magnified as much as possible to detect the onset of cracking during this program. This magnification level was much greater than typically used for PD to measure a growing macrocrack in a fatigue crack growth specimen.

H.2.6.3 Acoustic Emission.

When damage occurs in a material, the process results in a release of energy in a variety of forms including acoustic energy. The acoustic emission technique measures the acoustic activity in a specimen so as to infer damage and/or crack progression. The primary variables of interest include the frequency of the acoustic waveform as well as the energy associated with it. This method is exceptionally difficult to calibrate and, as such, the data can only be used as an indicator of damage; further interpretation must be based on some method linking activity to physically observed data.

During Phase A of the program, the acoustic emission setup consisted of two 0.75-inch-diameter, wide-band acoustic microphones connected to a LOCAN 320 (Physical Acoustics Corporation, PAC, Lawrenceville, NJ) computer for measurement and analysis of the results. In Phase B, a PAC MISTRAS 2001 system was used in conjunction with six NANO-30 acoustic emission transducers (0.30-inch-diameter footprint) fastened to the specimen using rubber bands. Four transducers were placed on the specimen at the ends of the gage section: two each, top and bottom, directly opposite each other on the opposing faces of the specimen. The remaining two transducers were placed on the sides of the specimen, opposing each other, on the centerline of the sample as shown in figure H-10.

The newer generation MISTRAS system incorporates several advantages over the earlier LOCAN system. It operates at a higher baseline sample rate and resolution (more robust

data acquisition capability) and is configured with software to triangulate the acoustic events to determine source location. This is a powerful feature that allows the user to filter acoustic activity that occurs remote from the area of interest. Whereas the earlier LOCAN 320 system measures acoustic hits (e.g., acoustic peaks), the MISTRAS 2001 represents data in terms of both hits and more importantly events. An acoustic event is defined as an acoustic waveform that is detected simultaneously throughout the array of microphones. This feature acts to filter acoustic activity that is not significant hence, effectively increasing the signal-to-noise ratio exhibited by the system.

Acoustic emission data were recorded continually and subdivided into blocks corresponding to the manually recorded data. All acoustic data exceeding user-set thresholds were written to disk. This allowed the user to vary analysis procedures and settings by replaying a test and performing posttest processing. However, this enhanced flexibility was costly in terms of data storage and replay time. It was not uncommon during fatigue testing to generate over a gigabyte of data for a single specimen.

H.2.6.4 Ultrasonic Technique.

During Phase A of this work, an ultrasonic method was also used to detect crack growth and progression. For the surface defects, ultrasonic surface wave and 45-degree shear wave techniques were used with a 10 MHz, 0.25-inch-diameter transducer. Alternatively, unfocused UT methods were used with 45-degree shear wave shoes (one in pulse echo and the other in pitch catch mode) to detect cracking in the interior defects.

The UT method generally proved to be the least reliable (relative to PD or AE) for achieving consistent, repeatable results. However, this is probably a consequence of the implementation rather than an overall comment on the usefulness of the method. Since the UT method was less effective than the other methods and discontinued in the Phase B testing, further details are omitted.

H.3 RESULTS AND DISCUSSION.

The results of the experiments described in the previous section are examined in this section, with particular attention paid to measured crack detection transducer data and the implications for overall cracking behavior. The results are presented first for the static loading case followed by the fatigue investigations. The fatigue testing is emphasized since (a) it is most applicable to rotor design, and (b) the wealth of information apparent from the fracture surfaces provides a sense of how the cracking process progressed. The description of the fatigue testing concludes with observations from tests of the naturally occurring defects as well as implications drawn from simulations of the experiments using the Flight_Life computer code.

H.3.1 CHARACTERIZATION OF SYNTHETIC DEFECT SPECIMENS.

Prior to discussing the observed cracking behavior, it is useful to summarize the results obtained from assessments of hardness and chemistry for the synthetic defects using specimen HA-SL-B1. A microprobe scan to determine chemical constituents was performed by Pratt and Whitney. The hard alpha core consisted of 5% nitrogen (weight percent), with the balance titanium. Recall

that the target nominal composition was 6%. The natural diffusion that occurred, as shown in the chemical profile in figure H-11, resulted in a high level of 4% nitrogen just outside the hard alpha core. This nitrogen composition then dropped sharply to a constant level of 0.8-1 percent at a radial location 0.002 inch deep into the DZ. Furthermore, the grading in mechanical properties was also apparent from the hardness profile shown in figure H-12. The defect core had a relatively constant hardness approximately 2.2 times greater (> R_C 64) than the base metal level.

The microstructure shown in figure H-11 was typical for the synthetic defect specimens. The HA core of the defect was typically smooth and either completely featureless or characterized by featureless regions surrounded by rougher regions (as in figure H-11). Conversely, the diffusion zone region exhibited a cross-hatched, textured microstructure that differed significantly from the speckled Ti-6-4 alpha-beta structure apparent in figure H-11.

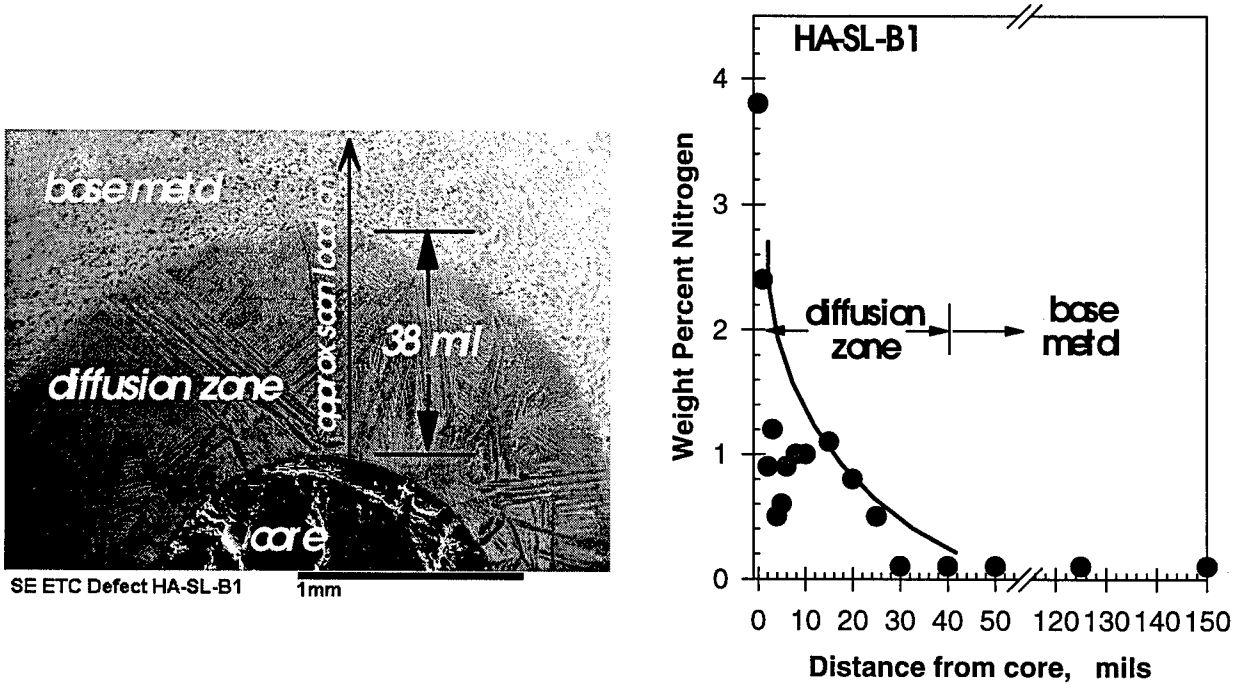
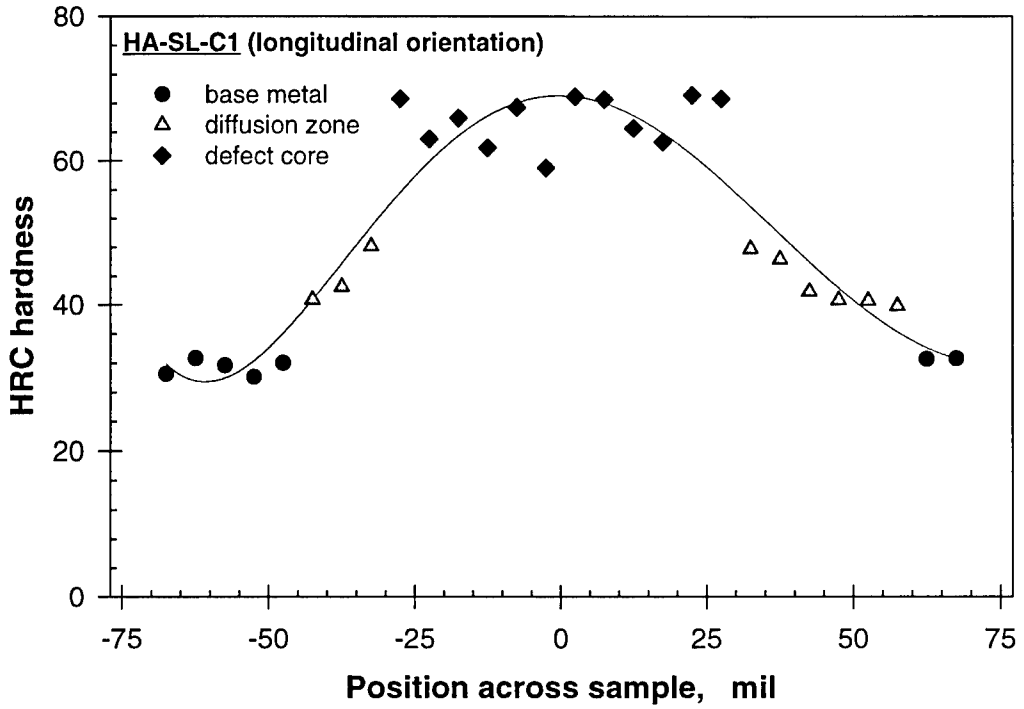


FIGURE H-11. ARTIFICIAL DEFECT COMPOSITION VARIATION AS A FUNCTION OF DISTANCE FROM CORE CENTER



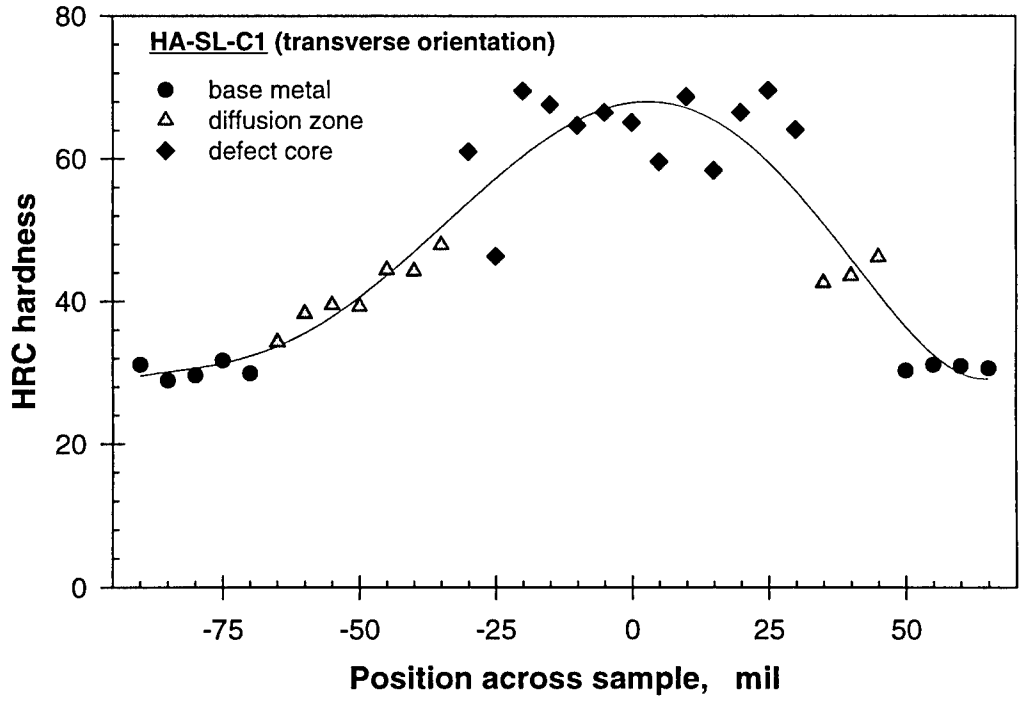


FIGURE H-12. HARDNESS PROFILE OF AN ARTIFICIAL HARD ALPHA SPECIMEN IN LONGITUDINAL AND TRANSVERSE DIRECTIONS

H.3.2 STATIC LOADING OF SYNTHETIC DEFECT SPECIMENS.

Damage and cracking behavior during static loading is relevant both to the forging operation and to the initial cycle of fatigue load. The following section addresses the results obtained from the static loading of the synthetic defect specimen.

H.3.2.1 Surface Defects.

Photomicrographs of cracks emerging from a HA core are shown for a large, high-nitrogen surface defect in figure H-13 with insets (a) and (b) being the left and right hands of the defect. The crack in figure H-13(a) is relatively flat with a large region of plasticity apparent on the surface at the DZ-base metal interface. This large region of plasticity implies that the progression of the crack was impeded by greater resistance in the base metal as the crack progressed to the end of the diffusion zone. The crack on the opposite side, figure H-13(b), exhibited a slightly different character with large periodic crack deflections but a similar region of plasticity at the intersection between the diffusion zone and base metal. Arrays of microcracks are also apparent, inclined along the axis of the segmental crack deflections, implying that cracking occurred along preferential planes of weakness, presumably crystollographic in nature.

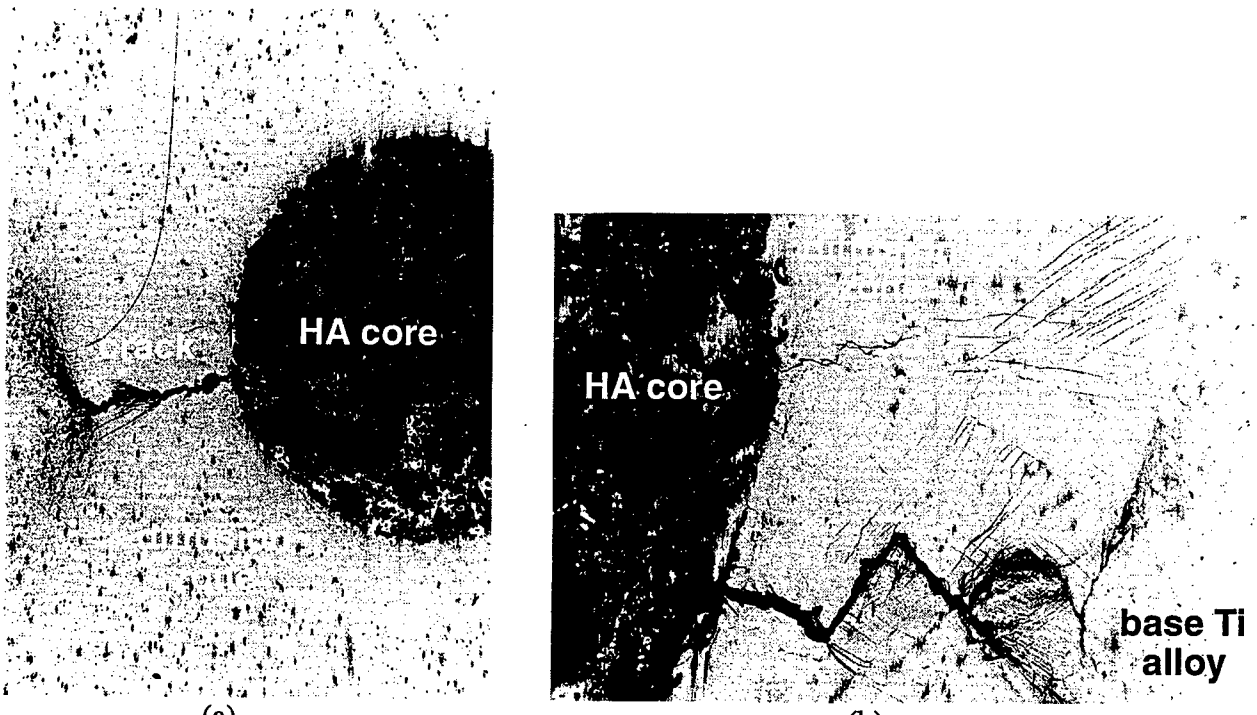


FIGURE H-13. CRACKING IN THE HA CORE AND THROUGH THE DIFFUSION ZONE IN A HIGH-NITROGEN, LARGE-DEFECT SPECIMEN

Typical test data are shown in figure H-14 for a large, high-nitrogen surface defect, illustrating how crack length, acoustic emission, ultrasonic, and potential drop output varied with applied stress. The normalized output signals for all three transducers increased steadily with an increase in stress and (correspondingly) crack length. Prior to the first visually observed surface crack growth at 8 ksi, the transducer output was constant. This data suggests that, at least for the surface defect case, a transducer signal change was indicative of crack growth.

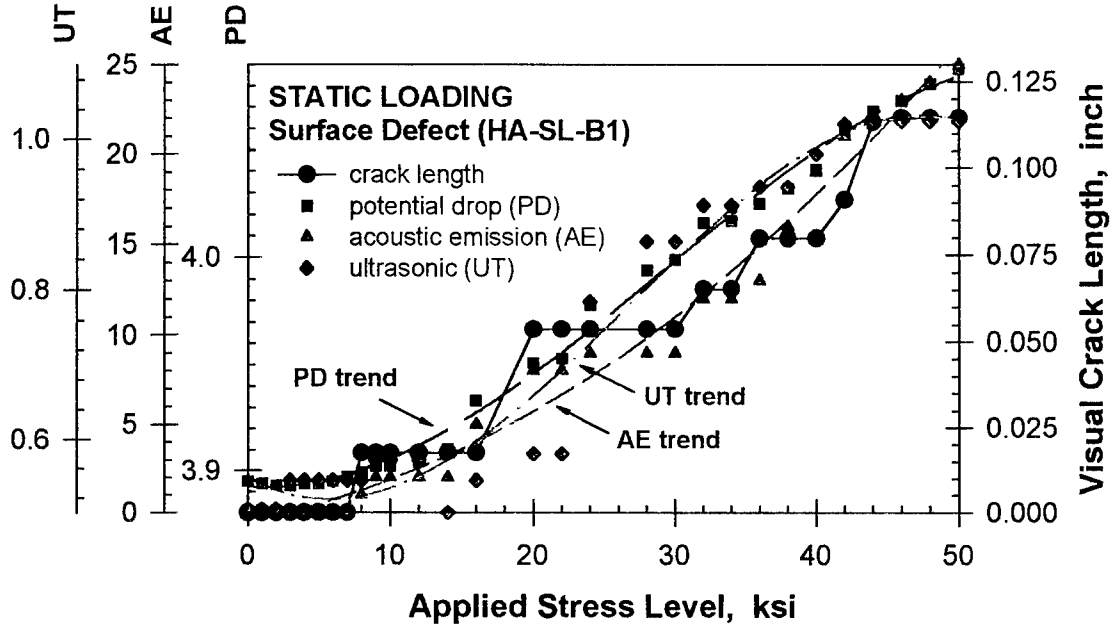


FIGURE H-14. CRACK LENGTH MEASUREMENTS AND ULTRASONIC, ACOUSTIC EMISSION, AND POTENTIAL DROP OUTPUT FOR A LARGE, HIGH-NITROGEN SURFACE DEFECT SUBJECTED TO STATIC LOADING

Further acoustic emission and potential drop data are shown in figures H-15 and H-16 for large defects with high- and low-nitrogen contents, respectively. The observed linear trend of AE and PD data was similar to that noted in figure 3-4. Note that even when surface crack length slowed or stabilized, in these cases at approximately 50-60 ksi (when the extent of the diffusion zone was reached), the increase in AE events and PD change also continued with an increase in applied stress. Presumably, this was indicative of cracking that was occurring subsurface in the portion of the defect and diffusion zone that was not visually apparent. Furthermore, note that the onset of cracking was delayed slightly in the low-nitrogen defect case (figure H-16) when compared with the high-nitrogen defect in figure H-15. The increase in potential drop signal for the high-nitrogen case also implies that the extent of cracking was higher for the loading shown. However, it is interesting to note that the number of acoustic events was approximately 50% smaller for the high-nitrogen case.

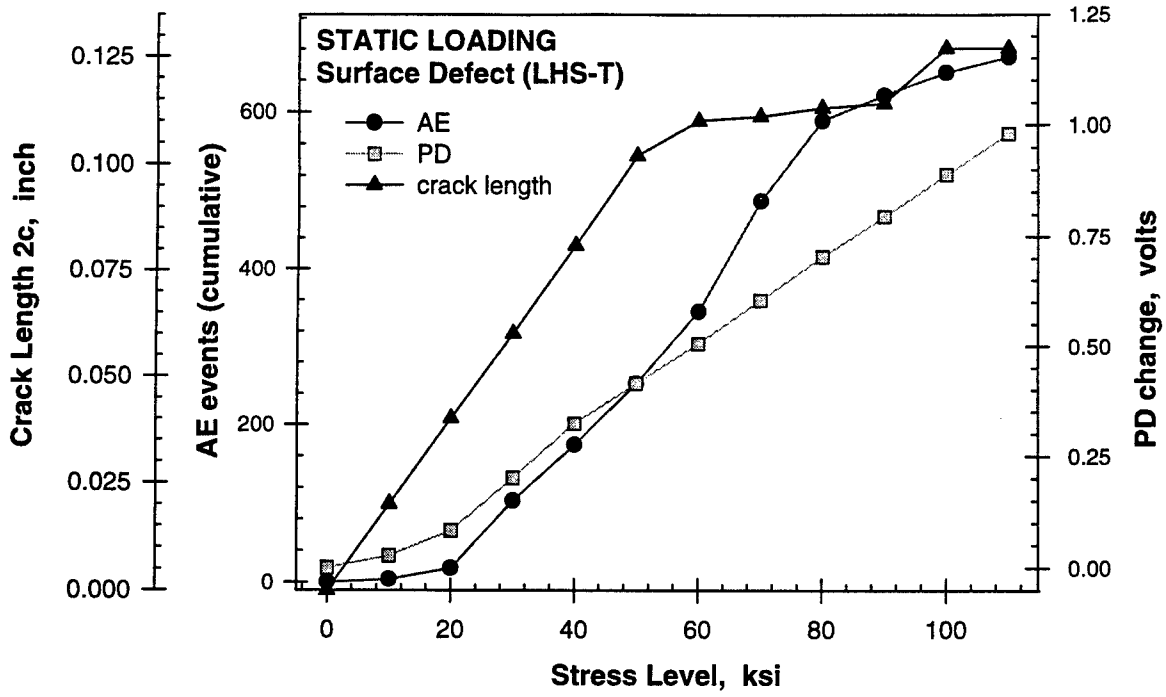


FIGURE H-15. TRANSDUCER OUTPUT AND CRACK LENGTH MEASUREMENTS FOR A LARGE, HIGH-NITROGEN SURFACE DEFECT

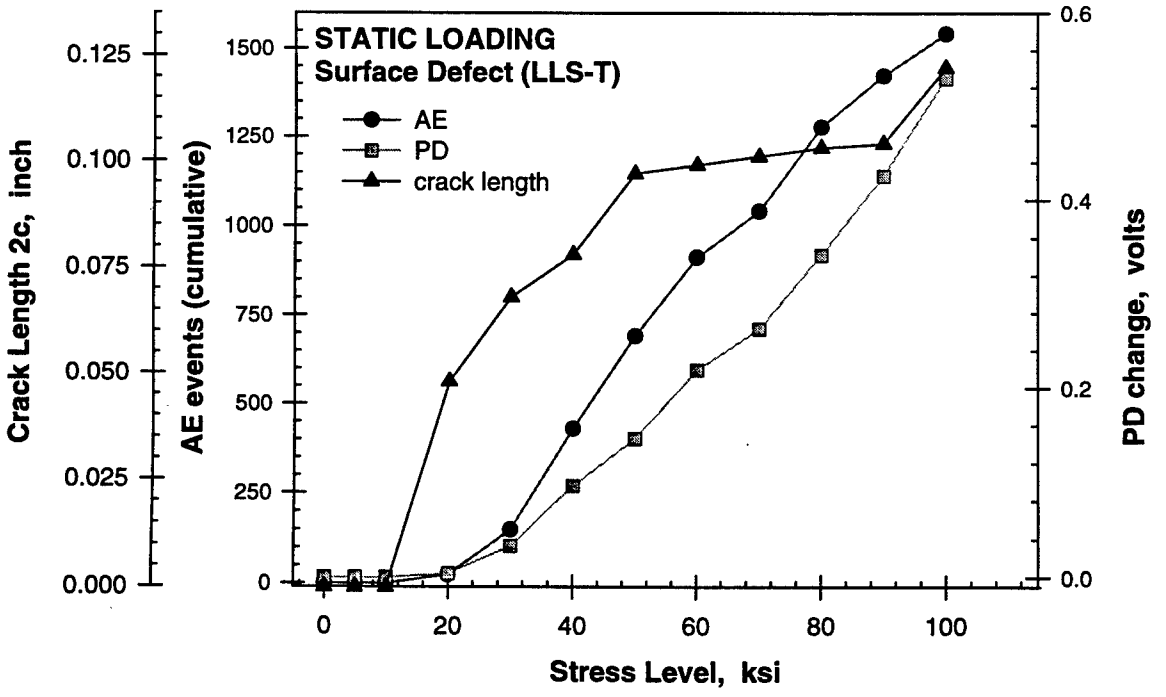


FIGURE H-16. TRANSDUCER OUTPUT AND CRACK LENGTH MEASUREMENTS FOR A LARGE, LOW-NITROGEN SURFACE DEFECT

Significantly different behavior was observed for the medium-nitrogen surface defects in figure H-17 with little transducer signal change up to 120 ksi loading. Note that the range for both AE and PD axes is only a fraction of that shown in figures H-15 and H-16. Recall from the earlier discussion that the pedigree of these defects was initially questioned since no apparent defect core was observed in what appeared to be the diffusion zone on the surface of the specimen. In fact, during this test no cracking whatsoever was observed on the surface of these specimens; although relatively high levels of deformation were observed. Clearly, the nature of these defects is quite different than that noted in figures H-14 through H-16. In view of the apparent lack of a defect core, the behavior shown in figure H-17 is probably not typical for a true medium-nitrogen level defect.

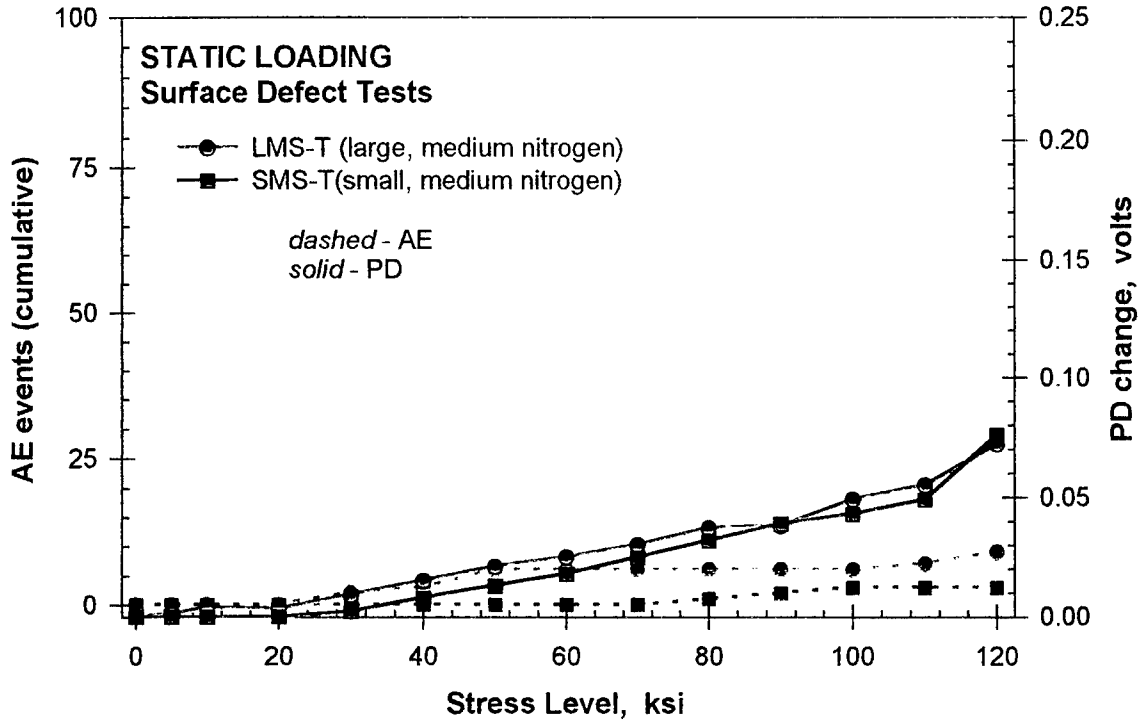


FIGURE H-17. TRANSDUCER OUTPUT FOR TWO MEDIUM NITROGEN LEVEL SURFACE DEFECTS (No cracking was observed during static loading which is consistent with the differences between these data and other static test data.)

Nevertheless, the absence of observed surface cracking is useful from the viewpoint of determining the lower threshold of AE and PD data not indicative of cracking (although the presence of localized deformation in the tests was indicative of local damage occurring). At the maximum loading condition in figure H-17, the number of acoustic events was approximately ten, whereas the change in PD output was approximately 0.075 volt. This level of acoustic activity is consistent with data obtained from tests on a solid Ti-6-4 specimen without any defects, where fewer than five events were observed under loading to 120 ksi. Conversely, the potential drop change manifested in figure H-17 is indicative of the localized deformation that occurred and a consequence of the relatively high gain employed with the PD so as to maximize the sensitivity to detect the onset of cracking. The obvious implication is that a potential drop change of greater than 0.075 volt must be observed before drawing the conclusion that cracking

is occurring (it must further be remembered that this conclusion is for a surface defect case only and how it applies to an interior defect is unknown).

H.3.2.2 Summary of Cracking Behavior in Surface Defects.

The visual observations of cracking in the defect cores and diffusion zone are summarized in table H-6. The stress levels corresponding to crack initiation in the core, initiation in the diffusion zone, and full cracking of the diffusion zone are shown for all specimens including the unusual medium-nitrogen level defects. Crack initiation is observed in the core in all cases at less than 20 ksi and in many cases at stress levels under 10 ksi. Crack initiation and propagation in the diffusion zone is consequently delayed to higher stress levels typically in excess of 30 ksi. However, diffusion zone initiations were observed in the low-nitrogen level defect and one of the high-nitrogen defects at under 30 ksi. The data further suggest that full-diffusion zone cracking does not occur until stresses on the order of 50-100 ksi have been achieved.

In the strictest sense, recording AE and PD data from surface defects is less critical since the damage formation in the defect and diffusion zone can be visually observed on the surface of the specimen. However, this data played a critical role in this investigation by providing confidence that the physical observations of cracking and damage can be correlated to data from the AE and PD transducers. This has been shown and in fact the AE and PD sensors were also useful for illustrating the atypical behavior noted in the medium nitrogen level case where a defect core was not visually observed in the apparent diffusion zone on the surface of the specimens.

TABLE H-6. CRACKING BEHAVIOR OBSERVED DURING STATIC LOADING OF SURFACE DEFECT SPECIMENS (The behavior indicated in the medium nitrogen level case is questionable due to an apparent lack of defect core visually observed in the specimens supplied.)

Specimen ID	Defect Size	Nitrogen Level	Applied Stress (in ksi) to Cause Cracks to:		
			Initiate in Core	Initiate in DZ	Fully Crack DZ
LLS-T	large	low	10-15	15-25	80
SMS-T	small	medium	***no cracking observed to 120 ksi loading (defect anomaly?)***		
LMS-T	large	medium	***no cracking observed to 120 ksi loading (defect anomaly?)***		
SHS-T	small	high	10-20	20-30	90
HA-SL-A1	large	high	6	32-36	≈100
HA-SL-B1	large	high	8	22	46
HA-SL-C1	large	high	5-10	28	-
LHS-T	large	high	<10	40	90
HA-SL-A2	large	high	10-18	42	70

H.3.2.3 Interior Defects.

Potential drop and acoustic emission data are shown for three interior defect specimens subjected to static loading in figure H-18. The variables involved in these specimens include both defect

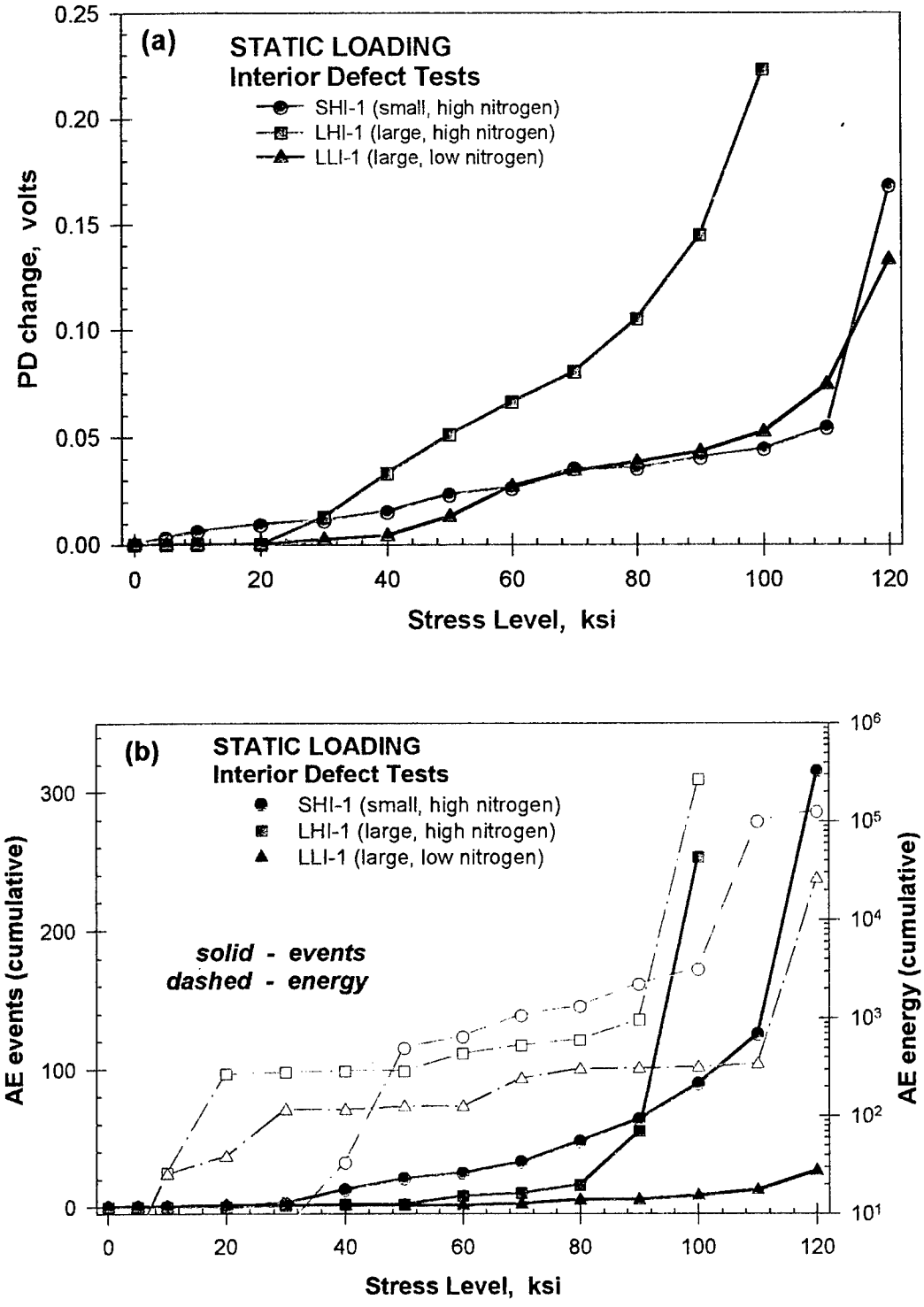


FIGURE H-18. TRANSDUCER OUTPUT DESCRIBING (a) POTENTIAL DROP AND (b) ACOUSTIC EMISSION FOR A VARIETY OF INTERIOR DEFECT SIZES AND NITROGEN LEVELS SUBJECTED TO STATIC LOADING

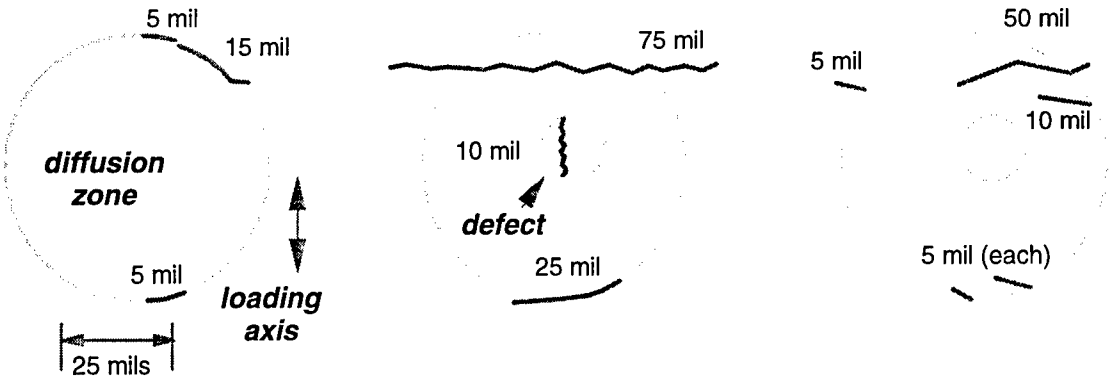
size and nitrogen level. In general, the data trends appear similar, although the large, high-nitrogen specimen tends to crack at a lower stress level as manifested by earlier increases in PD and acoustic emission events. Furthermore, it is interesting to note that the acoustic activity for the subsurface defects is considerably less than that observed in the surface defects in figures H-15 and H-16. Whereas for the surface defects AE events tended to steadily increase with loading, the acoustic event data for the interior defects (solid line data in figure H-18(b)) exhibit low emission until high stress levels (greater than 90-110 ksi) are achieved. This is especially true for the two large-defect cases in figure H-18(b). For the small-defect case, specimen SHI-1, the acoustic emission events spike at a high stress level, but this is offset by a steady stream of event data at lower stress levels.

The trend in the potential drop data in figure H-18(a) seems at first less easy to interpret than the corresponding acoustic data. To assist in interpreting the PD data, the 0.075-volt PD threshold noted for no cracking in the medium-nitrogen content surface defects is assumed to apply (in other words the PD must change by at least this amount to indicate onset of cracking). Using this criteria, the PD indicates the onset of cracking at stress levels on the order of 80 ksi for the large, high-nitrogen defect and in excess of 110 ksi for the other two cases shown in figure H-18(a). Consequently, when the PD data are interpreted in this manner, using the lower bound threshold noted for the medium-nitrogen content surface defect, the apparent onset of cracking is fairly consistent with that noted using the acoustic event data. These high stress levels for the onset of cracking are much different than noted for the surface defects. Presumably, the ability to load an embedded defect up to much higher stress levels must be a consequence of enhanced constraint provided by the surrounding Ti-6-4 material.

H.3.2.4 Metallographic Sectioning of Interior Defect Specimens.

In total, four interior defect specimens were sectioned to ascertain damage state after testing. All specimens exhibited some degree of cracking with the amount varying from specimen to specimen. It was typical to observe numerous sites of unconnected damage at each section for all specimens. Cracking was also observed in both the defect and diffusion zone, although the diffusion zone tended to exhibit a greater amount of cracking (consistent with its larger size).

During Phase A, two 6% nitrogen specimens, HA-IS-D1 (a small-defect specimen subjected to static and fatigue loading at 100 ksi maximum stress) and HA-IL-F1 (a large-defect specimen subjected to 100 ksi static loading only), were metallographically sectioned. The observed damage was quantified and a series of graphical depictions similar to those shown in figure H-19 were created. In the case of the large defect subjected to static loading, extensive HA core and DZ cracking was apparent in all sections. In the HA core region, the cracking was extensive with bands of microcracks indicative of core shattering evident. The diffusion zone was fully cracked in the central region of the defect. Conversely, virtually all of the observed cracking in the small defect was confined to the diffusion zone. Only one defect crack, illustrated in figure H-19, was observed, and it was parallel to the loading axis. In summary, for the small defect the cracking was predominantly confined to the diffusion zone, whereas for the large defect the most extensive cracking was in the HA core, although some also extended into the DZ region.



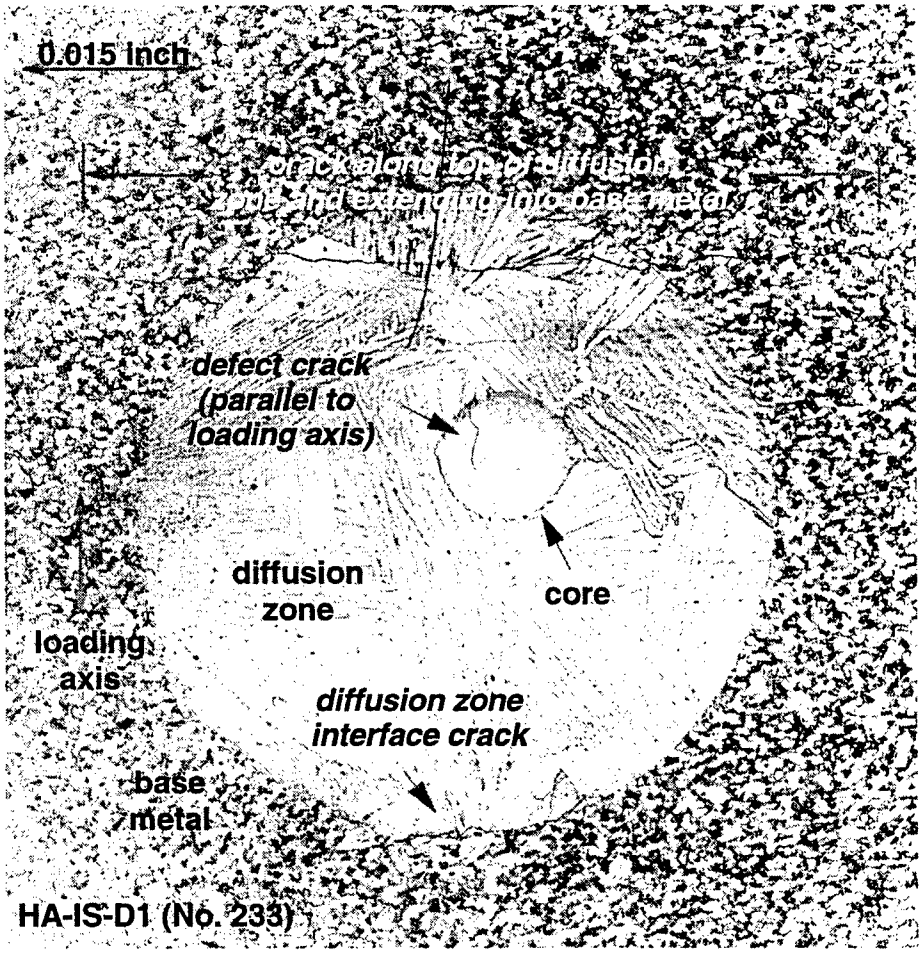


FIGURE H-19. SUMMARY METALLOGRAPHIC SECTIONS MADE FROM HA-IS-D1 AFTER STATIC AND FATIGUE TESTING

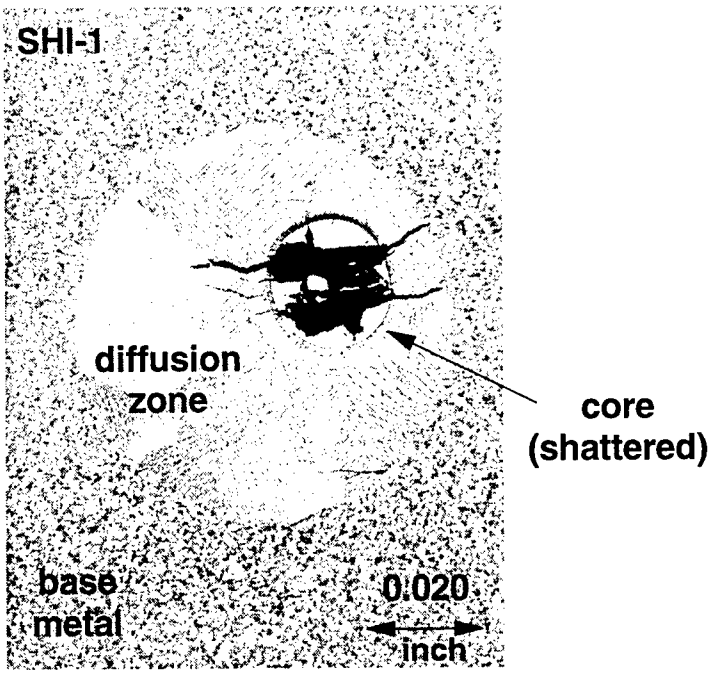
Two interior defect specimens subjected to static loading to 120 ksi during Phase B of the program were metallographically sectioned. The PD and AE responses of these specimens, namely LLI-1 and SHI-1, are shown in figure H-18. Typical metallographic sections are shown in figures H-20 and H-21 for the small and large defect, respectively. The nature of cracking differed from that observed in the Phase A effort. In the case of the small, high-nitrogen defect, the core was shattered, as illustrated in figure H-20(a). Cracking in the DZ endcap in figure H-20(b) was observed at the interface between the DZ and base metal as well as in the central area around the defect. Much less extensive cracking was observed in the large, low-nitrogen defect in figure H-21. For the majority of the length of the defect, the core and diffusion zone were intact, as shown in figure H-21(a). Deeper into the defect, figure H-21(b), some evidence of core cracking was observed (however it should be noted that in the low-nitrogen content defect the division between core and diffusion zone was somewhat unclear). However, most cross-sections exhibited some damage in the form of interface cracks between the DZ and base metal similar to that shown in figure H-21(c).

H.3.2.5 Additional Insight from Acoustic Data for Interior Defect Cracking.

Some of these apparent inconsistencies in cracking behavior can be better understood and rationalized by re-examining the acoustic data in figure H-18(b) knowing the results of the metallographic sectioning. All three specimens exhibited a spike in acoustic energy at or near the end of the static loading. Comparing SHI-1 (the shattered core) to LLI-1 (the generally intact defect), the key difference is the magnitude of energy and the number of events. In both cases, the shattered core specimen exhibited an order of magnitude increase for each measure of acoustic activity. Presumably, the lower degree of acoustic activity must be related to diffusion zone cracking since this predominated in LLI-1, the generally intact defect. It is reasonable to assume that the small high-nitrogen defect in Phase B was shattered due to the higher-stress levels imparted during Phase B (120 ksi versus 100 ksi on specimen HA-IS-D1). Note that the spike in energy and events for this specimen did not occur until 110 ksi, presumably the point when the core shattered, hence emitting the large amount of acoustic activity.

Understanding the behavior of specimen LHI-1 (an unsectioned specimen) requires employing some additional acoustic emission data analysis. One of the advantages of the MISTRAS 2001 system is that the software can perform acoustic event source locating. An example of the type of output provided is shown in figure H-22. In this case, the specimen loaded has a large surface defect, and the majority of the events are clearly grouped in the front, central region of the specimen in the same general area of the surface defect. This data provide confidence that the acoustic emission source detection algorithms are working reasonably well (however it should be noted that a truly definitive assessment of location is not possible due to the short specimen utilized, large footprint of the microphones, and relatively close proximity of the transducers).

The event location plots for the last two loading steps of interior defect specimen LHI-1 are shown in figure H-23. There is clearly a burst of acoustic activity during the last loading step that corresponds to events located in the center region of the specimen. In fact, the spike in acoustic energy exceeds the level noted in the case of the shattered small defect (specimen SHI-1). This observation implies that this specimen, too, probably exhibits a heavily cracked, and possible even shattered, core.



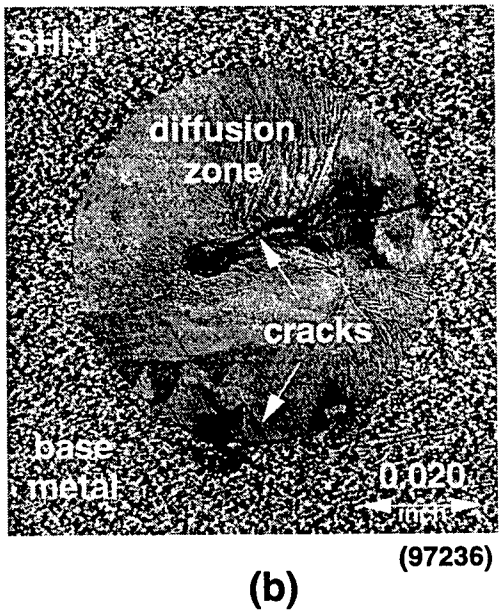
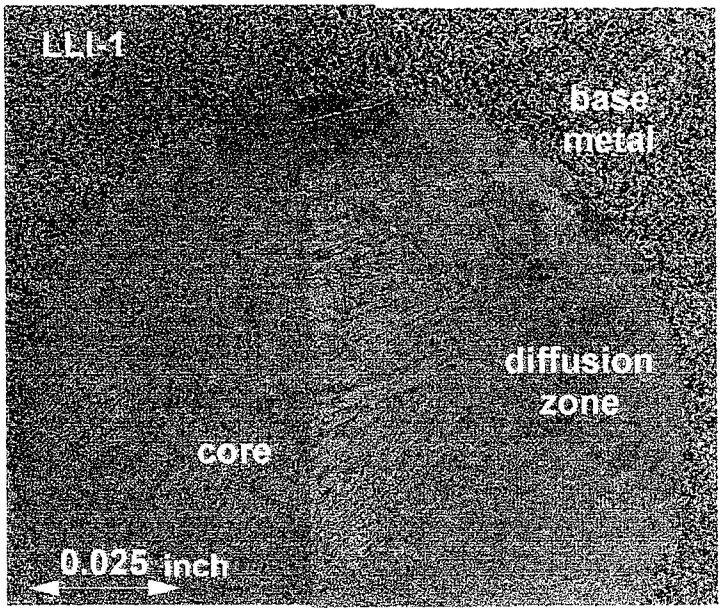
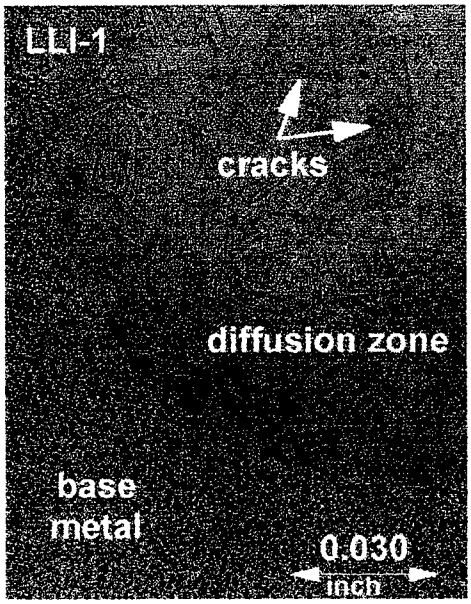


FIGURE H-20. METALLOGRAPHIC SECTIONS AFTER TESTING OF INTERIOR DEFECT SPECIMEN SHI-1 (SMALL, HIGH NITROGEN)
(In (a) the central region of the defect and (b) in a diffusion zone endcap.)



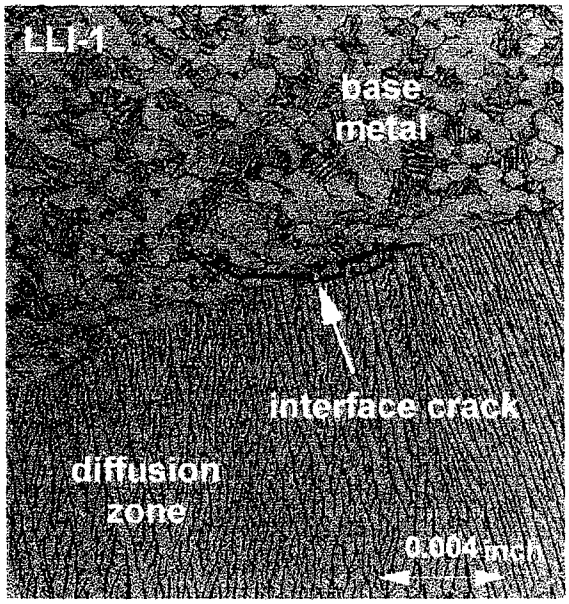
(97141/2)

(a)



(97208)

(b)



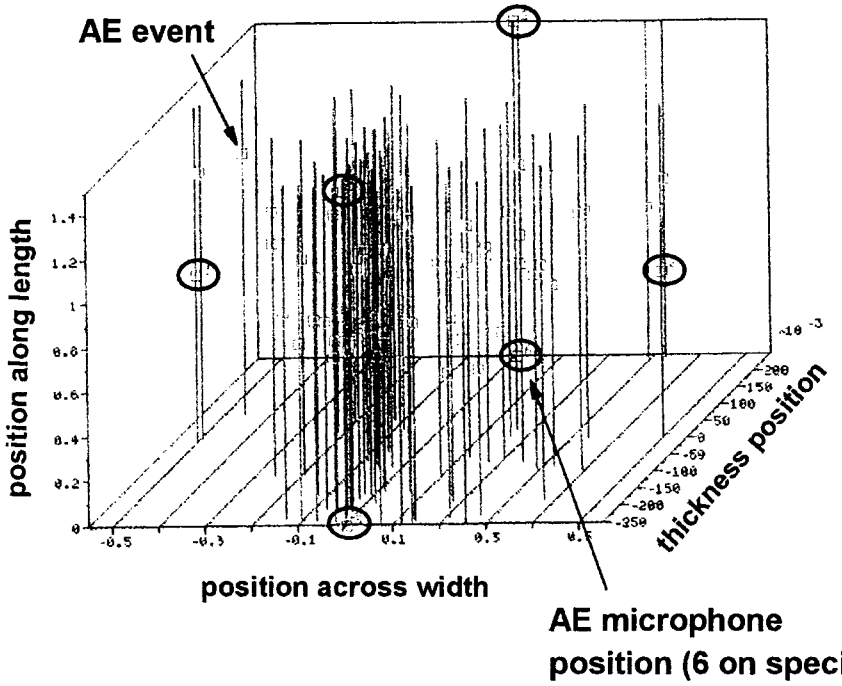
(97245)

(c)

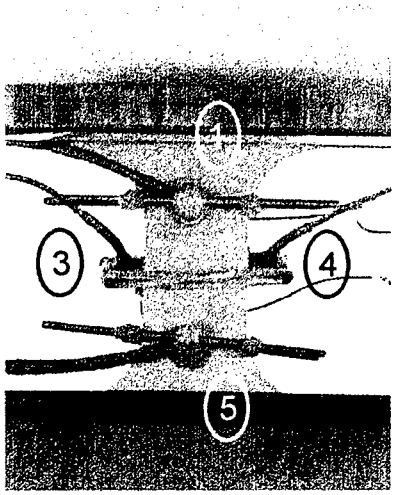
FIGURE H-21. METALLOGRAPHIC SECTIONS AFTER TESTING OF INTERIOR DEFECT LLI-1 (LARGE, LOW NITROGEN) (In (a-b) the central region of the defect and (c) illustrating an interface crack typical for the majority of the cracks.)

Specimen LHS-T
Large, high-nitrogen
surface breaker
static loading condition

AE event location
50 ksi loading step



Position Definition
AE microphones



Microphones No. 2 and 6 are on backside (mirroring 1 and 5)

FIGURE H-22. DESCRIPTION OF TYPICAL ACOUSTIC EMISSION SOURCE LOCATION DATA WITH STATIC LOADING RESULTS OF SPECIMEN LHS-T

Specimen LHI-1
Large, high-nitrogen
interior defect
static loading condition

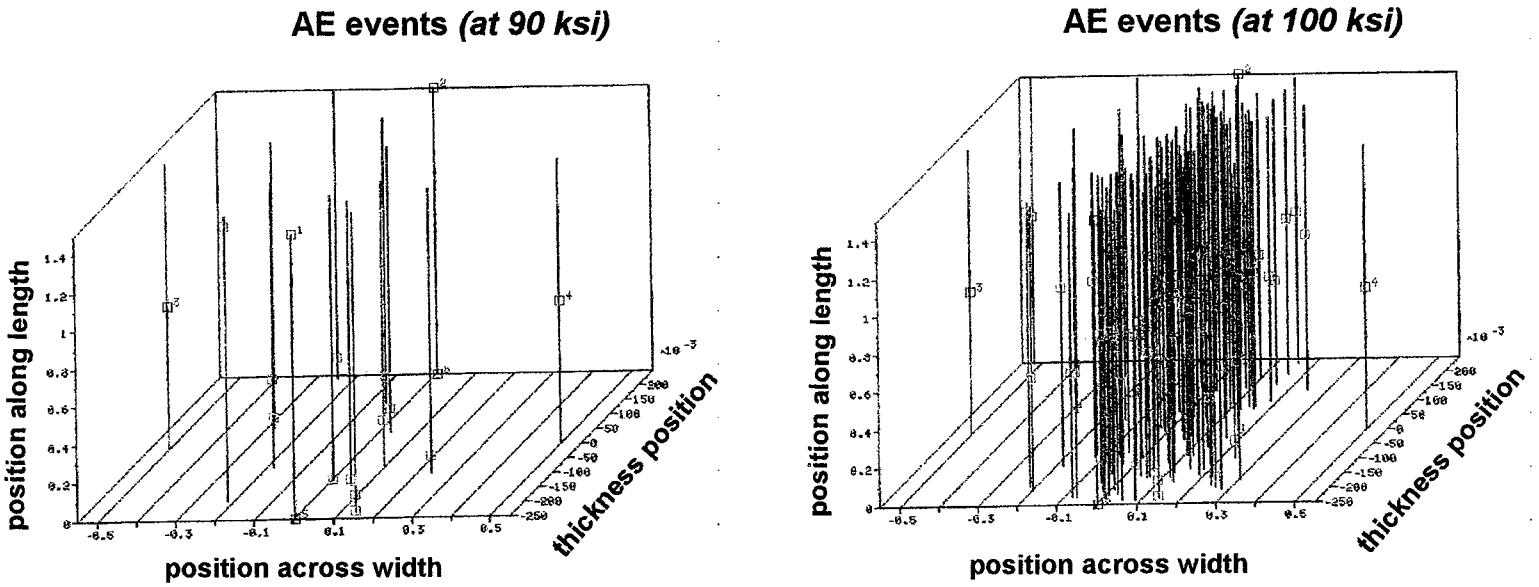


FIGURE H-23. ACOUSTIC EMISSION SOURCE LOCATION DATA FOR TWO CONSECUTIVE LOADING STEPS ON LARGE, HIGH-NITROGEN INTERIOR DEFECT SPECIMEN LHI-1

H.3.3 FATIGUE LOADING OF SYNTHETIC DEFECT SPECIMENS.

The behavior of the hard alpha defects under cyclic loading is of paramount importance to this program since the design methodologies under investigation focus on the fatigue problem. The previous characterization of the static loading case was an important prerequisite for understanding the resulting behavior under cyclic conditions.

H.3.3.1 Surface Defects.

Understanding the behavior of surface defects where damage and cracking are visible is important for interpreting the interior defect case where interpretation is confined only to changes in the external transducer data. Data are shown in figure H-24 for a large, high-nitrogen defect test performed in Phase A. As fatigue loading progressed at a maximum stress of 40 ksi, the output from the transducers as well as the observed crack growth all increased gradually. A slight decrease in the UT output was observed; recall that this transducer was not used in Phase B due to inconsistent data and repeatability problems related to how it was used in practice.

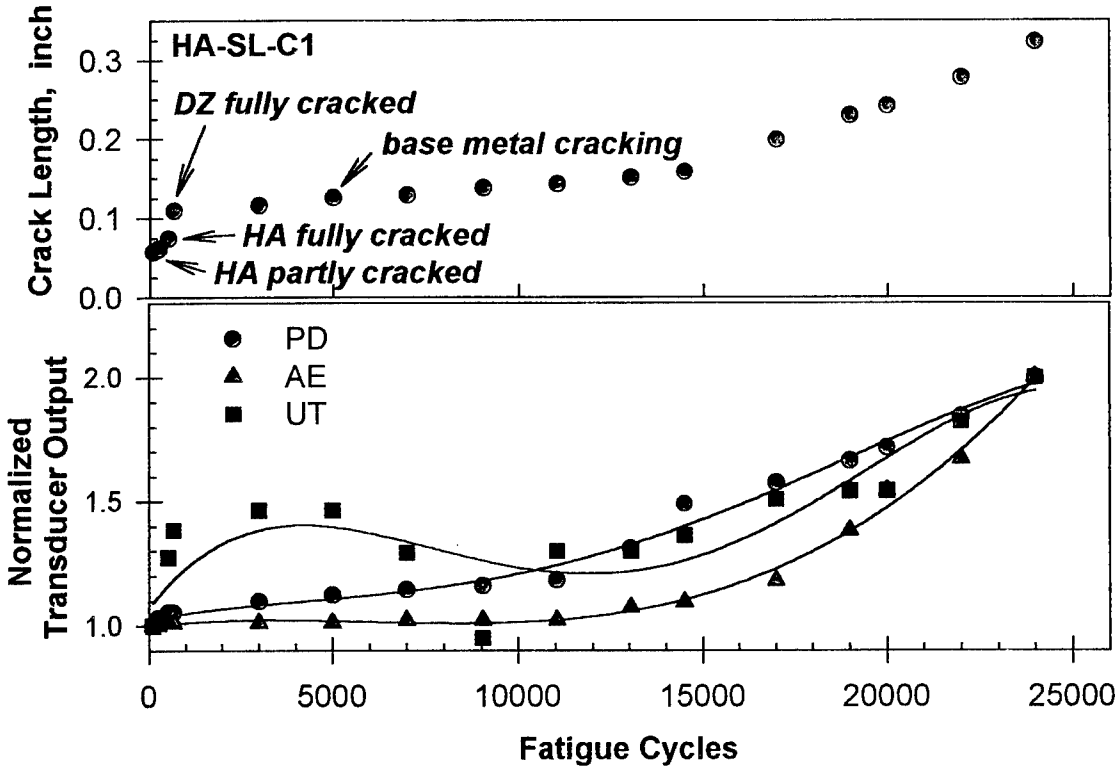


FIGURE H-24. PD, UT, AND AE DATA AND CRACK LENGTH FOR FATIGUE TESTING OF A LARGE, HIGH-NITROGEN SURFACE DEFECT

Generally, linear trends of acoustic data (on a log scale), PD change and surface crack length can be observed in figure H-25 for a high-nitrogen, large surface defect case. Only the initial portion of this data at 2c crack lengths less than 0.130-0.140 inch occurs in the diffusion zone of the

defect. The other data represent growth in the base Ti-6-4 material. Note that the maximum acoustic energy shown in figure H-25 for a large surface defect is on the same order as that observed in figure H-18 for an interior defect specimen. However, the number of acoustic events under fatigue loading conditions is approximately 20 times greater. The implication of similar energy levels but more events during fatigue suggests that the energy emitted during defect cracking is fixed while the events depend upon the nature of the loading. The latter follows from intuition since the fatigue loading is inherently a repeated process.

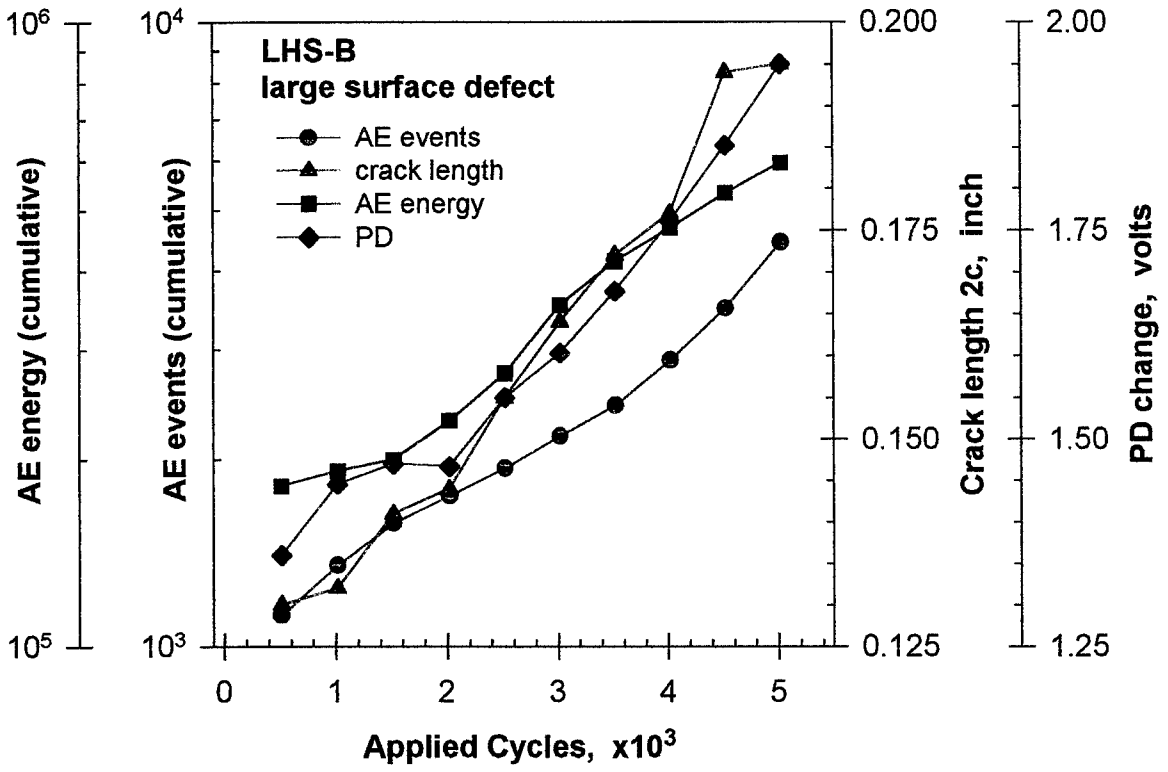


FIGURE H-25. AE, PD, AND CRACK LENGTH FOR A FATIGUE TEST ON A LARGE, HIGH-NITROGEN SURFACE DEFECT SPECIMEN

Initial data during Phase A suggested that the acoustic emission frequency might be a good indicator of cracking occurring in the defect, diffusion zone, and base material. This observation is further examined in figure H-26 by superimposing the acoustic emission frequency and PD data as a function of crack length for two tests: LHS-T (a static-loading test) and LHS-B (a fatigue test). The defect variables of these specimens are identical, and in fact the two specimens were formed from splitting the same original defect block. The acoustic frequency data shown in figure H-26 does vary as growth occurs through the defect core, diffusion zone, and base metal. However, this variation is probably not experimentally significant in view of the large standard deviation bands shown for each. Incidentally, the trilinear PD response is presumably a consequence of rapid diffusion zone cracking at the end of the static test followed by slower surface growth during the fatigue test as the crack assumes a stable aspect ratio.

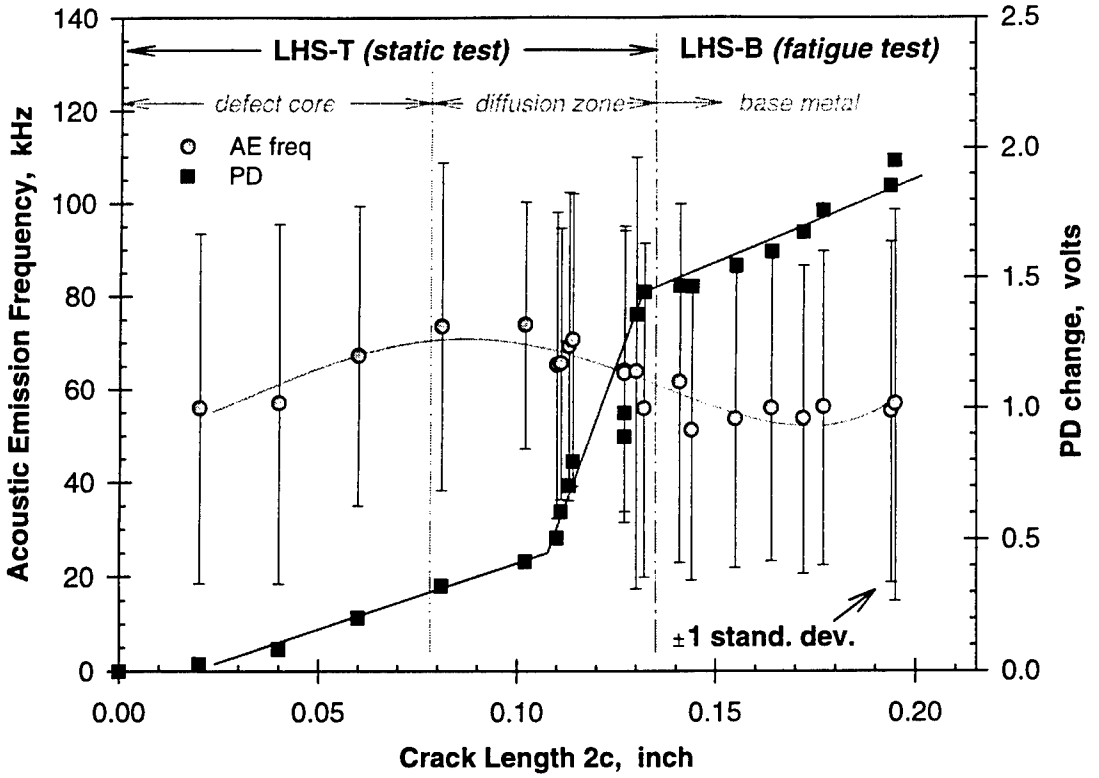


FIGURE H-26. VARIATION IN AE FREQUENCY AND PD WITH CRACK LENGTH FOR A STATIC AND FATIGUE TEST IN A HIGH-NITROGEN, LARGE SURFACE DEFECT

H.3.3.2 Interior Defects.

AE and PD data from the first two fatigue tests performed on interior defects in Phase B are shown in figure H-27 for (a) large and (b) small, high-nitrogen defects. Each of these tests was performed at a maximum stress of 50 ksi and subjected to a number of cycles (see table H-3 for load history). Both measures of acoustic activity increased rapidly over the first 20% of the applied cycles and then gradually increased with additional fatigue loading. The acoustic energy and number of events were consistent with the levels achieved in the static loading case shown in figure H-16. However, the PD data for the two interior defect specimens in figure H-27 exhibited virtually no change.

When the fatigue cycling was completed, the specimens were statically loaded to failure. An SEM micrograph of one of the fracture surfaces is shown in figure H-28. No conclusions can be made regarding fatigue crack growth inside the defect core and diffusion zone since the specimen was statically loaded to failure. However, it is clear from figure H-28 that there is no evidence of any crack progression into the base Ti-6-4 material from the edge of the defect. The same conclusion was made from the fracture surface of the other specimen (not shown). This implies that the acoustic data presented in figure H-27 corresponds only to defect core and diffusion zone cracking; the extent of which is unknown. Given this, the acoustic data presented can be used as a basis to estimate the lower bound of that required to fully crack the defect and diffusion zone. Based on the data presented in figure H-28, it is estimated that a minimum

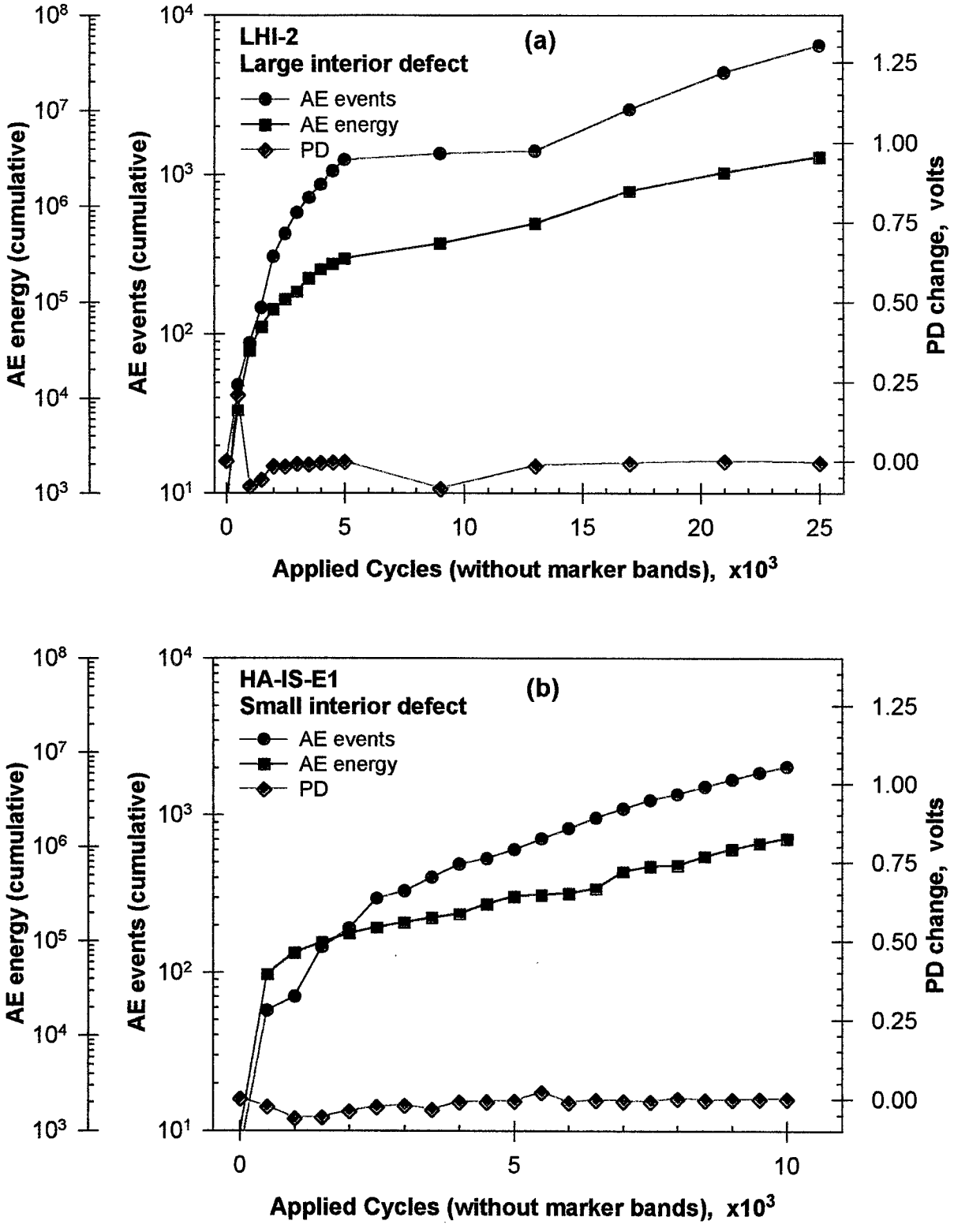


FIGURE H-27. AE AND PD DATA FOR TWO HIGH-NITROGEN INTERIOR DEFECTS ((a) LHI-2 (large) and (b) HA-IS-E1 (small), that exhibited no evidence of fatigue crack growth when statically failed after fatigue cycling.)

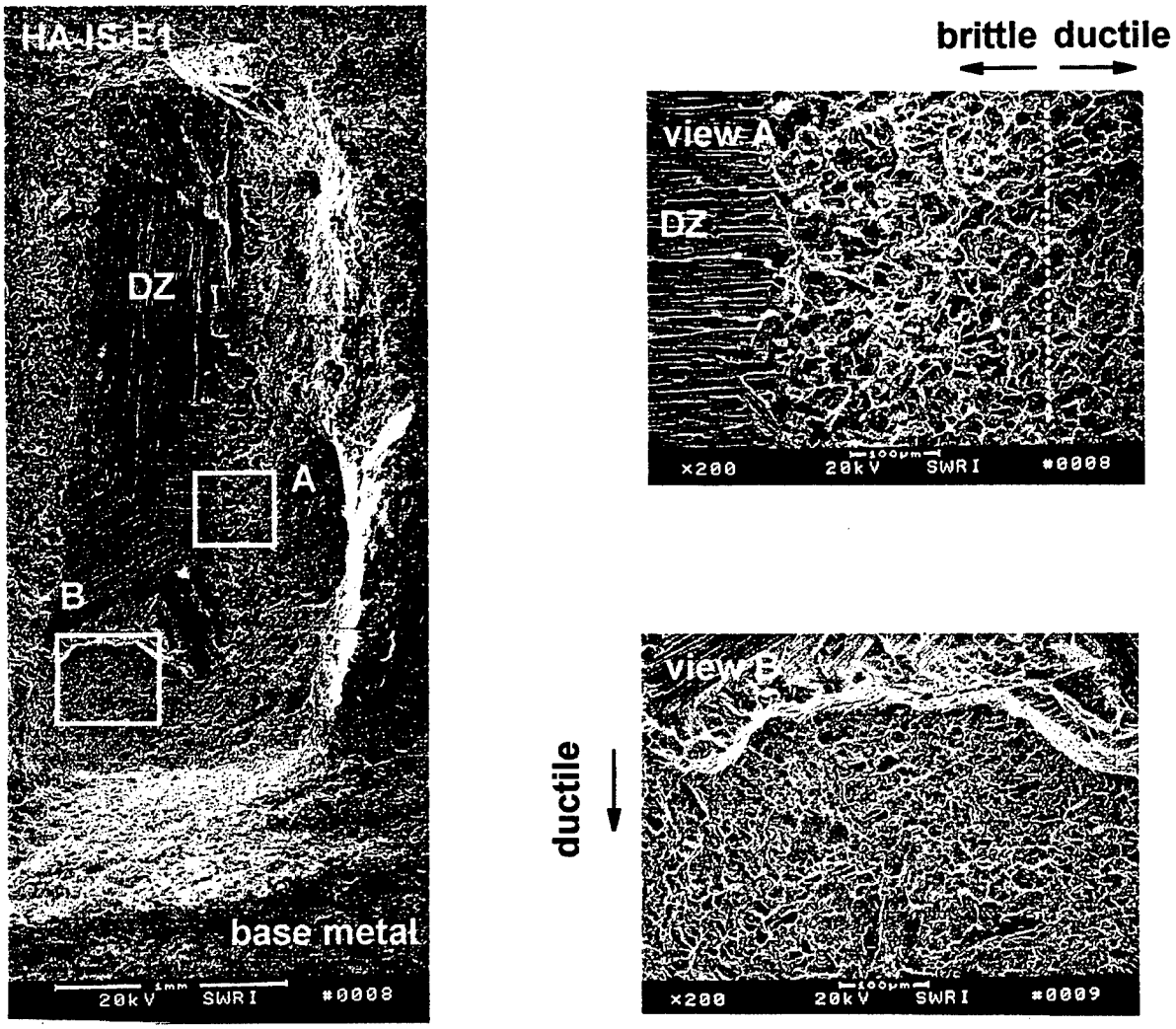


FIGURE H-28. SEM PHOTOMICROGRAPH OF THE FRACTURE SURFACE FOR SPECIMEN HA-IS-E1 (HIGH-NITROGEN, SMALL INTERIOR DEFECT) SHOWING NO FATIGUE CRACK GROWTH INTO THE MATRIX

of 6000 events (large defect) and 2000 events (small defect) are required with total acoustic energies in the range of 1-3(10^6) to result in (some degree of) core and diffusion zone cracking. These acoustic events and energy levels roughly scale with the ratio of planar areas (a factor of approximately four) of a small and large defect.

Transducer outputs from the next two fatigue tests, both on large defects (low- and medium-nitrogen content), are shown in figures H-29 and H-30 with the corresponding fracture surfaces in figure H-31. The maximum stress level in these two tests was increased to 75 ksi (see table H-3 for cyclic loading conditions), and crack growth into the base material can be observed in figure H-31. For the case of LLI-2 (figures H-29 and H-31(a)), the low *R*-ratio portion of the cycling corresponds to the lighter central region around the one end of the defect in the fractograph. The subsequent band of crack growth extending past this initial region (and to specimen failure) appears darker and corresponds to growth under the high *R*-ratio marker band.

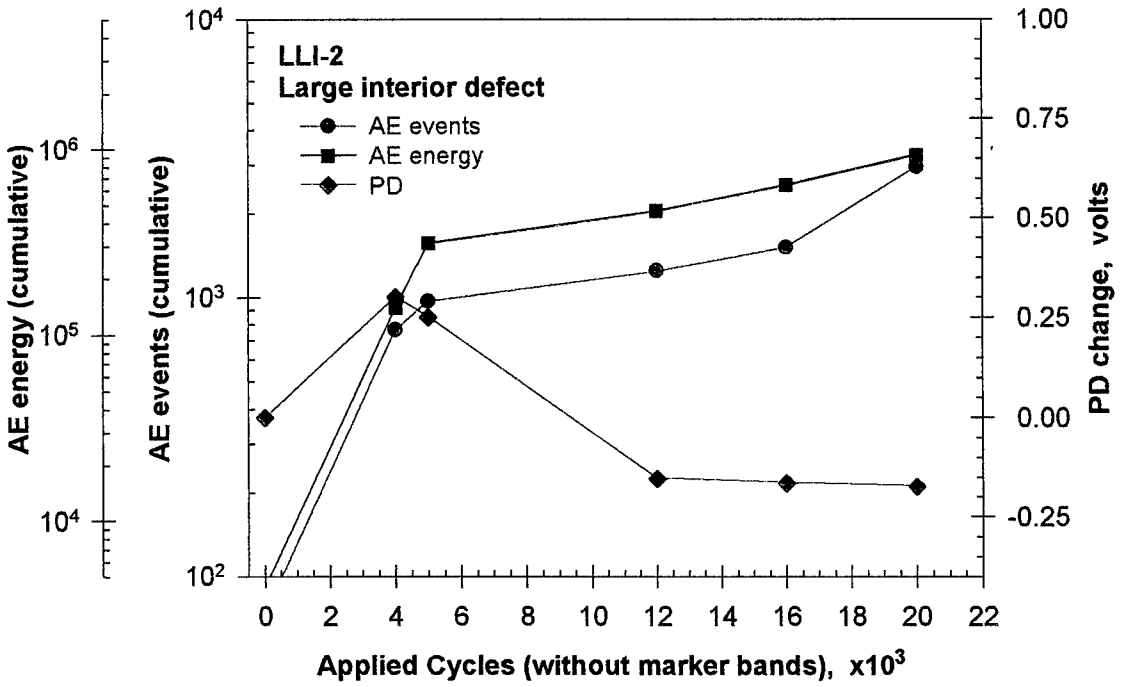


FIGURE H-29. FATIGUE TEST DATA FROM A LARGE INTERIOR DEFECT (LOW-NITROGEN) SPECIMEN

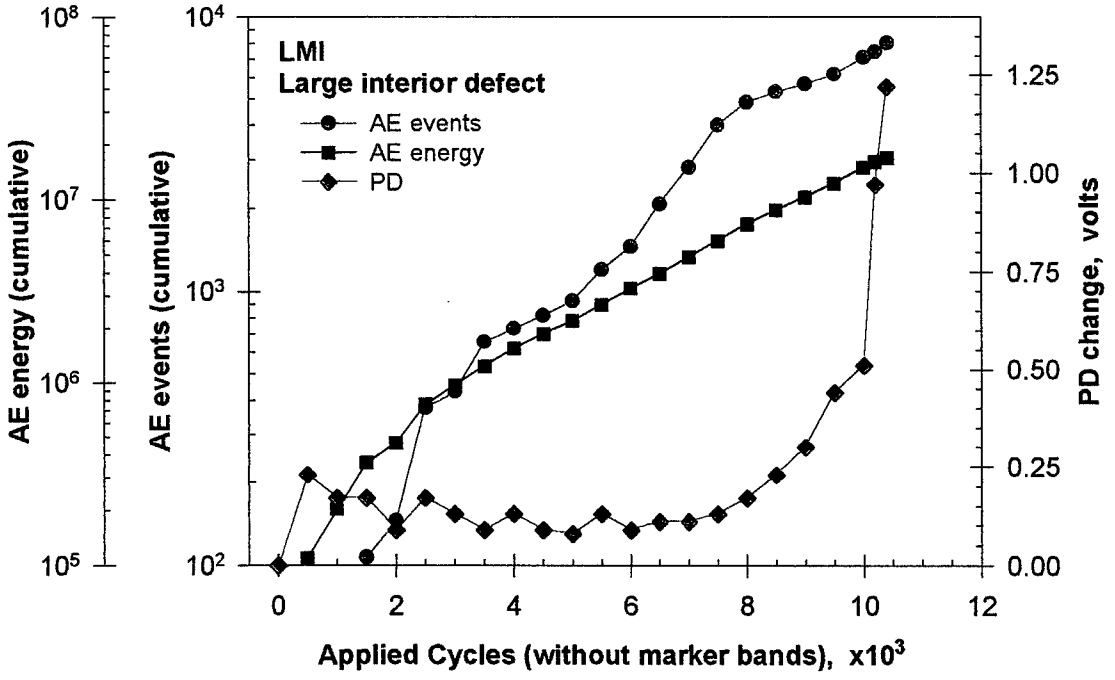


FIGURE 30. FATIGUE TEST DATA FROM A LARGE INTERIOR DEFECT (MEDIUM-NITROGEN) SPECIMEN

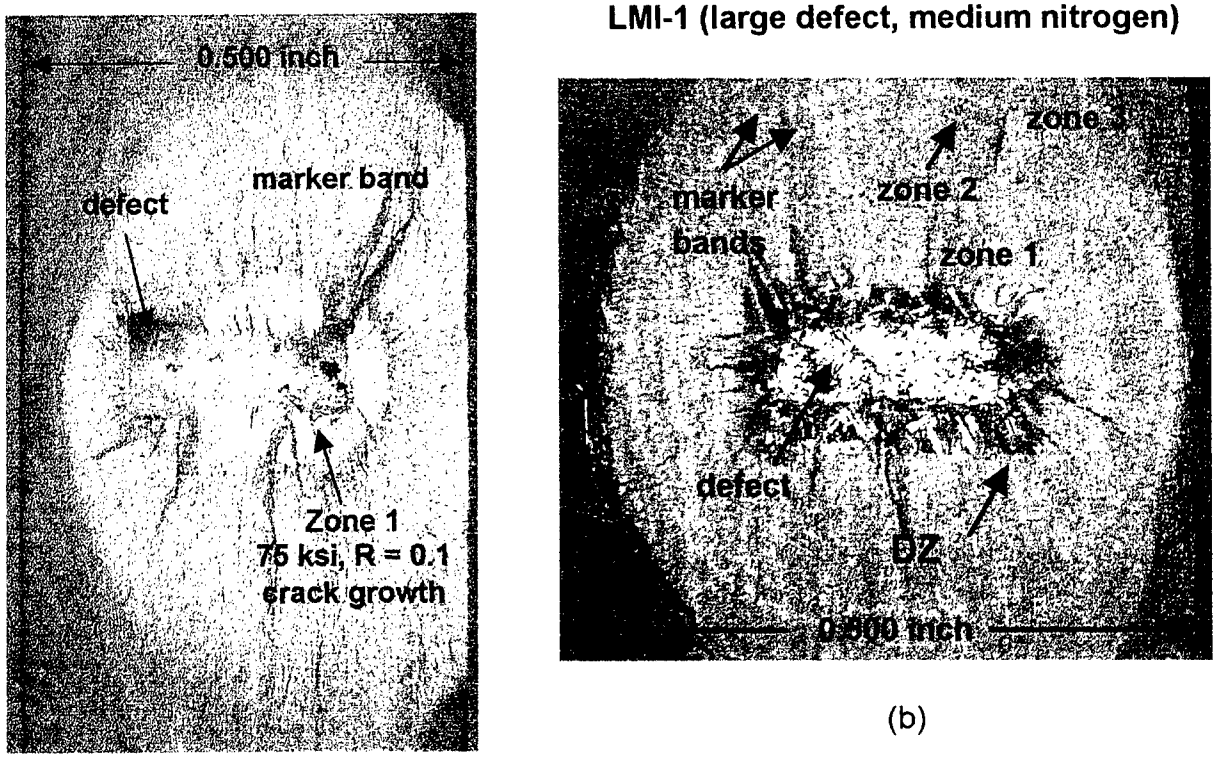


FIGURE H-31. FRACTURE SURFACES FOR TWO LARGE, INTERIOR DEFECT SPECIMENS SUBJECTED TO FATIGUE LOADING

The fracture surface marking suggests that at the end of the R = 0.1 loading, the crack had enveloped approximately 2/3 of the HA core and diffusion zone. However, as observed in figure H-29, the PD data did not provide any indication of this crack growth. Similarly, the acoustic event count and energy was approximately the same as the threshold levels noted from figure H-27 for the case of core/DZ cracking only. Presumably, the inability of the acoustic data to suggest any crack growth outside the defect is a consequence of the fact that the crack was small and similar in area to a fully cracked core/DZ.

The transducer data and fractograph for the final synthetic defect, LMI-1, are shown in figures H-30 and H-31(b), respectively. The fatigue crack marking procedure was more successful for this test as evidenced by the two marker bands on the fracture surface separating zones 1 and 2. For this specimen, the PD change indicated crack progression for the last 2000 cycles of growth. Conversely, the plot of acoustic events and energy is relatively smooth with no perturbation that can be obviously related to a change in conditions. Using the earlier derived acoustic threshold data, the event count exceeds the 6000 level for the last 2000 cycles while the energy exceeds the 3 million threshold for the last 4000 cycles of growth. Presumably, this is a reasonable estimate of the earliest period that crack propagation could have occurred from the defect.

In summary, these fatigue tests demonstrated the damage tolerance of specimens with initially uncracked artificial defects embedded in them. This testing has further shown that acoustic events, energy, and PD to some degree can be used as a first order indicator of when cracking progresses past the defect and into the base material. Although the data are few and the results far from definitive, this method appears to hold some promise for determining when cracking progresses outside the defect.

H.3.4 FATIGUE TESTING OF NATURALLY OCCURRING DEFECTS.

Test results are shown for naturally occurring surface and interior defects in figure H-32 (transducer data) and figure H-33 (fractographs). For the case of the surface defect, test RMI-E1 performed at a maximum stress of 50 ksi, the defect initiated in the central core region on the surface of the specimen and progressively grew down the thickness. The unusual shape of the fatigue crack is a consequence of continuous crack initiation along the diffusion zone extending through the thickness of the specimen. This is a significant observation since it implies that the material that appears to be diffusion zone was not fully cracked after the first cycle but rather was able to sustain significant fatigue loading.

The acoustic data for this test, figure H-32(a), was marked by an initial burst of activity, followed by a quiet period during which the crack grew steadily. This was followed by another burst of activity at the end of the test. It should also be noted that the acoustic data is represented in terms of hits since the smaller specimen size only allowed two (versus six) acoustic microphones. As such, it is impossible to compare the magnitudes of the acoustic activity to that observed in the synthetic defect cases.

The naturally occurring internal defect specimen, RMI-F1, proved more difficult to initiate and grow a crack than either the natural surface defect or any of the synthetic defect tests performed. As is apparent from table H-5 and figure H-32(b), four loading steps spanning a maximum stress from 50 to 100 ksi were required. At each step, there typically was a burst of activity after which the acoustic emission settled to near background conditions. The acoustic data in figure H-32(b) looks similar in form to that obtained with the natural surface defect. Events and energy initially climbed, followed by a settling in magnitude. It appears, however, that acoustic activity restarted and continued after the loading was increased to the 75 ksi level. The PD data suggest that crack growth definitely was occurring during the last portion of the 100 ksi block. However, it is impossible to identify when crack growth started.

Marking is clearly apparent on the fracture surface in figure H-33(b). However, in this case, the link between this marking and the applied loading is difficult to know definitively. The two regions (marked Region A and B) could subdivide the 75 from the 100 ksi loading bands (highly unlikely based on subsequent Flight_Life calculations presented in the next section) or they might represent changes during the last 100 ksi block between $R = 0.1$ from the $R = 0.7$ loading. Differences are also apparent when comparing the acoustic emission data to that obtained for the synthetic defects. Clearly, the acoustic emission observed in the natural subsurface defect was an order of magnitude or more greater (for both events and energy) than observed in the synthetic defects. Relating the acoustic data to earlier synthetic defect testing is problematic due to the differing defect sizes (the natural internal HA exposed on the fracture was tiny compared

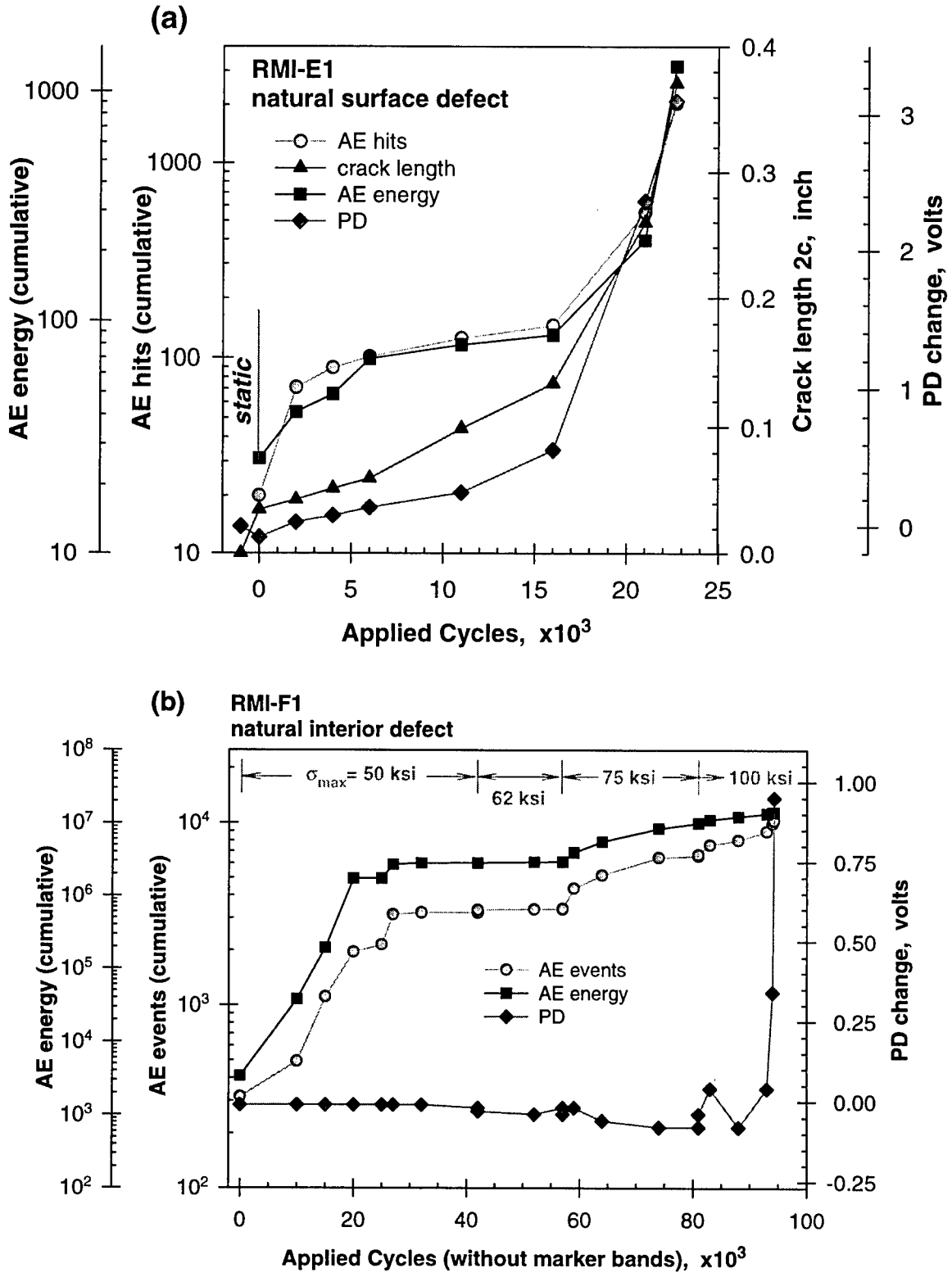


FIGURE H-32. AE AND PD DATA FROM THE TWO FATIGUE TESTS PERFORMED ON NATURALLY OCCURRING DEFECTS

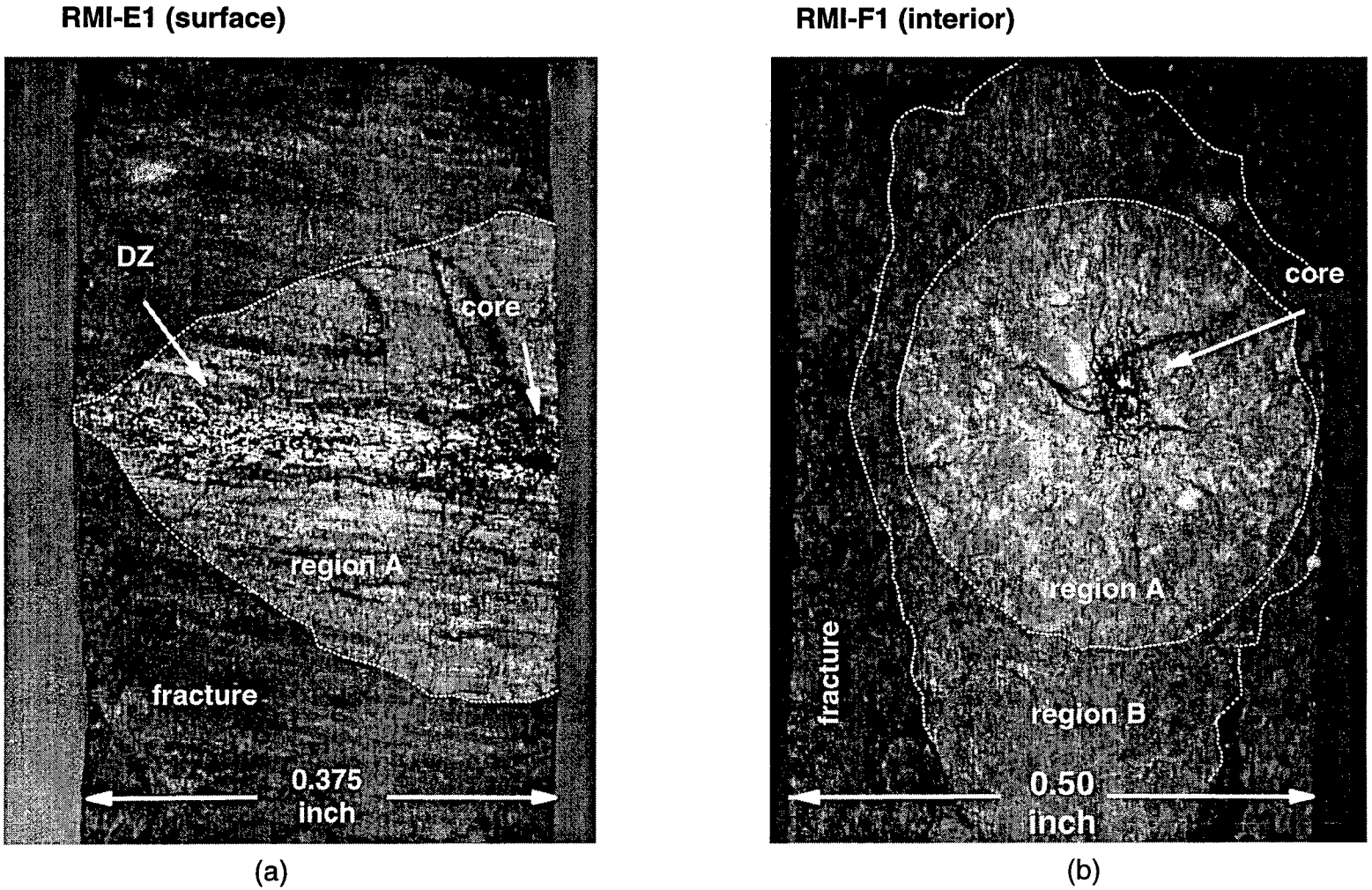


FIGURE H-33. FRACTURE SURFACES FOR TWO NATURALLY OCCURRING DEFECT (SURFACE AND INTERIOR) SPECIMENS SUBJECTED TO FATIGUE LOADING CONDITIONS

to the synthetic HA). Curiously, the observed trend seems counter intuitive based on what was observed in the synthetic defect testing; a smaller natural defect would have been expected to emit less acoustic energy and fewer events that the large synthetic variety. This apparent contradiction can, however, be explained. The exposed interior defect evident in figure H-33(b) is believed to be significantly smaller than the total embedded defect. The previously detailed SwRI UT study suggested that the defect was 0.7 inch axially and at one point 0.3 inch across – much bigger than the small exposed defect.

Perhaps the most notable observation from the natural defect testing is the cyclic life observed for the specimens. For the surface defect, crack breakthrough occurred after almost 25,000 cycles at 50 ksi maximum stress level and low R-ratio loading. Conversely, the interior defect specimen sustained over 90,000 cycles at various stress levels exceeding 50 ksi, including over 13,000 cycles at 100 ksi.

H.3.5 Flight_Life ANALYSIS OF FATIGUE TEST RESULTS.

H.3.5.1 Methodology.

The Flight_Life fatigue crack growth analysis module in the Design Assessment of Reliability With INspection (DARWIN) computer was used to simulate some of the fatigue experiments on specimens with internal defects. Comparisons between predicted (Flight_Life) and actual (experimentally observed) numbers of fatigue cycles to cause a given amount of crack growth provided some insight on the length of time required to nucleate a growing fatigue crack from the defect into the matrix.

Fatigue crack growth (FCG) properties for the Flight_Life analysis were based on the vacuum FCG data and regressions for Ti-6Al-4V that were generated in the current program (see appendix I). Vacuum data were selected, since the embedded defects were isolated from the atmosphere and hence grew in a vacuum-like environment. The specific FCG equations used in the Flight_Life analysis were based on the Paris regressions documented in appendix I, with specific cutoffs at both threshold and instability. In general, these equations followed the simple single linear Paris form. However, the regression lines for the vacuum data crossed above the regression lines for representative air data from the Damage Tolerant Design handbook (see again appendix I) at large values of ΔK, implying that crack growth occurred faster in vacuum than in air. In reality, vacuum and air data are seen to merge at high ΔK, and the crossover is an extrapolation artifact of the single linear Paris regressions. Therefore, a bilinear Paris equation form was adopted in which the lower regression line followed the vacuum data until the point of crossover with the relevant air Paris regression, and then the upper regression line followed the air data regression above the crossover. The specific Paris regressions for room temperature, $R = 0$, data employed in this analysis are shown in figure H-34 (the bilinear curve was offset graphically for clarity). Regressions for data at higher stress ratios were qualitatively similar. This adjustment had only a small impact on most calculations, since most of the crack growth lifetime is spent at lower ΔK values below the vacuum-air crossover.

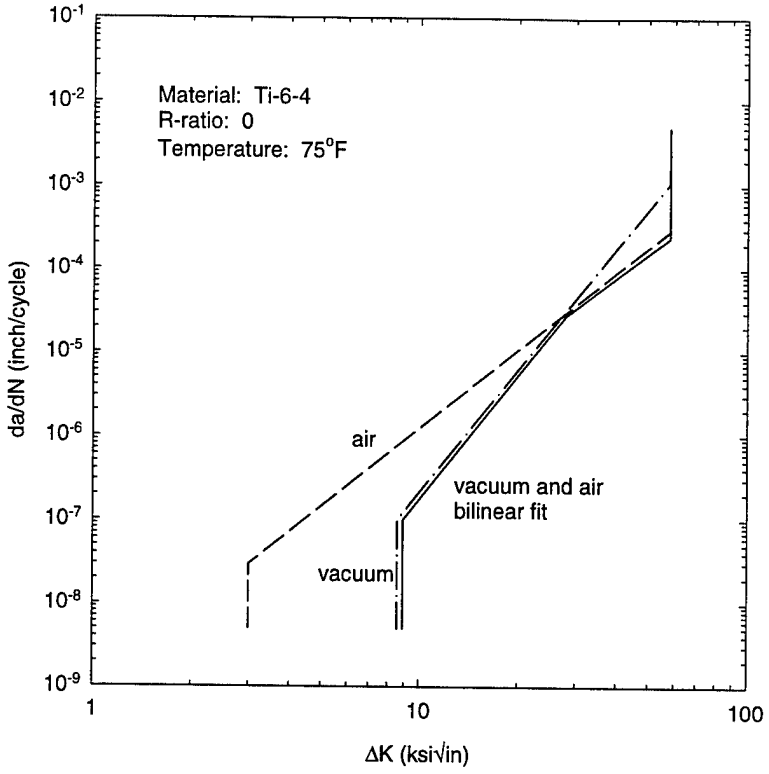


FIGURE H-34. FATIGUE CRACK GROWTH RELATIONSHIPS EMPLOYED IN Flight_Life ANALYSIS OF FATIGUE TESTS

It is important to establish some confidence in the suitability of the vacuum FCG regressions to describe subsurface crack growth in the specific specimens used in this study. This validation was performed by analyzing crack growth in the LMI specimen, where marker bands worked most effectively. This specimen (see again figure H-31(b)) exhibited two narrow marker bands for relatively large embedded cracks with regular elliptical shapes. The width of the marker bands themselves, resulting from the application of 2500 or 2000 cycles of $R = 0.7$, $\sigma_{max} = 75$ ksi loading, was measured to be about 0.010 inch and predicted to be between 0.008 and 0.009 inch. Crack growth between the two marker bands (Zone 2 in figure H-31(b)) was generated by the application of 200 cycles of $R = 0.1$, $\sigma_{max} = 75$ ksi loading. Flight_Life predicted this same amount of growth in approximately 120 cycles. The difference between the two values—less than a factor of two—is within the normal scatter in FCG behavior. These are all relatively unambiguous results, since the fatigue crack had fully nucleated in the matrix and was growing in a stable manner and initial and final cracks were distinct in size and had stable shapes.

Based on this validation, it is now possible to evaluate fatigue crack growth from the hard alpha defect itself. One of the purposes of this test program was to determine if a nonnegligible number of cycles was consumed during nucleation of a growing fatigue crack in the defect and surrounding matrix. In actual forged hardware, of course, it is possible that the hard alpha anomaly is voided and even extensively cracked before the rotor ever enters service, as a result of the forging deformation. Current probabilistic design practice assumes that the defect core and its surrounding diffusion zone is cracked on Cycle 1 and further assumes that the crack

begins to grow into the matrix material on the first fatigue cycle. Although, this is a conservative assumption, it is theoretically possible that it is overconservative under some conditions.

This assumption was evaluated by calculating the predicted life of each specimen and comparing with the actual observed fatigue life. The original defect size (core + diffusion zone) was measured from the fracture surface at the end of the test. The artificial hard alpha defects generally had a rectangular cross-section in the plane normal to the specimen axis. An initial elliptical fatigue crack was postulated with the same cross-sectional area and aspect ratio (length-to-width ratio) as the measured defect (core + diffusion zone). This approach is similar to the current probabilistic design practice, which assumes an initial fatigue crack of circular shape and equivalent area to the actual hard alpha anomaly. The number of cycles for this initial crack to grow to some known intermediate size, or to grow to final specimen failure, was then calculated with Flight_Life. If the actual number of cycles applied in the test was significantly larger than this calculated value, then the difference might indicate a nucleation period.

Calculations of this type were performed for four tests with artificial internal defects and one test with a natural internal defect. The calculations and comparisons are summarized in table H-7.

TABLE H-7. COMPARISON OF Flight_Life PREDICTIONS WITH EXPERIMENTAL RESULTS FOR FATIGUE TESTS WITH INTERNAL DEFECTS AND PERFORMED AT $R = 0.1$

Specimen	Maximum Stress	Observed Crack Growth	Cycles Applied	Cycles Predicted
HA-IS-E1	50 ksi	no growth	10,000	71,347 to failure
LHI-2	50 ksi	no growth	25,000	19,156 to failure
LLI-2	75 ksi	to 0.174″ × 0.214″ ellipse	20,000	2500
LMI	75 ksi	to 0.376″ × 0.419″ ellipse	10,000	2700
RMI-F1	50 ksi	unknown	42,000	No failure
	62 ksi	unknown	15,000	No failure
	75 ksi	unknown	24,000	23,312 to failure
	100 ksi	failure	13,285	5680 to failure

H.3.5.2 Results of Simulations.

In the first two seeded fatigue tests (HA-IS-E1 and LHI-2), the specimens were cycled at $R = 0.1$ and $\sigma_{max} = 50$ ksi for a predetermined number of cycles and then broken open statically. Posttest inspection of the fracture surface indicated that no fatigue crack growth had occurred in the titanium matrix. Flight_Life analysis of HA-IS-E1 indicated that a small amount of crack growth—a few mils—should have occurred during the 10,000 cycles of loading. However, Flight_Life analysis of LHI-2 predicted that the crack should have grown to failure in 19,156 cycles. In reality, 25,000 cycles (and even some additional marker band cycles) were applied without inducing any fatigue crack growth in the matrix (LLI-2 and LMI).

In the next two seeded fatigue tests, both conducted at $R = 0.1$ and $\sigma_{max} = 75$ ksi, marker bands provided a distinct intermediate crack size and shape as the termination of the initial growth

period. In both cases, the predicted number of cycles to achieve this size, based on the assumed initial flaw size as described above, was around 2500 cycles. In actuality, four to eight times greater number of cycles were applied to reach this size—10,000 in one case and 20,000 in the other case.

The final fatigue test with an internal defect was RMI-F1, with a naturally occurring defect from the RMI CBS material. This experiment was conducted somewhat like a step test. Since the original defect size was completely unknown until the end of the test, cycling started at a low stress level, and the applied stress was increased in steps until the specimen fractured. In this case, the initial defect size employed in the calculations probably corresponded more closely to the defect core, since a distinct diffusion zone was not readily apparent from the fracture surface. Further study of the fracture surface may be needed to identify an appropriate initial defect size more accurately. The posttest analysis predicted zero or minimal growth during the cycles at σ_{max} = 50 ksi and σ_{max} = 62 ksi. However, the analysis predicted specimen failure following about 23,000 cycles at σ_{max} = 75 ksi. Coincidentally, the specimen was subjected to 24,000 cycles at this stress level, but did not fail and (in retrospect) may have exhibited little or no fatigue crack growth at all at this stress level. The specimen failed following 13,285 cycles at the final stress level of 100 ksi, but the predicted life at this stress level was only about 5,700 cycles. Although, marker bands were also applied; these were unsuccessful in marking the surface clearly and ignoring them in the analysis is conservative for present purposes (the predicted life would have been slightly lower if they had been included).

H.3.5.3 Discussion.

Analysis of the four internally seeded fatigue tests and the single RMI test with an internal defect all indicated that some nonnegligible number of cycles was consumed by nucleation of a growing fatigue crack in the matrix. Predictions of crack growth life based on the assumption that a fatigue crack equal in size to the hard alpha defect plus the diffusion zone was growing on Cycle 1 were all conservative, sometimes excessively so.

However, it must be emphasized that this very small number of tests represents a very limited parameter range. Furthermore, these tests may not be fully representative of actual hardware under actual service conditions. Actual hardware would have experienced a complete forging operation after defect formation, and it is possible that this forging operation would have either nucleated more severe initial cracks in the hard alpha anomaly or even grown cracks into the matrix itself. There is some industry experience suggesting that some rotor fatigue cracks nucleated at hard alpha defects did, in fact, begin growing in the matrix at the very beginning of life. However, it is not known at the present time how the conditions in those events (defect size, applied stress level, etc.) compare to the current test matrix. It is possible that larger defects, or defects in higher stress fields, would form a matrix fatigue crack much more quickly.

Until additional testing and analysis are performed, it seems appropriate to continue to use the current conservative industry assumption: assume a growing fatigue crack in the matrix on Cycle 1 with initial size equal to the size of the defect core plus diffusion zone. However, additional testing and analysis should be performed to understand any differences between

laboratory tests and industry field experience and to quantify any nonnegligible nucleation life of practical significance.

H.4 SUMMARY.

The testing has provided a wealth of information regarding the behavior of both synthetic and naturally occurring hard alpha defects under static and fatigue loading. The results and observations from this testing are summarized and described below.

a. Of the different damage detection transducers used, the acoustic emission and potential drop methods provide the most promise for detecting damage and cracking in the absence of the time-consuming, but definitive, metallographic assessment by defect sectioning. The PD method proved only marginally successful for the case of internal defects with a significant drop in sensitivity when contrasted to the surface defect case. Both the PD and AE methods are exceptionally difficult to calibrate given the three-dimensional nature of damage and the sensitivity required to detect damage progression.

b. The core and diffusion zone from a synthetic defect (nominally 6% nitrogen) was characterized in terms of composition and hardness as a function of radial position. After a radial distance of 0.002 inch into the diffusion zone, the nitrogen composition was observed to drop sharply to 0.8-1.0 percent from a nominal 5% in the core. The defect core had a constant hardness on the order of an Rc of 64, which is approximately 2.2 times greater than the base metal.

c. Visual observations of cracking under static loading in surface defects suggest that the core/DZ cracks easily, but cracks arrest before extending into the base Ti-6-4 material. Crack initiation was observed in the defect cores at stress levels less than 20 ksi and often at stress levels below 10 ksi. Crack initiation and propagation through the diffusion zone typically occurs at stress levels in excess of 30 ksi with full diffusion zone cracking observed at stress levels on the order of 50-100 ksi.

d. The acoustic emission data suggest that significantly higher stresses can be sustained by internal defects prior to the onset of cracking. Significant levels of emission are first observed at stress levels typically in excess of 80 ksi and sometimes as high as 100 ksi or greater. Metallurgical sectioning of four specimens loaded to 100 ksi or greater revealed extensive damage and numerous continuous cracks distributed throughout the diffusion zone and core. For two of the cases, the defect core was generally intact, and in two others the defect was shattered. However, significant damage was noted in the diffusion zone region or at the interface between the diffusion zone and base metal.

e. Acoustic emission frequency variation is not a clear indicator of where the cracking predominantly occurs (e.g., in the core, diffusion zone, or base metal). However, other acoustic parameters, namely cumulative emission events and energy level, appear more promising for indicating extent of damage or onset of cracking into the base metal under fatigue loading conditions.

f. Crack coalescence and growth occurs rapidly in surface defect specimens subjected to fatigue loading. Conversely, the internal defects exhibit much greater resistance to crack propagation especially into the base metal. Both sizes of high-nitrogen defects were subjected to fatigue loading at 50 ksi (R = 0.1) for either 10 or 25 k cycles with no observed crack growth into the base metal. Maximum fatigue stresses needed to be increased to 75 ksi (R = 0.1) to cause growth into the base Ti-6-4 material.

g. The naturally occurring surface defect exhibited rapid initiation during fatigue loading at a maximum stress of 50 ksi (R = 0.1). The posttest fractographic evidence suggests that the complete diffusion zone was not completely cracked initially. Rather, crack initiation and propagation occurred gradually and in a sequential manner through the thickness with numerous initiations occurring at the interface between the diffusion zone and base metal.

h. The naturally occurring internal defect specimen required a stress level on the order of 75-100 ksi (R = 0.1) to cause fatigue crack formation and growth in the matrix. The natural internal defect was probably much larger than the synthetic defects; hence, explaining why the acoustic emission data proved to be an order of magnitude greater. Furthermore, the cyclic life of this small internal defect was quite large: it sustained over 90 k cycles at stress levels exceeding 50 ksi.

i. Flight_Life calculations simulating the test conditions suggest that both the low and high R-ratio, Ti-6-4 vacuum crack growth data are suitable for the materials used in this evaluation. The analytical simulations of the laboratory experiments generally provided good cyclic comparisons given a crack growing in the matrix remote from the defect. However, the fact that the simulations underpredicted the experimental cycle count for growth immediately from the defect suggests that there is a finite crack initiation and incubation time for the defect. Although this suggests that the assumption of matrix cracking for the first applied cycle is conservative, the applicability of these limited results to the behavior of real, forged defects is currently unknown and worthy of additional focus.

APPENDIX I—FATIGUE CRACK GROWTH RATE TESTING OF THREE TITANIUM ROTOR ALLOYS IN VACUUM

I.1 INTRODUCTION.

The focus of the current program is reduction of the risk from melt-related anomalies called hard alpha (HA), which are small zones in the microstructure where the alpha phase has been stabilized by the presence of nitrogen that can be introduced at various stages in the melting history. These hard zones are brittle, usually have cracks and voids associated with them, and have been responsible for the initiation of low-cycle fatigue cracks that resulted in disk failures. Although HA occurrence rates are extremely low and inspection techniques are improving, HA most commonly occurs at subsurface locations, where undetected fatigue cracks can potentially nucleate and grow. Since these cracks are not exposed to the atmosphere, they grow in a vacuum-like environment.

Numerous researchers have noted a difference between fatigue crack growth (FCG) rates in air and vacuum for titanium alloys [I-1 – I-11]. This previous work is summarized in table I-1. However, these investigations were generally limited to a single stress ratio (typically $R = 0.1$) and a single temperature (typically ambient). Information on systematic changes in vacuum behavior with stress ratio or temperature has not been available. Of greater significance for the current application, insufficient vacuum data were available to support a complete lifing system for FCG in turbine engine rotors, and therefore it has been difficult to accurately evaluate the risk associated with crack nucleation at subsurface HA anomalies.

TABLE I-1. PREVIOUS RESEARCH ON VACUUM EFFECTS IN TITANIUM

Authors	Alloy	Ratio	Temperature	Reference
Meyn (1971)	Ti-8-1-1	0.1	RT	[I-1]
Irving & Beevers (1974)	Ti-6-4	0.35	RT	[I-2]
Doker & Munz (1977)	Ti-6-4	0.1	RT	[I-3]
Ruppen & McEvily (1984)	Ti-6-2-4-2	0.05	RT, 1000°F	[I-4]
Peters, Gysler, Lutjering (1984)	Ti-6-4	0.2	RT	[I-5]
Gao, Simmons, Wei (1984)	Ti-6-4, Ti-5-2.5	0.1	RT	[I-6]
Vesier & Antolovich (1990)	Ti-6-2-4-2	0.1	RT	[I-7]
Ghonem & Foerch (1991)	Ti-1100	0.1	1100°F	[I-8, I-9]
Petit, Berata, Bouchet (1992)	Ti-6-4	0.1	RT, 572°F	[I-10]
Bache, Evans, McElhone (1997)	Ti-6-4	0.01	RT	[I-11]

In order to address this need and to provide adequate data to support a probabilistic damage tolerance assessment of cracking at internal hard alpha defects in titanium rotors, a major test program was conducted. Vacuum FCG tests were performed on three titanium alloys commonly used by the aircraft turbine engine industry: Ti-6Al-4V (more commonly denoted Ti-6-4), Ti-6Al-2Sn-4Zr-2Mo+Si (more commonly denoted Ti-6-2-4-2), and Ti-17 (nominal composition Ti-5Al-2Sn-2Zr-4Mo-4Cr). These tests were conducted in engine company laboratories, following standard industry practices for the generation of FCG design data. This appendix provides a comprehensive documentation of the materials tested, test procedures, and results,

including complete graphical and tabular representations of the test data, regressions of the data to conventional FCG models, and comparisons with representative air data.

I.2 MATERIALS TESTED.

I.2.1 Ti-6Al-4V.

The Ti-6-4 test specimens were machined from a production quality, triple vacuum arc remelt (VAR) melted, high by-pass ratio fan disk forging provided by General Electric Aircraft Engines (GEAE). The microstructure is shown in figure I-1. The pedigree of the forging is summarized below:

Processing:	Alpha + beta forged Solution treated below transus and water quenched + overaged
Certification:	Serial No. – WZA 63315 Heat No. – RT 4422 Mill – OREMET Conversion source – Wyman Gordan
Tensile Properties:	0.2% yield strength – 140 ksi Ultimate tensile strength – 152 ksi % elongation – 15 percent % RA – 37 percent

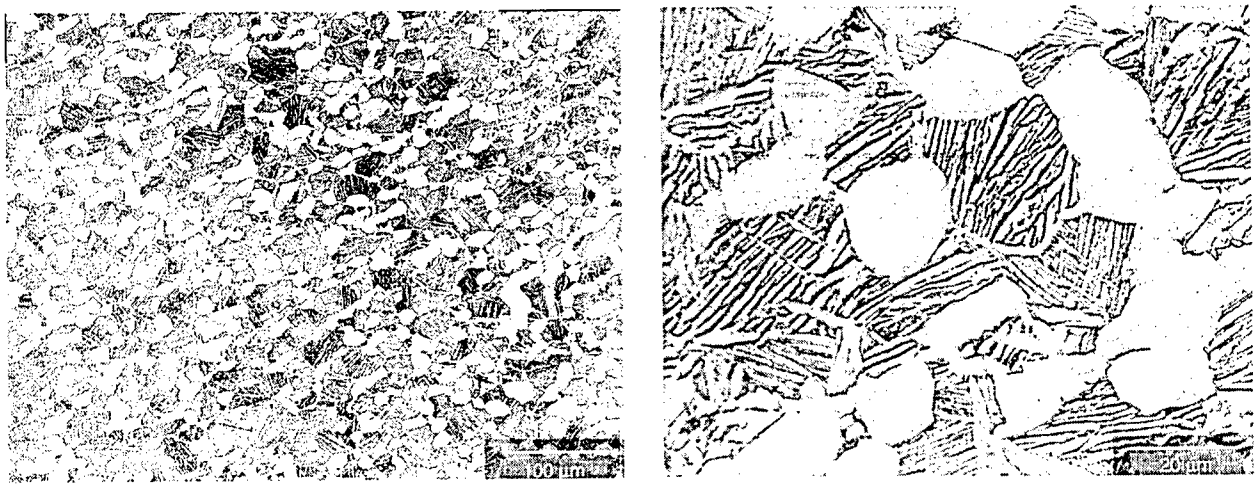


FIGURE I-1. MICROSTRUCTURE OF Ti-6Al-4V FORGING

I.2.2 Ti-6Al-2Sn-4Zr-2Mo+Si.

The Ti-6-2-4-2 material selected for the test program was triple VAR melted, extracted from a single radial compressor forging supplied by AlliedSignal Engines. The forging pedigree is summarized below.

Ingot to Billet Conversion: Converted from 30″-34″ diameter VAR ingot to 8″ diameter billet. Final billet conversion operations are conducted in the alpha-beta temperature range. Typical AMS 2380 macro levels of 20 to 30 are achieved.

Forging Practice:	Alpha-beta forged on conventional dies with an approximate 2.5:1 upset
Heat Treatment:	Solution treated at T_β – 25°F, rapid air cooled and aged at 1100°F for 8 hrs
Typical Tensile Properties:	0.2% yield strength – 133 ksi Ultimate tensile strength – 145 ksi % elongation – 18 percent % RA – 35 percent

The above process results in a uniform distribution of fine equiaxed alpha phase in a transformed beta matrix. The volume fraction of primary alpha phases in the test forging is 40 to 60 percent. This microstructure is shown in figure I-2.

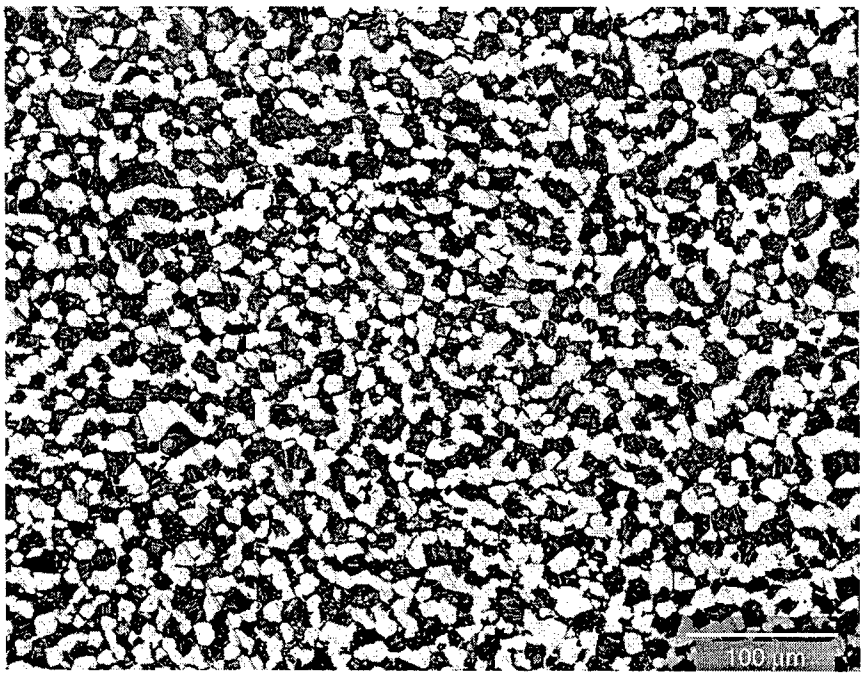


FIGURE I-2. MICROSTRUCTURE OF Ti-6-2-4-2 FORGING

I.2.3 Ti-17.

Ti-17 is a newer, deep hardenable engine disk alloy for intermediate operating temperatures below about 800°F. The nominal composition of Ti-17 is Ti-5Al-2Sn-2Zr-4Mo-4Cr, and the name Ti-17 is based on the sum total of substitutional alloying elements of its nominal composition. Further background on Ti-17 is available in the open literature [I-12, I-13].

The Ti-17 test specimens were machined from a production quality, triple VAR melted, high by-pass ratio compressor disk forging provided by GEAE. The microstructure is shown in figure I-3. The pedigree of the forging is summarized below:

Processing:	Forged above beta transus Solution heat treated below beta transus + water quenched + aged
Certification:	Serial No. – MZS 76863 Heat No. – T5125 Mill – TMC Forging vendor – Ladish
Tensile Properties:	0.2% yield strength – 155 ksi Ultimate tensile strength – 170 ksi % Elongation - 6 – 12 percent % RA - 12 – 21 percent

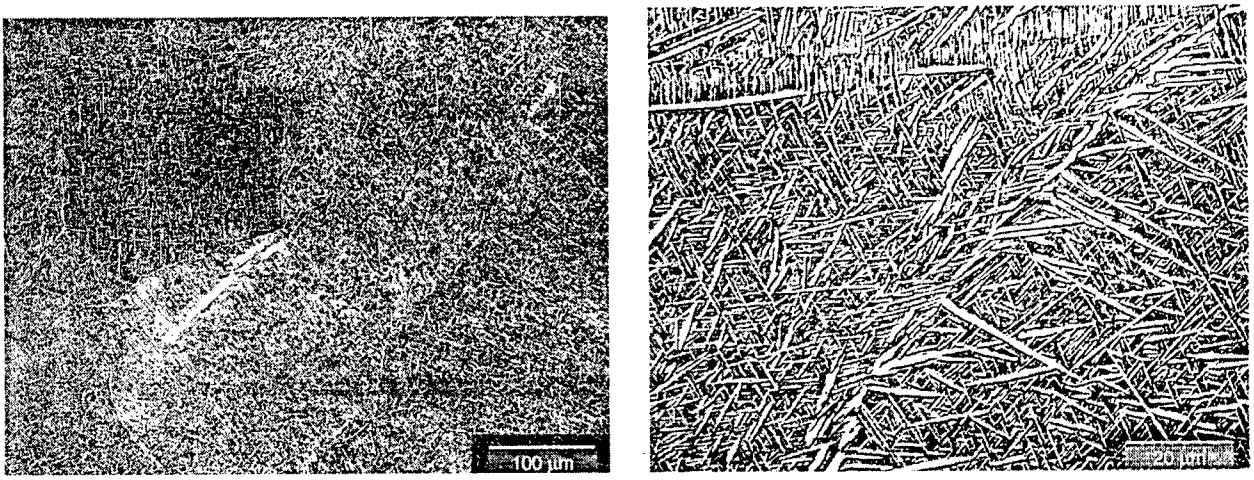


FIGURE I-3. MICROSTRUCTURE OF Ti-17 FORGING

I.3 VACUUM LEVEL STUDY.

In order to simulate the environment of a fully embedded internal crack, it is necessary to maintain a sufficiently high vacuum level in the test chamber. Since titanium is extremely reactive to air atmospheres, a weak vacuum may be inadequate. A brief literature study and adjunct test program was conducted to identify adequate vacuum levels to be implemented in the main vacuum FCG test program.

I.3.1 LITERATURE REVIEW.

Published investigations [I-1 – I-12] of vacuum FCG in various titanium alloys (mostly Ti-6-4) have reported a wide range of vacuum levels from about 10^{-5} Torr (e.g., Irving and Beevers [I-2], Davidson and Lankford [I-14]) to about $5(10)^{-9}$ Torr (Gao et al. [I-6]). Note that vacuum levels were sometimes originally reported in different units, so approximate conversions were carried out to obtain common units for quotation in this report.

None of these authors conducted any direct study of the effect of different vacuum levels on FCG rates. Irving and Beevers [I-2] cited the research of James (published only in an internal report [I-15]) on Ti-5-2.5. James performed tests at 100 Hz at two different vacuum levels, $(10)^{-5}$ Torr and $3(10)^{-8}$ Torr, and found no effect of these two vacuum levels on crack growth rate. Sugano et al. [I-16] examined the effect of vacuum level on S-N life of pure titanium from 10^{-5} Torr to atmospheric pressure, considering several intermediate vacuum levels. Total fatigue lives were an order of magnitude longer at 10^{-5} Torr compared to slightly higher pressures.

Of course, it must be noted that a single vacuum level does not tell the whole story. The amounts of oxygen and moisture available in the system, as would be influenced by leak rates and other considerations, are also crucial. Vacuum levels can also be measured at different points in the vacuum system. Some authors cited special traps in their system to further reduce water vapor or oxygen content.

Irving and Beevers [I-2] cited general evidence of the existence of a critical pressure for other materials (e.g., aluminum and steel). Below this pressure, no further effects on growth rates were observed with changes in vacuum pressure. They also noted that this critical pressure would scale with test frequency, increasing proportionally with frequency. However, except for the James work cited, there appear to be no systematic confirmations of these observations for titanium alloys. The Sugano et al. [I-16] work does not address vacuum levels high enough to confirm or deny this phenomenon.

I.3.2 TEST PROCEDURES FOR VACUUM LEVEL STUDY.

In order to assess what pressure levels were adequate to capture the full vacuum effect on FCG rates in titanium alloys, a very brief, informal test program was conducted at different vacuum levels ranging from 10^{-4} Torr to 10^{-9} Torr.

All tests in the vacuum level study were conducted at National Aeronautics and Space Administration (NASA) Langley Research Center, at no cost to the Federal Aviation Administration (FAA), on specimens provided by Southwest Research Institute (SwRI) from Ti-6Al-4V forging material provided by GEAE. The tests were conducted in a stainless steel constructed ultrahigh vacuum (UHV) chamber mounted on a servohydraulic test machine. A platinum electrode resistance "clam shell" oven, mounted along the test machine load line, and located inside the UHV chamber was used to heat the specimen to a constant elevated temperature. The UHV chamber is equipped with one 450 l/sec turbo-molecular vacuum pump, two 500 l/sec ion vacuum pumps, and a titanium sublimation vacuum pump. The entire chamber is also equipped with heaters for outgassing the system at 250°F. The vacuum environment was monitored by a thoriated-iriduim filament ionization gage (10^{-4} to 10^{-6} Torr), tungsten filament ionization gage (10^{-6} to 10^{-9} Torr), and a Leybold-Inficon quadrupole mass spectrometer. The NASA-Langley vacuum FCG test facility is shown in figure I-4.

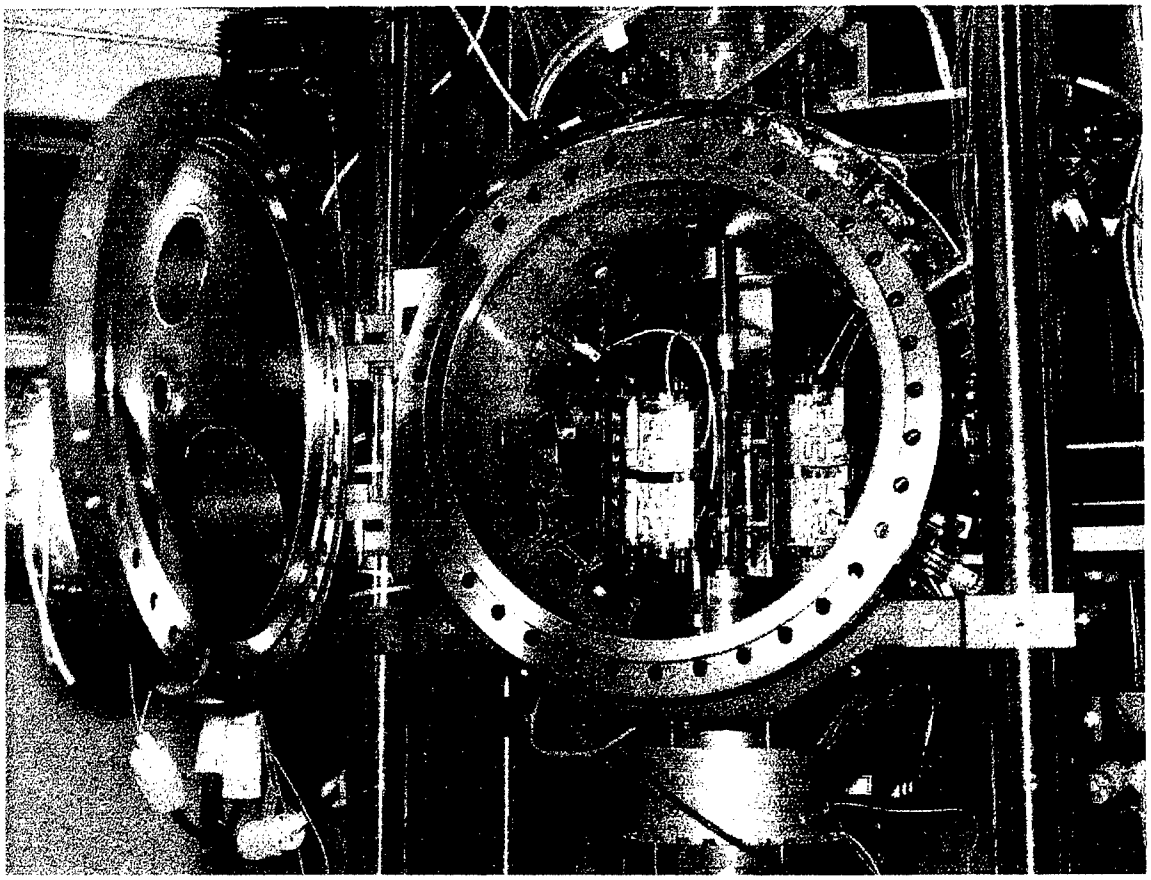


FIGURE I-4. NASA LANGLEY RESEARCH CENTER VACUUM FCG TEST FACILITY

The pin-loaded extended single-edge-cracked tension ESE(T) specimen, formerly known as the extended compact tension specimen [I-17], was used for the constant ΔK crack growth tests. A dimensioned specimen drawing is given in figure I-5. The constant ΔK tests were performed under load control, using a computer (load) controlled servohydraulic test machine. The specimen temperature was monitored in the crack growth region by attaching (spot welding) a thermocouple directly to the specimen in the mid-plane region. Specimen temperature was controlled to within ±2°F. Fatigue crack length was monitored continuously by using the crack mouth opening compliance measurement method. A long focal length microscope mounted to the side of the vacuum chamber which is capable of monitoring the specimen surface crack length to within ±0.0001 inch at high magnification (400 ×) was used to verify the compliance-based crack length measurements.

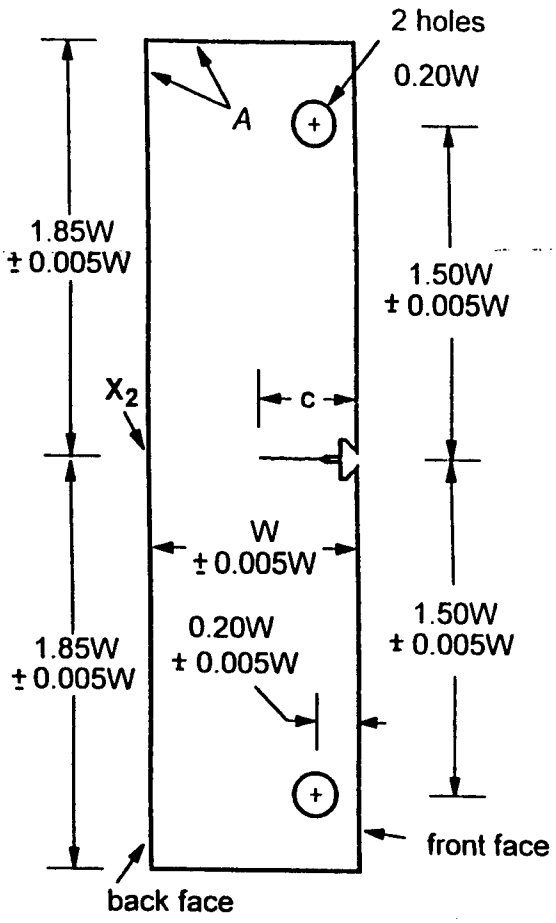


FIGURE I-5. ESE(T) SPECIMEN USED IN VACUUM LEVEL STUDY TESTS

I.3.3 RESULTS FROM VACUUM LEVEL TESTS.

The results of the constant ΔK test conducted at ΔK = 18 ksi$\sqrt{in.}$, R = 0.05, f = 0.33 Hz, and a temperature of 400°F are shown in figure I-6. Here, the plot of crack length (a) versus load cycle (N) is used to show extremely small changes in crack growth rate ($\Delta a/\Delta N$) under constant conditions of ΔK and six different levels of vacuum environment. Fatigue crack growth rate determinations were obtained by performing a linear regression analysis for selected regions of steady-state crack growth. The selected regions are identified by the bold data symbols in figure I-6. Because it is extremely difficult to maintain a constant vacuum level, each region of crack growth is characterized by a range of vacuum. For example, the 10^{-4} Torr level is characterized by the vacuum (2.2×10^{-4} Torr) reached at the start of the test interval and the vacuum (6×10^{-4} Torr) obtained at the end the test interval. Table I-2 summarizes the results from figure I-6. A factor of two reduction is observed in da/dN when the vacuum was changed from 10^{-4} Torr to 10^{-5} Torr. A small variation in the fatigue crack growth rate is observed for vacuum levels ranging from 10^{-5} Torr to 10^{-9} Torr. A linear regression analysis for this range in vacuum, the dashed line in figure I-6, reveals an average crack growth rate of 1.49×10^{-6} in./ cycle for crack lengths between 0.376 inch to 0.540 inch.

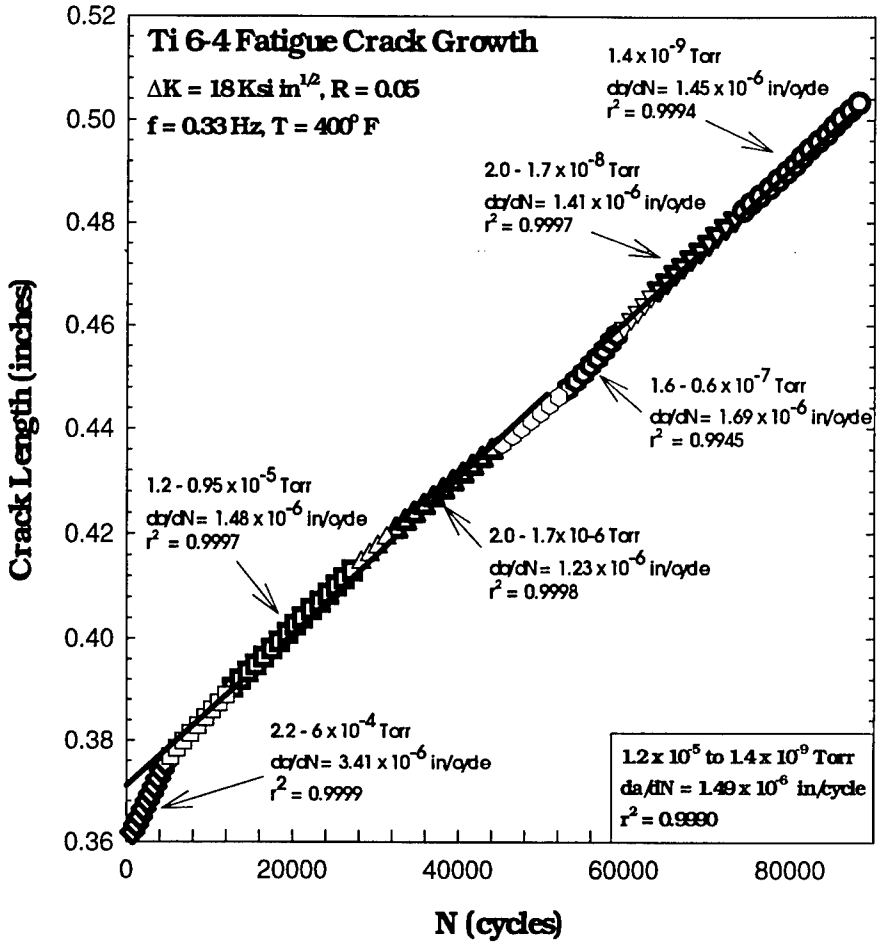


FIGURE I-6. CRACK LENGTH VERSUS LOAD CYCLES FOR A CONSTANT ΔK TEST CONDUCTED IN VACUUM AT ΔK = 18 ksi$\sqrt{in.}$, R = 0.05, f = 0.33 Hz, AND A TEMPERATURE OF 400°F

TABLE I-2. FATIGUE CRACK GROWTH RATES AT ΔK = 18 ksi$\sqrt{in.}$, R = 0.05, f = 0.33 Hz, T = 400°F

Crack Length (in.)	*da/dN* (in./cycle)	Vac. Range (Torr)
0.362 - 0.376	3.41×10^{-6}	10^{-4}
0.390 - 0.414	1.48×10^{-6}	10^{-5}
0.420 - 0.436	1.23×10^{-6}	10^{-6}
0.448 - 0.460	1.69×10^{-6}	10^{-7}
0.466 - 0.480	1.41×10^{-6}	10^{-8}
0.480 - 0.540	1.45×10^{-6}	10^{-9}

Load and displacement (clip gage) measurements (an example is shown in figure I-7) were obtained at each vacuum level. From the load-displacement results, crack closure levels (determined by the reduced-strain method) were found to range from $0.31P_{max}$ to $0.35P_{max}$ during the low R (R = 0.05) vacuum tests.

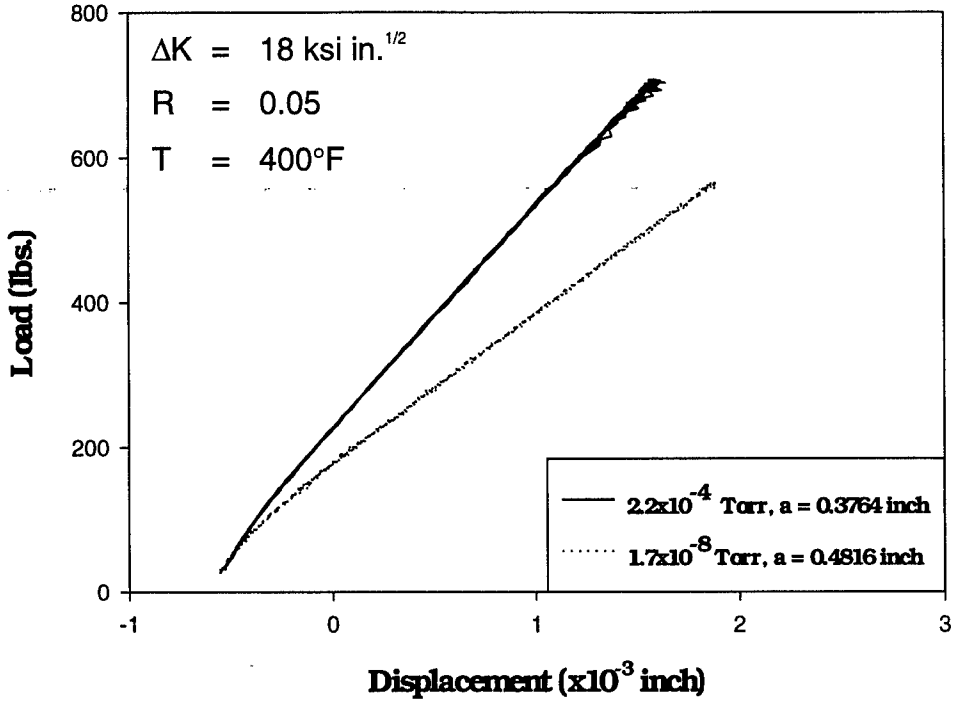


FIGURE I-7. LOAD VS. CRACK MOUTH OPENING DISPLACEMENT MEASURED BY A CLIP GAGE FOR A CRACK GROWN AT ΔK = 18 ksi$\sqrt{}$in., R = 0.05, f = 0.33 Hz, AND A TEMPERATURE OF 400°F

The results of the constant ΔK test conducted at ΔK = 8.9 ksi$\sqrt{}$in., R = 0.5, f = 0.33 Hz, and a temperature of 400°F are shown in figure I-8. After testing at constant ΔK level of 18 ksi$\sqrt{}$in. and prior to the ΔK = 8.9 ksi$\sqrt{}$in. test, a decreasing ΔK test was performed at constant K_{max} = 18.95 ksi$\sqrt{}$in., C = -8 in.$^{-1}$, and f = 5 Hz. This test allowed a rapid means of reducing the crack tip plastic zone size prior to performing the constant ΔK = 8.9 ksi$\sqrt{}$in. (R = 0.5) test. The fatigue crack was grown to an additional 0.012 inch at a constant ΔK = 8.9 ksi$\sqrt{}$in. (R = 0.5) to ensure steady state crack growth rates at UHV prior to obtaining the a versus N data shown in figure I-8 at the three levels of vacuum. At ultrahigh vacuum (2×10^{-9} Torr) and 1×10^{-6} Torr (with highly purified water vapor (H_2O) addition) similar fatigue crack growth rates were observed. A vacuum environment of 2×10^{-5} Torr, containing lab air additions, was shown to accelerate da/dN compared to the rates at a vacuum of 1×10^{-6} Torr. The results of the constant ΔK = 8.9 ksi$\sqrt{}$in. test are summarized in table I-3.

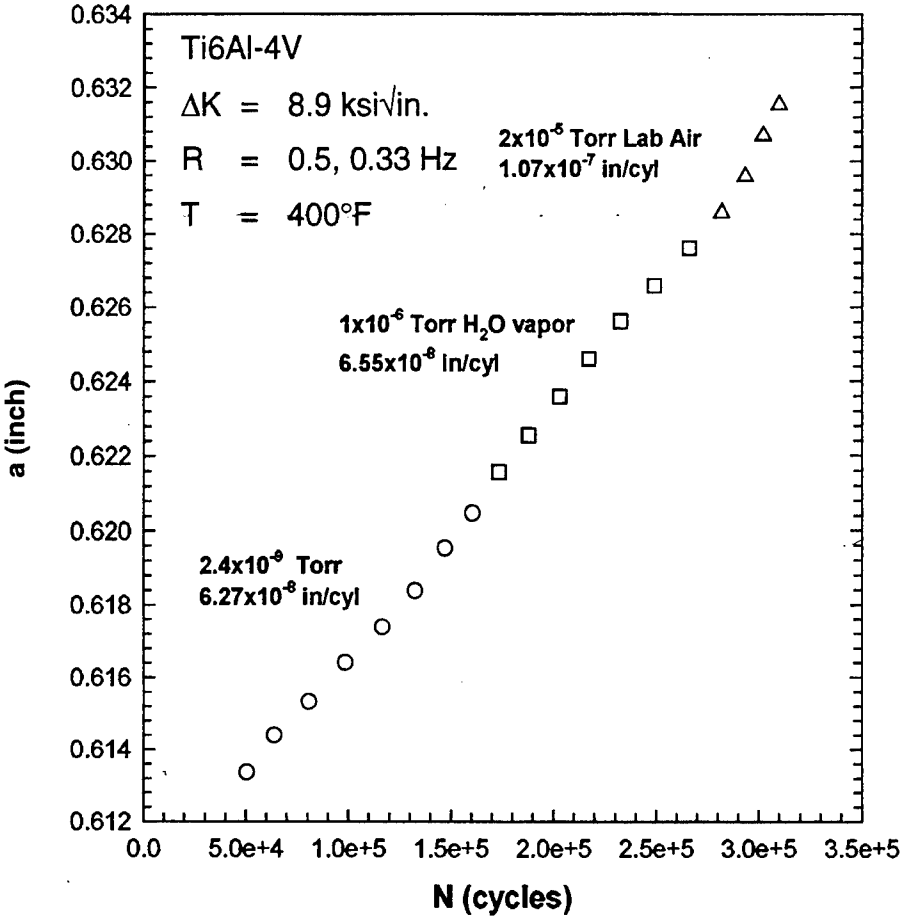


FIGURE I-8. CRACK LENGTH VERSUS LOAD CYCLES FOR A CONSTANT ΔK TEST CONDUCTED IN VACUUM AT ΔK = 8.9 ksi$\sqrt{}$in., R = 0.5, f = 0.33 Hz, AND A TEMPERATURE OF 400°F

TABLE I-3. FATIGUE CRACK GROWTH RATES AT ΔK = 8.9 ksi$\sqrt{}$in., R = 0.5, f = 0.33 Hz, T = 400°F

Crack Length (in.)	*da/dN* (in./cycle)	Vac. Range (Torr)
0.613 - 0.621	6.27×10^{-8}	10^{-9}
0.621 - 0.628	6.55×10^{-8}	10^{-6}
0.628 - 0.632	1.07×10^{-7}	10^{-5}

Obviously, this brief, informal study cannot definitively resolve the vacuum level question, and further testing at much lower growth rates (very near threshold) would be of particular value. However, the limited data available, in conjunction with the brief literature review, suggests that vacuum levels better than 10^{-6} Torr should be adequate to capture full vacuum effects for engineering purposes at crack growth rates greater than about 5×10^{-8} inches/cycle. All subsequent testing described in this report was conducted at vacuum levels better than 10^{-6} Torr.

I.4 TESTING PROCEDURES.

All Ti-6-4 and Ti-17 tests were conducted at GEAE, and all Ti-6-2-4-4-2 tests were conducted at AE. Although the specimen geometries and test procedures employed at the two labs were generally similar, there were minor variations in both approach and documentation, and those variations are reflected as appropriate in this report. Some further documentation of the AE test procedures is provided in a separate AlliedSignal Engines report [I-18].

Two types of specimen geometries were employed in this testing. Most tests were conducted using a surface-crack tension (SCT) specimen, also known as a Kb bar specimen. A specimen drawing for the GEAE Kb bar specimen is provided in figure I-9, and a specimen drawing for the AE SCT specimen is provided in figure I-10. These specimens have a rectangular cross-section in the gage section of nominal dimensions 0.168 by 0.400 inch (GEAE) or 0.226 by 0.450 inch AlliedSignal Engines. A semielliptical crack is centered on one of the wide faces. This crack is initiated from an electrodischarge machine (EDM) notch with initial dimensions 0.007 inch deep by 0.014 inch long (GEAE) or 0.010 inch deep by 0.020 inch long (AE). The GEAE specimen has buttonhead ends, and the AE specimen is threaded.

GEAE used a single-edge notch button head (SENBH) specimen to obtain near-threshold data. A specimen drawing is provided in figure I-11. This geometry has a nominal gage section of 0.100 by 0.400 inch with a 0.015-inch-deep EDM notch on one narrow face of the specimen.

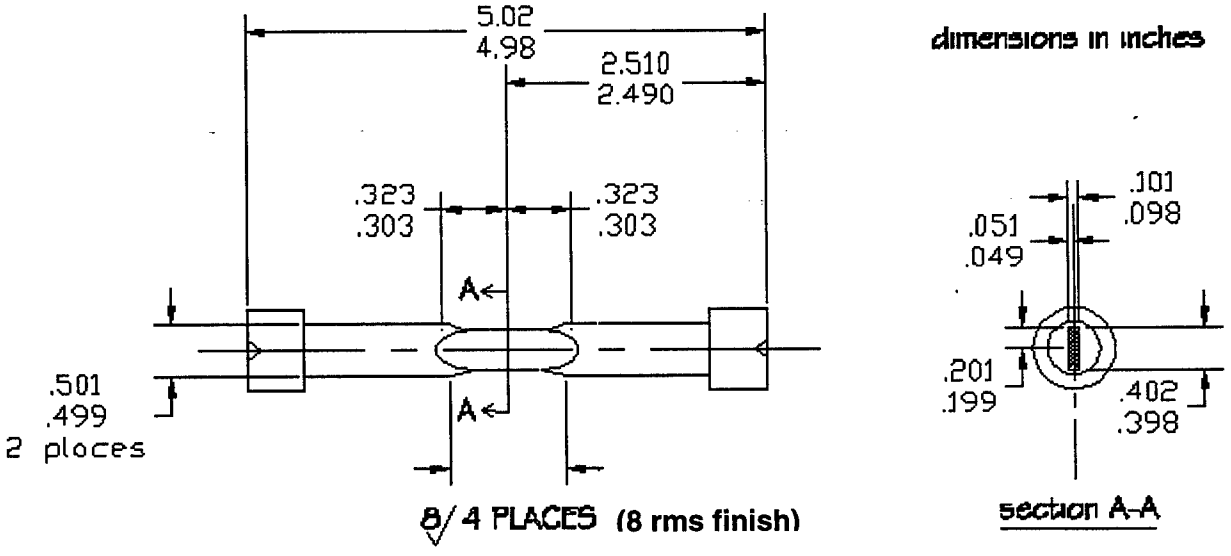


FIGURE I-9. GEAE Kb BAR SPECIMEN DRAWING

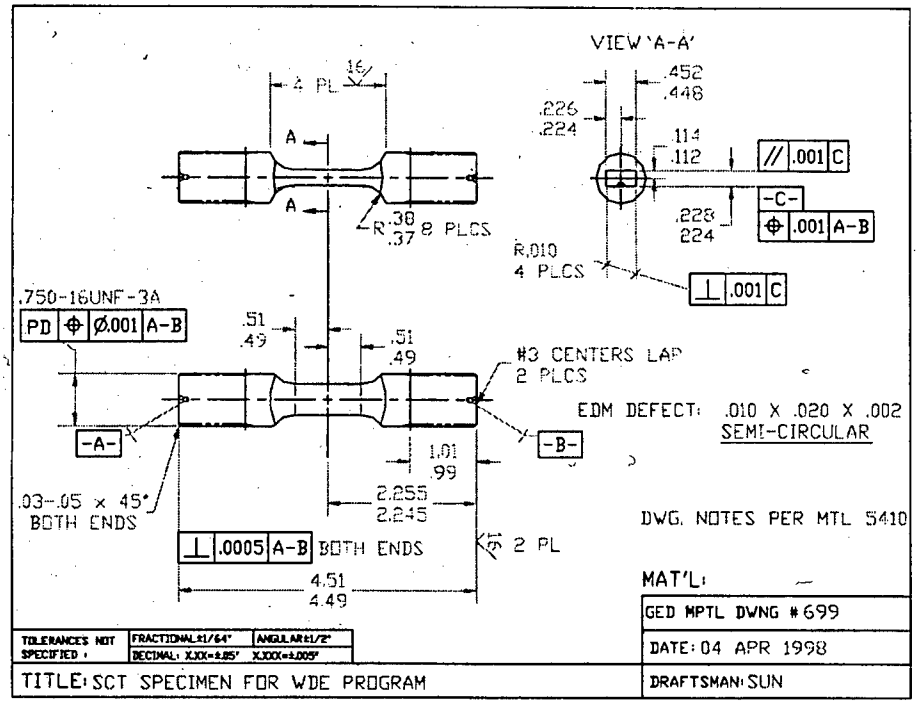


FIGURE I-10. ALLIEDSIGNAL SCT SPECIMEN DRAWING

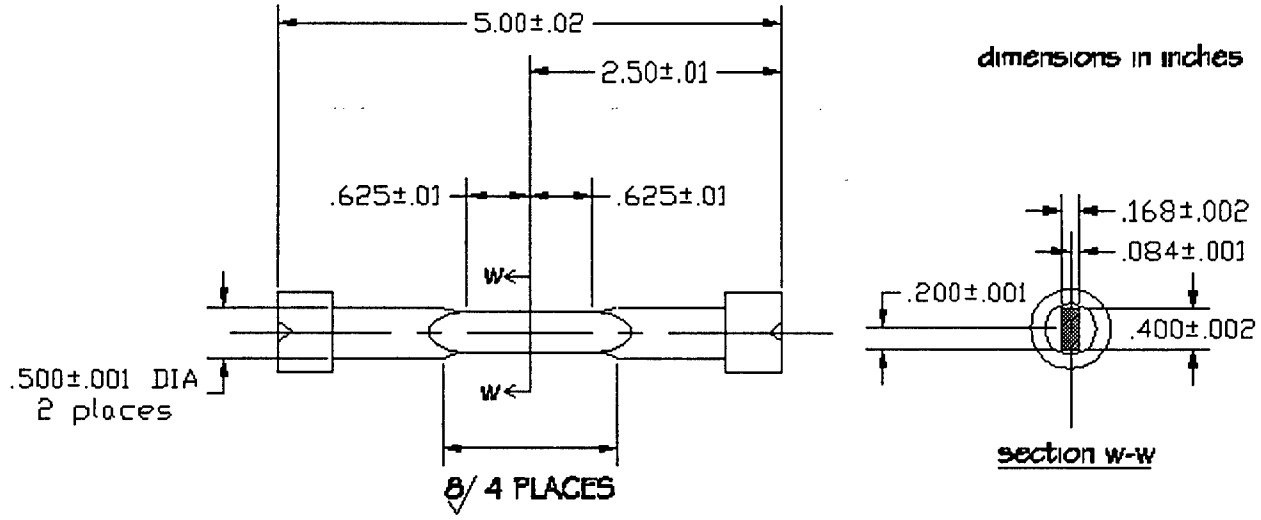


FIGURE I-11. GEAE SINGLE-EDGE NOTCH BUTTONHEAD SPECIMEN DRAWING

As noted earlier, all specimens were removed from production forgings. Schematic drawings showing the cutup plans for the Ti-6-4 forging are provided in figures I-12 and I-13. Schematic drawings for the Ti-6-2-4-2 specimen locations are provided in figures I-14 and I-15. Drawings for Ti-17 are provided in figure I-16. Note that the location and orientation of each individual specimen within each forging is specified.

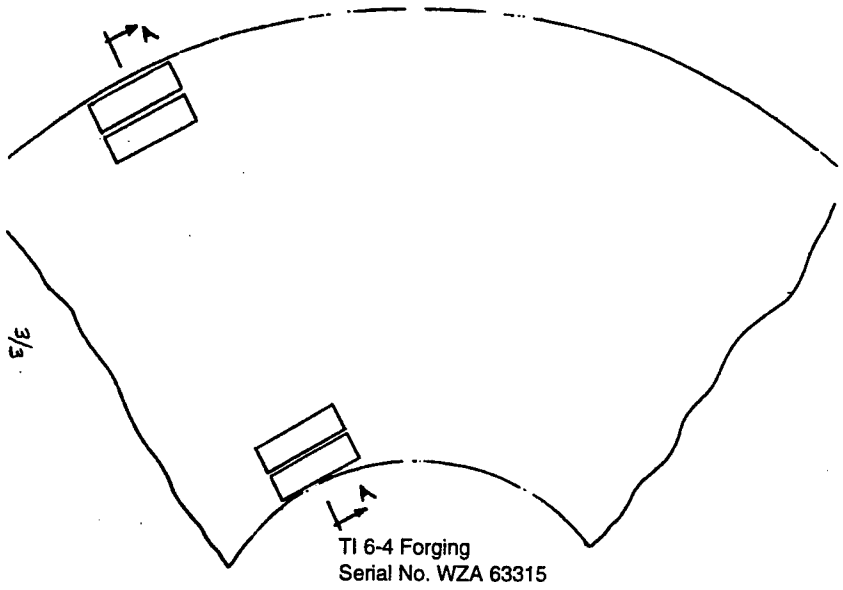


FIGURE I-12. Ti-6-4 SPECIMEN CUTUP PLAN (TOP VIEW)

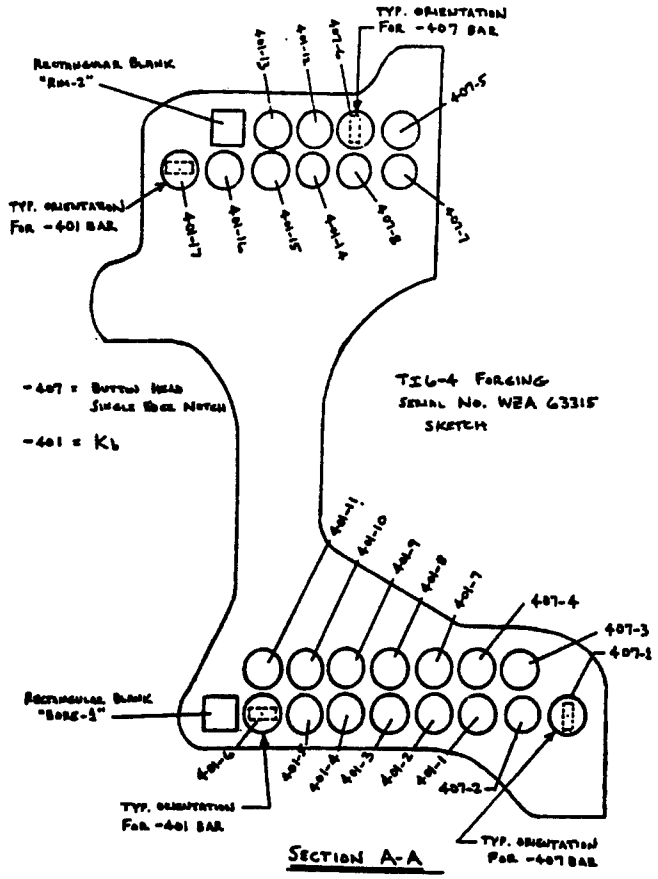


FIGURE I-13. Ti-6-4 SPECIMEN CUTUP PLAN (CROSS SECTION)

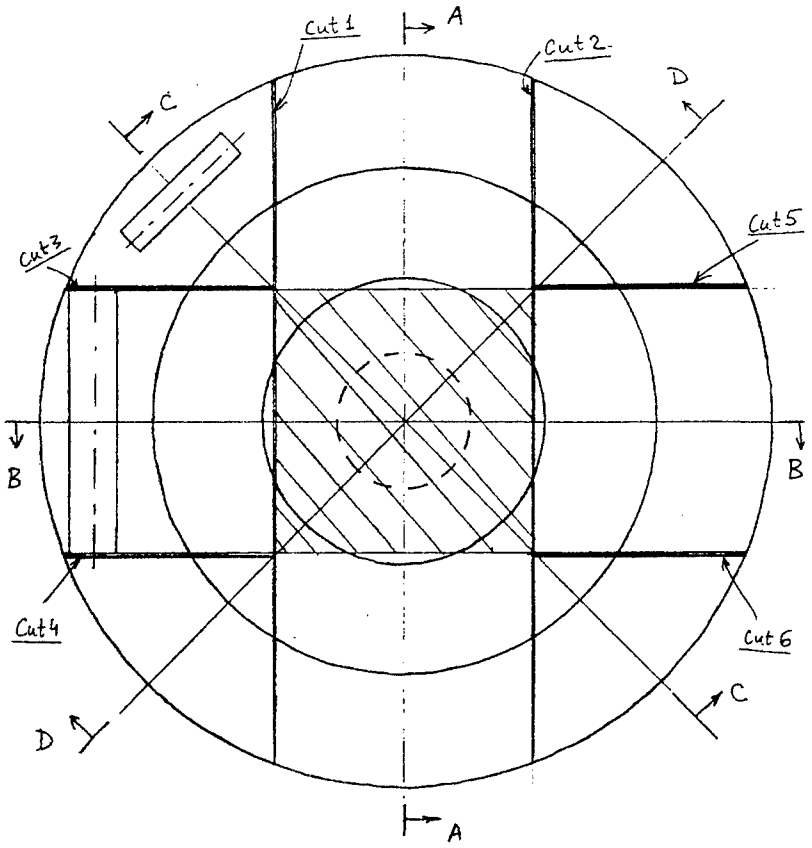


FIGURE I-14. Ti-6-2-4-2 SPECIMEN CUTUP PLAN (TOP VIEW)

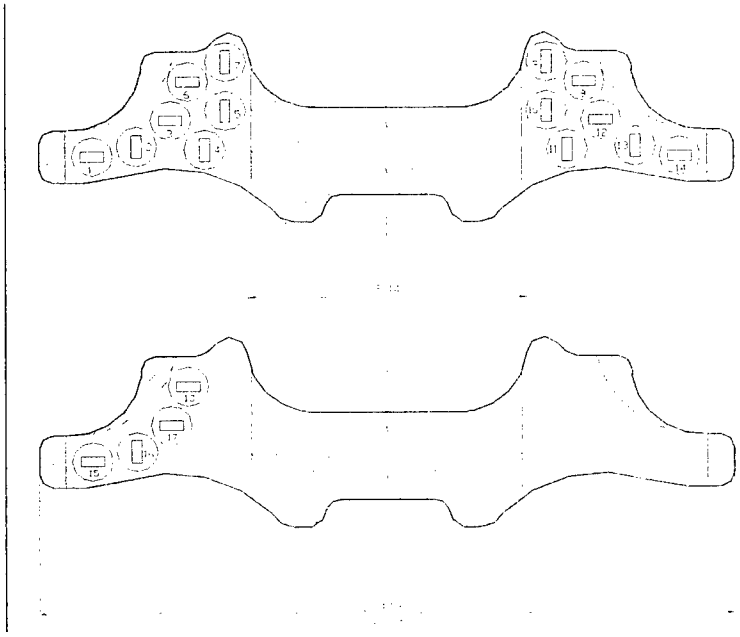
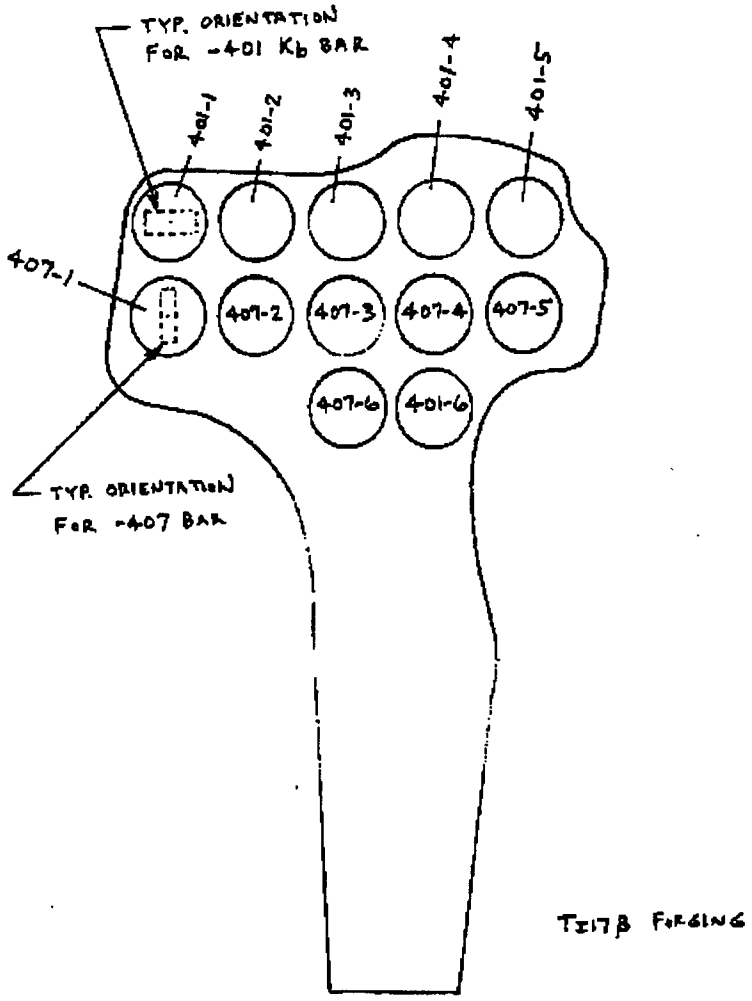


FIGURE I-15. Ti-6-2-4-2 SPECIMEN CUTUP PLAN (CROSS SECTION)



SECTION A-A

SCALE: FULL SIZE

FIGURE I-16. Ti-17 SPECIMEN CUTUP PLAN

Precracking of all specimens was conducted in laboratory air at room temperature under constant load conditions. Precrack loading frequencies were 10 Hz (GEAE) or 3.33 Hz (AlliedSignal Engines). Semicircular precracks in SCT or Kb specimens were grown to a nominal size of 0.015 by 0.030 inch, except for higher stress ratio tests at GE, where precracks were grown to approximately 0.030 inch deep by 0.060 inch long. Precracks in SENBH specimens at GEAE were grown to lengths between 0.040 and 0.060 inch.

Following precracking, all crack growth tests were conducted under high-vacuum conditions. Vacuum levels generally ranged between 10^{-7} and 10^{-8} Torr. Figure I-17 shows the vacuum fatigue crack growth test facility at AlliedSignal, including a view of the test specimen mounted inside the vacuum chamber.

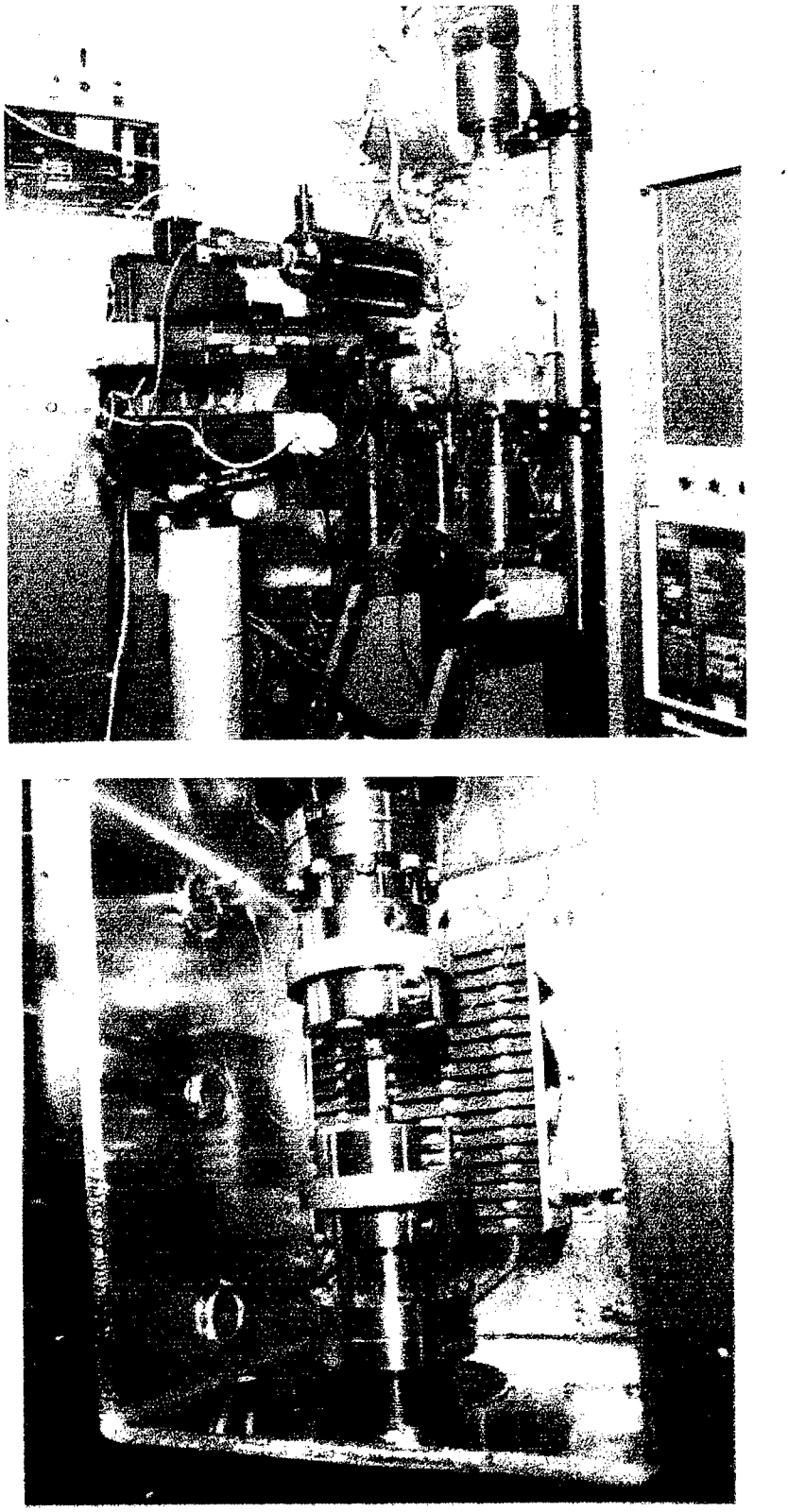


FIGURE I-17. ALLIEDSIGNAL VACUUM FATIGUE CRACK GROWTH TEST FACILITY

Bending loads were closely monitored to ensure proper specimen alignment.

Tests were conducted at cyclic frequencies of either 0.33 Hz (20 CPM) or 1 Hz. Most tests were conducted at 0.33 Hz. All room temperature Ti-6-2-4-2 tests at AlliedSignal and portions of two 400°F Ti-6-4 tests at GEAE were conducted at 1 Hz. A brief study of frequency effects was conducted at GEAE to confirm that no differences in growth rates were observed between 0.33 and 1 Hz.

The direct current (DC) electric potential drop (PD) method [I-19] was used to monitor crack growth in all tests. The adaptation of the PD method to the Kb or SCT geometry has been described previously by Van Stone and Richardson [I-20]. The Roe-Coffin potential solution [I-19] was used to convert potential data to crack length data for this geometry. Tests were stopped prior to reaching the cyclic toughness, and the test bar was then fractured using a monotonic tensile load at room temperature in air. The crack fronts corresponding to the end of the precrack and the end of the experiment were measured directly from the fracture surface. These crack fronts were defined more clearly by heat tinting or other surface marking techniques at the end of the precracking and the end of the experiment. The measured crack dimensions were used to correct the crack sizes determined from the PD technique and to infer the aspect ratio history of the crack during the test. Some visual measurements of surface crack length were also obtained during the tests with a long focal length microscope.

The Newman-Raju solution [I-21] was used to calculate the applied stress intensity factor values for the surface cracks in the Kb or SCT specimens. Crack growth rates and ΔK values were calculated at both the maximum depth position (the a-tip and the surface position (the c-tip) around the perimeter of the crack. Data reported in the tables and graphs that follow later in this appendix all correspond to the maximum depth a-tip.

The Johnson solution [I-22] was used to convert potential data to crack length data for the SENBH specimen. Applied stress intensity factor values for the SENBH geometry were calculated using the Harris solution [I-23].

Crack growth rates were calculated based on the test data (crack length vs. number of fatigue cycles) as a derivative of crack length with respect to number of cycles using the secant, five-point, or seven-point incremental polynomial methods. Most data were analyzed using the seven-point method.

The Kb bar tests at GEAE and some SCT tests at AlliedSignal were conducted under constant load amplitude cycling. The SENBH tests at GEAE and most SCT tests at AlliedSignal were conducted under K-gradient control. A normalized K-gradient can be defined as

$$C = \frac{1}{K}\frac{dK}{da} \tag{I-1}$$

The relationship between ΔK and crack length is then given by the equation

$$\Delta K = \Delta K_o \ \exp\left[c\left(a - a_o\right)\right] \tag{I-2}$$

where ΔK_0 is the initial ΔK at the beginning of the K-gradient, and a_0 is the corresponding crack length. In this control mode, the applied range of ΔK is steadily increased or decreased while holding the stress ratio constant.

Negative K-gradients correspond to decreasing load amplitudes and were used to determine thresholds and near-threshold growth rates. Positive K-gradients correspond to increasing load amplitudes and were primarily used to grow cracks into the Paris regime. Typically, K-control specimens were first subjected to a negative K-gradient to generate near-threshold data, and then a positive K-gradient was applied to generate Paris regime data, with some overlap, from the same specimen.

The value of the normalized K-gradient, C, was held constant in a single test segment. Values of C employed in these tests ranged from ±15 to ±20 inch^{-1} at AlliedSignal, to -30 inch^{-1} at GEAE. Some precracking at AlliedSignal was conducted with K-gradients on the order of -25 to -30 inch^{-1}. ASTM Test Method E647-95a recommends that the value of C be algebraically greater than or equal to -2 inch^{-1} for the determination of crack growth thresholds (i.e., a much slower load shed). However, a recent study by GEAE and Pratt & Whitney (P&W) [I-24] has shown that faster load sheds (e.g., -20 inch^{-1}) can be applied in threshold testing with Ti-6-4 without artificially influencing the results, as long as initial ΔK values at the beginning of the load shed are adequately small (less than about 20 ksi$\sqrt{\text{in.}}$). Corresponding analysis of fatigue crack closure during threshold load sheds under constant K-gradient [I-25] has confirmed that these faster load sheds do appear acceptable when initial ΔK is adequately small, although the material strength must also be taken into consideration. When load sheds are too fast for high initial ΔK or low material strength, the load shed causes anomalous crack closure, which in turn causes artificially high thresholds.

Test matrices for each material addressed two to three temperatures and two to three stress ratios. Tests on Ti-6-4 and Ti-6-2-4-2 were conducted at R = 0 (or 0.05), 0.5, and 0.75. Tests at the highest and lowest stress ratios covered both the near-threshold and Paris regimes (typically requiring two specimens), while only limited testing (a single specimen) addressing primarily the Paris regime was performed at the intermediate stress ratio. Tests on Ti-17 were performed only at R = 0 and 0.6.

Tests on Ti-6-4 were performed at room temperature and 400°F (originally planned tests at 200°F were cancelled after results at 400°F were found to agree closely with room temperature results). Ti-6-2-4-2 tests were performed at room temperature, 600°, and 1000°F, while Ti-17 tests were performed only at room temperature and 750°F.

I.5 RESULTS.

Detailed results of all fatigue crack growth tests are provided in tables I-4 through I-12. These tables provide specific values of cycle count, crack size, calculated crack growth rate, and applied stress-intensity factor range for each test. Tables I-4 through I-7 document all Ti-6-4 tests: room temperature, R = 0 data are summarized in table I-4; 400°F, R = 0 data in table I-5; R = 0.5 data for both temperatures in table I-6; and R = 0.75 data for both temperatures in table I-7. Data for Ti-6-2-4-2 are collected in tables I-8 through I-10 by stress ratio: all R = 0.05

data in table I-8, $R = 0.5$ data in table I-9, and $R = 0.75$ data in table I-10. Ti-17 data are given in tables I-11 and I-12: $R = 0$ data in table I-11 and $R = 0.6$ data in table I-12.

Electronic copies of the Excel spreadsheets from which these tables were directly printed are available from the authors at Southwest Research Institute.

TABLE I-4. FATIGUE CRACK GROWTH DATA FOR Ti-6-4 AT $R = 0$, ROOM TEMPERATURE

401-4	RT	R=0		407-4	RT	R=0		407-4	RT	R=0	
Const. Load (freq=20 cpm)				ΔK decreasing (freq=20 cpm)				ΔK increasing (freq=20 cpm)			
a	N	da/dN	ΔK	a	N	da/dN	ΔK	a	N	da/dN	ΔK
0.01491	420	8.06E-09	12.09	0.05251	27000	3.23E-06	17.45	0.10939	8141	1.60E-07	12.37
0.01493	840	9.77E-08	12.10	0.05542	27780	3.06E-06	17.35	0.10930	8361	1.76E-07	12.29
0.01496	1260	1.17E-07	12.12	0.05767	28684	2.65E-06	16.32	0.10928	8581	2.33E-07	12.29
0.01494	1680	1.28E-07	12.14	0.06019	29874	2.13E-06	15.72	0.10936	8801	3.41E-07	12.35
0.01502	2100	1.32E-07	12.16	0.06267	31347	1.70E-06	15.09	0.10958	9021	4.62E-07	12.42
0.01505	2520	1.42E-07	12.18	0.06530	33063	1.44E-06	14.52	0.10985	9241	5.12E-07	12.45
0.01512	2940	1.42E-07	12.20	0.06769	35008	1.22E-06	13.99	0.10976	9461	5.16E-07	12.47
0.01516	3360	1.54E-07	12.22	0.07001	37162	1.04E-06	13.48	0.10984	9681	4.62E-07	12.53
0.01523	3780	1.54E-07	12.25	0.07233	39526	8.99E-07	13.01	0.10996	9901	4.59E-07	12.52
0.01526	4200	1.76E-07	12.27	0.07434	42057	7.70E-07	12.60	0.11011	10121	4.63E-07	12.57
0.01537	4620	1.83E-07	12.29	0.07619	44743	6.59E-07	12.24	0.11015	10341	4.70E-07	12.58
0.01541	5040	2.12E-07	12.32	0.07776	47555	5.58E-07	11.93	0.11024	10561	5.46E-07	12.58
0.01547	5460	2.24E-07	12.35	0.07922	50479	4.81E-07	11.67	0.11038	10781	6.17E-07	12.63
0.01556	5880	2.27E-07	12.40	0.08066	53516	4.15E-07	11.39	0.11048	11001	7.07E-07	12.65
0.01560	6300	2.25E-07	12.43	0.08168	56628	3.70E-07	11.22	0.11075	11221	7.45E-07	12.73
0.01574	6720	2.25E-07	12.45	0.08282	59823	3.31E-07	11.00	0.11089	11441	7.66E-07	12.78
0.01582	7140	2.39E-07	12.49	0.08371	63081	2.93E-07	10.85	0.11105	11661	7.83E-07	12.81
0.01595	7560	2.51E-07	12.53	0.08481	66419	2.65E-07	10.67	0.11119	11881	7.89E-07	12.84
0.01602	7980	2.79E-07	12.57	0.08566	69815	2.41E-07	10.53	0.11139	12101	8.66E-07	12.91
0.01610	8400	2.92E-07	12.61	0.08630	73256	2.19E-07	10.42	0.11158	12321	9.53E-07	12.98
0.01618	8820	2.93E-07	12.66	0.08694	76739	2.10E-07	10.31	0.11180	12541	1.03E-06	13.01
0.01633	9240	2.90E-07	12.70	0.08778	80279	2.11E-07	10.20	0.11204	12761	1.07E-06	13.07
0.01644	9660	2.98E-07	12.74	0.08834	83859	2.19E-07	10.09	0.11230	12981	1.08E-06	13.14
0.01657	10080	2.67E-07	12.79	0.08944	87506	2.11E-07	9.91	0.11255	13201	1.15E-06	13.20
0.01671	10500	2.89E-07	12.82	0.08013	91202	1.89E-07	9.79	0.11277	13421	1.29E-06	13.27
0.01681	10920	2.89E-07	12.87	0.09103	94957	1.63E-07	9.66	0.11299	13637	1.46E-06	13.33
0.01692	11340	3.47E-07	12.90	0.09136	98729	1.23E-07	9.60	0.11335	13846	1.67E-06	13.43
0.01707	11760	3.58E-07	12.95	0.09175	102528	9.32E-08	9.54	0.11378	14055	1.88E-06	13.54
0.01721	12180	4.28E-07	13.01	0.09204	106344	7.31E-08	9.50	0.11421	14264	2.03E-06	13.65
0.01720	12600	4.55E-07	13.09	0.09222	110171	7.87E-08	9.46	0.11460	14473	2.16E-06	13.77
0.01749	13020	4.65E-07	13.14	0.09241	114020	8.56E-08	9.44	0.11507	14682	2.36E-06	13.92
0.01752	13440	5.21E-07	13.21	0.09278	117865	9.02E-08	9.38	0.11553	14891	2.51E-06	14.03
0.01788	13860	5.62E-07	13.27	0.09336	121783	1.01E-07	9.28	0.11611	15100	2.64E-06	14.19
0.01791	14280	6.34E-07	13.37	0.09377	125704	1.05E-07	9.24	0.11680	15309	2.82E-06	14.36
0.01828	14700	6.49E-07	13.45	0.09396	129637	9.67E-08	9.20	0.11730	15518	3.04E-06	14.52
0.01833	15120	6.87E-07	13.56	0.09454	133602	8.80E-08	9.12	0.11784	15727	3.30E-06	14.68
0.01865	15540	6.73E-07	13.65	0.09490	137595	7.57E-08	9.06	0.11863	15936	3.69E-06	14.83
0.01892	15960	6.64E-07	13.74	0.09508	141600	6.14E-08	9.03	0.11943	16145	4.20E-06	15.10
0.01930	16380	6.61E-07	13.82	0.09545	145625	5.08E-08	9.01	0.12034	16354	4.71E-06	15.33
0.01952	16800	6.92E-07	13.91	0.09541	149650	4.94E-08	8.99	0.12144	16563	5.06E-06	15.63
0.01979	17220	7.20E-07	13.99	0.09549	153695	5.34E-08	8.99	0.12251	16772	5.46E-06	15.97
0.02002	17640	7.63E-07	14.08	0.09595	157748	5.04E-08	8.93	0.12377	16981	5.91E-06	16.30
0.02033	18060	7.82E-07	14.18	0.09617	161813	4.91E-08	8.90	0.12492	17190	6.30E-06	16.62
0.02059	18480	8.31E-07	14.28	0.09644	165893	4.05E-08	8.84	0.12631	17399	6.93E-06	17.01
0.02089	18900	8.97E-07	14.39	0.09645	169973	2.99E-08	8.83	0.12778	17601	7.56E-06	17.40
0.02119	19320	9.70E-07	14.50	0.09646	174053	2.07E-08	8.83	0.12921	17799	8.44E-06	17.80
0.02152	19600	1.04E-06	14.62	0.09655	176144	1.75E-08	8.82	0.13108	17997	9.40E-06	18.33
0.02187	20000	1.10E-06	14.75	0.09680	182247	2.29E-08	8.80	0.13291	18195	1.06E-05	18.84
0.02218	20400	1.14E-06	14.89	0.09667	186357	3.56E-08	8.79	0.13511	18393	1.16E-05	19.48
0.02260	20800	1.14E-06	15.02	0.09685	190467	4.33E-08	8.78	0.13759	18591	1.32E-05	20.15
0.02308	21200	1.22E-06	15.14	0.09704	194582	4.79E-08	8.78	0.14041	18789	1.45E-05	20.97
0.02353	21600	1.34E-06	15.27	0.09751	198722	5.29E-08	8.70	0.14314	18977	1.56E-05	21.77
0.02397	21980	1.48E-06	15.42	0.09766	202877	4.64E-08	8.68	0.14633	19164	1.66E-05	22.70
0.02441	22360	1.63E-06	15.60	0.09777	207032	5.00E-08	8.66	0.14947	19351	1.76E-05	23.65
0.02481	22740	1.77E-06	15.79	0.09789	211193	5.33E-08	8.64	0.15281	19538	1.92E-05	24.62
0.02527	23120	1.84E-06	15.99	0.09795	215363	5.75E-08	8.62	0.15627	19719	2.16E-05	25.65
0.02597	23500	1.90E-06	16.17	0.09859	219563	5.63E-08	8.57	0.15980	19895	2.61E-05	26.71
0.02667	23880	1.97E-06	16.35	0.09891	223784	4.83E-08	8.50	0.16443	20071	3.26E-05	28.11
0.02733	24260	2.05E-06	16.55	0.09892	228014	2.79E-08	8.49	0.17024	20242	4.19E-05	29.88
0.02801	24620	2.16E-06	16.75	0.09898	232244	4.07E-09	8.49	0.17747	20407	5.58E-05	32.10
0.02869	24980	2.34E-06	16.96	0.09876	240704	6.58E-09	8.45				
0.02937	25340	2.54E-06	17.18	0.09881	244934	1.98E-08	8.46				
0.03020	25700	2.77E-06	17.40	0.09900	249184	3.06E-08	8.47				
0.03094	26060	3.03E-06	17.65	0.09924	253401	3.61E-08	8.47				
0.03172	26400	3.29E-06	17.91	0.09954	257681	2.01E-08	8.42				
0.03266	26740	3.53E-06	18.16								
0.03360	27080	3.77E-06	18.48								
0.03464	27400	3.96E-06	18.77								
0.03575	27720	4.24E-06	19.07								
0.03687	28040	4.58E-06	19.36								
0.03809	28340	5.02E-06	19.69								
0.03931	28640	5.66E-06	20.03								
0.04055	28940	6.30E-06	20.39								
0.04187	29220	6.95E-06	20.78								
0.04328	29500	7.57E-06	21.20								
0.04476	29760	8.06E-06	21.63								
0.04652	30020	8.40E-06	22.04								
0.04837	30260	8.62E-06	22.42								
0.05022	30500	9.06E-06	22.81								
0.05202	30720	9.52E-06	23.17								
0.05381	30920	1.02E-05	23.55								
0.05554	31120	1.10E-05	23.91								
0.05715	31300	1.18E-05	24.31								
0.05876	31480	1.26E-05	24.68								
0.06056	31640	1.33E-05	25.01								
0.06230	31800	1.42E-05	25.37								
0.06403	31940	1.48E-05	25.69								
0.06561	32080	1.55E-05	26.02								
0.06715	32180	1.65E-05	26.29								
0.06869	32280	1.75E-05	26.59								
0.07017	32380	1.91E-05	26.90								
0.07145	32460	2.05E-05	27.16								
0.07272	32540	2.20E-05	27.44								
0.07411	32620	2.38E-05	27.64								
0.07538	32680	2.55E-05	27.85								
0.07655	32740	2.65E-05	28.09								
0.07754	32780	2.65E-05	28.20								
0.07845	32820	2.68E-05	28.34								

TABLE I-5. FATIGUE CRACK GROWTH DATA FOR Ti-6-4 AT $R = 0$, 400°F

401-2 T=400F R=0
Const. Load (freq=20 cpm)

a	N	da/dN	ΔK
0.01691	280	1.57E-07	11.91
0.01689	560	1.77E-07	11.93
0.01697	840	1.57E-07	11.94
0.01702	1120	1.40E-07	11.96
0.01704	1400	1.55E-07	11.98
0.01712	1680	1.53E-07	11.99
0.01714	1960	1.78E-07	12.01
0.01720	2240	1.92E-07	12.02
0.01722	2520	2.05E-07	12.05
0.01725	2800	2.19E-07	12.07
0.01733	3080	2.21E-07	12.09
0.01738	3360	2.17E-07	12.12
0.01745	3640	2.21E-07	12.14
0.01750	3920	2.21E-07	12.17
0.01755	4200	2.39E-07	12.19
0.01763	4480	2.38E-07	12.22
0.01770	4760	2.55E-07	12.25
0.01774	5040	2.97E-07	12.27
0.01783	5320	3.05E-07	12.31
0.01786	5600	3.36E-07	12.34
0.01798	5880	3.43E-07	12.38
0.01803	6160	3.65E-07	12.41
0.01812	6440	3.81E-07	12.45
0.01826	6720	3.91E-07	12.49
0.01831	7000	4.30E-07	12.54
0.01844	7280	4.31E-07	12.58
0.01853	7560	4.50E-07	12.63
0.01865	7840	3.95E-07	12.68
0.01878	8120	4.23E-07	12.71
0.01890	8400	4.53E-07	12.75
0.01905	8680	5.02E-07	12.80
0.01914	8960	5.68E-07	12.85
0.01929	9240	6.09E-07	12.92
0.01936	9520	6.42E-07	12.99
0.01957	9800	5.90E-07	13.05
0.01970	10080	5.86E-07	13.11
0.01990	10360	6.40E-07	13.16
0.02009	10640	7.09E-07	13.22
0.02023	10920	7.31E-07	13.29
0.02037	11200	8.70E-07	13.38
0.02055	11480	9.36E-07	13.47
0.02072	11760	9.81E-07	13.57
0.02103	12040	9.75E-07	13.66
0.02127	12320	1.00E-06	13.76
0.02153	12600	1.03E-06	13.86
0.02181	12880	1.05E-06	13.96
0.02211	13160	1.08E-06	14.06
0.02239	13440	1.13E-06	14.16
0.02264	13720	1.16E-06	14.27
0.02296	14000	1.19E-06	14.38
0.02327	14280	1.23E-06	14.48
0.02357	14560	1.31E-06	14.59
0.02393	14840	1.41E-06	14.70
0.02426	15120	1.57E-06	14.83
0.02457	15400	1.77E-06	14.97
0.02494	15680	1.94E-06	15.12
0.02529	15920	2.07E-06	15.30
0.02573	16160	2.16E-06	15.46
0.02620	16440	2.23E-06	15.66
0.02675	16700	2.26E-06	15.85
0.02735	16960	2.23E-06	16.03
0.02792	17220	2.33E-06	16.21
0.02847	17480	2.47E-06	16.39
0.02906	17740	2.61E-06	16.59
0.02971	18000	2.74E-06	16.77
0.03029	18260	2.93E-06	16.97
0.03078	18520	3.14E-06	17.19
0.03157	18760	3.16E-06	17.42
0.03227	19000	3.35E-06	17.65
0.03297	19240	3.59E-06	17.88
0.03368	19480	3.86E-06	18.14
0.03450	19720	4.09E-06	18.36
0.03539	19960	4.35E-06	18.64
0.03606	20200	4.72E-06	18.92
0.03706	20420	5.05E-06	19.20
0.03802	20640	5.58E-06	19.51
0.03899	20860	6.26E-06	19.86
0.04002	21000	6.90E-06	20.22
0.04112	21300	8.02E-06	20.61
0.04239	21520	9.20E-06	21.06
0.04367	21720	1.05E-05	21.52
0.04517	21920	1.19E-05	22.06
0.04680	22120	1.38E-05	22.67
0.04841	22300	1.58E-05	23.28
0.05056	22480	1.81E-05	23.98
0.05274	22660	2.06E-05	24.69
0.05505	22820	2.35E-05	25.52
0.05753	22980	2.67E-05	26.34
0.06025	23120	2.96E-05	27.11
0.06335	23260	3.32E-05	27.98
0.06619	23380	3.57E-05	28.80
0.06995	23480	3.85E-05	29.70
0.07193	23560	4.00E-05	30.40
0.07468	23660	4.48E-05	31.21
0.07777	23740	4.79E-05	31.78
0.08029	23800	5.11E-05	32.42
0.08251	23860	5.06E-05	32.79

407-5 T=400F R=0
ΔK decreasing (1 Hz)

a	N	da/dN	ΔK
0.05704	4320	9.84E-06	29.7
0.06458	5160	8.43E-06	28.6
0.07329	6600	5.93E-06	27.5
0.07821	8040	4.35E-06	25.3
0.08437	9480	3.35E-06	23.6
0.08902	11460	2.60E-06	21.6
0.09381	13620	2.10E-06	20.8
0.09809	15780	1.74E-06	19.7
0.10133	17940	1.48E-06	18.8
0.10416	20100	1.26E-06	18.1
0.10647	22260	1.12E-06	17.6
0.10902	24420	1.04E-06	17.1
0.11081	26580	9.58E-07	16.5
0.11269	28740	8.85E-07	16.1
0.11497	30900	8.27E-07	15.7
0.11662	33600	7.43E-07	14.6
0.11653	36480	6.86E-07	15
0.12060	39360	5.09E-07	14.5
0.12206	42240	5.64E-07	14.2
0.12419	45120	5.09E-07	13.9
0.12497	48000	4.44E-07	13.7
0.12649	50880	3.93E-07	13.5
0.12745	53760	3.80E-07	13.1
0.12839	56640	3.50E-07	13.1
0.12945	59520	3.01E-07	12.9
0.13088	62400	2.65E-07	12.7
0.1308	65280	2.44E-07	12.4
0.13153	68160	2.25E-07	12.4
0.13203	71040	2.32E-07	12.4
0.13301	73920	2.63E-07	12.3
0.13367	76800	2.73E-07	12.2
0.13469	79680	2.64E-07	12
0.13522	82560	2.36E-07	11.9
0.13619	85440	2.31E-07	11.8
0.13649	88320	1.96E-07	11.7
0.13702	91200	1.26E-07	11.7
0.13791	94080	7.48E-08	11.5
0.13788	96960	8.14E-09	11.5
0.13705	99840	3.99E-08	11.4
0.13754	102720	1.16E-07	11.5
0.13688	105600	1.74E-07	11.4
0.13616	108480	2.27E-07	11.2
0.13955	111360	2.11E-07	11.2
0.14034	114240	1.84E-07	11.2
0.14107	117120	5.13E-08	11.1

407-8 T=400F R=0
ΔK decreasing (freq=20 cpm)

a	N	da/dN	ΔK
0.05812	11600	6.04E-06	25.36
0.06067	12032	5.10E-06	24.06
0.06212	12514	3.99E-06	23.36
0.06359	13048	3.09E-06	22.61
0.06517	13634	2.52E-06	22.21
0.06651	14265	2.31E-06	21.69
0.06817	14946	2.10E-06	21.14
0.06958	15670	1.91E-06	20.65
0.07091	16435	1.78E-06	20.17
0.07212	17235	1.68E-06	19.76
0.07355	18073	1.63E-06	19.29
0.07504	18954	1.60E-06	18.82
0.07649	19874	1.56E-06	18.38
0.07783	20833	1.51E-06	17.94
0.07943	21829	1.40E-06	17.50
0.08099	22863	1.26E-06	17.06
0.08227	23931	1.10E-06	16.65
0.08327	25033	9.43E-07	16.37
0.08406	26165	8.07E-07	16.14
0.08480	27265	7.24E-07	15.90
0.08574	28414	6.76E-07	15.69
0.08648	29580	6.29E-07	15.50
0.08724	30763	5.68E-07	15.29
0.08793	31961	5.24E-07	15.11
0.08846	33171	4.79E-07	14.97
0.08836	34391	4.41E-07	14.86
0.08953	35621	4.16E-07	14.72
0.09002	36864	4.07E-07	14.57
0.09051	38115	4.15E-07	14.44
0.09099	39379	4.21E-07	14.32
0.09151	40654	4.27E-07	14.21
0.09219	41940	4.21E-07	14.04
0.09275	43238	4.00E-07	13.91
0.09323	44545	3.57E-07	13.80
0.09367	45861	3.21E-07	13.69
0.09405	47186	3.06E-07	13.59
0.09432	48514	3.23E-07	13.52
0.09482	49853	3.90E-07	13.43
0.09526	51189	3.25E-07	13.35
0.09594	52556	2.75E-07	13.17
0.09624	53924	2.26E-07	13.11
0.09648	55298	1.94E-07	13.01
0.09634	56674	1.81E-07	13.00
0.09678	58050	2.02E-07	12.98
0.09715	59431	2.11E-07	12.91
0.09757	60822	2.19E-07	12.79
0.09786	62218	1.92E-07	12.75
0.09793	63618	1.79E-07	12.72
0.09817	65018	1.59E-07	12.68
0.09848	66422	1.70E-07	12.62
0.09878	67837	1.82E-07	12.53
0.09886	69253	1.98E-07	12.52
0.09928	70673	1.79E-07	12.43
0.09960	72100	1.63E-07	12.35
0.09987	73532	1.65E-07	12.30
0.09998	74964	1.30E-07	12.26
0.10008	76399	9.89E-08	12.26
0.10044	77839	9.25E-08	12.17
0.10036	79279	9.90E-08	12.15
0.10040	80719	8.83E-08	12.15
0.10066	82164	9.45E-08	12.13
0.10083	83612	1.06E-07	12.08
0.10091	85060	1.25E-07	12.06
0.10108	86512	1.31E-07	12.04
0.10126	87968	1.35E-07	12.02
0.10160	89427	1.36E-07	11.97
0.10181	90891	1.21E-07	11.92
0.10190	92355	9.65E-08	11.91
0.10204	93821	5.35E-08	11.88
0.10213	95293	5.69E-08	11.86
0.10217	96765	5.53E-08	11.84

407-5 T=400F R=0
ΔK increasing (freq=20 cpm)

a	N	da/dN	ΔK
0.15305	460120	6.63E-07	13.03
0.15318	460400	7.41E-07	13.09
0.15335	460680	6.05E-07	13.12
0.15357	460960	9.12E-07	13.18
0.15406	461240	1.00E-06	13.30
0.15414	461520	1.05E-06	13.36
0.15456	461800	1.05E-06	13.45
0.15479	462080	1.02E-06	13.51
0.15509	462360	1.07E-06	13.58
0.15542	462640	1.02E-06	13.67
0.15572	462920	1.05E-06	13.76
0.15596	463200	1.05E-06	13.82
0.15624	463480	1.06E-06	13.89
0.15657	463760	1.07E-06	13.98
0.15668	464040	1.05E-06	14.05
0.15718	464320	1.01E-06	14.14
0.15746	464600	6.98E-07	14.21
0.15780	465160	7.69E-07	14.26
0.15805	465440	7.13E-07	14.37
0.15825	465720	8.23E-07	14.43
0.15855	466000	9.06E-07	14.49
0.15663	466280	1.04E-06	14.55
0.15917	466548	1.21E-06	14.66
0.15937	466812	1.33E-06	14.72
0.15972	467078	1.47E-06	14.81
0.16027	467344	1.55E-06	14.95
0.16061	467610	1.69E-06	15.04
0.16106	467876	1.74E-06	15.17
0.16159	468142	1.75E-06	15.33
0.16205	468408	1.78E-06	15.41
0.16253	468674	1.78E-06	15.57
0.16301	468940	1.76E-06	15.70
0.16344	469206	1.74E-06	15.81
0.16392	469472	1.89E-06	15.94
0.16441	469738	1.66E-06	16.07
0.16481	470054	1.66E-06	16.13
0.16526	470270	1.69E-06	16.29
0.16571	470536	1.70E-06	16.42
0.16613	470802	1.98E-06	16.55
0.16667	471067	2.18E-06	16.67
0.16725	471319	2.28E-06	16.83
0.16792	471571	2.41E-06	17.04
0.16856	471823	2.39E-06	17.21
0.16906	472075	2.30E-06	17.33
0.16974	472327	2.21E-06	17.51
0.17024	472579	2.28E-06	17.65
0.17072	472831	2.54E-06	17.79
0.17130	473083	2.86E-06	17.96
0.17212	473335	3.19E-06	18.18
0.17312	473587	3.46E-06	18.45
0.17406	473839	3.66E-06	18.71
0.17485	474079	3.86E-06	18.95
0.17571	474317	4.13E-06	19.21
0.17670	474555	4.45E-06	19.43
0.17789	474793	4.87E-06	19.60
0.17917	475031	5.40E-06	20.15
0.18036	475269	5.93E-06	20.47
0.18174	475504	6.41E-06	20.84
0.18341	475728	6.84E-06	21.29
0.18502	475952	7.23E-06	21.78
0.18667	476176	7.48E-06	22.27
0.18834	476400	7.75E-06	22.74
0.18997	476614	8.30E-06	23.21
0.19165	476824	9.01E-06	23.70
0.19361	477034	9.79E-06	24.27
0.19587	477244	1.06E-05	24.92
0.19806	477440	1.14E-05	25.61
0.20028	477636	1.21E-05	26.27
0.20269	477832	1.28E-05	26.97
0.20516	478014	1.35E-05	27.72
0.20766	478196	1.48E-05	28.49
0.21013	478374	1.65E-05	29.27
0.21292	478542	1.86E-05	30.10
0.21625	478709	2.12E-05	31.13
0.21969	478863	2.40E-05	32.23
0.22356	479012	2.76E-05	33.49
0.22737	479152	3.22E-05	34.75
0.23143	479292	3.76E-05	36.12
0.23628	479402	4.58E-05	37.75

407-8 T=400F R=0
ΔK increasing (1 Hz)

a	N	da/dN	ΔK
0.10961	197640	2.17E-07	13.09
0.10974	198360	2.85E-07	13.26
0.11023	199080	3.20E-07	13.80
0.11051	199800	3.22E-07	13.84
0.11069	200520	2.95E-07	13.90
0.11079	201240	2.24E-07	13.90
0.11093	201960	1.83E-07	13.93
0.11117	202680	1.56E-07	13.97
0.11122	203400	1.48E-07	13.99
0.11127	204120	1.43E-07	14.00
0.11132	204840	1.63E-07	14.02
0.11149	205560	1.90E-07	14.04
0.11164	206280	2.09E-07	14.07
0.11191	207000	2.24E-07	14.11
0.11196	207720	2.14E-07	14.13
0.11210	208440	2.06E-07	14.14
0.11231	209160	2.10E-07	14.18
0.11241	209880	2.22E-07	14.26
0.11250	210600	2.22E-07	14.22
0.11280	211320	2.33E-07	14.27
0.11293	212040	2.45E-07	14.28
0.11307	212760	2.27E-07	14.32
0.11333	213480	2.01E-07	14.36
0.11346	214200	1.81E-07	14.40
0.11352	214920	1.58E-07	14.41
0.11361	215640	1.36E-07	14.42
0.11369	216360	1.47E-07	14.42
0.11384	217080	1.67E-07	14.46
0.11393	217800	1.63E-07	14.48
0.11409	218520	1.28E-07	14.51
0.11424	219240	1.04E-07	14.53
0.11425	219960	8.93E-08	14.55
0.11417	220680	8.73E-08	14.54
0.11433	221400	1.20E-07	14.55
0.11440	222120	1.57E-07	14.56
0.11454	222840	1.90E-07	14.57
0.11477	223560	2.01E-07	14.63
0.11464	224280	2.07E-07	14.66
0.11498	225000	2.03E-07	14.66
0.11519	225720	2.06E-07	14.70
0.11529	226440	2.26E-07	14.73
0.11544	227160	2.25E-07	14.72
0.11566	227880	2.09E-07	14.76
0.11582	228600	2.07E-07	14.81
0.11595	229320	1.81E-07	14.84
0.11603	230040	1.64E-07	14.85
0.11620	230760	1.75E-07	14.90
0.11623	231480	2.10E-07	14.90
0.11641	232200	2.46E-07	14.92
0.11662	232920	2.45E-07	14.96
0.11680	233640	2.56E-07	15.00
0.11706	234360	2.42E-07	15.03
0.11711	235080	2.62E-07	15.06
0.11733	235800	2.66E-07	15.07
0.11749	236520	2.89E-07	15.13
0.11791	237240	3.28E-07	15.18
0.11801	237960	3.51E-07	15.21
0.11824	238680	3.62E-07	15.21
0.11854	239400	3.53E-07	15.29
0.11887	240120	3.65E-07	15.36
0.11910	240840	3.84E-07	15.40
0.11934	241560	3.60E-07	15.42
0.11967	242280	3.32E-07	15.49
0.11991	243000	3.20E-07	15.53
0.12008	243720	3.34E-07	15.56
0.12026	244440	3.40E-07	15.62
0.12050	245160	3.87E-07	15.64
0.12092	245880	4.48E-07	15.74
0.12115	246600	5.16E-07	15.75
0.12158	247320	5.42E-07	15.83
0.12200	248040	5.42E-07	15.91
0.12251	248760	5.50E-07	16.01
0.12290	249480	5.05E-07	16.04
0.12315	250200	4.99E-07	16.13
0.12353	250920	5.07E-07	16.20
0.12374	251640	5.39E-07	16.22
0.12428	252360	5.63E-07	16.31
0.12473	253080	5.82E-07	16.39
0.12512	253800	6.46E-07	16.49
0.12555	254520	6.84E-07	16.54
0.12585	255240	7.44E-07	16.62
0.12670	255960	8.27E-07	16.77
0.12729	256680	8.95E-07	16.86
0.12790	257400	9.63E-07	16.99
0.12865	258120	1.06E-06	17.11
0.12935	258840	1.31E-06	17.22
0.13019	259560	1.59E-06	17.40
0.13138	260280	1.82E-06	17.76
0.13327	261000	2.00E-06	18.61
0.13464	261720	2.10E-06	18.87
0.13623	262440	2.15E-06	19.09
0.13764	263160	2.16E-06	19.34
0.13915	263880	2.32E-06	19.62
0.14057	264600	2.59E-06	19.91
0.14287	265320	2.99E-06	20.26
0.14490	266040	3.54E-06	20.61
0.14757	266760	4.18E-06	21.02
0.15083	267480	4.96E-06	21.52
0.15481	268200	5.95E-06	22.20
0.15911	268920	6.92E-06	22.99
0.16428	269640	7.89E-06	23.87
0.17100	270360	9.13E-06	24.98
0.17746	271080	1.08E-05	26.07
0.18475	271800	1.29E-05	27.25
0.19404	272520	1.67E-05	28.37

407-1 T=400F R=0
ΔK increasing (freq=20 cpm)

a	N	da/dN	ΔK
0.14254	63161	4.92E-07	13.97
0.14289	63741	5.80E-07	14.03
0.14324	64321	6.50E-07	14.15
0.14363	64901	7.14E-07	14.26
0.14409	65481	7.99E-07	14.38
0.14453	66061	8.82E-07	14.50
0.14503	66641	9.78E-07	14.63
0.14571	67221	1.11E-06	14.83
0.14632	67801	1.26E-06	15.01
0.14704	68381	1.39E-06	15.22
0.14809	68961	1.53E-06	15.50
0.14890	69541	1.69E-06	15.75
0.14986	70121	1.82E-06	16.00
0.15100	70701	1.93E-06	16.27
0.15213	71281	2.13E-06	16.52
0.15337	71861	2.30E-06	16.95
0.15471	72441	2.54E-06	17.31
0.15640	73021	2.88E-06	17.81
0.15798	73601	3.23E-06	18.24
0.15999	74181	3.53E-06	18.83
0.16234	74761	3.77E-06	19.52
0.16457	75341	4.03E-06	20.15
0.16683	75921	4.38E-06	20.84
0.16924	76501	5.04E-06	21.52
0.17198	77081	6.16E-06	22.30
0.17571	77661	7.70E-06	23.41
0.18051	78241	9.54E-06	24.84
0.18665	78821	1.20E-05	26.66
0.19411	79401	1.60E-05	28.91

TABLE I-6. FATIGUE CRACK GROWTH DATA FOR Ti-6-4 AT $R = 0.5$

401-5	RT	R=0.5		401-7	T=400F	R=0.5	
Const. Load (freq=20 cpm)				Const. Load (freq=20 cpm)			
a	N	da/dN	ΔK	a	N	da/dN	ΔK
0.02435	1040	2.48E-08	7.33	0.02721	1050	8.31E-08	7.76
0.02420	2080	6.15E-08	7.30	0.02723	2100	1.01E-07	7.76
0.02421	3120	6.62E-08	7.31	0.02726	3150	1.13E-07	7.80
0.02425	4160	8.84E-08	7.33	0.02736	4200	1.21E-07	7.82
0.02414	5200	1.11E-07	7.34	0.02747	5250	1.25E-07	7.84
0.02442	6240	9.17E-08	7.36	0.02758	6300	1.32E-07	7.87
0.02447	7280	1.21E-07	7.37	0.02773	7350	1.39E-07	7.89
0.02457	8320	1.45E-07	7.38	0.02785	8400	1.43E-07	7.92
0.02453	9360	1.73E-07	7.41	0.02796	9450	1.48E-07	7.94
0.02480	10400	1.79E-07	7.43	0.02812	10500	1.45E-07	7.96
0.02494	11440	1.96E-07	7.46	0.02826	11550	1.42E-07	7.99
0.02492	12480	2.13E-07	7.49	0.02843	12600	1.43E-07	8.01
0.02527	13520	2.03E-07	7.52	0.02860	13650	1.49E-07	8.03
0.02544	14560	2.10E-07	7.55	0.02873	14700	1.52E-07	8.06
0.02566	15600	2.11E-07	7.58	0.02890	15750	1.51E-07	8.08
0.02588	16640	2.11E-07	7.61	0.02901	16800	1.54E-07	8.11
0.02607	17680	2.13E-07	7.64	0.02917	17850	1.51E-07	8.13
0.02631	18720	2.12E-07	7.67	0.02937	18900	1.54E-07	8.16
0.02653	19760	2.13E-07	7.70	0.02954	19920	1.45E-07	8.16
0.02676	20800	2.17E-07	7.72	0.02968	20940	1.65E-07	8.20
0.02697	21840	2.33E-07	7.75	0.02990	21960	1.86E-07	8.23
0.02718	22880	2.46E-07	7.78	0.02997	22980	2.05E-07	8.26
0.02742	23920	2.59E-07	7.82	0.03012	24000	2.23E-07	8.30
0.02764	24960	2.56E-07	7.86	0.03034	25020	2.39E-07	8.34
0.02787	26000	2.74E-07	7.89	0.03036	26040	2.50E-07	8.36
0.02811	27040	2.86E-07	7.93	0.03073	27060	2.34E-07	8.42
0.02844	28040	2.95E-07	7.96	0.03098	28080	2.17E-07	8.45
0.02870	29040	3.06E-07	8.00	0.03122	29100	2.34E-07	8.46
0.02898	30040	3.11E-07	8.04	0.03146	30120	2.57E-07	8.52
0.02912	31040	3.14E-07	8.09	0.03171	31110	2.89E-07	8.56
0.02959	32040	2.98E-07	8.12	0.03192	32100	3.22E-07	8.60
0.02990	33040	3.03E-07	8.16	0.03214	33090	3.40E-07	8.66
0.03020	34040	3.21E-07	8.19	0.03224	34080	3.52E-07	8.72
0.03049	35040	3.49E-07	8.23	0.03272	35070	3.36E-07	8.77
0.03077	36040	3.81E-07	8.28	0.03305	35080	3.46E-07	8.81
0.03106	37040	4.03E-07	8.33	0.03343	37050	3.67E-07	8.86
0.03141	38040	4.17E-07	8.38	0.03374	38010	4.10E-07	8.91
0.03172	39040	4.33E-07	8.43	0.03401	38970	4.63E-07	8.97
0.03215	40040	4.46E-07	8.48	0.03436	39930	5.10E-07	9.05
0.03259	41000	4.57E-07	8.53	0.03470	40890	5.56E-07	9.13
0.03301	41960	4.71E-07	8.59	0.03511	41850	5.92E-07	9.20
0.03338	42920	4.87E-07	8.64	0.03558	42810	6.19E-07	9.28
0.03379	43880	5.02E-07	8.70	0.03610	43740	6.44E-07	9.37
0.03427	44840	4.94E-07	8.76	0.03666	44670	6.85E-07	9.45
0.03477	45800	5.03E-07	8.81	0.03721	45600	6.83E-07	9.54
0.03522	46760	5.32E-07	8.87	0.03778	46500	7.08E-07	9.63
0.03568	47720	5.63E-07	8.92	0.03837	47400	7.43E-07	9.72
0.03614	48640	6.81E-07	8.98	0.03897	48300	7.92E-07	9.81
0.03668	49560	7.88E-07	9.05	0.03960	49170	8.47E-07	9.91
0.03702	50480	8.94E-07	9.15	0.04021	50040	8.95E-07	10.01
0.03760	51400	9.63E-07	9.25	0.04082	50910	9.42E-07	10.13
0.03823	52320	1.03E-06	9.35	0.04151	51750	9.61E-07	10.24
0.03899	53240	1.09E-06	9.45	0.04225	52590	9.68E-07	10.35
0.04000	54120	1.13E-06	9.56	0.04307	53430	9.71E-07	10.46
0.04087	55000	1.19E-06	9.67	0.04387	54240	9.86E-07	10.56
0.04172	55880	1.27E-06	9.78	0.04461	55050	1.01E-06	10.67
0.04265	56760	1.41E-06	9.90	0.04543	55830	1.05E-06	10.77
0.04366	57600	1.56E-06	10.02	0.04615	56610	1.11E-06	10.88
0.04477	58440	1.70E-06	10.16	0.04690	57390	1.19E-06	11.00
0.04580	59280	1.84E-06	10.33	0.04766	58140	1.30E-06	11.12
0.04686	60090	1.94E-06	10.49	0.04847	58890	1.41E-06	11.24
0.04807	60880	2.02E-06	10.65	0.04925	59610	1.56E-06	11.38
0.04977	61680	2.09E-06	10.79	0.05013	60330	1.72E-06	11.53
0.05124	62440	2.23E-06	10.95	0.05105	61020	1.90E-06	11.70
0.05265	63200	2.38E-06	11.11	0.05202	61710	2.08E-06	11.87
0.05410	63920	2.59E-06	11.29	0.05316	62370	2.25E-06	12.05
0.05560	64640	2.85E-06	11.46	0.05425	63030	2.45E-06	12.24
0.05717	65320	3.17E-06	11.65	0.05553	63660	2.63E-06	12.45
0.05881	66000	3.51E-06	11.85	0.05687	64260	2.87E-06	12.65
0.06055	66640	3.82E-06	12.06	0.05816	64830	3.12E-06	12.86
0.06228	67280	4.19E-06	12.31	0.05960	65400	3.36E-06	13.08
0.06431	67880	4.58E-06	12.54	0.06105	65940	3.61E-06	13.31
0.06656	68480	5.00E-06	12.79	0.06259	66450	3.82E-06	13.54
0.06887	69040	5.43E-06	13.05	0.06404	66930	4.05E-06	13.77
0.07109	69560	5.89E-06	13.30	0.06571	67380	4.29E-06	13.98
0.07331	70080	6.39E-06	13.55	0.06727	67800	4.50E-06	14.20
0.07591	70580	6.85E-06	13.80	0.06875	68190	4.75E-06	14.41
0.07849	71000	7.47E-06	14.06	0.07027	68550	5.03E-06	14.63
0.08089	71400	7.93E-06	14.33	0.07165	68880	5.28E-06	14.84
0.08314	71760	8.28E-06	14.59	0.07306	69180	5.53E-06	15.04
0.08565	72120	8.52E-06	14.81	0.07457	69480	5.84E-06	15.22
0.08815	72440	8.90E-06	15.03	0.07585	69750	6.10E-06	15.43
0.09049	72720	9.24E-06	15.24	0.07721	69990	6.33E-06	15.61
0.09268	72960	1.01E-05	15.45	0.07841	70200	6.47E-06	15.77
0.09457	73200	1.07E-05	15.63	0.07960	70410	6.63E-06	15.93
0.09635	73400	1.14E-05	15.84	0.08074	70580	6.81E-06	16.07
0.09814	73600	1.16E-05	16.00	0.08178	70740	6.43E-06	16.21
0.09993	73760	1.17E-05	16.17	0.08268	70880	6.26E-06	16.31
0.10148	73920	1.18E-05	16.30	0.08354	71010	6.18E-06	16.40
0.10324	74040	1.17E-05	16.40	0.08428	71130	6.71E-06	16.48
0.10447	74160	1.24E-05	16.53	0.08495	71220	7.42E-06	16.53
0.10546	74240	1.27E-05	16.58	0.08549	71310	8.34E-06	16.61
0.10635	74320	1.30E-05	16.64	0.08578	71370	8.94E-06	16.70
0.10727	74400	1.36E-05	16.71	0.08617	71430	8.53E-06	16.75
				0.08657	71490	8.21E-06	16.80
				0.08718	71550	7.66E-06	16.85
				0.08752	71580	7.47E-06	16.88

TABLE I-7. FATIGUE CRACK GROWTH DATA FOR Ti-6-4 AT $R = 0.75$

401-1 RT R=0.75			
Const. Load (freq=20 cpm)			
a	N	da/dN	ΔK
0.03576	4400	7.20E-09	4.67
0.03571	8800	7.86E-09	4.66
0.03573	13200	1.15E-08	4.66
0.03576	17600	1.44E-08	4.66
0.03582	22000	1.60E-08	4.69
0.03585	26400	1.86E-08	4.69
0.03593	30800	1.99E-08	4.7
0.03598	35200	1.95E-08	4.71
0.03609	39600	1.35E-08	4.72
0.03617	44000	0.74E-08	4.72
0.03621	48400	5.70E-09	4.72
0.03623	52800	4.38E-09	4.72
0.03636	57200	6.54E-09	4.72
0.03642	61600	9.12E-09	4.72
0.03642	66000	1.23E-08	4.73
0.03639	70400	1.44E-08	4.74
0.03639	74800	1.55E-08	4.74
0.0365	79200	1.44E-08	4.75
0.03659	83600	1.46E-08	4.75
0.03665	88000	1.62E-08	4.78
0.03669	92400	1.18E-08	4.77
0.03675	96800	1.23E-08	4.77
0.03682	101200	1.28E-08	4.77
0.03691	105600	1.22E-08	4.78
0.03697	110000	1.39E-08	4.78
0.03707	114400	1.51E-08	4.79
0.03691	118800	1.80E-08	4.79
0.03714	123200	1.41E-08	4.8
0.03721	127600	1.39E-08	4.8
0.03722	132000	1.38E-08	4.81
0.03733	136400	1.24E-08	4.81
0.03738	140800	1.30E-08	4.82
0.03745	145200	1.25E-08	4.82
0.03751	149600	1.30E-08	4.83
0.03755	154000	1.32E-08	4.83
0.0376	158400	1.33E-08	4.84
0.03766	162800	1.32E-08	4.84
0.03774	167200	1.21E-08	4.84
0.03779	171600	1.21E-08	4.85
0.03784	176000	1.19E-08	4.85
0.03789	180400	1.11E-08	4.86
0.03795	184700	1.60E-08	4.87
0.03802	189000	1.51E-08	4.87
0.03804	193300	1.39E-08	4.88
0.03826	213000	1.26E-08	4.89
0.0384	217300	8.16E-09	4.89
0.03846	221600	8.96E-09	4.89
0.03849	225900	1.19E-08	4.9
0.03856	230200	1.48E-08	4.9
0.03859	234500	1.77E-08	4.91
0.0386	238800	1.95E-08	4.92
0.03862	243100	1.87E-08	4.92
0.03879	247400	1.30E-08	4.93
0.03864	251700	1.92E-08	4.94
0.03893	256000	1.34E-08	4.94
0.03899	260300	1.41E-08	4.94
0.03903	264600	1.45E-08	4.95
0.03908	268900	1.50E-08	4.95
0.03913	273200	1.46E-08	4.96
0.0392	277500	1.37E-08	4.96
0.03928	281800	1.33E-08	4.97
0.03933	286100	1.49E-08	4.97
0.03939	290400	1.36E-08	4.98
0.03945	294700	1.49E-08	4.98
0.03952	299000	1.55E-08	4.99
0.03955	303300	1.23E-08	5
0.03963	307300	1.34E-08	5
0.03974	312200	1.39E-08	5
0.03977	316500	1.56E-08	5.01
0.03983	320800	1.44E-08	5.02
0.03992	325100	1.46E-08	5.02
0.03982	329400	1.72E-08	5.03
0.04006	333700	1.45E-08	5.03
0.04011	338000	1.83E-08	5.03
0.04016	342300	1.77E-08	5.04
0.04015	346500	1.62E-08	5.05
0.04025	350700	1.56E-08	5.06
0.04037	354900	1.48E-08	5.06
0.04043	359100	1.31E-08	5.06
0.0405	363300	1.86E-08	5.06
0.04056	367500	1.90E-08	5.07
0.04061	371700	2.04E-08	5.07
0.04065	375900	2.06E-08	5.08
0.04075	380100	1.96E-08	5.08
0.04074	384300	1.85E-08	5.1
0.04068	388500	1.49E-08	5.1
0.04103	392700	1.68E-08	5.11
0.04108	396900	1.82E-08	5.12
0.04114	401100	1.94E-08	5.12
0.04122	405300	1.90E-08	5.13
0.04127	409500	1.97E-08	5.14
0.04136	413700	1.83E-08	5.15
0.04145	417900	1.95E-08	5.15
0.04154	422100	2.04E-08	5.15
0.04163	426300	2.15E-08	5.16
0.04169	430500	2.31E-08	5.17
0.04177	434700	2.39E-08	5.18
0.04186	438900	2.41E-08	5.18
0.04196	443100	2.20E-08	5.2
0.04206	447300	2.26E-08	5.2
0.04215	451500	2.43E-08	5.21
0.04226	455700	2.47E-08	5.21
0.04237	459900	2.56E-08	5.23
0.04246	464300	2.57E-08	5.24
0.04251	468100	2.61E-08	5.25
0.04264	472200	2.52E-08	5.25
0.04279	476300	2.56E-08	5.26
0.04287	480400	2.75E-08	5.26
0.04298	484500	2.80E-08	5.27
0.04305	488600	2.90E-08	5.28
0.04317	492700	2.82E-08	5.29

continued in next column

401-1 RT R=0.75			
Const. Load (freq=20 cpm)			
a	N	da/dN	ΔK
0.04329	496800	3.02E-08	5.3
0.04342	500900	2.59E-08	5.31
0.04355	505000	2.31E-08	5.32
0.04364	509100	2.79E-08	5.33
0.04373	513200	3.18E-08	5.33
0.0439	517300	3.95E-08	5.34
0.04405	521400	3.85E-08	5.36
0.04429	525500	4.05E-08	5.37
0.04459	529600	4.39E-08	5.38
0.0441	529600	4.04E-08	4.39
0.04445	533700	3.58E-08	5.4
0.0445	537800	3.65E-08	5.41
0.04472	541800	3.73E-08	5.42
0.04488	545800	3.82E-08	5.43
0.04501	549900	3.92E-08	5.44
0.04518	553900	4.09E-08	5.46
0.04532	557800	4.18E-08	5.47
0.04547	561800	4.32E-08	5.49
0.04561	565800	4.35E-08	5.5
0.0458	569800	4.29E-08	5.51
0.04595	573800	4.34E-08	5.52
0.04615	577800	4.35E-08	5.54
0.04631	581800	4.41E-08	5.55
0.0465	585800	4.34E-08	5.56
0.04665	589800	4.26E-08	5.58
0.04682	593700	4.25E-08	5.59
0.04701	597800	4.28E-08	5.6
0.04719	601800	4.36E-08	5.61
0.04735	605400	4.36E-08	5.63
0.0475	609300	4.30E-08	5.64
0.04764	613200	4.29E-08	5.65
0.04784	617100	4.25E-08	5.67
0.04803	621000	4.28E-08	5.68
0.0482	624900	3.91E-08	5.7
0.04834	628800	4.27E-08	5.71
0.04849	632700	4.46E-08	5.72
0.04867	636600	4.48E-08	5.73
0.0485	640500	4.52E-08	5.74
0.04903	644300	4.68E-08	5.76
0.04902	648100	4.68E-08	5.77
0.04939	651900	4.80E-08	5.79
0.04954	655700	4.89E-08	5.8
0.0497	659500	5.35E-08	5.81
0.04985	663300	5.87E-08	5.83
0.05004	667100	5.77E-08	5.85
0.05022	670900	5.91E-08	5.87
0.05045	674700	5.99E-08	5.89
0.05068	678500	5.72E-08	5.9
0.0503	682300	5.22E-08	5.82
0.05113	686000	5.59E-08	5.83
0.05132	689700	5.87E-08	5.85
0.05153	693400	5.70E-08	5.86
0.05181	697100	5.79E-08	5
0.04939	701900	8.66E-08	6.07
0.05238	704500	8.02E-08	6.03
0.05259	708200	8.06E-08	6.05
0.05282	711900	8.28E-08	6.07
0.05301	715600	8.43E-08	6.08
0.05327	719200	8.43E-08	6.1
0.05345	722800	8.74E-08	6.12
0.05363	726400	8.92E-08	6.14
0.05392	730000	7.24E-08	6.16
0.05419	733600	7.67E-08	6.18
0.0544	737200	8.11E-08	6.2
0.05463	740800	8.31E-08	6.22
0.05492	744400	9.39E-08	6.25
0.05519	748000	8.38E-08	6.27
0.0555	751600	8.33E-08	6.29
0.05582	755000	8.35E-08	6.32
0.0561	758500	8.61E-08	6.34
0.05636	762000	9.14E-08	6.36
0.05665	765500	9.61E-08	6.39
0.05695	769000	1.01E-07	6.41
0.05727	772500	1.05E-07	6.44
0.05757	775900	1.03E-07	6.47
0.0579	779300	1.08E-07	6.5
0.0583	782700	1.15E-07	6.53
0.05805	786100	1.30E-07	6.55
0.05901	789500	1.50E-07	6.59
0.05938	792800	1.74E-07	6.63
0.05958	796100	1.89E-07	6.66
0.06016	799400	1.92E-07	6.74
0.06066	802700	1.95E-07	6.79
0.06131	806000	1.94E-07	6.84
0.06197	809200	1.94E-07	6.89
0.06261	812400	1.97E-07	6.93
0.06324	815600	2.03E-07	6.98
0.06379	818700	2.18E-07	7.03
0.06433	821800	2.32E-07	7.09
0.06501	824900	2.41E-07	7.15
0.06563	827900	2.47E-07	7.21
0.06625	830900	2.48E-07	7.27
0.06693	833900	2.47E-07	7.33
0.06779	836800	2.48E-07	7.39
0.06852	839700	2.56E-07	7.45
0.06913	842600	2.63E-07	7.51
0.06966	845400	2.64E-07	7.56
0.07051	848200	2.63E-07	7.64
0.07124	851000	2.57E-07	7.7
0.07207	853700	2.49E-07	7.76
0.07273	856400	2.46E-07	7.82
0.07345	859100	2.50E-07	7.87
0.07403	861700	2.64E-07	7.93
0.07475	864300	2.88E-07	7.99
0.07539	866800	3.18E-07	8.05
0.07593	869400	3.48E-07	8.13
0.07661	871900	3.73E-07	8.21
0.07732	874400	3.97E-07	8.3
0.07815	876900	4.29E-07	8.38
0.07911	879200	4.72E-07	8.48
0.07999	881500	5.15E-07	8.58
0.08083	883800	5.57E-07	8.7
0.08181	886000	6.08E-07	8.82
0.08291	888000	6.81E-07	8.95
0.08403	890300	7.77E-07	9.08
0.08537	892400	8.24E-07	9.24
0.08647	894400	1.16E-06	9.43
0.08787	896300	1.50E-06	9.66
0.08919	898200	2.49E-06	9.9

402-6 RT R=0.75			
ΔK decreasing (freq=20 cpm)			
a	N	da/dN	ΔK
0.06645	21000	6.02E-07	8.56
0.06712	22000	5.36E-07	8.51
0.06757	23131	4.65E-07	8.41
0.06806	24121	4.03E-07	8.34
0.06843	25000	3.57E-07	8.26
0.06896	26939	3.45E-07	8.23
0.06943	28372	3.35E-07	8.18
0.06994	29834	3.21E-07	8.11
0.07048	31527	3.25E-07	8.04
0.07104	33217	3.14E-07	7.98
0.07159	35020	2.94E-07	7.91
0.07216	36920	2.71E-07	7.84
0.07265	38601	2.52E-07	7.78
0.07311	40100	2.41E-07	7.72
0.07356	41903	2.37E-07	7.68
0.07410	45256	2.36E-07	7.61
0.07470	47612	2.34E-07	7.55
0.07532	50025	2.25E-07	7.47
0.07579	52511	2.10E-07	7.41
0.0763	55075	1.90E-07	7.35
0.07690	57720	1.72E-07	7.29
0.07727	60435	1.58E-07	7.23
0.07765	63229	1.41E-07	7.26
0.07803	66037	1.33E-07	7.16
0.07835	68918	1.28E-07	7.12
0.07868	71845	1.24E-07	7.08
0.07916	74845	1.20E-07	7.04
0.07952	77900	1.17E-07	7.00
0.07982	80956	1.04E-07	6.96
0.08012	84139	0.86E-08	6.91
0.08049	87335	8.77E-08	6.90
0.08058	90540	1.06E-07	6.88
0.08083	93777	1.08E-07	6.87
0.08122	97031	1.05E-07	6.92
0.08216	100516	1.10E-07	6.73
0.08314	103946	9.26E-08	6.73
0.08226	107420	7.81E-08	6.69
0.08263	110940	5.71E-08	6.65
0.08274	114464	5.15E-08	6.69
0.08473	118036	3.20E-08	6.82
0.08319	121516	2.08E-08	6.81
0.08309	125196	4.62E-08	6.55
0.08298	128778	5.32E-08	6.56
0.08339	132332	6.32E-08	6.55
0.08423	136099	6.07E-08	6.52
0.08422	139818	5.10E-08	6.52
0.08419	143539	2.97E-08	6.50
0.08407	147256	1.91E-08	6.49
0.08429	150993	2.32E-08	6.49
0.08442	154753	3.45E-08	6.48
0.08473	158545	3.66E-08	6.45
0.08477	162345	3.84E-08	6.43
0.08479	166145	3.45E-08	6.43
0.08498	169971	3.45E-08	6.43
0.08520	173825	3.85E-08	6.40
0.08527	177688	3.84E-08	6.39
0.08550	181582	3.92E-08	6.37
0.08559	185502	2.79E-08	6.36
0.08567	189422	2.75E-08	6.35
0.08577	193342	2.80E-08	6.35
0.08583	197276	3.78E-08	6.34
0.08600	201236	5.07E-08	6.31
0.08621	205225	5.86E-08	6.28
0.08655	209251	5.52E-08	6.28
0.08692	213222	4.99E-08	6.24
0.08706	217423	4.01E-08	6.23
0.08700	221523	3.96E-08	6.22
0.08717	225535	3.56E-08	6.21
0.08730	229775	4.01E-08	6.20
0.08755	233931	3.82E-08	6.19
0.08788	238130	3.28E-08	6.16
0.08791	242347	2.55E-08	6.14
0.08783	246567	1.48E-08	6.12
0.08796	250805	1.32E-08	6.13
0.08804	255045	1.85E-08	6.13
0.08834	259214	1.95E-08	6.11
0.08846	272054	1.57E-08	6.10

401-5 T=400F R=0.75			
Const. Load (freq=20 cpm)			
a	N	da/dN	ΔK
0.03561	3780	1.85E-08	4.69
0.03557	7461	1.79E-08	4.7
0.03572	11140	1.72E-08	4.7
0.03562	14820	1.61E-08	4.71
0.0359	18500	1.70E-08	4.71
0.03594	22180	1.81E-08	4.72
0.036	25860	1.78E-08	4.72
0.03605	29540	1.64E-08	4.73
0.03612	33220	1.47E-08	4.73
0.03613	36900	1.27E-08	4.73
0.03628	40580	9.99E-09	4.73
0.03633	44260	1.48E-08	4.74
0.03637	47940	1.61E-08	4.75
0.0364	51620	1.40E-08	4.75
0.03649	55300	1.50E-08	4.75
0.03655	58980	1.30E-08	4.76
0.03662	62660	1.43E-08	4.76
0.03671	73360	1.73E-08	4.76
0.03678	77460	1.30E-08	4.77
0.03678	81060	1.13E-08	4.77
0.03683	84660	9.05E-09	4.77
0.03687	88260	7.87E-09	4.77
0.03702	91860	7.37E-09	4.78
0.03705	95460	1.07E-08	4.78
0.03694	100260	1.23E-08	4.79
0.03698	103860	1.41E-08	4.79
0.03705	107460	1.57E-08	4.79
0.03716	111060	1.77E-08	4.8
0.03724	114660	2.03E-08	4.8
0.03716	118260	2.08E-08	4.82
0.03738	125460	1.50E-08	4.82
0.03746	129060	1.42E-08	4.82
0.03754	132660	1.23E-08	4.79
0.03758	136260	1.34E-08	4.83
0.03763	139860	1.24E-08	4.83
0.03768	143460	1.20E-08	4.84
0.0377	147060	1.25E-08	4.84
0.03776	150660	1.26E-08	4.84
0.0378	154260	1.32E-08	4.85
0.03785	157860	1.43E-08	4.85
0.03788	161460	1.52E-08	4.85
0.03792	165060	1.53E-08	4.86
0.03799	168660	1.57E-08	4.86
0.03803	172260	1.63E-08	4.86
0.03808	175860	1.74E-08	4.87
0.0382	182960	1.78E-08	4.88
0.03825	186500	1.77E-08	4.88
0.03832	190020	1.75E-08	4.89
0.03838	193540	1.73E-08	4.89
0.03844	197063	1.75E-08	4.9
0.03852	200583	1.69E-08	4.9
0.03857	204100	1.69E-08	4.9
0.03862	207620	1.57E-08	4.91
0.03863	211143	1.39E-08	4.91
0.03874	214660	8.44E-09	4.92
0.03883	218180	1.86E-08	4.92
0.03887	221700	1.22E-08	4.92
0.03892	225220	2.74E-08	4.92
0.03895	228740	5.63E-08	4.92
0.03898	232260	1.01E-08	4.92
0.03862	235780	1.65E-08	4.92
0.03865	239300	1.57E-08	4.93
0.03902	242820	1.54E-08	4.93
0.03906	246363	1.64E-08	4.94
0.03911	253360	1.64E-08	4.94
0.03918	256900	1.56E-08	4.95
0.03923	260420	1.57E-08	4.95
0.03929	263940	1.52E-08	4.95
0.03934	267460	1.40E-08	4.96
0.0394	270980	1.28E-08	4.97
0.03947	274420	1.19E-08	4.96
0.03951	277860	1.08E-08	4.97
0.03956	281300	1.06E-08	4.97
0.03961	28474	2.15E-08	4.98
0.03963	288112	2.50E-08	4.98
0.03967	291622	2.55E-08	4.99
0.03971	295062	2.41E-08	5
0.03973	298500	2.07E-08	5
0.03990	301940	1.49E-08	5
0.04004	305380	1.81E-08	5.01
0.0401	308820	1.80E-08	5.01
0.04013	312260	2.09E-08	5.02
0.04018	315700	2.37E-08	5.02
0.04023	319140	2.43E-08	5.03
0.04031	322580	2.48E-08	5.03
0.04039	326020	2.53E-08	5.04
0.04046	329460	2.53E-08	5.05
0.04056	332900	2.40E-08	5.05
0.04067	336340	2.36E-08	5.06
0.04071	339780	2.40E-08	5.06
0.04082	343220	2.31E-08	5.07
0.04089	346660	2.32E-08	5.07
0.04099	350100	2.38E-08	5.08
0.04105	353460	2.83E-08	5.08
0.04113	356820	3.39E-08	5.09
0.04122	360180	3.82E-08	5.1
0.0413	363540	4.18E-08	5.11
0.04136	366900	3.76E-08	5.12

continued in next column

401-5 T=400F R=0.75			
Const. Load (freq=20 cpm)			
a	N	da/dN	ΔK
0.04147	370260	4.03E-08	5.13
0.04166	373620	3.91E-08	5.14
0.04183	376980	3.88E-08	5.15
0.04187	380340	4.02E-08	5.16
0.04209	383700	4.04E-08	5.17
0.04205	387060	3.92E-08	5.16
0.04229	390420	2.92E-08	5.16
0.04249	393780	2.75E-08	5.19
0.04262	397140	2.42E-08	5.2
0.04273	400340	2.31E-08	5.2
0.04281	403650	2.37E-08	5.21
0.04289	406900	2.47E-08	5.21
0.04295	410160	2.53E-08	5.22
0.04304	413400	2.00E-08	5.23
0.04311	416740	2.51E-08	5.22
0.04318	420030	3.27E-08	5.23
0.04329	423300	4.26E-08	5.24
0.04338	426560	4.65E-08	5.25
0.04344	429860	4.92E-08	5.27
0.04357	433140	4.73E-08	5.28
0.04371	436420	3.75E-08	5.29
0.04392	439680	3.45E-08	5.29
0.04408	442960	3.75E-08	5.3
0.04418	446100	4.10E-08	5.31
0.04427	449360	4.27E-08	5.32
0.04434	452500	4.17E-08	5.33
0.0445	455700	4.27E-08	5.34
0.04452	458900	3.85E-08	5.35
0.04483	462100	3.88E-08	5.35
0.04494	465300	3.53E-08	5.36
0.04503	468500	4.04E-08	5.37
0.04512	471700	4.82E-08	5.38
0.04525	474900	5.09E-08	5.39
0.04537	478020	5.56E-08	5.4
0.04547	481140	5.32E-08	5.42
0.04561	484260	5.55E-08	5.43
0.04582	487380	5.69E-08	5.44
0.046	490500	5.95E-08	5.45
0.04618	493620	6.13E-08	5.46
0.04633	496740	6.02E-08	5.48
0.04638	499860	6.28E-08	5.49
0.04672	502980	6.07E-08	5.5
0.04692	506020	6.55E-08	5.51
0.04711	509060	7.05E-08	5.53
0.04729	512100	7.49E-08	5.54
0.04735	515140	7.51E-08	5.56
0.04761	518160	7.06E-08	5.58
0.0473	521220	6.39E-08	5.59
0.04816	524260	6.05E-08	5.6
0.04835	527200	6.07E-08	5.61
0.04833	530180	6.43E-08	5.62
0.04873	533140	7.12E-08	5.64
0.04889	536100	8.21E-08	5.66
0.04905	539060	8.21E-08	5.66
0.04925	542020	8.55E-08	5.69
0.04946	544980	8.65E-08	5.71
0.04974	547860	8.68E-08	5.73
0.04996	550740	9.15E-08	5.74
0.05021	553620	9.76E-08	5.76
0.05046	556500	1.07E-07	5.78
0.05073	559380	1.18E-07	5.8
0.05096	562260	1.27E-07	5.82
0.05123	565060	1.31E-07	5.85
0.05152	567860	1.35E-07	5.87
0.05198	570660	1.38E-07	5.9
0.05228	573460	1.40E-07	5.93
0.0527	576160	1.38E-07	5.96
0.05303	578900	1.37E-07	5.98
0.05336	581620	1.32E-07	6.01
0.05362	584340	1.26E-07	6.03
0.05419	586960	1.24E-07	6.05
0.05454	589620	1.25E-07	6.07
0.05488	592260	1.35E-07	6.09
0.05517	594820	1.43E-07	6.11
0.05543	597380	1.55E-07	6.14
0.0559	599940	1.93E-07	6.17
0.05613	602500	2.03E-07	6.21
0.0565	604960	2.22E-07	6.25
0.05686	607420	2.47E-07	6.29
0.05742	609840	2.83E-07	6.32
0.05782	612420	2.81E-07	6.37
0.05856	614920	2.91E-07	6.42
0.05917	617220	3.03E-07	6.46
0.0598	619540	3.14E-07	6.51
0.06048	621860	3.20E-07	6.56
0.06124	624100	3.27E-07	6.61
0.06182	626340	3.41E-07	6.66
0.06249	628500	3.45E-07	6.71
0.06324	630660	3.43E-07	6.76
0.06386	632740	3.50E-07	6.8
0.06482	634820	3.71E-07	6.85
0.06533	636820	3.94E-07	6.9
0.06606	638740	4.26E-07	6.95
0.06667	640660	4.78E-07	7.01
0.06737	642500	5.41E-07	7.07
0.06807	644140	5.96E-07	7.14
0.06884	645700	6.55E-07	7.22
0.06973	647860	7.22E-07	7.29
0.07064	649540	8.04E-07	7.36
0.07157	651140	8.84E-07	7.47
0.0729	652860	9.83E-07	7.55
0.07302	654180	1.03E-06	7.67
0.07488	655620	1.17E-06	7.78
0.07577	656980	1.25E-06	7.86
0.07783	658260	1.34E-06	7.95
0.07902	659460	1.45E-06	8.06
0.08029	660540	1.59E-06	8.2
0.08187	661620	1.85E-06	8.3
0.08296	662580	2.15E-06	8.42
0.08472	663420	2.62E-06	8.54
0.08553	664260	3.03E-06	8.67
0.08681	664980	3.37E-06	8.81
0.08812	665620	3.53E-06	8.95
0.08983	666180	3.73E-06	9.06
0.09131	666660	3.77E-06	9.15
0.09291	667080	3.84E-06	9.2
0.09395	667380	3.53E-06	9.23

402-7 T=400F R=0.75			
ΔK decreasing (freq=20 cpm)			
a	N	da/dN	ΔK
0.06735	72140	3.18E-07	8.44
0.06761	72671	2.96E-07	8.44
0.06784	73617	2.69E-07	8.39
0.06804	74413	2.49E-07	8.32
0.06825	75243	2.20E-07	8.30
0.06832	76113	2.17E-07	8.29
0.06855	77021	2.28E-07	8.27
0.06877	77975	2.50E-07	8.23
0.06900	78899	2.67E-07	8.20
0.06936	80087	2.58E-07	8.15
0.06971	81241	2.44E-07	8.11
0.06998	82456	2.24E-07	8.07
0.06998

TABLE I-8. FATIGUE CRACK GROWTH DATA FOR Ti-6-2-4-2 AT $R = 0.05$

3 RT R = 0.05 Seg B - K Inc			
a	N	Δ Ka	da/dN
0.03217	2968	14.50	3.05E-03
0.03259	4237	14.63	3.31E-03
0.03297	5488	14.81	3.77E-03
0.03359	7004	15.01	4.32E-03
0.03419	8232	15.21	4.90E-03
0.03462	9152	15.40	5.47E-03
0.03514	10136	15.61	6.16E-03
0.03581	11162	15.83	7.10E-03
0.03648	12024	16.09	8.23E-03
0.03715	12845	16.34	9.53E-03
0.03783	13543	16.61	1.09E-02
0.03855	14181	16.88	1.23E-02
0.03926	14723	17.15	1.43E-02
0.03969	15171	17.41	1.61E-02
0.04056	15585	17.70	1.77E-02
0.04135	15955	17.98	1.94E-02
0.04219	16393	18.34	2.15E-02
0.04315	16933	18.69	2.42E-02
0.04383	17108	19.00	2.72E-02
0.04449	17358	19.29	3.10E-02
0.04523	17589	19.60	3.47E-02
0.04608	17813	19.96	3.88E-02
0.04699	18034	20.32	4.29E-02
0.04773	18204	20.68	4.55E-02
0.04858	18394	21.04	4.90E-02
0.04944	18560	21.42	5.21E-02
0.05030	18722	21.81	5.77E-02
0.05114	18877	22.22	6.23E-02
0.05204	19011	22.62	6.84E-02
0.05295	19124	23.00	7.10E-02
0.05373	19249	23.43	7.74E-02
0.05469	19375	23.88	8.55E-02
0.05559	19478	24.30	9.29E-02
0.05647	19562	24.73	1.01E-01
0.05739	19648	25.18	1.07E-01
0.05935	19739	25.67	1.14E-01
0.05932	19820	26.14	1.23E-01
0.06020	19894	26.61	1.33E-01
0.06110	19961	27.10	1.47E-01
0.06212	20028	27.60	1.64E-01
0.06308	20086	28.13	1.84E-01
0.06404	20135	28.65	2.03E-01
0.06506	20184	29.18	2.26E-01
0.06598	20224	29.72	2.47E-01
0.06693	20261	30.27	2.67E-01
0.06805	20301	30.86	2.98E-01
0.06907	20335	31.45	3.34E-01
0.07006	20368	32.09	3.77E-01
0.07121	20394	32.70	4.20E-01
0.07219	20416	33.33	4.64E-01
0.07328	20438	33.98	5.05E-01
0.07435	20460	34.39	5.57E-01

3 RT R = 0.05 Seg B - Const. Load			
a	N	Δ Ka	da/dN
0.08430	18	37.18	1.08E-04
0.08501	25	37.27	1.05E-04
0.08577	32	37.38	1.04E-04
0.08674	42	37.53	1.04E-04
0.08808	55	37.73	1.10E-04
0.08948	68	37.95	1.20E-04
0.09078	78	38.13	1.25E-04
0.09183	86	38.29	1.40E-04
0.09328	98	38.50	1.50E-04
0.09454	105	38.70	1.56E-04
0.09610	113	38.91	1.66E-04
0.09750	122	39.12	1.76E-04
0.09907	131	39.35	1.90E-04
0.10072	140	39.58	2.05E-04
0.10269	148	39.86	2.38E-04
0.10490	158	40.18	2.71E-04
0.10751	167	40.54	3.11E-04

4 RT R = 0.05 Seg B - K dec			
a	N	Δ Ka	da/dN
0.04044	1874	15.86	7.09E-07
0.04115	2982	15.51	6.65E-07
0.04189	4143	15.19	6.18E-07
0.04269	5824	14.92	5.48E-07
0.04384	7741	14.59	4.95E-07
0.04481	9978	14.27	4.42E-07
0.04591	12514	14.00	3.94E-07
0.04698	14934	13.78	3.45E-07
0.04743	17079	13.47	3.16E-07
0.04828	20289	13.27	2.77E-07
0.04931	24394	13.03	2.50E-07
0.05038	28426	12.78	2.36E-07
0.05130	32900	12.50	2.20E-07
0.05248	38958	12.28	2.01E-07
0.05347	43918	12.03	1.79E-07
0.05458	50000	11.80	1.62E-07
0.05588	57286	11.57	1.45E-07
0.05672	66621	11.36	1.33E-07
0.05779	74796	11.14	1.29E-07
0.05894	84505	10.94	1.15E-07
0.06010	93639	10.73	1.09E-07
0.06122	103892	10.52	1.01E-07
0.06237	117058	10.33	8.73E-08
0.06354	131792	10.14	7.27E-08
0.06466	150079	9.97	6.01E-08
0.06572	173084	9.80	4.90E-08
0.06698	197829	9.62	3.95E-08
0.06812	236800	9.46	2.96E-08
0.06931	293178	9.32	2.05E-08

17 T=600F R = 0.05 Seg B - K dec			
a	N	Δ Ka	da/dN
0.04009	305	17.70	2.10E-05
0.04066	634	17.30	1.63E-05
0.04147	1095	16.97	1.58E-05
0.04222	1658	16.57	1.32E-05
0.04302	2362	16.19	1.11E-05
0.04382	3329	15.87	8.23E-07
0.04473	4042	15.51	8.03E-07
0.04555	5461	15.21	7.18E-07
0.04634	6713	14.89	8.60E-07
0.04725	8227	14.59	6.28E-07
0.04826	9883	14.30	6.06E-07
0.04922	11395	13.99	5.69E-07
0.05013	12908	13.71	5.69E-07
0.05109	14662	13.44	5.38E-07
0.05210	16622	13.18	4.80E-07
0.05314	18838	12.91	4.39E-07
0.05416	21266	12.65	3.69E-07
0.05519	24491	12.40	3.38E-07
0.05631	28385	12.19	2.94E-07
0.05735	32014	11.92	2.61E-07
0.05849	35985	11.70	2.34E-07
0.05948	41700	11.48	2.04E-07
0.06058	48317	11.30	1.81E-07
0.06164	53945	11.07	1.66E-07
0.06280	60574	10.87	1.56E-07
0.06400	66963	10.69	1.40E-07
0.06512	77577	10.48	1.20E-07
0.06627	89036	10.28	9.87E-08
0.06752	104036	10.10	7.68E-08
0.06877	123479	9.91	6.25E-08
0.07006	152330	9.75	4.83E-08
0.07125	175819	9.57	4.02E-08
0.07228	214325	9.39	3.16E-08
0.07376	264630	9.27	2.70E-08

17 T=600F R = 0.05 Seg C - K Inc			
a	N	Δ Ka	da/dN
0.07705	5459	12.70	2.09E-07
0.07779	6611	12.92	2.61E-07
0.07850	11229	13.15	3.35E-07
0.07928	13454	13.39	4.26E-07
0.07999	15192	13.64	5.35E-07
0.08071	16479	13.88	6.46E-07
0.08147	17510	14.13	7.55E-07
0.08223	18516	14.41	8.65E-07
0.08301	19389	14.67	1.02E-06
0.08373	20082	14.94	1.13E-06
0.08445	20634	15.21	1.24E-06
0.08517	21187	15.48	1.37E-06
0.08589	21736	15.77	1.52E-06
0.08667	22235	16.05	1.75E-06
0.08739	22627	16.34	1.87E-06
0.08805	22934	16.65	2.17E-06
0.08883	23315	16.94	2.36E-06
0.08958	23590	17.26	2.53E-06
0.09059	23934	17.57	2.71E-06
0.09107	24169	17.89	2.89E-06
0.09176	24392	18.21	3.04E-06
0.09247	24621	18.54	3.29E-06

17 T=600F R = 0.05 Seg D - Const. Load			
a	N	Δ Ka	da/dN
#######	229	21.34	4.40E-06
#######	398	21.48	4.62E-06
0.10024	581	21.64	4.55E-06
0.10103	699	21.78	4.56E-06
0.10169	861	21.93	4.62E-06
0.10242	1037	22.10	4.66E-06
0.10311	1174	22.23	4.78E-06
0.10376	1310	22.37	5.02E-06
0.1045	1459	22.54	5.24E-06
0.10524	1589	22.70	5.31E-06
0.10603	1732	22.87	5.30E-06
0.10689	1856	23.02	5.23E-06
0.10794	1964	23.17	5.12E-06
0.10907	2131	23.34	5.09E-06
0.10972	2266	23.50	5.17E-06
0.10945	2404	23.67	5.34E-06
0.11011	2528	23.83	5.53E-06
0.11083	2652	24.00	5.81E-06
0.11152	2771	24.17	6.03E-06
0.11216	2882	24.34	6.32E-06
0.11288	2985	24.51	6.72E-06
0.11347	3078	24.67	6.96E-06
0.11417	3173	24.85	7.09E-06
0.11491	3264	25.03	7.12E-06
0.11551	3355	25.19	7.87E-06
0.11618	3450	25.39	8.34E-06
0.11685	3549	25.61	8.13E-06
0.11791	3610	25.81	7.97E-06
0.11823	3872	25.93	8.02E-06
0.11877	3769	26.12	7.51E-06
0.11940	3863	26.29	7.11E-06
0.12009	3949	26.48	7.87E-06
0.12074	4027	26.67	7.96E-06
0.12135	4103	26.86	8.13E-06
0.12203	4183	27.06	8.37E-06
0.12259	4257	27.24	8.58E-06
0.12314	4322	27.41	8.76E-06
0.12387	4397	27.63	9.03E-06
0.12444	4459	27.82	9.25E-06
0.125	4521	28.00	9.40E-06
0.12558	4584	28.19	8.56E-06
0.12622	4650	28.40	9.79E-06
0.1259	4719	28.63	1.01E-05
0.12751	4775	28.84	1.05E-05
0.12801	4827	29.02	1.08E-05
0.12868	4885	29.25	1.11E-05
0.12927	4937	29.46	1.15E-05
0.12985	4988	29.67	1.20E-05
0.13041	5036	29.86	1.23E-05
0.13098	5080	30.09	1.25E-05
0.13154	5121	30.29	1.27E-05
0.13211	5167	30.52	1.29E-05
0.1327	5213	30.74	1.30E-05
0.13323	5255	30.95	1.30E-05
0.13377	5296	31.17	1.34E-05
0.13434	5337	31.39	1.36E-05
0.13485	5376	31.61	1.45E-05
0.13538	5412	31.83	1.53E-05
0.13589	5445	32.04	1.58E-05
0.13643	5477	32.27	1.67E-05
0.13698	5508	32.50	1.77E-05
0.13747	5538	32.73	1.83E-05
0.13797	5566	32.95	1.88E-05
0.13852	5589	33.17	1.99E-05
0.13893	5614	33.39	1.91E-05
0.13946	5640	33.61	2.06E-05
0.13993	5668	33.83	2.22E-05
0.14048	5698	34.13	2.50E-05
0.14171	5732	34.67	2.45E-05
0.14198	5742	34.81	2.30E-05
0.14252	5759	35.00	2.32E-05
0.14279	5785	35.23	1.92E-05
0.14324	5815	35.49	2.06E-05
0.14368	5835	35.71	2.17E-05
0.1442	5854	35.97	2.38E-05
0.14461	5872	36.19	2.24E-05

5 1000F R = 0.05 Seg C - K dec			
a	N	Δ Ka	da/dN
0.07272	1420	9.95	6.85E-07
0.07282	2539	9.73	5.76E-07
0.07351	3827	9.52	5.14E-07
0.07421	5226	9.3	4.75E-07
0.07486	6634	9.1	4.40E-07
0.07577	8901	8.81	4.03E-07
0.07662	11109	9.72	3.70E-07
0.07746	13525	8.54	3.42E-07
0.07833	16245	8.37	3.14E-07
0.07927	19099	8.2	2.93E-07
0.08023	21948	8.03	2.84E-07
0.08126	27105	7.87	2.39E-07
0.08227	31696	7.71	2.18E-07
0.08329	36594	7.56	1.99E-07
0.08439	42249	7.42	1.75E-07
0.08538	49006	7.28	1.56E-07
0.08654	57243	7.14	1.39E-07
0.08766	66100	7.01	1.22E-07
0.08879	76075	6.88	1.06E-07
0.08996	88025	6.75	9.49E-08
0.09118	102315	6.63	8.06E-08
0.09235	118729	6.51	6.90E-08

7 1000F R = 0.05 Seg C - K Inc			
a	N	Δ Ka	da/dN
0.09630	578	10.1	7.53E-07
0.09656	1067	10.3	6.76E-07
0.09704	1725	10.4	6.84E-07
0.09755	2514	10.5	7.32E-07
0.09832	3126	10.7	7.73E-07
0.09853	3784	10.9	8.57E-07
0.09926	4523	11	9.03E-07
0.09975	5132	11.2	1.01E-06
0.09944	5708	11.4	1.09E-06
0.06101	6278	11.6	1.19E-06
0.06170	6810	11.8	1.31E-06
0.06228	7252	11.9	1.41E-06
0.06296	7713	12.1	1.53E-06
0.06354	8155	12.3	1.65E-06
0.06436	8559	12.6	1.78E-06
0.06534	8953	12.8	1.84E-06
0.06578	9314	13	2.10E-06
0.06766	9629	13.2	2.27E-06
0.06879	76075	6.68	1.06E-07
0.06716	9925	13.4	2.50E-06
0.06788	10226	13.6	2.72E-06
0.06858	10500	13.9	2.90E-06
0.06948	10738	14.1	3.01E-06
0.07015	10969	14.4	3.12E-06
0.07095	11274	14.6	3.22E-06
0.07175	11478	14.8	3.36E-06
0.07248	11700	15.1	3.64E-06
0.07328	11902	15.4	3.93E-06
0.07403	12096	15.7	4.26E-06
0.07494	12278	15.9	4.60E-06
0.07564	12445	16.2	4.93E-06
0.07641	12598	16.5	5.27E-06
0.07721	12748	16.8	5.84E-06
0.07800	12884	17.1	6.02E-06
0.07880	13014	17.4	6.45E-06
0.07982	13138	17.7	7.00E-06
0.06044	12255	18	7.59E-06
0.08128	13380	18.3	8.14E-06
0.06208	13455	18.6	8.66E-06
0.06291	13546	18.8	9.44E-06
0.06366	13629	19.1	1.03E-05
0.08440	13704	19.4	1.11E-05
0.08527	13771	19.7	1.17E-05
0.06602	13803	20	1.24E-05
0.08690	13904	20.4	1.30E-05
0.08788	13984	20.7	1.35E-05
0.08852	14025	21	1.43E-05
0.08933	14081	21.4	1.52E-05
0.09006	14130	21.7	1.65E-05
0.09002	14174	22	1.76E-05
0.09159	14216	22.4	1.92E-05
0.09245	14262	22.7	2.11E-05
0.09319	14295	23.1	2.28E-05
0.06397	14328	23.4	2.51E-05
0.08477	14360	23.8	2.82E-05
0.09560	14389	24.2	3.19E-05
0.09633	14411	24.5	3.57E-05
0.09706	14431	24.9	3.97E-05
0.09784	14450	25.3	4.38E-05
0.09839	14469	25.7	4.40E-05
0.09943	14483	26.1	4.65E-05
0.10008	14498	26.6	5.32E-05
0.10159	14531	27.2	9.73E-05
0.10257	14540	27.8	1.48E-04
0.10358	14547	28.5	1.86E-04

TABLE I-9. FATIGUE CRACK GROWTH DATA FOR Ti-6-2-4-2 AT $R = 0.5$

11	RT	R=0.5		16	T=600F	R=0.5		16	T=600F	R=0.5		10	T=1000F	R=0.5	
	Segm.B - K inc				Segm. B - K inc				Segm. C - Const. Load				Segm. B - K inc		
a	N	ΔKa	da/dN	a	N	ΔKa	da/dN	a	N	ΔKa	da/dN	a	N	ΔKa	da/dN
0.03346	4745	7.69	1.36E-07	0.04976	36192	8.38	8.82E-08	0.08083	1101	15.84	4.66E-06	0.04737	1737	7.63	6.79E-07
0.03413	9641	7.75	1.50E-07	0.05032	42002	8.51	1.00E-07	0.08157	1250	15.93	4.57E-06	0.04796	2753	7.76	6.63E-07
0.03486	14119	7.83	1.61E-07	0.05082	46843	8.64	1.13E-07	0.08231	1413	16.03	4.52E-06	0.04844	3463	7.86	7.09E-07
0.03555	18233	7.90	1.65E-07	0.05137	51455	8.80	1.26E-07	0.08302	1575	16.13	4.48E-06	0.04887	4095	7.96	7.52E-07
0.03605	21002	7.96	1.68E-07	0.05188	55376	8.91	1.36E-07	0.08373	1731	16.22	4.44E-06	0.04938	4713	8.06	8.12E-07
0.03652	23891	8.02	1.69E-07	0.05242	59066	9.03	1.47E-07	0.08445	1900	16.31	4.52E-06	0.04987	5316	8.17	8.92E-07
0.03720	28122	8.10	1.67E-07	0.05297	62753	9.15	1.59E-07	0.08514	2056	16.41	4.65E-06	0.05034	5841	8.27	9.90E-07
0.03797	32445	8.18	1.68E-07	0.05353	66255	9.27	1.75E-07	0.08581	2199	16.50	4.79E-06	0.05077	6283	8.38	1.09E-06
0.03870	36916	8.27	1.76E-07	0.05408	69545	9.40	1.99E-07	0.08660	2355	16.60	5.04E-06	0.05123	6674	8.48	1.23E-06
0.03940	41393	8.36	1.87E-07	0.05469	72511	9.53	2.30E-07	0.08732	2498	16.70	5.29E-06	0.05169	7038	8.58	1.37E-06
0.04017	45268	8.45	1.95E-07	0.05527	74908	9.66	2.62E-07	0.08810	2649	16.80	5.57E-06	0.05211	7345	8.69	1.50E-06
0.04094	48696	8.55	2.03E-07	0.05584	77007	9.79	2.96E-07	0.08885	2775	16.90	5.87E-06	0.05253	7590	8.79	1.59E-06
0.04176	52571	8.65	2.14E-07	0.05644	78892	9.93	3.35E-07	0.08949	2883	16.99	6.19E-06	0.05292	7842	8.91	1.77E-06
0.04257	56595	8.76	2.25E-07	0.05702	80658	10.07	3.79E-07	0.09024	3004	17.09	6.49E-06	0.05340	8106	9.01	2.02E-06
0.04335	60172	8.87	2.42E-07	0.05764	82262	10.21	4.25E-07	0.09097	3113	17.19	6.63E-06	0.05380	8334	9.14	2.35E-06
0.04415	63451	8.97	2.62E-07	0.05825	83553	10.35	4.65E-07	0.09173	3218	17.29	6.74E-06	0.05428	8507	9.25	2.66E-06
0.04497	66432	9.09	2.78E-07	0.05886	84823	10.50	5.11E-07	0.09243	3322	17.39	6.93E-06	0.05469	8655	9.37	3.16E-06
0.04577	68964	9.19	2.92E-07	0.05949	86033	10.65	5.59E-07	0.09316	3434	17.50	7.07E-06	0.05508	8780	9.49	3.71E-06
0.04656	71702	9.31	3.05E-07	0.06012	87157	10.80	6.03E-07	0.09387	3538	17.60	7.20E-06	0.05543	8891	9.61	4.40E-06
0.04738	74440	9.43	3.22E-07	0.06079	88219	10.96	6.59E-07	0.09463	3631	17.70	7.40E-06	0.05590	8975	9.73	5.28E-06
0.04822	77059	9.55	3.46E-07	0.06143	89136	11.11	7.15E-07	0.09536	3731	17.80	7.66E-06	0.05627	9046	9.86	6.04E-06
0.04908	79559	9.68	3.83E-07	0.06200	89973	11.27	7.75E-07	0.09611	3831	17.91	8.13E-06	0.05665	9113	9.98	7.02E-06
0.04993	81677	9.80	4.23E-07	0.06270	90820	11.43	8.59E-07	0.09678	3915	18.01	8.53E-06	0.05703	9154	10.1	7.84E-06
0.05074	83579	9.93	4.58E-07	0.06336	91586	11.60	9.55E-07	0.09745	3995	18.10	9.05E-06	0.05728	9196	10.2	9.18E-06
0.05159	85282	10.06	4.97E-07	0.06398	92231	11.77	1.03E-06	0.09825	4071	18.21	9.61E-06	0.05772	9240	10.3	1.11E-05
0.05247	86979	10.19	5.42E-07	0.06464	92811	11.93	1.11E-06	0.09893	4146	18.32	1.01E-05	0.05804	9271	10.5	1.44E-05
0.05334	88678	10.34	5.94E-07	0.06532	93384	12.10	1.20E-06	0.09969	4219	18.43	1.05E-05	0.05841	9294	10.6	2.66E-05
0.05427	90149	10.48	6.45E-07	0.06597	93960	12.29	1.27E-06	0.10040	4283	18.53	1.10E-05	0.05866	9310	10.7	3.78E-05
0.05511	91377	10.61	6.97E-07	0.06668	94484	12.47	1.36E-06	0.10109	4346	18.63	1.17E-05	0.05909	9326	11.1	7.51E-05
0.05598	92601	10.76	7.54E-07	0.06735	94958	12.64	1.48E-06	0.10183	4413	18.75	1.21E-05				
0.05686	93762	10.91	8.13E-07	0.06797	95413	12.83	1.64E-06	0.10257	4466	18.85	1.23E-05				
0.05778	94852	11.06	8.81E-07	0.06868	95821	13.01	1.80E-06	0.10322	4515	18.94	1.26E-05				
0.05866	95836	11.21	9.59E-07	0.06935	96178	13.21	1.97E-06	0.10389	4572	19.05	1.27E-05				
0.05954	96731	11.36	1.06E-06	0.07007	96516	13.40	2.14E-06	0.10467	4635	19.17	1.27E-05				
0.06046	97593	11.52	1.19E-06	0.07072	96820	13.59	2.31E-06	0.10544	4695	19.29	1.28E-05				
0.06138	98376	11.69	1.37E-06	0.07141	97109	13.79	2.53E-06	0.10611	4746	19.39	1.32E-05				
0.06231	99015	11.85	1.57E-06	0.07208	97387	13.99	2.77E-06	0.10683	4801	19.50	1.37E-05				
0.06314	99550	12.01	1.78E-06	0.07282	97636	14.20	3.01E-06	0.10760	4858	19.62	1.44E-05				
0.06409	100037	12.18	1.96E-06	0.07349	97838	14.40	3.23E-06	0.10829	4907	19.73	1.51E-05				
0.06501	100485	12.35	2.13E-06	0.07414	98042	14.60	3.44E-06	0.10908	4954	19.85	1.61E-05				
0.06596	100906	12.53	2.31E-06	0.07484	98245	14.82	3.69E-06	0.10975	4995	19.96	1.73E-05				
0.06682	101283	12.71	2.46E-06					0.11039	5035	20.07	1.85E-05				
0.06780	101675	12.89	2.64E-06					0.11115	5074	20.19	1.96E-05				
0.06874	102016	13.07	2.94E-06					0.11188	5106	20.30	2.10E-05				
0.06963	102318	13.25	3.22E-06					0.11255	5140	20.42	2.28E-05				
0.07053	102623	13.45	3.55E-06					0.11325	5173	20.54	2.37E-05				
0.07162	102863	13.64	3.81E-06					0.11397	5200	20.65	2.46E-05				
0.07247	103101	13.85	4.09E-06					0.11474	5227	20.77	2.53E-05				
0.07351	103345	14.04	4.39E-06					0.11537	5256	20.89	57E-05				
0.07437	103544	14.24	4.64E-06					0.11612	5283	21.0	0E-05				
0.07528	103732	14.44	4.98E-06					0.11674	5308	21.1	E-05				
0.07629	103931	14.65	5.43E-06					0.11742	5334	21.2	4E-05				
0.07728	104108	14.87	6.02E-06					0.11811	5358	21.36	3.21E-05				
0.07816	104260	15.09	6.66E-06					0.11878	5381	21.48	3.91E-05				
0.07916	104408	15.31	7.33E-06					0.11956	5402	21.63	5.37E-05				
0.08020	104537	15.53	7.96E-06					0.12036	5416	21.77	7.80E-05				
0.08105	104636	15.74	8.47E-06					0.12098	5425	21.89	1.08E-04				
0.08190	104739	15.96	8.70E-06					0.12179	5432	22.03	1.31E-04				
								0.12265	5437	22.17	1.52E-04				
								0.12350	5442	22.33	1.52E-04				

TABLE I-10. FATIGUE CRACK GROWTH DATA FOR Ti-6-2-4-2 AT $R = 0.75$

Spec. ID: 2 RT R=0.75
Segm. D - K dec

a	N	ΔK	da/dN
0.06450	22418	6.28	6.28E-08
0.06603	69163	6.17	3.66E-08
0.06810	138800	6.08	3.16E-08
0.07019	225663	5.98	3.03E-08
0.07260	291901	5.90	3.35E-08

5 RT R=0.75
Segm. B - Const. Load

a	N	ΔK	da/dN
0.04814	19936	7.27	7.00E-08
0.04892	29802	7.33	8.55E-08
0.04969	37709	7.40	8.82E-08
0.05053	46300	7.46	9.30E-08
0.05146	55466	7.53	9.38E-08
0.05230	65594	7.60	9.72E-08
0.05324	75412	7.68	1.03E-07
0.05415	85956	7.76	1.09E-07
0.05539	93930	7.84	1.10E-07
0.05616	100636	7.89	1.13E-07
0.05722	110734	7.98	1.16E-07
0.05825	120928	8.06	1.17E-07
0.05935	129946	8.14	1.27E-07
0.06045	138197	8.22	1.41E-07
0.06160	146448	8.31	1.59E-07
0.06277	153574	8.39	1.77E-07
0.06395	159886	8.48	1.98E-07
0.06518	165907	8.57	2.26E-07
0.06636	171268	8.66	2.65E-07
0.06771	176330	8.76	3.17E-07
0.06894	180188	8.85	3.85E-07
0.07042	183744	8.95	4.14E-07
0.07157	186346	9.03	4.57E-07
0.07285	189248	9.13	5.05E-07
0.07423	191895	9.23	5.44E-07
0.07570	194324	9.33	5.78E-07
0.07717	196746	9.43	6.14E-07
0.07865	199151	9.54	6.51E-07
0.08015	201529	9.65	7.03E-07
0.08168	203712	9.77	7.65E-07
0.08328	205720	9.88	8.18E-07
0.08488	207476	9.99	8.70E-07
0.08649	209265	10.11	9.32E-07
0.08805	211051	10.23	1.04E-06
0.08978	212749	10.36	1.27E-06
0.09152	214270	10.51	1.54E-06
0.09317	215194	10.62	1.59E-06
0.09486	215848	10.72	1.68E-06
0.09666	216996	10.87	1.77E-06
0.09847	218208	11.02	1.82E-06
0.10033	219264	11.16	2.01E-06
0.10224	220210	11.31	2.31E-06
0.10430	221035	11.47	2.67E-06
0.10622	221740	11.62	3.03E-06
0.10840	222436	11.79	3.52E-06
0.11068	223065	11.97	4.16E-06
0.11269	223557	12.14	4.96E-06
0.11480	223969	12.31	5.94E-06
0.11687	224314	12.47	7.20E-06
0.11904	224603	12.65	8.88E-06
0.12124	224857	12.83	1.12E-05
0.12357	225084	13.02	1.39E-05
0.12620	225244	13.23	2.28E-05
0.12902	225399	13.46	3.51E-05
0.13139	225507	13.65	7.88E-05

4 RT R=0.75
Segm. E - K dec

a	N	ΔK	da/dN
0.10204	2007	9.07	3.32E-07
0.10309	6279	8.96	2.51E-07
0.10410	11593	8.79	2.00E-07
0.10511	17425	8.62	1.72E-07
0.10609	23897	8.46	1.52E-07
0.10711	30733	8.31	1.37E-07
0.10806	37949	8.15	1.22E-07
0.10908	47504	8.01	1.06E-07
0.11007	58547	7.86	9.09E-08
0.11110	70983	7.73	7.92E-08
0.11210	85124	7.59	7.01E-08
0.11310	100110	7.45	6.31E-08
0.11411	116699	7.32	5.65E-08
0.11519	138571	7.20	5.07E-08
0.11613	158273	7.06	4.61E-08
0.11714	180896	6.96	4.21E-08
0.11802	206231	6.83	3.79E-08
0.11905	233565	6.73	3.41E-08
0.12008	264551	6.60	3.11E-08

13 T=600F R=0.75
Segm. B - K dec

a	N	ΔK	da/dN
0.09099	3219	7.49	4.22E-07
0.09150	4243	7.52	4.39E-07
0.09211	5533	7.56	5.05E-07
0.09284	6823	7.61	5.92E-07
0.09357	8032	7.66	6.45E-07
0.09431	9152	7.71	6.99E-07
0.09513	10186	7.76	7.50E-07
0.09603	11420	7.82	8.13E-07
0.09700	12580	7.89	8.60E-07
0.09788	13539	7.94	8.92E-07
0.09884	14557	8.01	9.39E-07
0.09983	15645	8.09	9.86E-07
0.10087	16692	8.15	1.05E-06
0.10195	17700	8.23	1.12E-06
0.10309	18707	8.31	1.22E-06
0.10417	19554	8.39	1.32E-06
0.10525	20392	8.48	1.44E-06
0.10654	21229	8.57	1.58E-06
0.10763	21918	8.66	1.70E-06
0.10884	22599	8.75	1.85E-06
0.11012	23246	8.85	2.01E-06
0.11130	23864	8.95	2.18E-06
0.11256	24419	9.05	2.33E-06
0.11385	24919	9.15	2.61E-06
0.11509	25426	9.27	2.93E-06
0.11636	25897	9.39	3.34E-06
0.11784	26248	9.50	3.72E-06
0.11903	26590	9.62	4.07E-06
0.12049	26924	9.76	4.28E-06
0.12180	27200	9.87	4.40E-06
0.12316	27500	10.00	4.88E-06
0.12452	27828	10.15	9.82E-06
0.12596	28116	10.36	1.98E-05
0.12754	28278	10.46	1.24E-04

8 T=1000F R=0.75
Segm. C - K dec

a	N	ΔK	da/dN
0.05150	2320	4.03	4.53E-07
0.05193	3645	3.94	3.39E-07
0.05245	5579	3.84	2.61E-07
0.05302	8188	3.75	2.11E-07
0.05355	11471	3.67	1.77E-07
0.05408	14599	3.57	1.54E-07
0.05471	18875	3.49	1.31E-07
0.05530	24651	3.41	1.11E-07
0.05588	30434	3.33	9.30E-08
0.05653	37907	3.25	7.69E-08
0.05715	48931	3.17	6.31E-08
0.05786	61671	3.11	5.29E-08
0.05842	74098	3.03	4.61E-08
0.05912	89995	2.96	4.09E-08

8 T=1000F R=0.75
Segm. D - K inc

a	N	ΔK	da/dN
0.06086	1529	4.36	4.80E-07
0.06132	2657	4.43	4.63E-07
0.06180	3705	4.49	4.80E-07
0.06228	4209	4.54	4.95E-07
0.06267	5391	4.62	5.28E-07
0.06352	7042	4.69	6.04E-07
0.06420	8041	4.77	6.69E-07
0.06479	8896	4.85	7.29E-07
0.06547	9750	4.92	7.95E-07
0.06614	10605	5.00	8.59E-07
0.06684	11431	5.08	9.42E-07
0.06761	12200	5.16	1.04E-06
0.06836	12912	5.24	1.17E-06
0.06914	13566	5.32	1.33E-06
0.06987	14136	5.40	1.52E-06
0.07070	14638	5.49	1.96E-06
0.07152	15106	5.57	2.69E-06
0.07224	15443	5.67	3.59E-06
0.07331	15630	5.74	4.07E-06
0.07404	15792	5.83	4.40E-06
0.07490	15981	5.91	4.95E-06
0.07569	16163	6.00	5.39E-06
0.07655	16328	6.09	6.44E-06
0.07756	16475	6.17	8.08E-06
0.07850	16599	6.27	1.05E-05
0.07951	16691	6.36	1.41E-05
0.08040	16755	6.46	1.90E-05
0.08149	16813	6.55	2.62E-05
0.08257	16855	6.65	3.52E-05
0.08376	16883	6.74	4.74E-05
0.08481	16907	6.77	6.38E-05
0.08571	16923	6.78	8.94E-05
0.08691	16934	6.80	1.15E-04
0.08809	16946	6.79	1.77E-04

9 T=1000F R=0.75
Segm. B - K inc

a	N	ΔK	da/dN
0.04362	5724	3.77	2.56E-07
0.04422	8208	3.83	2.78E-07
0.04476	9814	3.88	2.95E-07
0.04508	10841	3.93	3.01E-07
0.04562	12676	3.99	3.15E-07
0.04627	14633	4.05	3.30E-07
0.04667	16025	4.11	3.59E-07
0.04730	17900	4.18	4.09E-07
0.04806	19585	4.25	4.82E-07
0.04857	20484	4.31	5.29E-07
0.04893	21269	4.36	5.96E-07
0.04957	22330	4.43	6.66E-07
0.05021	23295	4.50	7.98E-07
0.05082	23874	4.56	8.71E-07
0.05135	24521	4.63	9.92E-07
0.05198	25157	4.70	1.17E-06
0.05248	25629	4.78	1.32E-06
0.05328	26187	4.86	1.64E-06
0.05396	26553	4.94	1.89E-06
0.05454	26897	5.03	2.19E-06
0.05540	27246	5.07	2.59E-06
0.05587	27429	5.14	2.92E-06
0.05650	27639	5.20	3.39E-06
0.05717	27841	5.26	3.94E-06
0.05783	27995	5.33	4.66E-06
0.05843	28118	5.39	5.45E-06
0.05895	28224	5.46	6.49E-06
0.05973	28336	5.52	8.41E-06
0.06035	28414	5.59	1.12E-05
0.06096	28469	5.66	1.54E-05
0.06163	28513	5.73	2.23E-05
0.06235	28549	5.81	4.08E-05
0.06311	28565	5.88	7.29E-05
0.06359	28573	6.00	8.90E-05

TABLE I-11. FATIGUE CRACK GROWTH DATA FOR Ti-17 AT $R = 0$

KbA RT R=0 Const. Load			
a	N	da/dN	ΔK
0.01821	320	5.90E-07	12.97
0.01828	640	6.75E-07	13.05
0.01835	960	7.39E-07	13.14
0.01863	1280	7.67E-07	13.22
0.01886	1600	8.08E-07	13.31
0.01906	1920	8.69E-07	13.40
0.01928	2240	9.18E-07	13.51
0.01954	2560	9.68E-07	13.63
0.01982	2880	1.00E-06	13.74
0.02013	3200	1.04E-06	13.85
0.02039	3520	1.09E-06	13.97
0.02073	3840	1.14E-06	14.09
0.02104	4160	1.17E-06	14.21
0.02141	4480	1.21E-06	14.34
0.02174	4800	1.24E-06	14.47
0.02210	5120	1.26E-06	14.61
0.02250	5440	1.29E-06	14.74
0.02292	5760	1.34E-06	14.87
0.02327	6080	1.42E-06	15.01
0.02373	6400	1.48E-06	15.16
0.02410	6720	1.56E-06	15.31
0.02452	7040	1.63E-06	15.46
0.02498	7360	1.70E-06	15.61
0.02547	7680	1.73E-06	15.76
0.02595	7960	1.79E-06	15.93
0.02642	8260	1.84E-06	16.10
0.02695	8580	1.87E-06	16.27
0.02749	8900	1.92E-06	16.44
0.02805	9160	1.91E-06	16.62
0.02856	9460	2.01E-06	16.79
0.02917	9760	2.10E-06	16.97
0.02973	10060	2.19E-06	17.14
0.03033	10360	2.23E-06	17.33
0.03095	10660	2.37E-06	17.51
0.03139	10940	2.49E-06	17.71
0.03218	11220	2.51E-06	17.90
0.03283	11500	2.58E-06	18.10
0.03349	11780	2.65E-06	18.31
0.03404	12060	2.72E-06	18.53
0.03495	12340	2.73E-06	18.72
0.03565	12620	2.83E-06	18.91
0.03637	12900	2.94E-06	19.12
0.03706	13180	3.09E-06	19.33
0.03779	13420	3.26E-06	19.55
0.03853	13680	3.48E-06	19.76
0.03931	13940	3.74E-06	20.01
0.04012	14200	4.03E-06	20.26
0.04095	14460	4.31E-06	20.53
0.04184	14700	4.48E-06	20.81
0.04275	14940	4.66E-06	21.10
0.04374	15180	4.73E-06	21.38
0.04484	15420	4.80E-06	21.66
0.04600	15660	4.96E-06	21.93
0.04703	15880	5.22E-06	22.20
0.04803	16100	5.59E-06	22.51
0.04914	16320	5.93E-06	22.80
0.05016	16540	6.33E-06	23.12
0.05131	16760	6.65E-06	23.46
0.05250	16980	6.92E-06	23.80
0.05372	17160	7.30E-06	24.14
0.05505	17360	7.69E-06	24.48
0.05640	17560	8.17E-06	24.84
0.05769	17740	8.63E-06	25.18
0.05897	17920	9.02E-06	25.56
0.06033	18100	9.20E-06	25.96
0.06178	18260	9.18E-06	26.30
0.06315	18420	9.12E-06	26.65
0.06466	18580	9.09E-06	26.99
0.06604	18720	9.30E-06	27.31
0.06731	18860	9.58E-06	27.60
0.06855	19000	9.95E-06	27.92
0.06978	19140	1.02E-05	28.27
0.07083	19260	1.02E-05	28.61
0.07204	19380	1.00E-05	28.89
0.07333	19500	9.85E-06	29.17
0.07455	19620	1.04E-05	29.42
0.07564	19720	1.12E-05	29.71
0.07653	19820	1.24E-05	30.04
0.07752	19920	1.37E-05	30.34
0.07849	20020	1.48E-05	30.67
0.07946	20120	1.59E-05	31.04
0.08083	20200	1.65E-05	31.31
0.08185	20280	1.74E-05	31.63
0.08304	20360	1.83E-05	31.95
0.08410	20420	2.02E-05	32.27
0.08505	20480	2.25E-05	32.65
0.08616	20540	2.38E-05	32.95
0.08725	20600	2.50E-05	33.27
0.08839	20660	2.64E-05	33.60
0.08927	20700	2.62E-05	33.97
0.09050	20740	2.63E-05	34.11
0.09151	20780	2.68E-05	34.31
0.09247	20820	2.72E-05	34.48
0.09314	20840	2.72E-05	34.67
0.09358	20860	2.78E-05	34.84

SENBH-20P RT R=0 ΔK decreasing			
a	N	da/dN	ΔK
0.04445	29268	2.00E-06	15.67
0.04595	30195	1.74E-06	14.93
0.04766	31334	1.48E-06	14.50
0.04942	32684	1.32E-06	14.06
0.05133	34259	1.21E-06	13.61
0.05340	36061	1.11E-06	13.12
0.05562	38101	1.03E-06	12.62
0.05772	40360	9.38E-07	12.15
0.06003	42848	8.42E-07	11.65
0.06211	45534	7.48E-07	11.23
0.06407	48398	6.61E-07	10.84
0.06587	51423	5.77E-07	10.49
0.06756	54594	5.09E-07	10.17
0.06907	57889	4.58E-07	9.89
0.07047	61297	4.16E-07	9.65
0.07181	64813	3.80E-07	9.40
0.07328	68435	3.50E-07	9.16
0.07444	72148	3.24E-07	8.95
0.07566	75939	2.97E-07	8.76
0.07665	79809	2.69E-07	8.60
0.07773	83755	2.49E-07	8.42
0.07866	87765	2.29E-07	8.28
0.07949	91832	2.11E-07	8.15
0.08033	95952	1.96E-07	8.03
0.08111	100124	1.90E-07	7.92
0.08187	104343	1.79E-07	7.81
0.08261	108609	1.66E-07	7.69
0.08348	112930	1.54E-07	7.62
0.08395	117280	1.43E-07	7.50
0.08450	121663	1.33E-07	7.43
0.08510	126083	1.26E-07	7.35
0.08566	130535	1.26E-07	7.28
0.08622	135021	1.26E-07	7.20
0.08679	139539	1.25E-07	7.13
0.08729	144086	1.25E-07	7.06
0.08794	148668	1.23E-07	6.99
0.08851	153285	1.19E-07	6.91
0.08908	157933	1.09E-07	6.83
0.08956	162610	9.68E-08	6.77
0.09006	167312	8.89E-08	6.71
0.09028	172027	8.36E-08	6.66
0.09066	176764	7.87E-08	6.62
0.09111	181522	7.33E-08	6.58
0.09153	186304	7.06E-08	6.51
0.09178	191098	6.41E-08	6.49
0.09202	195904	5.81E-08	6.47
0.09229	200724	5.20E-08	6.43
0.09258	205559	5.07E-08	6.39
0.09277	210404	4.83E-08	6.36
0.09303	215263	4.52E-08	6.34
0.09324	220132	4.30E-08	6.32
0.09342	225007	4.15E-08	6.31
0.09363	229897	4.00E-08	6.28
0.09383	234795	4.31E-08	6.26
0.09399	239703	4.45E-08	6.23
0.09422	244623	4.47E-08	6.22
0.09455	249556	4.46E-08	6.18
0.09471	254502	4.34E-08	6.15
0.09491	259454	4.06E-08	6.13
0.09513	264419	3.67E-08	6.12
0.09528	269388	3.37E-08	6.09
0.09548	274368	3.03E-08	6.08
0.09562	279363	2.95E-08	6.05
0.09568	284358	3.35E-08	6.06
0.09583	289353	3.15E-08	6.04

SENBH-20P RT R=0 ΔK increasing			
a	N	da/dN	ΔK
0.10608	11530	3.61E-07	10.92
0.10625	11890	3.93E-07	10.97
0.10645	12250	4.60E-07	11.00
0.10662	12610	4.94E-07	11.05
0.10679	12970	4.98E-07	11.12
0.10702	13330	4.70E-07	11.17
0.10712	13690	4.63E-07	11.19
0.10736	14050	4.81E-07	11.27
0.10744	14410	5.17E-07	11.31
0.10763	14770	5.90E-07	11.34
0.10789	15130	6.37E-07	11.41
0.10815	15490	6.84E-07	11.49
0.10842	15850	7.16E-07	11.56
0.10867	16210	7.42E-07	11.63
0.10887	16570	7.13E-07	11.70
0.10921	16930	5.97E-07	11.78
0.10953	17290	5.41E-07	11.86
0.10963	17650	5.43E-07	11.93
0.10997	18010	5.92E-07	11.94
0.10986	18370	6.86E-07	11.98
0.11024	18730	6.40E-07	12.06
0.11065	19090	9.82E-07	12.19
0.11093	19450	1.02E-06	12.28
0.11128	19810	1.06E-06	12.36
0.11170	20170	1.14E-06	12.47
0.11212	20530	1.22E-06	12.60
0.11256	20890	1.26E-06	12.72
0.11310	21249	1.33E-06	12.88
0.11350	21590	1.36E-06	12.96
0.11399	21932	1.35E-06	13.10
0.11447	22274	1.30E-06	13.25
0.11494	22616	1.33E-06	13.36
0.11534	22958	1.39E-06	13.49
0.11583	23300	1.42E-06	13.63
0.11634	23642	1.48E-06	13.76
0.11687	23984	1.60E-06	13.92
0.11740	24326	1.66E-06	14.09
0.11797	24668	1.71E-06	14.24
0.11870	25010	1.77E-06	14.44
0.11925	25352	1.82E-06	14.64
0.11979	25694	1.87E-06	14.77
0.12045	26036	1.97E-06	14.96
0.12115	26378	2.15E-06	15.16
0.12190	26720	2.34E-06	15.36
0.12275	27062	2.62E-06	15.62
0.12367	27404	2.95E-06	15.88
0.12462	27746	3.27E-06	16.14
0.12594	28088	3.54E-06	16.53
0.12718	28417	3.80E-06	16.87
0.12844	28741	3.99E-06	17.21
0.12970	29065	4.10E-06	17.58
0.13111	29389	4.32E-06	17.99
0.13249	29713	4.59E-06	18.37
0.13394	30037	4.92E-06	18.81
0.13564	30361	5.36E-06	19.30
0.13742	30685	5.86E-06	19.81
0.13931	31009	6.54E-06	20.36
0.14148	31315	7.17E-06	21.01
0.14368	31621	7.97E-06	21.65
0.14631	31927	9.04E-06	22.44
0.14899	32233	1.03E-05	23.25
0.15220	32537	1.17E-05	24.19
0.15593	32825	1.34E-05	25.33
0.15998	33113	1.56E-05	26.57
0.16495	33401	1.93E-05	27.91
0.16953	33671	2.40E-05	29.51
0.17618	33940	3.11E-05	31.58
0.18434	34192	4.44E-05	34.25

KbA T=75oF R=0 Const. Load			
a	N	da/dN	ΔK
0.01786	2970	1.00E-06	11.18
0.01816	3300	1.09E-06	11.27
0.01844	3630	1.18E-06	11.39
0.01875	3960	1.24E-06	11.51
0.01906	4290	1.34E-06	11.63
0.01944	4620	1.42E-06	11.75
0.01989	4950	1.51E-06	11.88
0.02031	5270	1.62E-06	12.02
0.02071	5590	1.72E-06	12.18
0.02112	5910	1.80E-06	12.34
0.02170	6230	1.84E-06	12.50
0.02221	6550	1.92E-06	12.68
0.02291	6870	1.99E-06	12.81
0.02367	7190	2.06E-06	12.97
0.02396	7500	2.15E-06	13.14
0.02455	7810	2.25E-06	13.31
0.02517	8120	2.35E-06	13.49
0.02584	8430	2.47E-06	13.66
0.02651	8730	2.61E-06	13.85
0.02715	9030	2.76E-06	14.05
0.02789	9330	2.89E-06	14.25
0.02864	9630	3.03E-06	14.45
0.02940	9920	3.19E-06	14.68
0.03012	10200	3.26E-06	14.90
0.03086	10500	3.48E-06	15.11
0.03199	10790	3.71E-06	15.33
0.03290	11070	3.93E-06	15.58
0.03395	11350	4.16E-06	15.81
0.03484	11620	4.46E-06	16.05
0.03566	11890	4.78E-06	16.33
0.03636	12160	5.00E-06	16.60
0.03806	12420	5.31E-06	16.86
0.03920	12680	5.64E-06	17.16
0.04040	12930	5.94E-06	17.46
0.04172	13180	6.24E-06	17.76
0.04305	13420	6.58E-06	18.05
0.04440	13660	6.89E-06	18.37
0.04579	13890	7.17E-06	18.66
0.04723	14110	7.40E-06	18.98
0.04869	14330	7.72E-06	19.29
0.05016	14540	8.09E-06	19.59
0.05168	14740	8.50E-06	19.91
0.05314	14940	8.98E-06	20.23
0.05463	15130	9.51E-06	20.54
0.05612	15320	1.01E-05	20.87
0.05773	15500	1.07E-05	21.20
0.05932	15670	1.12E-05	21.54
0.06085	15830	1.18E-05	21.87
0.06245	15990	1.24E-05	22.20
0.06413	16140	1.30E-05	22.53
0.06573	16280	1.38E-05	22.87
0.06738	16410	1.44E-05	23.18
0.06892	16540	1.51E-05	23.52
0.07052	16660	1.58E-05	23.85
0.07208	16770	1.64E-05	24.16
0.07364	16880	1.70E-05	24.48
0.07520	16980	1.74E-05	24.78
0.07673	17070	1.77E-05	25.08
0.07815	17160	1.84E-05	25.33
0.07954	17240	1.85E-05	25.57
0.08084	17310	1.96E-05	25.82
0.08205	17380	2.08E-05	26.04
0.08313	17440	2.25E-05	26.29
0.08422	17500	2.36E-05	26.50
0.08532	17550	2.43E-05	26.71
0.08613	17600	2.50E-05	26.89
0.08729	17640	2.51E-05	27.07
0.08818	17680	2.56E-05	27.24
0.08899	17710	2.59E-05	27.37
0.08970	17740	2.69E-05	27.49
0.09040	17770	2.82E-05	27.61
0.09099	17790	2.91E-05	27.75
0.09149	17810	2.59E-05	27.80
0.09202	17830	2.74E-05	27.90
0.09257	17850	2.76E-05	27.95
0.09290	17860	2.74E-05	28.02
0.09323	17870	2.73E-05	28.09

SENBH-30P T=75oF R=0 ΔK decreasing			
a	N	da/dN	ΔK
0.04026	13690	3.43E-06	15.46
0.04126	14559	2.93E-06	14.53
0.04246	15893	2.35E-06	13.57
0.05015	17906	1.86E-06	12.63
0.05389	20237	1.52E-06	11.73
0.05739	22072	1.25E-06	10.91
0.06087	26227	1.03E-06	10.18
0.06392	29687	8.40E-07	9.55
0.06656	33401	6.81E-07	9.05
0.06889	37321	5.40E-07	8.63
0.07069	41395	4.33E-07	8.31
0.07217	45595	3.49E-07	8.03
0.07341	49893	2.86E-07	7.83
0.07450	54276	2.44E-07	7.66
0.07548	58736	2.15E-07	7.50
0.07631	63257	1.98E-07	7.38
0.07719	67839	1.84E-07	7.25
0.07806	72485	1.73E-07	7.12
0.07884	77184	1.62E-07	7.00
0.07959	81936	1.45E-07	6.90
0.08026	86737	1.30E-07	6.80
0.08087	91578	1.20E-07	6.71
0.08126	96445	1.16E-07	6.65
0.08184	101349	1.13E-07	6.59
0.08241	106294	1.12E-07	6.51
0.08310	111279	1.11E-07	6.42
0.08361	116295	1.02E-07	6.35
0.08410	121344	9.31E-08	6.29
0.08452	126422	8.54E-08	6.22
0.08489	131520	8.06E-08	6.17
0.08530	136645	7.87E-08	6.13
0.08576	141796	7.83E-08	6.06
0.08609	146969	7.67E-08	6.02
0.08654	152165	7.33E-08	5.98
0.08693	157382	7.41E-08	5.93
0.08726	162624	7.42E-08	5.93
0.08758	167881	7.44E-08	5.88
0.08814	173172	7.62E-08	5.79
0.08844	178484	8.00E-08	5.75
0.08890	183811	8.03E-08	5.72
0.08932	189164	7.71E-08	5.68
0.08982	194552	7.34E-08	5.61
0.09017	199956	6.70E-08	5.58
0.09054	205378	6.28E-08	5.51
0.09075	210808	6.14E-08	5.49
0.09108	216256	6.35E-08	5.45
0.09147	221727	6.90E-08	5.42
0.09190	227219	6.93E-08	5.37
0.09226	232738	6.33E-08	5.30
0.09279	238274	5.87E-08	5.27
0.09291	243825	5.29E-08	5.25
0.09308	249378	4.60E-08	5.24
0.09350	254958	4.49E-08	5.19
0.09372	260548	4.96E-08	5.15
0.09383	266148	4.87E-08	5.14
0.09430	271763	4.99E-08	5.10
0.09458	277395	5.67E-08	5.09
0.09472	283043	5.93E-08	5.05
0.09520	288704	5.43E-08	5.02
0.09565	294398	5.03E-08	4.96
0.09585	300084	4.76E-08	4.95
0.09605	305795	4.13E-08	4.93
0.09617	311507	4.25E-08	4.91
0.09648	317230	5.01E-08	4.87
0.09675	322966	4.93E-08	4.86
0.09718	328724	4.52E-08	4.83
0.09759	334500	3.81E-08	4.77
0.09751	340278	3.39E-08	4.77
0.09763	346055	3.09E-08	4.77
0.09783	351847	3.32E-08	4.76
0.09813	357653	4.18E-08	4.72
0.09838	363472	4.08E-08	4.69
0.09864	369296	3.64E-08	4.67
0.09892	375139	3.09E-08	4.64
0.09895	380995	2.63E-08	4.62
0.09909	386851	2.50E-08	4.63
0.09924	392707	2.76E-08	4.63
0.09939	398573	3.36E-08	4.60
0.09959	404445	4.13E-08	4.57
0.09990	410327	4.32E-08	4.57
0.10013	416217	3.82E-08	4.54
0.10059	422130	2.76E-08	4.50
0.10064	428050	1.83E-08	4.48
0.10058	433970	1.53E-08	4.48
0.10050	439890	1.39E-08	4.46
0.10067	445810	1.82E-08	4.46
0.10097	451737	2.59E-08	4.48

SENBH-30P T=75oF R=0 ΔK increasing			
a	N	da/dN	ΔK
0.10206	466475	1.28E-06	9.52
0.10220	466635	1.16E-06	9.56
0.10234	466795	9.92E-07	9.60
0.10250	466955	9.56E-07	9.65
0.10265	467115	1.05E-06	9.69
0.10282	467275	1.17E-06	9.74
0.10297	467435	1.33E-06	9.78
0.10324	467595	1.46E-06	9.85
0.10348	467755	1.49E-06	9.92
0.10379	467915	1.44E-06	10.01
0.10401	468075	1.37E-06	10.07
0.10417	468235	1.28E-06	10.14
0.10432	468395	1.24E-06	10.18
0.10459	468555	1.26E-06	10.25
0.10475	468715	1.36E-06	10.30
0.10500	468875	1.38E-06	10.36
0.10523	469035	1.34E-06	10.45
0.10546	469195	1.35E-06	10.48
0.10564	469355	1.33E-06	10.57
0.10584	469515	1.37E-06	10.61
0.10607	469675	1.42E-06	10.70
0.10630	469835	1.50E-06	10.75
0.10658	469995	1.55E-06	10.82
0.10681	470155	1.57E-06	10.91
0.10707	470315	1.57E-06	10.98
0.10731	470475	1.57E-06	11.05
0.10757	470635	1.59E-06	11.14
0.10760	470795	1.61E-06	11.19
0.10808	470955	1.62E-06	11.28
0.10834	471115	1.66E-06	11.35
0.10862	471275	1.75E-06	11.43
0.10885	471435	1.81E-06	11.50
0.10917	471595	1.89E-06	11.59
0.10952	471755	1.96E-06	11.71
0.10982	471915	2.08E-06	11.76
0.11016	472075	2.23E-06	11.86
0.11045	472231	2.34E-06	11.99
0.11090	472383	2.40E-06	12.09
0.11131	472535	2.38E-06	12.22
0.11166	472687	2.35E-06	12.32
0.11196	472839	2.26E-06	12.41
0.11226	472991	2.27E-06	12.51
0.11264	473143	2.44E-06	12.61
0.11299	473295	2.70E-06	12.73
0.11343	473447	2.95E-06	12.86
0.11390	473599	3.10E-06	12.96
0.11444	473751	3.29E-06	13.14
0.11495	473903	3.61E-06	13.29
0.11540	474055	3.90E-06	13.44
0.11600	474207	4.29E-06	13.60
0.11683	474359	4.50E-06	13.81
0.11760	474511	4.58E-06	14.06
0.11828	474663	4.53E-06	14.27
0.11888	474815	4.35E-06	14.45
0.11950	474967	4.32E-06	14.64
0.12021	475119	4.47E-06	14.85
0.12085	475271	4.71E-06	15.04
0.12157	475423	4.92E-06	15.26
0.12236	475573	5.11E-06	15.48
0.12313	475717	5.34E-06	15.71
0.12388	475861	5.49E-06	15.95
0.12469	476005	5.61E-06	16.16
0.12552	476149	5.83E-06	16.41
0.12635	476293	6.12E-06	16.67
0.12721	476437	6.36E-06	16.93
0.12820	476581	6.63E-06	17.22
0.12920	476725	6.87E-06	17.51
0.13017	476869	7.16E-06	17.81
0.13120	477013	7.49E-06	18.12
0.13229	477157	7.95E-06	18.44
0.13346	477301	8.49E-06	18.79
0.13468	477439	8.96E-06	19.14
0.13596	477575	9.41E-06	19.53
0.13727	477711	9.84E-06	19.95
0.13861	477847	1.04E-05	20.33
0.14000	477963	1.11E-05	20.77
0.14154	478119	1.20E-05	21.22
0.14320	478255	1.29E-05	21.73
0.14505	478391	1.36E-05	22.29
0.14700	478520	1.42E-05	22.89
0.14890	478648	1.45E-05	23.43
0.15065	478776	1.46E-05	24.01
0.15258	478904	1.48E-05	24.61
0.15443	479032	1.55E-05	25.18
0.15632	479160	1.66E-05	25.74
0.15836	479282	1.79E-05	26.40
0.16066	479402	1.93E-05	27.10
0.16314	479522	2.10E-05	27.89
0.16570	479642	2.27E-05	28.67
0.16835	479761	2.47E-05	29.51
0.17123	479873	2.79E-05	30.44
0.17434	479985	3.21E-05	31.43
0.17782	480097	3.77E-05	32.52
0.18233	480202	4.39E-05	33.98
0.18698	480306	5.04E-05	35.48
0.19254	480406	5.67E-05	37.30
0.19835	480502	6.71E-05	39.23

TABLE I-12. FATIGUE CRACK GROWTH DATA FOR Ti-17 AT $R = 0.6$

Kb-2A RT R=0.6 Const. Load				SEN08-8DP RT R=0.6 ΔK decreasing				SEN08-6BP RT R=0.6 ΔK increasing				Kb-4A T=250F R=0.6 Const. Load				SEN08-8DP T=250F R=0.6 ΔK decreasing				SEN08-4DP T=250F R=0.6 ΔK increasing			
a	N	da/dN	ΔK	a	N	da/dN	ΔK	a	N	da/dN	ΔK	a	N	da/dN	ΔK	a	N	da/dN	ΔK	a	N	da/dN	ΔK
0.02721	2160	1.72E-07	6.74	0.06378	26379	2.15E-06	11.52	0.11357	350513	3.29E-08	5.37	0.02691	1740	8.74E-08	5.86	0.06366	15000	2.71E-06	11.79	0.11243	360934	1.93E-07	5.58
0.02748	4320	1.90E-07	6.79	0.06529	27260	1.85E-06	11.12	0.11360	351203	5.48E-08	5.37	0.02902	3480	8.32E-08	5.89	0.06559	15832	2.27E-06	11.48	0.11257	361584	1.54E-07	5.62
0.02779	6480	2.06E-07	6.85	0.06699	28094	1.58E-06	10.74	0.11366	351893	5.65E-08	5.37	0.02921	5220	6.30E-08	5.91	0.06751	16910	1.87E-06	11.05	0.11287	362274	1.75E-07	5.65
0.02816	8640	2.22E-07	6.90	0.06859	28734	1.34E-06	10.34	0.11369	352583	5.72E-08	5.37	0.02935	6960	6.15E-08	5.92	0.06960	18247	1.54E-06	10.63	0.11279	362984	1.89E-07	5.67
0.02855	10800	2.31E-07	6.95	0.07064	31295	1.20E-06	9.96	0.11373	353273	5.82E-08	5.37	0.02953	8700	6.03E-08	5.92	0.07180	19947	1.31E-06	10.20	0.11291	363654	2.03E-07	5.67
0.02894	12960	2.35E-07	7.01	0.07268	33060	1.07E-06	9.60	0.11377	353963	5.63E-08	5.37	0.02967	10440	6.45E-08	5.93	0.07388	21681	1.16E-06	9.80	0.11307	364344	2.15E-07	5.70
0.02945	15080	2.28E-07	7.07	0.07464	35031	9.51E-07	9.25	0.11381	354653	5.74E-08	5.37	0.02979	12180	7.15E-08	5.95	0.07592	23754	1.02E-06	9.44	0.11323	365034	2.23E-07	5.74
0.02992	17200	2.18E-07	7.12	0.07655	37195	8.54E-07	8.91	0.11385	355343	5.60E-08	5.37	0.02998	13920	8.20E-08	5.96	0.07835	26074	9.06E-07	9.01	0.11338	365724	2.23E-07	5.78
0.03042	19320	2.08E-07	7.17	0.07844	39543	7.58E-07	8.58	0.11388	356033	5.41E-08	5.38	0.02981	15660	8.88E-08	5.98	0.08043	28603	7.98E-07	8.67	0.11356	366414	2.30E-07	5.81
0.03094	21400	1.92E-07	7.21	0.08030	42068	6.62E-07	8.27	0.11392	356723	5.62E-08	5.38	0.03009	17400	8.08E-08	6.00	0.08243	31326	6.79E-07	8.34	0.11370	367104	2.24E-07	5.83
0.03145	23480	1.85E-07	7.25	0.08185	44733	5.84E-07	7.99	0.11395	357413	5.69E-08	5.38	0.03022	19140	8.19E-08	6.01	0.08416	34214	5.51E-07	8.05	0.11385	367794	2.18E-07	5.86
0.03187	25560	1.67E-07	7.29	0.08316	47514	5.13E-07	7.80	0.11400	358103	6.07E-08	5.38	0.03036	20880	8.34E-08	6.03	0.08589	37240	4.52E-07	7.82	0.11403	368484	2.12E-07	5.90
0.03226	27640	1.69E-07	7.33	0.08453	50410	4.45E-07	7.59	0.11405	358793	6.12E-08	5.38	0.03050	22620	8.49E-08	6.05	0.08670	40357	3.65E-07	7.65	0.11414	369174	2.11E-07	5.93
0.03263	29680	1.61E-07	7.38	0.08604	53432	3.83E-07	7.37	0.11409	359483	6.66E-08	5.38	0.03067	24360	8.52E-08	6.06	0.08762	43553	3.05E-07	7.51	0.11429	369864	2.05E-07	5.95
0.03300	31720	1.60E-07	7.42	0.08709	55539	3.35E-07	7.19	0.11413	360173	7.29E-08	5.38	0.03079	26100	8.74E-08	6.08	0.08866	46838	2.72E-07	7.37	0.11444	370554	2.23E-07	5.97
0.03335	33760	1.67E-07	7.46	0.08792	59715	2.89E-07	7.09	0.11417	360863	6.74E-08	5.38	0.03092	27840	8.88E-08	6.10	0.08931	50178	2.71E-07	7.26	0.11458	371244	2.41E-07	6.02
0.03375	35800	1.63E-07	7.50	0.08867	62949	2.49E-07	6.96	0.11421	361553	1.02E-07	5.39	0.03108	29580	8.75E-08	6.11	0.09019	53591	2.62E-07	7.15	0.11471	371934	2.52E-07	6.02
0.03419	37800	1.81E-07	7.54	0.08947	66247	2.22E-07	6.85	0.11432	362243	1.02E-07	5.39	0.03124	31320	8.01E-08	6.13	0.09114	57076	2.30E-07	7.03	0.11488	372624	2.52E-07	6.09
0.03454	39960	1.86E-07	7.58	0.09026	69604	2.05E-07	6.74	0.11443	362933	1.05E-07	5.39	0.03140	33060	8.19E-08	6.15	0.09242	60664	2.13E-07	6.85	0.11513	373283	2.54E-07	6.11
0.03492	41800	1.94E-07	7.62	0.09092	73013	1.86E-07	6.65	0.11448	363623	1.04E-07	5.41	0.03154	34800	9.71E-08	6.16	0.09293	64298	1.80E-07	6.79	0.11530	373965	2.61E-07	6.14
0.03526	43800	2.08E-07	7.66	0.09142	76458	1.65E-07	6.58	0.11455	364313	9.82E-08	5.42	0.03168	36540	1.02E-07	6.18	0.09330	67955	1.55E-07	6.72	0.11547	374632	2.41E-07	6.16
0.03560	45760	2.24E-07	7.70	0.09204	79947	1.50E-07	6.50	0.11460	365003	9.38E-08	5.44	0.03185	38280	1.04E-07	6.20	0.09367	71639	1.35E-07	6.60	0.11564	375299	2.46E-07	6.21
0.03598	47720	2.37E-07	7.74	0.09250	83468	1.40E-07	6.44	0.11468	365693	9.97E-08	5.44	0.03199	40020	1.03E-07	6.22	0.09425	75367	1.43E-07	6.61	0.11573	375966	2.51E-07	6.23
0.03634	49680	2.47E-07	7.79	0.09295	87025	1.34E-07	6.38	0.11475	366383	1.06E-07	5.46	0.03218	41700	1.02E-07	6.24	0.09498	78148	1.39E-07	6.54	0.11594	376633	2.43E-07	6.26
0.03677	51640	2.52E-07	7.84	0.09342	90613	1.26E-07	6.31	0.11482	367073	1.13E-07	5.46	0.03235	43380	1.04E-07	6.26	0.09542	82957	1.34E-07	6.47	0.11613	377300	2.53E-07	6.30
0.03721	53560	2.51E-07	7.90	0.09397	94237	1.30E-07	6.25	0.11491	367763	1.16E-07	5.48	0.03254	45060	1.05E-07	6.27	0.09611	86830	1.33E-07	6.35	0.11632	377967	2.80E-07	6.33
0.03770	55480	2.49E-07	7.94	0.09433	97690	1.32E-07	6.20	0.11498	368453	1.19E-07	5.48	0.03273	46740	1.08E-07	6.29	0.09620	90715	1.32E-07	6.35	0.11645	378634	3.02E-07	6.35
0.03822	57400	2.51E-07	7.99	0.09484	101577	1.38E-07	6.13	0.11508	369143	1.19E-07	5.51	0.03287	48420	1.16E-07	6.31	0.09677	94625	1.20E-07	6.30	0.11668	379301	3.10E-07	6.40
0.03870	59320	2.62E-07	8.04	0.09536	105298	1.41E-07	6.06	0.11516	369833	1.29E-07	5.53	0.03302	50100	1.20E-07	6.33	0.09760	98591	1.12E-07	6.22	0.11693	379968	3.14E-07	6.45
0.03914	61200	2.82E-07	8.09	0.09599	109055	1.41E-07	6.02	0.11523	370523	1.46E-07	5.55	0.03322	51780	1.23E-07	6.35	0.09811	102556	1.16E-07	6.15	0.11718	380635	3.14E-07	6.50
0.03963	63080	3.08E-07	8.14	0.09651	112854	1.41E-07	5.94	0.11532	371213	1.69E-07	5.57	0.03343	53460	1.27E-07	6.38	0.09893	106501	1.20E-07	6.13	0.11734	381302	3.03E-07	6.52
0.04007	64960	3.44E-07	8.20	0.09699	116687	1.40E-07	5.89	0.11547	371903	1.91E-07	5.58	0.03360	55140	1.32E-07	6.40	0.09956	110636	1.15E-07	6.10	0.11752	381969	3.07E-07	6.57
0.04055	66800	3.76E-07	8.26	0.09747	120549	1.38E-07	5.82	0.11561	372588	2.05E-07	5.62	0.03381	56820	1.33E-07	6.42	0.09926	114712	1.18E-07	6.02	0.11770	382636	3.20E-07	6.60
0.04107	68640	4.06E-07	8.34	0.09809	124450	1.34E-07	5.76	0.11578	373258	2.15E-07	5.65	0.03404	58500	1.34E-07	6.45	0.10004	118844	1.31E-07	5.92	0.11794	383303	3.33E-07	6.64
0.04155	70480	4.30E-07	8.41	0.09861	128385	1.35E-07	5.69	0.11591	373923	2.10E-07	5.67	0.03423	60180	1.36E-07	6.47	0.10026	122996	1.11E-07	5.86	0.11820	383970	3.57E-07	6.69
0.04231	72280	4.48E-07	8.49	0.09912	132351	1.34E-07	5.62	0.11605	374583	2.09E-07	5.69	0.03446	61860	1.41E-07	6.49	0.10063	127171	8.34E-08	5.85	0.11844	384626	3.69E-07	6.74
0.04302	74080	4.57E-07	8.57	0.09961	136347	1.28E-07	5.56	0.11618	375257	2.07E-07	5.72	0.03470	63540	1.45E-07	6.52	0.10134	131385	8.77E-08	5.76	0.11865	385269	3.73E-07	6.79
0.04381	75840	4.85E-07	8.64	0.10019	140377	1.25E-07	5.52	0.11631	375924	2.11E-07	5.74	0.03494	65220	1.51E-07	6.54	0.10127	135516	1.12E-07	5.75	0.11891	385913	3.72E-07	6.84
0.04457	77500	5.38E-07	8.72	0.10071	144439	1.17E-07	5.45	0.11647	376591	2.27E-07	5.77	0.03514	66900	1.58E-07	6.57	0.10133	139646	1.23E-07	5.76	0.11915	386557	3.73E-07	6.87
0.04535	79320	5.79E-07	8.82	0.10113	148528	1.10E-07	5.41	0.11661	377259	2.47E-07	5.78	0.03537	68520	1.64E-07	6.60	0.10259	144136	1.19E-07	5.66	0.11941	387201	3.65E-07	6.92
0.04617	81040	6.18E-07	8.92	0.10161	152644	1.02E-07	5.37	0.11675	377925	2.75E-07	5.83	0.03556	70140	1.64E-07	6.63	0.10345	148493	1.12E-07	5.54	0.11964	387845	3.58E-07	6.97
0.04697	82720	6.52E-07	9.02	0.10192	156778	9.68E-08	5.33	0.11688	378592	3.11E-07	5.88	0.03589	71760	1.58E-07	6.65	0.10371	152863	7.81E-08	5.52	0.11986	388489	3.52E-07	7.01
0.04772	84400	6.84E-07	9.12	0.10234	160939	1.01E-07	5.29	0.11717	379259	3.46E-07	5.91	0.03613	73380	1.56E-07	6.68	0.10382	157245	2.72E-06	5.50	0.12006	389133	3.72E-07	7.04
0.04900	86040	6.80E-07	9.22	0.10274	165122	1.00E-07	5.23	0.11743	379926	3.66E-07	5.95	0.03640	75000	1.55E-07	6.70	0.10373	161623	2.01E-05	5.50	0.12030	389777	3.96E-07	7.09
0.05000	87640	7.14E-07	9.33	0.10314	169326	9.18E-08	5.21	0.11772	380593	4.20E-07	6.00	0.03668	76620	1.56E-07	6.73	0.10360	166003	2.24E-05	5.50	0.12059	390421	4.32E-07	7.14
0.05100	89240	7.39E-07	9.43	0.10377	173569	7.79E-08	5.14	0.11787	381260	4.62E-07	6.05	0.03695	78240	1.61E-07	6.75	0.10359	170363	4.56E-06	5.49	0.12086	391065	4.54E-07	7.19
0.05204	90960	7.62E-07	9.53	0.10402	177825	7.28E-08	5.09	0.11828	381927	5.02E-07	6.12	0.03718	79860	1.68E-07	6.78	0.10372	174763	8.78E-06	5.50	0.12117	391709	4.71E-07	7.27
0.05314	92320	7.60E-07	9.64	0.10406	182081	7.35E-08	5.09	0.11867	382604	5.55E-07	6.18	0.03741	81480	1.71E-07	6.81	0.10392	179145	1.11E-07	5.51	0.12150	392353	4.78E-07	7.32
0.05428	93800	8.52E-07	9.75	0.10424	186350	6.82E-08	5.10	0.11902	383261	5.95E-07	6.24	0.03765	83100	1.77E-07	6.84	0.10554	183621	1.12E-07	5.34	0.12178	392974	4.75E-07	7.37
0.05531	95280	8.30E-07	9.85	0.10480	190648	6.97E-08	5.02	0.11942	383905	5.99E-07	6.32	0.03794	84720	1.82E-07	6.87	0.10599	188132	8.60E-06	5.26	0.12209	393595	4.55E-07	7.44
0.05642	96720	1.01E-06	9.97	0.10532	194975	7.63E-08	4.97	0.11990	384549	5.63E-07	6.41	0.03821	86280	1.86E-07	6.90	0.10603	192647	4.72E-06	5.26	0.12238	394216	4.53E-07	7.52
0.05755	98120	1.07E-06	10.09	0.10540	199316	8.10E-08	4.97	0.12026	385183	5.61E-07	6.48	0.03850	87840	1.93E-07	6.93	0.10572	210707	5.76E-09	5.27	0.12264	394837	4.57E-07	7.55
0.05995	99480	1.11E-06	10.23	0.10557	203655	7.22E-08	4.95	0.12056	385827	5.36E-07	6.54	0.03876	89400	2.13E-07	6.96	0.10579	215222	4.48E-08	5.28	0.12293	395459	4.55E-07	7.60
0.06299	100960	1.13E-06	10.37	0.10605	208017	6.56E-08	4.91	0.12089	386471	5.24E-07	6.61	0.03900	90960	2.27E-07	6.99	0.10596	219737	6.63E-06	5.28	0.12321	396079	4.71E-07	7.67
0.06147	102160	1.13E-06	10.50	0.10691	212415	7.25E-08	4.86	0.12120	387115	5.46E-07	6.68	0.03934	92520	2.30E-07	7.03	0.10614	224255	7.23E-08	5.27	0.12350	396700	5.00E-07	7.70
0.06269	103440	1.18E-06	10.52	0.10667	216825	7.27E-08	4.84	0.12158	387759	5.76E-07	6.75	0.03966	94080	2.40E-07	7.07	0.10735	226957	6.90E-06	5.14	0.12380	397321	5.34E-07	7.76
0.06432	104880	1.19E-06	10.75	0.10691	221206	6.39E-08	4.80	0.12196	388403	6.10E-07	6.83	0.03999	95640	2.57E-07	7.11	0.10736	233435	5.39E-06	5.12	0.12415	397942	5.91E-07	7.83
0.06557	105960	1.28E-06	10.87	0.10733	225670	5.91E-08	4.79	0.12237	389037	6.75E-07	6.90	0.04036	97200	2.76E-07	7.15	0.10724	236040	3.03E-06	5.12	0.12453	398563	6.62E-07	7.91
0.06693	107040	1.35E-06	11.00	0.10763	230122	6.10E-08	4.76	0.12275	389659	7.94E-07	6.98	0.04074	98760	2.92E-07	7.19	0.10739	242645	8.19E-09	5.12	0.12492	399174	7.57E-07	7.99
0.06820	109160	1.48E-06	11.14	0.10770	234577	5.30E-08	4.76	0.12323	390279	7.90E-07	7.09	0.04114	100320	3.09E-07	7.23	0.10736	247250	2.44E-09	5.12	0.12536	399772	9.47E-07	8.07
0.06953	109240	1.58E-06	11.29	0.10804	239043	4.55E-08	4.73	0.12378	390900	8.45E-07	7.18	0.04153	101620	3.17E-07	7.26	0.10743	251855	6.40E-09	5.12	0.12597	400370	9.92E-07	8.10
0.07059	110280	1.71E-06	11.43	0.10823	243523	4.79E-08	4.72	0.12435	391521	8.66E-07	7.28	0.04192	103320	3.22E-07	7.33	0.10763	256460	8.70E-06	5.11	0.12662	400988	9.26E-07	8.31
0.07219	111260	1.83E-06	11.56	0.10828	248003	5.13E-08	4.70	0.12488	392142	8.91E-07	7.38	0.04235	104820	3.23E-07	7.38	0.10815	261090	9.73E-08	5.07	0.12715	401568	9.52E-07	8.42
0.07362	112240	1.92E-06	11.74	0.10864	252500	5.41E-08	4.69	0.12548	392763	9.06E-07	7.47	0.04293	106320	3.24E-07	7.42	0.10941	265791	8.70E-06	4.94	0.12761	402184	9.55E-07	8.50
0.07519	113160	2.01E-06	11.90	0.10898	257013	5.59E-08	4.65	0.12588	393383	9.44E-07	7.58	0.04337	107820	3.30E-07	7.47	0.10956	270516	8.14E-06	4.93	0.12820	402751	9.72E-07	8.61
0.07674	114040	2.10E-06	12.05	0.10917	261535	5.45E-08	4.63	0.12652	393984	1.05E-06	7.70	0.04366	109320	3.47E-07	7.52	0.10957	275241	2.79E-06	4.93	0.12882	403325	1.02E-06	8.72
0.07834	114960	2.20E-06	12.21	0.10946	266072	4.22E-08	4.61	0.12715	394582	1.17E-06	7.82	0.04431	110760	3.63E-07	7.57	0.10944	279966	1.23E-06	4.90	0.12939	403901	1.05E-06	8.85
0.07995	115920	2.34E-06	12.37	0.10963	270622	3.65E-08	4.59	0.12781	395183	1.35E-06	7.94	0.04478	112200	3.84E-07	7.62	0.10940	284691	4.10E-06	4.90	0.13001	404478	1.06E-06	8.94
0.08145	116440	2.47E-06	12.53	0.10976	275172	3.74E-08	4.58	0.12868	395769	1.49E-06	8.10	0.04524	113640	4.05E-07	7.68	0.10943	289416	7.10E-06	4.90	0.13064	405051	1.12E-06	9.10
0.08298	117160	2.60E-06	12.70	0.10975	279722	3.74E-08	4.58	0.12972	396333	1.61E-06	8.29	0.04579	115080	4.18E-07	7.73	0.11011	294159	9.34E-06	4.89	0.13124	405621	1.16E-06	9.21
0.08452	117840	2.72E-06	12.87	0.11004	284285	4.01E-08	4.56	0.13066	396903	1.69E-06	8.43	0.04631	116520	4.36E-07	7.79	0.11105	298955	9.84E-06	4.80	0.13192	406173	1.23E-06	9.35
0.08601	118480	2.80E-06	13.03	0.11033	288860	3.77E-08	4.53	0.13163	397483	1.66E-06	8.87	0.04684	117960	4.48E-07	7.85	0.11144	303770	8.53E-06	4.77	0.13262	406725	1.32E-06	9.47
0.08752	119080	2.83E-06	13.16	0.11049	293440	3.29E-08	4.52	0.13266	398044	1.66E-06	8.94	0.04742	119340	4.56E-07	7.91	0.11172	306595	5.33E-06	4.74	0.13330	407277	1.36E-06	9.59
0.08909	119640	2.84E-06	13.32	0.11065	298032	2.52E-08	4.51	0.13355	398566	1.66E-06	9.03	0.04806	120720	4.64E-07	7.97	0.11183	313426	2.32E-06	4.75	0.13417	407829	1.41E-06	9.74
0.09059	120160	2.86E-06	13.45	0.11062	302624	2.75E-08	4.50	0.13434	399149	1.65E-06	9.13	0.04868	122100	4.78E-07	8.03	0.11188	316273	8.95E-09	4.71	0.13499	408383	1.45E-06	9.91
0.09186	120640	2.89E-06	13.57	0.11068	307216	3.11E-08	4.51	0.13528	399700	1.75E-06	9.37	0.04925	123480	4.96E-07	8.09					0.13569	408989	1.52E-06	10.06
0.09316	121080	2.88E-06	13.67	0.11085	311815	3.41E-08	4.49	0.13625	400230	1.65E-06	9.55	0.04969	124800	5.21E-07	8.16					0.13642	409418	1.55E-06	10.20
0.09430	121480	3.02E-06	13.75	0.11126	316426	4.45E-08	4.47	0.13728	400758	1.91E-06	9.73	0.05048	126120	5.46E-07	8.23					0.13727	409847	1.91E-06	10.36
0.09529	121840	3.08E-06	13.87	0.11135	321070	4.74E-08	4.45	0.13833	401289	2.01E-06	9.94	0.05114	127440	5.65E-07	8.30					0.13825	410450	2.21E-06	10.54
0.09629	122160	3.04E-06	13.96	0.11143	325704	4.05E-08	4.43	0.13932	401803	2.11E-06	10.14	0.05179	128760	5.80E-07	8.37					0.13949	410984	2.52E-06	10.79
0.09706	122440	2.88E-06	14.05	0.11108	330355	4.07E-08	4.41	0.14035	402309	2.17E-06	10.33	0.05248	130080	6.19E-07	8.44					0.14099	411402	2.92E-06	11.09
0.09791	122720	2.99E-06	14.13	0.11198	335017	4.51E-08	4.39	0.14161	402815	2.22E-06	10.57	0.05317	131340	6.69E-07	8.52					0.14232	411945	3.41E-06	11.32
0.09869	122960	3.03E-06	14.19	0.11195	339679	4.09E-08	4.39	0.14274	403305	2.23E-06	10.79	0.05398	132600	7.20E-07	8.59					0.14382	412423	4.01E-06	11.61
0.09943	123200	3.21E-06	14.27	0.11245	344358	2.82E-08	4.34	0.14375	403799	2.55E-06	11.00	0.05483	133860	8.13E-07	8.68					0.14500	412883	4.66E-06	12.03
0.10004	123400	3.32E-06	14.34	0.11261	349040	2.24E-08	4.33	0.14485	404271	2.92E-06	11.20	0.05543	135120	8.99E-07	8.76					0.14912	413329	5.42E-06	12.48
0.10057	123600	3.44E-06	14.40	0.11250	353730	1.61E-08	4.33	0.14623	404735	3.50E-06	11.46	0.05623	136320	9.71E-07	8.89					0.15065	413753	6.15E-06	12.95
0.10114	123960	3.52E-06	14.45	0.11249	358420	1.51E-08	4.33	0.14794	405195	4.14E-06	11.79	0.05712	137520	1.04E-06	9.01					0.15329	414162	6.91E-06	13.45
0.10171	123960	3.53E-06	14.50	0.11257	363118	3.05E-08	4.33	0.14998	405638	4.72E-06	12.20	0.05819	138720	1.11E-06	9.12					0.15600	414551	7.82E-06	13.99
0.10223	124120	3.58E-06	14.56	0.11261	367808	4.61E-08	4.33	0.15234	406082	5.32E-06	12.85	0.05917	139920	1.23E-06	9.24					0.15887	414918	9.09E-06	14.55
0.10273	124240	3.59E-06	14.60	0.11310	372515	5.23E-08	4.26	0.15448	406476	6.17E-06	13.08	0.06050	141000	1.34E-06	9.37					0.16203	415290	1.06E-05	15.19
0.10307	124360	3.88E-06	14.63	0.11354	377248	4.58E-08	4.24	0.15871	406868	7.08E-06	13.50	0.06159	142080	1.48E-06	9.52					0.16545	415573	1.33E-05	15.87
0.10352	124480	3.83E-06	14.67					0.15838	407244	7.90E-06	14.04	0.06276	143160	1.55E-06	9.67								
0.10382	124560	4.03E-06	14.71					0.16283	407598	8.67E-06	14.72	0.06401	144180	1.58E-06	9.84								
0.10410	124640	4.24E-06	14.75					0.16598	407925	1.01E-05	15.34	0.06537	145200	1.84E-06	9.96								
0.10440	124720	4.28E-06	14.77					0.16865	408235	1.22E-05	15.87	0.06709	146160	1.73E-06	10.13								
0.10468	124800	4.20E-06	14.79									0.06858	147120	1.88E-06	10.29								
0.10498	124880	4.07E-06	14.82									0.07008	148020	2.09E-06	10.46								
0.10525	124920	3.80E-06	14.83									0.07145	148920	2.35E-06	10.64								
0.10538	124960	3.94E-06	14.86									0.07269	149760	2.58E-06	10.84								
0.10554	125000	3.94E-06	14.86									0.07447	150600	2.84E-06	11.06								
												0.07619	151380	3.01E-06	11.29								
												0.07789	152100	3.22E-06	11.51								
												0.07964	152820	3.41E-06	11.72								
												0.08185	153480	3.60E-06	11.95								
												0.08362	154080	3.85E-06	12.17								
												0.08563	154620	4.11E-06	12.38								
												0.08718	155160	4.41E-06	12.61								

I.5.1 EFFECTS OF STRESS RATIO AND TEMPERATURE.

Test results are summarized graphically by stress ratio and temperature in figures I-18 through I-32.

Figure I-18 shows 75°F Ti-6-4 data at all three stress ratios, and figure I-19 shows 400°F Ti-6-4 data at the same three stress ratios. Typical stress ratio effects—slightly higher FCG rates and slightly lower thresholds at higher stress ratios—were observed. Figure I-20 provides a direct comparison of $R = 0$ data at the two different temperatures, while figures I-21 and I-22 provide similar comparisons of Ti-6-4 data from the two temperatures at $R = 0.5$ and $R = 0.75$. Temperature appeared to have no significant effect on FCG rates in the 75° to 400°F range except at the highest stress ratio ($R = 0.75$), where some of the 400°F data exhibited slightly higher growth rates.

Figures I-23 through I-25 document the effects of different stress ratios on Ti-6-2-4-2 growth rates at a common temperature for each of the three test temperatures. Typical stress ratio effects were again observed, and these effects were more pronounced at higher temperatures. The two higher stress ratios (0.5 and 0.75) exhibited similar growth rates at room temperature, but $R = 0.75$ cycling produced substantially faster growth rates than $R = 0.5$ cycling at the elevated temperatures. Figures I-16 through I-28 more clearly show the effects of temperature on Ti-6-2-4-2 data at common stress ratios. Changes in temperature between 75° and 600°F had essentially no effect on FCG rates at $R = 0$ and $R = 0.5$ and a relatively small effect at $R = 0.75$. Increasing the temperature further to 1000°F had a small effect at $R = 0$ but a very strong effect at the two higher stress ratios.

Figures I-29 through I-32 illustrate FCG rate data for Ti-17. Figures I-29 and I-30 show the effect of different stress ratios ($R = 0$ and $R = 0.6$) at common temperatures (75° and 750°F), and figures I-31 and I-32 show the effect of different temperatures at common stress ratios. Neither variable had a strong effect on growth rates over the ranges investigated.

I.5.2 COMPARISONS WITH AIR DATA.

The critical issue for the vacuum FCG data is the potential difference between vacuum and air growth rates. Both GEAE and AlliedSignal Engines have performed comparisons of these vacuum data with their own proprietary air data. However, due to the confidential nature of those proprietary air databases, those comparisons cannot be shown in this report.

Fortunately, some public domain air data are available for comparable materials and test conditions, so that vacuum vs. air comparisons can be shown in this report. The data selected for comparison were taken from the Damage Tolerant Design Handbook (DTDH) [I-26]. Comparisons based on DTDH data were qualitatively similar to comparisons based on proprietary data.

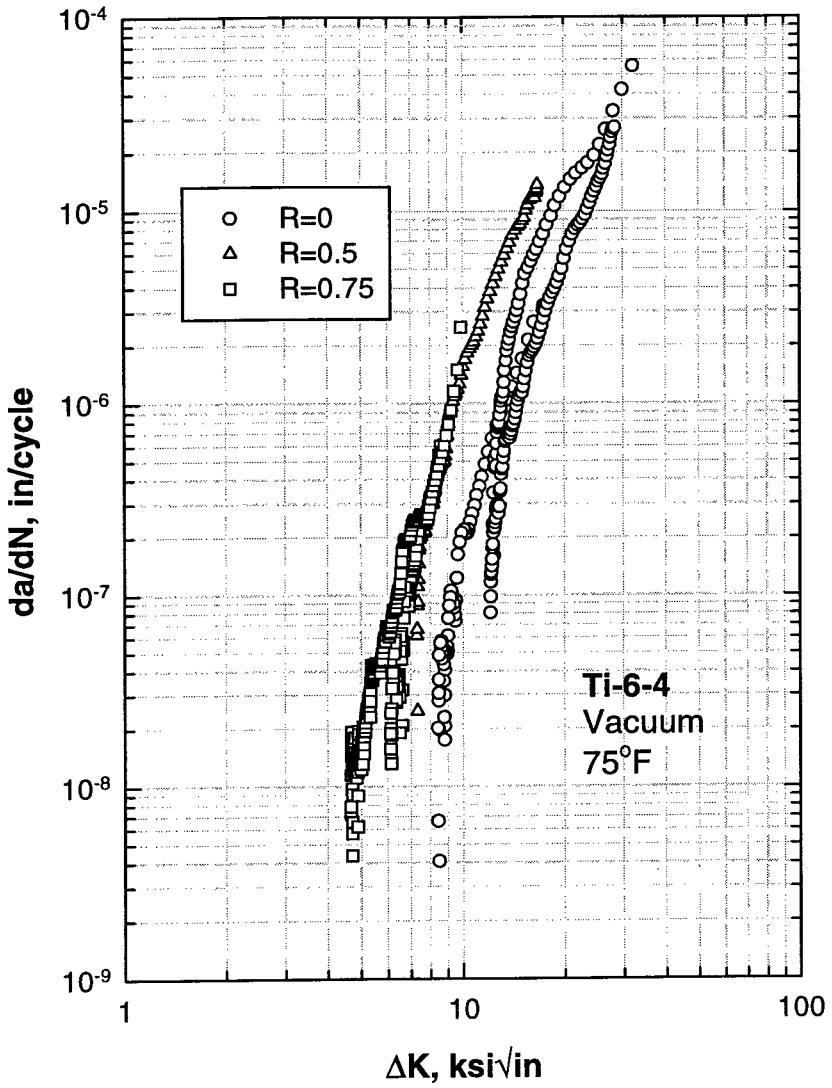


FIGURE I-18. VACUUM FCG DATA FOR Ti-6Al-4V AT ALL STRESS RATIOS (75°F)

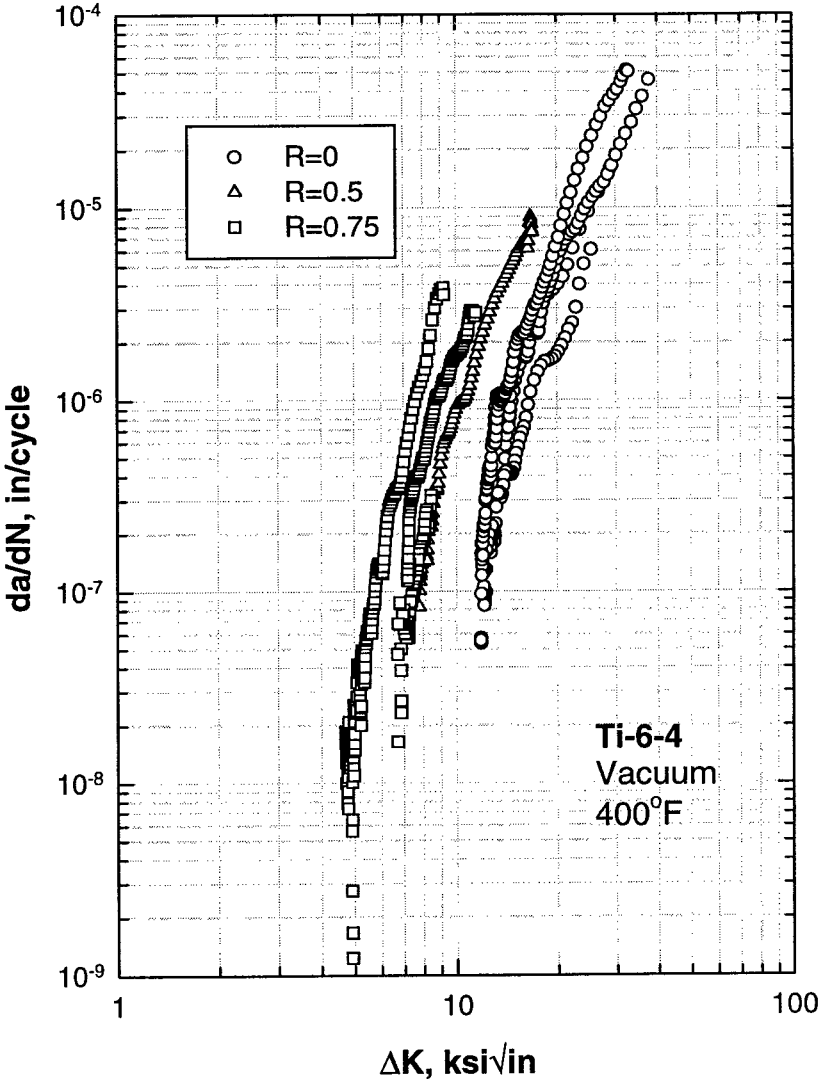


FIGURE I-19. VACUUM FCG DATA FOR Ti-6Al-4V AT ALL STRESS RATIOS (400°F)

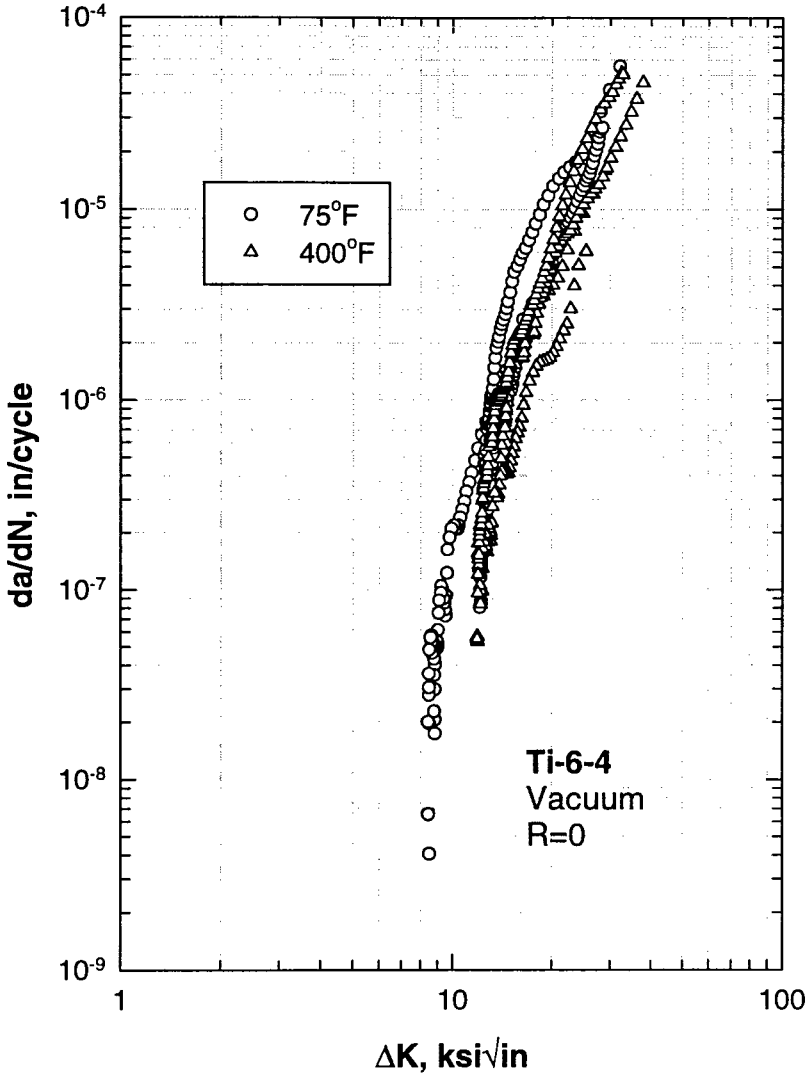


FIGURE I-20. VACUUM FCG DATA FOR Ti-6Al-4V AT ALL TEMPERATURES ($R = 0$)

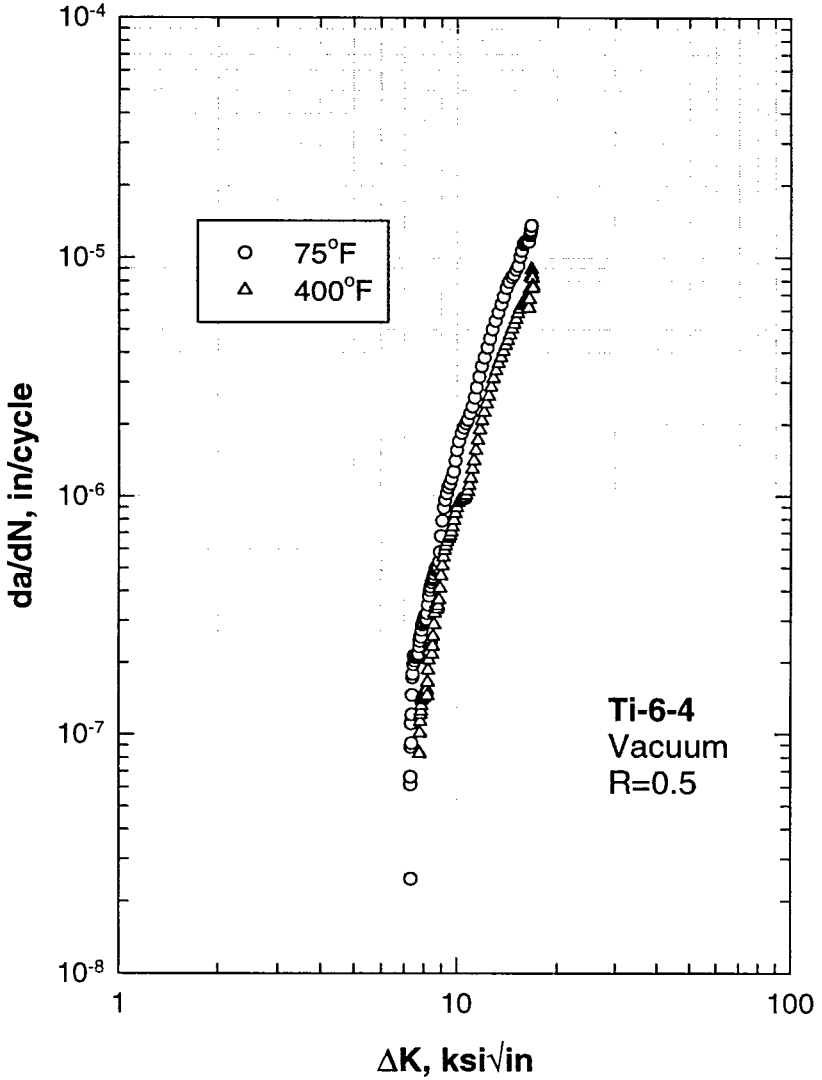


FIGURE I-21. VACUUM FCG DATA FOR Ti-6Al-4V AT ALL TEMPERATURES ($R = 0.5$)

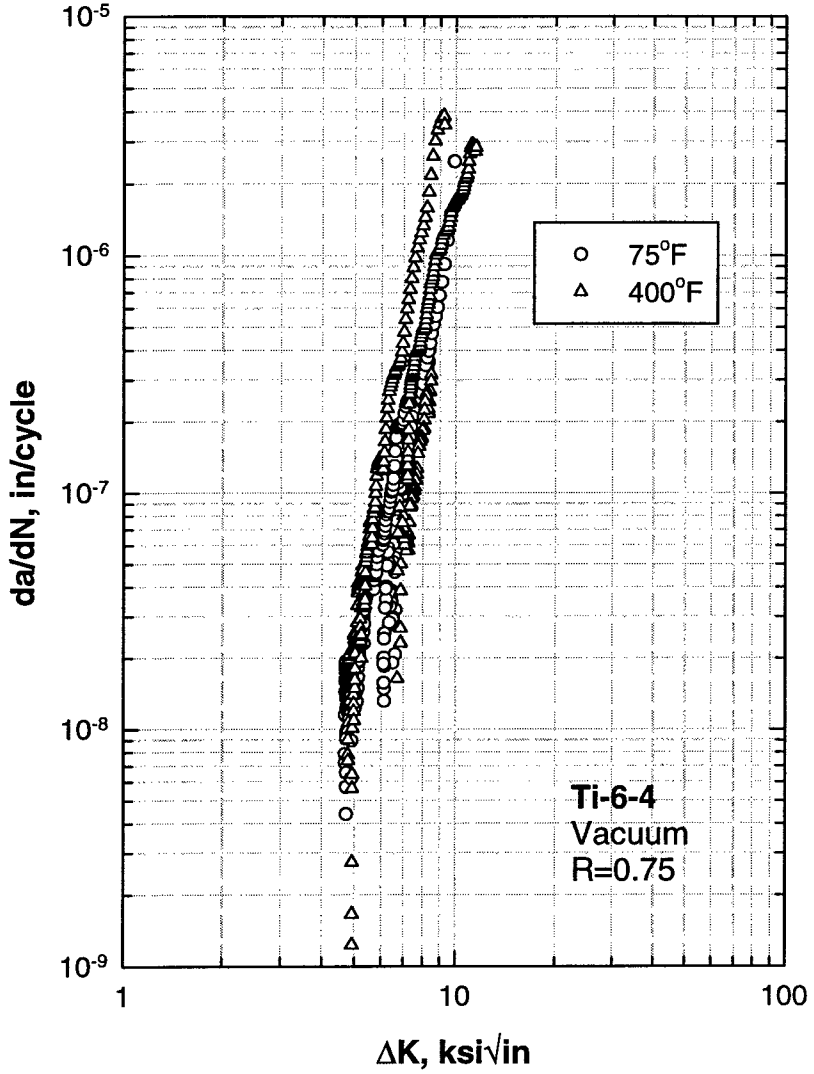


FIGURE I-22. VACUUM FCG DATA FOR Ti-6Al-4V AT ALL TEMPERATURES ($R = 0.75$)

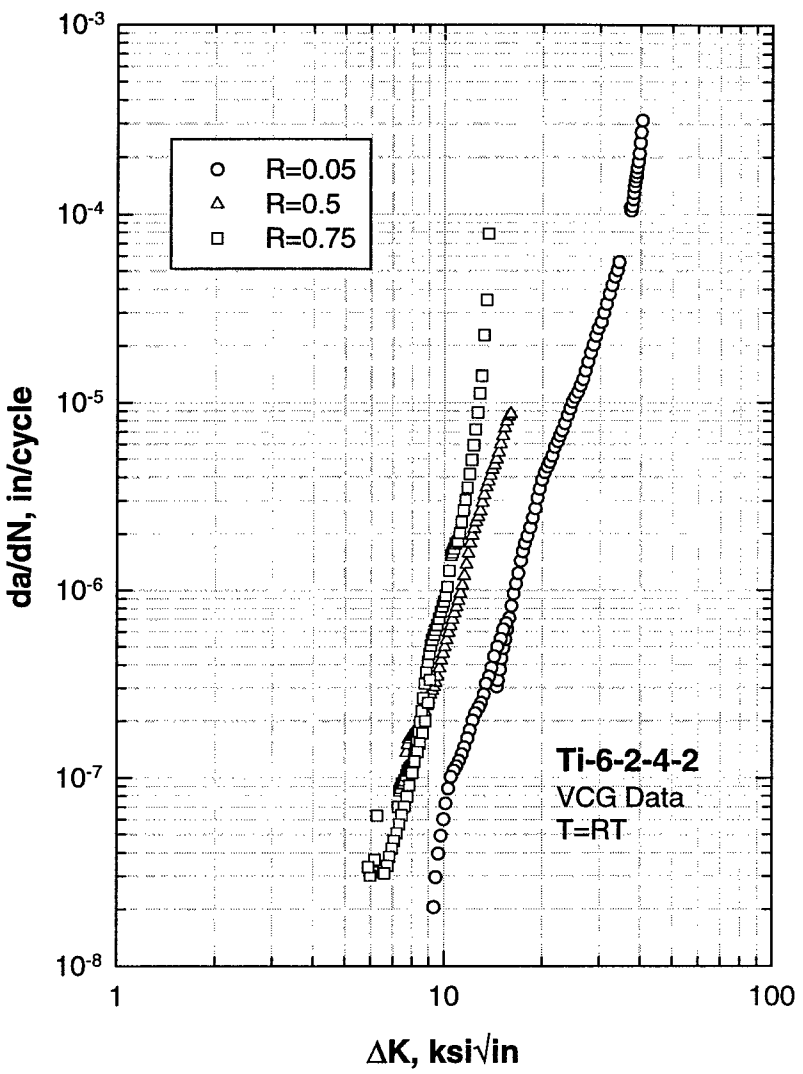


FIGURE I-23. VACUUM FCG DATA FOR Ti-6-2-4-2 AT ALL STRESS RATIOS (75°F)

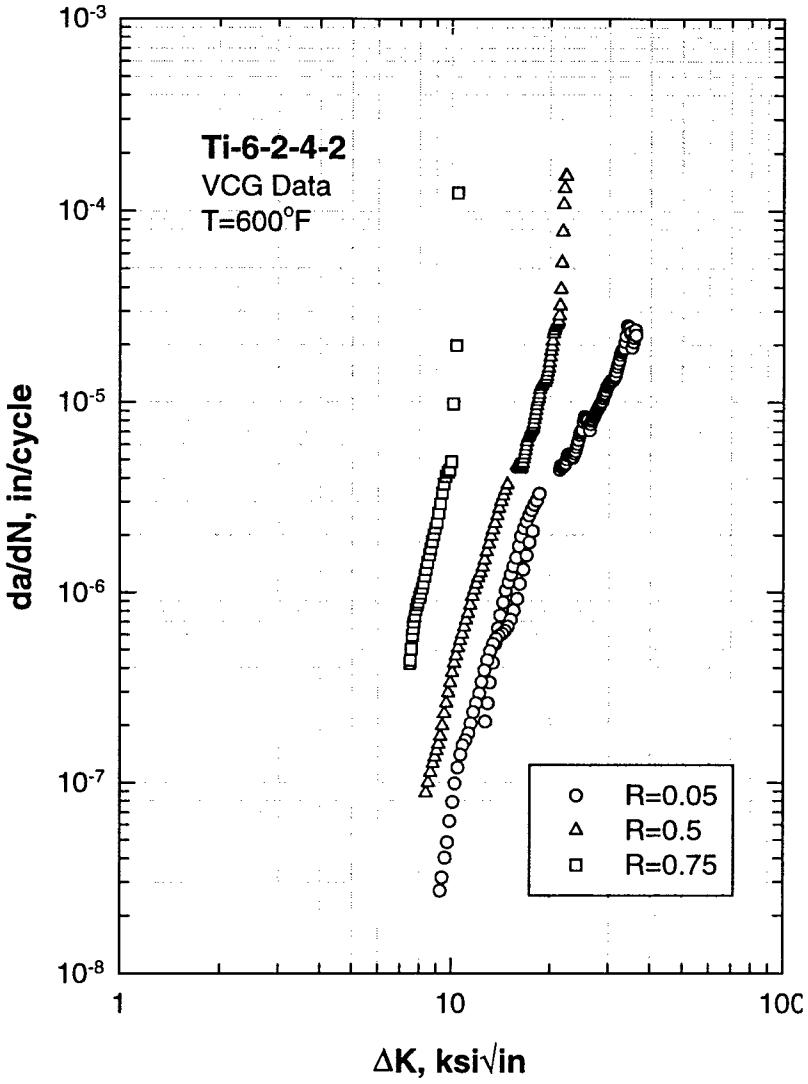


FIGURE I-24. VACUUM FCG DATA FOR Ti-6-2-4-2 AT ALL STRESS RATIOS (600°F)

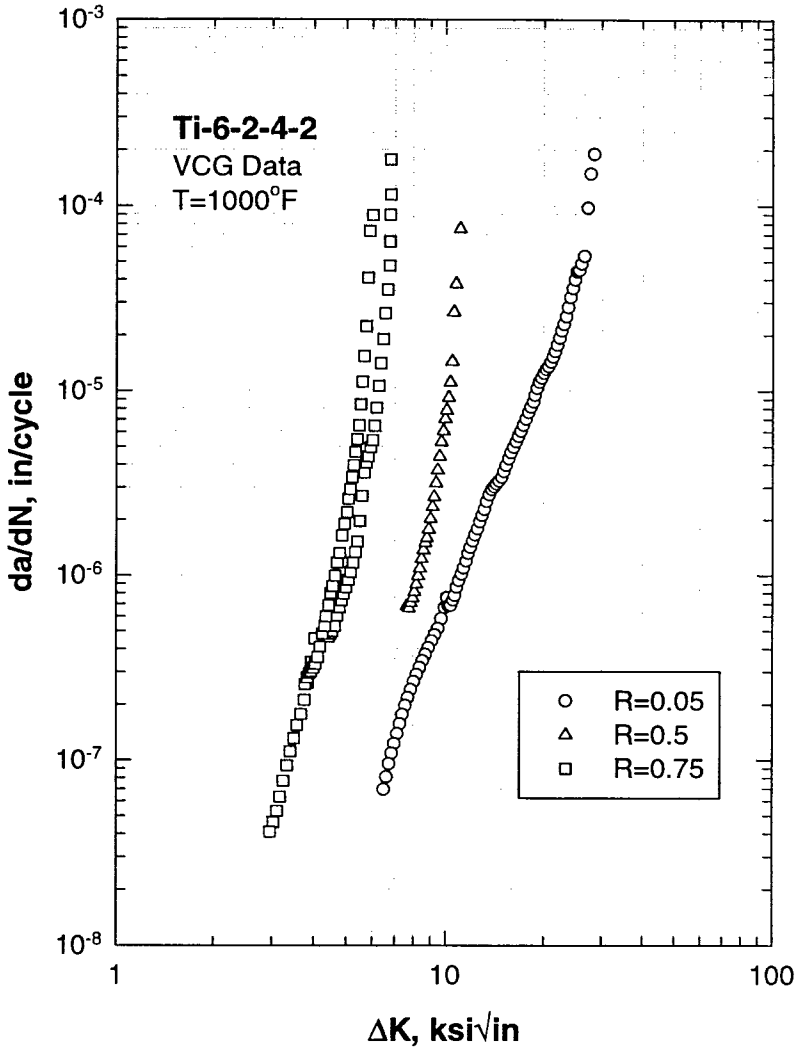


FIGURE I-25. VACUUM FCG DATA FOR Ti-6-2-4-2 AT ALL STRESS RATIOS (1000°F)

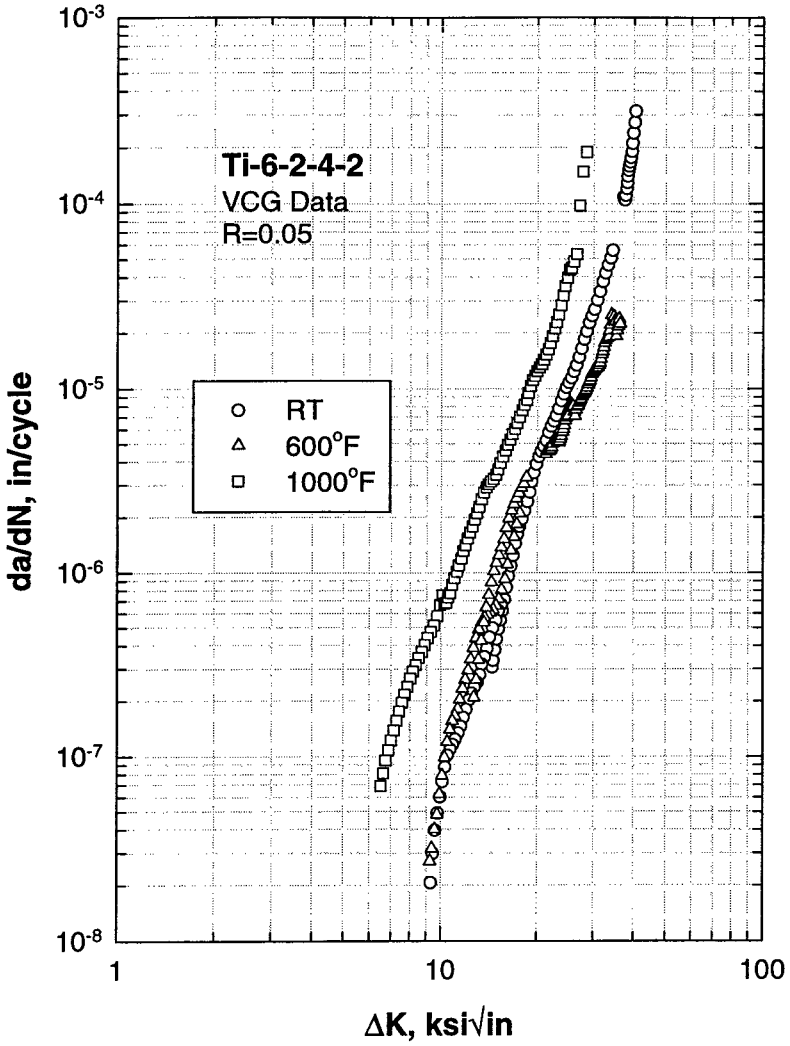


FIGURE I-26. VACUUM FCG DATA FOR Ti-6-2-4-2 AT ALL TEMPERATURES ($R = 0$)

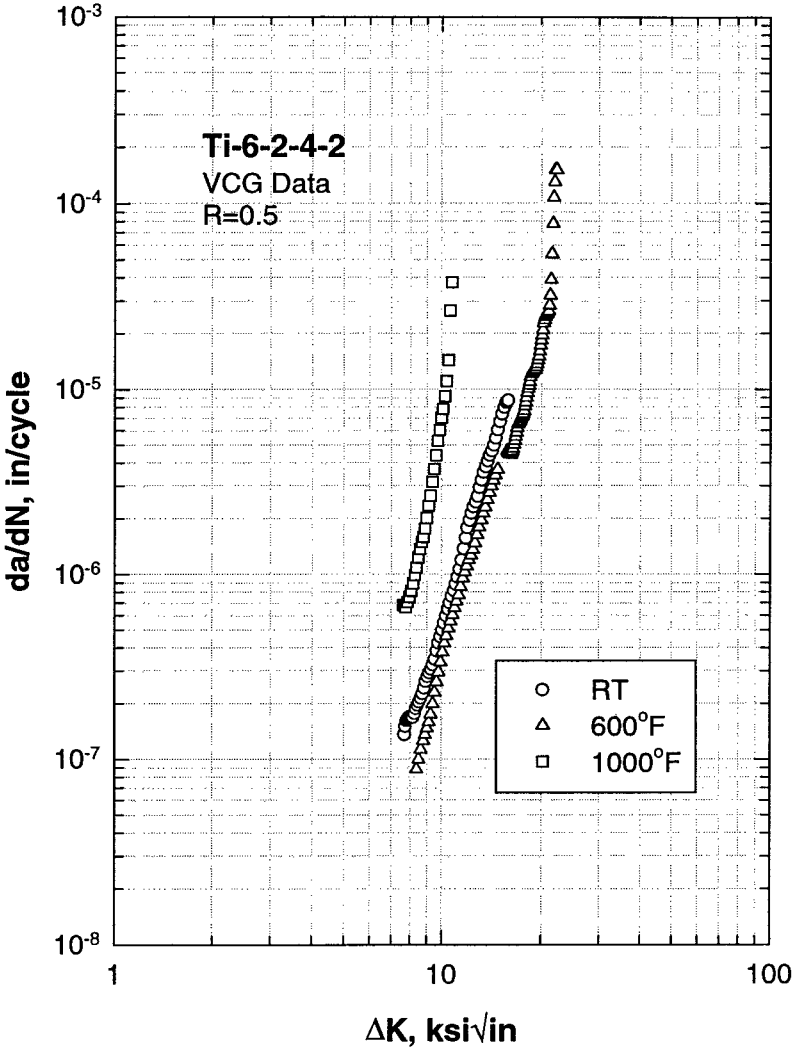


FIGURE I-27. VACUUM FCG DATA FOR Ti-6-2-4-2 AT ALL TEMPERATURES ($R = 0.5$)

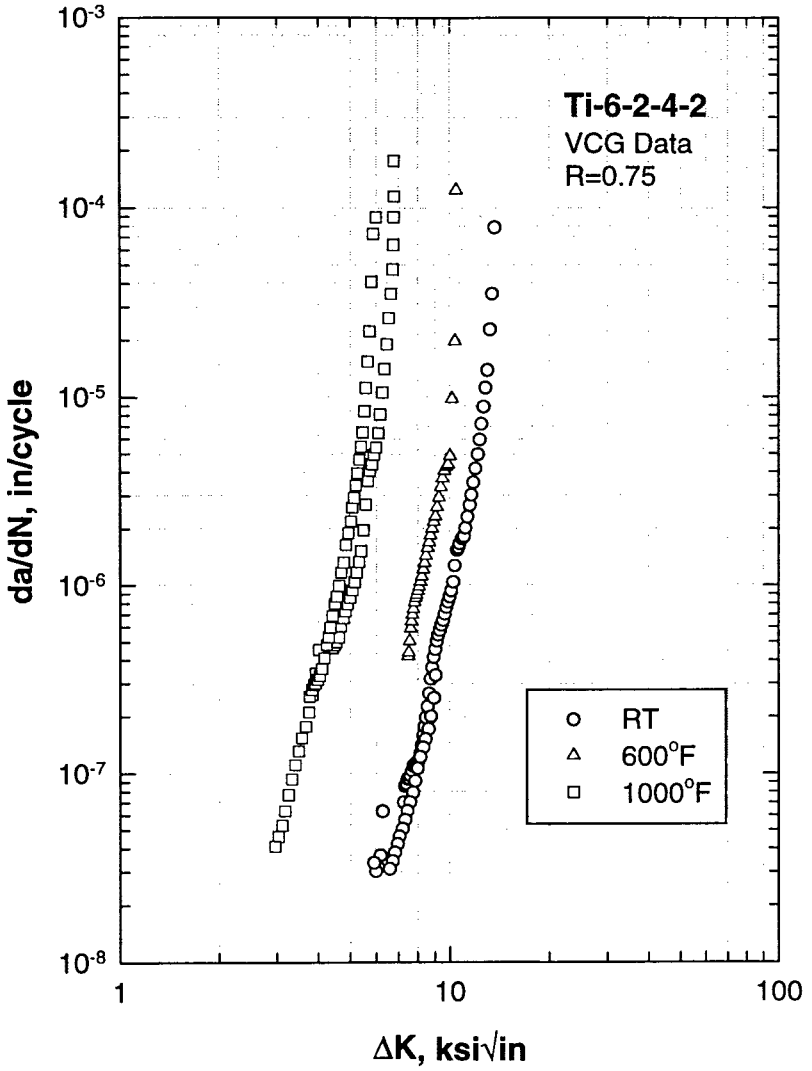


FIGURE I-28. VACUUM FCG DATA FOR Ti-6-2-4-2 AT ALL TEMPERATURES (R = 0.75)

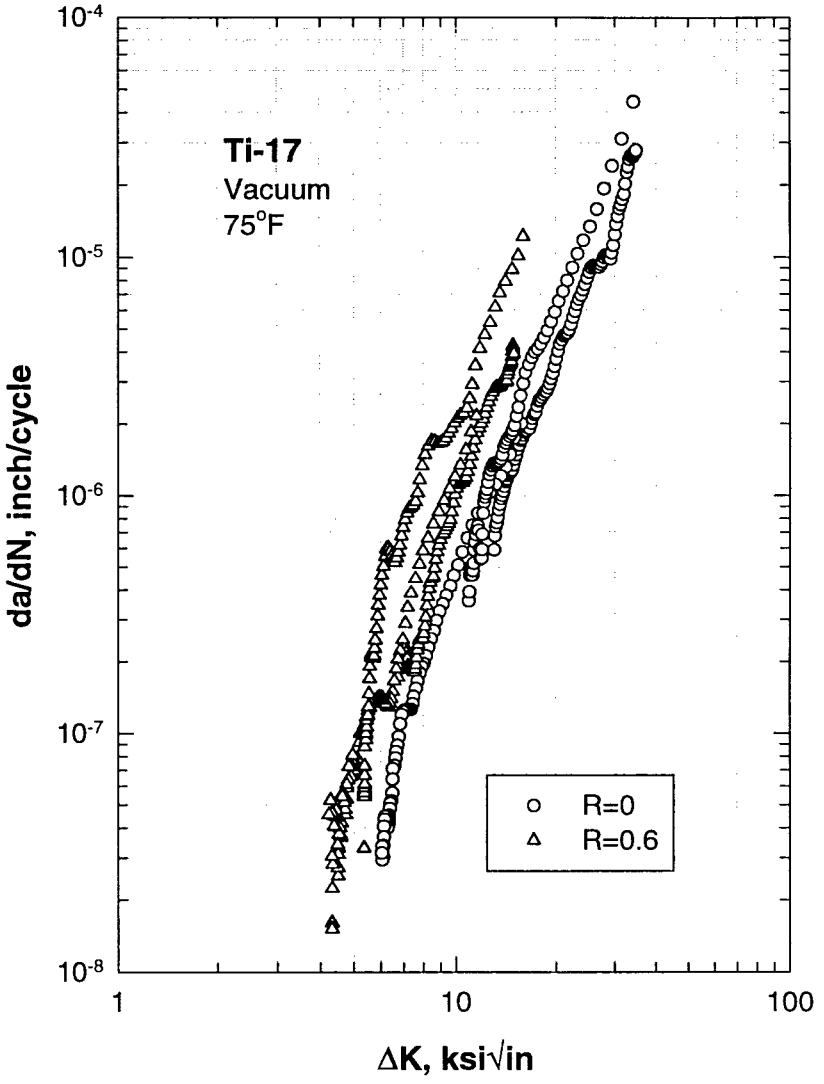


FIGURE I-29. VACUUM FCG DATA FOR Ti-17 AT BOTH STRESS RATIOS (75°F)

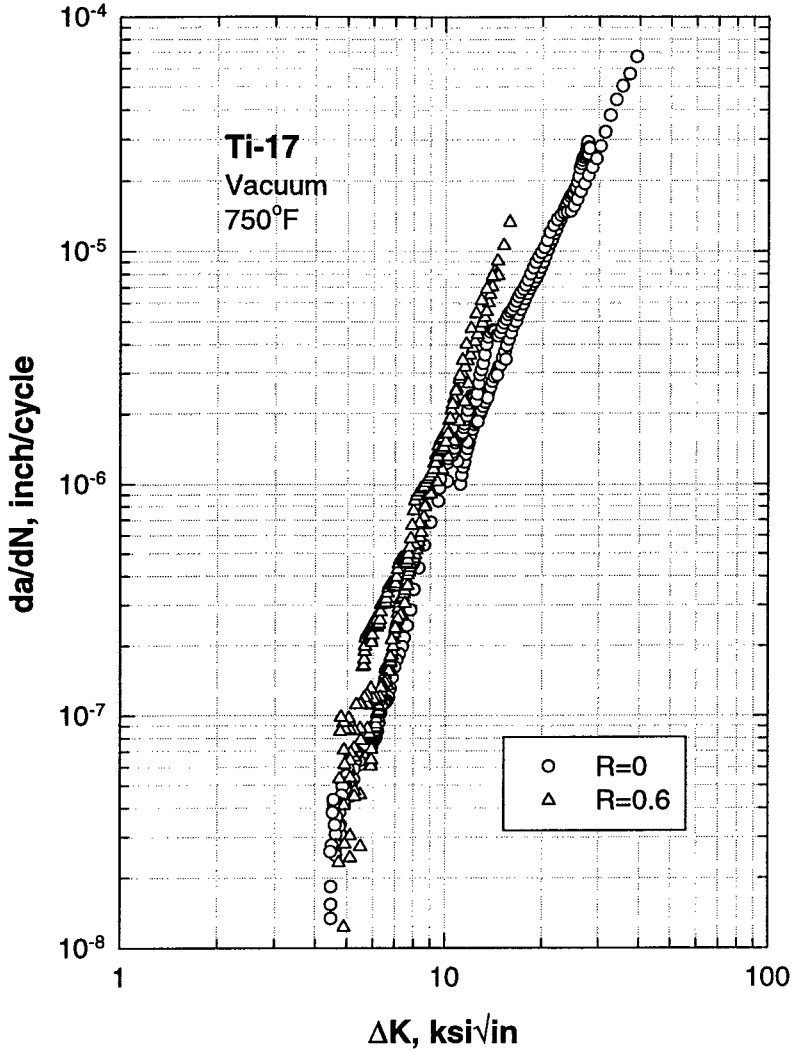


FIGURE I-30. VACUUM FCG DATA FOR Ti-17 AT BOTH STRESS RATIOS (750°F)

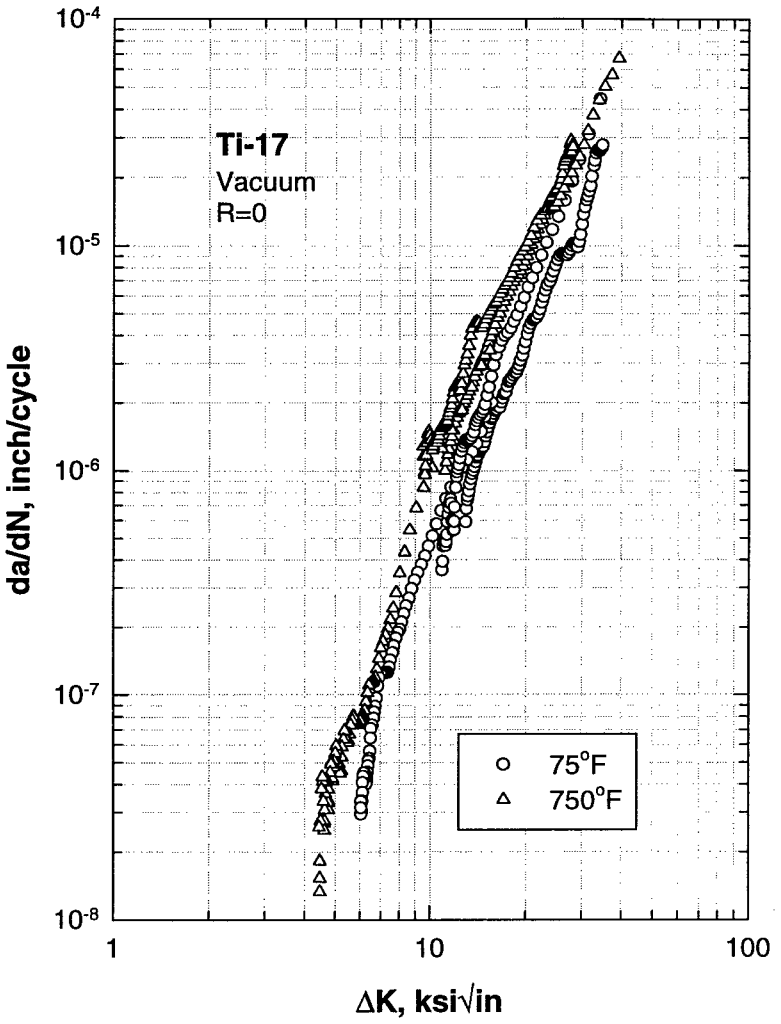


FIGURE I-31. VACUUM FCG DATA FOR Ti-17 AT BOTH TEMPERATURES ($R = 0$)

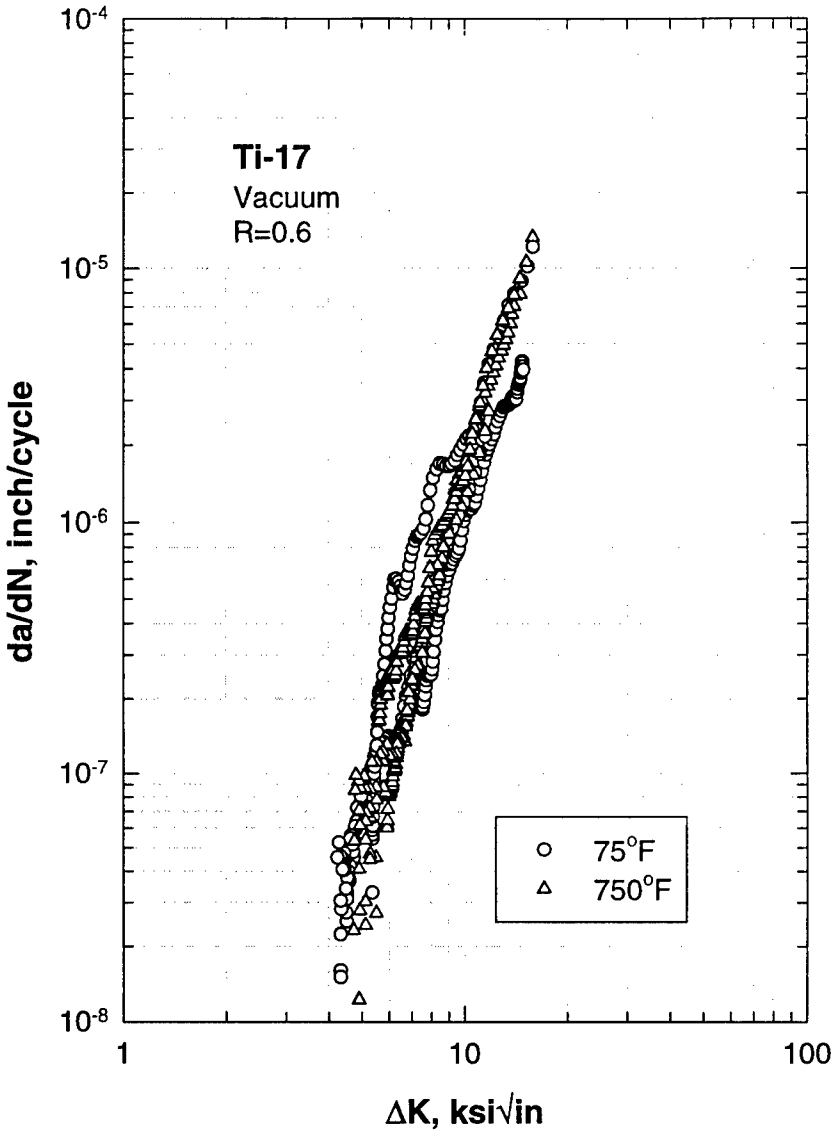


FIGURE I-32. VACUUM FCG FOR Ti-17 AT BOTH TEMPERATURES (R = 0.6)

Air FCG data for Ti-6-4 selected for comparison were originally provided to the DTDH by GEAE in October 1982 and were generated using Kb bar specimens in the TF34 Damage Tolerance Analysis (DTA) Effort. The material and test conditions as documented in the DTDH are summarized in table I-13. Some additional comparisons were made against Ti-6-4 air data provided to the DTDH compilers by P&W (DTDH Reference PW003) for which only limited documentation was available.

Air FCG data for Ti-6-2-4-2 selected for comparison were originally provided to the DTDH by P&W and were taken from an Air Force contract report [I-27]. The material and test conditions as documented in the DTDH are summarized in table I-14.

TABLE I-13. MATERIAL CONDITION AND TEST CONDITIONS FOR SELECTED Ti-6Al-4V AIR DATA FROM DAMAGE TOLERANT DESIGN HANDBOOK

Condition/HT: 1775°F 1 HR WQ 1675°F 1 HR WQ 1000°F – 1200°F 2-8 HR AC	
Form: 0.94 – 1.15-in. Disk	Yield Strength: 145 – 150 ksi
Specimen Type: Kb Bar	Ult. Strength:
Orientation: C-R	Specimen Thk: 0.251 – 0.253 in.
Frequency: 0.3 Hz	Specimen Width: 0.995 – 1.002 in
Environment: LAB AIR	Ref: GE007
Temperature: RT, 300°F, 600°F	
Stress Ratios: 0.03, 0.25, 0.54	

TABLE I-14. MATERIAL CONDITION AND TEST CONDITIONS FOR SELECTED Ti-6-2-4-2 AIR DATA FROM DAMAGE TOLERANT DESIGN HANDBOOK

Condition/HT: 1790°F 1 HR AC 1100°F 8 HR AC	
Form: 2-in. Forging	Yield Strength: 139.4 – 140.9 ksi
Specimen Type: CCP (max load specified)	Ult. Strength: 151.6 – 152.3 ksi
Orientation: C-R	Specimen Thk: 0.073 – 0.083 in.
Frequency: 0.16 – 30 Hz	Specimen Width: 1.75 in
Environment: LAB AIR	Ref: PW002
Temperature: 80°F, 800°F, 1000°F	
Stress Ratios: 0.1, 0.5, 0.7	

Comparisons of the current vacuum data against scatterbands constructed from the DTDH air data are shown graphically in figures I-33 through I-40. In general, the vacuum and air data exhibited similar growth rates in the upper Paris regime, sometimes denoted as Region II growth. Cracks in vacuum grew at much slower rates than cracks in air at lower ΔK values, and vacuum data exhibited higher apparent values of the fatigue crack growth threshold, ΔK_{th}. These general trends appear to hold for both materials examined at all stress ratios and temperatures examined. The same general trends were observed in the open literature reviewed previously [I-1 – I-11].

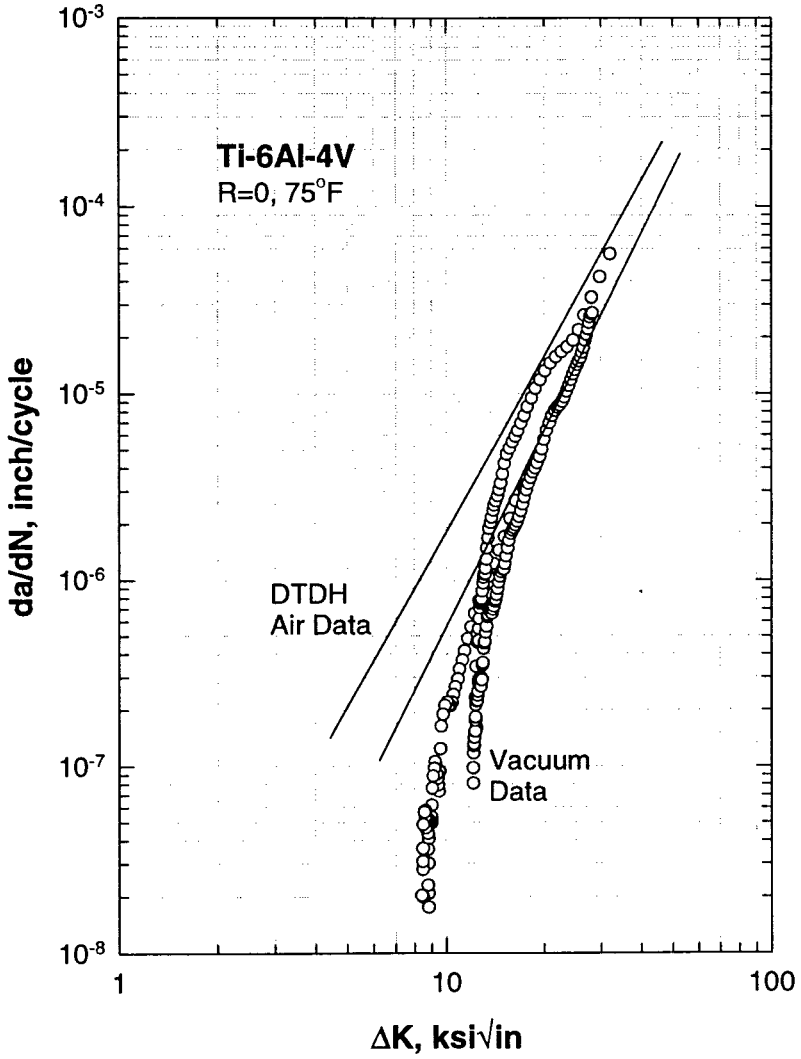


FIGURE I-33. COMPARISON OF VACUUM FCG DATA WITH AIR DATA FROM DTDH FOR Ti-6Al-4V AT 75°F AND $R = 0$

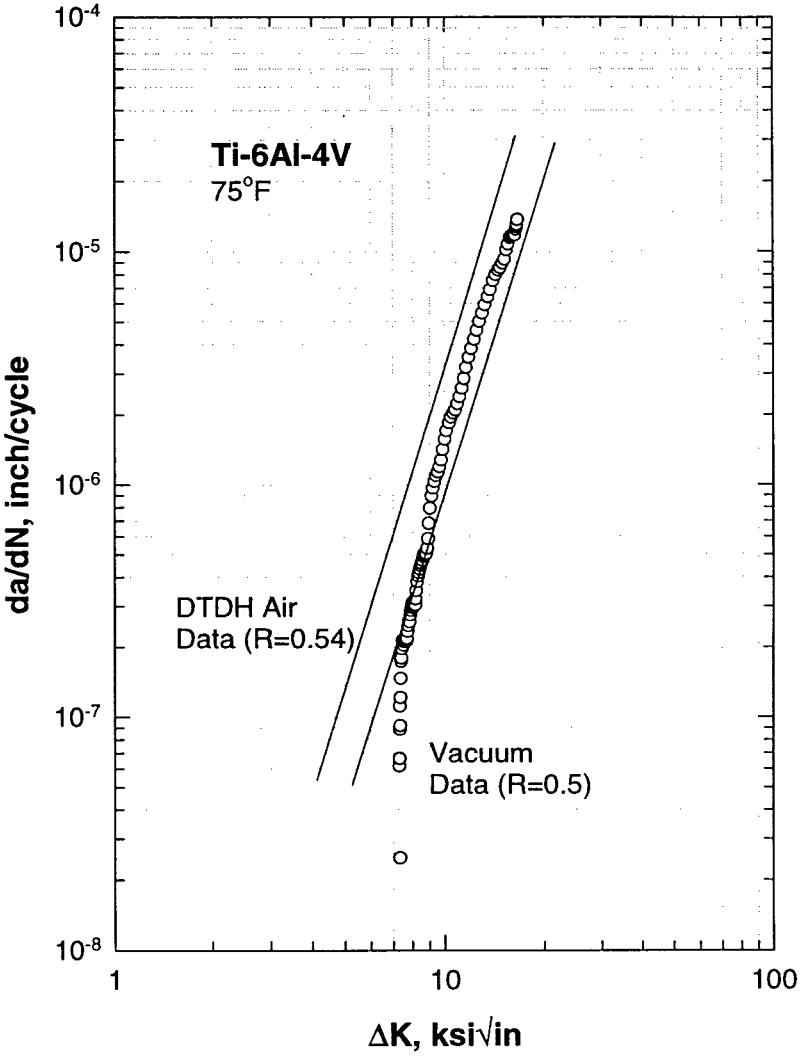


FIGURE I-34. COMPARISON OF VACUUM FCG DATA WITH AIR DATA FROM DTDH FOR Ti-6Al-4V AT 75°F AND $R = 0.5$

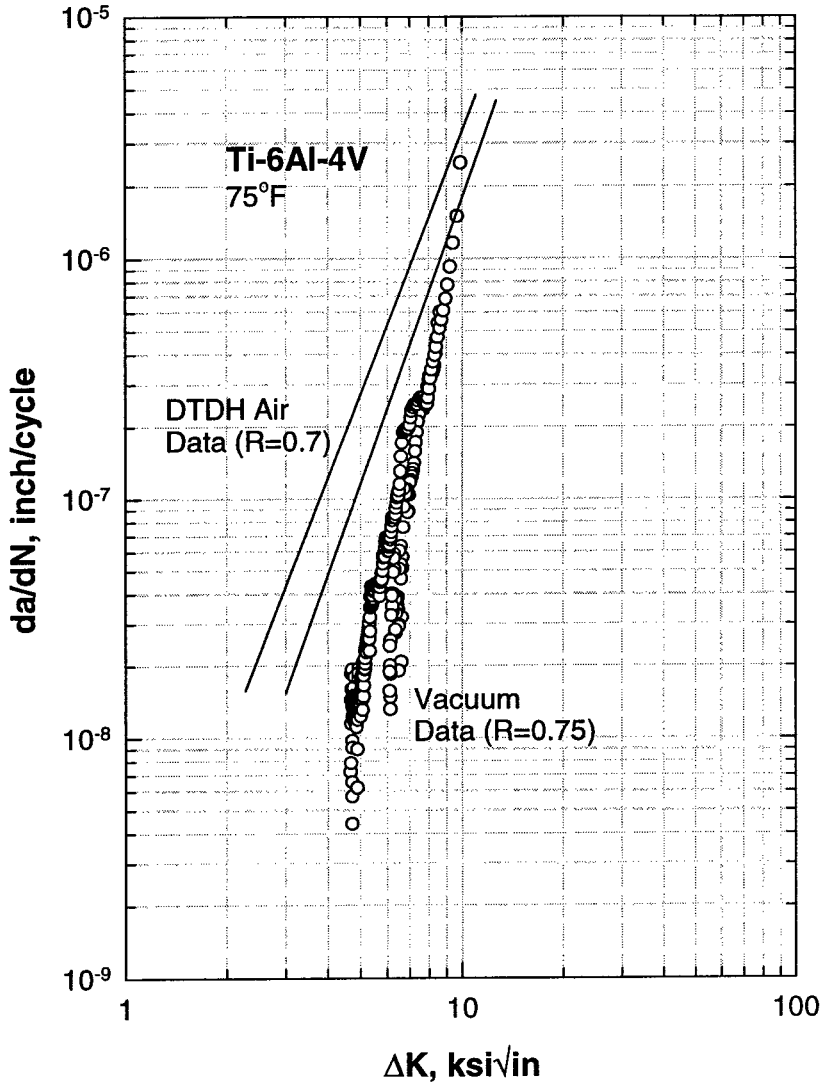


FIGURE I-35. COMPARISON OF VACUUM FCG DATA WITH AIR DATA FROM DTDH FOR Ti-6Al-4V AT 75°F AND $R = 0.75$

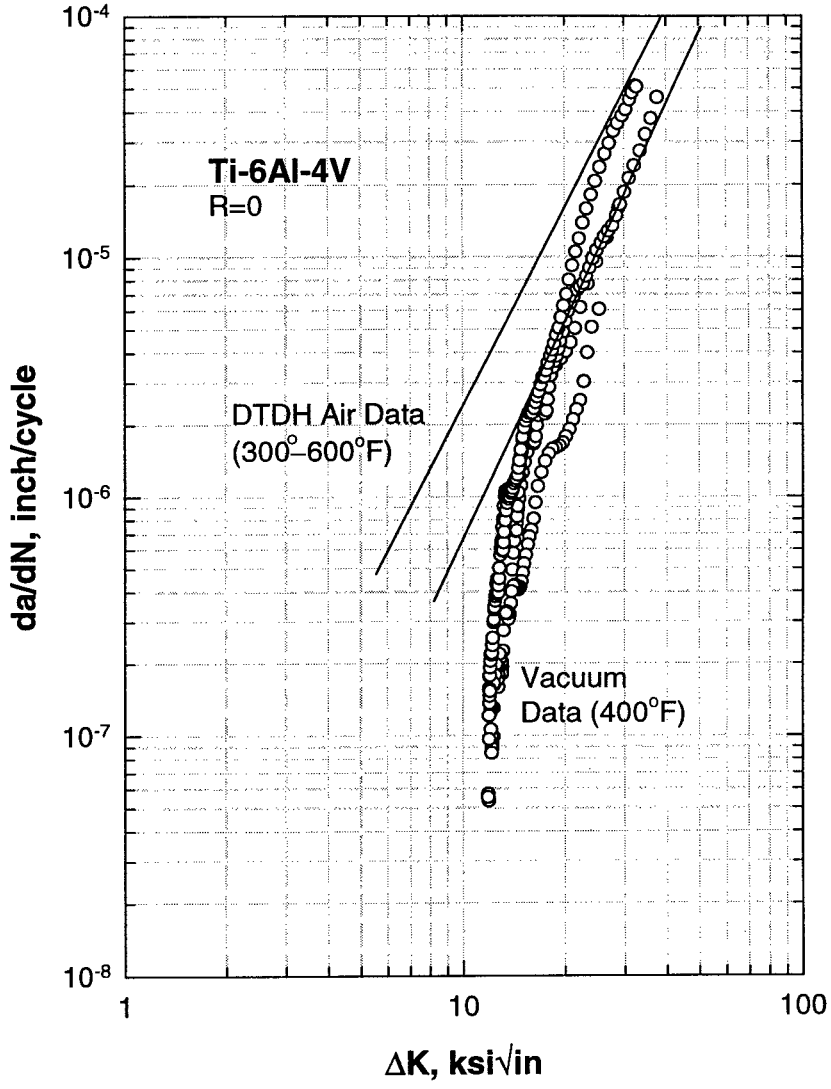


FIGURE I-36. COMPARISON OF VACUUM FCG DATA WITH AIR DATA FROM DTDH FOR Ti-6Al-4V AT 300°-600°F AND $R = 0$

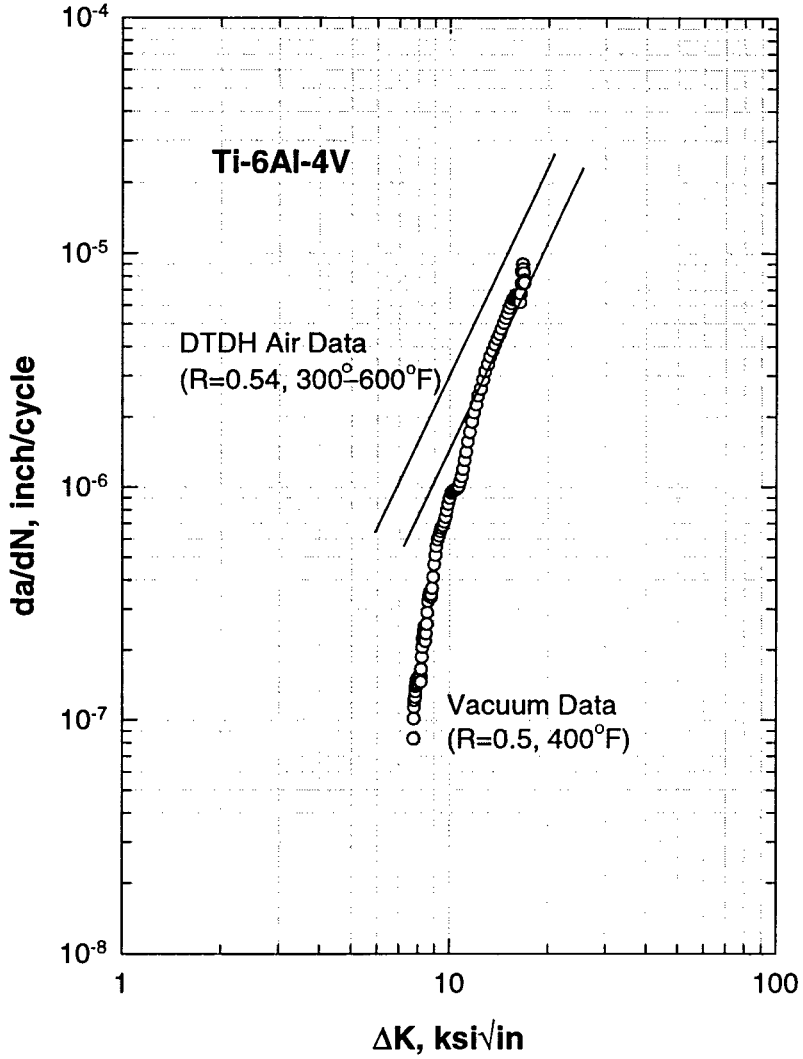


FIGURE I-37. COMPARISON OF VACUUM FCG DATA WITH AIR DATA FROM DTDH FROM Ti-6Al-4V AT 300°-600°F AND $R = 0.5$

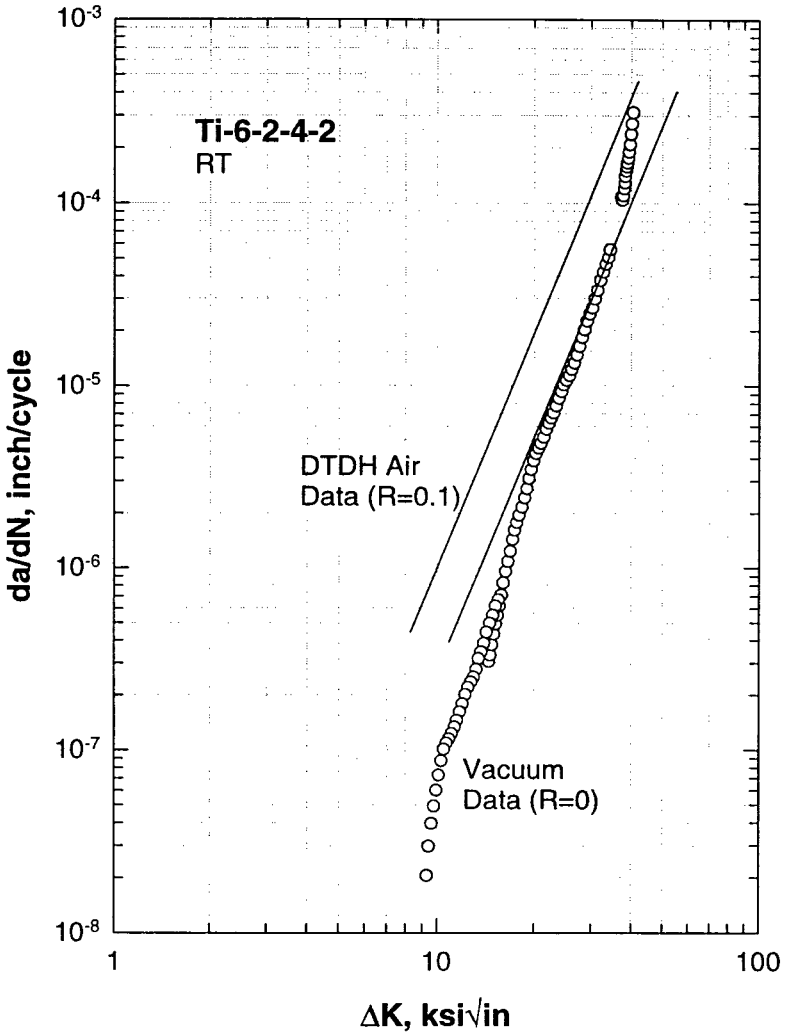


FIGURE I-38. COMPARISON OF VACUUM FCG DATA WITH AIR DATA FROM DTDH FOR Ti-6-2-4-2 AT 75°F AND $R = 0$

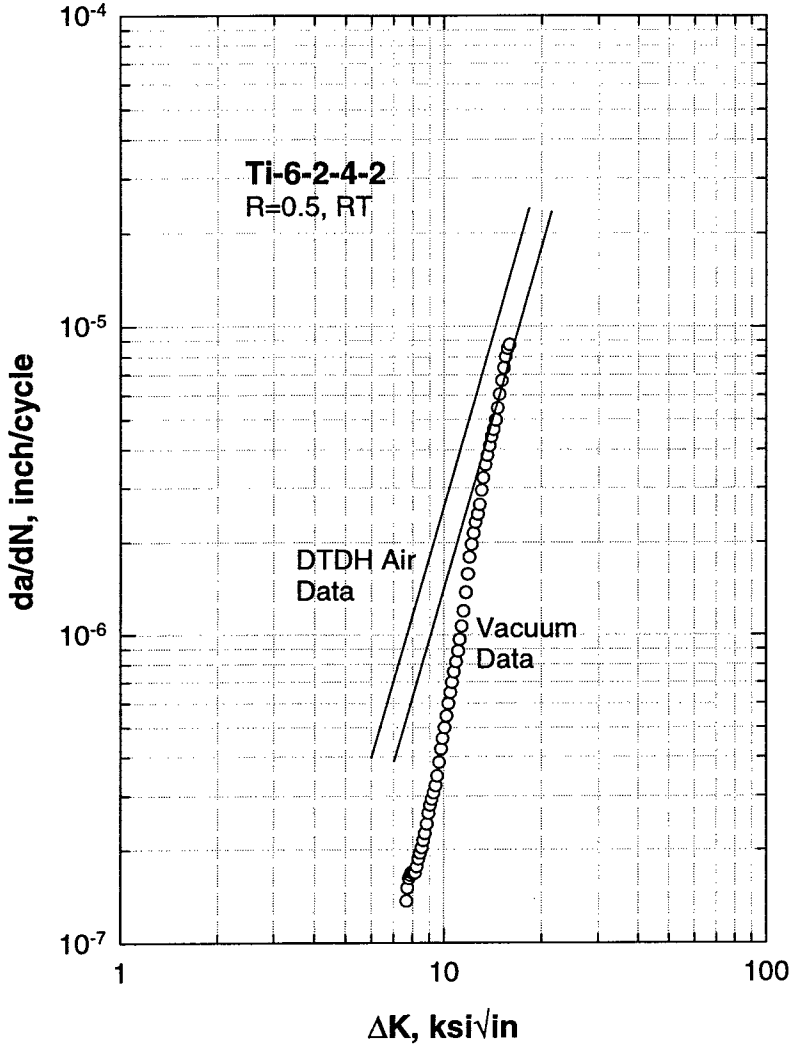
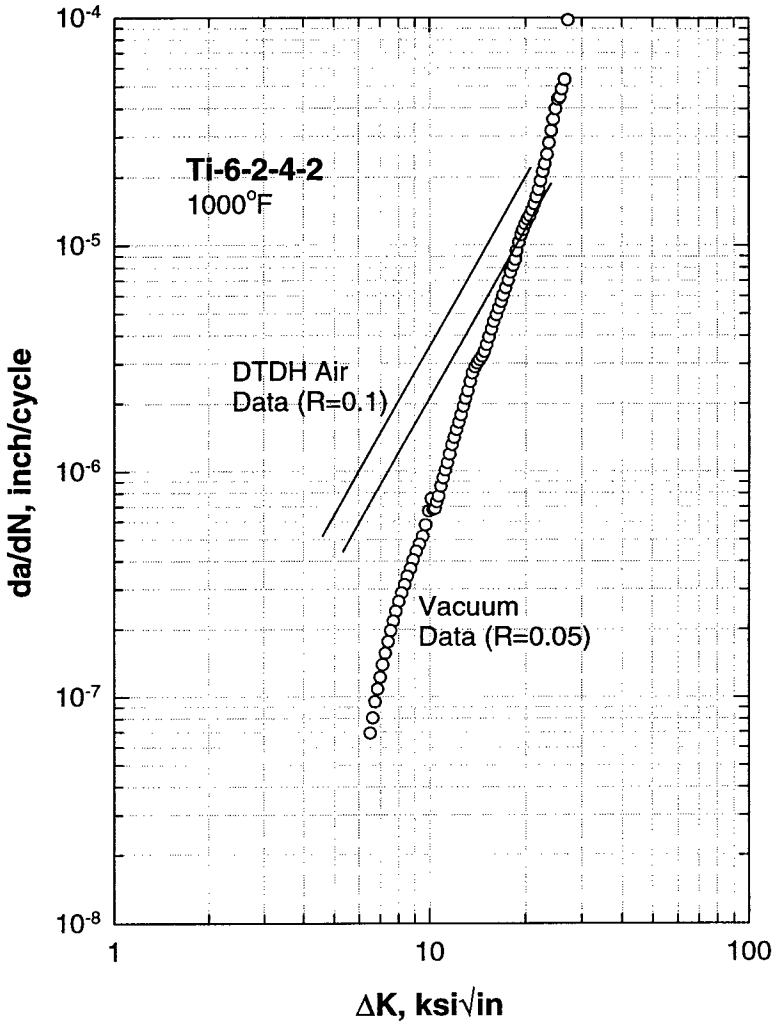


FIGURE I-39. COMPARISON OF VACUUM FCG DATA WITH AIR DATA FROM DTDH FOR Ti-6-2-4-2 AT 75°F AND $R = 0.5$



FGURE I-40. COMPARISON OF VACUUM FCG DATA WITH AIR DATA FROM DTDH FOR Ti-6-2-4-2 AT 1000°F AND $R = 0$

The true significance of these differences in growth rates is reflected in the differences in lifetime predictions for vacuum vs. air properties. In order to illustrate these lifetime differences, a simple set of reference life calculations was performed using the room temperature Ti-6-4 vacuum and air properties shown in figures I-33 and I-35. In these calculations, an initial embedded crack with circular shape was assumed to exist in an infinite body subjected to remote, constant amplitude, uniaxial tension cycling. The crack growth life to failure (the critical fracture toughness K_c = 58 ksi$\sqrt{in}$. was assumed to be the same for air and vacuum) was calculated as a function of the initial crack size.

The specific crack growth equations used in this comparison are illustrated in figure I-41 for $R = 0$. Note that the vacuum and air regression lines cross at a high growth rate. In reality, however, the data do not cross, but rather merge at high growth rates. The observed crossing in figure I-41 is an extrapolation artifact of the simple equation form. Therefore, to avoid overpredicting vacuum growth rates at high ΔK values, a bilinear equation was adopted which follows the actual vacuum data at low ΔK, but follows the air regression line above the crossing point, up to the fracture toughness. This bilinear equation is also shown in figure I-41 (the slight offsets were included for visual clarity and do not indicate any shift in the actual bilinear equation).

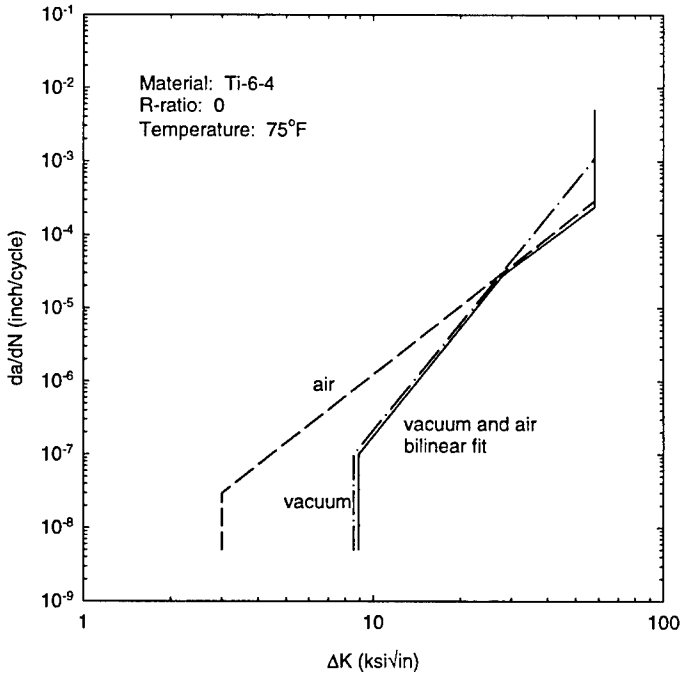


FIGURE I-41. VACUUM AND AIR FCG MODELS USED FOR LIFETIME COMPARISONS

The resulting lifetime comparisons for vacuum vs. air are shown in figure I-42 for three different maximum stresses at $R = 0$. Similar results (not shown here) were found for $R = 0.75$. Both the single linear vacuum and bilinear vacuum plus air results are shown to illustrate the small difference that the bilinear correction makes.

The threshold crack size (the smallest crack size that will grow) under vacuum conditions is about three times larger than the threshold crack size under air for these conditions. The fatigue lifetime for this threshold crack size is about three times longer in vacuum than for the same crack size in air.

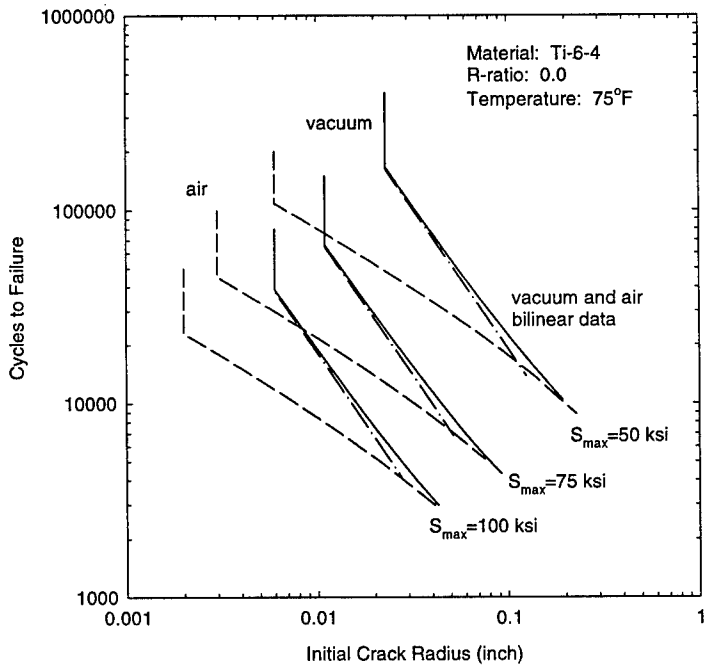


FIGURE I-42. COMPARISON OF FCG LIFETIMES FOR EMBEDDED CIRCULAR CRACKS BASED ON VACUUM AND AIR PROPERTIES

I.5.3 DATA REGRESSIONS.

One of the principal deliverables of the FAA program supporting this study is a probabilistic damage tolerance computer code called Design Assessment of Reliability With INspection (DARWIN). DARWIN includes a default FCG analysis module called Flight_Life, which was specifically designed with the capabilities and computational speed for the probabilistic rotor integrity problem. Flight_Life provides different options for common FCG equations and models for stress ratio and temperature effects, along with tabular FCG data capability and a user-defined equation module. Flight_Life also permits FCG properties to change automatically from vacuum to air at embedded-to-surface transitions. Further information on DARWIN and Flight_Life is provided in section 2.5 of the main body of this report.

A variety of statistical regressions of the vacuum FCG data were performed in order to obtain library properties for the DARWIN code. The regressions documented in this report are based on a simple Paris equation with and without various stress ratio models. Near-threshold data were regressed independently to obtain values of the FCG threshold.

I.5.3.1 Paris Regressions.

The basic Paris equation (with no stress ratio model) is given by the form

$$\frac{da}{dN} = C(\Delta K)^n \tag{I-3}$$

where C and n are empirically determined regression constants. Regressions of this form were performed on each data set at a given stress ratio and temperature.

The Paris equation with a Walker stress ratio model is given by

$$\frac{da}{dN} = C\left(\Delta K_{eff}\right)^n \tag{I-4}$$

where

$$\Delta K_{eff} = U_W \Delta K \tag{I-5}$$

and

$$U_W = (1 - R)^{m-1} \tag{I-6}$$

Here the stress ratio, R, is given by $R = K_{min}/K_{max}$. The Walker exponent m takes the different values m^+ when $R \geq 0$ and m^- when $R < 0$. However, since no vacuum data were generated at $R < 0$, the regressions here can only determine values of m^+.

The Paris equation with a Newman crack closure model is given by

$$\frac{da}{dN} = C\left(\Delta K_{eff}\right)^n \tag{I-7}$$

where

$$\Delta K_{eff} = U_C \Delta K \tag{I-8}$$

and

$$U_C = \frac{1 - S_{open} / S_{max}}{1 - R} \tag{I-9}$$

Here U_c has physical meaning as the effective stress-intensity factor range ratio. The crack opening stress ratio, S_{open}/S_{max}, is calculated based on equations derived by Newman [I-28]. For simplicity, the dependence of S_{open}/S_{max} on S_{max}/σ_0 in the original Newman equations has been eliminated by setting $S_{max}/\sigma_0 = 0.6$ in both the current regressions and the current DARWIN

implementation of the Newman model. This simplification leaves S_{open}/S_{max} as a function of stress ratio, R, and the Newman constraint factor, α, which now serves as a fitting parameter. However, in order to preserve some semblance of physical meaning, the Newman constraint factor was limited to the range $1 \leq \alpha \leq 3$.

Note that the effective stress range ratio, ΔK_{eff}, has an entirely different interpretation in the Walker and Newman formulations. In the Newman closure formulation, $\Delta K_{eff}/\Delta K \leq 1$, while in the Walker formulation, $\Delta K_{eff}/\Delta K \geq 1$. The Walker U_W and the Newman closure U_C have no direct relationship to each other.

All of these regressions involved a single linear Paris relationship with no curvature for threshold or instability, but many of the data sets included the conventional deviations from linearity near threshold or near instability. Therefore, before these regressions were conducted, engineering judgement was applied to censor those data near threshold or near instability that exhibited noticeable deviations from the Region II linear trends, in order to insure that the regressions would most accurately represent the Region II data.

The regressions are documented graphically in figures I-43 through I-73. Each figure documents a single regression and shows all data sets grouped together for that particular regression. All data in each data set are shown, including any censored data not included in the regression analysis, in order to permit the reader to assess the suitability of the regression for the available data. Individual specimens and test segments (e.g., K-increasing or K-decreasing portions of a particular test) are denoted by different symbols. These specimen and segment identifications are the same as those employed in the tabulated test data in tables I-4 through I-12. Note that in a few cases, data from two temperatures were grouped together into a single data set for a single regression, when the temperature appeared to have no significant impact on the FCG behavior.

Figures I-43 through I-52 show the regressions for Ti-6-4, while figures I-53 through I-65 show Ti-6-2-4-2 regressions and figures I-66 through I-73 show Ti-17 regressions. For each material, individual Paris regressions are documented first, followed by regressions for the Walker and then the Newman crack closure stress ratio models.

Note that included in figure I-44 are the data from the brief frequency effect study. Ti-6-4 data for 400°F collected at 1 Hz and 0.33 Hz exhibited similar growth rates.

The significantly higher growth rates observed in the Kb bar specimen for Ti-6-4 at 400°F, $R = 0.75$, in comparison to the SEN data at the same conditions, raised some concerns (see again figure I-48). A replicate Kb bar test (data not shown here) gave nearly identical results to the first Kb bar test. Therefore, the data appear to accurately reflect the response of a growing fatigue crack in a Kb bar specimen. The difference between the Kb and SEN data may be related to time-dependent deformation at elevated temperatures under high mean stresses in the Kb bar specimen.

All calculated regression constants are documented in tables I-15 through I-17: table I-15 for Ti-6-4, table I-16 for Ti-6-2-4-2, and table 5-17 for Ti-17.

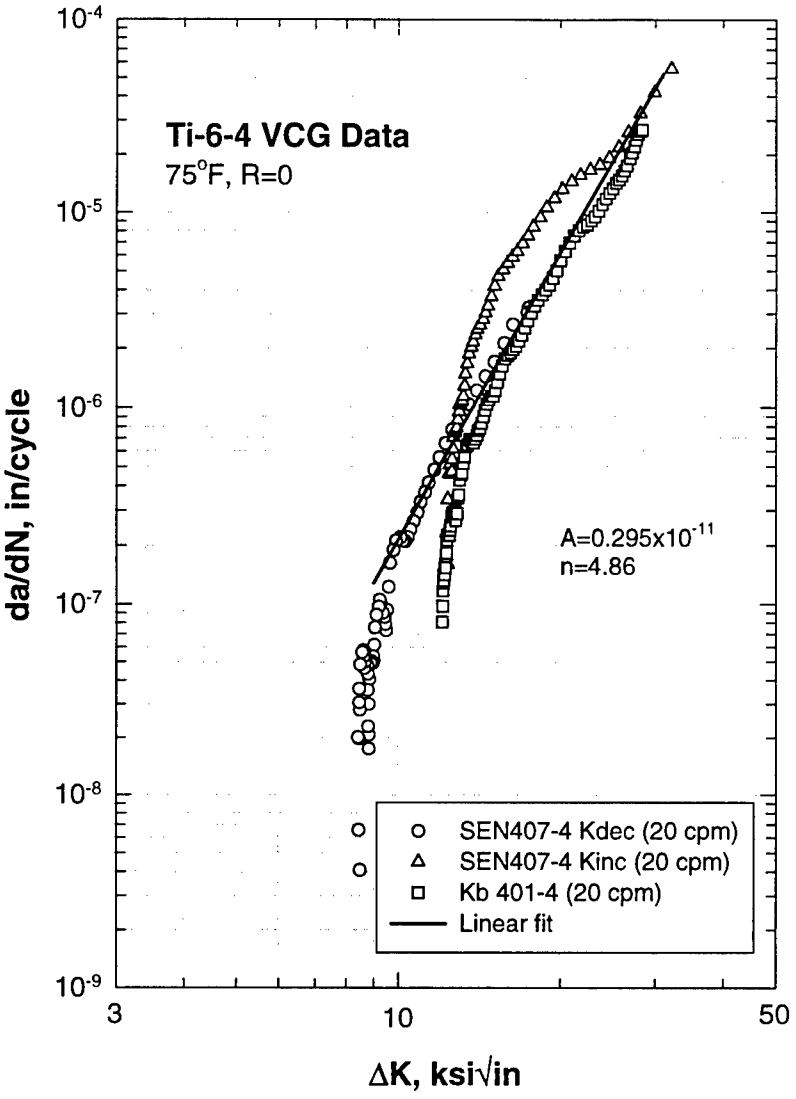


FIGURE I-43. VACUUM FCG DATA AND PARIS REGRESSION FOR Ti-6Al-4V AT 75°F, *R*=0

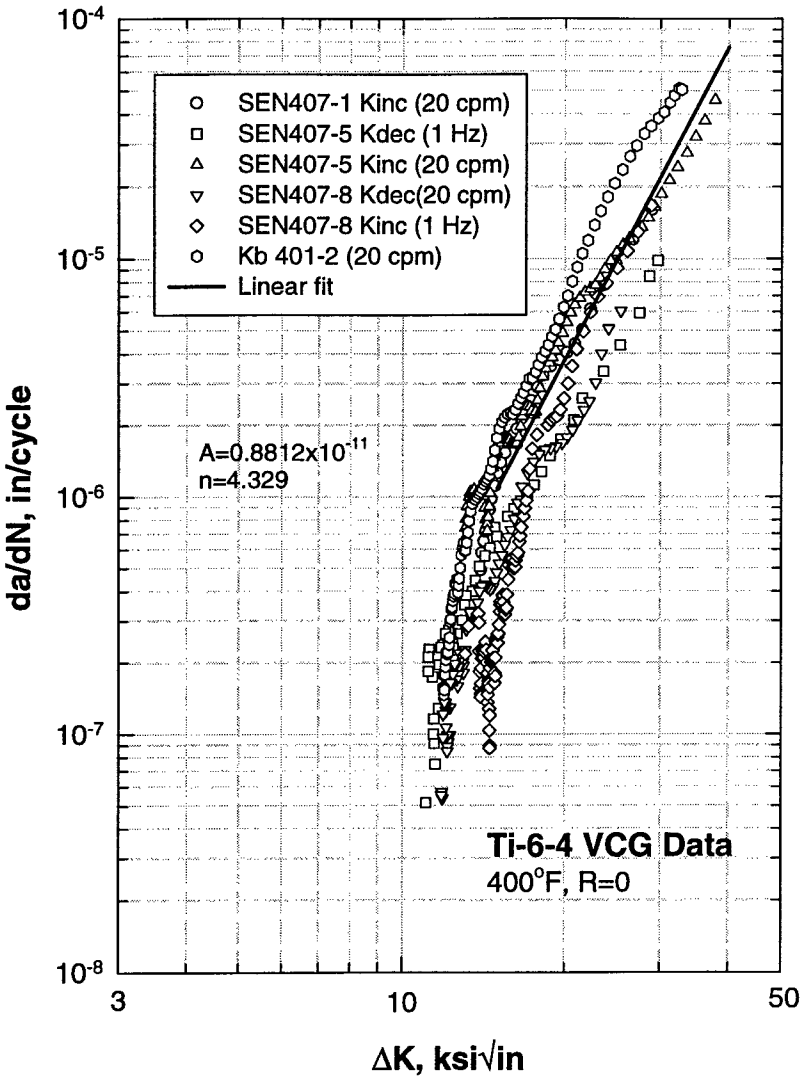


FIGURE I-44. VACUUM FCG DATA AND PARIS REGRESSION FOR Ti-6Al-4V AT 400°F, $R = 0$

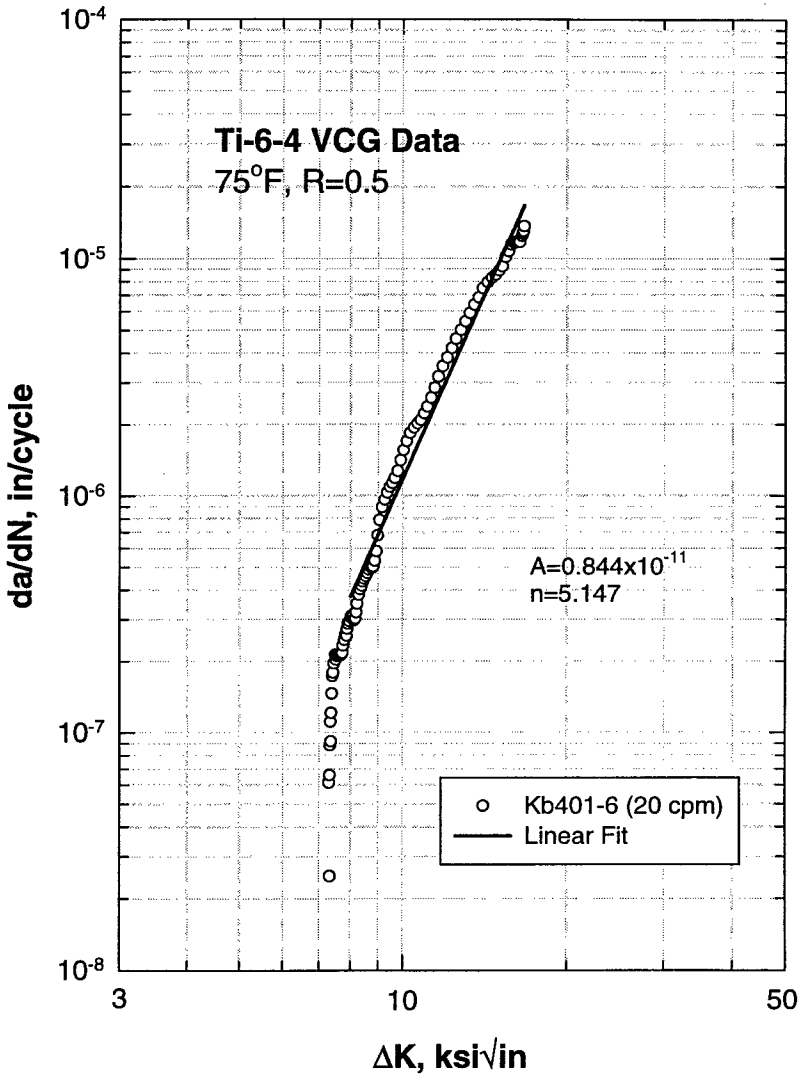


FIGURE I-45. VACUUM FCG DATA AND PARIS REGRESSION FOR Ti-6Al-4V AT 75°F, $R = 0.5$

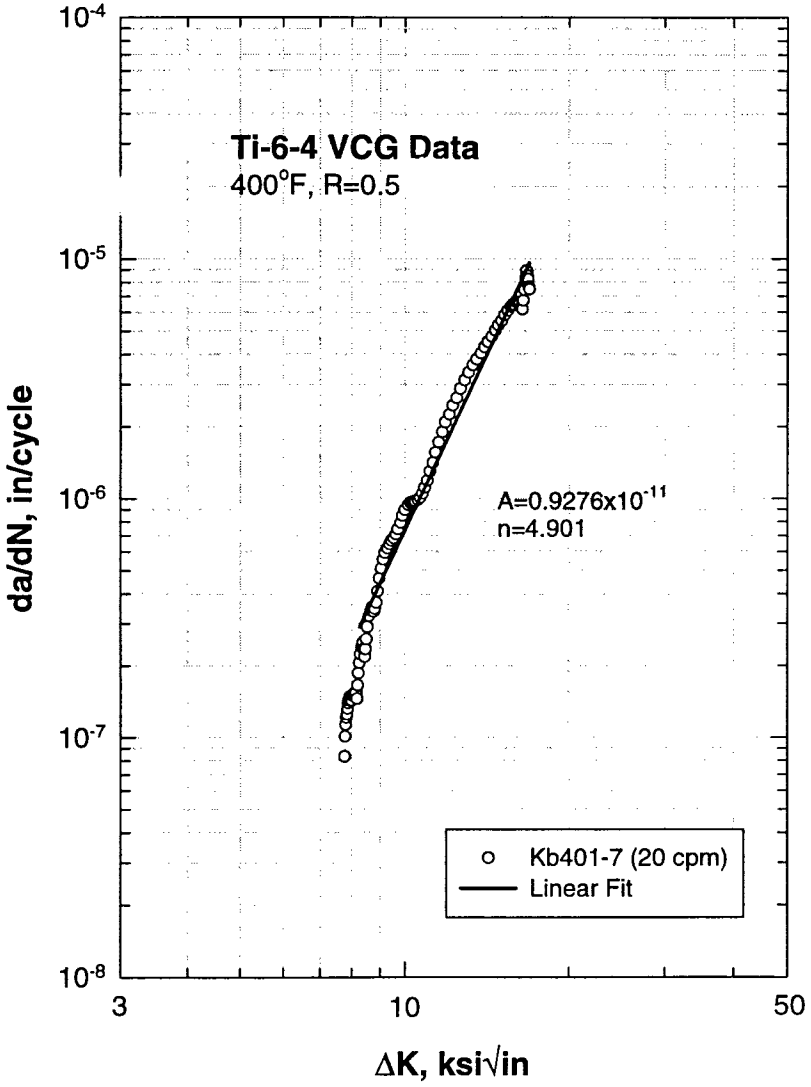


FIGURE I-46. VACUUM FCG DATA AND PARIS REGRESSION FOR Ti-6Al-4V AT 400°F, $R = 0.5$

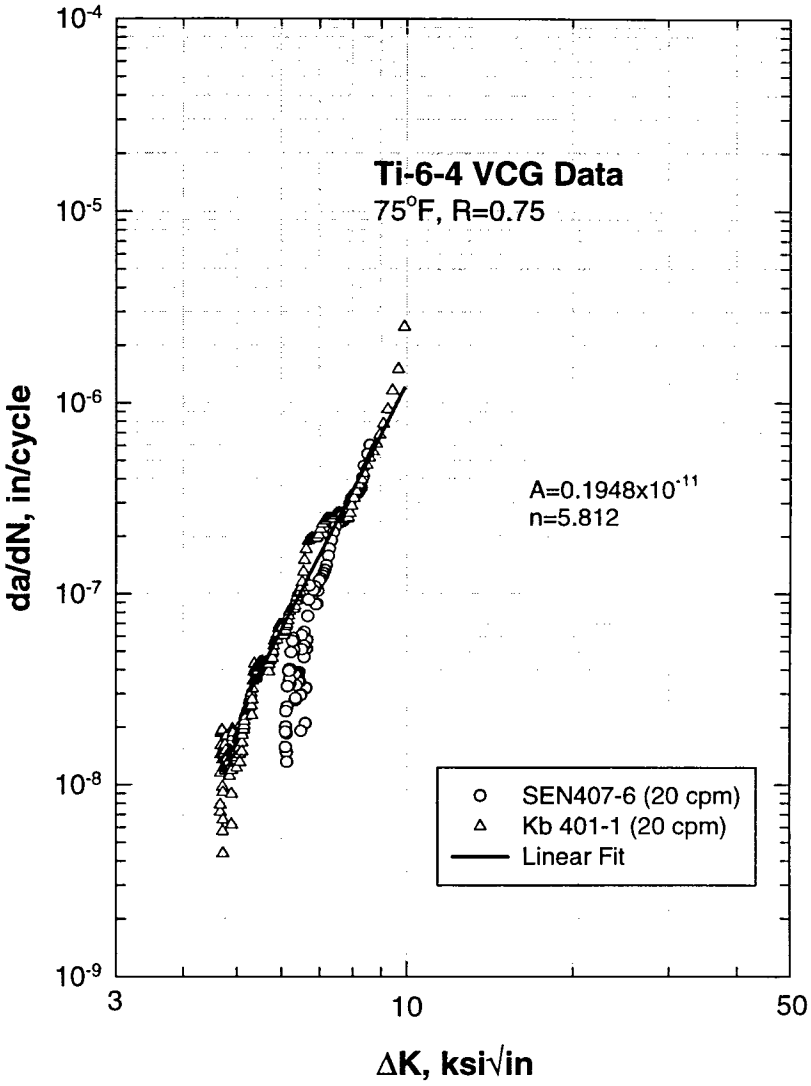


FIGURE I-47. VACUUM FCG DATA AND PARIS REGRESSION FOR Ti-6Al-4V AT 75°F, $R = 0.75$

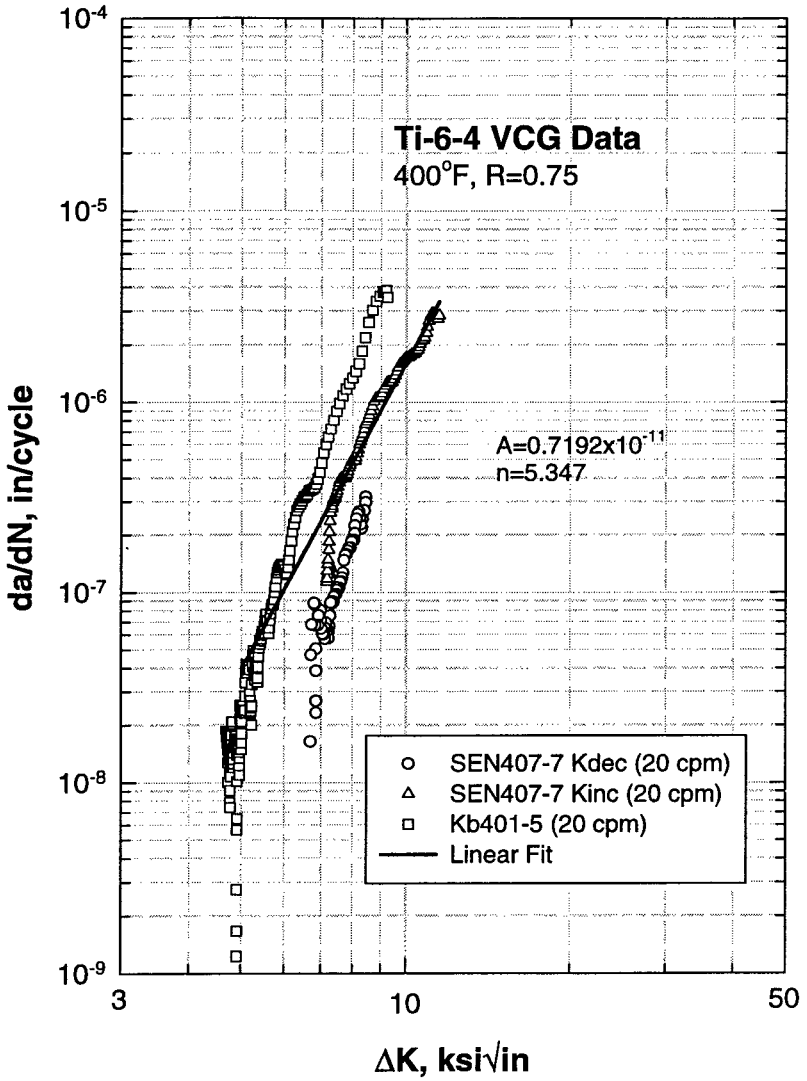


FIGURE I-48. VACUUM FCG DATA AND PARIS REGRESSION FOR Ti-6Al-4V AT 400°F, $R = 0.75$

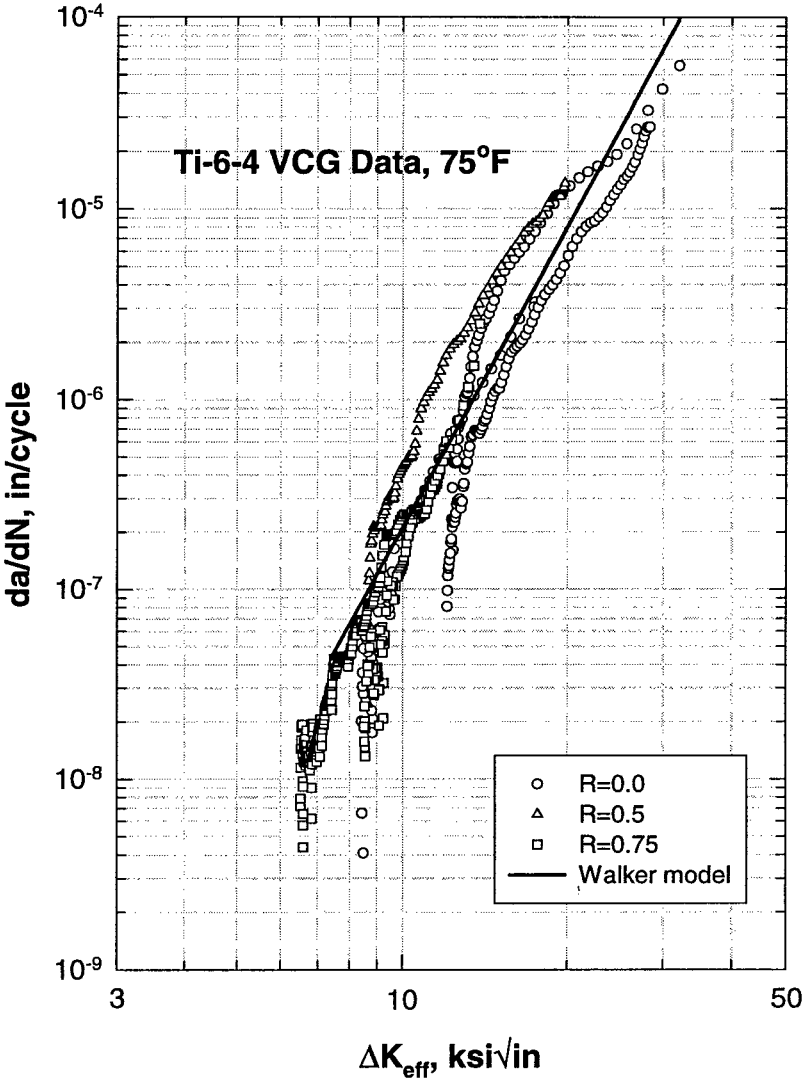


FIGURE I-49. VACUUM FCG DATA AND WALKER MODEL REGRESSION FOR Ti-6Al-4V AT 75°F

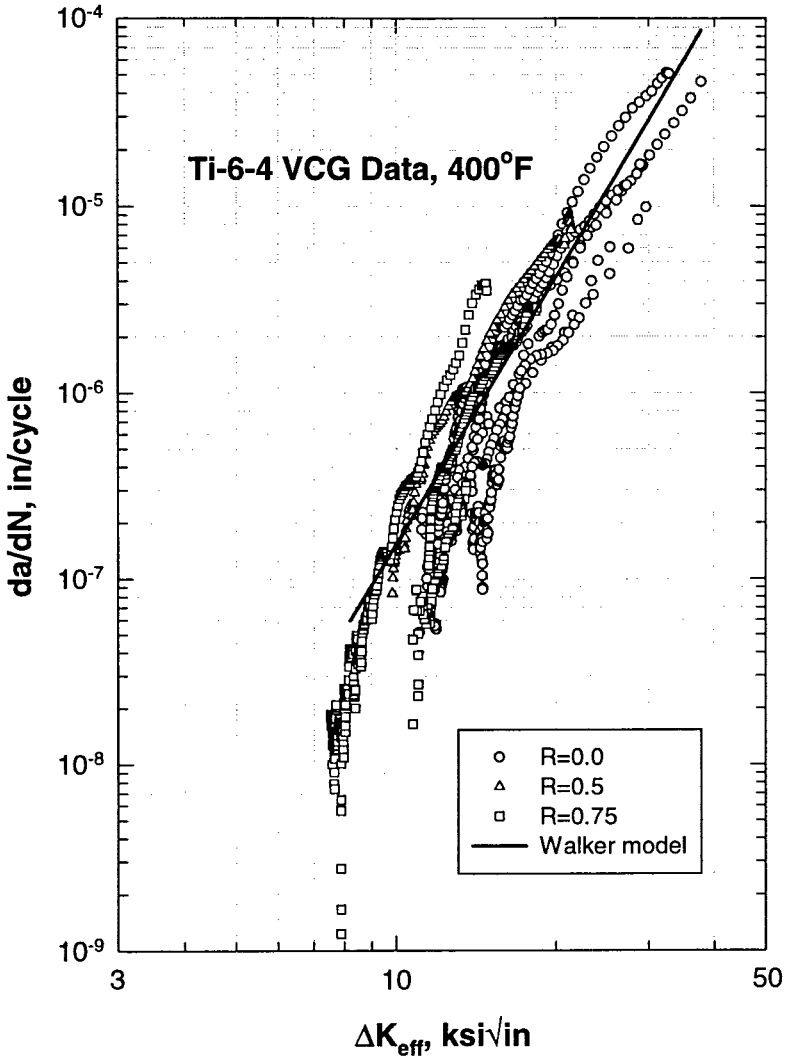


FIGURE I-50. VACUUM FCG DATA AND WALKER MODEL REGRESSION FOR Ti-6Al-4V AT 400°F

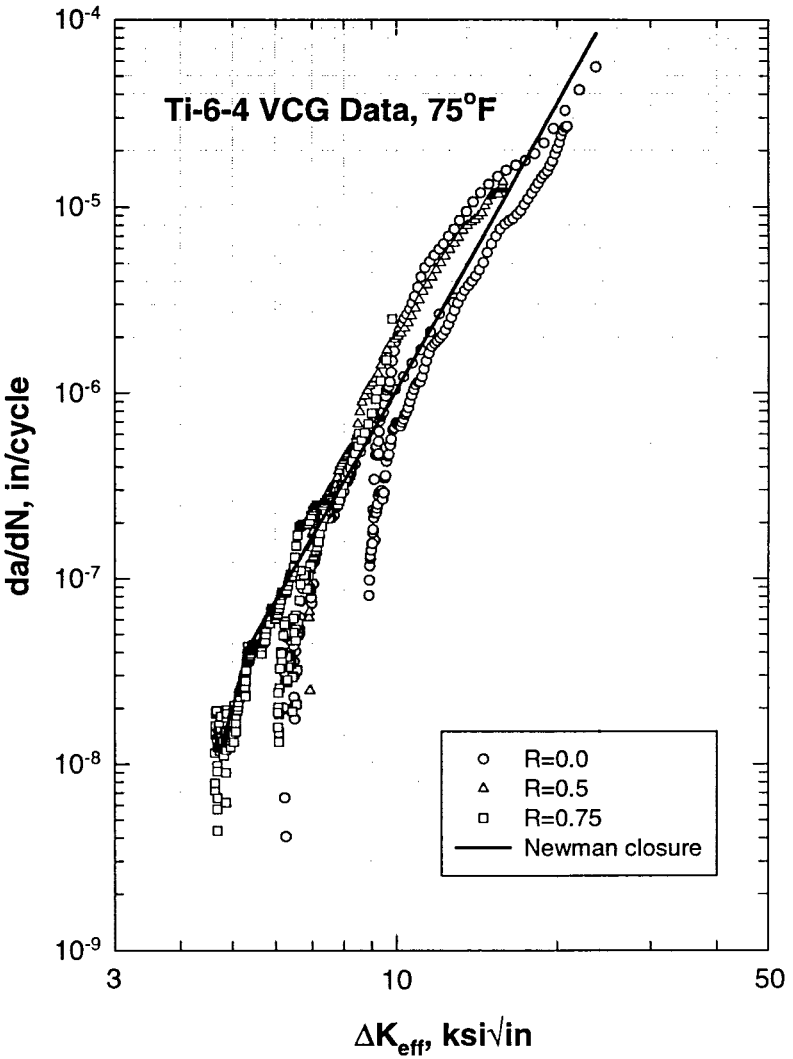


FIGURE I-51. VACUUM FCG DATA AND NEWMAN CLOSURE MODEL REGRESSION FOR Ti-6Al-4V AT 75°F

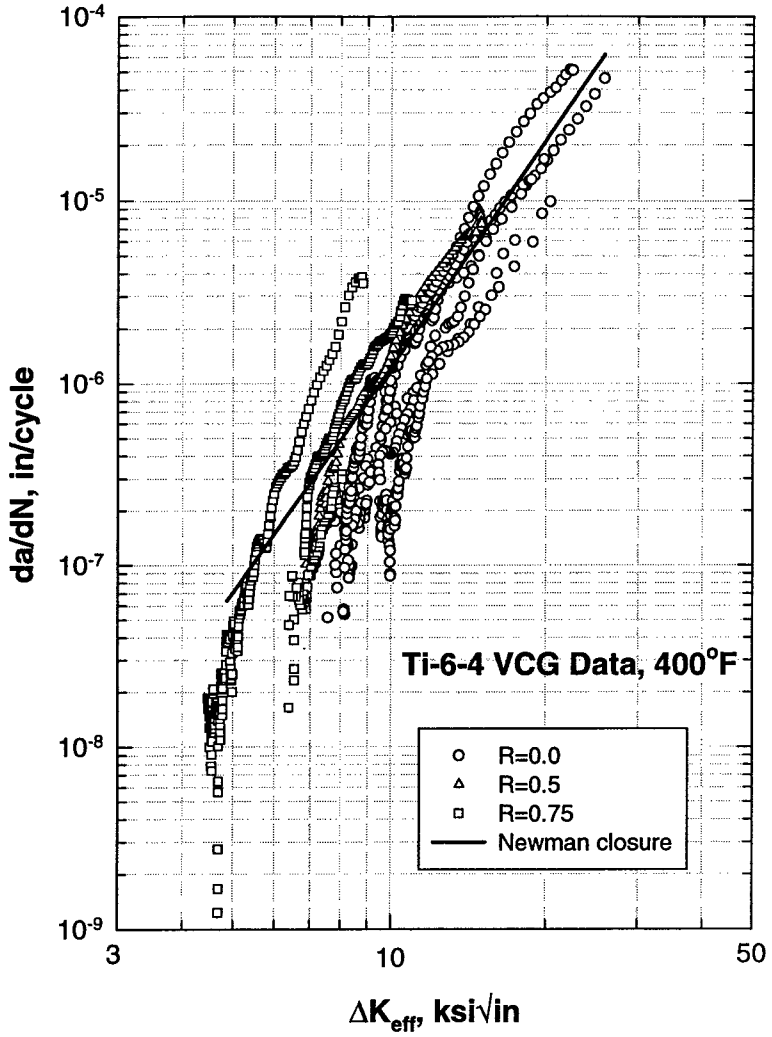


FIGURE I-52. VACUUM FCG DATA AND NEWMAN CLOSURE MODEL REGRESSION FOR Ti-6Al-4V AT 400°F

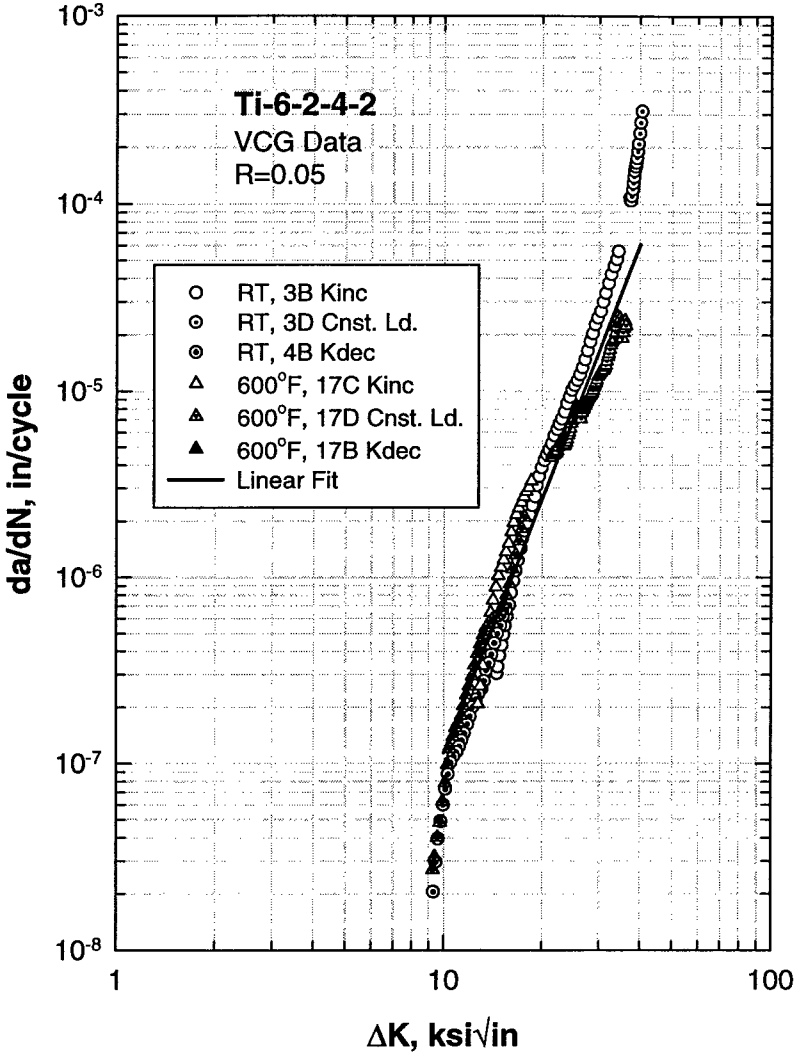


FIGURE I-53. VACUUM FCG DATA AND PARIS REGRESSION FOR Ti-6-2-4-2 AT 75°F AND 600°F, $R = 0$

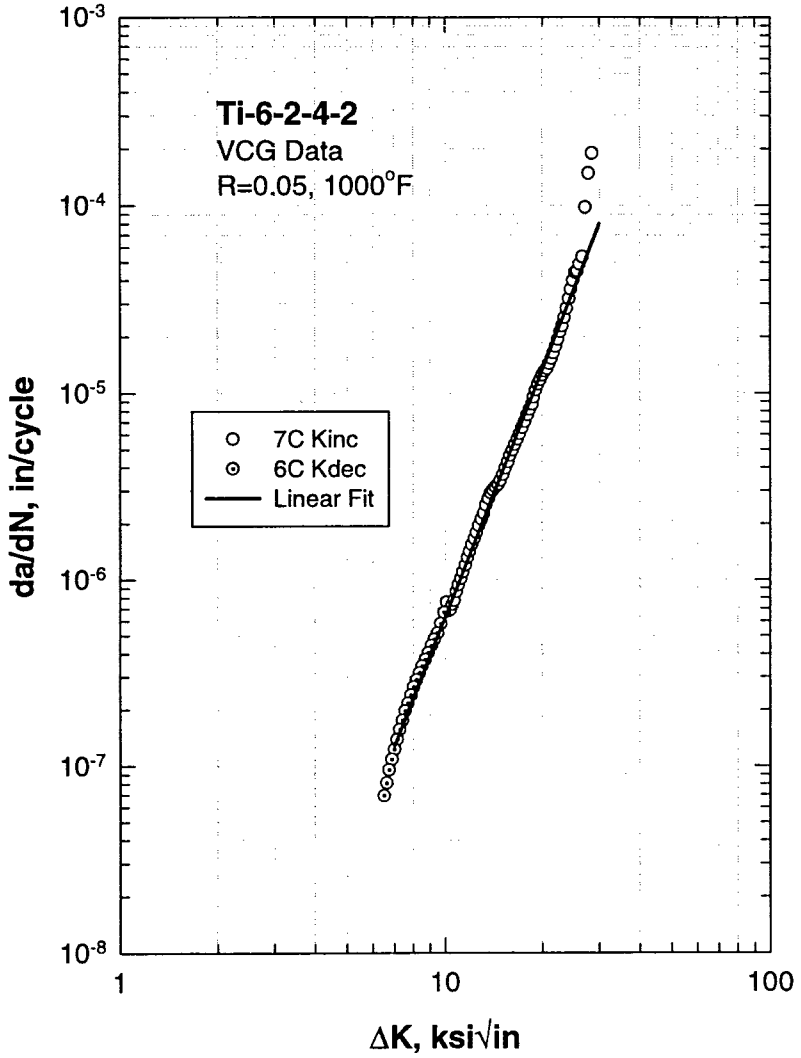


FIGURE I-54. VACUUM FCG DATA AND PARIS REGRESSION FOR Ti-6-2-4-2 AT 1000°F, $R = 0$

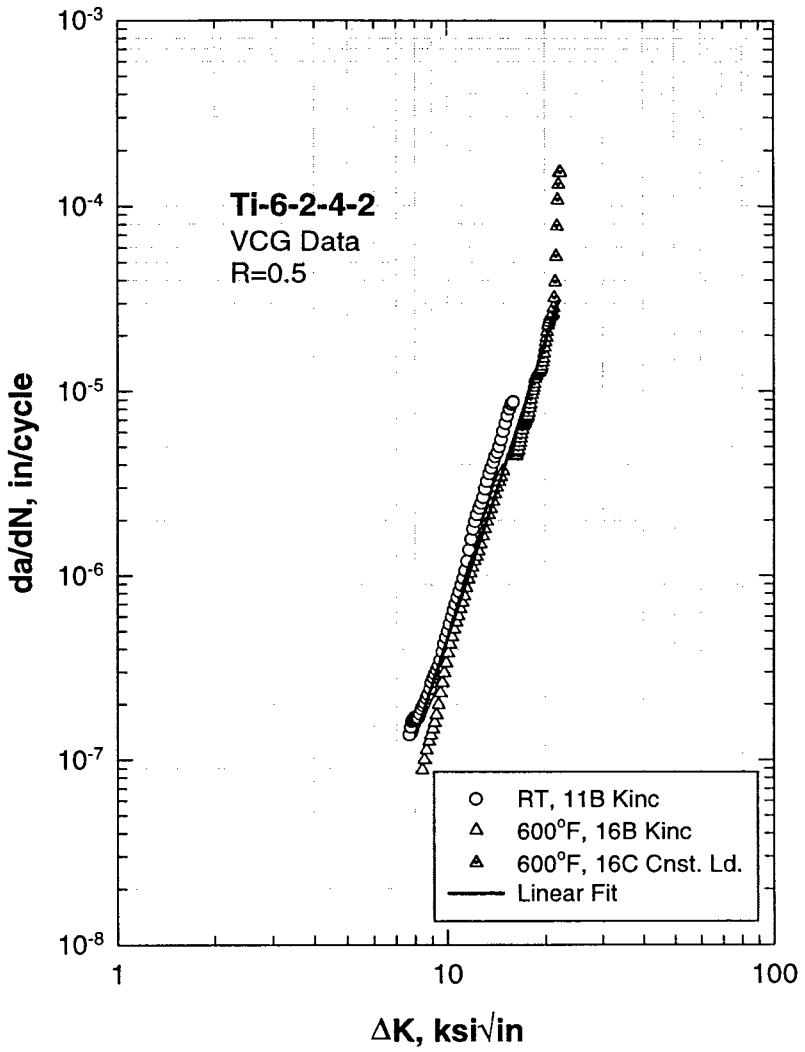


FIGURE I-55. VACUUM FCG DATA AND PARIS REGRESSION FOR Ti-6-2-4-2 AT 75°F AND 600°F, $R = 0.5$

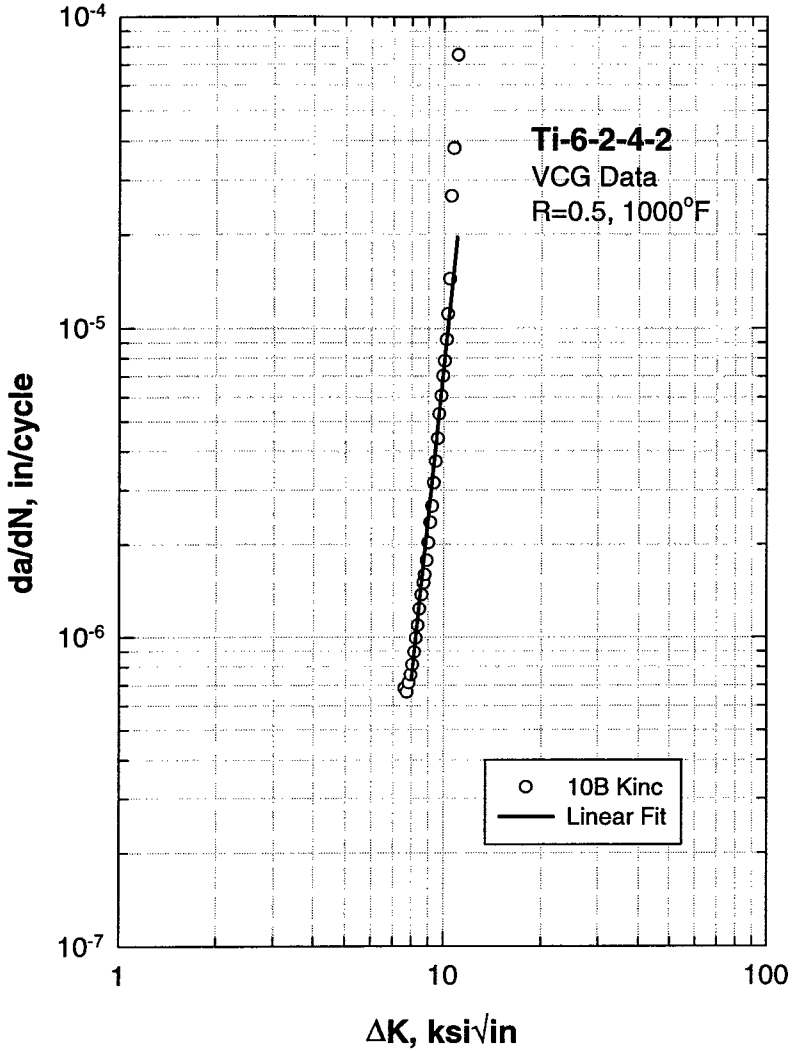


FIGURE I-56. VACUUM FCG DATA AND PARIS REGRESSION FOR Ti-6-2-4-2 AT 1000°F, $R = 0.5$

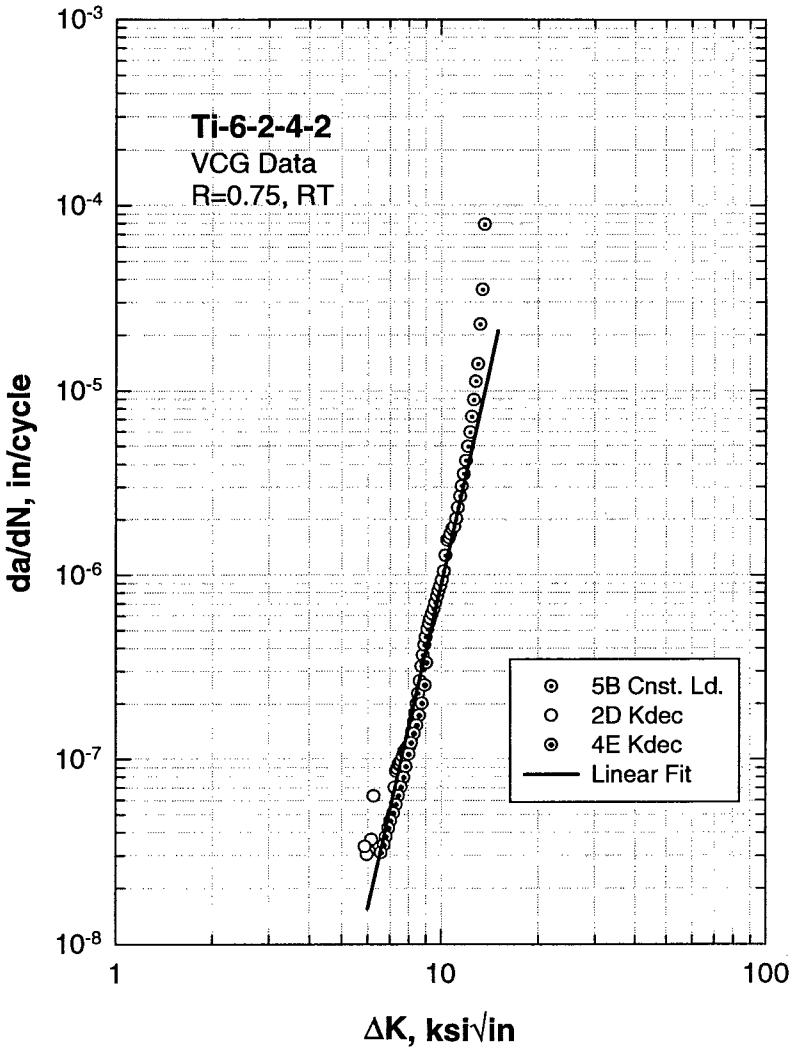


FIGURE I-57. VACUUM FCG DATA AND PARIS REGRESSION FOR Ti-6-2-4-2 AT 75°F, $R = 0.75$

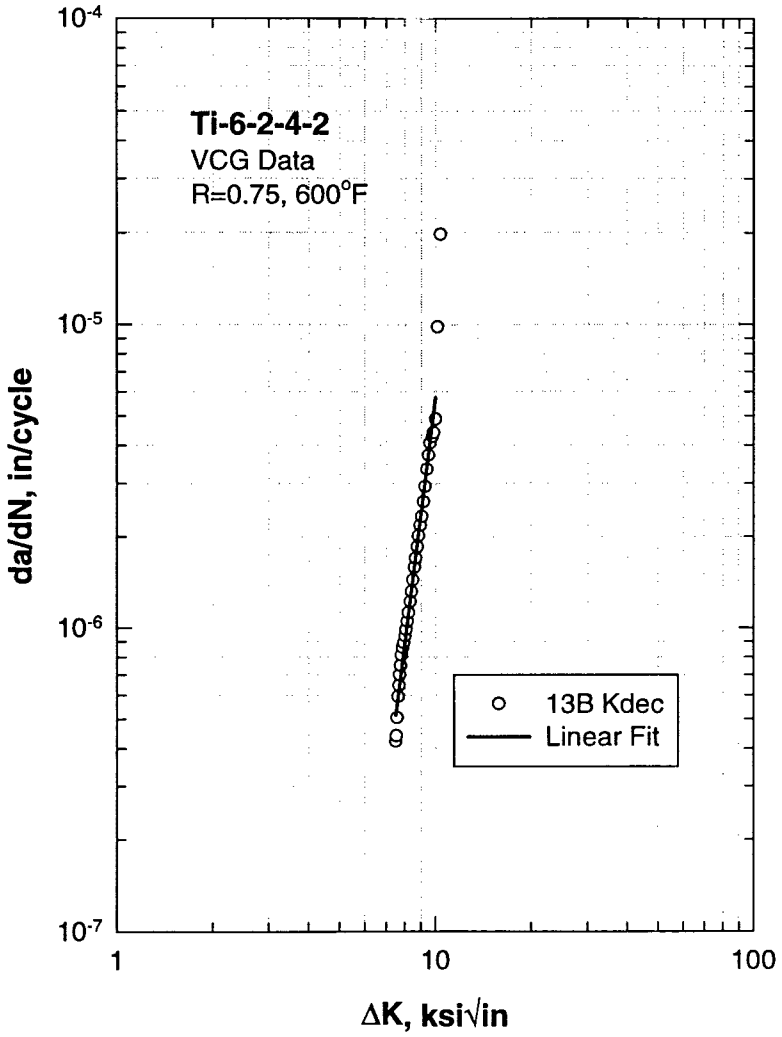


FIGURE I-58. VACUUM FCG DATA AND PARIS REGRESSION FOR Ti-6-2-4-2 AT 600°F, $R = 0.75$

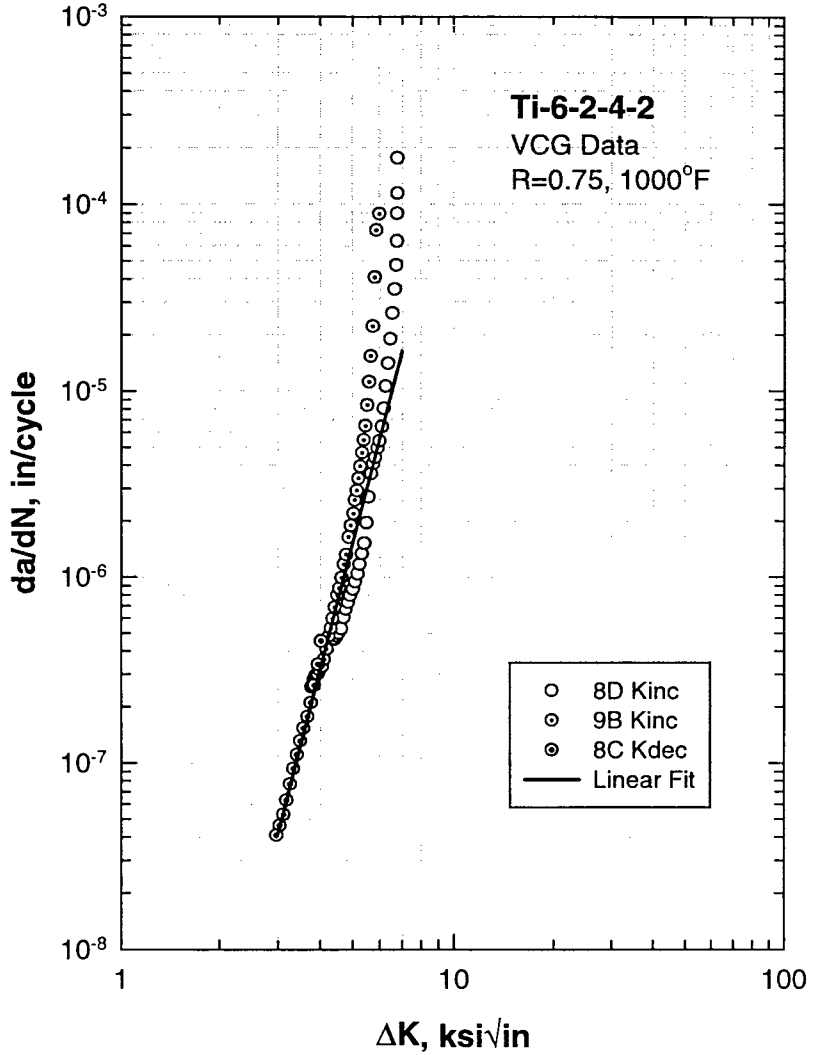


FIGURE I-59. VACUUM FCG DATA AND PARIS REGRESSION FOR Ti-6-2-4-2 AT 1000°F, $R = 0.75$

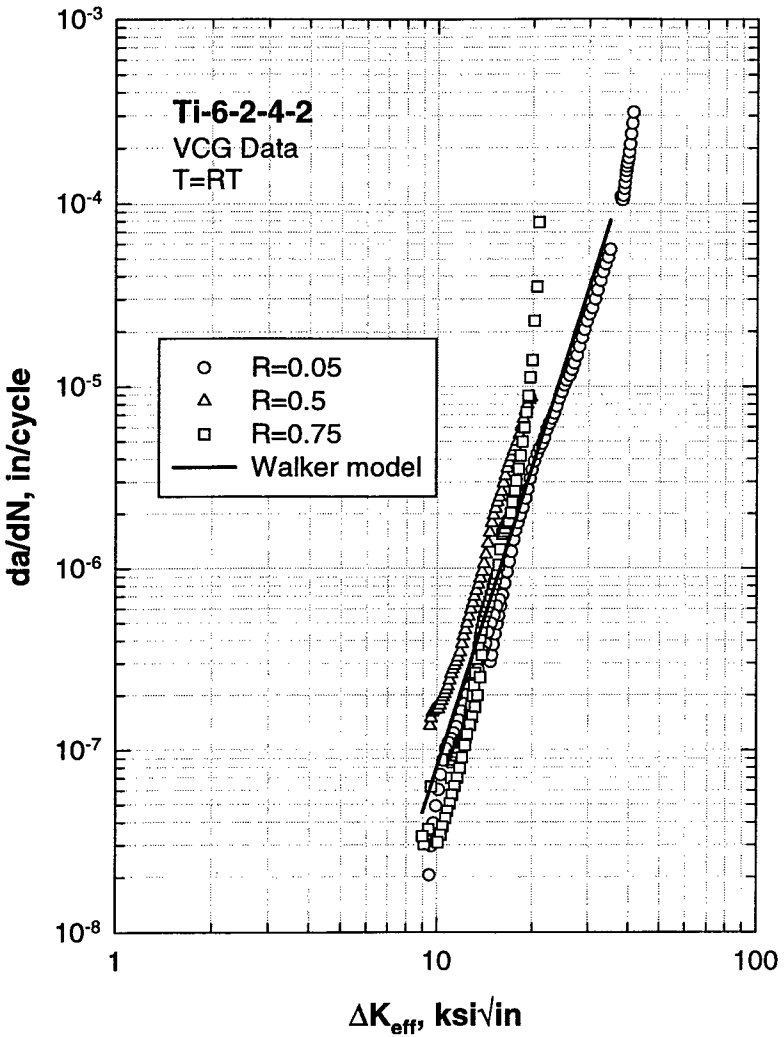


FIGURE I-60. VACUUM FCG DATA AND WALKER MODEL REGRESSION FOR Ti-6-2-4-2 AT 75°F

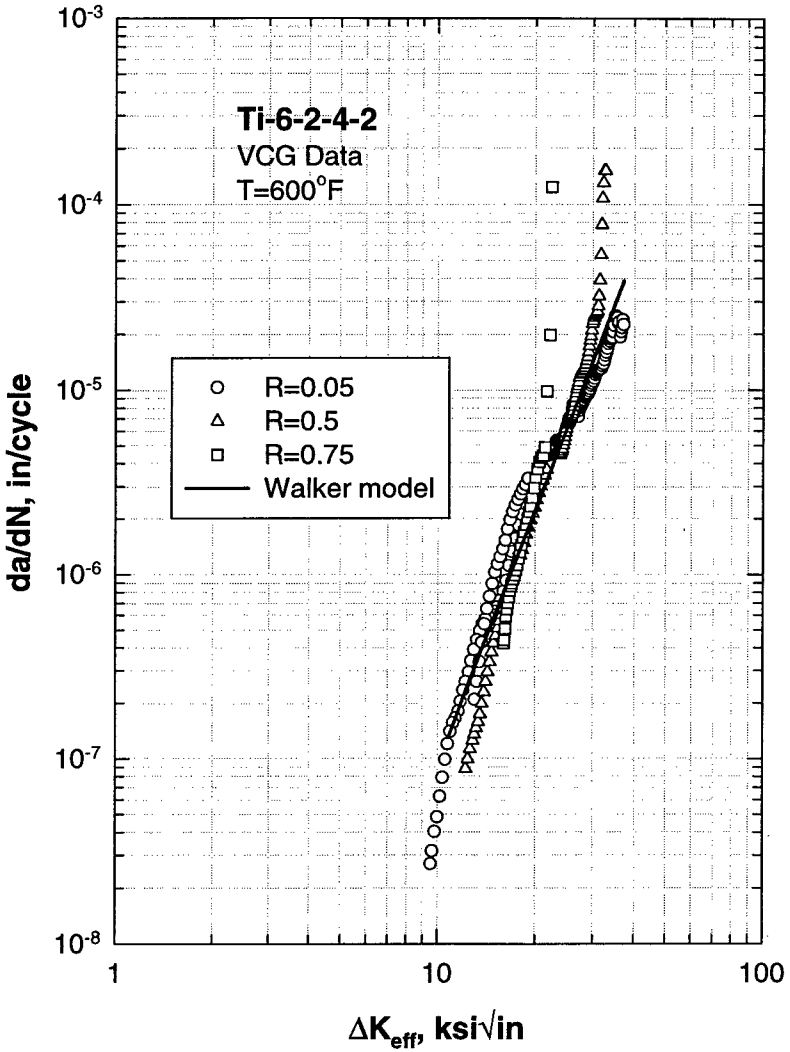


FIGURE I-61. VACUUM FCG DATA AND WALKER MODEL REGRESSION FOR Ti-6-2-4-2 AT 600°F

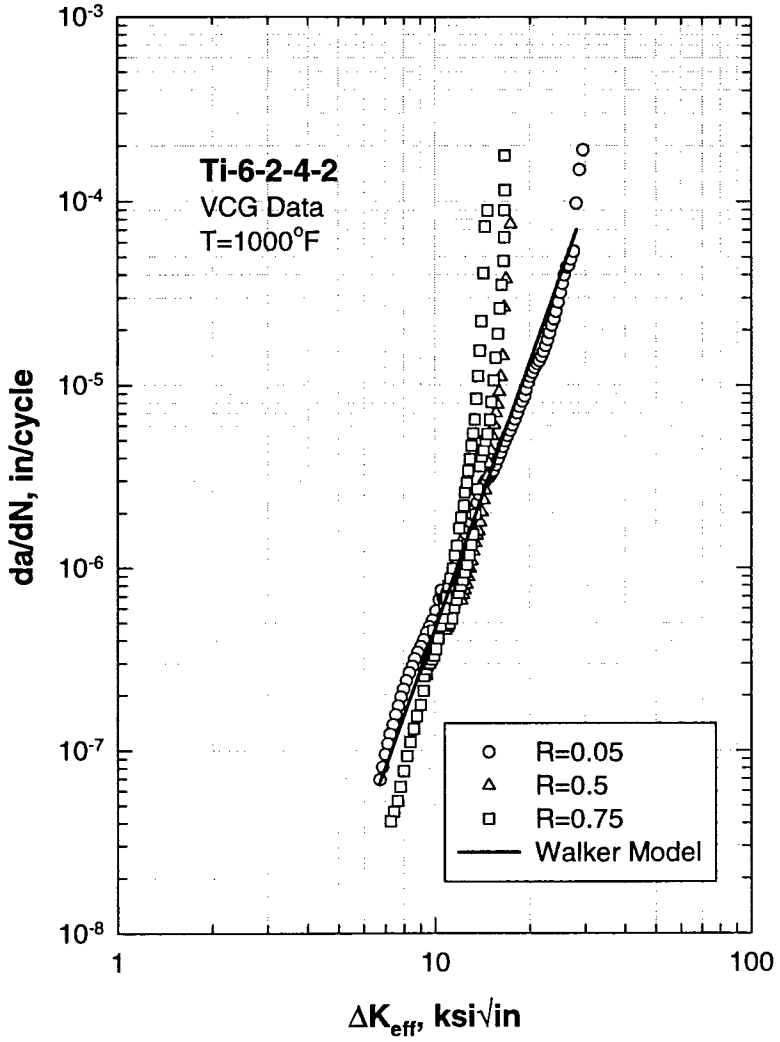


FIGURE I-62. VACUUM FCG DATA AND WALKER MODEL REGRESSION FOR Ti-6-2-4-2 AT 1000°F

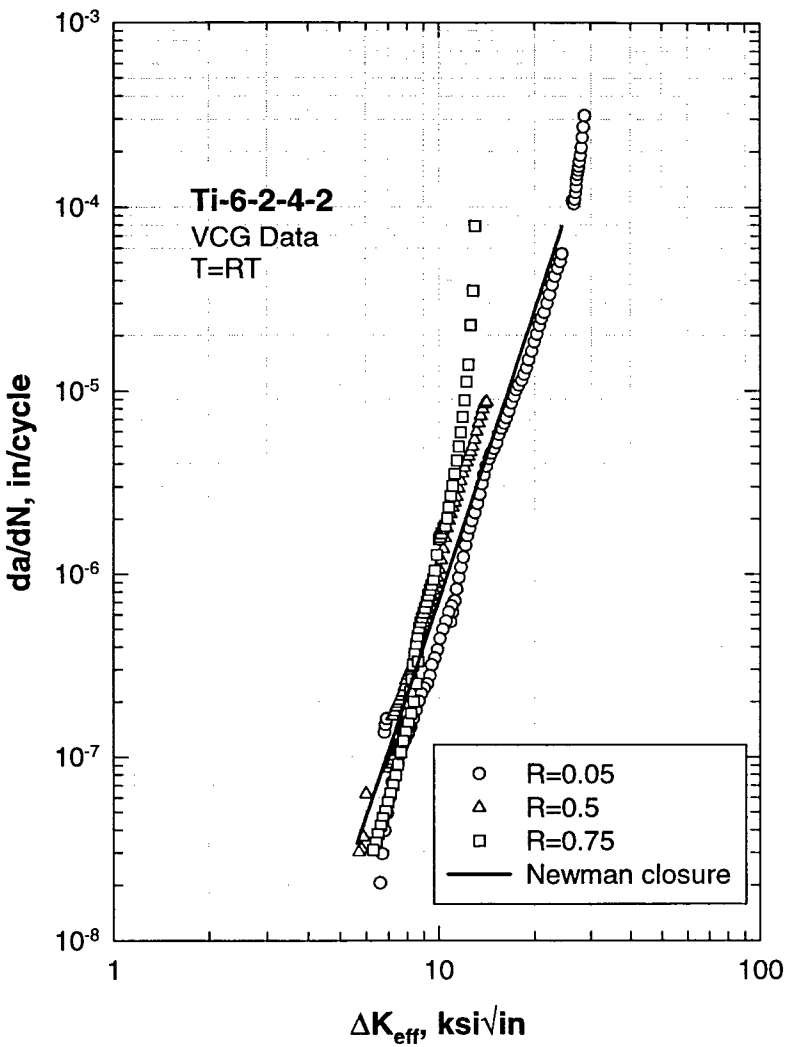


FIGURE I-63. VACUUM FCG DATA AND NEWMAN CLOSURE MODEL REGRESSION FOR Ti-6-2-4-2 AT 75°F

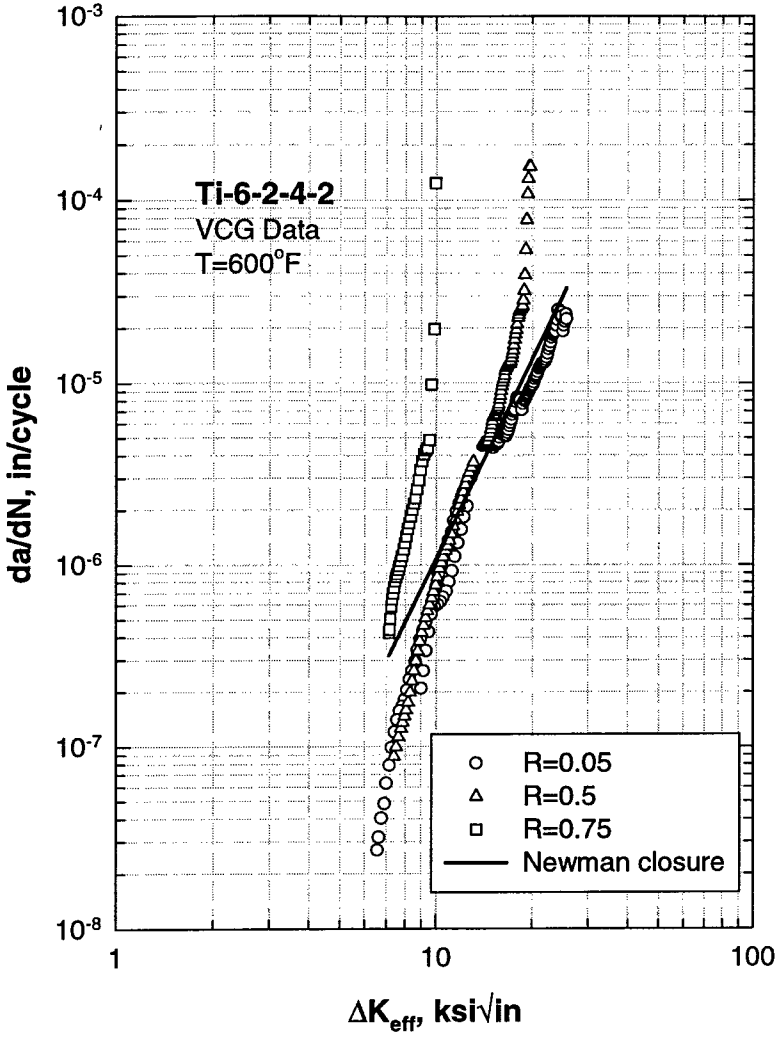


FIGURE I-64. VACUUM FCG DATA AND NEWMAN CLOSURE MODEL REGRESSION FOR Ti-6-2-4-2 AT 600°F

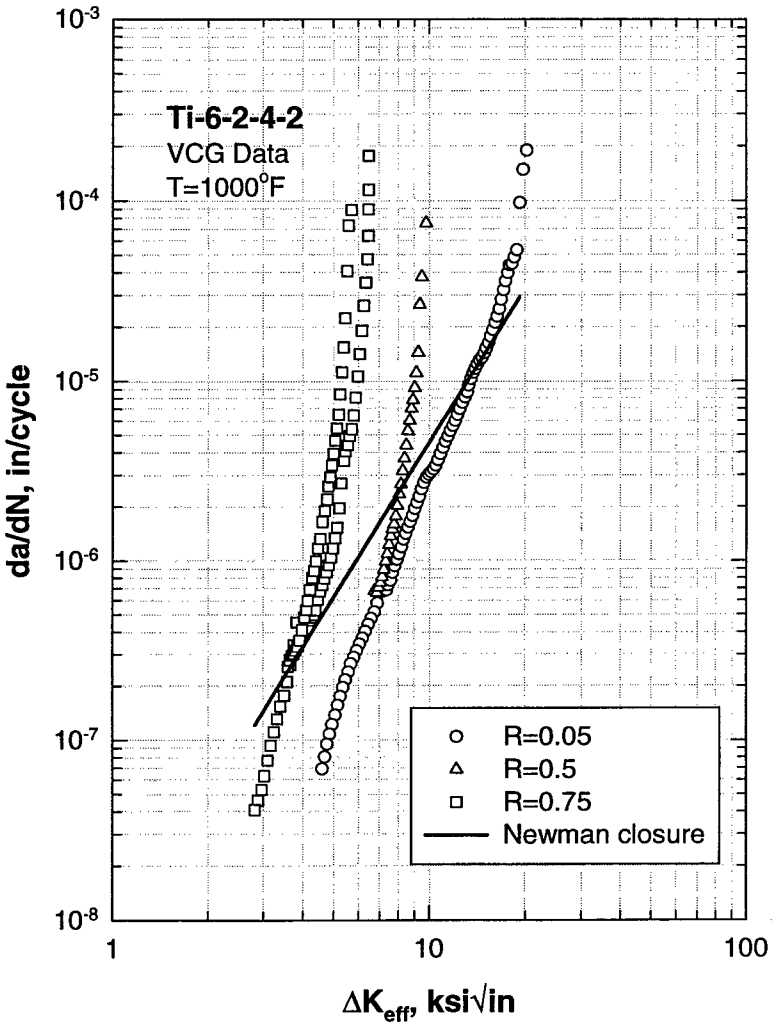


FIGURE I-65. VACUUM FCG DATA AND NEWMAN CLOSURE MODEL REGRESSION FOR Ti-6-2-4-2 AT 1000°F

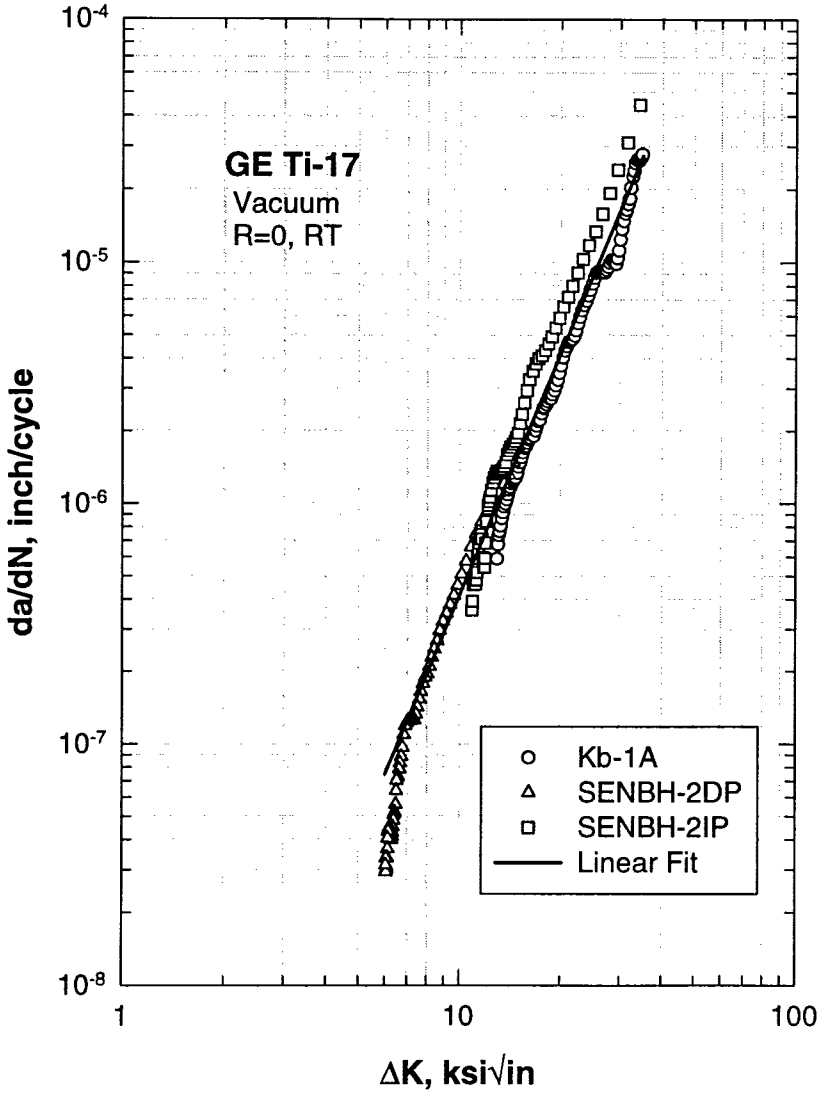


FIGURE I-66. VACUUM FCG DATA AND PARIS REGRESSION FOR Ti-17 AT 75°F, $R = 0$

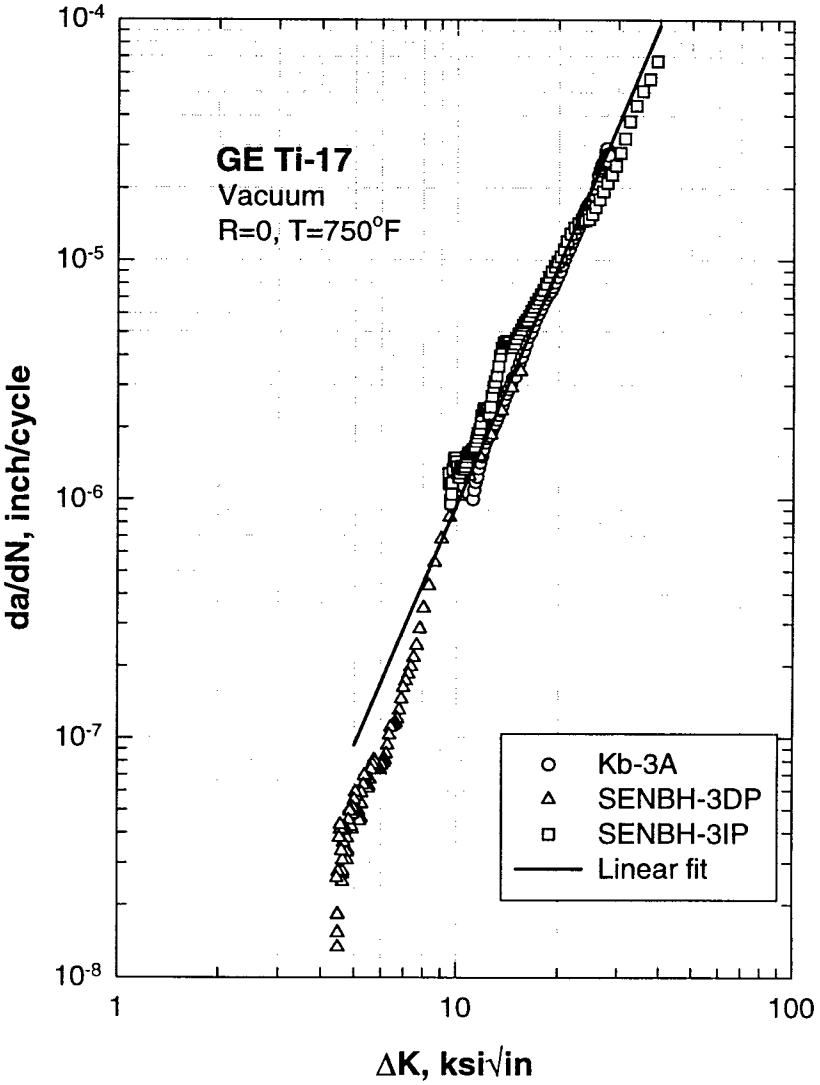


FIGURE I-67. VACUUM FCG DATA AND PARIS REGRESSION FOR Ti-17 AT 750°F, $R = 0$

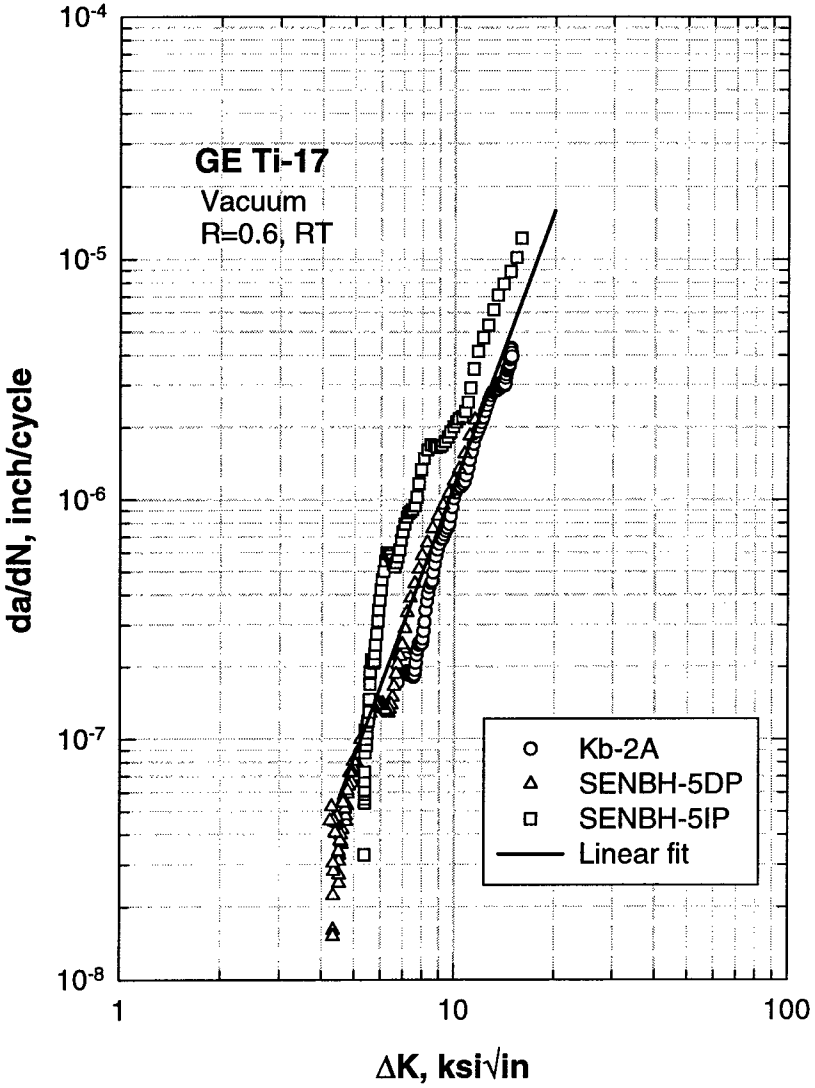


FIGURE I-68. VACUUM FCG AND PARIS REGRESSION FOR Ti-17 AT 75°F, $R = 0.6$

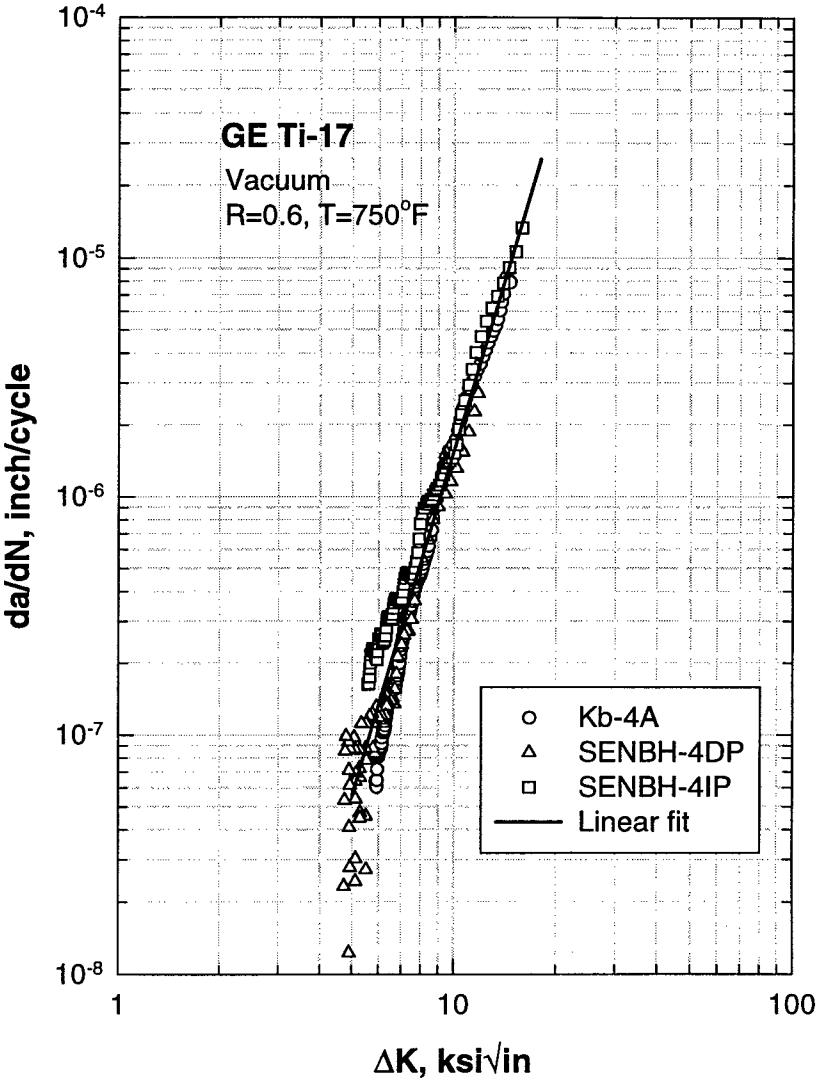


FIGURE I-69. VACUUM FCG DATA AND PARIS REGRESSION FOR Ti-17 AT 750°F, $R = 0.6$

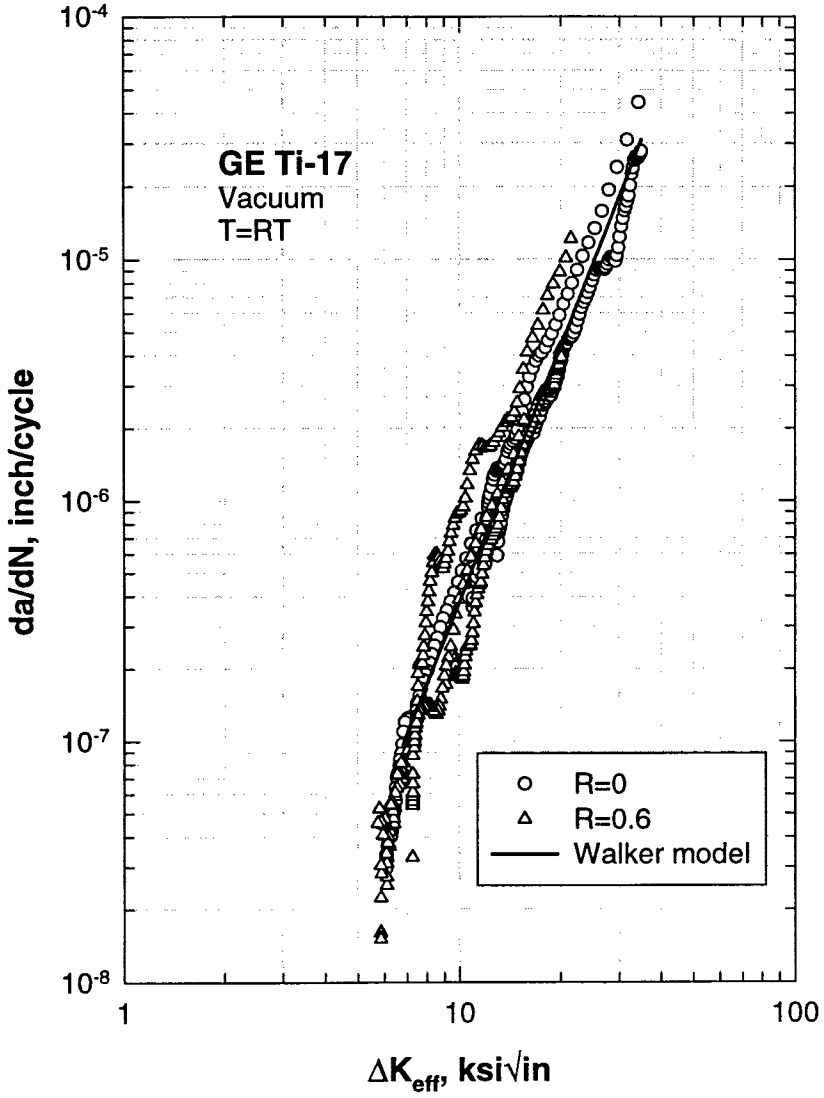


FIGURE I-70. VACUUM FCG DATA AND WALKER MODEL REGRESSION FOR Ti-17 AT 75°F

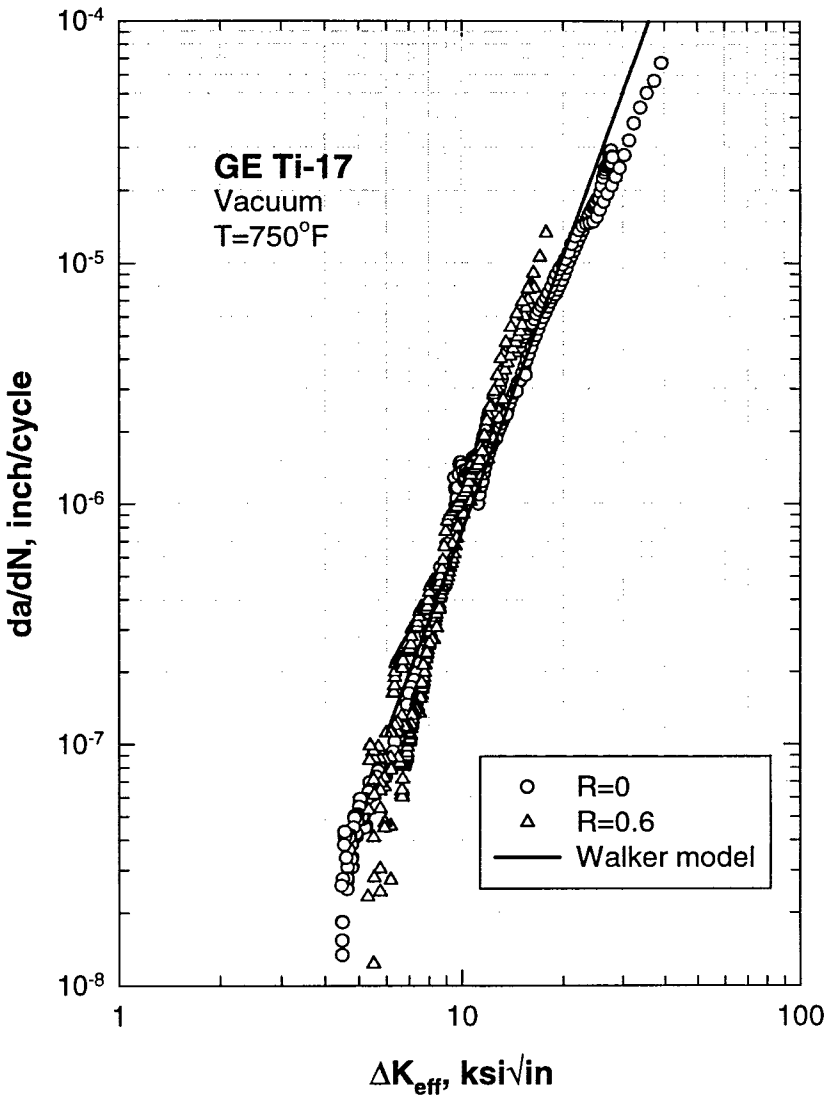


FIGURE I-71. VACUUM FCG DATA AND WALKER MODEL REGRESSION FOR Ti-17 AT 750°F

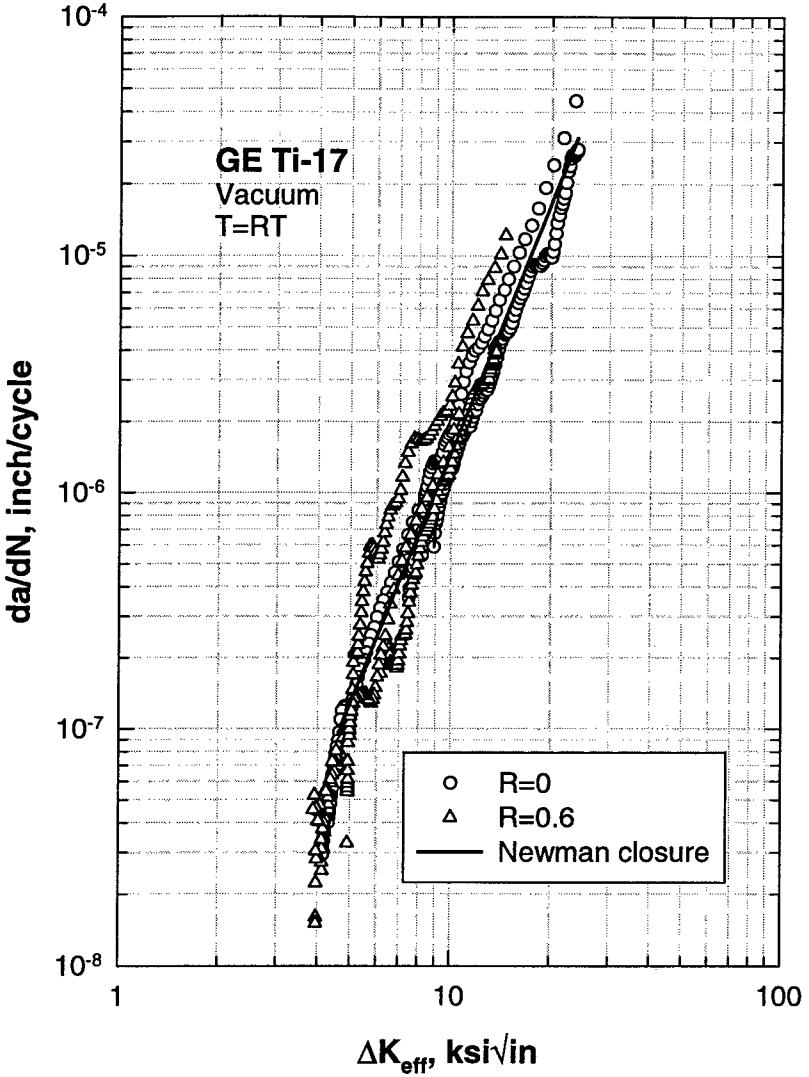


FIGURE I-72. VACUUM FCG DATA AND NEWMAN CLOSURE MODEL REGRESSION FOR Ti-17 AT 75°F

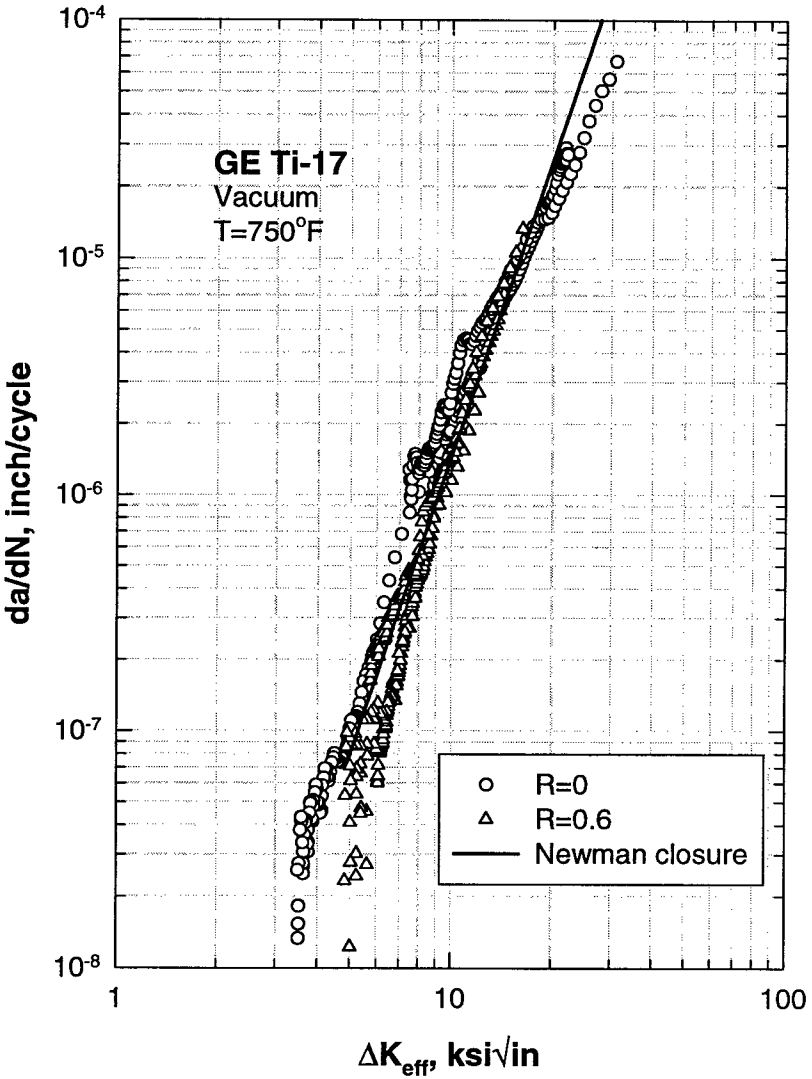


FIGURE I-73. VACUUM FCG DATA AND NEWMAN CLOSURE MODEL REGRESSION FOR Ti-17 AT 750°F

TABLE I-15. CALCULATED REGRESSION CONSTANTS FOR Ti-6-4 VACUUM DATA

Individual Paris Equations			
Temperature (°F)	R	A	n
75	0	2.950E-12	4.860
400	0	8.812E-12	4.329
75	0.5	8.440E-12	5.147
400	0.5	9.276E-12	4.901
75	0.75	1.948E-12	5.812
400	0.75	7.192E-12	5.347
Walker Model			
Temperature (°F)	m	A	n
75	0.759	1.151E-12	5.262
400	0.659	2.587E-12	4.771
Newman Crack Closure Model			
Temperature (°F)	α	A	n
75	2.027	8.093E-12	5.105
400	1.145	9.306E-11	4.122

TABLE I-16. CALCULATED REGRESSION CONSTANTS FOR Ti-6-2-4-2 VACUUM DATA

Individual Paris Equations			
Temperature (°F)	R	A	n
RT/600	0.5	0.3365E-11	4.53
1000	0.5	0.2346E-10	4.421
RT/600	0.5	0.1929E-11	5.363
1000	0.5	0.3269E-15	10.35
RT	0.75	0.1166E-13	7.87
600	0.75	0.2339E-13	8.389
1000	0.75	0.1855E-10	7.037
Walker Model			
Temperature (°F)	m	A	n
RT	0.696	2.44E-13	5.52
600	0.452	2.33E-12	4.597
1000	0.353	6.22E-12	4.868
Newman Crack Closure Model			
Temperature (°F)	α	A	n
RT	1.164	3.68E-12	5.282
600	1.099	2.49E-10	3.635
1000	1.115	6.24E-09	2.858

TABLE I-17. CALCULATED REGRESSION CONSTANTS FOR Ti-17 VACUUM DATA

Individual Paris Equations			
Temperature (°F)	R	A	n
RT	0	1.861E-10	3.347
750	0	4.369E-10	3.329
RT	0.6	1.914E-10	3.78
750	0.6	2.476E-11	4.793
Walker Model			
Temperature (°F)	m	A	n
RT	0.671	1.123E-10	3.529
750	0.873	1.203E-10	3.804
Newman Crack Closure Model			
Temperature (°F)	α	A	n
RT	1.19	4.570E-10	3.506
750	2.952	9.937E-11	4.160

The suitability of the stress-ratio model (Walker and Newman) regressions can be informally assessed by comparing the slopes of the individual Paris regressions for the constituent data with the slopes of each Paris-Walker or Paris-Newman regression. Those slopes should be approximately the same. Furthermore, note that the Walker or Newman regressions implicitly assume that the slopes of the individual data sets at different stress ratios are the same, since all the data are fitted by a single common slope. Therefore, for material-temperature combinations where the Paris slope changes significantly from stress ratio to stress ratio, it may be concluded that neither the simple Walker nor the simple Newman models are entirely appropriate representations of stress ratio effects. These changes in Paris slope (typically, an increase in Paris slope with increasing stress ratio) are often indicative of some change in the FCG mechanism, such as contributions from time-dependent crack growth mechanisms. These mechanism changes are generally not addressed satisfactorily by simple empirical regression models.

By these standards, the stress-ratio model regressions of the Ti-6-4 data were reasonably acceptable, although the Paris slopes did increase slightly with increasing stress ratio. Slopes of both Walker regressions and the 75°F Newman regression reflected the average of the individual regression slopes. The 400°F Newman regression was less satisfactory since the slope was less than any of the individual regression slopes.

The stress-ratio model regressions were more problematic for the Ti-6-2-4-2 data, since the individual Paris slopes increased more dramatically with increasing stress ratio. The Walker regressions were still reasonably useful except at higher ΔK values, where the data spread. The Newman regressions were generally not useful, especially at the two higher temperatures, where the Newman regression slope was substantially lower than any of the individual regression slopes.

The stress-ratio model regressions for Ti-17 were all reasonably successful because the slopes of the individual regressions were all reasonably similar and because data were available at only two stress ratios.

Although the motivations and derivations of the Walker and Newman models are substantially different, the two models give similar results for moderately positive stress ratios, and in fact, it may be shown that the two models are almost mathematically equivalent in this range. The two models differ more substantially, however, at high positive stress ratios and at negative stress ratios. At high stress ratios, the Walker model predicts a large effect of increasing stress ratio (e.g., changing the stress ratio from 0.5 to 0.75), while the Newman model predicts a relatively small effect for the same change from one high stress ratio to another. The Newman model behaves in this manner because it has a physical basis in crack closure behavior, and crack closure is known to change little between different high stress ratios. The Walker model, on the other hand, is a more empirical model effectively driven by K_{max} values. If the changes in FCG rate with stress ratio are due primarily to crack closure behavior, then the Newman model will be a more satisfactory model, and the Walker model may even over estimate stress ratio effects at high R. On the other hand, if the changes in FCG rate with stress ratio are due to other phenomena, such as time-dependent deformation, then the Newman model may be inadequate and the Walker model may be preferable. This appears to be the case for some of the high-temperature titanium data in the present test program. On the other hand, if the superposition of time-dependent deformation and crack growth mechanisms lead to substantial changes in the Paris slope with increasing stress ratio, then both the Walker and Newman models may be inadequate representations of the data. In this case, it may be necessary to employ a tabular approach with stress ratio interpolation or to employ alternative crack growth equations that include implicit or explicit time-dependent terms.

Note that a single Walker exponent does not satisfactorily correlate data at both positive and negative stress ratios (positive and negative minimum stresses). It is customary in some design systems to derive two different Walker exponents, denoted m^+ and m^-, applicable to positive and negative stress ratios respectively. However, since no negative stress ratio testing was conducted in the present test program, values for m^- could not be determined. The values of m presented in the previous tables are, more exactly, values of m^+.

I.5.3.2 Threshold Regressions.

Fatigue crack growth thresholds are an important element of rotor design systems, identifying conditions under which FCG is not expected to occur at significant rates. Reliable experimental characterization of the threshold is therefore an important element of the materials testing required to support these design systems. In fact, as noted earlier, one of the most significant differences between air and vacuum data for titanium alloys is the large difference in threshold values. Vacuum thresholds appear to be substantially higher than air thresholds.

Although it is possible to estimate threshold values approximately from simple inspection of the available FCG data in the near-threshold regime, it is preferable to determine threshold values from a more rigorous analytical process. Such a process is recommended by ASTM E 647,

"Standard Test Method for Measurement of Fatigue Crack Growth Rates," which defines a procedure based on a linear regression of near-threshold crack growth data in which log *da/dN* is the independent variable and log ΔK is the dependent variable.

Since this regression line will, in general, have a finite nonzero slope, some operational definition of the threshold FCG rate must be established as a common point of reference for all regressions. The ASTM test method stipulates a growth rate of 10^{-10} m/cycle $(4(10)^{-9}$ inch/cycle) as the operational definition of threshold. However, with a few exceptions, the available vacuum FCG data generally only extended down to a minimum growth rate between 10^{-7} and 10^{-8} inch/cycle. Furthermore, for the low cycle fatigue (LCF) histories of primary concern to rotor design, FCG rates in the 10^{-9} inch/cycle range are less significant, because the total number of available cycles is relatively small. Therefore, in this analysis, the threshold FCG rate was defined as 10^{-8} inch/cycle. This value still required extrapolation beyond the available data for some vacuum FCG tests, although data sets were generally excluded from consideration if the minimum growth rate was no lower than about 10^{-7} inch/cycle. Data sets were filtered by inspection to include only true near-threshold data in the analysis. No data corresponding to growth rates faster than $2(10)^{-7}$ inch/cycle were ever included in a regression. In general, only *K*-decreasing tests were analyzed to determine threshold values, but constant load Kb bar tests were analyzed in a few cases where *K*-decreasing tests were unavailable or appeared questionable.

Representative threshold regressions are illustrated graphically in figure I-74. The SEN 407-4 data are from a Ti-6-4 *K*-decreasing test at room temperature, $R = 0$, in which available data straddled the 10^{-8} inch/cycle threshold crack growth rate, but with a very shallow slope. The 17B data are from a *K*-decreasing test for Ti-6-2-4-2 at $R = 0.05$, 600°F in which available data had to be extrapolated downward to 10^{-8} inch/cycle.

Note that, in general, the near-threshold regressions for Ti-6-4 exhibited much shallower slopes (as plotted above) than the other two materials. These near-threshold data appeared to be converging more quickly to a true threshold. In contrast, the near-threshold data for Ti-6-2-4-2 usually exhibited larger slopes without a strong sense of imminent convergence to a bounding ΔK_{th} value.

The threshold values resulting from all regressions are summarized in table I-18. It is encouraging to note the remarkably close agreement between values from replicate tests. For example, the two Ti-6-2-4-2 tests at $R = 0.75$, room temperature gave the same threshold value to within 1%. Similar agreement was observed between the two Ti-6-4 tests at $R = 0$, 400°F.

Ti-6-4 threshold values at room temperature vs. 400°F were remarkably similar for both $R = 0.5$ and $R = 0.75$, which made the substantial temperature difference at $R = 0$ somewhat puzzling. Another slightly puzzling result is that *K*-decreasing SENBH tests for Ti-6-4 at $R = 0.75$ (not analyzed here, but shown previously in figures I-47 and I-48) gave apparent threshold values much higher than the constant load Kb bar tests shown in the same figures. The threshold values shown in table I-18 were conservatively based on the Kb tests only for these conditions.

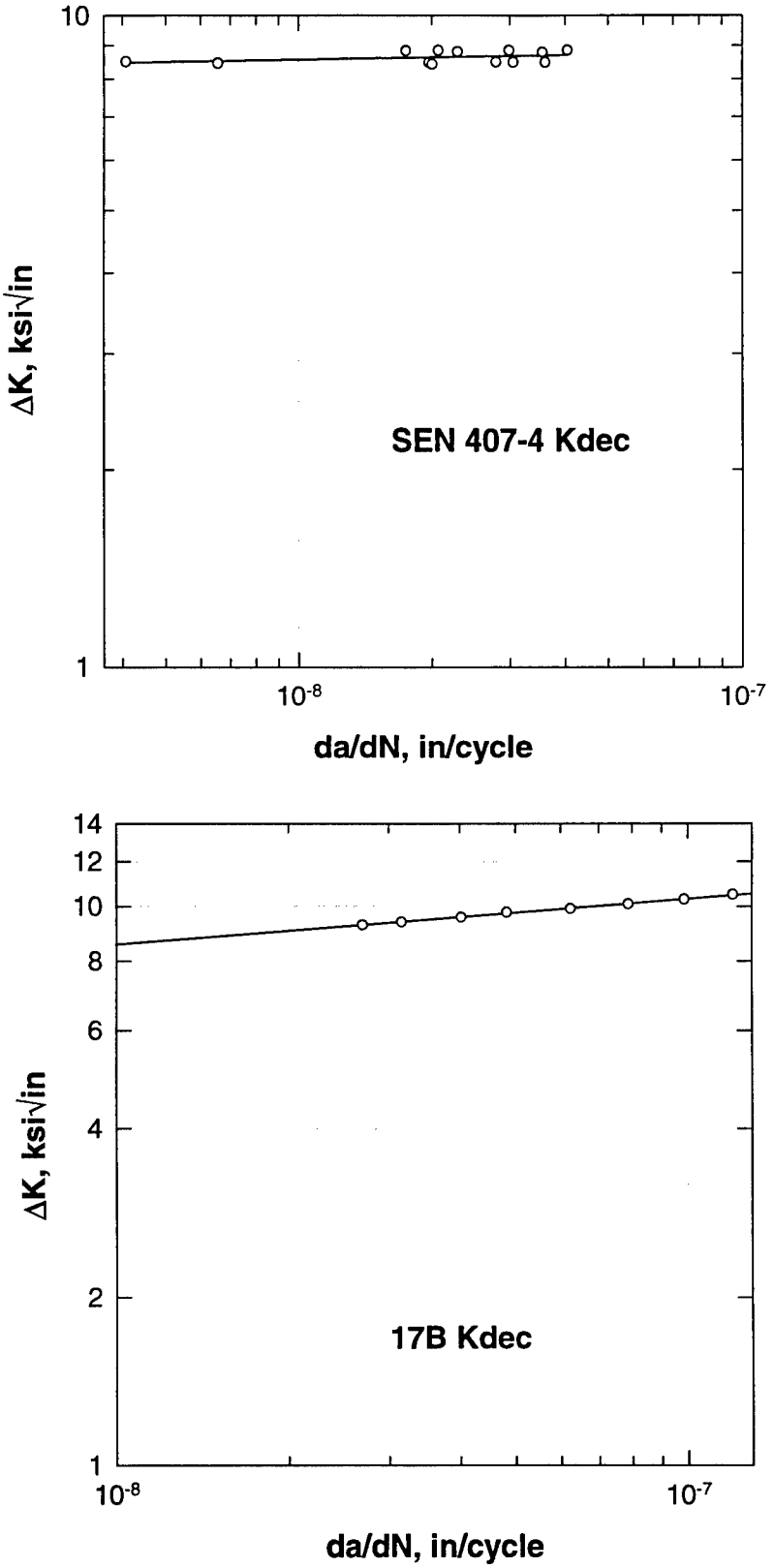


FIGURE I-74. REPRESENTATIVE EXAMPLES OF THRESHOLD REGRESSIONS

TABLE I-18. SUMMARY OF THRESHOLD VALUES OBTAINED FROM REGRESSIONS

GE Ti-6-4 Vacuum Data			
Specimen No.	R	T (°F)	ΔK_{th} (ksi$\sqrt{in.}$)
SEN 407-4 Kdec	0	RT	8.553
SEN 407-5 Kdec	0	400	11.216
SEN 407-8 Kdec	0	400	11.310
Kb 401-6	0.5	RT	7.185
Kb 401-7	0.5	400	7.326
Kb 401-1	0.75	RT	4.798
Kb 401-5	0.75	400	4.814
AlliedSignal Ti-6-2-4-2 VCG Data			
4B Kdec	0.05	RT	8.725
17B Kdec	0.05	600	8.558
6C Kdec	0.05	1000	4.933
2D Kdec	0.75	RT	5.575
4E Kdec	0.75	RT	5.528
13B Kdec	0.75	600	6.045
8C Kdec	0.75	1000	2.458
GE Ti-17 VCG Data			
SENBH-2DP	0	RT	5.425
SENBH-3DP	0	750	4.370
SENBH-5DP	0.6	RT	4.285
SENBH-4DP	0.6	750	4.892

I.6 SUMMARY AND CONCLUSIONS.

Fatigue crack growth design data were generated under high-vacuum conditions for three different titanium rotor alloys, Ti-6-4, Ti-6-2-4-2, and Ti-17. Thermal/forging histories, tensile properties, and microstructures of each material were documented. Data were generated for each material at room temperature and one or two elevated temperatures appropriate to each material, at stress ratios ranging from $R = 0$ to 0.75, in both the near-threshold and Paris regimes. Tests were conducted by engine company laboratories using specimens and test procedures typical of standard industry practice.

A brief vacuum level effects study conducted at NASA-Langley Research Center indicated, consistent with the limited available literature, that vacuum levels better than 10^{-6} Torr should be adequate to capture full vacuum effects for engineering purposes at crack growth rates greater than about 5×10^{-8} inch/cycle.

Comparisons of the resulting vacuum fatigue crack growth data with available air data for Ti-6-4 and Ti-6-2-4-2 indicate that growth rates under vacuum conditions are considerably slower than growth rates under air conditions at the same ΔK values in the lower Paris and near-threshold regimes. Apparent threshold values (ΔK_{th}) at growth rates on the order of 10^{-8} inch/cycle are considerably higher in vacuum than in air. At faster growth rates, in the upper Paris regime, vacuum growth rates increase to merge with air data.

Regressions were performed to obtain appropriate constants for single linear Paris equations, two different mean stress equations (Walker and Newman crack closure models), and to determine ΔK_{th} values.

All vacuum FCG data generated and all regressions were thoroughly documented in both graphical and tabular forms.

I.8 REFERENCES.

I-1. D. A. Meyn, "An Analysis of Frequency and Amplitude Effects on Corrosion Fatigue Crack Propagation in Ti-8Al-1Mo-1V," *Metallurgical Transactions*, Vol. 2, pp. 853-865, 1971.

I-2. P. E. Irving and C. J. Beevers, "The Effect of Air and Vacuum Environments on Fatigue Crack Growth Rates in Ti-6Al-4V," *Metallurgical Transactions*, Vol. 5, pp. 391-398, 1974.

I-3. H. Doker and D. Munz, "Influence of Environment on the Fatigue Crack Propagation of Two Titanium Alloys," *The Influence of Environment on Fatigue*, London: MEP Ltd, pp. 123-130, 1977.

I-4. J. A. Ruppen and A. J. McEvily, "Influence of Microstructure and Environment on the Fatigue Crack Growth Fracture Topography of Ti-6Al-2Sn-4Zr-2Mo-0.1Si," *Fractography and Materials Science, ASTM STP 733*, American Society for Testing and Materials, pp. 32-50, 1981.

I-5. M. Peters, A. Gysler, and G. Lutjering, "Influence of Texture on Fatigue Properties of Ti-6Al-4V," *Metallurgical Transactions*, Vol. 15A, pp. 1597-1605, 1984.

I-6. S. J. Gao, G. W. Simmons, and R. P. Wei, "Fatigue Crack Growth and Surface Reactions for Titanium Alloys Exposed to Water Vapor," *Materials Science and Engineering*, Vol. 62, pp. 65-78, 1984.

I-7. L. S. Vesier and S. D. Antolovich, "Fatigue Crack Propagation in Ti-6242 as a Function of Temperature and Waveform," *Engineering Fracture Mechanics*, Vol. 37, pp. 753-775, 1990.

I-8. Ghonem and R. Foerch, "Frequency Effects on Fatigue Crack Growth Behavior in a Near-α Titanium Alloy," *Materials Science and Engineering*, Vol. A138, pp. 69-81, 1991.

I-9 R. Foerch, A. Madsen, and H. Ghonem, "Environmental Interactions in High-Temperature Fatigue Crack Growth of Ti-1100," *Metallurgical Transactions*, Vol. 24A, pp. 1321-1332, 1993.

I-10. J. Petit, W. Berata, and B. Bouchet, "Fatigue Crack Growth Behavior of Ti-6Al-4V at Elevated Temperature," *Titanium '92 Science and Technology*, Warrendale, PA, TMS, pp. 1819-1826, 1993.

I-11. M. R. Bache, W. J. Evans, and M. McElhone, "The Effects of Environment and Internal Oxygen on Fatigue Crack Propagation in Ti-6Al-4V," *Materials Science and Engineering*, Vol. A234-236, pp. 918-922, 1997.

I-12. T. K. Redden, "Processing and Properties of the Ti-17 Alloy for Aircraft Gas Turbine Applications," *Beta Titanium Alloys in the 80's*, TMS-AIME, pp. 239-254, 1984.

I-13. H. W. Rosenberg, "Ti-17 Properties," *Beta Titanium Alloys in the 80's*, TMS-AIME, pp. 433-439, 1984.

I-14. D. L. Davidson and J. Lankford, "Fatigue Crack Growth Mechanics for Ti-6Al-4V (RA) in Vacuum and Humid Air," *Metallurgical Transactions A*, Vol. 15A, pp. 1931-1940, 1984.

I-15. D. M. James, RAE Technical Memorandum CPM 66, October 1966.

I-16. M. Sugano, S. Kanno, and T. Satake, "Fatigue Behavior of Titanium in Vacuum," *Acta Metallurgica*, Vol. 37, pp. 1811-1820, 1989.

I-17. R. S. Piascik, J. C. Newman, Jr., and J. H. Underwood, "The Extended Compact Tension Specimen," *Fatigue and Fracture of Engineering Materials and Structures*, Vol. 20, pp. 559-563, 1997.

I-18. M. Gorelik, T. Gill, and C. Date, "Vacuum Fatigue Crack Growth Rate Testing of Ti-6-2-4-2 Alloy: Test Report," AlliedSignal Engines & Systems Report 11-0197A, August 1999.

I-19. R. P. Gangloff, D. C. Slavik, R. S. Piascik, and R. H. Van Stone, "Direct Current Electric Potential Measurement of the Growth of Small Cracks," *Small-Crack Test Methods, ASTM STP 1149*, American Society for Testing and Materials, pp. 116-168, 1992.

I-20. R. H. Van Stone and T. L. Richardson, "Potential-Drop Monitoring of Cracks in Surface-Flawed Specimens," *Automated Test Methods for Fracture and Fatigue Crack Growth, ASTM STP 877*, pp. 148-166, 1983.

I-21. J. C. Newman, Jr. and I. S. Raju, "Stress Intensity Factor Equations for Cracks in Three-Dimensional Finite Bodies," *Fracture Mechanics: Fourteenth Symposium—Volume 1, ASTM STP 791*, pp. I-238-I-265, 1983.

I-22. H. H. Johnson, "Calibrating the Electric Potential Method for Studying Slow Growth," *Materials Research and Standards*, Vol. 5, pp. 442-445, 1965.

I-23. D. O. Harris, "Stress Intensity Factors for Hollow Circumferentially Notched Round Bars," *Journal of Basic Engineering*, Vol. 89, pp. 49-54, 1967.

I-24. J. W. Sheldon, K. R. Bain, and J. K. Donald, "Investigation of the Effects of Shed-Rate, Initial K_{max}, and Geometric Constraint on ΔK_{th} in Ti-6Al-4V at Room Temperature," *International Journal of Fatigue*, in press, 1999.

I-25. R. C. McClung, "Analysis of Fatigue Crack Closure During Simulated Threshold Testing," *Fatigue Crack Growth Thresholds, Endurance Limits, and Design, ASTM STP 1372*, American Society for Testing and Materials, in press, 1999.

I-26. Damage Tolerant Design Handbook, Vol. 2, WL-TR-94-4053, CINDAS/USAF, 1994.

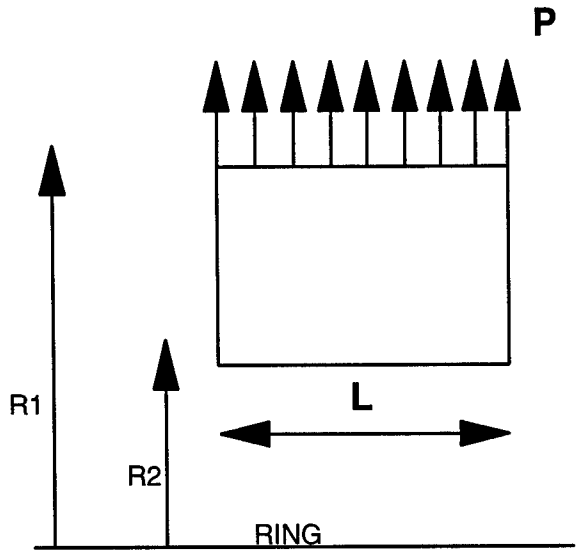
I-27. J. R. Beyer, D. L. Sims, and R. M. Wallace, "Titanium Damage Tolerant Design Data for Propulsion Systems," United Technologies Corp., Pratt and Whitney Aircraft Group, West Palm Beach, FL, Report AFML-TR-77-101, Contract No. F33615-75-C-5130, June 1977.

I-28. J. C. Newman, Jr., "A Crack Opening Stress Equation for Fatigue Crack Growth," *International Journal of Fracture*, Vol. 24, pp. R131-R135, 1984.

APPENDIX J—DARWIN ANALYSIS OF ADVISORY CIRCULAR (AC) TEST CASE

J.1 DESCRIPTION OF ADVISORY CIRCULAR (AC) TEST CASE.

The AC Test Case consists of a titanium ring disk as shown in figure J-1. The design life of the disk is 20,000 flight cycles, and the maximum disk speed during each flight cycle is 6,000 RPM. A 50 MPa external pressure load is applied to the outer surface of the disk to simulate blade loading.



R1 = 0.425 m (16.73 in.) L = 0.1 m (3.94 in.)
R2 = 0.3 m (11.81 in.) P = 50 MPa (7.25 ksi)

FIGURE J-1. ADVISORY CIRCULAR TEST CASE GEOMETRY

Design of Reliability With INspection (DARWIN) uses a zone based risk computation procedure, in which a component is partitioned into zones of approximately equal risk. The material properties, stresses, and temperatures within each zone must be approximately constant. It is assumed that the probability of occurrence of a single hard alpha defect in each zone is relatively low, and the probability of occurrence of two defects within the same zone is negligible. It is assumed that embedded cracks propagate from defects in interior zones, and surface cracks propagate from defects in exterior zones.

The AC Test Case disk is divided into 21 zones as indicated in figure J-2. Defects are located in the geometric center of the interior zones. Surface defects are located on the exterior surfaces of the exterior zones. Exterior zones are assumed to have a thickness of 0.5 mm (0.020 in) to simulate the approximate depth limit of surface defects.

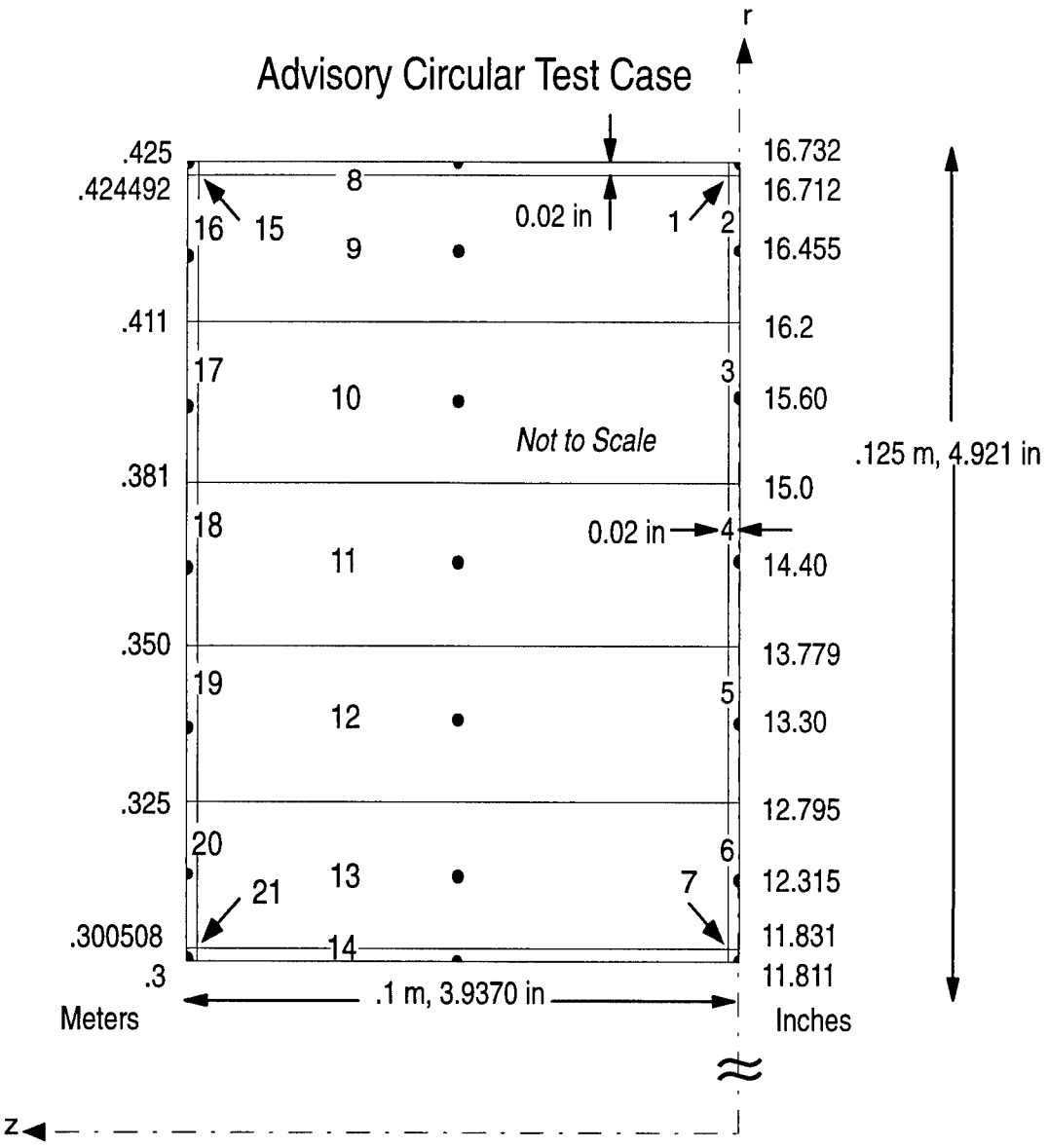


FIGURE J-2. ZONE DEFINITION AND INITIAL DEFECT LOCATIONS

Values for the input variables for the AC Test Case are indicated in table J-1. The defect distribution and probability of detection (PoD) curve are defined in the No. 3 flat bottom hole (FBH) and are shown in figures J-3 and J-4, respectively. All other random variables (e.g., stress multiplying factor, life scatter factor, inspection time) are modeled as deterministic quantities. A single inspection is performed at 10,000 cycles, and all detected defects are removed at the time of inspection.

The probability of fracture versus cycles for the AC Test Case is shown in figure J-5. At 20,000 cycles, the probability of fracture without inspection is 2.37E-5, which corresponds to probability of fracture of 1.18E-9 per flight cycle. If the disk is inspected at 10,000 cycles and all detected defects are removed, the probability of fracture (with inspection) at 20,000 cycles is 1.46E-5, which corresponds to probability of fracture of 7.31E-10 per flight cycle.

TABLE J-1. INPUT VALUES FOR AC TEST CASE VARIABLES

Variable	Input Value
Fracture Mechanics Method	Flight_Life – Paris Crack Growth – No Mean Stress
Fatigue Crack Growth Constant (C)	5.248E-11
Fatigue Crack Growth Exponent (n)	3.87
Risk Computation Method	Monte Carlo Simulation @10,000 samples
Failure Toughness Factor	1.0
Stress Multiplying Factor Median	1.0
Stress Multiplying Factor COV	0.0
Defect Distribution	Post 1995 #3/#3 FBH Defect Dist
PoD Curve	1-1 #3 FBH PoD Curve
Life Scatter Factor Median	1.0
Life Scatter Factor COV	0.0
Inspection Time Mean	10,000 cycles
Inspection Time COV	0.0
Percentage of Samples Not Inspected	0%

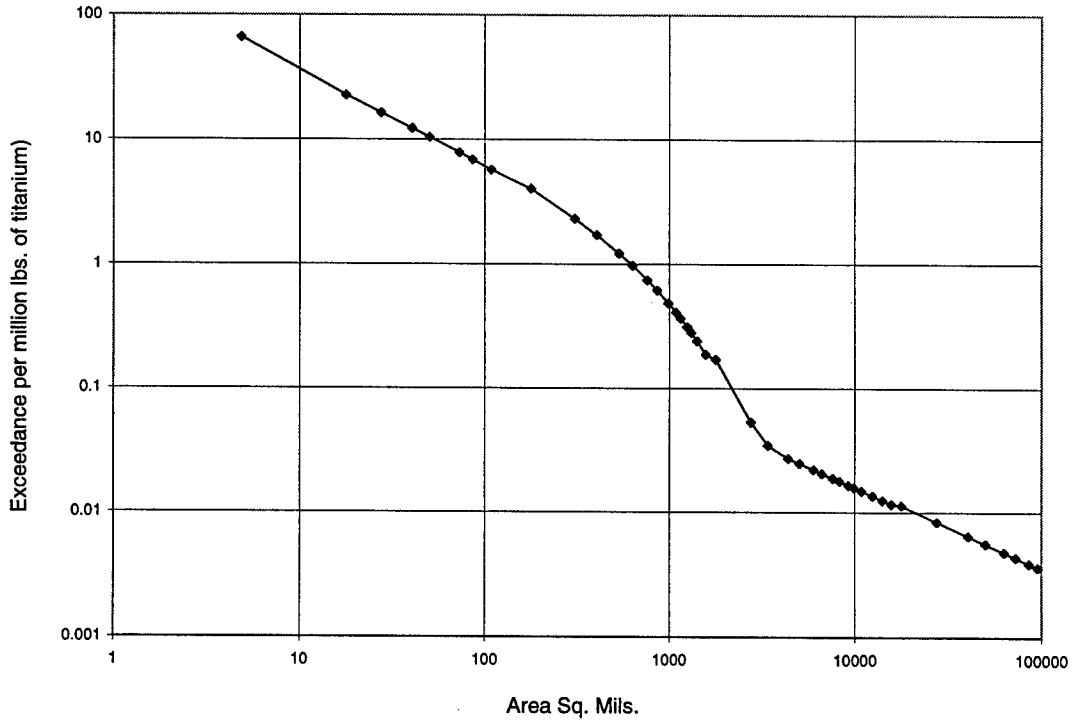


FIGURE J-3. INITIAL DEFECT DISTRIBUTION

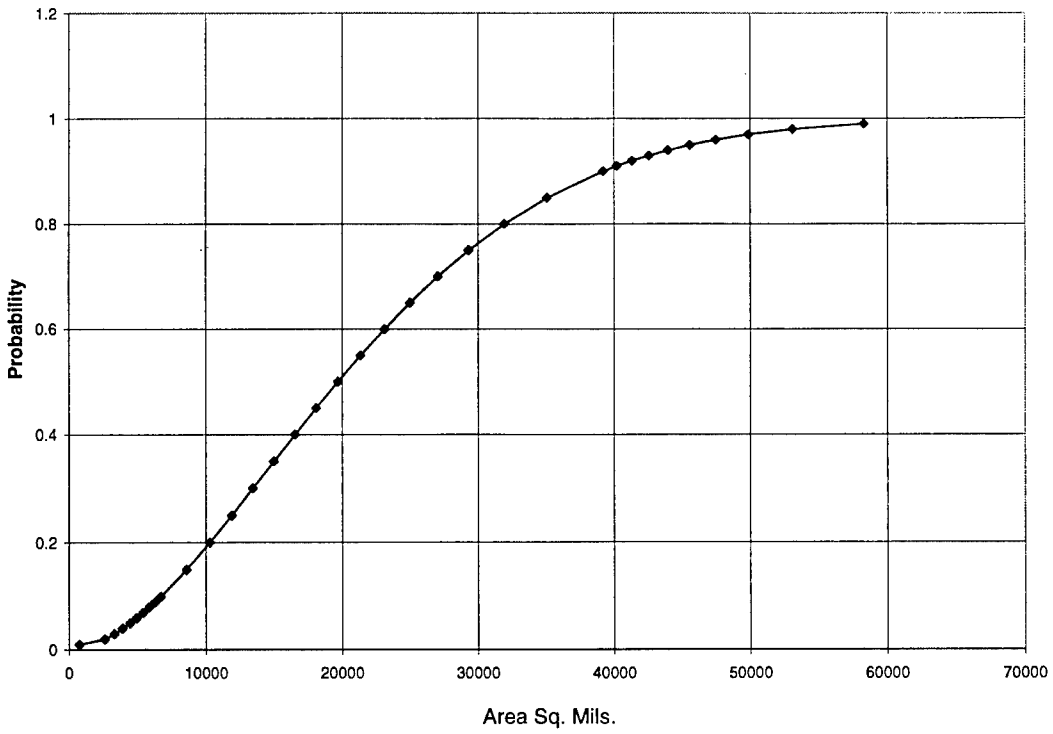


FIGURE J-4. PROBABILITY OF DETECTION (PoD) CURVE

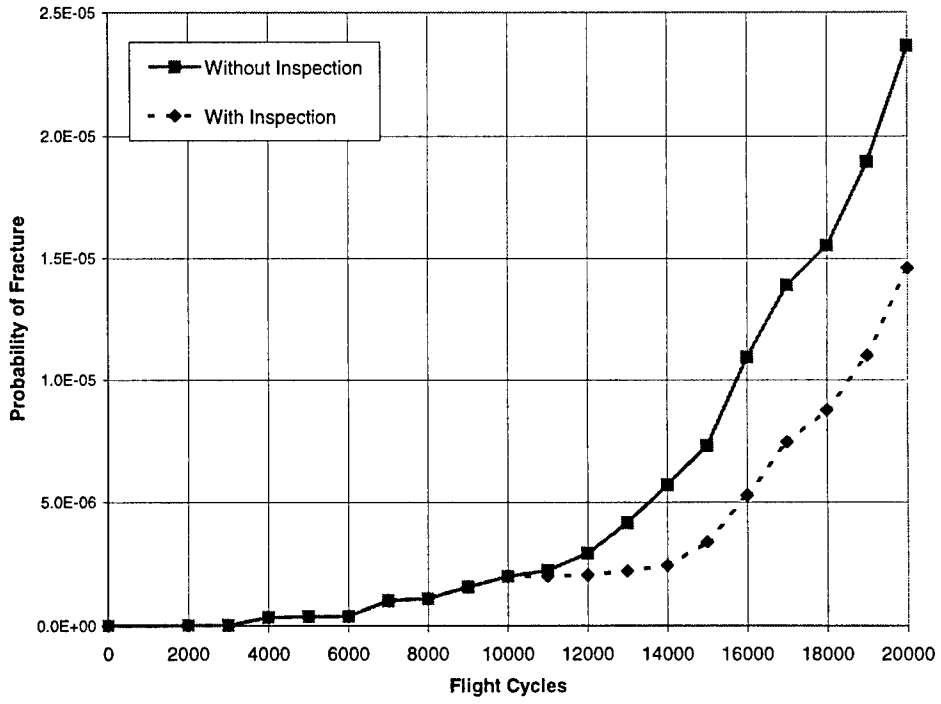


FIGURE J-5. PROBABILITY OF FRACTURE VS FLIGHT CYCLES FOR AC TEST CASE